$BiVO_4$-based Photoanodes for Photoelectrochemical Water Splitting

Towards strategies to overcome major drawbacks of the most promising photoanode material

vorgelegt von
Diplom-Chemiker
Martin Rohloff
geb. in Neubrandenburg

von der Fakultät II - Mathematik und Naturwissenschaften
der Technischen Universität Berlin
zur Erlangung des akademischen Grades

Doktor der Naturwissenschaften
- Dr. rer. nat. -

genehmigte Dissertation

Promotionsausschuss:

Vorsitzender: Prof. Dr. Martin Kaupp
Gutachter: Prof. Dr. Arne Thomas
Gutachterin: Prof. Dr. Anna Fischer

Tag der wissenschaftlichen Aussprache: 18. Oktober 2017

Berlin 2018

1. Abstract

Global warming refers to the rise in average surface temperatures on Earth and is considered as the major environmental problem humanity is facing today. An overwhelming scientific consensus maintains that climate change is primarily caused by the combustion of fossil fuels, which releases carbon dioxide and other greenhouse gases into the atmosphere. Consequently, this gives rise to a range of severe changes in the planet's ecosystem. For this reason, humanity urgently needs a clean energy supply. This can be provided by the use of hydrogen as energy carrier which solely leaves energy and water when it is combusted. An indispensable prerequisite for the environmental friendly use of hydrogen is a sustainable hydrogen generation. Direct photoelectrochemical (PEC) water splitting using sunlight as energy source is considered as the Holy Grail of sustainable hydrogen production. In this context, one of the most promising photoanode materials for the PEC water oxidation reaction is the n-type semiconductor bismuth vanadate ($BiVO_4$) which exhibits a range of beneficial material properties for this approach. However, the main drawback of this material is the poor bulk conductivity which limits its overall PEC performance.

In this thesis, principles to overcome the sluggish electron transport properties of $BiVO_4$ are presented. Anion doping, i.e. partial O/F substitution by fluorination of $BiVO_4$ powder samples is demonstrated to be a viable method to improve the PEC behavior. Significant enhancement of the PEC performance is revealed for the fluorinated $BiVO_4$ compared to its pristine counterpart.

Furthermore, the development of a new bottom-up synthesis approach for the direct deposition of $BiVO_4$ thin films is demonstrated. The new synthesis allows the adjustment of the photoanode design to the materials properties. Combining the new synthesis method

with cation doping and optimizing the photoanode morphology as well as PEC-relevant properties, unleashes tremendous PEC performance regarding water oxidation accounting for photocurrent densities up to 4.6 mA/cm² at 1.23 V vs RHE (illumination of white light, 400-700 nm at 100 mW/cm² at neutral pH).

Additionally, the concepts of anion and cation doping were combined to form F/Mo:$BiVO_4$ thin film photoanodes. The co-doped $BiVO_4$ photoanodes exhibit enhanced PEC performance in terms of photocurrent densities accounting for 5.4 mA/cm² at 1.23 V vs RHE (illumination of white light, 400-700 nm at 100 mW/cm² at neutral pH); a higher photocurrent density has not been reported so far for a single-material photoanode regarding water oxidation.

With the new synthesis method in hands, the preparation of a well-performing WO_3/$BiVO_4$ heterojunction photoanode was enabled. In a first step, a WO_3 sol was used for dip coating an FTO substrate resulting after subsequent calcination in a WO_3 thin film homogeneously covering the rough FTO substrate morphology. Thereafter, the WO_3 thin film was coated with a $BiVO_4$ thin film in a second synthesis step. Photocurrent densities of ~ 6.8 mA/cm² at 1.23 V vs RHE (illumination of white light, 400-700 nm at 100 mW/cm² at neutral pH) were obtained for the heterojunction photoanode which easily outperforms heterojunction photoanodes of comparably facile design and also competes well with the best performing WO_3/$BiVO_4$ photoanodes reported of advanced nanostructure.

2. Zusammenfassung

Die globale Erderwärmung, d.h. der Anstieg der mitteleren Temperatur an der Erdoberfläche, wird als das größte Umweltproblem der Menschheit der heutigen Zeit betrachtet. Es herrscht breiter, wissenschaftlicher Konsens, dass für die globale Erwärmung maßgeblich die Verbrennung fossiler Energieträger und die damit verbundene Treibhausgasemission, insbesondere von CO_2, verantwortlich ist. Infolge der globalen Erwärmung treten bedrohliche Veränderungen im Ökosystem des gesamten Planeten auf, weshalb die Menschheit dringend eine umweltfreundliche Energieversorgung benötigt. Dies könnte basierend auf Wasserstoff als Energieträger erreicht werden, da bei dessen Verbrennung lediglich Wasser und Energie frei werden. Eine unabdingbare Voraussetzung für die umweltfreundliche Nutzung von Wasserstoff ist hierbei die nachhaltige und umweltfreundliche Wasserstoffgewinnung. Direkte photoelektrochemische Wasserspaltung unter Verwendung von solarer Energie gilt als der Heilige Gral der nachhaltigen Wasserstoffproduktion. Im Kontext der photoelektrochemischen Wasseroxidation wird das n-Typ Halbleitermaterial Bismutvanadat ($BiVO_4$) als besonders vielversprechend betrachtet, da es eine Reihe vorteilhafter Eigenschaften für diese Anwendung besitzt. Der gravierendste Nachteil und gleichzeitig leistungslimitierende Faktor des $BiVO_4$ ist jedoch die geringe elektrische Leitfähigkeit im Material.

In dieser Arbeit werden grundlegende Strategien vorgestellt, um das Problem geringen elektrischen Leitfähigkeit des $BiVO_4$ zu überwinden und somit die photoelektrochemische Leistungsfähigkeit zu erhöhen. Es wird gezeigt, dass Anionendotierung, d.h. partielle O/F-Substitution durch Fluorierung, eine nützliche Methode darstellt, um die photoelektrochemischen Eigenschaften von pulverbasierten $BiVO_4$-Photoanoden zu steigern. Eine signifikante Verbesserung der photoelektrochemischen Leistung des fluorierten $BiVO_4$ im Vergleich zum reinen $BiVO_4$ wird dargelegt.

Des Weiteren wird die Entwicklung eines neuen bottum-up Syntheseansatzes für die direkte Abscheidung von $BiVO_4$-Dünnschichten erläutert, welche die Anpassung des Elektrodendesigns an die Materialeigenschaften ermöglicht. Durch Kombination des neuen Syntheseansatzes mit Kationendotierung und durch Optimierung der Morphologie und aller photoelektrochemisch relevanten Photoanodeneigenschaften konnten bemerkenswerte Photostromdichten für photoelektrochemische Wasseroxidation von bis zu 4.6 mA/cm² bei einem angelegten Potential von 1.23 V vs RHE (unter weißem Licht, 400-700 nm bei 100 mW/cm² und neutralem pH-Wert) erreicht werden.

Ferner wird dargestellt, dass durch Kombination der Konzepte der optimierten, kationendotierten $BiVO_4$-Dünnschicht und der Anionendotierung durch Fluorierung die photoelektrochemische Leistungsfähigkeit weiter erhöht werden kann. Die erzielten Photostromdichten bzgl. Wasseroxidation der ko-dotierten, CoPi-modifizierten F/Mo:$BiVO_4$-Dünnschichtphotoanoden von bis zu 5.4 mA/cm² bei einem angeleten Potential von 1.23 V vs RHE (unter weißem Licht, 400-700 nm bei 100 mW/cm² und neutralem pH-Wert) sind einzigartig in der Fachliteratur für eine Einzelmaterial-Photoanode.

Außerdem wird gezeigt, dass die neue bottum-up Synthesemethode zur Darstellung von leistungsfähigen Wolframoxid/Bismutvanadat (WO_3/$BiVO_4$) Heterostruktur-Photoanoden genutzt werden kann. Ein Wolframoxid-Sol wird zunächst zur Tauchbeschichtung eines leitfähigen Substrates verwendet und kalziniert. Die resultierende Wolframoxid-Dünnschicht, welche die Oberfläche des Substrates homogen bedeckt, wird anschließend mit einem $BiVO_4$-Film beschichtet. Die erzielten Photostromdichten dieser CoPi-modifizierten WO_3/$BiVO_4$ Heterostruktur-Photoanode von bis zu 6.8 mA/cm² bei 1.23 V vs RHE (unter weißem Licht, 400-700 nm bei 100 mW/cm² und neutralem pH-Wert) übertreffen vergleichbar einfach aufgebaute WO_3/$BiVO_4$- Photoanoden deutlich und können sich auch mit den leistungsstärksten, bisher veröffentlichen, $BiVO_4$-basierten Heterostruktur-Photoanoden messen.

3. Table of Contents

1. Abstract II

2. Zusammenfassung IV

3. Table of Contents VII

4. Abbrevations XI

5. Introduction 1

5.1. Motivation 1

5.1.1. Hydrogen as future energy carrier 1

5.1.2. Aim of this thesis 4

5.2. Direct PEC water splitting 6

5.3. Semiconductor 8

5.3.1. Basic principles of intrinsic semiconductors 8

5.3.2. Doping 12

5.3.3. Semiconductor-liquid junction 13

5.3.4. Semiconductor under illumination 16

5.4. Materials 17

5.4.1. General material requirements 17

5.4.2. $BiVO_4$ – a suitable candidate for PEC water oxidation? 20

5.5. Methods 25

5.5.1. Introduction 25

5.5.2. Synthesis methods ... *26*

5.5.3. (Photo-)Electrochemistry ... *30*

6. Experimental ... **38**

6.1. Materials ... 38

6.2. Synthesis ... 38

6.2.1. $BiVO_4$ powder electrodes by EPD ... *38*

6.2.2. Synthesis of $BiVO_4$ and Mo-doped $BiVO_4$ thin films ... *39*

6.2.3. Variation of Synthesis parameters ... *41*

6.2.4. Fluorination of $BiVO_4$ and 10% Mo:$BiVO_4$ thin films ... *43*

6.2.5. Synthesis of WO_3/$BiVO_4$ heterojunctions ... *43*

6.3. Characterization methods ... 44

6.4. Electrochemical characterization ... 46

7. Fluorine-doped $BiVO_4$ ... **49**

7.1. Introduction ... 49

7.2. Synthesis and characterization of F:$BiVO_4$ ... 51

7.3. Photoelectrochemical investigations of F:$BiVO_4$ ... 60

7.4. Conclusion ... 72

8. $BiVO_4$ and Mo:$BiVO_4$ thin film photoanodes ... **75**

8.1. Introduction ... 75

8.2. $BiVO_4$ thin films by bottom-up synthesis approach ... 77

8.2.1. Synthesis of $BiVO_4$ thin films ... *77*

8.2.2. Structural and morphological characterization of $BiVO_4$ thin films ... *80*

8.2.3. (Photo-)electrochemical investigations ... *85*

8.2.4. Conclusion ... *89*

8.3. Molybdenum-doped $BiVO_4$ thin films ... 90

8.3.1. Introduction ... *90*

8.3.2. Synthesis ... *90*

8.3.3. Structural and morphological characterization ... *92*

8.3.4. (Photo-)electrochemical investigations ... *104*

8.3.5. Conclusion ... *114*

8.4. Variation of parameters influencing the PEC performance ... 117

8.4.1. Introduction ... *117*

8.4.2. Domain morphology ... *117*

8.4.3. Calcination temperature ... *134*

8.4.4. CoPi deposition ... *152*

9. F:$BiVO_4$ and F/Mo:$BiVO_4$ thin film photoanodes ... 183

9.1. Introduction ... 183

9.2. Partial O/F substituted $BiVO_4$ thin films ... 183

9.3. Partial O/F substituted 10% Mo:$BiVO_4$ thin films ... 197

9.4. Conclusion ... 206

10. WO_3/Mo:$BiVO_4$ heterojunction photoanodes ... 208

10.1. Introduction ... 208

10.2. Synthesis and Characterization of WO_3 thin films ... 208

10.3. Synthesis and Characterization of WO_3/Mo:$BiVO_4$ heterojunction ... 221

10.4. Optimization of composite electrode design ... 236

10.4.1. Introduction ... *236*

10.4.2. Optimization of WO_3 thin films ... *236*

10.4.3. Application of optimized WO_3 thin films in WO_3/$BiVO_4$ composite electrodes ... *244*

10.4.4. Conclusion ... *258*

11. Conclusion and Outlook 260

12. Appendix 263

12.1. Supplementary data 263

12.1.1. Supplementary data for chapter 7: Fluorine-doped $BiVO_4$ 263

12.1.2. Supplementary data for chapter 8: $BiVO_4$ and Mo:$BiVO_4$ thin film photoanodes 265

12.1.3. Supplementary data for chapter 9: F:$BiVO_4$ and F/Mo:$BiVO_4$ thin film photoanodes 286

12.1.4. Supplementary data for chapter 10: WO_3/Mo:$BiVO_4$ heterojunction photoanode 291

12.2. List of publications 296

13. References 298

14. List of Figures 311

15. List of Tables 325

16. Acknowledgement XIII

17. Eidesstattliche Erklärung XIV

4. Abbrevations

ABPE	-	Applied bias photon to current efficiency
BET	-	Physisorption measurement acc. to Brunauer, Emmet and Teller
CoPi	-	Cobalt phosphate water oxidation catalyst
e^-	-	Electron
EBSD	-	Electron backscatter diffraction
ED	-	Electrodeposition of CoPi
EDX	-	Energy-dispersive X-ray spectroscopy
E_F	-	Fermi energy
EIS	-	Electrochemical impedance spectroscopy
EPD	-	Electrophoretic deposition
FTO	-	Fluorine-doped tin oxide
FWHM	-	Full width at half maximum
GI-XRD	-	gracing incidence X-ray diffraction
hν	-	Photon
h+	-	Hole
ICP-OES	-	Inductively-coupled plasma optical emission spectroscopy
IMPS	-	Intensity modulated photocurrent spectroscopy
IPCE	-	Incident photon to electron conversion efficiency
PD	-	Photochemical depositon

PEC	-	Photoelectrochemical/Photoelectrochemistry
PED	-	Photo-assisted electrodeposition
PEIS	-	Potentio-electrochemical impedance spectroscopy
P-XRD	-	Powder X-ray diffraction
RHE	-	Reversible hydrogen electrode
SAED	-	Selected area electron diffraction

5. Introduction

5.1. Motivation

5.1.1. Hydrogen as future energy carrier

According to the Fifth Assessment Report on Climate Change by the Intergovernmental Panel on Climate Change (IPCC, endorsed by the United Nations Environment Program (UNEP) and the World Meteorological Organization (WMO)), warming of the climate system is unequivocal, and since the 1950s, many of the observed changes in the climate system are unprecedented over decades to millennia.[1] Since 1880 the mean global temperature has increased by 0.85 °C. The last three decades have been successively warmer than all previous decades. Consequently, ongoing warming of the atmosphere and oceans causes a sharp decline of snow and ice, which in turn results in a rising mean sea level. Furthermore, a plenty of extreme weather and climate events come along with global warming like an increase of extreme hot temperature episodes, a severe decrease of cold temperature episodes as well as a drastic increase of heavy rainfalls in some regions of the world. Grave consequences for humanity are related to these changes of the climate system. Despite water shortages, crop failures, epidemics of tropical diseases and floods, also extinction of 15-37 % of all species of the world are dramatic but conceivable scenarios.[2] To avoid these appalling consequences, it is indispensable that the eventual global warming is kept below 2 °C.[3]

The main reason for global warming is in all probability the anthropogenic greenhouse gas emission which has drastically increased since the pre-industrial era and which is largely driven by economic and population growth. This has led to atmospheric concentrations of methane, nitrous oxide and in particular of carbon dioxide that are unprecedented and at its highest level since at least the last 800,000 years (see Figure 5-1).[4] Their effects have been detected throughout the climate system and are considered to be the dominant cause of the

observed global warming since middle of the 20th century.[1] An ongoing increase of atmospheric CO_2 concentration is predicted based on the further increasing worldwide hunger for energy which still is mostly produced by the combustion of fossil fuels.[5]

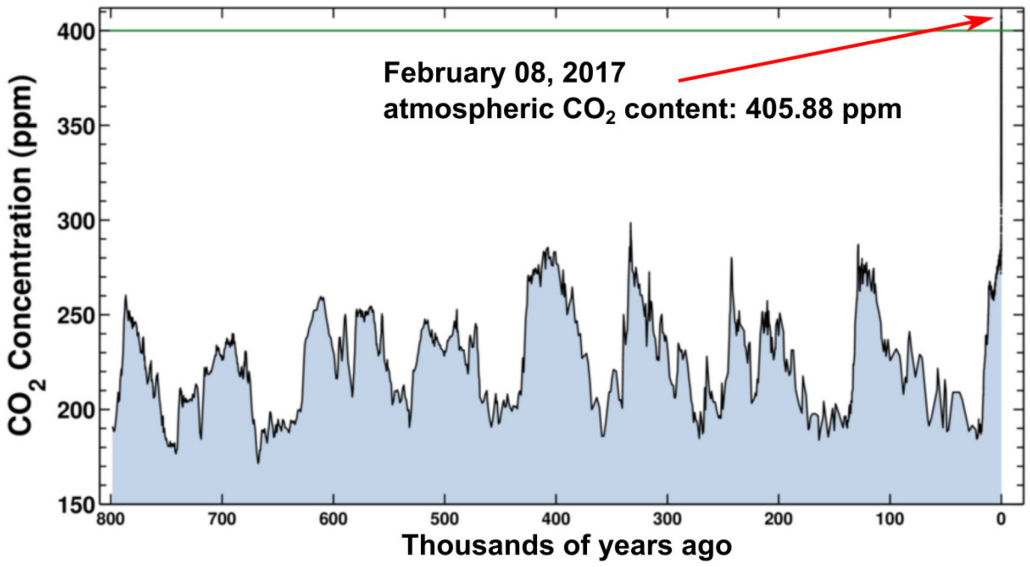

Figure 5-1. Atmospheric CO_2 content over a time period of 800,000 years. Ice-core data considered for estimation of CO_2 content before 1958. Data after 1958 by Scripps CO_2 measurements at Mauna Loa, Hawaii, USA.[4]

To restrain the mean global warming to a total of 2 °C, greenhouse gas emissions have to be reduced drastically in a very rapid manner.[3] Despite a variety of appropriate measures like environmental friendly and energy-efficient technology, housing and infrastructure as well as development of efficient energy saving strategies to reduce the energy consumption, first and foremost energy production has to be decarbonized to pull the root of further CO_2 emission to the atmosphere.

Renewable energy sources like wind energy, geothermal energy, hydropower and solar energy are nearly inexhaustible. Taking advantage of these environmental friendly energy sources does not imply any emission of CO_2 which makes them promising candidates to discard combustion of fossil fuels. Amongst these renewable energy sources, by far the largest energy resource is provided by the sun. In two hours more solar energy strikes the

earth ($8.6 \cdot 10^{20}$ J)[6] than all energy consumed worldwide in the whole year 2015 ($5.62 \cdot 10^{20}$ J).[7] However, the most considerable detriment of using solar energy is its availability which is directly connected to day and night times. This would lead to severe intermittency of an energy supply which was solely based on the direct use of solar energy. For this reason the development of energy storages becomes crucial. Despite impressive progress made in the field of batteries,[8–12] conversion of solar energy to chemical fuels is an attractive strategy as it provides energy storage in the smallest possible configuration – chemical bonds – which enables energy storage in high energy density materials.

Amongst all chemical fuels, hydrogen has the highest gravimetric energy density (143 MJ/kg[13]) which is ~6 times the energy density of coal. Hydrogen can directly be gained out of water by the water splitting reaction (Equation 5-1), an uphill reaction which requires an energy input of $\Delta G = 237.2$ kJ/mol to occur.[14] Once produced, hydrogen is a clean, highly volatile, non-toxic synthetic fuel which produces solely water and energy when it is combusted in lean mixtures.

Equation 5-1. Overall water splitting reaction given for acidic media.

$$2\,H_2O \rightarrow H_2 + 2\,O_2 \qquad \Delta G = +237.2\,kJ/mol$$

However, the biggest problem when considering the usage of hydrogen is its poor volumetric energy density. At room temperature and atmospheric pressure 1 kg of H_2 occupies a volume of 11.25 m³.[13] This problem can be overcome by converting H_2 with CO_2 by a reverse water-gas shift reaction[15,16] to CO which in turn can be transformed to various liquid hydrocarbon fuels by Fischer-Tropsch processes.[17]

A sustainable future for humanity's further growing energy demand could be based on the sun's nearly inexhaustible energy supply in application for water splitting and hydrogen production, respectively. The energy needed for water splitting is provided very well by visible-light-photons enabling the formation of hydrogen and successively its feasible conversion to liquid fuels in an environmental friendly manner.

5.1.2. Aim of this thesis

There are several pathways for hydrogen production using solar energy.[18–21] This thesis copes with direct photoelectrochemical (PEC) water splitting, i.e. semiconductor electrodes harvesting solar energy are in direct contact to an aqueous electrolyte and carry out the water splitting reaction. Investigations focus on bismuth vanadate ($BiVO_4$), the most promising photo-anode material up to date. As will be elucidated in the upcoming sections, the main drawback of $BiVO_4$ and at the same time main PEC performance-limiting factor was figured out to be its poor electron transport properties.[22–24] In the context of enhancing electron transport through the electrode material, different methodologies are conceivable: i) n-type doping to increase the number of free charge carriers in the conduction band, ii) improved electrode design involving advanced nanostructuration and iii) setting-up of a staggered-type heterojunction photoanode with another semiconductor material resulting in enhanced charge carrier transport. The objective of this thesis was to pursue the mentioned optimization strategies to overcome the limiting factors to develop well-performing $BiVO_4$-based photoanodes for PEC water oxidation.

N-type cation doping of $BiVO_4$ is well known and a widely used method to overcome the problem of slow electron transport. Especially doping with hexavalent cations like W^{6+} or Mo^{6+} were demonstrated to significantly improve PEC performance.[25–28] The concept of anion doping applied to $BiVO_4$ is by far less studied. The positive impact of anion substitution in terms of improving the number of free charge carriers and also in terms of band gap engineering is well-known.[29–31] However, no profound study on anion substitution in $BiVO_4$ was reported. Answering the question whether anion doping, choosing fluorine as dopant, is beneficial for the PEC performance of $BiVO_4$-based photoanodes is therefore one subject of this thesis. A clean and robust synthetic route to fluorine-doped $BiVO_4$ needed to be developed which on the one hand allows extensive chemical and structural characterization and on the other hand enables (photo-)electrochemical investigations.

Charge carrier transport through an electrode can be facilitated by improvement of the interfaces (at the back contact and at the electrolyte) and especially by reduction of charge transport impeding artifacts like a high number of grain and particle boundaries as well as

by morphological adjustments to the materials properties. For this reason, improvement of the electrode design and morphology is a viable tool to enhance the PEC performance of $BiVO_4$ photoanodes. However, most synthesis methods for the direct deposition of $BiVO_4$ thin films on conducting substrates are for some very sophisticated from a technical point of view and for some questionable in terms of scalability.[32–34] A straight-forward, robust and facile method to synthesize $BiVO_4$ thin film photoanodes which at the same time enables fine-tuning of various material and electrode properties, is still missing. For this reason, the development of a molecular synthesis route to well-performing $BiVO_4$ and doped $BiVO_4$ thin film photoanodes with controllable properties is another objective of this thesis.

Application of fine-tuned doped $BiVO_4$ thin films to advanced electrode systems is conceivable in order to further enhance PEC performance of $BiVO_4$-based photoanodes. In principle, the synthesis method developed for fluorine doping of $BiVO_4$ could also be applied to fine-tuned pristine and cation-doped $BiVO_4$ thin film photoanodes. The influence of combining both synthesis approaches on the photoelectrochemical properties of the resulting co-doped $BiVO_4$-based thin film photoanodes is another aim of this thesis.

Furthermore, a molecular synthesis approach for $BiVO_4$ thin film photoanodes can be used to fabricate a staggered-type heterojunction with WO_3 as interlayer between $BiVO_4$ and the conducting substrate. Setting-up of $WO_3/BiVO_4$ heterojunctions is reported to be a powerful method to further enhance PEC performance regarding water oxidation of $BiVO_4$ based photoanodes.[35–38] However, only strongly advanced nanostructuration of $WO_3/BiVO_4$ heterojunction photoanodes was demonstrated to yield best PEC performances which, unfortunately, seriously impedes up-scaling for industrial applications. For this reason, the development of a facile preparation route to $WO_3/BiVO_4$ composite electrodes is another objective of this thesis.

5.2. Direct PEC water splitting

Direct photoelectrochemical water splitting combines harvesting of solar energy and the electrolysis of water into a single device. It has been investigated for decades since Fujishima and Honda demonstrated in 1972 the "Electrochemical Photolysis of Water at a Semiconductor Electrode".[39] In Figure 5-2 a simplified schematic illustration of a PEC cell is shown. As can be seen, the illustrated PEC cell is comprised of a single photoanode and a metal cathode which is the PEC cell configuration that is used throughout this thesis to characterize the photoelectrochemical properties of fabricated electrodes regarding the water oxidation reaction. The main component of this PEC cell is the semiconductor photoanode in which electron-hole pairs are excited by incident photons ($h\nu$). Photo-generated electrons and holes are separated spatially from each other due to the presence of an electric field inside the semiconductor (*vide infra*). The photo-generated electrons are swept to the conducting back-contact and to the metal counter electrode via the outer circuit, respectively. At the metal cathode, the electrons are used to reduce water to form hydrogen gas. The photo-generated holes are transported to the semiconductor-electrolyte interface and are used to oxidize water to evolve oxygen gas.

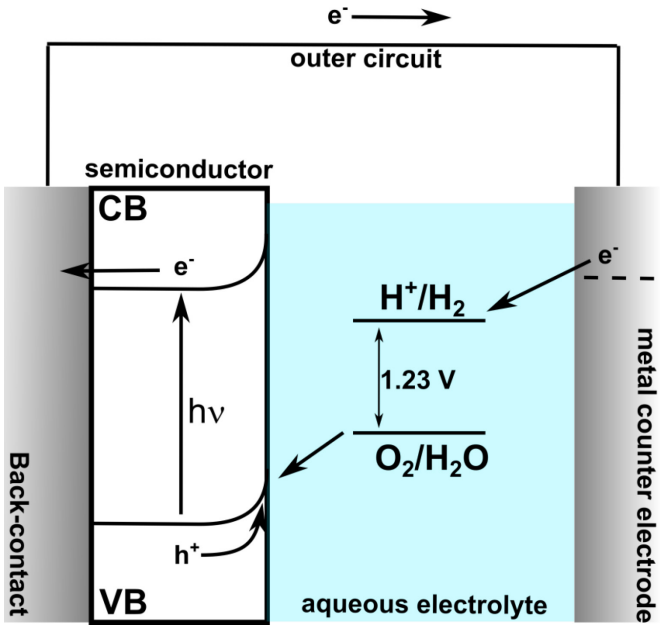

Figure 5-2. Schematic illustration of a PEC cell comprised of a semiconductor photoanode and a metal counter electrode.

Respective half reactions occurring at the electrode using acidic electrolytes can be written as:

Equation 5-2. Water splitting half reactions in acidic media (pH = 0).

$$4H^+ + 4e^- \rightarrow 2H_2 \qquad E^0_{red} = 0.00\ vs\ NHE$$

$$2H_2O + 4h^+ \rightarrow 4H^+ + O_2 \qquad E^0_{ox} = 1.23\ vs\ NHE$$

In alkaline media the appropriate reactions are as follows:

Equation 5-3. Water splitting half reactions in alkaline media (pH = 14).

$$4H_2O + 4e^- \rightarrow 2H_2 + 4OH^- \qquad E^0_{red} = -0.83\ vs\ NHE$$

$$4OH^- + 4h^+ \rightarrow 2\ H_2O + O_2 \qquad E^0_{ox} = 0.40\ vs\ NHE$$

For media the overall water splitting reaction is:

Equation 5-4. Overall water splitting reaction.

$$2H_2O \overset{h\nu}{\rightarrow} 2H_2 + O_2$$

For this reaction the free enthalpy (also known as Gibbs free energy, *ΔG*) can be calculated according to Equation 5-5:

Equation 5-5. Free enthalpy change calculated by the electrochemical cell voltage.

$$\Delta G = -nF(E^0_{red} - E^0_{ox}) = -nF\Delta E$$

where n is the chemical amount and F the Faradaic constant. For standard conditions (298 K, 1 bar, 1 mol/l) the chemical cell voltage *ΔE* equals -1.23 V which corresponds according to Equation 5-5 to a free enthalpy change of 237.2 kJ (n = 2). The positive free enthalpy of this reaction reveals the reaction to be thermodynamically unfavorable, i.e. uphill as illustrated in Figure 5-3.

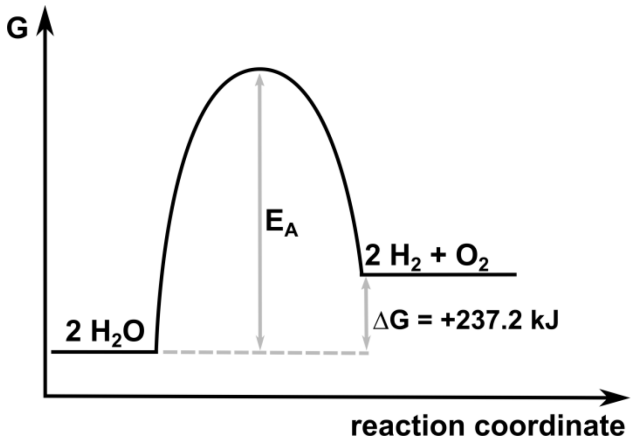

Figure 5-3. Energy diagram for the thermodynamically unfavorable water splitting reaction with E_A as activation energy.

5.3. Semiconductor

The main component of a PEC cell is the semiconductor as it converts the incident photons to electron-hole pairs. With respect to PEC water splitting, basic principles of semiconductors which are useful to understand occurring phenomena when a semiconductor is brought into contact with an electrolyte will be discussed in this section. Note: This chapter only gives a brief introduction to subjects relevant to the use of semiconductors in a PEC cell. For detailed and comprehensive information on this topic the reader is referred to outstanding text books by Bard and Faulkner,[40] Memming[41] and van de Krol and Grätzel.[42]

5.3.1. Basic principles of intrinsic semiconductors

To describe energy states in an ideal single crystal, the energy band model is appropriate. According to quantum mechanics the energy levels of a single atom are discrete. If two atoms are approaching each other, the energy levels split up due to electrostatic interactions. Translating this assumption to a crystal and assuming atoms to be arranged in a periodic lattice, several quantum mechanical energy states arise which are energetically very similar. For this reason, the energy states can be considered as continuum or energy bands. This is illustrated in Figure 5-4a. The broadness of the bands is different for

different energy levels. This is a consequence of electrons at lower energy levels being tightly bound to an atom which results in only low interaction with neighboring atoms. Hence, the energy bands are narrow. Electrons of higher energy levels are less tightly bound. For this reason they can overcome atomic potentials between the lattice atoms easier and interact more strongly with neighboring atoms, hence, the band becomes broader (see Figure 5-4b).

For the electric conductivity of a crystal/material the highest occupied energy level named valence band and the lowest unoccupied levels named conduction band are of interest. Both bands are separated by an energy band gap (E_g) in which no energy states are allowed. According to the size of the band gap, materials can be categorized in conducting materials, semiconducting materials and isolators/non-conducting materials. Valence and conduction bands are overlapping in case of conducting materials ($E_g = 0$ eV) which leads to a high amount of free energetic states resulting in good electric conductivity. In case of semiconducting materials there is a moderately sized band gap ($E_g \sim 1.0$ - 3.5 eV) between valence band and conduction band in which no energy states are allowed. The immobile electrons of the valence band need to be excited (by heat or photons) to overcome the band gap and reach energy levels of the conduction band to become mobile. Upon such an excitation, two mobile charge carriers are created: the electron in the conduction band and the hole (or defect electron) in the valence band. Both charge carriers are of utmost importance in PEC water splitting as they are used for the water splitting half reactions. In case of isolators, the band gap is very big ($E_g > 3.5$ eV) and for this reason it is impossible to excite electrons to the conduction band.

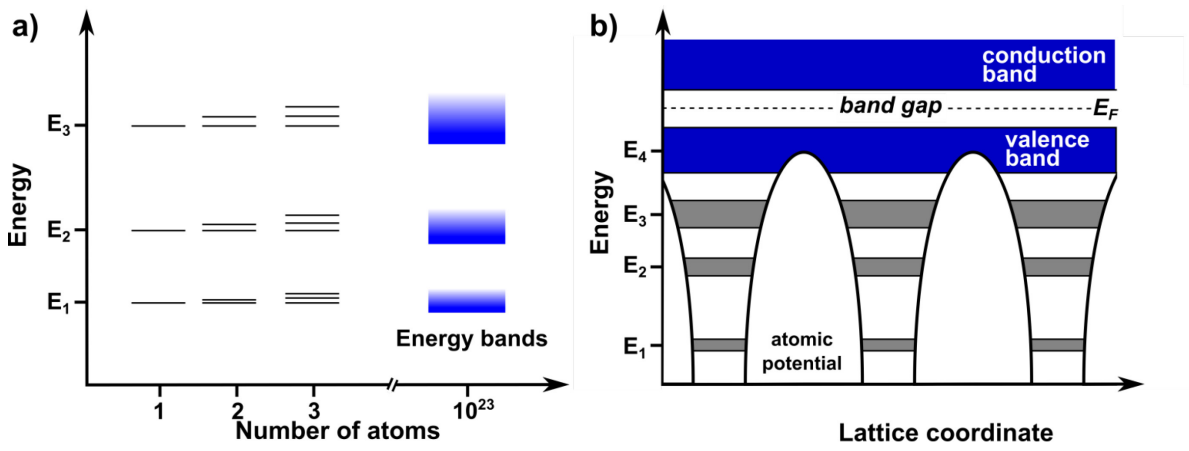

Figure 5-4. Split-up of energy levels of atoms in a periodic lattice forming energy bands.

In Figure 5-4b, a dashed line is shown within the band gap region which is assigned to the Fermi energy level E_F (Fermi level) which is defined as the energy level at which the probability of being occupied by an electron is exactly one half. At a temperature of 0 K, the Fermi level is exactly half way between the valence and conduction band as the whole valence band is filled with electrons and the whole conduction band is completely empty. However, for temperatures above absolute zero, the probability of an electron being thermally excited is larger than zero. As a consequence the number of electrons occupying levels in the conduction band is given by Equation 5-6:

Equation 5-6. Number of electrons occupying levels in the conduction band.

$$n_e = \int_{E_C}^{\infty} N(E) f(E)\, dE$$

in which $N(E)$ is the total number of energy states up to a certain energy level and $f(E)$ is the Fermi-Dirac distribution as given by Equation 5-7:

Equation 5-7. Fermi-Dirac distribution.

$$f(E) = \frac{1}{1 + \exp\left(\frac{E - E_F}{k_B T}\right)}$$

where k_B is the Boltzmann constant and T is the temperature. Equation 5-6 can only be solved by the approximation that $(E\text{-}E_F)/k_BT \gg 1$. This is valid for degenerated

semiconductors under equilibrium conditions and results in the concentration of free electrons occupying energy states in the conduction band which is given by Equation 5-8:

Equation 5-8. Concentration of free electrons occupying states in the conduction band and density of energy states above the conduction band edge.

$$n_e = N_C \, exp\left(-\frac{E_C - E_F}{k_B T}\right) \qquad with \qquad N_C = \frac{2(2\pi m_e^* k_B T)^{3/2}}{h^3}$$

where N_c is the density of energy states within few k_BT above the conduction band edge, m_e^* is the effective mass of an electron and h is the Planck constant. In a similar manner, expressions can be derived for the concentration of free holes in the valence band (Equation 5-9):

Equation 5-9. Number of holes occupying states in the valence band.

$$n_h = \int_{-\infty}^{E_V} N(E)\big(1 - f(E)\big)\, dE$$

Using the same approximations like above the concentration of free holes in the valence band is given by Equation 5-10:

Equation 5-10. Concentration of free holes occupying states in the valence band and density of energy states below the valence band edge.

$$n_h = N_V \, exp\left(\frac{E_V - E_F}{k_B T}\right) \qquad with \qquad N_V = \frac{2(2\pi m_h^* k_B T)^{3/2}}{h^3}$$

where N_V is the density of energy states around the top of the valence band edge and m_h^* is the effective mass of a hole.

For an intrinsic semiconductor the concentrations of holes and electrons occupying states in the valence and conduction band, respectively, must be equal. Hence, the position of the Fermi level can be calculated from Equation 5-8 and Equation 5-10 as follows (Equation 5-11):

Equation 5-11. Calculation of the Fermi level out of the concentration of free holes and electrons.

$$E_F = \frac{E_C + E_V}{2} + \frac{k_B T}{2} ln\left(\frac{N_V}{N_C}\right) = \frac{E_C + E_V}{2} + \frac{k_B T}{2} ln\left(\frac{m_h^*}{m_e^*}\right)^{3/2}$$

In accordance to Equation 5-11, the Fermi level is located close to the middle of the energy gap. Additionally, the intrinsic carrier density can be obtained by multiplying Equation 5-8 and Equation 5-10, revealing the intrinsic density of charge carriers (Equation 5-12):

Equation 5-12. Intrinsic electron and hole density.

$$n_h n_e = N_V N_C \, exp\left(-\frac{E_g}{k_B T}\right) = n_i^2$$

where E_g is the band gap energy. For intrinsic semiconductors, thermal excitation is the dominant excitation process. In accordance, the density of electrons and holes becomes very small for big band gap energies (Equation 5-12).

5.3.2. Doping

Due to their low conductivity, intrinsic semiconductors are only rarely used for practical applications. The conductivity can be drastically enhanced by doping an intrinsic semiconductor with impurities. A doped semiconductor is referred to as extrinsic semiconductor. The impurities, i.e. the dopants, are either electron donating or electron accepting atoms and are referred to as donors/n-type and acceptors/p-type. In Figure 5-5 band diagrams of an intrinsic semiconductor (a), an n-type extrinsic semiconductor (b) and an extrinsic p-type semiconductor (c) are illustrated. As can be seen, doping of a semiconductor leads to introduction of energy levels within the band gap. The donor level E_D is located close to the conduction band and the acceptor level E_A close to the valence band. Extra electrons of a donor dopant are only loosely bound to the donor atom. Hence, it can be easily excited to energy levels of the conduction band. On the opposite, electrons of the valence band can easily be excited to the acceptor levels close to it leaving additional holes within the valence band.

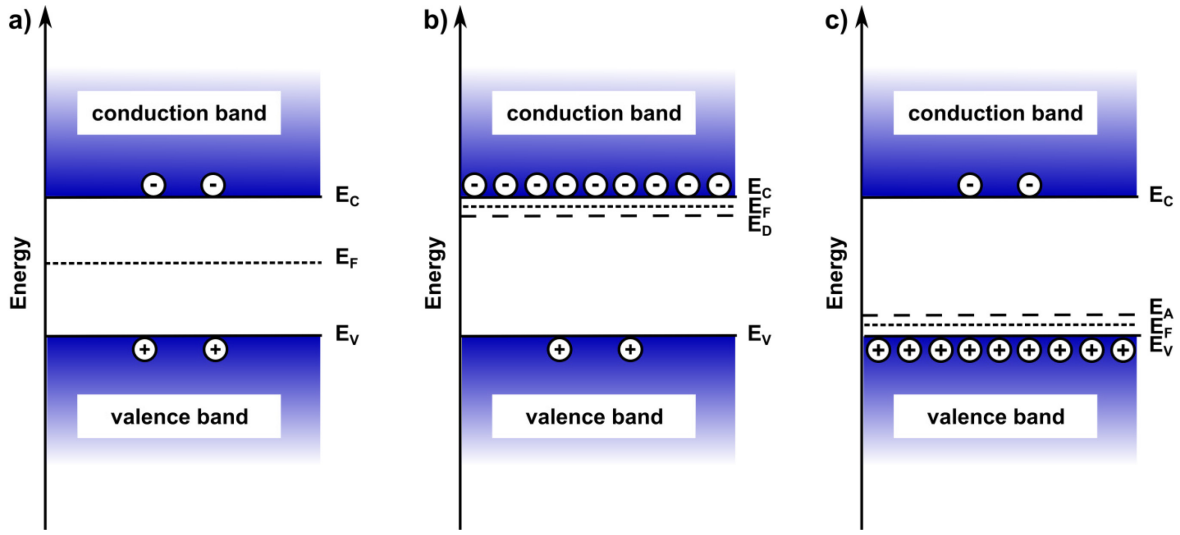

Figure 5-5. Energy diagram of a) an intrinsic semiconductor b) an n-type doped semiconductor and c) a p-type doped semiconductor.

If the energetic distance between dopant level and conduction band and valence band, respectively, is sufficiently small, dopants can be thermally excited to the respective bands already at moderate temperatures – this is referred to as shallow donors and acceptors, respectively. In metal oxide photoelectrodes like presented in this thesis, shallow donors and acceptors are necessary because of the low intrinsic charge carrier mobilities. The conductivity σ of a material can be determined according to Equation 5-13:

Equation 5-13. Conductivity of a material.

$$\sigma = n_e e \mu_e + n_h e \mu_h$$

where e is the elementary charge, n_e and n_h are the number of electrons and holes and μ_e and μ_h are the electron and hole mobilities, respectively. Small charge carrier mobilities can be compensated by an increase of n_e and n_h, respectively.

5.3.3. Semiconductor-liquid junction

In PEC water splitting, a semiconductor is brought into contact with an aqueous electrolyte. When the Fermi levels of both, i.e. of the semiconductor material and the redox species in the electrolyte, are different, charge carriers are transferred between the semiconductor and

the electrolyte until the electrochemical equilibrium condition is achieved. This process is illustrated in Figure 5-6 for an n-type semiconductor brought into contact with an aqueous electrolyte. As can be seen in Figure 5-6a, before being brought into contact the Fermi levels of the semiconductor and the corresponding redox level of the electrolyte are different. If the level of the semiconductor's conduction band is more cathodic as the redox level of the electrolyte, electrons of the electrode's conduction band are transferred to the electrolyte after being brought into contact (Figure 5-6b). This results in an upward bending of the bands at the semiconductor-electrolyte interface. The Fermi levels of both materials approach and this process continues until both Fermi levels converge and the electrochemical equilibrium is reached, respectively. As a result, a region at the semiconductors surface is created in which the concentration of electrons is depleted. This region is referred to as depletion layer or space charge region. Due to band bending, a potential Φ_{SC} is created which results in an electric field which is beneficial for the spatial separation of electrons and holes. The width of the space charge region W depends on Φ_{SC} and can be calculated according to Equation 5-14:

Equation 5-14. Width of the space charge region.

$$W = \sqrt{\frac{2\varepsilon_0\varepsilon_r}{eN_D}\left(\Phi_{SC} - \frac{k_B T}{e}\right)}$$

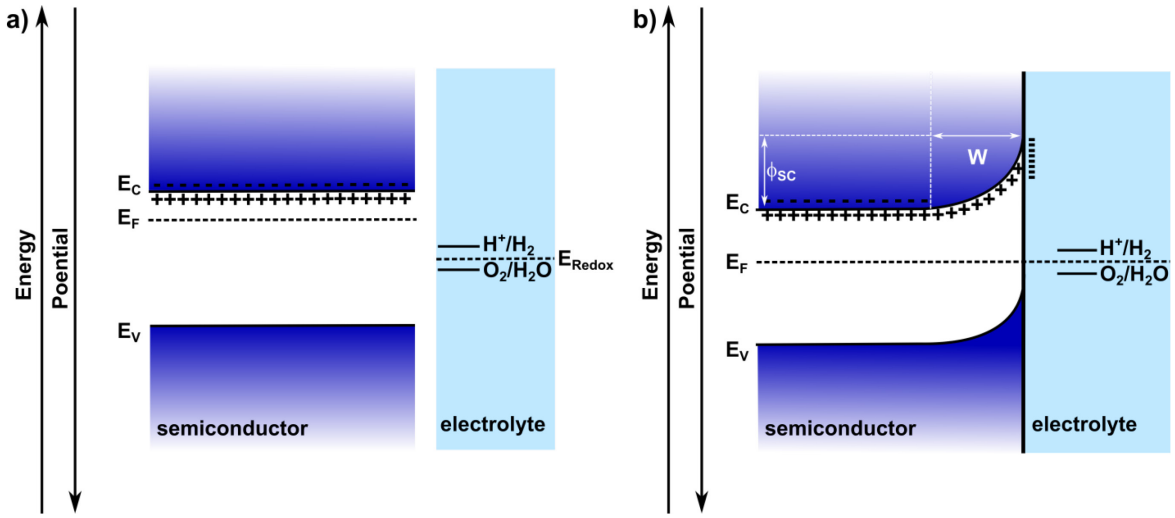

Figure 5-6. Band diagrams of an n-type semiconductor-liquid junction. a) before being brought into contact and b) after beeing brought into contact.

Band diagrams are very useful tools to estimate whether a certain reduction or oxidation reaction is thermodynamically possible. As can be seen in the example given in Figure 5-6b, the O_2/H_2O redox energy is positioned above the top of the valence band edge which is a crucial condition for a semiconductor to carry-out the water oxidation reaction.

The potential within the space charge region Φ_{SC} can be influenced by applying an external bias potential. In Figure 5-7a, a band diagram comprised of a semiconductor in contact with an aqueous electrolyte and the energy level of a reference electrode is illustrated. Application of a positive bias to the n-type semiconductor (Figure 5-7b) results in a downshift of the Fermi level and therefore to increased band bending. As a consequence the Φ_{SC} is enhanced and, according to Equation 5-14, the width of the space charge region W increases. Application of a negative external bias potential lifts the Fermi level upwards and therefore decreases band bending (not shown).

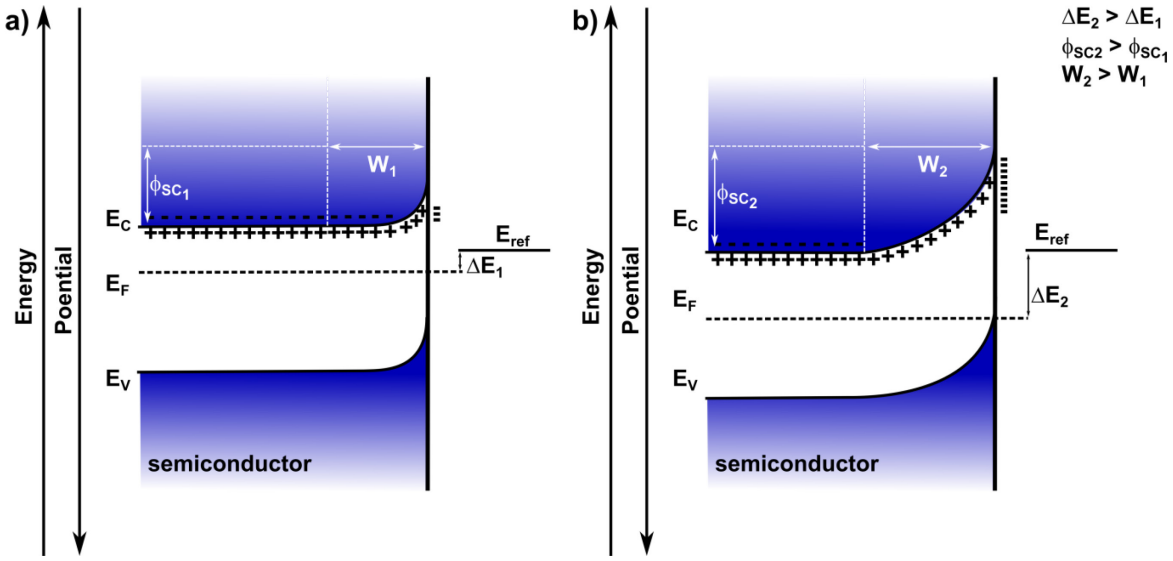

Figure 5-7. Band diagram of an n-type semiconductor in contact with an electrolyte. a) unbiased and b) application of a positive bias potential to the semiconductor.

5.3.4. Semiconductor under illumination

Illumination of a semiconductor represents a disturbance of the thermal equilibrium. Consequently, electron and hole densities are increased to above their equilibrium values and exceed the intrinsic electron density (n_i), i.e. $n_h n_e > n_i^2$. For this reason, it is useful to define quasi-Fermi levels $E_{F,h}$ and $E_{F,e}$ for holes and electrons separately which can be written as follows (Equation 5-15):

Equation 5-15. Quasi-Fermi level for holes and electrons.

$$E_{F,h} = E_V + ln\left(\frac{N_V}{n_h}\right) \qquad and \qquad E_{F,e} = E_C - ln\left(\frac{N_C}{n_e}\right)$$

In Figure 5-8a, the band diagram of an n-type semiconductor in contact with an aqueous electrolyte in the dark and in thermal equilibrium, respectively, is depicted. The Fermi level energy E_F equals $E_{F,h}$ and $E_{F,e}$ in the dark. In case of excitation of the extrinsic n-type semiconductor, the number of additional electrons excited to the conduction band is much smaller compared to the number of electrons already thermally excited to the conduction band ($\Delta n_e \ll n_e^0$). On the contrary, the number of holes in the valence band increases drastically upon illumination ($\Delta n_h \gg n_h^0$). For this reason, the Fermi level of the electrons

$E_{F,e}$ remains unchanged whereas the Fermi level of holes $E_{F,h}$ is shifted significantly to the valence band. This is illustrated in Figure 5-8b.

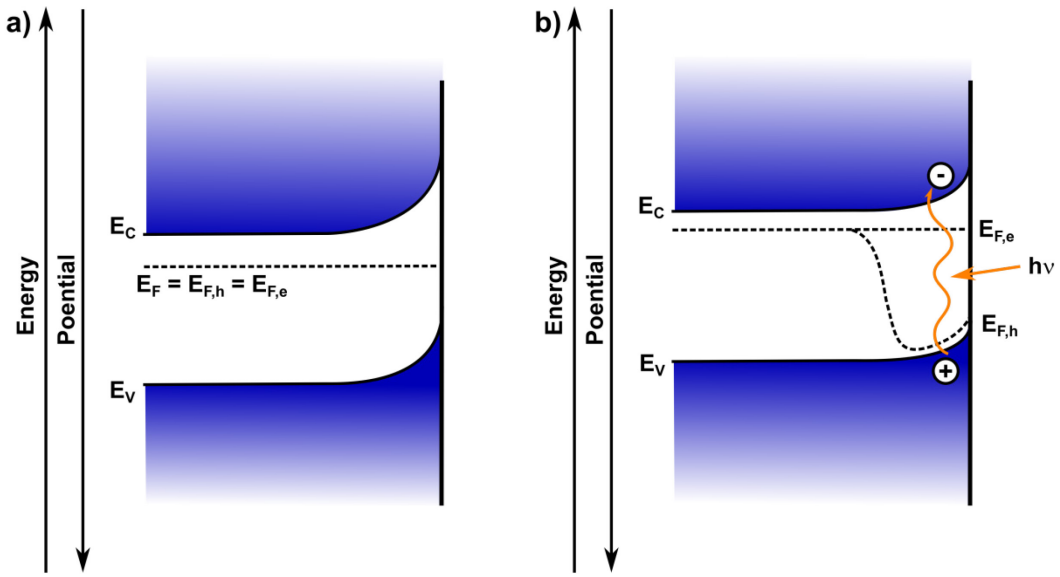

Figure 5-8. Band diagramm of an n-type semiconductor in contact with an aqueous electrolyte. a) in the dark and b) upon illumination.

The concept quasi-Fermi levels is a viable tool to understand processes at the semiconductor-liquid junction, as the relative position of the quasi-Fermi levels with respect to the redox Fermi levels in the electrolyte allows an assumption of the thermodynamic driving force for an electrochemical reaction.

5.4. Materials

5.4.1. General material requirements

Shining light onto some basic principles of semiconductors with respect to photoelectrochemical water splitting already gave some hints to general material requirements for the use as photoelectrode for photoelectrochemical water splitting. Some general aspects have to be considered when the suitability of an electrode material for PEC

water splitting is under discussion. They have been summarized and discussed extensively in literature, for instance by Grätzel and van de Krol:[42,43]

i) Strong (visible) light absorption
ii) High chemical stability in the dark and under illumination
iii) Suitable band edge positions
iv) Efficient charge transport in the semiconductor
v) Low overpotentials for the reduction/oxidation reactions
vi) Low cost

i) The band gap of a semiconductor determines the spectral range in which light is absorbed. The minimal band gap energy required for a semiconductor to perform water splitting can be estimated by taking into account the energy needed for water splitting (1.23 eV), some losses attributed to thermodynamics/entropy (0.3-0.4 eV)[44,45] and overpotentials due to slow reaction kinetics (0.4-0.6 eV). Based on all energy contributions, the minimal band gap of a material can be estimated to be 1.9 eV. The upper band gap limit is determined by the solar spectrum. As the intensity of sunlight rapidly declines in the UV range, an upper limit of 3.1 eV can be estimated. The band gap of a semiconductor therefore needs to be somewhere between 1.9 and 3.1 eV.

ii) Chemical stability in aqueous media in the dark and upon illumination is indispensable for an electrode material to be used for direct photoelectrochemical water oxidation. Most non-oxide materials dissolve or form a passivating oxide layer which is severely impeding electron transfer. Most metal oxide semiconductors are stable in aqueous media but may be decomposed upon application of a bias potential and/or illumination.

iii) Suitable band edge positions are crucial to drive the water splitting half reactions. For the reduction reaction, the conduction band must be positioned above the energy level for the reduction of H^+ to H_2. To drive the water oxidation reaction, the valence band should be positioned below the energy level for the H_2O/O_2 oxidation reaction. If the band edges of a semiconductor material straddle the potentials of both water splitting half reactions, it is principally possible to use this semiconductor to evolve both, H_2 and O_2 from water. However, most semiconducting materials only fulfill one of the band edge criteria.

According to their band energies, most non-oxide semiconductors are rather suitable to drive the water reduction reaction whereas most oxide semiconductors are better suited to carry out the water oxidation reaction. An overview of recently investigated semiconductor materials fulfilling the requirement of suitable band positions was provided by Roland Marschall.[46]

iv) Being fulfilled easily for some semiconducting materials, e.g. WO_3, the requirement of efficient charge transport can also be the main limiting factor for other materials. Slow charge transport within a semiconductor leads to inefficient separation of the photo-generated charge carriers and therefore results in fast recombination. Intrinsic and extrinsic factors influence the charge transport properties of a semiconducting material. Extensively overlapping 3d orbitals and overlapping O-2p orbitals determine the electron and hole mobilities, respectively, in most metal oxides. Furthermore, extrinsic effects like shallow donors/acceptors are important factors with respect to charge transport properties of a semiconductor. A measure to estimate the charge transport properties of a material is the minority charge carrier diffusion length L_D (Equation 5-16), which is directly related to the carrier lifetime τ_r and the diffusivity, given by the Nernst-Einstein term, which includes the charge carrier mobility μ:

Equation 5-16. Minority charge carrier diffusion length.

$$L_D \simeq \sqrt{\frac{k_B T \mu \tau_r}{e}}$$

The diffusion length ranges from several nanometers in some oxides to several hundred micrometers.

v) Considering an n-type semiconductor, the requirement of low overpotentials for the water oxidation reaction is fulfilled if hole transfer from the semiconductor to the electrolyte is fast enough to avoid accumulation of photo-generated holes at the electrode-electrolyte interface, i.e. at the semiconductor surface. Surface hole accumulation leads to enhanced electron-hole recombination at the surface. Interfacial charge transfer kinetics

can be improved by the deposition of a catalytically active species onto the semiconductor surface. Despite precious metal-based catalysts like IrO_2,[47–49] recently, Co-based[50–52] and Ni-based[53–55] alternatives were shown to improve water oxidation kinetics efficiently at different pH ranges.

5.4.2. $BiVO_4$ – a suitable candidate for PEC water oxidation?

Up to this day, no material has been found which fulfills all requirements. Binary metal oxides and particularly α-Fe_2O_3 (hematite) or TiO_2 have been investigated exhaustively with respect to PEC water splitting. However, as a consequence of their high ionic character, binary metal oxides often suffer from a very large band gap (e.g. $E_g(Al_2O_3) = 8.8$ eV). For this reason, research on more complex, ternary metal oxides has been growing. Since Kudo et al. reported in 1998 on "Photocatalytic O_2 evolution under visible light irradiation on $BiVO_4$ in aqueous $AgNO_3$ solution",[56] the ternary oxide bismuth vanadate ($BiVO_4$) has become one of the most investigated electrode materials for photoelectrochemical water oxidation[57–61] and is the semiconductor material in the focus of this thesis. Some of its materials properties are elucidated in the next sections.

5.4.2.1. Crystal structure

$BiVO_4$ is known to exist in three polymorphs. The mineral pucherite (space group: *Pnca* with $a = 5.328$ Å, $b = 5.052$ Å, $c = 12.003$ Å) exhibits an orthorhombic crystal structure.[62,63] However, the orthorhombic $BiVO_4$ does only occur in nature and has never been prepared synthetically. Synthetic $BiVO_4$ crystallizes either in a zircon-type or in a scheelite-type structure. The zircon-type has a tetragonal crystal system (space group: $I4_1/a$ with $a = b = 7.303$ Å and $c = 6.584$ Å)[64] while the scheelite-type $BiVO_4$ can either have a monoclinic crystal system (space group: I2/b with $a = 5.1787$ Å, $b = 5.1042$ Å, $c = 11.6953$ Å, $\gamma = 90.260$ °) referred to as monoclinic scheelite[65,66] or a tetragonal crystal system ($I4_1/a$, $a = b = 5.147$ Å, $c = 11.721$ Å) referred to as tetragonal scheelite.[67] The monoclinic scheelite structure represents a slightly distorted modification of the tetragonal scheelite structure.

Zircon-type $BiVO_4$ usually is prepared by precipitation methods at room temperature.[68–70] Heat treatment at ~ 400-500 °C irreversibly transforms the zircon-type $BiVO_4$ to the monoclinic scheelite-type. A reversible transition between the monoclinic scheelite structure and the tetragonal scheelite structure is observed at 255 °C. The phase transitions are illustrated schematically in Figure 5-9.

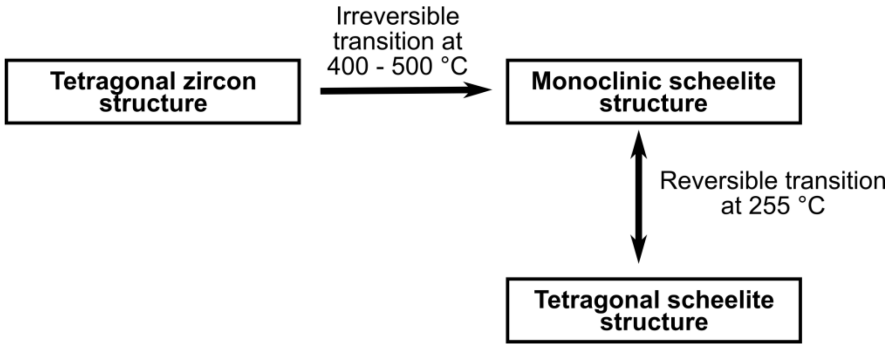

Figure 5-9. Phase transitions of $BiVO_4$ according to Tokunaga et al.[67]

The unit cell of monoclinic $BiVO_4$ with corresponding coordination polyhedra is shown in Figure 5-10. Each vanadium ion is tetrahedrally coordinated by four oxygen ions. The bismuth coordination environment consists of eight oxygen ions in dodecahedral coordination. The oxygen ions are thereby provided by a different VO_4 tetrahedral each. This coordination system is valid for both scheelite-type structures. The main difference between tetragonal and monoclinic scheelite $BiVO_4$ is a slight distortion of the local environments of bismuth and vanadium ions in the monoclinic structure which results in the loss of the four-fold symmetry.

As shown by Kudo et al., the scheelite-type polymorph of $BiVO_4$ is most interesting for photocatalytic applications. This is attributed to the much smaller band gap of the scheelite-type $BiVO_4$ compared to its zircon-type analogue (2.4 eV and 2.9 eV, respectively).[71] Further Tokunaga et al. demonstrated the monoclinic scheelite-type $BiVO_4$ to exhibit a significantly higher photocatalytic activity regarding water oxidation when compared to the tetragonal analogue.[67] The distortion in the monoclinic scheelite structure is considered to

be the origin of higher photocatalytic activity. According to Tokunaga et al., the distortion probably positively influences the charge separation and delocalization of photo-generated electrons and holes.[67]

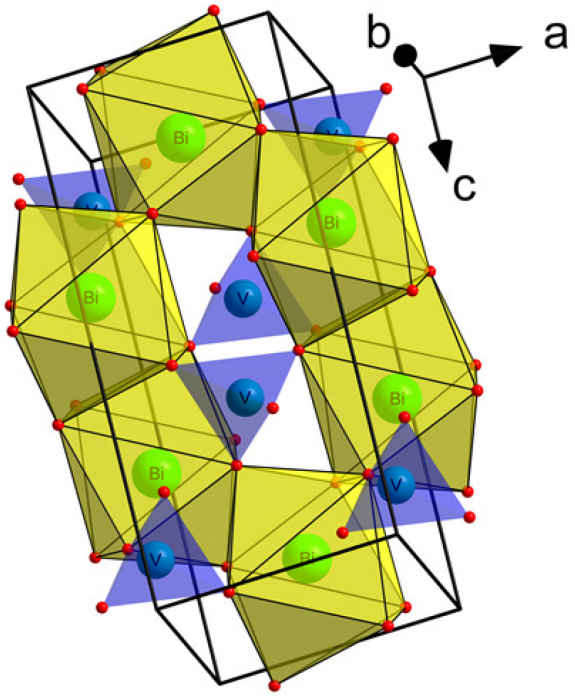

Figure 5-10. Unit cell and coordination polyhedra of monoclinic scheelite-type $BiVO_4$. Bi colored green, V colored blue, O colored red. V-O_4-tetrahedra colored blue, Bi-O_8-polyhedra colored yellow.

5.4.2.2. Electronic structure

A very recent study on the electronic structure of monoclinic scheelite-type $BiVO_4$ was reported by the group of Sharp in 2014.[23] By combining density functional theory calculations (DFT) with results of various spectroscopy methods, a complete portrait of the orbital character of the valence and conduction bands was obtained. According to the results of this study, the energy level diagram including dominant orbital character is illustrated in Figure 5-11.

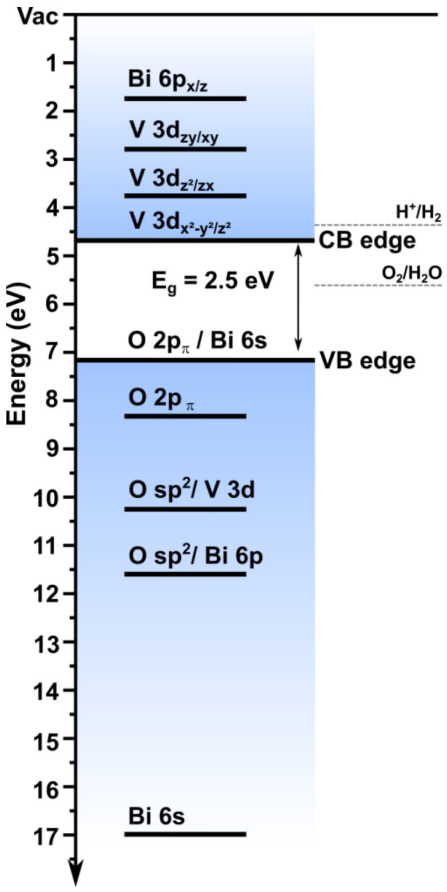

Figure 5-11. Energy diagram of monoclinic scheelite-type $BiVO_4$ according to Cooper et al.[23]

According to Cooper et al.,[23] the valence band edge is primarily comprised of O 2p orbitals, with the valence band maximum being comprised of non-bonding O $2p_\pi$ states with a slight contribution of Bi 6s orbitals. The conduction band is mainly comprised of V 3d orbitals. As can be seen, the valence band edge is positioned significantly below the oxidation potential of O_2/H_2O. However, the conduction band edge is slightly below the $H+/H_2$ reduction potential. With respect to PEC water splitting, this reveals $BiVO_4$ to be a material suitable only for the water oxidation reaction. Cooper et al. also showed the V d-orbitals to be only poorly overlapping with the Bi 6p orbitals which results in poor electron mobility in $BiVO_4$. In line with these results, slow bulk electronic conductivity in $BiVO_4$ has independently been shown by the group of van de Krol.[22]

5.4.2.3. Evaluation

Based on the materials properties, the suitability of $BiVO_4$ as material for PEC water splitting can be evaluated according to the material requirements elucidated in chapter 5.4.1. In the following, only the monoclinic scheelite-type $BiVO_4$ is considered as it is the most interesting modification with respect to photoelectrochemical applications.

The band gap of $BiVO_4$ is determined to be 2.4-2.5 eV which is perfectly matching the required band gap of 1.9-3.1 eV for water splitting.

Like most metal oxides, $BiVO_4$ is chemically stable in aqueous electrolytes depending on the pH of the solution. At low pH values $BiVO_4$ is prone to dissolution whereas it is stable in neutral and alkaline electrolytes. However, the photochemical stability of $BiVO_4$ is still under debate. Toma et al. reported in 2016, that $BiVO_4$ is susceptible to photochemical corrosion resulting in a non-stoichiometric composition of the surface. Self-passivation of $BiVO_4$ by the formation of a chemically stable bismuth oxide surface phase is not observed.[72] For this reason, the $BiVO_4$-electrolyte interface needs to be modified, e.g. ideally with a catalytically active passivation layer, to improve the durability of $BiVO_4$ photoanodes for sustained water oxidation operation.

The band edge positions of $BiVO_4$ do not straddle the water oxidation and reduction potentials. However, the valence band edge is positioned significantly below the water oxidation potential which enables the PEC water oxidation reaction. The conduction band edge is positioned slightly below the H^+/H_2 reduction potential. Consequently, $BiVO_4$ can only be used for photoelectrochemical water oxidation. With respect to the water oxidation reaction, the conduction band edge located close to the thermodynamic H_2 evolution potential is beneficial, as it promotes an earlier photocurrent onset and the generation of a higher photocurrent in the low bias region.[24]

Efficient charge carrier transport was figured out to be the main drawback for $BiVO_4$ for the use as photoanode material. The V 3d orbitals and the Bi 6s orbitals of the conduction band only slightly overlap.[23] Furthermore, the V-O_4 tetrahedra in the monoclinic scheelite $BiVO_4$ structure are not directly connected to each other; both resulting in very low electronic conductivity.[73] A further result is a rather short hole diffusion length of

70-100 nm.[22,74,75] To overcome the problem of low electronic conductivity, efficient n-type doping strategies need to be applied to $BiVO_4$.

Considerable overpotentials regarding water oxidation are observed for $BiVO_4$. This is a consequence of the sluggish water oxidation kinetics of the $BiVO_4$ surface.[76] For $BiVO_4$ single crystals the photocatalytic activity regarding oxidative processes depends on the crystal facet.[77–81] As reported by the group of Rohrer,[79] oxidation reactions are strongly favored on (hk0) surfaces. However, with respect to isotropic, polycrystalline $BiVO_4$-based photoanodes, the application of suitable water oxidation catalysts needs to be taken into account.

Finally, $BiVO_4$ is a non-toxic material comprised of earth-abundant elements. Taylor estimated the concentration of vanadium within the earth's continental crust to be as high as 135 ppm, while bismuth's concentration is estimated to 0.17 ppm.[82] The high abundance of the constituting elements therefore results in low material cost.

In consideration of the mentioned arguments and despite some severe drawbacks which need to be overcome, $BiVO_4$ is a promising electrode material for photoelectrochemical water oxidation.

5.5. Methods

5.5.1. Introduction

In the upcoming chapters, the synthesis of $BiVO_4$-based photoanodes will be elucidated and obtained photoanodes will be characterized profoundly. Basically, two different electrode synthesis approaches have been used: i) dip coating out of sol-gel-based solutions and ii) electrophoretic deposition of pre-synthesized powders. Key aspects of both synthesis approaches will be pointed up in the following.

Obtained electrodes were characterized by various different techniques. Quantitative methods (inductively coupled plasma optical emission spectrometry, ICP-OES), nitrogen an krypton physisorption (BET model), spectroscopic methods (UV/Vis spectroscopy in total reflectance and in transmission mode) and structural analysis methods (powder x-ray

diffraction, P-XRD, and x-ray diffraction in gracing incidence of the x-ray beam, GI-XRD), and different electron microscopy methods (scanning electron microscopy, SEM, transmission electron microscopy, TEM, scanning transmission electron microscopy, STEM) and related characterization methods (energy-dispersive x-ray spectroscopy, EDX, selected area electron diffraction, SAED, electron backscatter diffraction, EBSD) have been used. These characterization methods are commonly used to identify thin film structure, composition, crystallinity etc. and are very well described in various excellent textbooks.[83–90]

Less commonly used and therefore worth a closer look are several methods of electrochemistry and photoelectrochemistry. Three principal methods used throughout this thesis for characterization of the photoelectrochemical properties of the different photoanodes will be presented briefly in the following sections.

5.5.2. Synthesis methods

5.5.2.1. Sol-gel dip coating

In this thesis, thin film photoanodes were synthesized by different sol-gel-based methods in combination with dip coating as thin film deposition method.

The dip coating process can be applied to all kinds of precursor solutions. The sol-gel-based precursor solutions, as long as homogeneous and stable, offer most possibilities to influence the thin film properties.[91] Starting from inorganic or metal-organic precursors in aqueous or organic solvents, the precursors are hydrolyzed and condensed to form inorganic polymeric networks characterized by M-O-M bonds. Commonly used molecules are metal alkoxides as they readily react with water. Exemplarily, hydrolysis and condensation reactions for a metal alkoxide solved in its parent alcohol are given in Equation 5-17 and Equation 5-18. The hydrolysis reaction is characterized by a hydroxyl ligand being attached to the metal atom accompanied by the release of ROH. In case of R being a proton, a water molecule is released, in case of R being an alkyl, an alcohol ROH is released. Depending on the present amount of water and catalyst, e.g. acid, metal organic

precursors may be hydrolyzed completely ($x = n$) or partially ($x < n$). Two partially hydrolyzed molecules can be interconnected in a condensation reaction forming an oxo-bridged M-O-M species accompanied by liberation of a small molecule (alcohol – alkoxolation; water – oxolation).

Equation 5-17. Hydrolysis of a metal-alkoxide.

$$M(OR)_n + xH_2O \rightarrow [(OR)_{n-x} - M - (OH)_x] + xROH \qquad \text{hydrolysis}$$

Equation 5-18. Condensation reactions of a hydrolyzed alkoxide.

$$-M - OH + RO - M- \rightarrow -M - O - M - + ROH \qquad \text{alkoxolation}$$

$$-M - OH + HO - M- \rightarrow -M - O - M - + H_2O \qquad \text{oxolation}$$

By ongoing hydrolysis and condensation oligomers are created, which can be further interconnected to polymers or particles forming a colloidal dispersion of solids in a solvent, referred to as sol. Progressive hydrolysis/condensation leads to an amorphous inorganic polymer, referred to as gel.

The sol can be used for dip coating to process metal oxide thin films. As such, dip coating is one of the easiest and fastest methods to prepare thin films from chemical solutions allowing at the same time the highest degree of control about the thin film properties. Hence, it is the thin film deposition method of choice in this thesis. Briefly explained, a substrate is dipped vertically into a solution and is withdrawn at a constant speed v. As illustrated in Figure 5-12, by withdrawing the substrate out of the sol, some solution remains at the substrate. As the solvent is draining and evaporating, the inorganic species of the sol are progressively concentrated leading to aggregation and gelation. Finally, the film collapses and is deposited at the substrate.

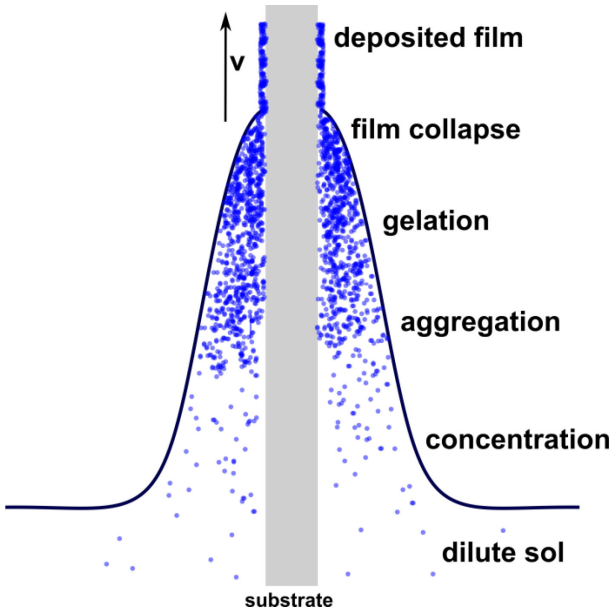

Figure 5-12. Evaporation-induced processes during dip coating according to Brinker et al.[92]

Despite the chemical factors influencing the properties of the resulting thin film like concentration, presence of a surfactant, quantities of water or acid, the processing factors are of utmost importance for adjustment of the thin film. The thickness of the deposited film d is influenced by the viscosity η of the solution, the withdraw speed v, the surface tension γ, the density ρ, and the gravitational constant g according to the Landau-Levich equation (Equation 5-19):[93]

Equation 5-19. Landau-Levich equation.

$$d = 0.94 \frac{(\eta \cdot v)^{2/3}}{\gamma^{1/6}(\rho \cdot g)^{1/2}}$$

Consequently, the film thickness can be influenced by the withdraw speed and by adjustment of the solution properties. Furthermore, temperature and relative humidity inside the coating cabinet need to be controlled precisely as these environmental factors have a strong impact on the evaporation of the solvent. As reported by Grosso et al.,[94,95] it is likely that the quantity of water in the films after drying of the deposited film varies with the relative humidity inside the dip coating cabinet which influences the thin film's final organization. The content of volatile species in the film can be modulated by indirect

adjustment of the vapor pressures. Variation of solution parameters and dip coating under controlled conditions allows fine-tuning of the thin film properties.

5.5.2.2. Electrophoretic deposition

To enable (photo-)electrochemical investigations of powder samples, fabrication of electrodes out of the powders is crucial. For this approach, an electrophoretic deposition (EPD) method based on the work from Abe et al. was used in this thesis.[96] First, a dispersion of the powder samples in an electrically conductive solvent is prepared. Two conductive substrates are immersed parallel into the dispersion (Figure 5-13a). Application of a potential between these electrodes results in the formation of a homogeneous electric field (Figure 5-13b). Particles between both electrodes are grafted electrophoretically due to the electric field and are deposited onto the substrate. The drift speed v of the dispersed particles thereby depends on the strength of the electric field E, the charge of the particles q, the particle radius r, and the viscosity of the solvent η according to Equation 5-20.

Equation 5-20. Electrophoretic drift speed for dispersed spherical particles.

$$v = \frac{q \cdot E}{6\pi \cdot r \cdot \eta}$$

Thereafter electrodes are taken out of the dispersion and are ready for (photo-)electrochemical usage. In most cases, the as-deposited particles at the substrates need to be interconnected to improve charge transport through the deposited particle layer. This can either be achieved by a simple heat treatment or by a certain necking treatment.

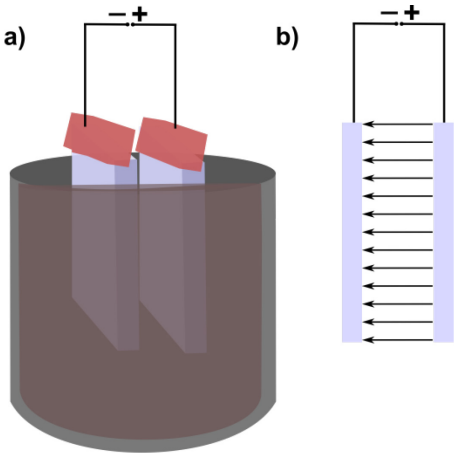

Figure 5-13. a) Sketch of EPD-setup b) Homogeneous electric field between electrodes.

5.5.3. (Photo-)Electrochemistry

5.5.3.1. Measurement of j-V curves and IR-drop compensation

Measurement of the j-V curves is the most widely used technique for acquiring information about electrochemical reactions. In practice, the electrochemical method used to acquire j-V curves is cyclic voltammetry. Typically, in a three-electrode configuration (see chapter 6.4) comprised of working electrode, counter electrode and reference electrode, a certain voltage V_0 is applied to the working electrode with respect to the reference electrode. The voltage is varied linearly between two limits with a scan rate of dV/dt; a triangular voltage is generated (see Figure 5-14a). When an electrochemical reaction occurs, the effective voltage is different from the applied voltage which is balanced by the potentiostat by a current flow to the counter electrode according to Ohm's law (Equation 5-21):

Equation 5-21. Ohm's law.

$$V = R \cdot I$$

As illustrated in Figure 5-14b, sweeping the voltage in anodic direction leads to oxidation of the reduced species which is expressed by a positive current with the maximum current density at $V = V_{ox}$. When sweeping the voltage back the oxidized species is reduced, expressed by a negative current with the maximum current density at $V = V_{red}$. For an

irreversible electrochemical reaction only the oxidation or the reduction current is observed (Figure 5-14c). Water oxidation is considered to be an irreversible electrochemical reaction, as the reaction product O_2 is leaving the electrochemical cell and is not available for the reduction reaction. In terms of a photoelectrochemical oxidation reaction using an n-type semiconductor as working electrode, the gained photovoltage V_{photo} is added to the applied voltage $V_{app.}$ Consequently, the observed oxidation current is shifted cathodically as less voltage needs to be applied by the potentiostat. This is illustrated by the blue curve in Figure 5-14c.

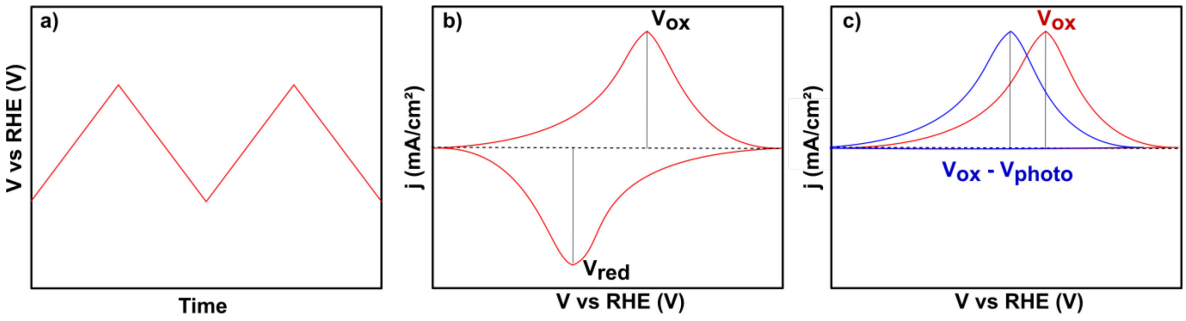

Figure 5-14. a) triangular voltage used for CV measurements, b) typical cyclic voltammogram for a reversible electrochemical reaction, c) cyclic voltammogram for an irreversible (photo-)electrochemical reaction conducted in darkness (red curve) and under illumination (blue curve).

The electrolyte in the electrochemical cell acts like a resistance R according to Ohm's law. As a consequence, between the current-carrying counter and working electrodes and between the working electrode and the reference electrode the voltage drops; a phenomenon which is referred to as IR-drop. This voltage drop distorts the measurement of the electrode potential of the working electrode about the value of I·R. Hence, to obtain proper j-V measurements, the IR-drop needs to be corrected. Besides the optimization of the cell setup to shorten current pathways between the electrodes, optimization of the electrode geometry and improvement of the electric conductivity of the electrolyte, a commonly used method is the electronic IR-drop compensation. The uncompensated resistance R_u of the electrochemical measurement setup is determined by a simple impedance measurement at high frequencies (~ 100 kHz) and a compensation voltage

determined by IR_u is added to the set voltage V_{set} according to Equation 5-22 to yield the corrected applied voltage V_{app}.

Equation 5-22. IR-drop compensation.

$$V_{app} = V_{set} + IR_u$$

5.5.3.2. Electrochemical impedance spectroscopy according to Mott-Schottky

The position of the band edges with respect to the redox potentials of the electrolyte is commonly called flat-band potential, E_{FB} or V_{FB}. As already suggested by its name, the flat-band potential corresponds to the potential that needs to be applied to a semiconductor under depletion conditions to decrease the band bending to zero, i.e. to flatten the bands. Hence, the flat band potential corresponds to the Fermi level of the semiconductor with respect to the reference electrode.[42] In case of an n-type semiconductor in contact with an electrolyte, the flat-band potential is positioned slightly below the conduction band edge. Gathering information about the flat band potential therefore allows estimation of the thermodynamic ability of an n-type semiconductor to carry out the water reduction reaction.

Amongst several methods to gain information about the flat-band potential,[97] the most common and most applied method to estimate the flat-band potential is electrochemical impedance spectroscopy (EIS) according to the Mott-Schottky relationship given in Equation 5-23:

Equation 5-23. Mott-Schottky equation.

$$\frac{1}{C_{SC}^2} = \frac{2}{\varepsilon_0 \varepsilon_r A^2 e N_D}\left(E - E_{FB} - \frac{k_B T}{e}\right)$$

where C_{SC} is the capacitance of the space charge region, ε_0 is permittivity in vacuum, ε_r is the relative permittivity of the semiconductor, A is the surface area of the semiconductor in contact with the electrolyte, e is the charge of an electron and N_D is the free charge carrier density. This method relies on measurement of the capacitance of the space charge region as a function of the applied potential at a fixed frequency. For an n-type semiconductor a

positive slope is expected which ascends linearly in a certain potential range. By extrapolation of the linear part of the Mott-Schottky-plot, the flat-band potential is given by the intercept on the potential axis minus k_BT/e. Furthermore, by the slope of the Mott-Schottky-plot the density of free charge carriers N_D can be calculated if the exact electrode surface area A in contact with the electrolyte is known.

These calculations are based on two assumptions:

i) Two capacitances need to be considered, the capacitance of the space charge layer C_{SC} and the capacitance of the Helmholtz layer C_{HL}. Since capacitances are considered to be connected in series, the total capacitance C_{total} is calculated by the sum of the reciprocals of the single capacitances, given by Equation 5-24:

Equation 5-24. Calculation of the total capacitance.

$$\frac{1}{C_{total}} = \frac{1}{C_{SC}} + \frac{1}{C_{HL}}$$

As the capacitance of the space charge region is much smaller than the capacitance of the Helmholtz layer ($C_{SC} \ll C_{HL}$),[41,42] the contribution of the C_{HL} to the total capacitance C_{total} is negligibly small. Therefore, the measured capacitances are assumed to be the values of the space charge capacitance.

ii) Possible faradaic and non-faradaic processes that can occur at the electrode surface need to be taken into account. For this purpose a modified Randles circuit shown in Figure 5-15 is used to model the electrode-electrolyte interface. The only possible faradaic process involves the water oxidation reaction which is represented by a resistance R_{CT} in the circuit. A Warburg impedance Z_W is connected in series to R_{CT} which represents diffusion of electroactive species towards the electrode surface. The non-faradaic electrode capacitance caused by the build-up of charge at the electrode surface connected in parallel with R_{CT} and Z_W and is represented by a constant-phase-element CPE. The CPE takes into account any inhomogeneity of the electrode surface, e.g. surface roughness. The impedance Z_{CPE} of a CPE in an ac circuit is given by Equation 5-25:

Equation 5-25. Impedance of a CPE in an ac circuit.

$$Z_{CPE} = \sigma\omega^{-m}\left[\cos\left(\frac{m\pi}{2}\right) - \mathrm{i}\sin\left(\frac{m\pi}{2}\right)\right]$$

with σ as CPE prefactor, ω as the angular frequency, m as the CPE exponent and i as the imaginary number ($\mathrm{i} = \sqrt{-1}$). The final component in the modified Randles circuit is R_S, which takes into account the voltage drop in the electrolyte owing to the passage of current between the electrode surface and the reference electrode.

Assuming the electrode to act like an ideal capacitor (CPE exponent m in Equation 5-25 equals 1), the interfacial capacitance C can be determined directly from the CPE prefactor σ and a Mott-Schottky plot can be established.

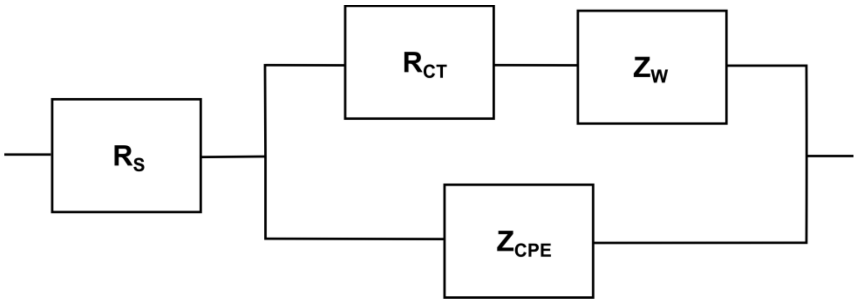

Figure 5-15. Modified Randles circuit used to model the electrode-electrolyte interface for Mott-Schottky analysis.

5.5.3.3. Photocurrent transient analysis

The competition between the desired water oxidation reaction on the one hand and the loss of photo-generated holes due to recombination processes determines the efficiency of any photoanode used for solar water splitting. Despite bulk recombination of the photo-generated charge carriers due to impurities and defects within the crystal lattice, surface recombination seems to be the most important loss mechanism for many semiconductor photoanodes. Surface recombination can be deduced directly from photocurrent-voltage measurements under chopped illumination. The obtained photocurrent response/photocurrent transient can then be analyzed.

An example of a typical photocurrent transient recorded for a Mo-doped $BiVO_4$ thin film photoanode exhibiting significant features is given in Figure 5-16. When the light is switched on, an initial photocurrent "spike" j_{ini} is observed. From this spike the photocurrent response shows a characteristic decay to a steady-state photocurrent j_{ss}. When the light is switched off again, an overshoot and decay back to the dark current/zero current is observed. Qualitatively, the recorded transient features can be interpreted as follows: When switching-on the light, electron-hole pairs are generated and charge carriers are separated. Electrons are swept to the bulk while holes migrate towards the anode surface. This initial displacement of charge carriers results in a charging or displacement current (spike) j_{ini}. As the concentration of holes at the surface increases, a recombination flux of electrons is induces which corresponds to a current of opposite sign with respect to the hole current. Consequently, a decay of the initial photocurrent spike is observed until a steady-state concentration of holes at the surface is reached which is balanced by interfacial hole transfer and recombination at the surface. Hence, the measured steady-state current j_{ss} is the sum of hole and electron currents. When switching-off the light, hole migration to the surface is immediately interrupted. However, electrons still migrate back to the surface to recombine with remaining holes at the surface; process which is observed as negative photocurrent overshoot. The overshoot therefore corresponds to the decay of surface hole concentration as a result of ongoing recombination and interfacial hole transfer.

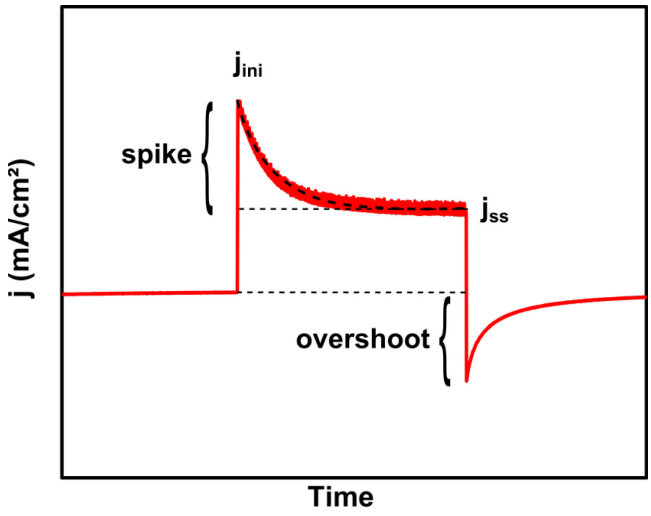

Figure 5-16. Example of a photocurrent transient.

As rationalized by Laurence Peter from the University of Bath, the photocurrent transients can be analyzed according to a simple kinetic model.[98,99] Assuming that hole transfer and surface hole recombination follow pseudo-first order rate laws with respect to the surface hole concentration, the hole transfer efficiency $\eta_{transfer}$ can be expressed by first order rate constants of hole transfer k_{trans} and surface recombination k_{rec} (Equation 5-26):

Equation 5-26. Hole transfer efficiency expressed by first order rate constants for hole transfer and surface hole recombination.

$$\eta_{transfer} = \frac{j_{ss}}{j_{ini}} = \frac{k_{trans}}{k_{trans} + k_{rec}}$$

The exponential decay from the photocurrent spike to the steady state current is characterized by $(k_{trans} + k_{rec})^{-1}$. The decay of the recorded photocurrent transient can be exponentially fitted and k_{trans} and k_{rec} can be separated according to Equation 5-26 allowing the analysis of the water oxidation kinetics at the semiconductor surface.

5.5.3.4. Applied bias photon to current efficiency

A viable diagnostic tool to characterize and understand materials' PEC performances is the solar-to-hydrogen efficiency (STH) which is defined by the chemical energy of the evolved hydrogen divided by the solar energy input from sunlight. This can be expressed in terms of the current density, the voltage, and the Faradaic efficiency for hydrogen generation divided by the power of the incident light (Equation 5-27):

Equation 5-27. Solar-to-hydrogen efficiency.

$$STH = \frac{j \cdot V \cdot \eta_F}{P_{light}}$$

with j the photocurrent density normalized to the illuminated electrode area, V the thermodynamic water splitting potential based on ΔG^0, η_F the Faradaic efficiency, and P_{light} the power of the incident light.

Application of a bias potential between the working and the counter electrodes is considered as additional energy input and does not reflect a true STH process. Hence, a new efficiency value is necessary. For this purpose, Chen et al. introduced the applied bias photon to current efficiency (ABPE, Equation 5-28) which assumes the Faradaic efficiency $\eta_F = 1$ and corrects the electrical power term by the electrical power provided by the bias source.[97]

Equation 5-28. Applied bias photon to current efficiency.

$$ABPE = \frac{j \cdot (V - V_{bias})}{P_{light}}$$

ABPE and STH principally are defined for a two-electrode PEC cell. As suggested by Peter,[100] ABPE still can be used for three-electrode PEC cells if V_{bias} is replaced by the electrode potential with respect to the reversible hydrogen electrode. As in a three-electrode PEC setup ohmic losses are compensated, this definition of the ABPE corresponds to the STH obtained in a two-electrode configuration with negligible cathode overpotential and ohmic resistance.

6. Experimental

6.1. Materials

All chemicals were used as received without further purification. Fluorine-doped SnO_2 glass slides (30 cm x 30 cm, FTO layer thickness ~ 200 µm, R = 8-12 Ω, Aldrich) were cut into pieces of about 2 cm x 1.2 cm and washed by means of ultrasonication (Emmi-20 HC ultrasonication bath, 27 kHz) for 20 min in ethanol, isopropanol and acetone before usage.

6.2. Synthesis

6.2.1. $BiVO_4$ powder electrodes by EPD

6.2.1.1. Synthesis of $BiVO_4$ powders

$BiVO_4$ powders were synthesized by Dipl.-Chem. Björn Anke under supervision of Prof. Dr. Martin Lerch from the Technische Universität Berlin (TU Berlin). $BiVO_4$ was synthesized in an aqueous medium at room temperature under ambient pressure. Bi_2O_3 (7.29 g, 15.6 mmol, 99.9 % Aldrich) and $NaVO_3$ (3.81 g, 31.2 mmol, 98 % AlfaAesar) were dissolved each in small amounts of concentrated HNO_3 (65 %, ~14 mol/l). After mixing both solutions, NaOH was added until the pH value reached basic conditions (pH = 12). The solution was stirred for 4 h. The resultant yellow precipitate was washed with distilled water several times, filtered, and dried at 60 °C for 12 h.

6.2.1.2. Fluorination of $BiVO_4$ powders

Fluorination was performed by Dipl.-Chem. Björn Anke under supervision of Prof. Dr. Martin Lerch from TU Berlin. F-containing $BiVO_4$ was prepared by a solid-vapor reaction using an indirect gas flow apparatus (*vide infra*, Figure 7-1). Loose powder of pure $BiVO_4$ (~500 mg) was loaded in a small corundum boat, which in turn was placed inside a

larger corundum boat containing varying amounts (typically ~2 g) of polyvinylidene difluoride (PVDF, Aldrich). The nested boats were then placed inside a corundum tube with one closed end and placed in a horizontal tube furnace with a low nitrogen gas flow of 5 l/h. The temperature was set to 380 °C for 24 h and after a final heating step in air at 450 °C for 30 min an orange powder was obtained. Note: For comparability the pristine $BiVO_4$ passed the same calcination procedure solely leaving out the PVDF.

6.2.1.3. Electrode fabrication out of $BiVO_4$ and F:$BiVO_4$ powders

An electrophoretic deposition method (EPD) based on a procedure Abe et al. initially reported for TaON was used to fabricate electrodes for photoelectrochemical investigations.[96] In a first step, the pristine as well as the F-containing powders were treated for 15 min in a mixer mill (Retsch GmbH, MM301) to provide a small particle sizes (verified by SEM-investigations). 80 mg of the respective $BiVO_4$ powder were dispersed in iodine-containing acetone (total volume 50 ml, I_2 content 2 mg/ml) by 20 min of ultrasonication (Emmi-20 HC, 27 kHz) at room temperature. Two fluorine-doped tin oxide coated glass slides (FTO) were immersed parallel in the dispersion with 1.0 cm of distance. Particles were deposited by application of a potential of 10 V for 5 min. This procedure was applied twice in total. After electrophoretic deposition, the as-prepared electrodes were calcined at 450 °C or 550 °C for 30 min under air to interconnect the deposited particles by sintering.

6.2.2. Synthesis of $BiVO_4$ and Mo-doped $BiVO_4$ thin films

6.2.2.1. Synthesis of $BiVO_4$ thin films

A solution of $VO(OEt)_3$ (123 µl, 0.7 mmol, Aldrich) in 1.5 ml $CHCl_3$ (>99 %, dry, Aldrich) was prepared. After stirring for 10 min, the solution was added to Bi(2-ethyl-hexanoate)$_3$ (445 mg, 0.7 mmol, AlfaAesar) and stirred for 4 h. The obtained red solution was used for dip coating various substrates (Si or FTO-coated glass slides) under controlled conditions (<30 % relative humidity, 30 °C, 300 mm/min withdrawal speed, 2 s dwell time). After solvent evaporation, all deposited films were aged at 100 °C for 12 h followed by calcination at 450 °C for 2 h in air (heating ramp: 0.5 K/min).

6.2.2.2. Synthesis of Mo:$BiVO_4$ thin films

A solution of $VO(OEt)_3$ (123 µl, 0.7 mmol, Aldrich) in 1.5 ml $CHCl_3$ (>99 %, dry, Aldrich) was prepared. Amounts of 11.3 mg (0.035 mmol), 22.6 mg (0.070 mmol), 33.9 mg (0.105 mmol) or 45.2 mg (0.140 mmol) of $MoO_2(acac)_2$ which correspond to a Mo-content with respect to the Bi content of 5, 10, 15 and 20 at% in the resulting Mo:$BiVO_4$-solution, respectively, were added (see Table 6-1 for an overview of different synthesis solution compositions). After stirring for 10 min, the solution was added to Bi(2-ethyl-hexanoate)$_3$ (445 mg, 0.7 mmol, AlfaAesar) and stirred for 4 h. The obtained red solution was used for dip coating Silicon wafers or FTO-coated glass slides under controlled conditions (< 30 % relative humidity, 30 °C, 300 mm/min withdrawal speed, 2 s dwell time). After solvent evaporation all deposited films were aged at 100 °C for 12 h followed by calcination at 450 °C for 2 h in air (heating ramp: 0.5 K/min).

Table 6-1. Composition of the precursor solution used for the synthesis of X% Mo:$BiVO_4$ thin film photoanodes.

sample	Bi(-OHex-2-Et)$_3$	$VO(OEt)_3$	$MoO_2(acac)_2$
0% Mo:$BiVO_4$	445 mg / 0.70 mmol	140 mg / 123 µl / 0.70 mmol	-
5% Mo:$BiVO_4$	445 mg / 0.70 mmol	140 mg / 123 µl / 0.70 mmol	11.3 mg / 0.035 mmol
10% Mo:$BiVO_4$	445 mg / 0.70 mmol	140 mg / 123 µl / 0.70 mmol	22.6 mg / 0.070 mmol
15% Mo:$BiVO_4$	445 mg / 0.70 mmol	140 mg / 123 µl / 0.70 mmol	33.9 mg / 0.105 mmol
20% Mo:$BiVO_4$	445 mg / 0.70 mmol	140 mg / 123 µl / 0.70 mmol	45.2 mg / 0.140 mmol

6.2.3. Variation of Synthesis parameters

6.2.3.1. Synthesis of $BiVO_4$ and Mo-doped $BiVO_4$ thin films with worm-like morphology

A solution of 123 µl (0.7 mmol) of $VO(OEt)_3$ in 1.5 ml $CHCl_3$ containing 112.5 mg of BASF Pluronic© F127 (ethylene oxide- *block* -propylene oxide- *block* -ethylene oxide, $(PEO)_{101}$-$(PPO)_{56}$-$(PEO)_{101}$) corresponding to 50 w% of $BiVO_4$ in solution was prepared. For Mo-doped $BiVO_4$ thin films amounts of 11.3 mg (0.036 mmol), 22.6 mg (0.07 mmol), 33.9 mg (0.10 mmol) or 45.2 mg (0.14 mmol) of $MoO_2(acac)_2$ which correspond to a Mo-content of 5, 10, 15 and 20 at% with respect to the Bi content in the resulting Mo:$BiVO_4$-solution, respectively, were added. After stirring for 10 min, the solution was added to Bi(2-ethyl-hexanoate)$_3$ (445 mg, 0.7 mmol) and stirred for 4 h. The obtained red solution was used for dip coating Silicon wafers or FTO-coated glass slides under controlled conditions (<30 % relative humidity, 30 °C, 300 mm/min withdrawal speed, 2 s dwell time). After solvent evaporation all deposited films were aged at 100 °C for 12 h followed by calcination at 450 °C for 2 h in air (heating ramp: 0.5 K/min).

6.2.3.2. Variation of the calcination procedure

For the variation of the calcination procedure 10% Mo:$BiVO_4$ thin films were prepared. A solution of $VO(OEt)_3$ (123 µl, 0.7 mmol) in 1.5 ml $CHCl_3$ (>99 %, dry) was prepared. $MoO_2(acac)_2$ (22.6 mg, 0.07 mmol) corresponding to 10% Mo with respect to the Bi content within the synthesis solution was added to the solution. After stirring for 10 min, the solution was added to Bi(2-ethyl-hexanoate)$_3$ (445 mg, 0.7 mmol) and stirred for 4 h. The obtained red solution was used for dip coating FTO-coated glass slides under controlled conditions (< 30 % relative humidity, 30 °C, 300 mm/min withdrawal speed, 2 s dwell time). After solvent evaporation all deposited films were aged at 100 °C for 12 h in air. Final calcination temperatures were varied from 350 °C to 550 °C in increments of 50 K. Note: The heating ramp was kept constant at 0.5 K/min for all final calcination times.

6.2.3.3. Variation of CoPi deposition methods

For all CoPi depositions 10% Mo:$BiVO_4$ thin films prepared according to the method described in chapter 6.2.2.2 were used.

6.2.3.3.1. Electrodeposition of CoPi

An electrochemical cell equipped with a RHE reference electrode, a Pt counter electrode and a 10% Mo:$BiVO_4$ thin film as working electrode described in chapter 6.4 (*vide infra*) was used for CoPi electrodeposition. The cell was filled with potassium phosphate solution (20 ml, 0.1 mol/l, Carl Roth) containing $Co(NO_3)_2$. (0.5 mmol/l, Aldrich). The deposition was carried out at an applied potential of 1.9 V vs RHE in the dark without stirring and without IR-correction and was stopped after a certain amount of charge was transferred.

6.2.3.3.2. Photodeposition of CoPi

The electrochemical cell equipped with RHE reference electrode, Pt counter electrode and the 10% Mo:$BiVO_4$ thin film as working electrode described in chapter 6.4 (*vide infra*) was used for CoPi electrodeposition. The cell was filled with potassium phosphate solution (20 ml, 0.1 mol/l, Carl Roth) containing $Co(NO_3)_2$. (0.5 mmol/l, Aldrich). Without application of any bias potential the working electrode was irradiated by white light (400-700 nm) of an intensity of 100 mW/cm² in frontside mode (*frontside* PD) or in backside mode (*backside* PD). The deposition was carried out without stirring. By variation of the irradiation time between 20 min and 40 min the amounts of deposited CoPi was varied.

6.2.3.3.3. Photo-assisted electrodeposition

A slightly modified PED method based on methods reported by Gamelin and Grätzel[101] as well as Ma and Durrant[102] was performed to functionalize 10% Mo:$BiVO_4$ photoanodes by CoPi. The electrochemical cell equipped with a RHE reference electrode, a Pt counter electrode and a 10% Mo:$BiVO_4$ thin film as working electrode described in chapter 6.4 (*vide infra*) was used for CoPi electrodeposition. The cell was filled with potassium phosphate solution (20 ml, 0.1 mol/l, Carl Roth) containing $Co(NO_3)_2$. (0.5 mmol/l, Aldrich). The working electrode was irradiated by white light (400-700 nm) of an intensity of 100 mW/cm² in frontside illumination mode. At the same time a bias potential of 1.2 V vs RHE was applied. The deposition was carried out without stirring and without IR-correction and was stopped after a certain amount of charge was transferred.

6.2.4. Fluorination of $BiVO_4$ and 10% Mo:$BiVO_4$ thin films

$BiVO_4$ and 10% Mo:$BiVO_4$ thin films on FTO-coated glass slides were prepared by the methods elucidated in chapter 6.2.2.1 and 6.2.2.2. The thin films were fluorinated by the solid-vapor reaction using the indirect gas flow method described in chapter 6.2.1.2 (Figure 6-1). A maximum of samples were fluorinated at once. The amounts of PVDF were varied from 1-3 g in increments of 1 g, the temperature was varied from 350 °C to 400 °C in increments of 10 K. A final heat treatment at 450 °C for 30 min in air was applied as finishing step.

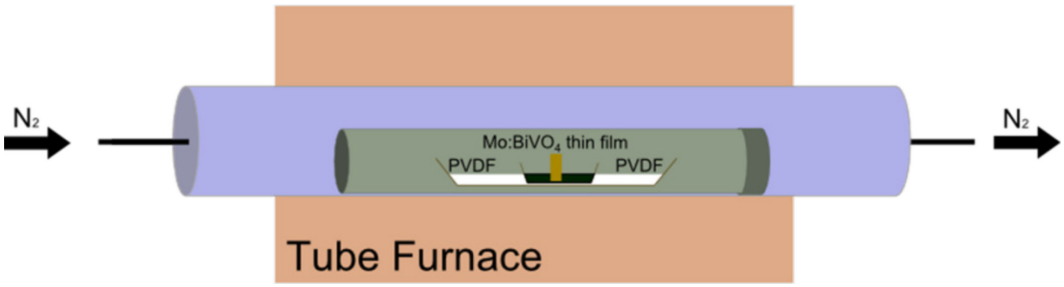

Figure 6-1. Scheme of the tube furnace used for fluorination of $BiVO_4$ and Mo:$BiVO_4$ thin films.

6.2.5. Synthesis of WO_3/$BiVO_4$ heterojunctions

6.2.5.1. Synthesis of WO_3 thin films

To fabricate WO_3 thin films on FTO substrates an adjusted sol-gel-approach based on the method reported by Brezesinski et al.[103] was used. WCl_6 (385 mg, 1 mmol, AlfaAesar) was dissolved in ethanol (1.5 ml, 98%, Carl Roth). After stirring for 4 h, the deep blue sol was used for dip coating of FTO substrates under controlled conditions (200 mm/min, 55% relative humidity, room temperature, 2 s dwell time). After evaporation of the solvent, as-coated thin films were aged at 100 °C for 12 h and subsequently calcined at 550 °C for 30 min in air (heating ramp: 0.5 K/min) resulting in colorless, transparent thin films.

6.2.5.2. Synthesis of WO_3/$BiVO_4$ and WO_3/Mo:$BiVO_4$ thin film heterojunctions

The synthesis of $BiVO_4$ and Mo:$BiVO_4$ thin films were performed according to chapter 6.2.2.1 and 6.2.2.2. Instead of FTO-coated glass slides WO_3 thin films deposited on FTO-coated glass slides were used as substrates.

6.2.5.3. Optimized synthesis of WO_3 thin films

A solution of 4.5 mg BASF Pluronic© F127 in 1.5 ml ethanol (1.5 ml, 98%) was prepared. Afer 10 min of ultrasonication (27 kHz, room temperature), WCl_6 (385 mg, 1 mmol) was added to the clear, colorless solution. After stirring for 4 h, the blue sol was used for dip coating FTO substrates under controlled conditions (100 mm/min, relative humidity 25 %, 30 °C, 8 s dwell time). After evaporation of the solvent the as-coated thin films were aged at 100 °C for 12 h and subsequently calcined at 550 °C for 30 min in air (heating ramp: 0.5 K/min) resulting in colorless, transparent thin films.

6.2.5.4. Optimized Synthesis of $WO_3/BiVO_4$ and WO_3/Mo:$BiVO_4$ thin film heterojunctions

The optimized synthesis of $WO_3/BiVO_4$ and WO_3/Mo:$BiVO_4$ thin film heterojunctions was performed according to the method described in chapter 6.2.3.1. Instead of 112.5 mg F127 only 3.0 mg were used. Optimized WO_3 thin films on FTO substrates were used as substrates.

6.3. Characterization methods

UV/Vis spectroscopy was carried out using a Perkin-Lambda 20 spectrometer operated in transmission mode. For diffuse reflectance UV/Vis spectroscopy a Jasco V670 with MgO as white standard was used.

The elemental composition of the thin films and of the reference powders was determined by inductively coupled plasma optical emission spectroscopy (ICP-OES) using a Varian ICP-OES 715 ES equipped with a radial argon plasma torch. For ICP-OES analysis either 10 mg of powder or 10 thin films were dissolved in HCl (1 mol/l) by ultrasonication.

The specific surface area of the thin films was determined by Kr physisorption (5-point BET measurement) using a Quantachrome Instrument ASI-C-11 operated at 77 K. For this purpose, $BiVO_4$ and Mo:$BiVO_4$ thin films were deposited on double-side polished silicon. For measurements 8-12 thin films were placed inside a measuring cell. Prior to every measurement, the samples were degassed under vacuum at 100 °C for at least 12 h.

X-ray diffraction of powder samples was carried out using a PANalytical X'Pert Pro powder diffractometer equipped with Cu-K_α radiation. The structural refinements were performed with the program *FullProf* Suite Version 2009 using a pseudo-Voigt function.[104,105] XRD of thin films using gracing incidence of the x-ray beam was performed using a Seifert XRD 3003 TT with Cu-K_α radiation equipped with a multilayer mirror or a Rigaku *SmartLab* 3kW with Cu-K_α radiation.

Scanning electron microscopy (SEM) was performed using a FEG-SEM SU8030 from Hitachi equipped with a 30 mm² silicon drift detector (SDD) from EDAX for energy dispersive X-ray spectroscopy (EDX).

Transmission electron microscopy (TEM), selective area electron diffraction (SAED) and TEM/EDX were performed using a FEI Tecnai G² 20 S-TWIN transmission electron microscope equipped with an EDAX r-TEM SUTW detector. Scanning transmission electron microscopy (STEM) was performed in cooperation with the group of Prof. Dr. Scheu at MPIE Duesseldorf using a FEI Titan Themis operated at 300 kV with aberration-corrected probe-forming lenses equipped with a QUANTAX EDX system by Bruker. All TEM samples were prepared as follows: a) chunks of $BiVO_4$ thin films were scraped off the substrate and transferred to a TEM grid, or b) a TEM lamella was cut out of a thin film using a FEI Helios Nanolab 600 focussed ion beam device (FIB).

Electron backscatter diffraction (EBSD) analyses were carried out using a Zeiss DSM 982 GEMINI equipped with an EDAX Hikari XP detector. Measurements were carried-out by Christoph Fahrenson from TU Berlin. No further sample treatment was performed prior to EBSD analysis.

6.4. Electrochemical characterization

Electrochemical measurements were carried out in a home-built PTFE electrochemical cell. Pictures of the EC cell are shown in Figure 6-2. As can be seen in Figure 6-2a, the $BiVO_4$ working electrode is contacted by conventional copper tape with conductive acrylic glue onto the sample holder made of stainless steel. The sample holder has a bore (∅ = 1 cm) onto which the working electrode is placed. For tightening the cell, a rubber ring is placed on the electrode before the body of the EC cell is mounted on top of the working electrode (Figure 6-2b). The working electrode area exposed to the electrolyte is 0.5 cm². The mounted cell is now ready to be equipped with electrolyte, reference electrode and counter electrode (3-electrode-setup, shown in Figure 6-2c). A wound Pt-wire and a reversible hydrogen reference electrode (RHE) from Gaskatel were used as counter and reference electrodes, respectively. The potential of the working electrode with respect to the reference electrode was controlled by a potentiostat (Biologic SP150). The photoanode was illuminated by a 150 W Xe-lamp by Lumatec Superlite, equipped with an UV cut-off filter and providing the spectral range between 400-700 nm. The lamp was mounted at a reproducible and constant distance of 5 cm from the $BiVO_4$ photoanode surface (Figure 6-2c and d). The light intensity at the electrode surface was adjusted to 100 mW/cm² using a light meter (Si-diode) from Extech. For this purpose, the working electrode was replaced by the Si diode of the light meter. Following this procedure ensured a reproducible light intensity of 100 mW/cm² at the electrode surface which is independent from any deviations for instance due to light reflection at the PTFE body of the cell.

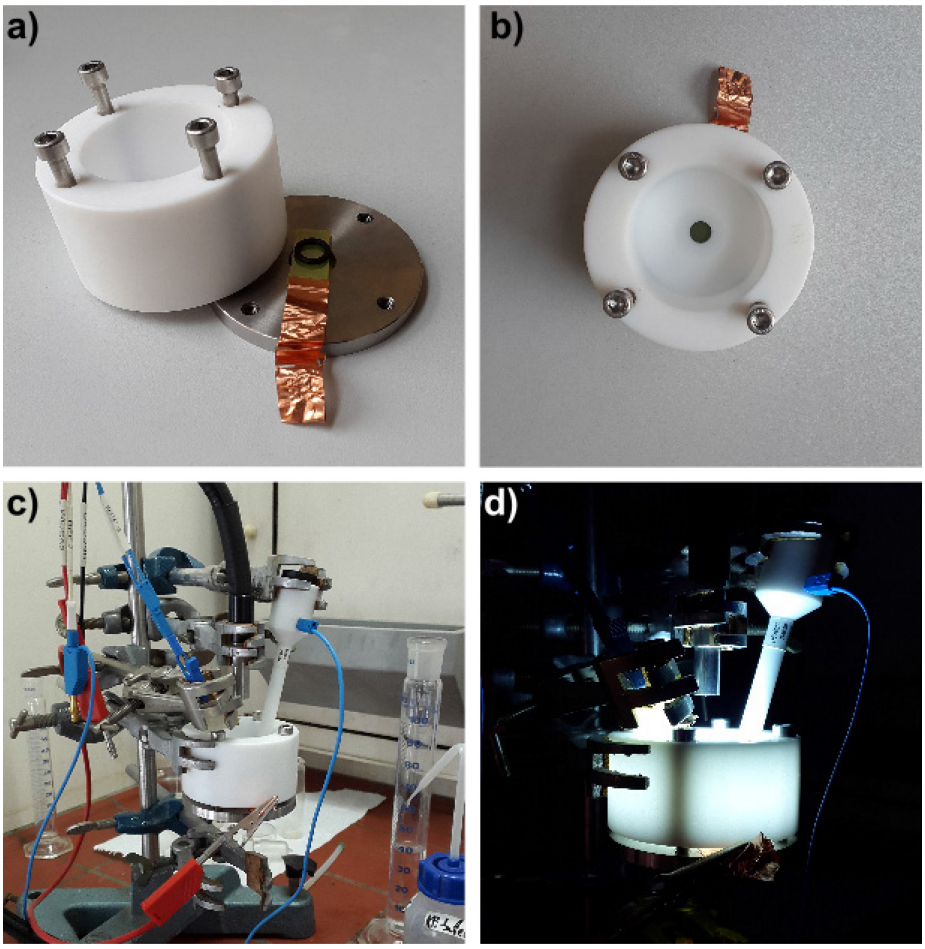

Figure 6-2. Photographs of the home-build photoelectrochemical cell. a) demounted cell, b) top-view of mounted cell, c) cell equipped with wired electrodes and installed light fiber of the light source in frontside illumination and d) cell under working conditions in frontside illumination mode.

Illumination was performed in two different modes which are illustrated schematically in Figure 6-3. In *frontside illumination*, the light source is mounted on top of the electrochemical cell. Hence, the illumination is incident from the $BiVO_4$-side. When *backside illumination* is applied, the light fiber is mounted underneath the EC cell. Hence, the illumination is incident from the FTO-side.

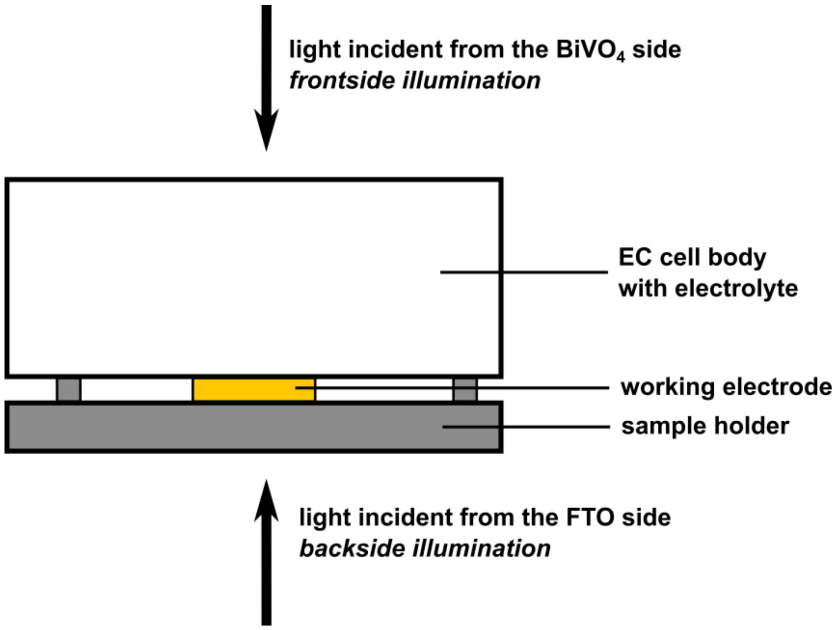

Figure 6-3. Schematic illustration of frontside and backside illumination.

All j-V measurements were conducted in potassium phosphate buffer (0.1 mol/l, KPi) at pH = 7.3 using a scan rate of 20 mV/s. Electronic IR-drop correction was used for all measurements unless it is stated otherwise. Throughout the whole thesis, the forward scan of the second cycle of the recorded cyclovoltammogramm is shown and referred to as j-V curve. Chopped-light measurements were obtained by switching the light on/off every 2.5 s corresponding to potential intervals of 50 mV.

For chronoamperometric measurements of the photocurrent transients a potential of 1.23 V vs. RHE was applied to the working electrode. Potassium phosphate buffer (0.1 mol/l, KPi) at pH 7.3 was used. The samples were illuminated with blue light (440 nm) at an intensity of 2 mW/cm².

Staircase potentio-electrochemical impedance spectroscopy (PEIS, Mott-Schottky) was carried out in potassium phosphate buffer (0.5 mol/l, KPi) at pH 7.3 scanning from anodic to cathodic potentials and using a sinusoidal modulation of 10 mV at frequencies of 500 Hz and 1 kHz. Estimation of the amount of free charge carriers in the thin film and evaluation of the flat band potential (V_{FB}) was performed by Mott-Schottky analysis (see chapter 5.5.3.2).

7. Fluorine-doped $BiVO_4$

Parts of this chapter have been published:

"Improved photoelectrochemical performance of bismuth vanadate by partial O/F-substitution"

B. Anke[1], M. Rohloff[1], M.G. Willinger, W. Hetaba, A. Fischer, M. Lerch, *Solid State Sciences* **2017**, *63*, 1-8.

[1] equally contributed

7.1. Introduction

As elucidated above there are many parameters influencing the photoelectrochemical performance of semiconductors with respect to water oxidation. For instance, the crystal structure of a semiconductor material like $BiVO_4$ is a very important factor to be considered. Among the three polymorphs of $BiVO_4$ (see chapter 5.4.2.1) the monoclinic phase shows the highest activity for water oxidation; a result which is ascribed to the smaller band gap of the monoclinic phase (2.4 eV) compared to the one of tetragonal zircon-type structure (3.1 eV).[67] Another way to influence the photoelectrochemical behavior of a semiconductor is to change its electronic structure by, for example, partial cation substitution. Molybdenum and tungsten were found to be suitable cationic dopants improving the photoelectrochemical properties due to enhancement of the amount of free charge carriers within the $BiVO_4$ material (*vide infra*).[25,28,32,106–109]

In contrast, anion doping is by far less explored. Anion-doping of TiO_2-based photocatalysts (e.g. with F^-, S^{2-}, N^{3-}) has been demonstrated to result in improved photocatalytic activity.[29,110–112] As shown by Junqi et al.,[30] among these non-metal

dopants, fluorine incorporated into the TiO_2 crystal lattice could reduce hole trapping at the TiO_2/electrolyte interface because of the strong electronegativity of surface bound fluorine. Hence, the photocatalytic performance regarding degradation of methyl orange was enhanced upon fluorine doping. The concept of fluorine incorporation has meanwhile been expanded to non-TiO_2-based semiconductor materials. Fluorination of Bi_2WO_6 reported by the group of Zhu enhanced photocatalytic activity for Rhodamine B degradation. This has mainly been ascribed to F ions serving as electron trapping sites and therefore enhancing interfacial electron-transfer rates by tightly holding trapped electrons which is beneficial for oxidative processes.[113,114]

However, only little efforts have been made to investigate anion doping in $BiVO_4$. Only very few reports on fluorinated $BiVO_4$ can be found in literature. Li et al. reported in 2013 a two-step hydrothermal fabrication method towards F-doped $BiVO_4$ (F:$BiVO_4$) microspheres.[115] It was found that fluorine incorporation results in an improvement of the optical absorption properties by shifting the absorption edge to higher wavelengths. Furthermore, it was shown that F-doped $BiVO_4$ spheres exhibited higher photocatalytic activity than undoped $BiVO_4$ regarding degradation of methylene blue under visible light irradiation. This was ascribed to the F-introduced electron traps leading to restrained recombination of photo-generated electron–hole pairs. In consideration of these results, fluorine incorporation into $BiVO_4$ seems to be a promising way to enhance its photocatalytic properties. However, such materials have not been studied in detail so far.

One possible route to fluorine incorporation into oxides involves polyvinylidene fluoride (PVDF) as fluoride source and was reported by Slater in 2002.[116] Heating PVDF in inert gas atmosphere results in the release of HF(g) according to Equation 7-1 which is used in-situ for solid-vapor fluorination reactions. Following Slaters method the HF-releasing polymer and the reactants must be mixed, which in terms of photo(electro-)catalytic applications might represent a big disadvantage because of potential carbon contamination of the final product.

Equation 7-1. Thermal decomposition of PVDF in inert gas atmosphere.

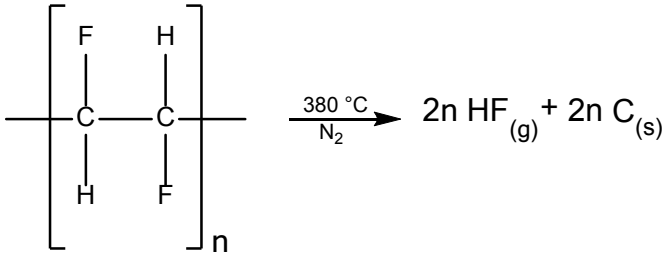

In this chapter, the application of a new process for the synthesis of F-containing $BiVO_4$ (F:$BiVO_4$) based on a solid-vapor reaction of $BiVO_4$ powder with $HF_{(g)}$ at ambient pressure and in inert gas atmosphere; process which was developed by Dipl.-Chem. Björn Anke under the supervision of Prof. Dr. Martin Lerch at the TU Berlin, is presented. Obtained powder samples were characterized extensively by means of chemical and structural analysis as well as by electron microscopy. Using electrophoretic deposition and taking advantage of the low-temperature sintering of $BiVO_4$, the as-synthesized powders could be processed to photoanodes, allowing the (photo-)electrochemical characterization of F:$BiVO_4$ regarding photoelectrochemical water oxidation. In addition, by comparison with undoped $BiVO_4$ photoanodes, the effect of F-doping on the PEC performance could be investigated.

7.2. Synthesis and characterization of F:$BiVO_4$

To synthesize $BiVO_4$ powder samples a precipitation method was used. Bi_2O_3 and $NaVO_3$ were each solved in concentrated HNO_3. After mixing both solutions, NaOH was added until the pH of the reaction mixture reached alkaline conditions. After stirring for 4 h, the raw $BiVO_4$ precipitate was washed several times and dried at 60 °C. Thereafter, a solid-vapor reaction using an indirect gas flow apparatus illustrated in Figure 7-1 was used to prepare F:$BiVO_4$. Loose powder of pure $BiVO_4$ was loaded in a small corundum boat, which in turn was placed inside a larger corundum boat containing varying amounts of PVDF. This arrangement advantageously prevents contact between the reagents in either solid or liquid form. The nested boats were then placed inside a corundum tube with one closed end and placed in a horizontal tube furnace with a gentle nitrogen gas flow. The

temperature was set to 380 °C for 24 h and after a final heating step in air at 450 °C for 30 min, the F:$BiVO_4$ powder was obtained. Note: For comparability the pristine $BiVO_4$ passed the same calcination procedure solely leaving out the PVDF.

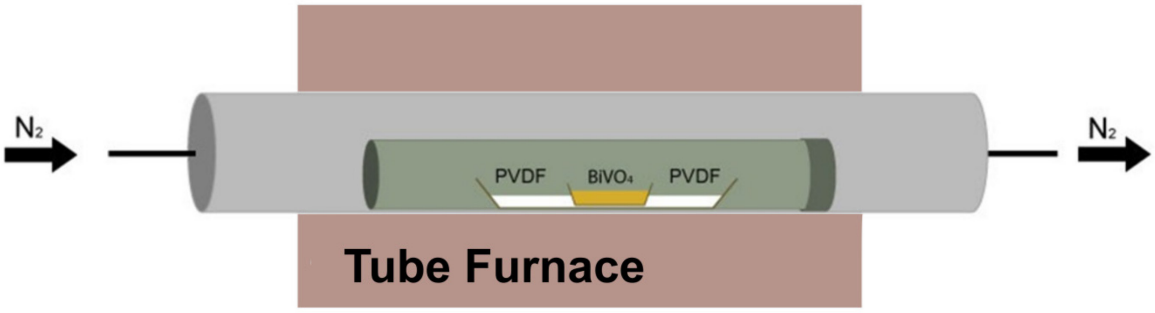

Figure 7-1. Sketch of fluorination apparatus. The inner corundum boat contains the sample to be fluorinated and the outer boat is filled with PVDF.

Following this synthesis procedure allowed the successful fabrication of F:$BiVO_4$ as phase-pure material. Quantitative chemical analysis by means of ICP-OES revealed a Bi:V ratio of 0.999:1. Hot gas extraction was used to measure the amount of oxygen within both powder samples. In pristine $BiVO_4$ the experimental value of 19.7 wt% is identical with the theoretical one. For F:$BiVO_4$ a slightly lower value of 18.2 wt% was obtained which is a reasonable result considering an O/F substitution.

Li et al. hypothesized that the substitution of O^{2-} anions by F^- anions could result in a decrease of the $BiVO_4$ lattice parameters and influence the chemical environment surrounding the Bi, V and O elements.[115] For a deeper understanding of the influence of fluorine incorporation into $BiVO_4$ on the crystal structure, X-ray diffraction experiments and structural refinements were performed by Dipl.-Chem. Björn Anke under supervision of Prof. Dr. Martin Lerch at the TU Berlin. Figure 7-2 depicts the X-ray powder diffraction patterns of pristine (a) and F containing (b) $BiVO_4$ along with the results of the Rietveld refinements. The structural refinements were started from the coordinates reported for the clinobisvanite structure of monoclinic $BiVO_4$ (space group I2/b (No. 15), JCPDS

14-0688).[117] The results clearly evidence that fluorine incorporation does not change the structure type. The Debye-Waller factors were not refined and set identically for both phases. Whereas the lattice parameters show some significant change, the positional parameters are very similar as can be seen e.g. by the resulting bond lengths for $BiVO_4$ and $F:BiVO_4$ given Table 7-1. The obtained bond lengths are more or less identical with no systematic trend. On the opposite, a look at the refined site occupation factors given in Table 7-3 is worth efforts. For pristine bismuth vanadate a small but significant underoccupation for bismuth and an overoccupation for vanadium are observed. In contrast, severe underoccupations for both cations resulted from Rietveld refinements of diffraction data of the F-containing material. Note: Unfortunately, the elements oxygen and fluorine cannot be distinguished using X-ray or even neutron diffraction methods. As also generally described by Fuertes,[118] Paulings second rule cannot be applied to predict a preferred position for fluorine because both anion positions are coordinated by three cations.

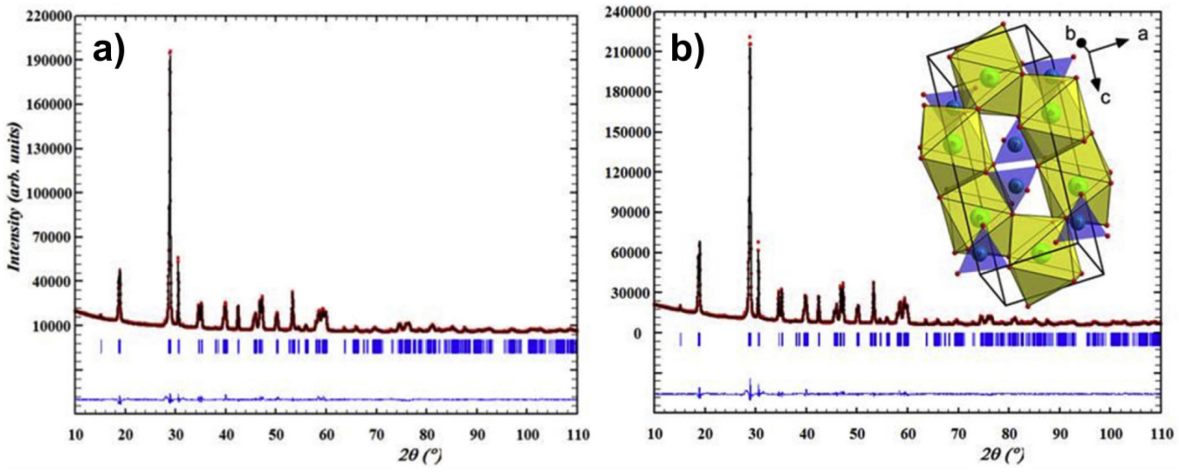

Figure 7-2. X-ray powder diffraction patterns of a) $BiVO_4$ and b) $F:BiVO_4$ with the results of the Rietveld refinements. Inset: Unit cell of $F:BiVO_4$ and polyhedral representation of the crystal structure. $Bi(O,F)_8$ polyhedra are drawn in yellow, $V(O,F)_4$ tetraheda are shown in blue. Reproduced from: Anke et al. Improved photoelectrochemical performance of bismuth vanadate by partial O/F-substitution. Solid State Sciences 2017, 63, 1-8. Copyright © 2017 Elsevier Masson SAS. All rights reserved.

Table 7-1. Determined Bi/V-(O,F) bond lengths in $BiVO_4$ and F:$BiVO_4$.

Bonds	$BiVO_4$ bond lengths (Å)	F:$BiVO_4$ bond lengths (Å)	Difference (Å)
Bi-O1	2.409(9)	2.387(9)	- 0.02
Bi-O1	2.458(9)	2.412(9)	- 0.05
Bi-O2	2.557(8)	2.544(7)	- 0.01
Bi-O2	2.645(8)	2.703(6)	+ 0.06
V-O1	1.669(8)	1.723(9)	+ 0.05
V-O2	1.632(8)	1.599(8)	- 0.03

Table 7-2. Refined structural parameters of $BiVO_4$ in comparison to F:$BiVO_4$.

Composition	$BiVO_4$	F:$BiVO_4$
Crystal system Space group	monoclinic *I2/b* (No. 15)	
Formular units	Z = 4	
Lattice parameters	a = 5.1787(5) Å	a = 5.1863(4) Å
	b = 5.1042(5) Å	b = 5.1003(4) Å
	c = 11.6953(11) Å	c = 11.6998(8) Å
	γ = 90.260(2) °	γ = 90.3082(12) °
Unit cell volume	V = 309.16(5) $Å^3$	V = 309.47(5) $Å^3$
Calculated density	6.962 g/cm^3	See discussion of the defect models in the text
Meas. density	6.89(2) g/cm^3	6.68(2) g/cm^3
R_{wp}	0.0300	0.0358
R_{Bragg}	0.0301	0.0421
R_{exp}	0.0101	0.0097
S	2.97	3.69

For a deeper understanding of the fluorine-containing material a closer look at possible mechanisms of fluorine incorporation is helpful. Besides fluorine incorporation on interstitial sites or partial reduction of vanadium, the most reasonable defect model is the formation of cation vacancies which can be expressed according to the Kröger-Vink notation[119] given in Equation 7-2. As can be seen, the introduction of HF into the $BiVO_4$ lattice results in the formation of a threefold negatively charged vacancy at a Bi site (V_{Bi}'''), a fivefold negatively charged vacancy at a V site (V_V''''''), eight onefold positively charged fluorine ions occupying oxygen sites ($8F_O^\bullet$) and the release of water.

Equation 7-2. Kröger-Vink notation of the formation of cation vacancies as a possible defect model for F:$BiVO_4$.

$$Bi_{Bi}^X + V_V^X + 8O_O^X + 8HF = V_{Bi}''' + V_V'''''' + 8F_O^\bullet + BiVO_4(sf) + 4H_2O$$

Taking into consideration the experimentally determined oxygen content of 18.2 wt%, a chemical formula of $Bi_{0.94}V_{0.94}O_{3.54}F_{0.46}$ can be calculated. The corresponding theoretical density calculated using the volume from the Rietveld refinement accounts for 6.66 g/cm³. The experimentally determined density of 6.68 g/cm³ for the F-containing material is in excellent agreement with the calculated value. Furthermore, the presence of cation vacancies is supported by the strong underoccupation of the cation positions, as determined from the Rietveld refinement (see Table 7-3). In addition, the calculated chemical composition of $Bi_{0.94}V_{0.94}O_{3.54}F_{0.46}$ is in good agreement with the composition coming from the refined site occupation factors $Bi_{0.93}V_{0.92}(O,F)_4$.

Table 7-3. Structural parameters for $BiVO_4$ and F:$BiVO_4$.

$BiVO_4$	Wyckoff	x	y	z	B_{iso}	s.o.f.
Bi	4e	0	¼	0.63277(10)	0.9	0.960(4)
V	4e	0	¼	0.1297(4)	0.6	1.014(4)
O1	8f	0.1349(18)	0.4906(15)	0.2061(8)	1.2	1
O2	8f	0.2680(13)	0.3729(18)	0.4477(8)	1.2	1
F:$BiVO_4$	Wyckoff	x	y	z	B_{iso}	s.o.f.
Bi	4e	0	¼	0.63283(10)	0.9	0.930(6)
V	4e	0	¼	0.1302(4)	0.6	0.922(6)
O1	8f	0.1444(18)	0.4969(14)	0.2082(8)	1.2	1
O2	8f	0.2733(51)	0.3765(18)	0.4438(7)	1.2	1

In consideration of the previous results, there are strong indications for the presence of cation vacancies as major defect in fluorine-containing bismuth vanadate. It should be mentioned that large concentrations of cation vacancies are also reported for other $BiVO_4$-based phases. For example, partial substitution of V^{5+} by Mo^{6+} leads to the formation of phases of the $Bi_{1-x/3}Mo_xV_{1-x}O_4$ type.[120]

In addition to the crystal structure, semiconductors' optical absorption properties play an important role for the photocatalytic behavior. For this reason, the influence of fluorine incorporation into $BiVO_4$ on the optical absorption properties was investigated by means of UV/Vis spectroscopy in diffuse reflectance mode. Absorbance spectra were calculated from the measured diffuse reflectance data using the Kubelka-Munk function (Equation 7-3):

Equation 7-3. Kubelka-Munk function.

$$(R) = \frac{(1-R)^2}{2R} = \varepsilon c \frac{1}{s}$$

Where R is the reflectance, ε is the absorption coefficient, c the concentration of absorbing species and s the scattering coefficient. Application of the Tauc method[121] allowed an estimation of the optical band gap according to Equation 7-4:

Equation 7-4. Tauc equation.

$$[F(R)h\nu]^{\frac{1}{n}} = A(h\nu - E_g)$$

with *F(R)* the Kubelka-Munk function, $h\nu$ the photon energy, E_g the optical band gap energy and *A* the proportionality constant.[122] The value of the exponent *n* denotes the nature of the transition. For $BiVO_4$ a direct transition is present, therefore n is set to ½.[123,124]

Resulting Tauc plots for $BiVO_4$ and F:$BiVO_4$ powder samples based on diffuse reflectance spectroscopy are shown in Figure 7-3. By extrapolation of the linear part of the Tauc plots the optical band gap can be estimated. For the pristine $BiVO_4$, a band gap 2.45 eV was estimated. In good agreement with the orange color of the F:$BiVO_4$, the absorption onset for the F:$BiVO_4$ sample is red-shifted resulting in an estimated band gap of 2.38 eV. This band gap reduction is beneficial in terms of light absorption as a bigger portion of the visible spectrum is absorbed by the F:$BiVO_4$.

Note: Although often applied in literature reports, the Tauc method is principally not appropriate for band gap determination of crystalline semiconductors.[125] However, it also allows a rough estimation of the optical band gap of a material.

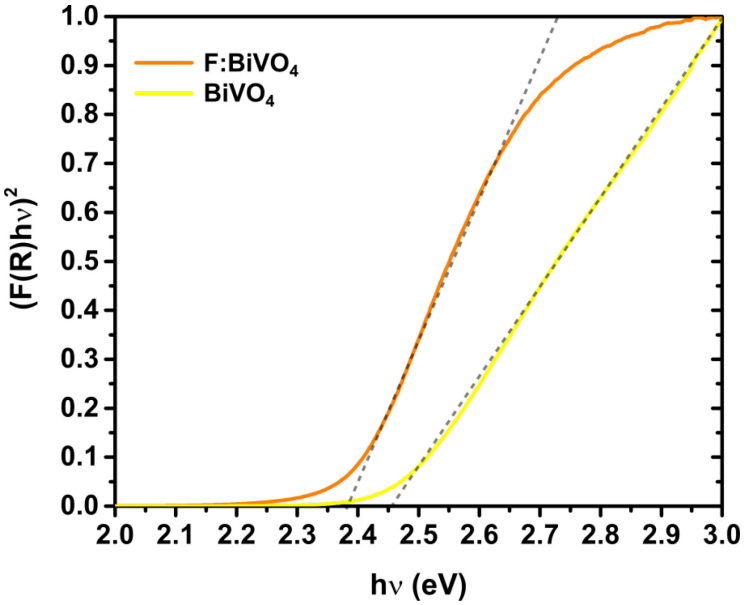

Figure 7-3. Tauc plot for $BiVO_4$ and F:$BiVO_4$ based on UV/Vis diffuse reflectance spectroscopy. Reproduced from: Anke et al. Improved photoelectrochemical performance of bismuth vanadate by partial O/F-substitution. Solid State Sciences 2017, 63, 1-8. Copyright © 2017 Elsevier Masson SAS. All rights reserved.

Electron microscopy methods were applied to gain information about the microstructure of F:$BiVO_4$ and the distribution of fluorine within the material. TEM investigations were carried out by Dr. Walid Hetaba under supervision of Dr. Marc Willinger from the Department of Inorganic Chemistry of the Fritz Haber Institute of the Max Planck Society. Figure 7-4a depicts a bright-field transmission electron microscopy overview image of the fluorine-containing sample while in Figure 7-4b a high-resolution TEM (HRTEM) image is shown. From Figure 7-4b the crystalline structure of the particles is evident. Fast-Fourier-transformation (FFT) of this region shows spatial frequencies due to the lattice fringes, which can be assigned to the monoclinic $BiVO_4$ structure.

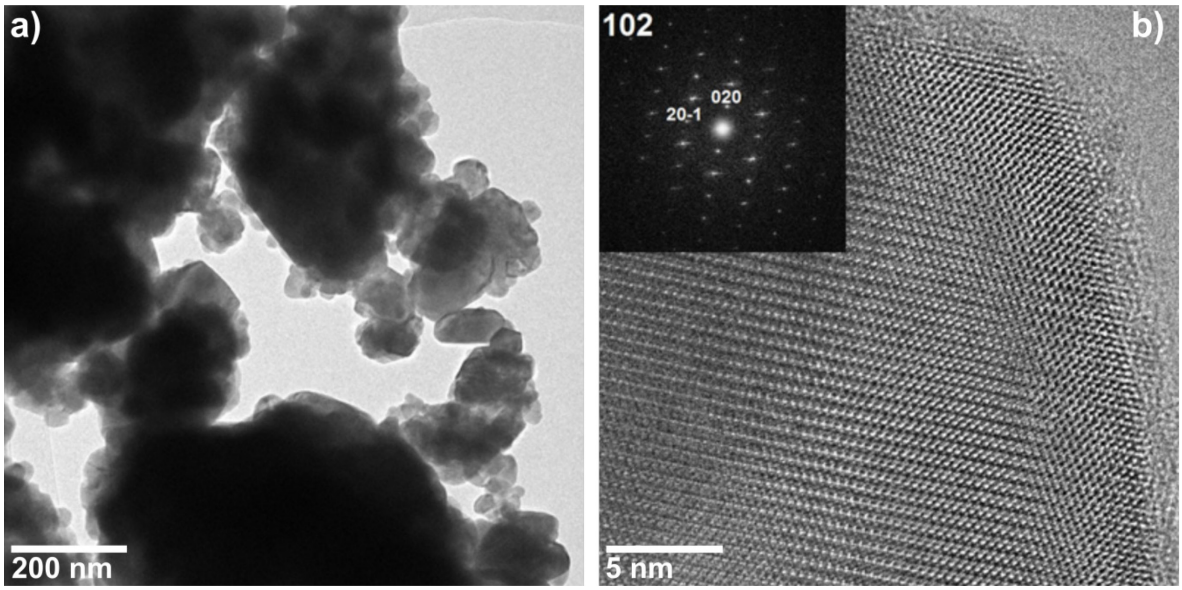

Figure 7-4. TEM investigations of F:$BiVO_4$. a) bright field TEM overview image of F:$BiVO_4$ and b) high resolution TEM image with inset showing the corresponding FFT. Spots due to the (020) and (20-1) lattice planes of the [102] oriented particle are labelled. Reproduced from: Anke et al. Improved photoelectrochemical performance of bismuth vanadate by partial O/F-substitution. Solid State Sciences 2017, 63, 1-8. Copyright © 2017 Elsevier Masson SAS. All rights reserved.

Figure 7-5 presents a high angle annular dark field overview image with the corresponding EDX maps of F (yellow), Bi (green) and V (red), revealing a homogeneous distribution of these elements in the material. Due to the limited energy resolution of the EDX detector, the oxygen K (around 530 eV) and vanadium L (around 518 eV) ionization edges overlap to a single peak and cannot be distinguished. For this reason, the oxygen content could not be determined by EDX. The vanadium content was quantified using the vanadium K-edge. A homogeneous distribution of fluorine in the material was confirmed by elemental quantification performed in the SEM and TEM at different magnifications. According to the quantification results, the samples contain equal amounts of Bi and V. Due to the low amount of fluorine present within the sample, unfortunately, precise quantification of the fluorine content was not possible. A fluorine content of ~ 5at% was estimated based on EDX data.

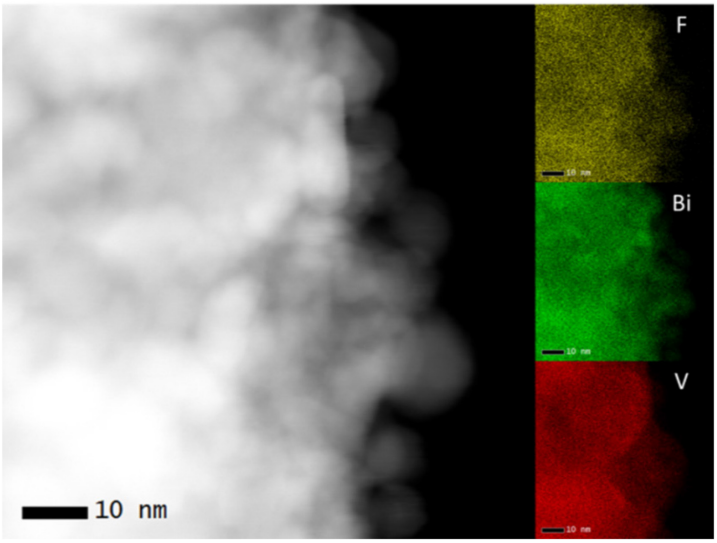

Figure 7-5. High angle annular dark field image of F:$BiVO_4$ (left) with corresponding EDX maps of F (yellow), Bi (green) and V (red) (right from top to bottom). Reproduced from: Anke et al. Improved photoelectrochemical performance of bismuth vanadate by partial O/F-substitution. Solid State Sciences 2017, 63, 1-8. Copyright © 2017 Elsevier Masson SAS. All rights reserved.

To sum-up briefly, by application of a new, clean and simple solid-vapor-reaction a F:$BiVO_4$ powder was synthesized. Detailed structural analysis by Rietveld refinements of powder diffraction data revealed the monoclinic scheelite structure to remain upon fluorine incorporation. Furthermore, it was shown that incorporation of fluorine mainly leads to the formation of cation vacancies. UV/Vis spectroscopy revealed the optical band gap to be reduced from 2.45 eV for pristine $BiVO_4$ to 2.38 eV for F:$BiVO_4$. HR-TEM/EDX analysis confirmed the presence of fluorine within the material and proved its homogeneous distribution. In the following section, the as-synthesized $BiVO_4$ and F:$BiVO_4$ powder samples are used for electrode fabrication and investigation of their PEC performance regarding water oxidation.

7.3. Photoelectrochemical investigations of F:$BiVO_4$

To enable (photo-)electrochemical investigations, fabrication of electrodes out of the pre-synthesized powders is necessary. For this approach, an electrophoretic deposition (EPD) method based on the work from Abe et al. was used.[96] The synthesis procedure is

illustrated schematically in Figure 7-6. Via electrophoretic deposition from a dispersion of powder samples of $BiVO_4$ and F:$BiVO_4$, particles are deposited onto an FTO substrate followed by a post-treatment/calcination to interconnect the particles with each other. The single synthesis steps have been followed by SEM and by screening of the PEC performance of the resulting photoanodes after each step regarding water oxidation. Results for a calcination temperature of 450 °C are shown in Figure 7-7, results for electrodes calcined at 550 °C are shown in Figure 7-8.

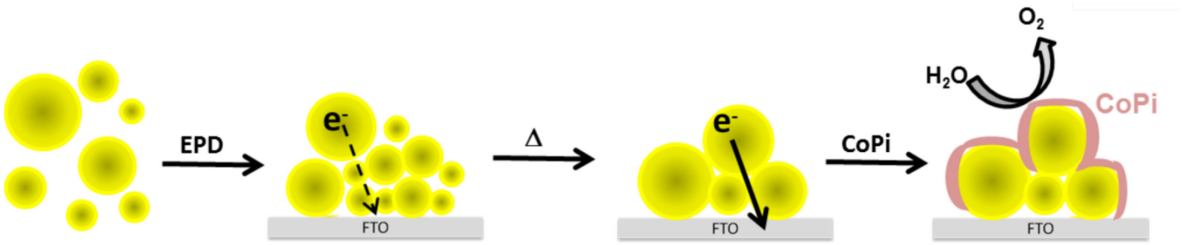

Figure 7-6. Illustration of synthesis steps for the preparation of electrodes out of the pre-synthesized $BiVO_4$ and F:$BiVO_4$ powders.

In a first step, the pristine and the F-containing $BiVO_4$ powder samples were ball-milled to provide small particle sizes for both powders. After that, the milled samples were dispersed in iodine-containing acetone. Two fluorine-doped tin oxide coated glass slides (FTO) were immersed parallel in the dispersion. By application of a potential of 10 V for 5 min, particles were deposited onto the substrate. This procedure was repeated once. As can be seen in Figure 7-7a and Figure 7-8a, the as-prepared electrodes consist of a loosely packed particle layer of ~5 µm thickness which is homogeneously spread over the entire FTO substrate. To establish a good particle connection, the as-prepared electrodes were calcined at 450 °C or 550 °C for 30 min in air (Figure 7-7b and Figure 7-8b). As can be seen, the thermal treatment comes along with material densification/sintering. After the thermal treatment, the electrodes consist of a denser layer of bigger, interconnected particles due to sintering of the deposited $BiVO_4$ and F:$BiVO_4$ particles, respectively. In Table 7-4 the sizes of the deposited particles for $BiVO_4$ and F:$BiVO_4$ electrodes after the thermal treatment are summarized. There is no significant difference in particle sizes of both electrodes for one calcination temperature accounting for an average particle diameter of 418 ±32 µm and

0.448 ±29 µm at a calcination temperature of 450 °C and 0.844 ±42 µm and 0.863 ±58 µm at 550 °C, respectively, for the pristine $BiVO_4$ and its fluorine-containing analogue. Material densification is more pronounced at a calcination temperature of 550 °C which results in bigger average particle sizes for both samples.

Table 7-4. Particle sizes after thermal treatment for F:$BiVO_4$ and $BiVO_4$ photoanodes.

Calcination temperature	Average particle diameter (µm)	
	$BiVO_4$	F:$BiVO_4$
450 °C	0.418 ±32	0.448 ±29
550 °C	0.844 ±42	0.863 ±58

After calcination, the photoanodes can be used for electrochemical investigations as well as for deposition of cobalt phosphate water oxidation catalyst (CoPi) first reported by Kanan and Nocera (Figure 7-7c and Figure 7-8c).[51,52] As can be seen, the particle surface of both electrodes is homogeneously covered by a thin layer after CoPi deposition.

As shown by the PEC performance screening for F:$BiVO_4$ electrodes calcined at 450 °C in Figure 7-7d, and F:$BiVO_4$ electrodes calcined at 550 °C in Figure 7-8, the photocurrent for the as-prepared F:$BiVO_4$ electrode is rather low accounting for 0.05 mA/cm^2 at 1.23 V vs. RHE for the 450 °C sample and the 550 °C sample.

After the calcination step, generally higher photocurrents are obtained accounting for 0.32 mA/cm^2 at an applied potential of 1.23 V vs. RHE for the F:$BiVO_4$ photoanode calcined at 450 °C and 0.39 mA/cm² for the sample calcined at 550 °C. Sintering of the particles improves ohmic contact within the film. Hence, it is beneficial for the overall charge carrier transport properties and photoelectrochemical behavior, respectively.

After deposition of CoPi water oxidation catalyst photocurrents were further enhanced and photocurrents as high as 0.64 mA/cm^2 and 1.51 mA/cm^2 at 1.23 V vs. RHE were yielded for the 450 °C and the 550 °C F:$BiVO_4$ photoanodes, respectively. Additional deposition of a layer of CoPi on the respective photoanodes further enhances PEC performance by improving the water oxidation kinetics and by suppression of possible surface

recombination of the photo-generated charge carriers.[102,126] Photocurrents as high as 0.64 mA/cm^2 at 1.23 V vs. RHE were yielded for the 450 °C treated F:$BiVO_4$ photoanode.

Note: In order to ensure that the fluorine content of the material did not change during the described procedures, hot gas extraction measurements were performed after the milling step and after the heat treatment steps at 450 °C and 550 °C for 30 min, respectively, for the F:$BiVO_4$ powders. The determined oxygen contents of 18.2 wt% are the same for all samples. This indicates good thermal stability of the fluorine-containing material and proves the legitimacy of the calcination step.

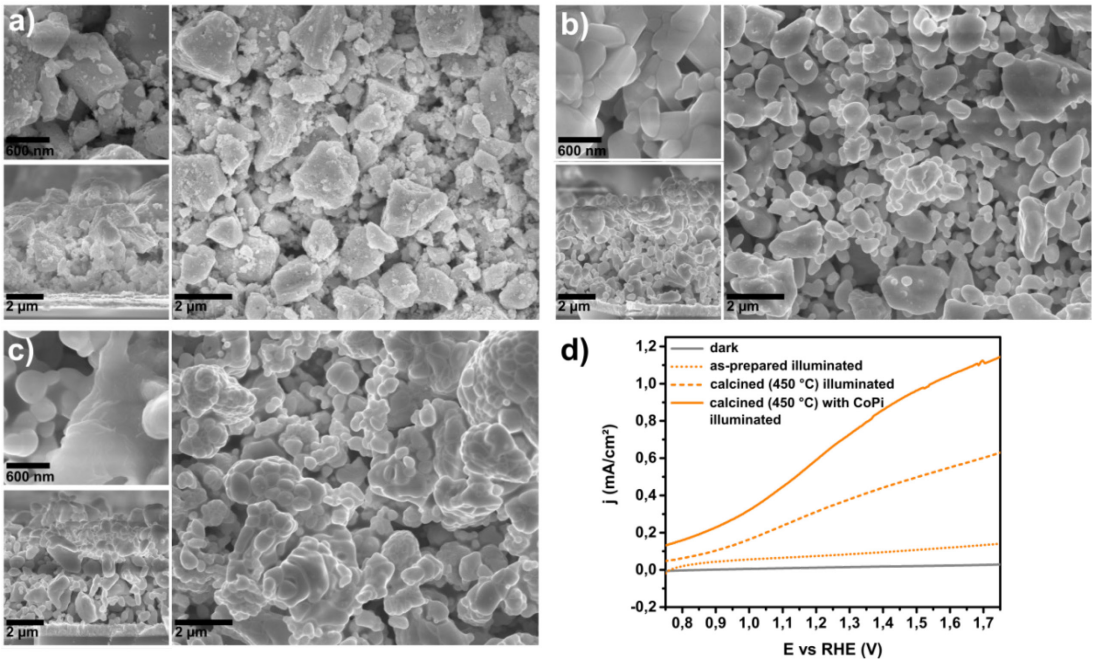

Figure 7-7. Illustration of electrode fabrication process: SEM top-view and cross-sectional images of a) as-prepared electrodes, b) calcined electrodes (450 °C, air), c) calcined electrodes with deposited CoPi co-catalyst layer and d) j-V-curves of as-prepared F:$BiVO_4$, calcined F:$BiVO_4$ and F:$BiVO_4$ with a deposited CoPi layer (0.1 M KPi buffer, pH 7.3, 20 mV/s, 150 W Xe-lamp, 400-700 nm, 100 mW/cm², backside illumination).

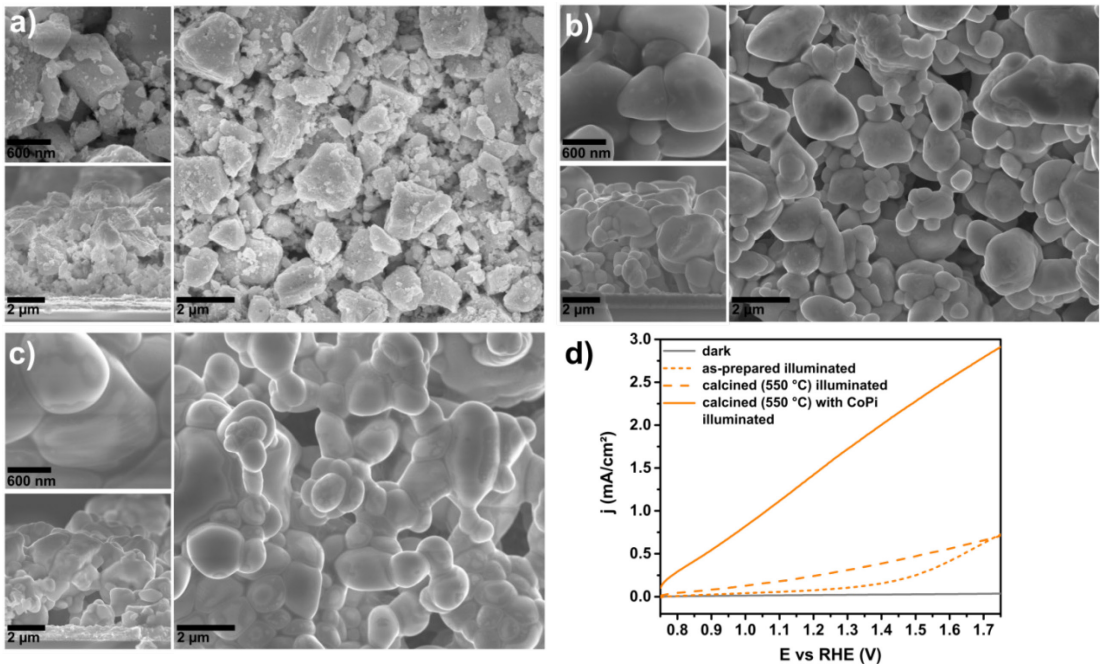

Figure 7-8. Illustration of electrode fabrication process: SEM top-view and cross-sectional images of a) as-prepared electrodes, b) calcined electrodes (550 °C, air), c) calcined electrodes with deposited CoPi co-catalyst layer and d) j-V-curves of as-prepared F:$BiVO_4$, calcined F:$BiVO_4$ and F:$BiVO_4$ with a deposited CoPi layer (0.1 M KPi buffer, pH 7.3, 20 mV/s, 150 W Xe-lamp, 400-700 nm, 100 mW/cm², backside illumination).

The effect of fluorine incorporation on the performance of $BiVO_4$ concerning photoelectrochemical water oxidation was investigated by comparing the performance of F:$BiVO_4$ with pristine $BiVO_4$ photoanodes prepared under the same conditions and with comparable amounts of deposited powder (3.5 mg per electrode, ~ 1.2 mg/cm²). Figure 7-9 shows j-V curves for corresponding electrodes calcined at 450 °C and 550 °C without and with CoPi water oxidation catalyst deposited onto the surface together with corresponding applied bias photon-to-current efficiency (ABPE) curves. All photocurrents were obtained by application of backside illumination of white light (wavelength range 400-700 nm) at an intensity of 100 mW/cm². Frontside illumination resulted in very low PEC performance. This can be assigned to the materials slow electron transport as well as to trap-limited charge transport through the electrode material when frontside illumination is used (exemplary j-V curves obtained in frontside illumination are given in the Appendix, chaper 12.1.1.1).[22,127] A summary of yielded photocurrents at a reference potential of 1.23 V vs RHE and the corresponding ABPE maxima is provided by Table 7-5.

As can be seen for the samples calcined at 450 °C (Figure 7-9a), a significant increase in photocurrent is observed for the F-containing electrodes with and without CoPi deposited accounting for 0.14 mA/cm² and 0.32 mA/cm² for the $BiVO_4$ and F:$BiVO_4$ photoanodes before CoPi deposition and 0.44 mA/cm² and 0.64 mA/cm² after CoPi deposition, respectively; all values given for an applied potential of 1.23 V vs RHE. Raising the calcination temperature to 550 °C only has a slight positive impact on yielded photocurrents for the non-modified photoanodes accounting for 0.15 mA/cm² for the pristine $BiVO_4$ sample and 0.39 mA/cm² for the F:$BiVO_4$ sample at 1.23 V vs RHE. However, photocurrents of the CoPi-modified electrodes are drastically enhanced leading to maximum photocurrents of 0.92 mA/cm² for the CoPi-modified $BiVO_4$ photoanode and 1.51 mA/cm² for the CoPi-modified fluorine-containing photoanode at an applied potential of 1.23 V vs RHE. In agreement with the j-V curves, the ABPE curves (applied-bias-to-photocurrent efficiency) reveal same trends. A maximum ABPE of 0.19 % is achieved for the CoPi-modified F:$BiVO_4$ sample calcined at 550°C.

Note: In all cases the water oxidation photocurrents are low compared to the highest reported photocurrent values for $BiVO_4$ photoanodes (~4.5-5.0 mA/cm^2 at 1.23 V vs RHE)[24,26,128,129] but are fully in line with photocurrents achieved for EPD-processed $BiVO_4$ electrodes (about 0.6 mA/cm^2).[130,131]

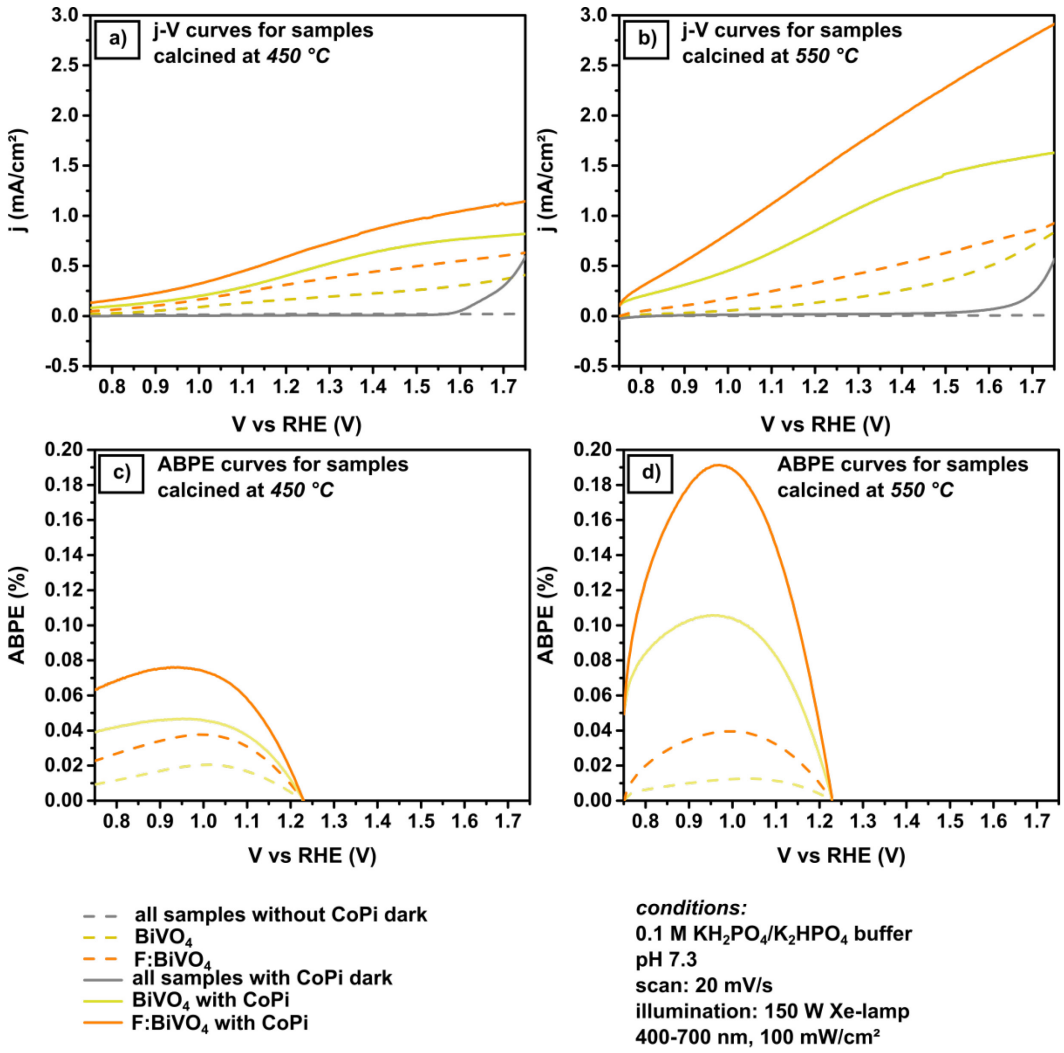

Figure 7-9. j-V curves of $BiVO_4$ and F:$BiVO_4$ photoanodes a) calcined at 450 °C, b) calcined at 550 °C and corresponding ABPE curves for $BiVO_4$ and F:$BiVO_4$ photoanodes c) calcined at 450 °C and d) calcined at 550 °C.

Table 7-5. Summary of obtained photocurrents at 1.23 V vs RHE and ABPE maxima of $BiVO_4$ and F:$BiVO_4$ photoanodes calcined at 450 °C and 550 °C.

Calcination temperature	*j at 1.23 V vs RHE (mA/cm²)*				*ABPE (%)*			
	$BiVO_4$		F:$BiVO_4$		$BiVO_4$		F:$BiVO_4$	
	w/o CoPi	With CoPi	w/o CoPi	With CoPi	w/o CoPi	With CoPi	w/o CoPi	With CoPi
450 °C	0.14	0.44	0.32	0.64	0.02	0.05	0.04	0.08
550 °C	0.15	0.92	0.39	1.51	0.01	0.11	0.04	0.19

Rise of the calcination temperature from 450 °C to 550 °C results in advanced sintering of the electrode particles. Accordingly, less particle boundaries which act as recombination and charge scattering sites are present at and therefore charge carrier transport properties are improved. Hence, the overall PEC performance is improved. Furthermore, in all cases the fluorine containing samples outperform their pristine counterparts which in first approximation can be assigned to the improved optical absorption properties of the F-containing material (*vide supra*) as well as to improved charge carrier transport properties due to F-doping (*vide infra*).

In order to gain deeper insights into the origin of the improvement of photoelectrochemical performance of F:$BiVO_4$, photocurrent transient measurements were carried out and obtained transients were analyzed according to the phenomenological approach described in chapter 5.5.3.3. Photocurrent transients for $BiVO_4$ and F:$BiVO_4$ photoanodes calcined at 450 °C and 550 °C without CoPi and with CoPi deposited are presented in Figure 7-10; results of the transient analysis are summarized in Table 7-6.

As can be seen in Figure 7-10, the photocurrent transients exhibit photocurrent spikes when the light is switched on followed by a decrease/decay of initial photocurrent. When switching-off the light a little cathodic photocurrent overshoot is observed. The overshoot is generally more pronounced for the samples calcined at 550 °C.

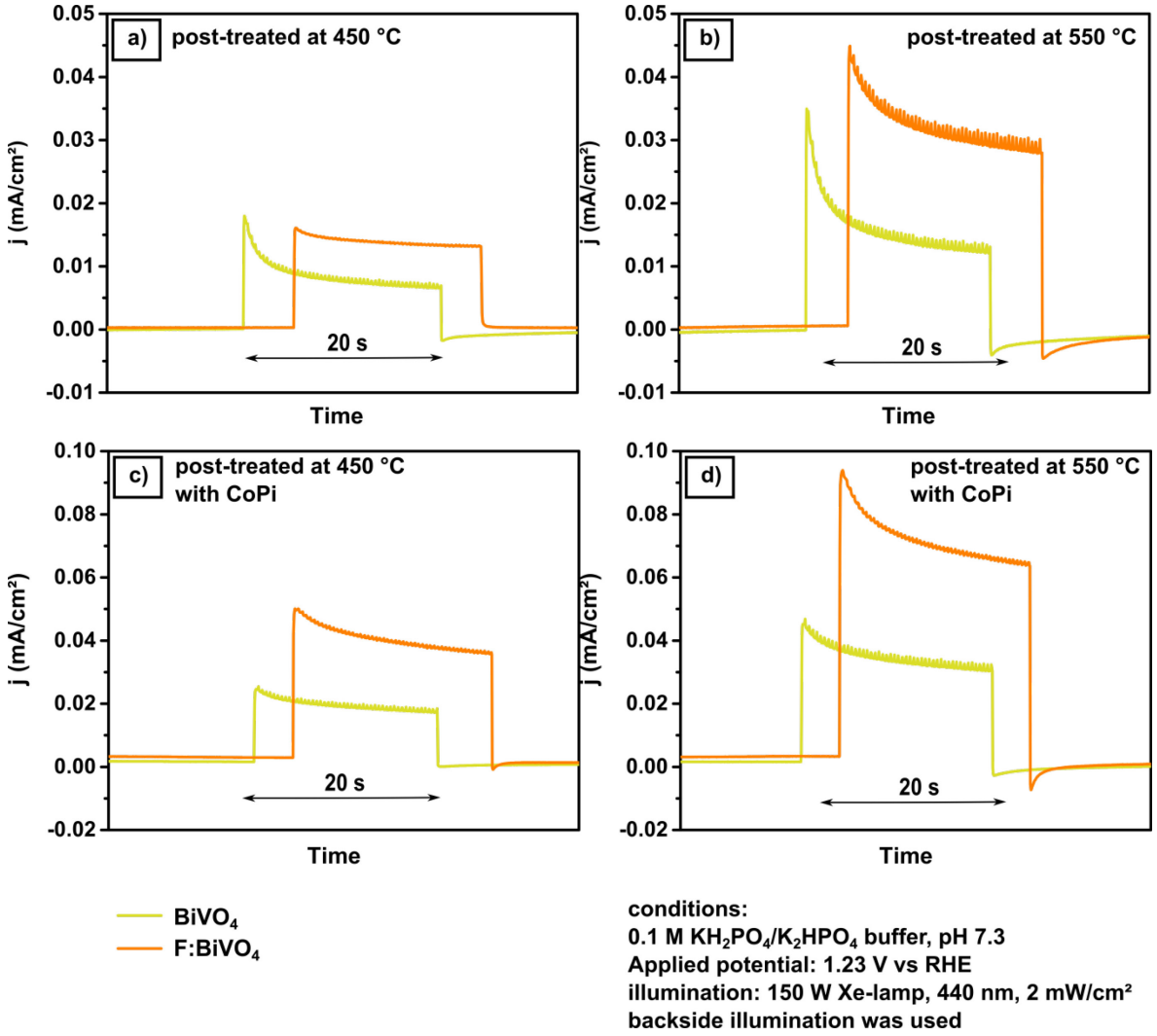

Figure 7-10. Photocurrent transients for $BiVO_4$ and F:$BiVO_4$ photoanodes calcined at 450 °C and 550 °C without CoPi and with CoPi deposited.

Analysis of the photocurrent transients for the samples without CoPi deposited reveals interesting insights into the water oxidation kinetics of the electrodes. For the $BiVO_4$ and the F:$BiVO_4$ samples calcined at 450 °C nearly identical hole transfer rates k_{trans} are observed accounting for 0.223 s^{-1} and 0.248 s^{-1}, respectively. However, surface hole recombination rates k_{rec} are significantly different. k_{rec} of the F-containing $BiVO_4$ sample is much smaller accounting for 0.044 s^{-1} compared to the k_{rec} of the pristine $BiVO_4$ sample accounting for 0.299 s^{-1}. In consequence, the hole transfer efficiency $\eta_{transfer}$ of F:$BiVO_4$ is

considerably higher compared to the pristine $BiVO_4$ photoanode accounting for 0.849 and 0.427, respectively.

Having a look at corresponding samples calcined at 550 °C, the overall trend is similar with the samples calcined at 450 °C in terms of smaller surface recombination rates for the F:$BiVO_4$ sample and in turn significantly higher hole transfer efficiencies. The surface hole recombination rate for the F:$BiVO_4$ of 0.097 s^{-1} is twice as high as for the corresponding sample calcined at 450 °C. As a result, the $\eta_{transfer}$ for the F:$BiVO_4$ is smaller accounting for 0.694 when electrodes are calcined at 550 °C. $\eta_{transfer}$ for $BiVO_4$ samples calcined at 450 °C and 550 °C are more or less identical. Furthermore, k_{trans} values for F:$BiVO_4$ are smaller compared to pristine $BiVO_4$ when calcining at 550 °C accounting for 0.248 s^{-1} for the pristine $BiVO_4$ and 0.219 s^{-1} for the F:$BiVO_4$ sample, respectively.

Surface hole recombination rates are very small for the F-containing $BiVO_4$ photoanodes. These findings are in good agreement with literature reports assigning the improved PEC performance of F:$BiVO_4$ to the high electronegativity of fluorine. According to DFT calculations by Wen et al., adsorption of water molecules is facilitated at the fluorinated $BiVO_4$ surface due to the formation of strong F-H bonds.[132] According to Li et al., fluorination of $BiVO_4$ results in F-related electron traps leading to restrained recombination of photo-generated electron–hole pairs at the surface.[115]

Raising the calcination temperature from 450 °C to 550 °C increases the overall PEC performance of both, the pristine $BiVO_4$ and the F:$BiVO_4$ samples, in terms of observed photocurrents. However, from a kinetic point of view, raising the calcination temperature is related with reduced hole transfer rates and slightly increased surface hole recombination rates. Most probably, the small trade-off in kinetic behavior of the electrode surfaces is reimbursed by a strong enhancement of charge transport due to advanced material densification.

Table 7-6. Summary of results of the photocurrent transient analysis for $BiVO_4$ and F:$BiVO_4$ photoanodes calcined at 450 °C and 550 °C without CoPi and with CoPi deposited.

with or w/o CoPi	Sample calcination temperature	current densities (mA/cm^2)	$\eta_{transfer}$	rate constants (s^{-1})
Without CoPi	$BiVO_4$ 450 °C	$j_{ini} = 0.018$	0.427	$k_{trans} = 0.223$
		$j_{ss} = 0.008$		$k_{rec} = 0.299$
	F:$BiVO_4$ 450 °C	$j_{ini} = 0.016$	0.849	$k_{trans} = 0.246$
		$j_{ss} = 0.014$		$k_{rec} = 0.044$
	$BiVO_4$ 550 °C	$j_{ini} = 0.035$	0.432	$k_{trans} = 0.248$
		$j_{ss} = 0.015$		$k_{rec} = 0.326$
	F:$BIVO_4$ 550 °C	$j_{ini} = 0.045$	0.694	$k_{trans} = 0.219$
		$j_{ss} = 0.031$		$k_{rec} = 0.097$
With CoPi	$BiVO_4$ 450 °C	$j_{ini} = 0.026$	0.755	$k_{trans} = 0.188$
		$j_{ss} = 0.019$		$k_{rec} = 0.061$
	F:$BiVO_4$ 450 °C	$j_{ini} = 0.050$	0.793	$k_{trans} = 0.160$
		$j_{ss} = 0.040$		$k_{rec} = 0.042$
	$BiVO_4$ 550 °C	$j_{ini} = 0.207$	0.726	$k_{trans} = 0.200$
		$j_{ss} = 0.165$		$k_{rec} = 0.075$
	F:$BiVO_4$ 550 °C	$j_{ini} = 0.179$	0.750	$k_{trans} = 0.224$
		$j_{ss} = 0.140$		$k_{rec} = 0.075$

Having a look at the CoPi-modified $BiVO_4$ and F:$BiVO_4$ electrodes calcined at 450 °C Figure 7-10c), only slight photocurrent spikes, a moderate photocurrent decay and very little overshoots are present. According to the photocurrent transient analysis, hole transfer rates k_{trans} are very similar for both samples accounting for 0.188 s^{-1} and 0.160 s^{-1} for the $BiVO_4$ and F:$BiVO_4$ samples, respectively. By CoPi deposition, the surface hole recombination rate for $BiVO_4$ is reduced to a minimum and is similar to the k_{rec} of the CoPi functionalized F:$BiVO_4$ sample accounting for 0.061 s^{-1} and 0.042 s^{-1}, respectively. In consequence, hole transfer efficiencies are similar as well, accounting for 0.755 and 0.793 for the pristine and the F-containing samples calcined at 450 °C, respectively. Same trends are observed for corresponding samples calcined at 550 °C (Figure 7-10d). k_{rec} of 0.075 s^{-1} is identical for both samples; k_{trans} slightly higher for the F:$BiVO_4$ compared to its pristine

counterpart accounting for 0.224 s^{-1} and 0.200 s^{-1}, respectively. As a result, hole transfer efficiencies for $BiVO_4$ and F:$BiVO_4$ electrodes calcined at 550 °C are very similar accounting for 0.726 and 0.750.

As revealed by photocurrent transient analysis, after surface functionalization with CoPi the water oxidation kinetics of the pristine $BiVO_4$ and the F:$BiVO_4$ photoanodes are comparable. However, PEC performance of the F:$BiVO_4$ electrodes is higher in terms of higher photocurrents. Most probably, this is a result of the smaller band gap and an enhanced amount of free charge carriers due to F incorporation.

To further clarify the origin of improved photocatalytic properties of F:$BiVO_4$ Mott-Schottky-type potentio-electrochemical impedance spectroscopy measurements (PEIS) for both materials were performed. Due to the particulate morphology of the electrodes, it was uncertain whether Mott-Schottky analysis would provide convincing results. However, for one type of electrode, measuring the electrode capacitance using different frequencies resulted in identical values for the flat band potential V_{FB} which validates obtained data. Respective plots are shown in the Appendix, chapter 12.1.1.1.

A comparing Mott-Schottky plot for $BiVO_4$ and F:$BiVO_4$ anodes calcined at 550 °C is shown in Figure 7-11. By the slope of the linear regions of the graph the number of free charge carriers can be assumed. A gradual slope is observed for the F:$BiVO_4$ and a much steeper slope for the pristine $BiVO_4$ electrodes revealing a higher number of free charge carriers for the F:$BiVO_4$ sample. By extrapolation of the linear part of the Mott-Schottky graphs, the flat band potential can be determined by the intersection with the potential axis. For the pristine $BiVO_4$ a V_{FB} of 0.06 V vs RHE is determined; a result which is in good agreement with reported values for the V_{FB} of $BiVO_4$.[26,28,74,133] The V_{FB} of the F:$BiVO_4$ is shifted cathodically to -0.06 V vs RHE.

Mott-Schottky analysis of the $BiVO_4$ and F:$BiVO_4$ anodes confirms a higher number of free charge carriers upon fluorine-incorporation which is in good agreement with results of the photocurrent transient analysis and photocurrent measurements. Furthermore, the flat band potential is shifted to more cathodic values which is a favorable situation regarding photoelectrochemical oxidation reactions. For the same applied potential more positive

with respect to the flat band potential, band bending is more intense for the F:$BiVO_4$ electrode compared to the pristine $BiVO_4$ electrode which largely improves charge separation. That means for the same applied potential the driving force for water oxidation is higher for the F:$BiVO_4$ material.

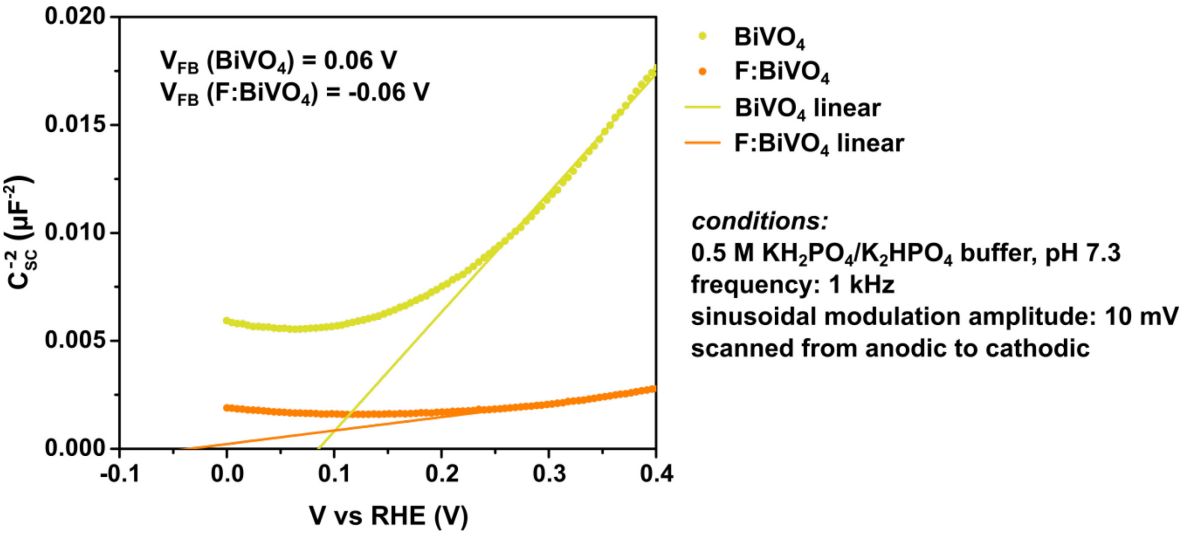

Figure 7-11. Mott-Schottky-Plots for $BiVO_4$ and F:$BiVO_4$ electrodes calcined at 550 °C. Linear parts of the Mott-Schottky-plots are linearly extrapolated.

7.4. Conclusion

In this chapter the synthesis of fluorine-containing $BiVO_4$ powder using a new, clean, and simple solid-vapor reaction was presented. By detailed structural analysis of the powders, it was revealed that the monoclinic scheelite structure which is favorable for photoelectrochemical applications because of a smaller band gap and superior local charge separation compared to the other polymorphs is preserved upon fluorine incorporation. Moreover, it was shown that the incorporation of fluorine mainly leads to the formation of cation vacancies. UV/Vis spectroscopy revealed the optical band gap of $BiVO_4$ to be reduced upon fluorination. HR-TEM/EDX analysis confirmed the presence of fluorine within the material and proved its homogeneous distribution. To enable (photo-)electrochemical investigations, electrodes were fabricated out of pre-synthesized $BiVO_4$ and F:$BiVO_4$ powders by electrophoretic depositions and subsequent heat treatment

to interconnect loosely deposited particles due to sintering. Obtained electrodes were used to investigate the PEC performance concerning water oxidation. Higher photocurrents were obtained for the fluorine-containing $BiVO_4$ anodes. By photocurrent transient analysis it was shown that surface hole recombination is drastically reduced for the F:$BiVO_4$ sample. This most probably is a consequence of surface-bound fluorine acting as electron traps and facilitating H_2O adsorption at the electrode surface. Additionally, Mott-Schottky-type PEIS revealed the F:$BiVO_4$ material to profit from a bigger amount of free charge carriers compared to its pristine counterpart as well as by a cathodically shifted flat band potential; both beneficial for improved PEC performance.

In summary, as shown in Figure 7-12, fluorine incorporation into $BiVO_4$ leads to higher PEC performance regarding water oxidation by i) a smaller band gap allowing the absorption of a bigger portion of the visible spectrum(Figure 7-12a), ii) a larger number of free charge carriers (Figure 7-12a), iii) a favorable shift of the flat band potential leading to increased band bending and hence enhanced charge separation and driving force (Figure 7-12a), and iv) by its fluorinated electrode surface which is beneficial for water oxidation (Figure 7-12b).

As such, fluorination of $BiVO_4$ turns out to be a powerful tool to improve its photoelectrochemical properties regarding water oxidation. Fluorination to other oxide-based semiconductor materials may result in similar benefits for their PEC water oxidation performance and certainly is an interesting research route to follow in the next years.

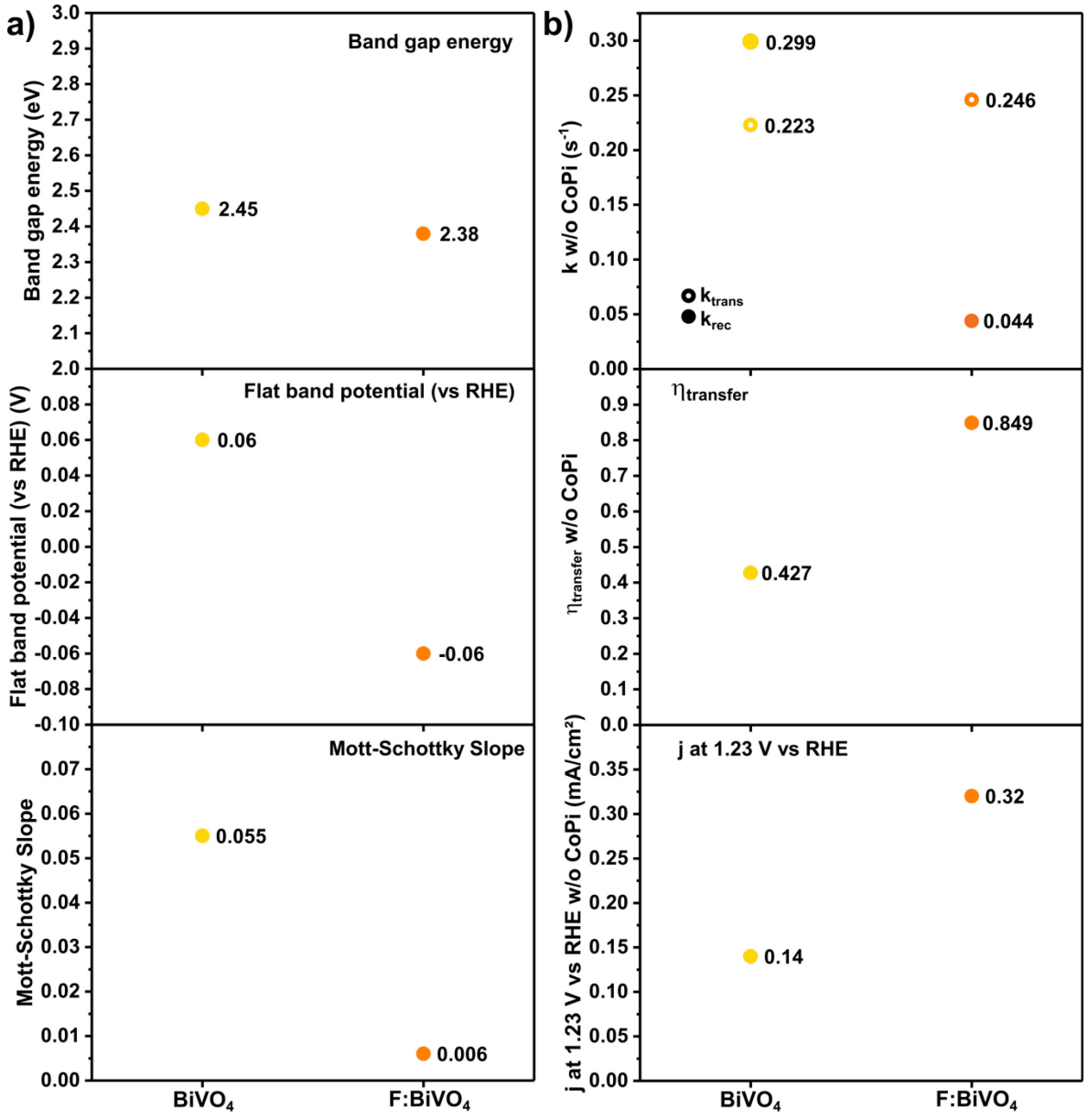

Figure 7-12. Comparison of $BiVO_4$ and F:$BiVO_4$. a) materials properties and b) kinetics of the electrodes' surfaces and obtained photocurrent densities (illumination: 400-700 nm, 100 mW/cm²) regarding water oxidation.

8. $BiVO_4$ and Mo:$BiVO_4$ thin film photoanodes

Parts of this chapter have been published:

"Mo-doped $BiVO_4$ thin films – high photoelectrochemical water splitting performance achieved by tailored structure and morphology"

M. Rohloff, B. Anke, Z. Siyuan, U. Gernert, C. Scheu, M. Lerch, A. Fischer, *Sustainable Energy Fuels* **2017**, *1*, 1830-1846.

8.1. Introduction

Yielded photocurrents regarding PEC water oxidation for powder-based $BiVO_4$ electrodes presented in the previous section were low compared to the highest reported values for $BiVO_4$-based systems. Furthermore, in frontside illumination only very low photocurrents for these electrodes could be observed. Most likely, the reason for the unsatisfactory photoelectrochemical performance can be found in the electrode design which is far away from an ideal photoanode design adjusted to the material properties.

As discussed in chapter 5.4, the five most important criteria a photoanode material has to fulfill are i) strong (visible) light absorption, ii) high chemical stability in darkness and under illumination, iii) suitable band edge positions with respect to the water oxidation reaction, iv) efficient charge transport and v) low overpotential regarding water oxidation. At this time, no single material has been found which fulfills all requirements. Optimization of the photoanode design allows getting around some intrinsic materials limitations. Main drawback of $BiVO_4$ is its poor electron transport.[22] Charge carrier transport through an electrode can be facilitated by improvement of the interfaces (at the back contact and at the electrolyte), by morphological adjustments matching the materials

properties (adjustment of film thickness to the minimum thickness needed for sufficient light absorption according to the material's extinction coefficient and material sizes/pore walls in the size range of the minority charge carrier diffusion length of the material) and especially by reduction of charge transport impeding artifacts like a high number of grain and particle boundaries.

In this context, a solution-based synthesis method allowing the fabrication of tailored thin film photoanodes comprised of wide-spread single-crystalline domains is desirable. As reported by Lange in 1996, this goal can be achieved by using suitable precursors within a sol-gel approach and by processing the thin films by spin coating or dip coating.[134]

Furthermore, for the use as electrodes, direct and scalable deposition methods are essential, allowing the synthesis of high quality thin films with precise control of the deposited thin film properties. The group of Mullins showed in 2011 that nanostructured $BiVO_4$ thin films can be synthesized directly by co-evaporation of bismuth and vanadium in oxygen atmosphere, a process referred to as reactive ballistic deposition. Water oxidation photocurrents under simulated sunlight of ~1 mA/cm² at 1.23 V vs RHE were yielded with a cobalt species deposited onto the surface as an electrocatalyst.[25] Gaining more knowledge about the nature/limitations of $BiVO_4$ and applying spray pyrolysis as new method for the direct deposition of $BiVO_4$ thin films, van de Krol et al. showed in 2013 that W-doping allows enhancing the charge transport efficiency in $BiVO_4$ thin film photoanodes, yielding, after an optimized electrodeposition of CoPi (a cobalt based water oxidation catalyst developed by Kanan and Nocera[52]), water oxidation photocurrents as high as 2.3 mA/cm² at 1.23 V vs RHE.[32] Introducing the concept of gradient doping, the group of van de Krol further improved charge separation in $BiVO_4$ thin films yielding photocurrents as high as 4 mA/cm² at 1.23 V vs. RHE.[26] By further improving the oxygen evolution catalysts and the nanostructuration of the $BiVO_4$, Choi and Kim could further increase photocurrent densities to values close to 4.5 mA/cm² at 1.23 V.[135]

However, to a certain extent these synthesis procedures are for some technically advanced and their scalability and reproducibility is not always granted. As such, a simple, wet chemical synthesis method for the direct deposition of photoelectrocatalytically active $BiVO_4$ thin film photoanodes with optimized light induced charge carrier generation,

separation, and transport through the electrode material is still missing. This issue is adressed in the upcoming chapters in which a new bottom-up synthesis approach allowing the fabrication of tailored $BiVO_4$ and Mo-doped $BiVO_4$ thin films is presented.

8.2. $BiVO_4$ thin films by bottom-up synthesis approach

8.2.1. Synthesis of $BiVO_4$ thin films

A new, wet chemical synthesis method for $BiVO_4$ thin films was developed. Synthesis steps are illustrated schematically in Figure 8-1. Starting from metal-organic precursor solution (Figure 8-1a), amorphous Bi- and V-containing thin films of $BiVO_4$ can be processed by dip coating of various substrates (Figure 8-1b). Subsequent calcination in air results in crystalline $BiVO_4$ thin films (Figure 8-1c).

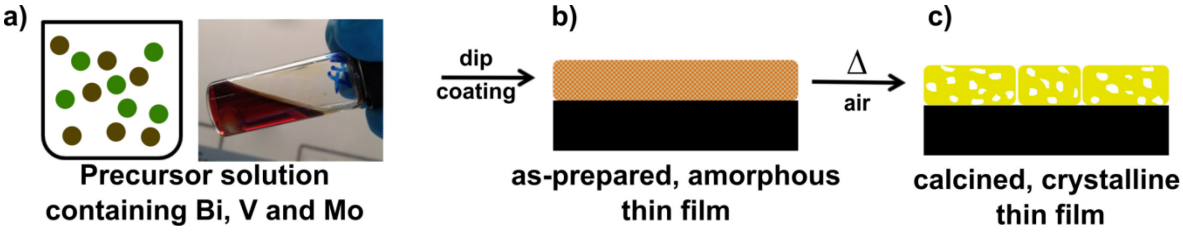

Figure 8-1. Synthesis scheme: a) precursor solution, b) as-deposited amorphous thin film and c) calcined, crystalline $BiVO_4$ thin film.

As demonstrated by the group of Vest in the early 1990s, metal hexanoates are suitable compounds for solution-based synthesis of metal oxide thin films because they are quantitatively transformed into metal oxides upon pyrolysis.[136] However, for a ternary oxide like $BiVO_4$, the exclusive use of bismuth and vanadium hexanoates is not appropriate as metal hexanoates do not tend to react which each other. Probably this would lead to certain compositional inhomogeneity. However, according to Fred Lange, once mixed with metal alkoxides, metal hexanoates react to form so called “hybrid-alkoxide” precursors with defined cationic ratios.[134] As such, by using metal hexanoate and metal alkoxide

precursors, metalorganic single-source precursors are formed in-situ with a 1:1 stoichiometry as demonstrated for example for $PbTiO_3$.

This synthesis concept was adapted and applied to the synthesis of $BiVO_4$, i.e. bismuth(III) 2-ethyl-hexanoate and vanadium(V) oxytriethoxide were mixed to form a bismuth-vanadium hybrid-alkoxide precursor in-situ in the starting precursor solution which results in a clear, deep red precursor solution after 4 hours of stirring. The solution was then used to deposit thin films on various substrates (silicon wafers, FTO) by dip coating. The dip-coating process leads to the formation of soapy, amorphous thin films on the substrates (as can be see TEM images and SAED diffraction pattern in Figure 8-2a).

Equation 8-1. a) Bismuth(V) 2-ethylhexanoate and b) Vanadium(V) oxytriethoxide and c) Formation of a Bi-V hybrid-alkoxide precursor out of the corresponding metal organic precursors.

a) Bismuth 2-ethylhexanoate

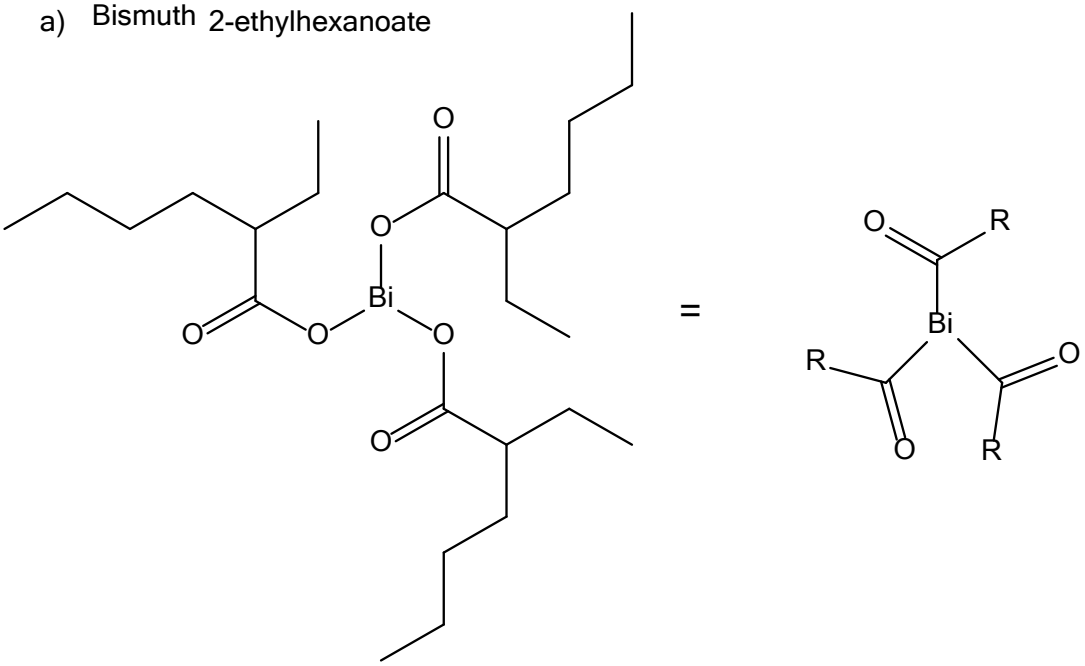

b) Vanadium oxytriethoxide

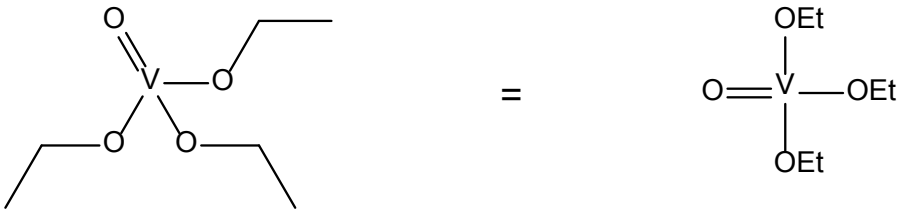

c) in-situ formation of Bi-V-hybrid precursor

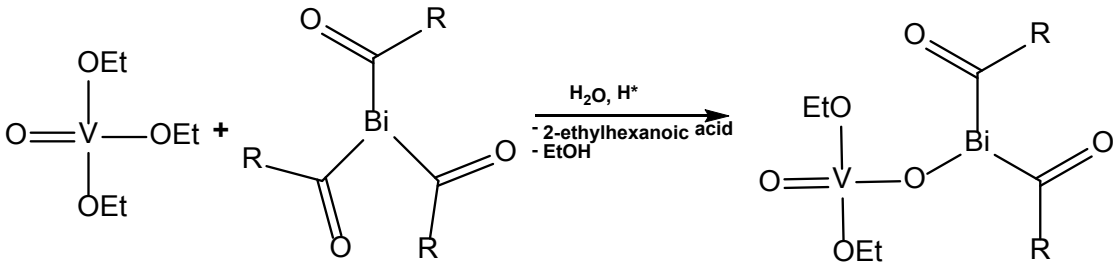

Calcination at 450 °C leads to grain/crystallite growth driven by the change in free energy due to elimination of grain boundaries by either coalescence or dissolution of smaller grains as well as decomposition of the organic residues.[134,137] As a result, a crystalline thin film of $BiVO_4$ comprised of large, porous, single-crystalline 2D-domains (*vide infra*) is obtained which is proven by an FFT of the HR-TEM image revealing spatial frequencies due to lattice fringes which can be assigned to $BiVO_4$ in monoclinic scheelite structure (see Figure 8-2).

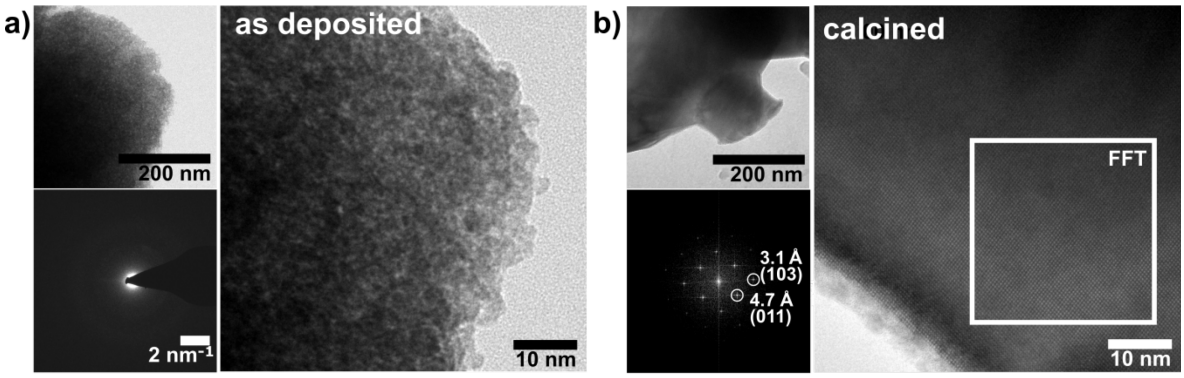

Figure 8-2. Synthesis steps followed by TEM for a $BiVO_4$ thin film: a) as-deposited amorphous thin film and b) crystalline $BiVO_4$ thin film with FFT pattern of the HR-TEM image.

8.2.2. Structural and morphological characterization of $BiVO_4$ thin films

By means of chemical and structural analysis the formation of $BiVO_4$ thin films by the sol-gel approach using bismuth hexanoate and vanadium oxytriethoxide was investigated. Structural characterization of the thin films was carried out by XRD under gracing incidence of the X-ray beam (GI-XRD), while the structural characterization of the corresponding $BiVO_4$ powder samples was performed by conventional powder-XRD (P-XRD). The powder sample was obtained by drying and calcining the synthesis solution used for dip coating according to the same calcination procedure applied to the thin films. Results of the structural characterization are shown in Figure 8-3. All obtained reflections of the pattern could be indexed according to $BiVO_4$ in the monoclinic scheelite structure as the included reference pattern illustrates (PDF: 01-083-1698). The

thin films as well as the powder samples exhibit isotropic, polycrystalline character. No side phases like Bi_2O_3 or V_2O_5 could be traced within the detection limit of the equipment.

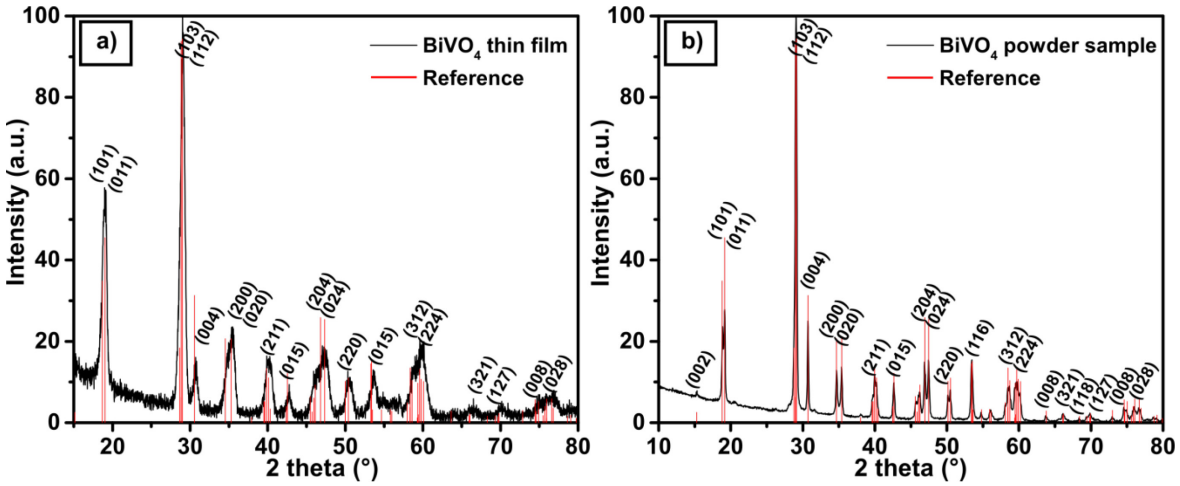

Figure 8-3. GI-XRD and P-XRD pattern of $BiVO_4$ thin films on Si substrate (left) and $BiVO_4$ powder samples (right), reference pattern of monoclinic scheelite $BiVO_4$ (PDF 01-083-1698) included in both figures.

By UV/Vis spectroscopy the absorption of visible light of the thin film deposited on FTO substrate was investigated. As shown in Figure 8-4a, the light of wavelengths smaller than 515 nm is absorbed by the thin film which corresponds to a band gap of 2.42 eV and is in good agreement with reported band gaps for monoclinic scheelite $BiVO_4$ in literature.[71,138,139] Furthermore, ICP-OES analysis of $BiVO_4$ thin films and powder samples, respectively, revealed a Bi:V ratio of 1.00:1.01 in both cases. By krypton physisorption experiments and BET analysis of the obtained isotherm, an average geometric surface area of 8.20 $cm^2_{film}/cm^2_{substrate}$ was determined. The krypton physisorption isotherm with corresponding BET plot is shown in Figure 8-4b.

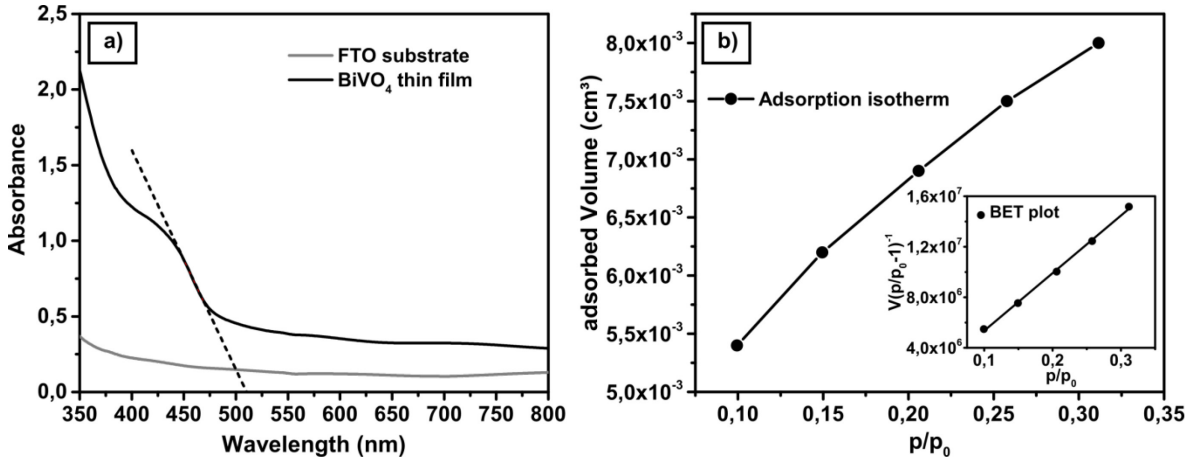

Figure 8-4. a) UV/Vis spectrum of $BiVO_4$ thin film on FTO substrate and b) Kr physisorption isotherm of $BiVO_4$ thin films, inset: corresponding BET plot.

The morphology and composition of the $BiVO_4$ thin films was investigated by electron microscopy and EDX. As shown by SEM top view and cross section images in Figure 8-5a-c, the thin films exhibit a domain-like morphology and are spread homogeneously over the substrate. The domains are separated from another by a thin groove. An average geometrical domain size of 7.2 ±3.3 µm² was determined. Every single domain consists of thin material streaks of an average thickness of 68 ±7 nm. The course of orientation of the inner domain material streaks shows that the material of one domain was grown surrounding a centered crystallization spot. By the cross section images (Figure 8-5d and e) the average film thickness was determined to be 270 nm. The cross section image indicates that the thin film consists of rarely porous material. Furthermore, the thin film does not exhibit particulate morphology. Additionally, it is shown that thin grooves separate the domains throughout the whole thin film down to the substrate. The discussed features are illustrated within Figure 8-5.

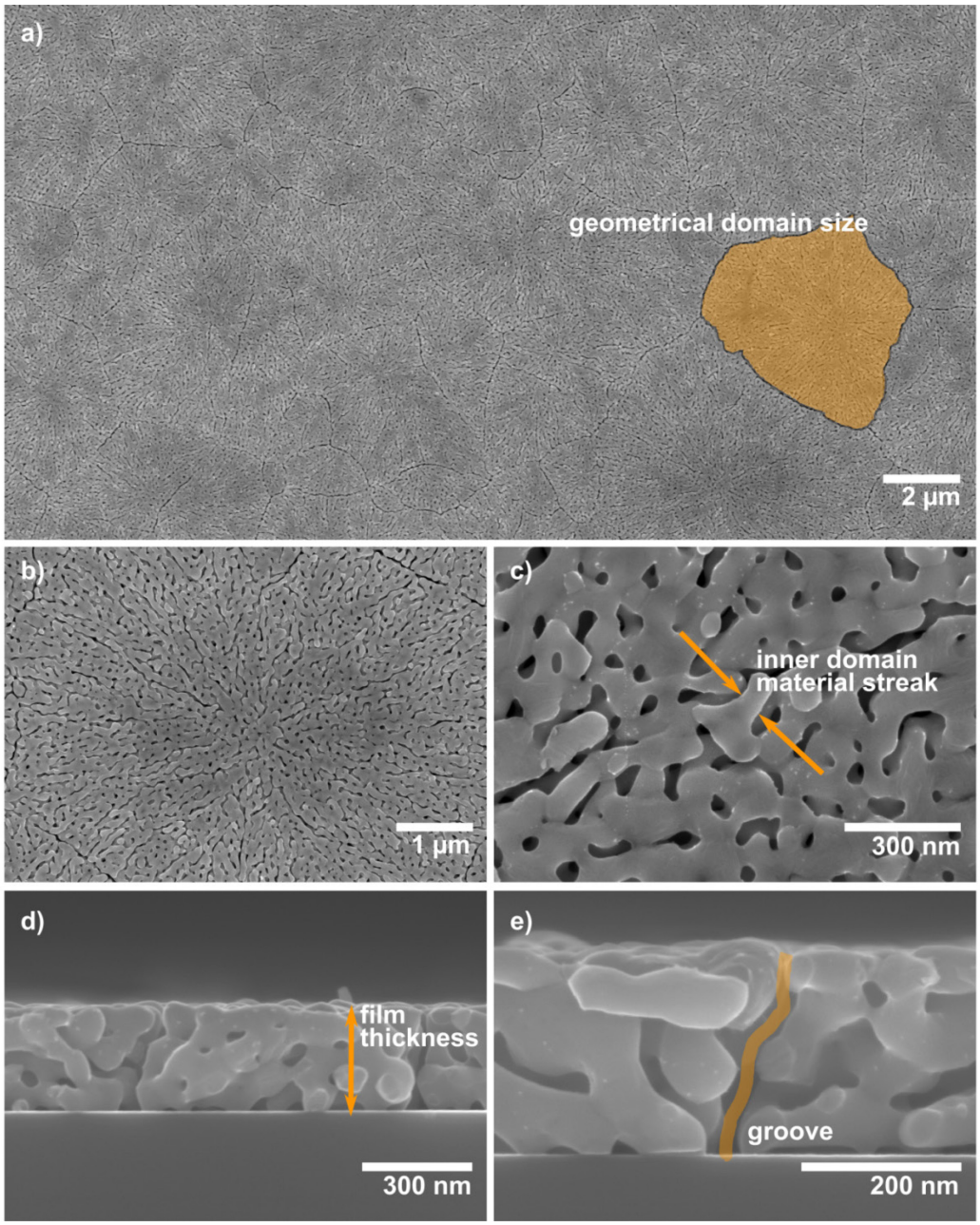

Figure 8-5. a-c) SEM top-view images of $BiVO_4$ thin film Si substrate, d and e) SEM cross-section image of $BiVO_4$ thin films at Si substrate. Characteristic thin film features are highlighted.

For TEM analysis, the $BiVO_4$ thin films were scraped off the substrate and transferred to a TEM-grid. Results of TEM/SAED and EDX investigations are shown in Figure 8-6. Generally, as shown by the overview image given in Figure 8-6a, the domain-like shape of the thin films assumed by SEM can be confirmed by the TEM. As can be seen in Figure

8-6b, the corresponding SAED pattern (diameter of 0.5 µm diameter of circular selected area) is comprised of separated reflections; a pattern which is referred to as dot pattern and which indicates single-crystallinity of the sample within the selected area. Analysis of the reflections reveals d-spacings of 4.8 Å and 4.7 Å, respectively which can be assigned to the (101) and the (011) plane of the monoclinic scheelite structure of $BiVO_4$. Furthermore, the high resolution image with respective FFT pattern (Figure 8-6c and d) exhibits only one set of lattice fringes which can be associated to the (011) lattice plane with a d-spacing of 4.7 Å. This further confirms the $BiVO_4$ thin film to be highly crystalline.

SEM and TEM/SAED investigations prove the thin film to consist of wide-spread domains which exhibit a preferred orientation. This can be explained by secondary grain growth processes during calcination of the thin films. As rationalized by Thompson,[140] general features of grain growth in thin films can be summarized as follows:

Normal grain growth occurs as long as the grain sizes are smaller than the film thickness. The formation of a columnar grain structure, i.e. all grain boundaries intersect the top and bottom surfaces of the film, leads to the cessation of normal grain growth. Advancing crystallization in films with columnar structures occurs via secondary or abnormal grain growth. That means few grains which are oriented energetically favorable in terms of interfacial and surface energy grow at the expense of the static matrix of the normal grains. Secondary grain growth usually continues until abnormal grains impinge on other abnormal grains. As a result, the thin film obtained after calcination is comprised of large grains which exhibit restricted crystallographic orientations.

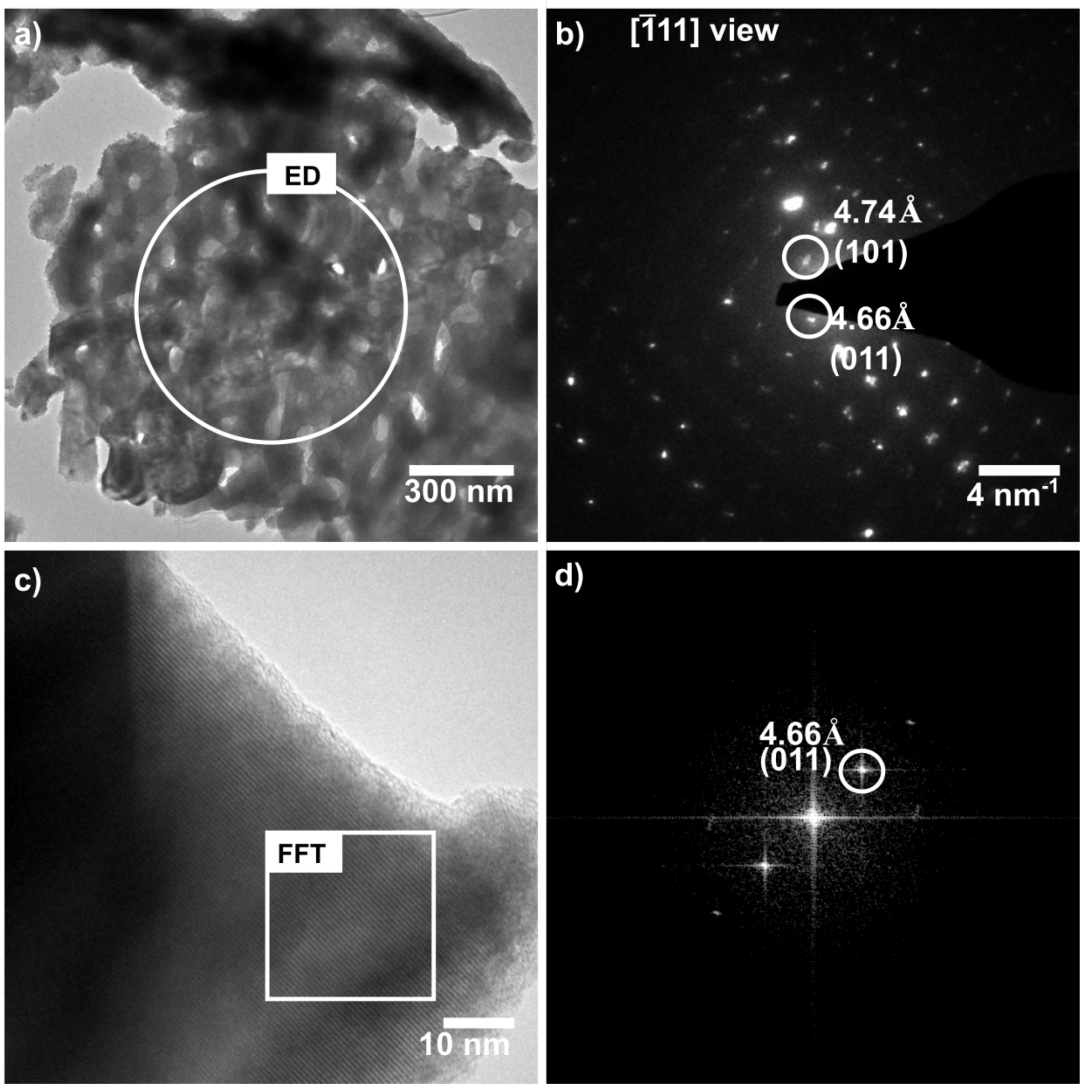

Figure 8-6. TEM/SAED investigations of thin films scraped off the substrate and transferred to a TEM grid: a) overview image, b) corresponding SAED pattern, c) high resolution image and d) corresponding FFT pattern.

8.2.3. (Photo-)electrochemical investigations

To investigate the photoelectrochemical properties of the $BiVO_4$ thin films with respect to water oxidation, an electrochemical cell was equipped with a reversible hydrogen electrode (RHE) as reference electrode and a wound Pt wire as counter electrode, respectively. $BiVO_4$ thin films were used as working electrodes in 0.1 mol/l potassium phosphate buffer at pH 7.3 and was illuminated with white light (400-700 nm) at an intensity of

100 mW/cm^2 using a 150 W Xe-lamp. A thin layer of CoPi water oxidation catalyst[52] was deposited using a photo-assisted electrodeposition method[50] (see chapter 6.4).

j-V curves of the $BiVO_4$ thin film photoanodes are shown in Figure 8-7a. Observed photocurrents of the pristine $BiVO_4$ thin films are low, accounting for 0.1 mA/cm² at 1.23 V vs. RHE in frontside illumination and 0.2 mA/cm² at 1.23 V vs. RHE in backside illumination, respectively. Depositing a thin layer of CoPi water oxidation catalyst enhances the photoelectrochemical performance and observed photocurrents, respectively. With CoPi deposited, photocurrents of 0.5 mA/cm² at 1.23 V vs. RHE were observed in frontside illumination; in backside illumination, photocurrents of 2.1 mA/cm² at 1.23 V vs. RHE were yielded. Deposition of CoPi water oxidation catalyst improves the water oxidation kinetics at the surface and therefore enhances the overall photoelectrochemical performance of the $BiVO_4$ thin films (*vide infra*, see chapter 8.4.4).

Generally, higher photocurrents were observed in backside illumination. Same trend is shown by the j-V-curves under chopped illumination presented in Figure 8-7b and c. When the light was switched on, a photocurrent spike is followed by a fast decrease in initial photocurrent. When the light was switched off, a negative overshoot was observed irregularly over the scanned potential range. This “spike and overshoot” behavior qualitatively indicates surface recombination of photo-generated charge carriers to be a PEC performance-limiting factor. The observed photocurrents are amongst the highest reported for undoped $BiVO_4$ thin film photoanodes in combination with CoPi water oxidation catalyst. This proves the synthesis method and the obtained photoanodes to be able to keep up with other synthesis approaches.[102,141,142]

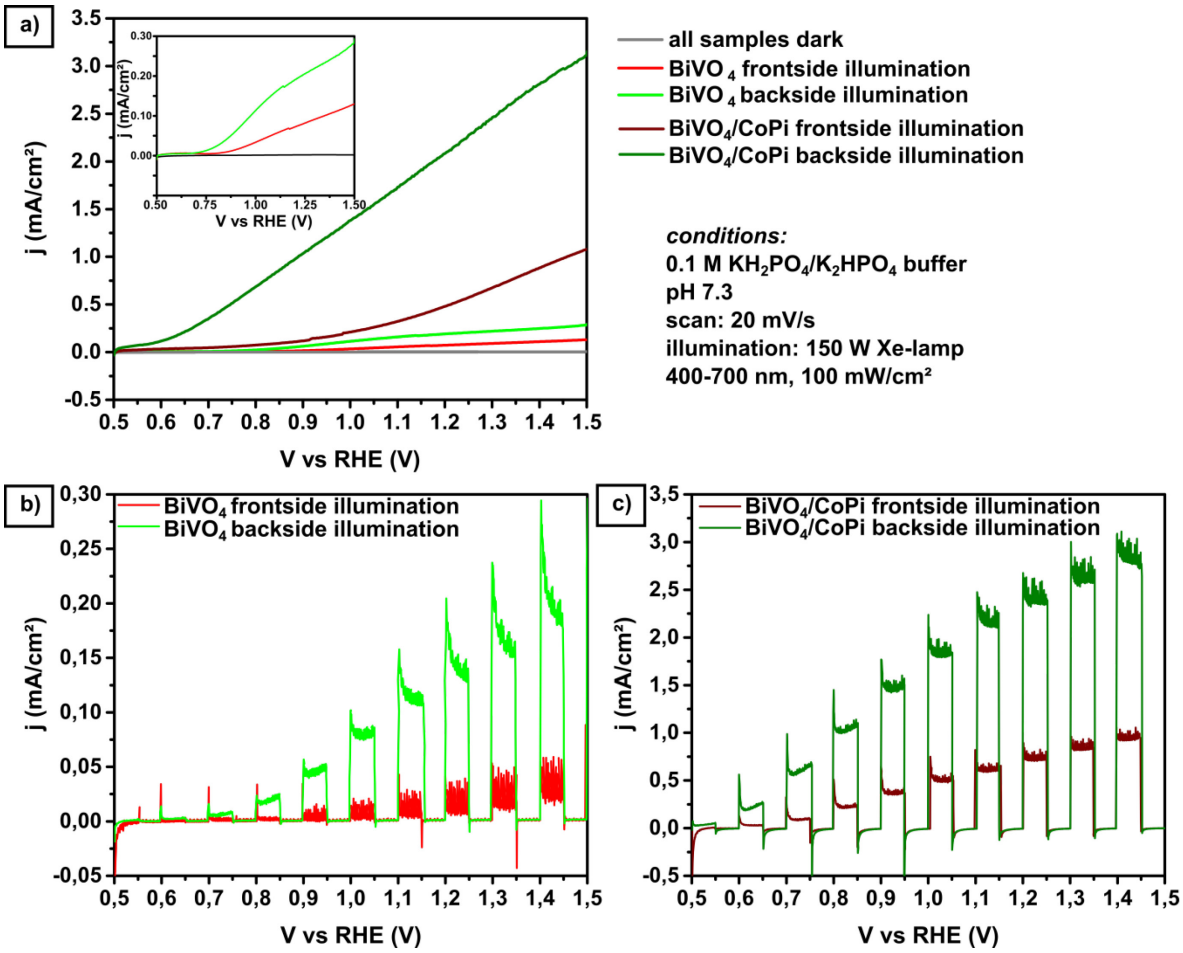

Figure 8-7. a) j-V-curves of $BiVO_4$ thin films with and without a layer of CoPi water oxidation catalyst under continous illumination (inset: magnified view on j-V curves of pristine samples), b and c) j-V-curves of $BiVO_4$ thin films without (b) and with (c) a layer of CoPi water oxidation catalyst under chopped illumination.

Investigation of the yielded photocurrents in frontside and backside illumination, respectively, is an efficient tool to elucidate photocurrent limiting factors for a photoanode material. When frontside illumination is used, holes are generated near to the anode/electrolyte interface and can be injected easily to the electrolyte whereas electrons need to travel through the whole thin film to the conductive substrate. As a consequence, fast electron transport properties are of utmost importance to obtain high photocurrents in frontside illumination. At the opposite, when backside illumination is used, photo-generated holes need to travel through the whole thin film to the anode/electrolyte interface whereas electrons only have to migrate a short distance to be collected at the conductive

substrate. In this case, hole conductivity is more important than electronic conductivity to yield high photocurrents. The obtained j-V-curves already indicate slow electron transport through the material to be impeding the PEC performance. To rule out surface-related effects on the obtained photocurrents, $BiVO_4$ thin films were used for sulfite oxidation. The oxidation of sulfite is thermodynamically ($E^0_{SO_3^{2-}/SO_4^{2-}}$= 0.6 – 0.7 V vs RHE[143,144]) and kinetically[135,145] much more facile than the water oxidation reaction. Hence, surface recombination becomes negligible. Results of the sulfite oxidation experiments are shown in Figure 8-8.

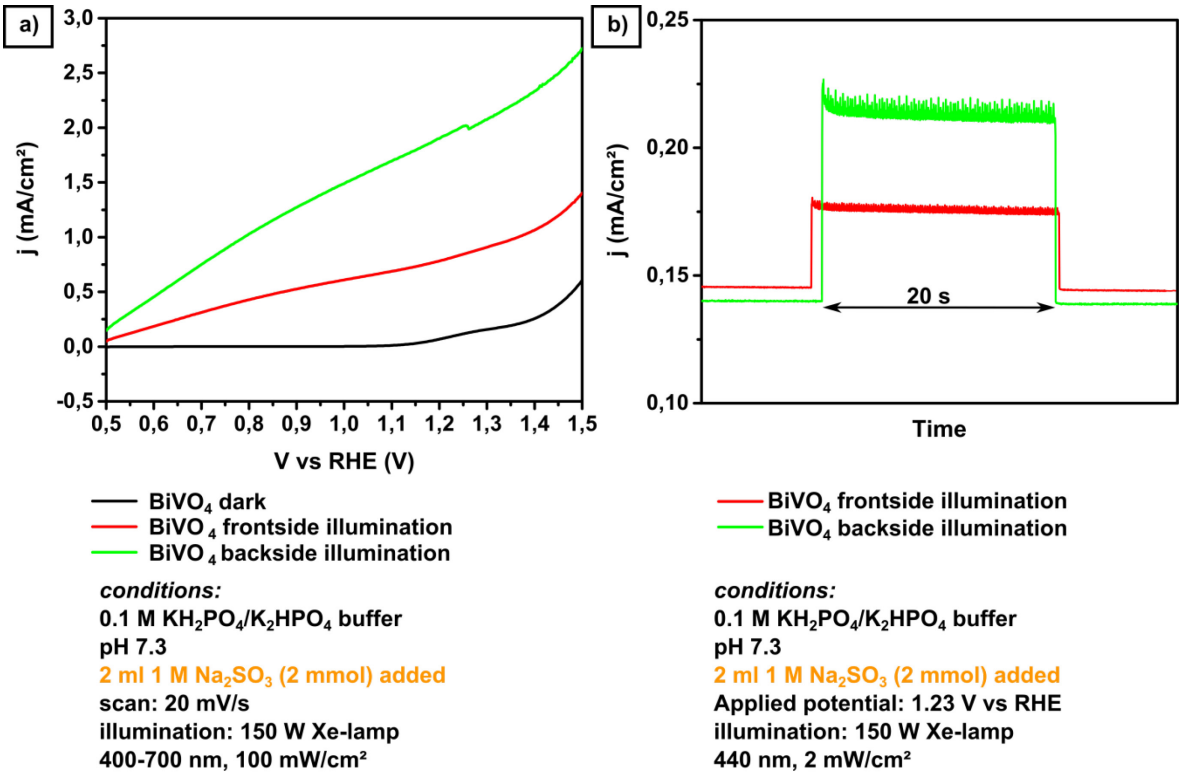

Figure 8-8. Results of PEC sulfite oxidation, a) j-V curves with and without CoPi water oxidation catalyst, b) photocurrent transients acquired in frontside and backside illumination mode.

As shown in Figure 8-8a, the obtained dark currents show an onset of the sulfite oxidation at about 1.15 V vs RHE. In frontside illumination photocurrents of 0.8 mA/cm² at 1.23 V vs RHE were yielded; photocurrents of 2.0 mA/cm² were obtained in backside

illumination. Furthermore, the photocurrent transients shown in Figure 8-8b, reveal surface hole recombination to be negligible (no significant spike and overshoot). Hence, surface related limitation effects were ruled out by the use of sulfite as hole scavenger.

The obtained photocurrents for unmodified $BiVO_4$ photoanodes for sulfite oxidation are considerably higher than for water oxidation. This indicates that the majority of the surface-reaching holes were lost due to surface recombination. The obtained photocurrents for the CoPi-modified $BiVO_4$ electrodes concerning water oxidation are in excellent agreement with the results of sulfite oxidation of unmodified $BiVO_4$ electrodes; a result which confirms the deposition of a thin layer of CoPi to sufficiently suppress surface recombination.

In addition to water oxidation experiments, results of sulfite oxidation reveal higher photocurrents when illuminated from the backside. As surface hole recombination is ruled out by the use of sulfite, this clearly indicates electron transport within the $BiVO_4$ thin film to be an important PEC performance-limiting factor. These results are in good agreement with literature. The group of van de Krol investigated the incident photon to current efficiency (IPCE) of undoped $BiVO_4$ photoanodes at different light intensities. The obtained IPCE at low light intensities is much higher (≈90 %) than for high light intensities (≈20 %) which exposes the charge separation to be limited by slow electron transport.[141] Furthermore, the group of Yang used intensity-modulated photocurrent spectroscopy (IMPS) to investigate the photoelectrochemical performance of $BiVO_4$ photoanodes in frontside and backside illumination. They suggested a trap-free electron transport region vicinal to the FTO substrate which leads to a higher charge separation efficiency when backside illumination was used.[127]

8.2.4. Conclusion

To sum-up briefly, the new one-step synthesis method allows the direct deposition of $BiVO_4$ thin films. Starting from metal organic Bi and V precursors, thin films can be fabricated by simple dip coating and subsequent calcination. Structural and morphological analysis revealed the porous $BiVO_4$ thin films to crystallize in monoclinic scheelite

structure. Investigations of the thin film morphology and microstructure revealed the thin films to be comprised of several micrometer large, porous domains which exhibit single-crystalline character. Photoelectrochemical performance concerning water oxidation was investigated for unmodified and CoPi-decorated $BiVO_4$ thin films. Observed photocurrents are in line with PEC performances reported in literature for similar photoanode systems. Furthermore, by means of sulfite oxidation experiments in frontside and backside illumination, slow electron transport was elucidated to be a very important factor limiting photoelectrochemical performance for water oxidation.

8.3. Molybdenum-doped $BiVO_4$ thin films

8.3.1. Introduction

As shown in the previous section, the slow electron transport is mainly limiting the PEC performance of $BiVO_4$ thin film electrodes regarding water oxidation. This drawback can be overcome by appropriate doping strategies. N-type doping of $BiVO_4$, i.e. partial substitution of the penta-valent vanadium cation by hexa-valent cations like molybdenum or tungsten, was shown by various groups to be a viable method to improve electron transport properties of the material.[25,26,28,74,107,109] In the following section, the new bottom-up synthesis approach for $BiVO_4$ thin film photoanodes is expanded by the addition of a suitable molybdenum precursor. The influence of Mo-doping on the $BiVO_4$ thin film structure, morphology and photoelectrochemical properties regarding water oxidation is presented.

8.3.2. Synthesis

The new bottom-up approach described in chapter 8.2.1 was used to fabricate molybdenum-doped $BiVO_4$ thin films. A suitable molybdenum precursor (Molybdenum diacetylacetonate dioxide, $MoO_2(acac)_2$) was added in atomic ratios of 5 to 20% (with respect to the used amount of Bi) to the synthesis solution. After 4 hours of stirring, the Bi, V and Mo containing solution was used for dip coating of FTO-coated glass slides or silicon substrates. After dip coating the thin films were aged for 12 h at 100 °C and

calcined at 450 °C for 2 h in air resulting in crystalline Mo-doped $BiVO_4$ thin films (Mo:$BiVO_4$). To correlate results of some characterization methods, it was necessary to analyze respective powder samples. Powder samples were synthesized by drying the synthesis solutions in air followed by a similar calcination procedure as used for the thin films.

In Figure 8-9, UV/Vis spectra of the synthesis solutions containing different amounts of Mo, acquired after 4h of stirring, are shown. The stirring time was not sufficient to solve the whole amount of used Mo precursor. As a consequence, the solutions' turbidity increases with increasing Mo content which results in a very strong absorbance over the whole spectral range.

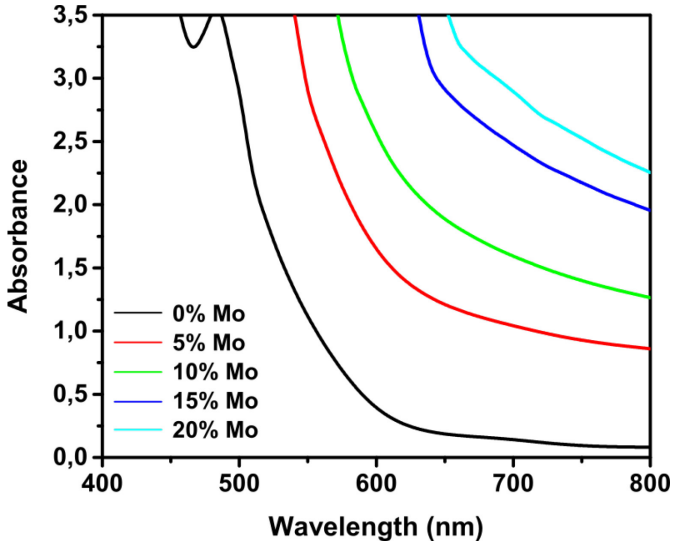

Figure 8-9. UV/Vis spectra of synthesis solutions containing different amounts of Mo.

However, using the turbid solutions for dip coating of FTO substrates, $BiVO_4$ thin films are obtained with a certain amount of Mo incorporated into the material. This is confirmed by ICP-OES analysis. An overview of the used Mo percentages with respect to the (determined) amounts of Bi is given in Figure 8-10 (left). Mo ratios within the powder samples are in agreement with the used Mo contents of the synthesis solutions. A significantly lower amount of Mo was traced within the thin film material. The relationship

between the used Mo amount in the solution and the Mo amount incorporated within the thin films as determined by ICP-OES is illustrated in Figure 8-10 (right). The relationship could be fitted linearly (R^2 = 0.9986). By the slope of the linear graph an incorporation coefficient of 0.55 was obtained. That means only 55 % of the used Mo precursor ratio within the synthesis solution is present within the thin film material. Nevertheless, the Mo content within the $BiVO_4$ thin films is tunable by adjustment of the Mo-content within the synthesis solution according to this relationship.

From now on the $BiVO_4$ thin films are referred to as Mo:$BiVO_4$, adding percentages as used for the corresponding synthesis solutions, e.g. 10% Mo:$BiVO_4$.

Mo-% in solution (atomic ratio)	Mo-% in powders (atomic ratio)	Mo-% in thin films (atomic ratio)
0	0	0
5	4	3
10	9	6
15	15	8.5
20	18	10.5

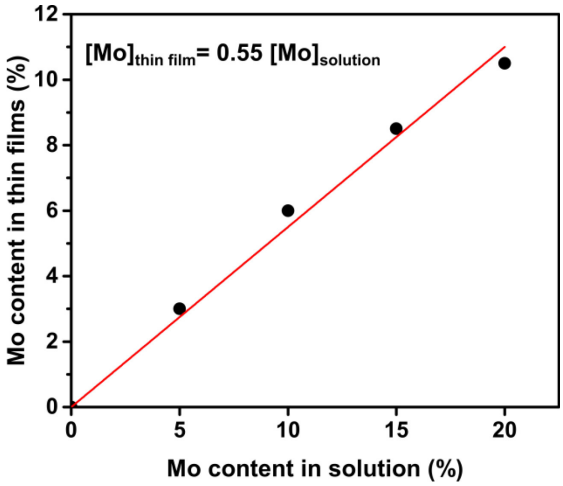

Figure 8-10. Overview of ICP-OES results for Mo:$BiVO_4$ thin films (left) and illustration of the relationship between Mo content in solution and in thin films (right). Mo-% is given in atomic ratios with respect to the used (synthesis solutions) or determined (thin films and powders) amount of Bi.

8.3.3. Structural and morphological characterization

In order to obtain information about the crystal structure of the Mo-doped $BiVO_4$ thin films, gracing incidence X-ray diffraction (GI-XRD) was performed. Figure 8-11a gives an overview of the obtained diffraction patterns. The GI-XRD data clearly reveal the $BiVO_4$ thin films to be polycrystalline with no preferred orientation.

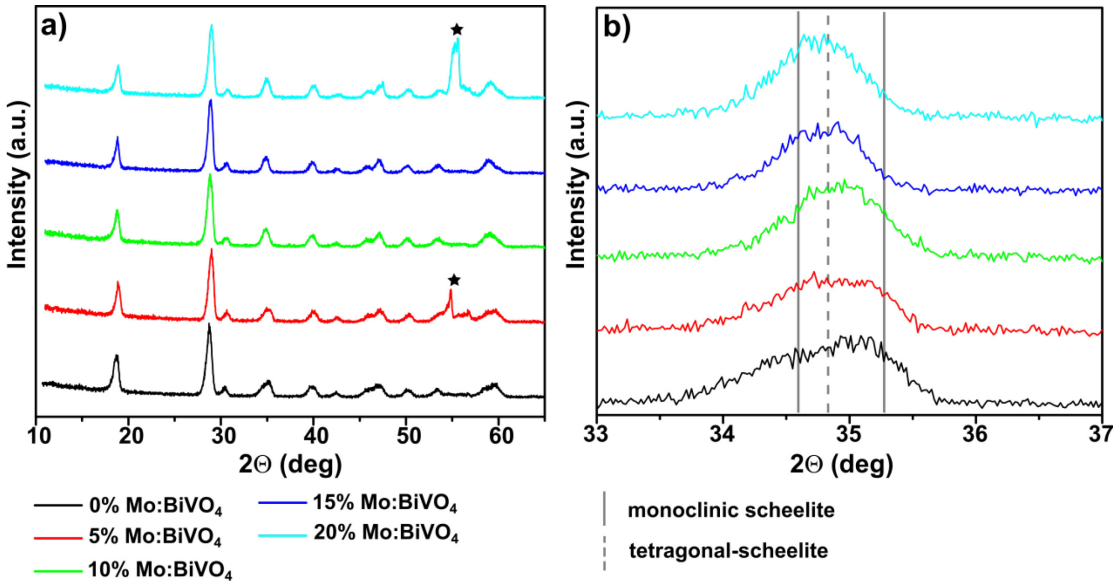

Figure 8-11. a) GI-XRD pattern of Mo:$BiVO_4$ thin films. Reflections marked with a star are measurement artefacts, b) magnified view on the (200) and (020) reflections (34.5 ° and 35.3 °) of the monoclinic scheelite structure.

As discussed in chapter 5.4.2.1, $BiVO_4$ exhibits three different crystal structures: the tetragonal zircon-type structure, the monoclinic scheelite-type structure and the tetragonal scheelite-type. It should be mentioned that the crystal structures of the monoclinic and tetragonal scheelite modifications are very similar. The space group of the monoclinic low temperature phase, *I*2/*b*, a non-standard setting of *C*2/*c*, is a maximal non-isomorphic subgroup (*translationengleich,* index 2) of $I4_1/a$, the space group of the tetragonal scheelite-type polymorph. The monoclinic crystal structure of $BiVO_4$ shows only slight deviations from the tetragonal one, which is expressed for example by an only minimal change in gamma angle between the monoclinic and the tetragonal phase (monoclinic gamma-angle ~90.3 °; tetragonal gamma-angle ~90 °). As such, the diffraction patterns of the monoclinic and tetragonal scheelite phase are very similar and hence not easy to distinguish. In Figure 8-11b, a magnified view on the diffraction pattern centered around 33-37 ° is given. The reflections at 34.5 ° and 35.3 ° corresponding to the (200) and (020) planes of the monoclinic scheelite structure are merged to a single reflection corresponding to (200) plane of the tetragonal scheelite structure. Due to the resolution limitations of

GI-XRD measurements, all reflections are broadened, making an unambiguous phase identification challenging for the thin film samples.

For this reason, high-quality powder diffraction measurements along with structural refinements using the Rietveld method are indispensable prerequisites to gather reliable structural information. To reveal eventual composition effects on the crystal structure as well as to gain information about the ideal (crystal) and real (defect) structure of the pristine and Mo-doped $BiVO_4$ thin film samples, reference powder samples were analyzed. Diffraction measurements and corresponding Rietveld refinements and defect model analyses were carried out by Dipl-Chem. Björn Anke under supervision of Prof. Dr. Martin Lerch from TU Berlin.

Figure 8-12a gives an overview of the diffraction patterns of the Mo-doped $BiVO_4$ powder samples. Details about the powder diffraction measurements as well as the outcome of the Rietveld refinements can be found in Appendix, chapter 12.1.2.1. From these data one can see that a continuous phase transition from the monoclinic scheelite to the tetragonal scheelite phase occurs with increasing molybdenum concentration. This is expressed by a shrinking a/b ratio and a decreasing gamma angle of the unit cell, respectively (see Figure 8-12c). As can be seen in Figure 8-12b, the monoclinic scheelite structure forms for the $BiVO_4$, 5% Mo:$BiVO_4$, 10% Mo:$BiVO_4$ and 15% Mo:$BiVO_4$ samples. Only the 20% Mo:$BiVO_4$ sample crystallizes in the tetragonal scheelite structure, as revealed by the completed merge of the (200) and (020) reflections of the monoclinic scheelite structure into a single reflection corresponding to the (200) plane of the tetragonal scheelite structure. This molybdenum-induced phase transition is in line with previous literature reports and is directly related to the larger ionic radius of the Mo^{6+} (0.41 Å) cations when compared to the V^{5+} (0.35 Å) cations.[28] (Note: both values are given for a coordination number of 4).

For a better understanding of the Mo-doped materials, a closer look was given at the possible defects arising from substituting V^{5+} by Mo^{6+}. All reasonable defect models are summarized in the Appendix, chapter 12.1.2.1. The observed underoccupation of the bismuth position revealed by Rietveld refinements clearly points to the presence of bismuth vacancies as main defects in the Mo-doped $BiVO_4$ structure. The stoichiometric formula

accordingly should be written as $Bi_{1-x/3}Mo_xV_{1-x}O_4$. This is in good agreement with single crystal diffraction results on such phases, as reported for example by Cesari et al.[120] Starting from the structural information gained from the powder samples, one would expect the thin films to exhibit the same crystal structure as the corresponding $BiVO_4$ powders.

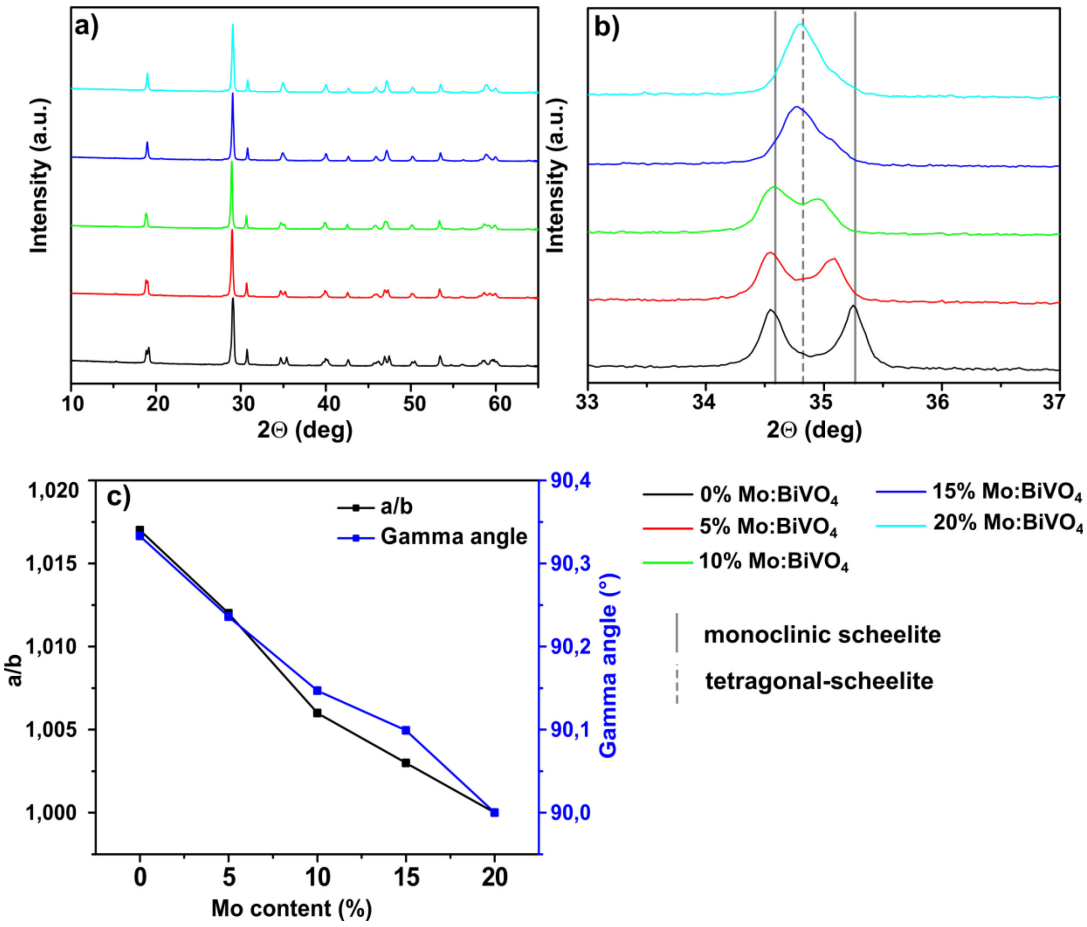

Figure 8-12. a) X-ray diffraction pattern of Mo:$BiVO_4$ powder samples containing different amounts of Mo, b) magnified view on merging reflections at 33-37 ° and c) change of the a/b ratio and gamma-angle with increasing Mo content acc. to Rietveld refinements.

UV/Vis spectroscopy was performed to determine the optical absorption properties of the differently doped Mo:$BiVO_4$ thin films on FTO coated glass substrates. Results and photographs of the measured samples are given in Figure 8-13. The absorbance of the Mo:$BiVO_4$ thin films increases with increasing Mo content. The highest absorbance was

observed for the 10% and 15% Mo:$BiVO_4$ samples. With increasing amount of Mo incorporated within the material, the absorbance all over the whole measured spectrum increases too. This correlates with the increasing turbidity of the samples as can be seen in the photographs in Figure 8-13. As there is no other deviation in the synthesis protocol than the used amount of Mo precursor for all samples, the change in absorbance probably has its origin in a change of the morphology and the crystal structure of the thin films caused by the incorporation of different amounts of Mo. This is reasonable as the thin film morphology is directly affected by the amount of Mo incorporated within the material (*vide infra*).

Although often applied in literature reports, the Tauc method is principally not appropriate for band gap determination of crystalline semiconductors.[125] Unfortunately, also the derivation of absorption spectrum fitting method (DASF method) introduced by Souri et al.[146] did not deliver appropriate results. Most probably, the high absorbance over the whole measured spectrum due to the thin film turbidity impedes the derivation of the absorption spectra. However, to get a qualitative idea of the optical band gap of the Mo:$BiVO_4$ thin films, the absorption onset was determined by the intersection of the extrapolation of the linear region of the absorbance graph with the wavelength-axis. The pristine $BiVO_4$ sample exhibits typical absorption of visible light starting at wavelengths of about 510 nm which is in good agreement with the band gap of 2.43 eV for $BiVO_4$ in the monoclinic scheelite phase[67]. All samples with Mo incorporated exhibit nearly the same onset starting at about 525 nm which corresponds to a band gap of 2.36 eV. The slightly smaller band gap of the Mo-doped $BiVO_4$ thin films reveals Mo incorporation to affect improved light absorption properties.

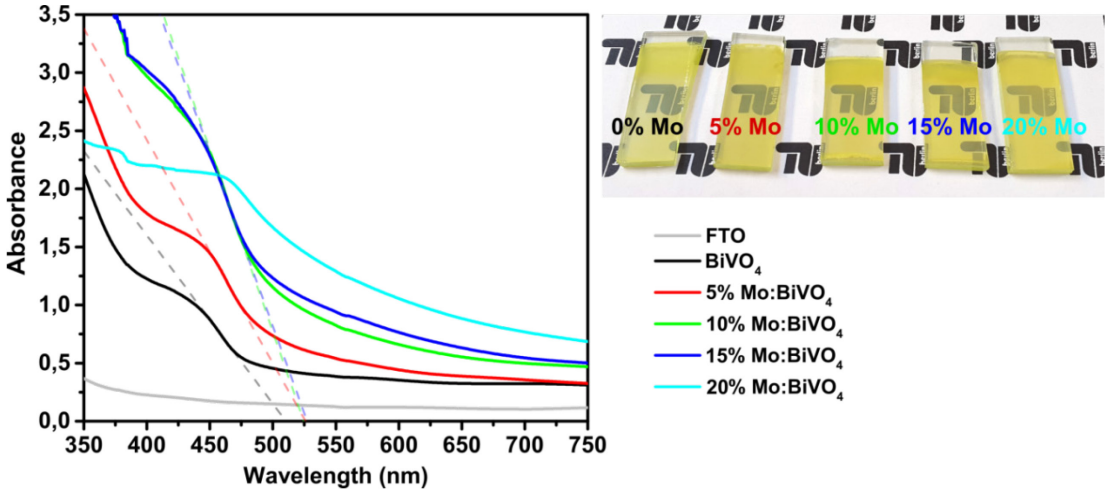

Figure 8-13. UV/Vis spectra of Mo:$BiVO_4$ thin films on FTO substrate.

The morphology of the different Mo:$BiVO_4$ thin films was investigated extensively by electron microscopy methods. Top view and cross-sectional images with corresponding EDX spectra of pristine $BiVO_4$ and Mo:$BiVO_4$ thin films deposited onto a FTO substrate are shown in Figure 8-14. All films consist of differently sized domains which are separated down to the substrate from each other by a thin groove. Like previously described (chapter 8.2.2), these areas are referred to as domains. The material within one domain is referred to as inner domain material streaks (see illustrations of analyzed features within Figure 8-14). By the cross-sectional images it is shown that all films exhibit a comparable film thickness of about 215 to 270 nm. Additionally, the cross-sectional images show all films to consist of barely porous material, homogeneously covering the rough FTO surface. EDX of Mo:$BiVO_4$ thin films deposited on FTO substrates proves the thin film material to consist of Bi, V, O and Mo. Due to overlaying peaks of V/O and Mo/Bi the quantifications of the EDX spectra did not reveal reliable results. Hence, EDX spectra only can provide qualitative information of the elemental composition.

The molybdenum content strongly influences the morphology of the thin films. The average geometrical domain size and thickness of the material streaks within the domains depend on the Mo content. As summarized in Table 8-1, undoped $BiVO_4$ thin films have an average domain size (geometrical area from top-view) of 7.2 µm², an average inner domain material streak size of 68 nm, and a film thickness of 270 nm. With increasing Mo content,

the average domain size decreases from 7.2 µm² for the 5% Mo:$BiVO_4$ sample to 1.7 µm² for the 15% Mo:$BiVO_4$ sample. In case of the 20% Mo-doped sample, the domain morphology is distorted and the geometrical domain size becomes smaller than 1 µm². Same tendency is observed for the film thickness which decreases from 245 nm for the 5% Mo:$BiVO_4$ sample to 214 nm for the 20% Mo:$BiVO_4$ sample. An inverse trend is observed for the inner domain material streak size which increases from 68 nm for the undoped $BiVO_4$ sample to 139 nm for the sample with the highest Mo content. The average inner domain material streak sizes of the 5% Mo:$BiVO_4$ and 10% Mo:$BiVO_4$ of 80 nm and 84 nm, respectively, match the diffusion length of 70-100 nm of $BiVO_4$.[22,74,75] The inner domain material streak size of 105 nm for the 15% Mo:$BiVO_4$ sample already exceeds the diffusion length.

Kudo et al. showed that $BiVO_4$ in the tetragonal scheelite structure tends to form bigger particles whereas $BiVO_4$ in the monoclinic scheelite type more likely forms smaller particles.[67] As shown by XRD investigations (*vide supra*), the $BiVO_4$ thin films exhibit increasing character of the tetragonal scheelite structure with increasing Mo content. Connecting Kudos findings with our XRD results, it seems reasonable that the inner domain material streaks sizes become bigger with increasing Mo content. In good agreement with these findings, the results of the krypton adsorption experiments reveal a decrease in specific geometrical surface area of the differently doped $BiVO_4$ thin films with increasing Mo content (see Appendix, chapter 12.1.2.2 for Kr physisorption isotherms and corresponding BET plots).

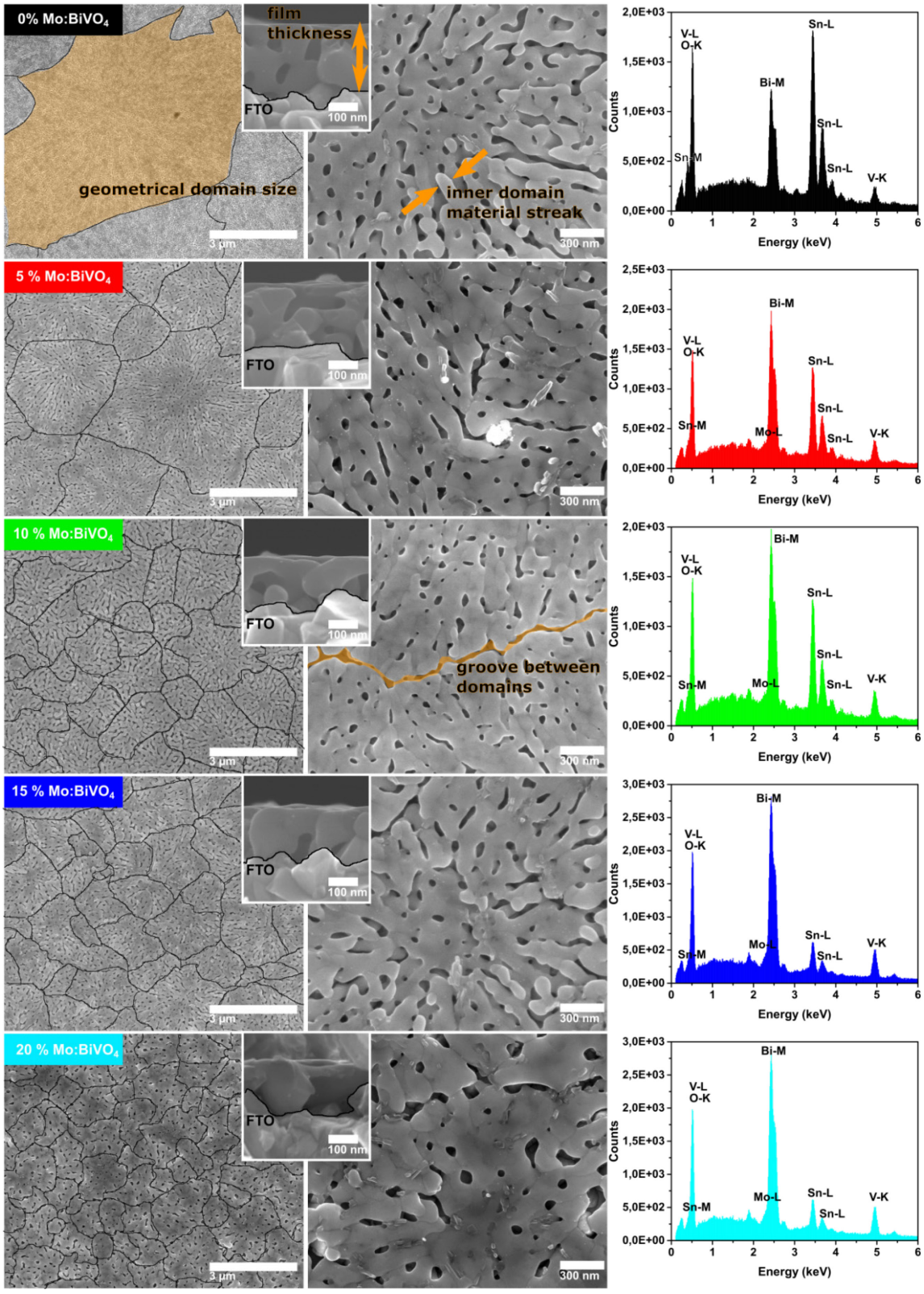

Figure 8-14. Top view and cross section images of Mo:$BiVO_4$ with corresponding EDX spectra. The Mo-L peak overlaps with the Bi-M peak at 2.3 keV.

Table 8-1. Summary of analyzed thin film features.

Mo percentage (at% with respect to Bi)	Mo content determined by ICP-OES (at% with respect to Bi)	Average geometrical domain size by SEM (μm²)	Average inner domain streak size (nm)	Average film thickness (nm)	Specific geom. surface area by Kr-Adsorption ($cm^2_{film}/cm^2_{substrate}$)
0	0	7.2 ±3.3	68 ±7	269 ±5	8.2
5	3	6.4 ±2.4	80 ±7	245 ±12	8.0
10	6	2.8 ±1.7	84 ±9	238 ±10	7.0
15	8.5	1.7 ±1.1	105 ±9	223 ±12	5.5
20	10.5	<1	139 ±8	214 ±14	2.9

The thin film crystallinity and orientation was further investigated by selected area electron diffraction (TEM/SAED) and electron backscatter diffraction (SEM/EBSD). Representative results of TEM/SAED experiments obtained for a 5%-Mo-doped $BiVO_4$ sample are shown in Figure 8-15a (respective analysis of other samples are given in the Appendix, chapter 12.1.2.4). Analysis of three different spots along one thin film domain reveals the same single-crystalline diffraction pattern corresponding to the (200) plane and the (004) plane in [010] viewing direction. As already assumed for pristine $BiVO_4$ thin films (see chapter 8.2.2), this result strongly indicates that the whole domain exhibits one preferred orientation. This is further confirmed by EBSD analysis. EBSD measurements were performed by Christoph Fahrenson from ZELMI/TU Berlin. Figure 8-15b illustrates the results of EBSD investigations of a 5%-Mo-doped $BiVO_4$ thin film deposited on Si substrate which was chosen for EBSD as the average domain size is compatible to the limitations of the EBSD measurement equipment. The single orientations of each domain are sketched in by the orientation of the respective unit cells. The misorientation exceeds 10 ° in some cases. However, like already suggested by SAED, every domain of the thin film reveals single-crystalline character. The orientations of the domains differ from each other resulting in the formation of a polycrystalline thin film with large crystallites; a result which is in line with the GI-XRD results, where no specific orientation/texture can be seen in the film. Both methods, EBSD and TEM/SAED, evidence all $BiVO_4$ thin films (pristine

and Mo-doped) to be comprised of differently oriented, single-crystalline domains. As similar thin film morphology can be observed for thin films deposited onto Si and FTO substrate, no substrate dependence could be derived for the thin film morphology (see Appendix, chapter 12.1.2.3 for SEM investigations of Mo:$BiVO_4$ thin films on Si substrate).

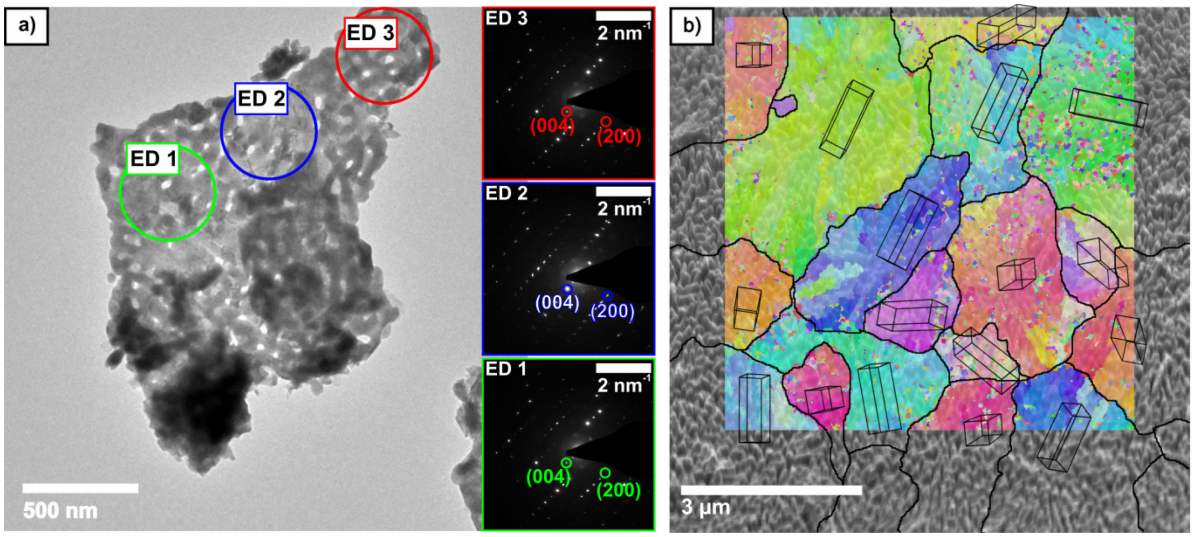

Figure 8-15. a) TEM/SAED investigations of one flake of a 5% Mo:$BiVO_4$ thin film (sample scraped-off the substrate and transferred to TEM grid), b) SEM/EBSD pattern of 5% Mo:$BiVO_4$ thin film with corresponding unit cells sketched in.

To further investigate the thin film properties with respect to usage as photoanodes for PEC water oxidation, high-resolution STEM was used to analyze the interface between the FTO substrate and the $BiVO_4$. The STEM and STEM/EDX analysis were carried out by Dr. Siyuan Zhang and were supervised by Prof. Dr. Christina Scheu from Max-Planck-Institut für Eisenforschung. For this purpose, a TEM lamella was prepared by FIB cutting of a 10% Mo-doped $BiVO_4$ sample; sample which was chosen exemplarily as it featured the best PEC performance for water oxidation (*vide infra*). The lamella cutting was performed by Dr. Dirk Berger from Zelmi/TU Berlin. Because of the single-crystalline character of the single domains of the thin films, epitaxial growth of the material depending on the orientation of the FTO is conceivable. Exemplarily for several investigated spots

along the TEM lamella, the interface between FTO and Mo:$BiVO_4$ was investigated (see Figure 8-17). The FFT pattern of the Mo:$BiVO_4$ crystal exhibits only one set of reflections corresponding to a d-spacing of 2.9 Å and the (004) plane, respectively. In the adjacent area, signals corresponding to the (110) plane with a d-spacing of 3.4 Å of the FTO substrate, respectively, can be seen. At the interface region of 5 nm in width, signals of both crystals were traced within the FFT pattern and no amorphous interlayer between the FTO substrate and the Mo-doped $BiVO_4$ thin film is observed. The crystalline character of the interface favors the interfacial transfer of electrons and therefore reduces ohmic resistivity. No epitaxial relationship between $BiVO_4$ and FTO was observed in this and all other analyzed areas.

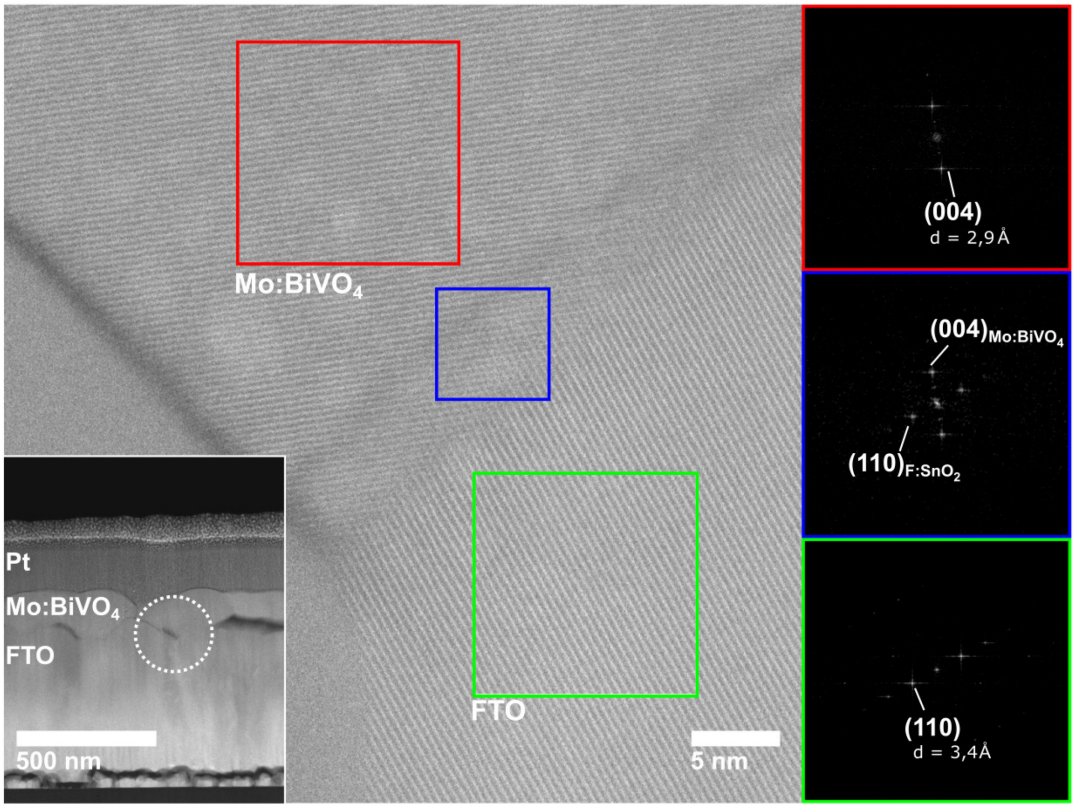

Figure 8-16. HR-STEM image of the interface between 10% Mo-doped $BiVO_4$ and FTO substrate with corresponding FFT pattern, inset: overview of TEM lamella. Pt protection layer was deposited during the FIB-SEM lamella preparation.

The distribution of Mo within the Mo-doped $BiVO_4$ thin film (cross-section) was furthermore investigated by EDX on the cut lamella. In Figure 8-17 the results of STEM-EDX element mapping for Mo (green), Bi (blue) and V (red) performed on the TEM-lamella of a 10% Mo:$BiVO_4$ sample are shown. The homogenous distribution of Mo all over the thin film is proven. This indicates the incorporation of Mo within the $BiVO_4$ lattice and excludes phase segregation.

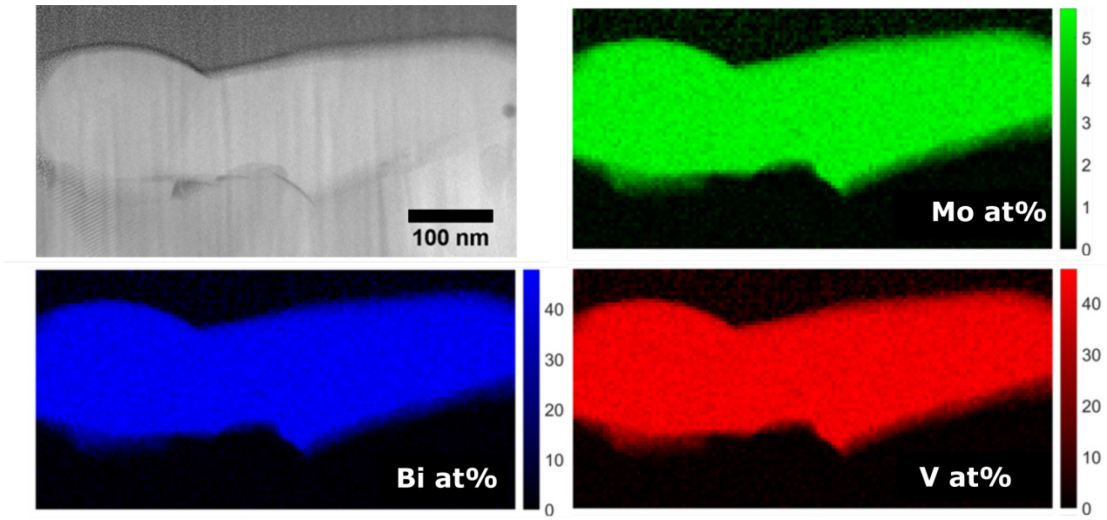

Figure 8-17. STEM image of 10% Mo:$BiVO_4$ lamella and corresponding single element EDX maps. The EDX quantification was performed for the cation sites Bi, V, and Mo.

Briefly summarized, starting from a solution containing suitable metalorganic Bi, V and Mo precursors, homogeneous and reproducible thin films can be fabricated by dip-coating under controlled conditions and subsequent calcination. Structural and morphological characterization reveals the polycrystalline Mo:$BiVO_4$ thin films to crystallize in the favorable monoclinic scheelite structure in micrometer large, randomly oriented, single-crystalline domains. The monoclinic scheelite structure can be kept upon Mo-insertion Light absorption was enhanced upon Mo incorporation as a result of a smaller band gap. The influence of Mo-doping on the photoelectrochemical performance regarding water oxidation is discussed in the following section.

8.3.4. (Photo-)electrochemical investigations

Photoelectrochemical performance of the Mo:$BiVO_4$ thin films regarding water oxidation was investigated by using an electrochemical cell which was equipped with the commonly used counter and reference electrodes (RHE – reference, Pt-wire – counter electrode). Measurements were carried out in 0.1 mol/l potassium phosphate buffer at pH 7.3 and illuminated with white light (400-700 nm) adjusted to an intensity of 100 mW/cm^2 using a 150 W Xe-lamp. A thin layer of CoPi water oxidation catalyst[52] was deposited using a photo-assisted electrodeposition method.[50]

In Figure 8-18a j-V curves of undoped and Mo-doped $BiVO_4$ thin films are presented. Yielded photocurrents at an applied potential of 1.23 V vs RHE are summarized in Table 8-2. For the undoped $BiVO_4$ samples, low photocurrents accounting for 0.20 mA/cm² at 1.23 V were observed. With increasing Mo content, the photocurrent could be increased up to tenfold. At an applied potential of 1.23 V vs. RHE, maximum photocurrents up to 1.76 mA/cm² and 1.93 mA/cm² for 5% Mo:$BiVO_4$ and 10% Mo:$BiVO_4$ were obtained, respectively. Exceeding the 10% Mo content leads to a decrease in photocurrent accounting for 1.17 mA/cm² and 1.02 mA/cm² at 1.23 V vs RHE for the 15% Mo and the 20% Mo sample, respectively.

j-V-curves of $BiVO_4$ photoanodes with a deposited layer of CoPi at the semiconductor-electrolyte interface are shown in Figure 8-18b**.** As can be seen, CoPi deposition onto the semiconductor surface further enhances observed photocurrents for all samples yielding values up to 4.6 mA/cm² at 1.23 V vs. RHE for the 10 % Mo:$BiVO_4$ photoanode. This value is amongst the highest photocurrents reported so far for a $BiVO_4$-based photoanode (see Table 8-3).

The 5% Mo and 10% Mo samples show highest PEC performance regarding water oxidation with and without CoPi deposited onto the surface. The 10% Mo:$BiVO_4$ sample marks an optimum for the Mo content which strongly correlates with morphology and structure of the respective thin films (see Figure 8-14 and Table 8-1). The 15% and 20% Mo:$BiVO_4$ samples show less PEC performance in terms of lower photocurrents. This, in first approach, most probably is a consequence of the inner domain material streaks

exceeding the minority carrier diffusion length of $BiVO_4$ and the more tetragonal scheelite character which is disadvantageous for PEC applications.[67]

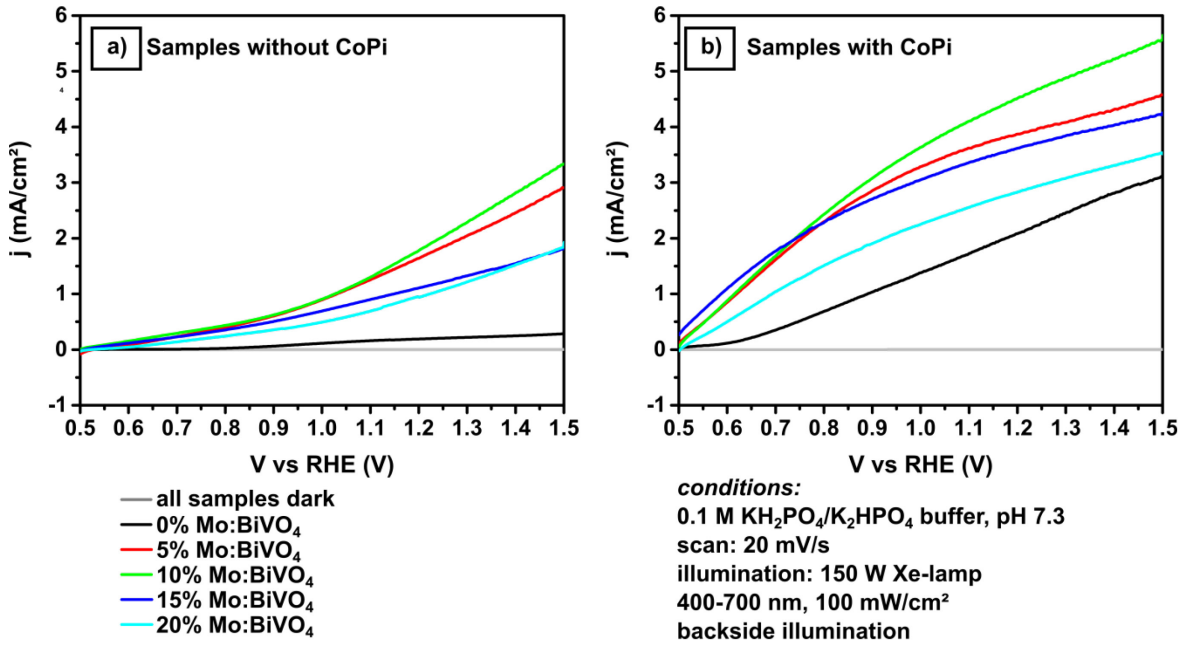

Figure 8-18. j-V curves of pristine and Mo-doped $BiVO_4$ obtained in backside illumination, a) without water oxidation catalyst, b) with CoPi water oxidation catalyst deposited onto the $BiVO_4$ and Mo:$BiVO_4$ surface.

Table 8-2. Summary of yielded photocurrents of the $BiVO_4$ and Mo:$BiVO_4$ photoanodes at an applied potential of 1.23 V vs RHE.

Sample	j at 1.23 V vs RHE (mA/cm²)			
	without CoPi		with CoPi	
	frontside illumination	backside illumination	frontside illumination	backside illumination
$BiVO_4$	0.08	0.20	0.54	2.19
5% Mo:$BiVO_4$	1.75	1.76	4.02	3.94
10% Mo:$BiVO_4$	1.74	1.93	3.81	4.64
15% Mo:$BiVO_4$	1.13	1.17	4.00	3.69
20% Mo:$BiVO_4$	1.12	1.02	3.25	2.91

Table 8-3. Overview of literature reports on highly active $BiVO_4$-based photoanodes.

anode/catalyst	j at 1.23 V vs RHE without co-catalyst (mA/cm²)	j at 1.23 V vs RHE with co-catalyst (mA/cm²)	electrolyte/pH	author/ reference	Publication year
Mo-doped $BiVO_4$					
Mo:BiVO4/CoPi	0.2	1.0	0.5 M Na_2SO_4, pH = 7	Pilli et al.[106]	2011
Mo:BiVO4/FeOOH	-	2.1	0.1 M KH_2PO_4, pH = 6.8	Chen et al.[147]	2015
Mo:$BiVO_4$/RhO_2	n.a.	2.9	natural seawater	Luo et al.[129]	2011
Mo:BiVO4/FeOOH	1.1	3.0	0.1 M KH_2PO_4, pH = 7	Park et al.[145]	2014
Mo:$BiVO_4$/CoPi	1.9	4.6	0.1 M KH_2PO_4, pH = 7.3	this work	2016
Other well-performing $BiVO_4$ based photoanodes					
$BiVO_4$/FeOOH	0.2	2.3	0.1 M KH_2PO_4, pH = 7	Seabold et al.[34,34]	2012
$BiVO_4$/CoO_x/NiO	1.1	3.5	0.1 M KH_2PO_4, pH = 7	Zhong et al.[128]	2015
W:$BiVO_4$/CoPi	1.1	4.0	0.1 M KH_2PO_4, pH = 7.3	Abdi et al.[26]	2013
$BiVO_4$/FeOOH/NiOOH	1.9	4.5	0.5 M KH_2PO_4, pH = 7	Kim et al.[135]	2014
Mo:$BiVO_4$/CoPi	1.9	4.6	0.1 M KH_2PO_4, pH = 7.3	this work	2016
H_2-treated Mo:BiVO4/CoPi	2.5	4.9	0.1 M KH_2PO_4, pH = 7	Kim et al.[148]	2015
N_2-treated $BiVO_4$/FeOOH	3.0	5.0	0.5 KH_2PO_4, pH = 7	Kim et al.[24]	2015

As discussed in chapter 8.2, for pristine $BiVO_4$ thin films, the photocurrents obtained in frontside-illumination are about 5 times lower compared to the photocurrents yielded in backside illumination. For all Mo-doped $BiVO_4$ thin films and as shown exemplarily in Figure 8-19a for a 10% Mo-doped $BiVO_4$ sample, the obtained photocurrents in frontside and backside illumination with and without CoPi water oxidation catalyst deposited onto the surface are comparable. This points to an improvement of electron transport properties of the material and to a decrease of bulk recombination, respectively. See Appendix, chapter 12.1.2.5 for results of similar measurements for other Mo:$BiVO_4$ samples.

The j-V curve in light on/off mode of a 10% Mo:$BiVO_4$ sample shown in Figure 8-19b reveals a photocurrent spike when light is switched on at high anodic potentials starting at about 0.9 V vs RHE. The occurrence of spikes when light is switched on and the missing overshoot when switching light off appears unusual in a first approach as bulk recombination was minimized by Mo doping and surface recombination was suppressed by CoPi deposition. Observed spikes and the fast decrease of initial photocurrent probably are caused by energetic surface states and Fermi level pinning. Both phenomena have not been investigated comprehensively within this thesis.[27,149]

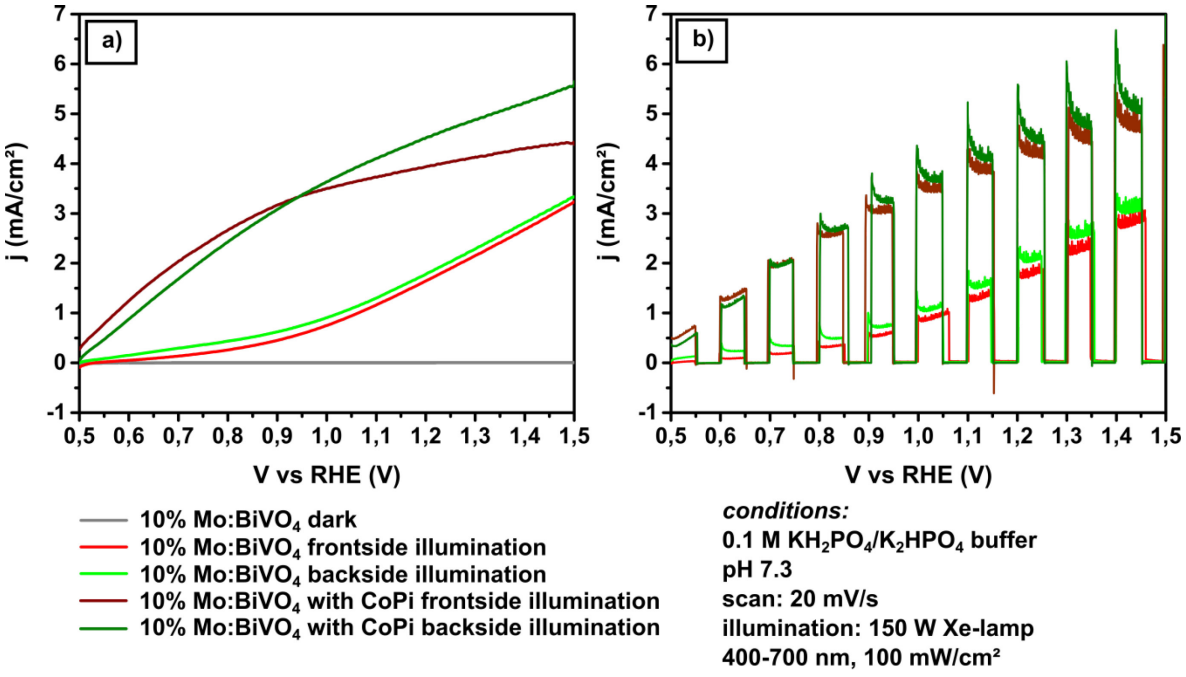

Figure 8-19. a) j-V curve in frontside and backside illumination and b) j-V curve in light on/off mode in frontside and backside illumination of a 10% Mo:$BiVO_4$ sample with and without CoPi deposited onto the surface.

To have a closer look at the water oxidation kinetics of the electrode surface, chronoamperometric investigations in light on/off mode at a potential of 1.23 V vs RHE and illuminated with blue light (440 nm) at an intensity of 2 mW/cm² were carried out to record the photocurrent transients. Results for all samples are shown in Figure 8-20.

The photocurrent transients can be analyzed according to the phenomenological approach described in chapter 5.5.3.3. Results of of the analysis of photocurrent transients acquired in backside illumination with and without CoPi deposited are summarized in Table 8-4.

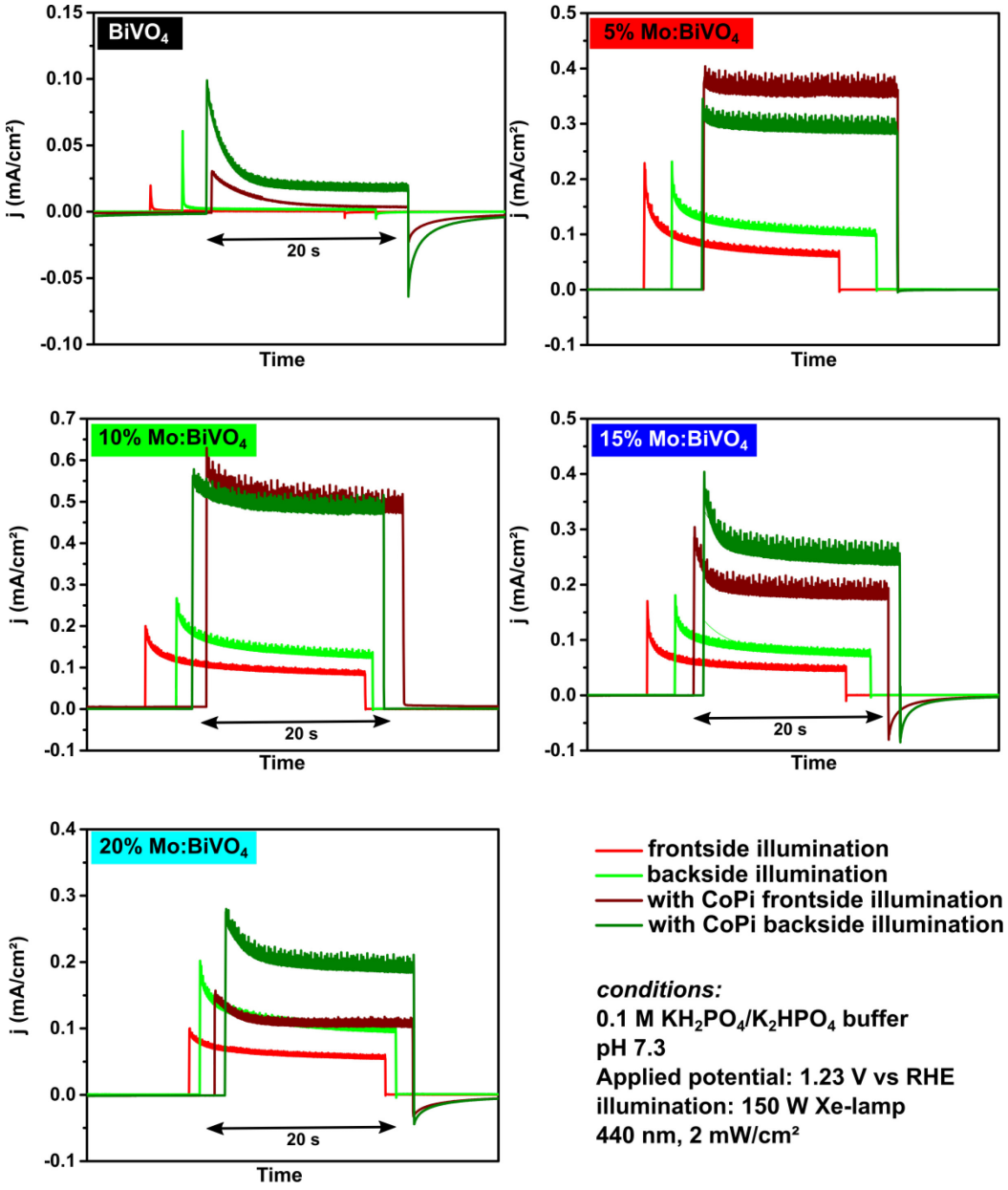

Figure 8-20. Chronoamperometry in light on/off mode for pristine and Mo-doped $BiVO_4$ samples.

As can be seen in Figure 8-20**,** the undoped $BiVO_4$ sample shows a typical "spike and overshoot" behavior during light-on/off experiments, accounting for an initial photocurrent j_{ini} of 0.055 mA/cm² which is rapidly decreased to the steady state photocurrent j_{ss} of 0.002 mA/cm². This response is typical for a system with pronounced surface electron–hole

recombination. In addition, the hole transfer efficiency $\eta_{transfer}$ of the pristine $BiVO_4$ sample was determined to be very low accounting for 0.033.

In case of the Mo-doped $BiVO_4$ samples the situation is different. Only a moderate photocurrent spike is observed for the Mo-doped samples while any overshoot is suppressed. This result is in good agreement with previous reports on charge carrier dynamics in undoped and doped $BiVO_4$ photoanodes.[150,151] The absence of any overshoot can be explained by two effects related to n-type doping in $BiVO_4$: i) decrease of the space charge width due to increased donor concentration reducing back electron-hole recombination with surface accumulated holes and ii) removal of surface trapping states upon doping, therefore reducing the number of surface accumulated holes which would cause back electron-hole recombination when the light is switched off. Consequently, Mo-doping also substantially increases the hole transfer efficiencies $\eta_{transfer}$ from 0.45 for the 5% Mo:$BiVO_4$ sample up to 0.53 for the 20% Mo:$BiVO_4$ sample.

Deposition of a layer of CoPi onto the undoped $BiVO_4$ anode increases the steady state photocurrent by a factor of 4, as a result of improved water oxidation kinetics. However, the CoPi deposition does not affect the spike and overshoot behavior positively, indicating that the undoped CoPi-modified $BiVO_4$ sample still suffers from a high degree of electron-hole recombination, which most probably occurs because of the limited electron transport of the undoped $BiVO_4$.[22]

For all Mo:$BiVO_4$ samples the observed photocurrents are largely increased after CoPi deposition indicating a drastic reduction of surface recombination due to CoPi-enhanced heterogeneous electron transfer rates at the semiconductor-electrolyte interface. Indeed, recombination rates k_{rec} become very small compared to hole transfer rates k_{trans} for the 5% Mo:$BiVO_4$ sample and the 10% Mo:$BiVO_4$ sample (factor of 6 and 7.5, respectively). A maximum hole transfer efficiency $\eta_{transfer}$ of 0.877 was yielded for the 10% Mo:$BiVO_4$ sample which is in good agreement with obtained j-V-curves and photocurrents, respectively.

Table 8-4. Summary of photocurrent transient analysis for pristine and Mo-doped $BiVO_4$ samples. Transients acquired at 1.23 V vs RHE with 2 mW/cm² of 440 nm light in backside illumination.

Sample	with or w/o CoPi	current densities (mA/cm²)	$\eta_{transfer}$	rate constants (s^{-1})
$BiVO_4$	without CoPi	j_{ini} = 0.055 mA/cm²	0.033	k_{trans} = 0.040
		j_{ss} = 0.002 mA/cm²		k_{rec} = 1.189
	with CoPi	j_{ini} = 0.097 mA/cm²	0.191	k_{trans} = 0.105
		j_{ss} = 0.018 mA/cm²		k_{rec} = 0.446
5% Mo:$BiVO_4$	without CoPi	j_{ini} = 0.225 mA/cm²	0.445	k_{trans} = 0.274
		j_{ss} = 0.100 mA/cm²		k_{rec} = 0.341
	with CoPi	j_{ini} = 0.341 mA/cm²	0.844	k_{trans} = 0.356
		j_{ss} = 0.288 mA/cm²		k_{rec} = 0.066
10% Mo:$BiVO_4$	without CoPi	j_{ini} = 0.267 mA/cm²	0.477	k_{trans} = 0.170
		j_{ss} = 0.127 mA/cm²		k_{rec} = 0.186
	with CoPi	j_{ini} = 0.563 mA/cm²	0.877	k_{trans} = 0.302
		j_{ss} = 0.494 mA/cm²		k_{rec} = 0.042
15% Mo:$BiVO_4$	without CoPi	j_{ini} = 0.168 mA/cm²	0.438	k_{trans} = 0.275
		j_{ss} = 0.074 mA/cm²		k_{rec} = 0.345
	with CoPi	j_{ini} = 0.393 mA/cm²	0.629	k_{trans} = 0.481
		j_{ss} = 0.247 mA/cm²		k_{rec} = 0.284
20% Mo:$BiVO_4$	without CoPi	j_{ini} = 0.199 mA/cm²	0.528	k_{trans} = 0.233
		j_{ss} = 0.105 mA/cm²		k_{rec} = 0.208
	with CoPi	j_{ini} = 0.278 mA/cm²	0.687	k_{trans} = 0.386
		j_{ss} = 0.191 mA/cm²		k_{rec} = 0.176

To further clarify the origin of the high photoelectrochemical performance, Mott-Schottky-type electrochemical impedance spectroscopy was applied (see chapter 5.5.3.2). The obtained values for the flat band potential V_{FB} are summarized in Table 8-5. It was uncertain whether accurate results would be provided by Mott-Schottky-analysis. However, as exemplarily shown for a 10% Mo-sample in Figure 8-21c, the determined flat band potentials are frequency independent and in line with previously reported V_{FB} values for $BiVO_4$ electrodes (see Appendix, chapter 12.1.2.5 for detailed measurements for other samples).[74,135] Flat band potentials of the Mo-doped $BiVO_4$ thin films are slightly more anodic with respect to the undoped $BiVO_4$ thin film. For the doped samples, the flat band

potential is shifted cathodically with increasing Mo content from 0.17 V vs RHE for the 5% Mo:$BiVO_4$ sample to 0.11 V vs RHE for the 20% Mo:$BiVO_4$ sample.

Table 8-5. Summary of flatband potentials determined by Mott-Schottky analysis.

Sample	V_{FB} vs RHE (V) measured at 500 Hz	V_{FB} vs RHE (V) measured at 1 kHz
$BiVO_4$	0.11	0.07
5% Mo:$BiVO_4$	0.17	0.16
10% Mo:$BiVO_4$	0.15	0.15
15% Mo:$BiVO_4$	0.13	0.13
20% Mo:$BiVO_4$	0.11	0.12

Based on the Mott-Schottky equation the number of free charge carriers N_D can be calculated from the slope of the linear parts of the Mott-Schottky graphs. Results are summarized in Table 8-6. As can be seen in Figure 8-21a**,** the slope of the undoped sample is much steeper than the one of the Mo-doped samples. Consequently, a low number of free charge carriers accounting for $1.38 \cdot 10^{18}$ cm^{-3} was calculated. In good agreement with the determined photocurrents and flat band potentials, a dramatic increase of free charge carriers upon Mo incorporation into the $BiVO_4$ thin films is revealed. The amount of Mo within the $BiVO_4$ thin films directly influences the amount of free charge carriers. With exception of the 20% Mo-sample, all samples, exhibit nearly equal slopes, and considering all other parameters accounting for the Mott-Schottky slope to be constant among the samples, they exhibit nearly the same free number of free charge carriers accounting for $24.0 \cdot 10^{18}$ cm^{-3} up to $33.0 \cdot 10^{18}$ cm^{-3}. The most gentle slope was obtained for the 20% Mo:$BiVO_4$ sample which in turn results in the highest number of free charge carriers accounting for $310 \cdot 10^{18}$ cm^{-3}.

Table 8-6. Number of free charge carriers in $BiVO_4$ and Mo:$BiVO_4$ thin film photoanodes. Calculations are based on the Mott-Schottky equation, an applied potential of 1.23 V vs RHE, and the specific surface areas of the electrodes determined by Kr physisorption.

sample	N_D (cm^{-3})
$BiVO_4$	$1.38 \cdot 10^{18}$
5% Mo: $BiVO_4$	$24.0 \cdot 10^{18}$
10% Mo: $BiVO_4$	$31.3 \cdot 10^{18}$
15% Mo: $BiVO_4$	$33.0 \cdot 10^{18}$
20% Mo: $BiVO_4$	$310 \cdot 10^{18}$

According to our results, the 20% Mo-doped $BiVO_4$ exhibits the highest number of free charge carriers. However, this is not translated into the highest photocurrents. As shown by SEM investigations (*vide supra*), the streak size of the single-crystalline domain of the 20% Mo sample is about 139 nm, which is bigger than the hole diffusion length for $BiVO_4$ of 70-100 nm. Additionally, the morphology of the single-crystalline domains of the 20% Mo:$BiVO_4$ sample exhibits more grain boundaries per square centimeter due to decreasing domain size with increasing Mo-incorporation. As grain boundaries potentially act as recombination centers and negatively affect the electron transport properties of a thin film, the observed lower photocurrents for the 20% Mo:$BiVO_4$ sample are lower than for the less doped ones.

To briefly sum-up, in line with other literature reports,[22] the main limiting factor for the PEC performance of the undoped $BiVO_4$ photoanodes was figured out to be the poor electron transport properties through the $BiVO_4$ bulk. According to our results, this problem can be overcome by Mo-doping, which increases the density of free charge carriers in the material and therefore boosts the PEC performance regarding water oxidation. Depositing a layer of CoPi enhances water oxidation kinetics and preeminently reduces possible surface recombination within the space charge region.

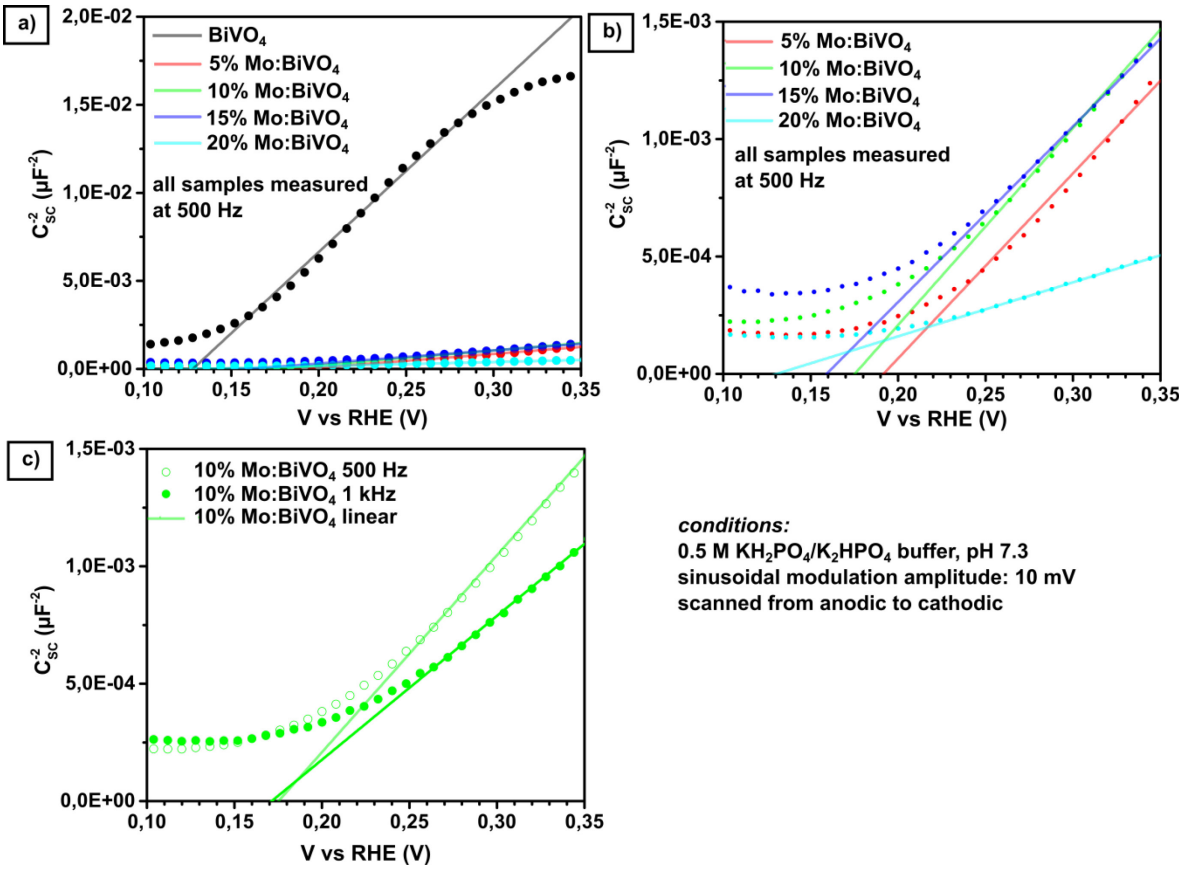

Figure 8-21. Results of Mott-Schottky-analysis: a) Mott-Schottky-Plot for all samples, b) magnified view on the Mo:$BiVO_4$ Mott-Schottky-Plots, c) Mott-Schottky-Plot of a 10% Mo:$BiVO_4$ sample measured at different frequencies.

8.3.5. Conclusion

In summary, the new synthesis method based on a one-pot solution of metalorganic Bi, V and Mo precursors was applied to directly deposit Mo-doped $BiVO_4$ thin films by simple dip coating and subsequent calcination. Structural characterization reveals the thin films to crystallize in the monoclinic scheelite structure. Morphologic characterization proved the thin films to be porous and comprised of differently oriented, single-crystalline domains. crystal structure and morphology of the Mo:$BiVO_4$ thin films are affected by the Mo-content as follows: with increasing Mo content i) the monoclinic scheelite structure gains more tetragonal scheelite character ii) the domain size is decreased and the inner domain material streak size is increased with increasing Mo content. (see Figure 8-22a) Investigations of the photoelectrochemical performance regarding water oxidation of

pristine and CoPi-decorated $BiVO_4$ and Mo:$BiVO_4$ thin films revealed drastically increased PEC performance upon Mo-doping (see Figure 8-22b and c) The obtained photocurrent of 4.6 mA/cm² at 1.23 V vs. RHE under an illumination of white light of an intensity of 100 mW/cm² for CoPi-decorated Mo-doped $BiVO_4$ is amongst the highest reported so far for single-layer $BiVO_4$ thin film photoanodes of comparably facile design. Further investigation using photocurrent transients and Mott-Schottky-type EIS gave insights to dominant recombination mechanisms and electronic properties of the material. The new bottom-up synthesis approach turns out to be a powerful method for the direct fabrication of fine-tuned photoanodes for PEC water oxidation which, in principle, can be applied to other oxide-based photoanode materials.

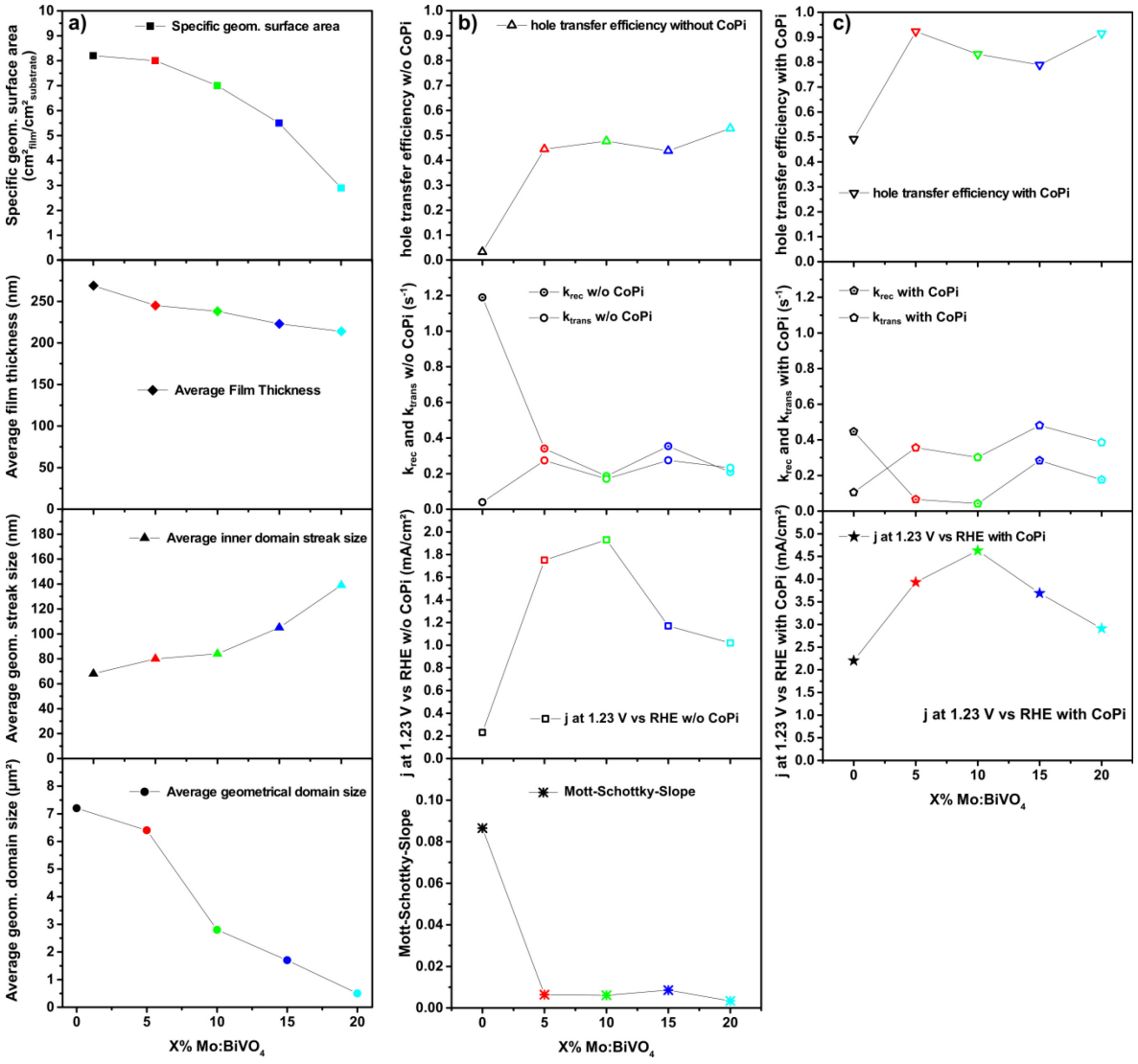

Figure 8-22. a) Morphological features, b) Photoelectrochemical properties without CoPi surface functionalization, and c) Photoelectrochemical properties with CoPi surface functionalization of the $BiVO_4$ and Mo:$BiVO_4$ thin film photoanodes illustrated as a function of Mo content.

8.4. Variation of parameters influencing the PEC performance

8.4.1. Introduction

In chapter 8.2 and 8.3 the main PEC performance-limiting factor for $BiVO_4$ as anode material was figured out to be its poor charge transport properties; a result which is in excellent agreement with other literature reports. For the $BiVO_4$ thin film photoanodes this problem was tackled by two strategies: i) Mo doping to enhance the materials conductivity and ii) adjustment of the thin film nanostructures to sizes comparable to the minor carrier diffusion length L_D of $BiVO_4$ in order to enhance the separation of photo-generated charge carriers. Additionally, the deposition of CoPi water oxidation catalyst onto the $BiVO_4$ thin film photoanodes was used to overcome the sluggish kinetics of the $BiVO_4$ surface regarding the water oxidation reaction. However, nanostructuration of photoanodes can also have disadvantageous effects on PEC performance.[152,153]

In order to evidence the strong positive impact of the domain-like morphology of the here developed $BiVO_4$ thin film photoanodes, $BiVO_4$ thin films with worm-like morphology were fabricated by the same synthesis method with only a slight deviation in the synthesis protocol. Photoelectrochemical performance regarding water oxidation was investigated. Furthermore, the influence of the calcination temperature on the structure and morphology of the Mo:$BiVO_4$ thin films and its impact on the photoelectrochemical performance was investigated. Finally, the impact of the deposition method of the CoPi water oxidation catalyst on the photoelectrochemical performance of Mo:$BiVO_4$ photoanodes was investigated. Results of the variation of the mentioned synthesis parameters are presented in the upcoming sections.

8.4.2. Domain morphology

The new bottom-up synthesis approach was adjusted to fabricate $BiVO_4$ and Mo:$BiVO_4$ thin film photoanodes exhibiting worm-like morphology. Practically, this was achieved by addition of 50 wt% of F127, a triblock copolymer composed of a central hydrophobic block of poly(propylene oxide) surrounded by two hydrophilic blocks of poly(ethylene oxide) at chain ends (50 wt% with respect to the mass of $BiVO_4$ in solution). Despite

adding the polymer, the whole synthesis procedure remained unchanged. Resulting worm-like $BiVO_4$ and Mo:$BiVO_4$ thin films were characterized and photoelectrochemical performance regarding water oxidation was investigated. Results are presented in the following sections.

The influence of the polymer on the crystal structure of the worm-like $BiVO_4$ and Mo:$BiVO_4$ thin films was investigated by GI-XRD. Representative for all samples, a worm-like $BiVO_4$ thin film on FTO was analyzed; results are shown in Figure 8-23. All observed reflections can be assigned to $BiVO_4$ in the monoclinic scheelite structure. The worm-like $BiVO_4$ thin films exhibit isotropic and polycrystalline character. No side phases could be traced within the detection limit of the equipment. No influence of addition of the F127 polymer to the synthesis solution on the crystal structure of the calcined $BiVO_4$ thin film could be observed.

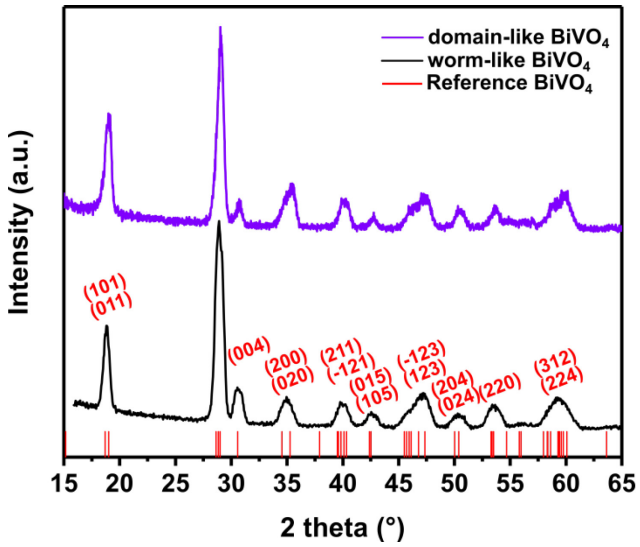

Figure 8-23. XRD (gracing incidence) patterns of domain-like and worm-like $BiVO_4$ thin films on FTO together with reference reflections acc. to PDF 01-083-1698 (monoclinic scheelite phase).

Changes in the nanostructure of thin films can affect their light absorption properties considerably. UV/Vis spectroscopy was applied to investigate light absorption properties of the worm-like $BiVO_4$ and Mo:$BiVO_4$ thin films. In Figure 8-24a, a comparison of the

absorption spectra of a 5% Mo:$BiVO_4$ thin films deposited on FTO in domain-like morphology and worm-like morphology is shown. As can be seen, the absorbance of the worm-like thin film is significantly increased compared to the domain-like thin film. This is reasonable as advanced thin film structuring on the nanoscale comes along with enhanced light distribution within the electrode material due to light scattering. For both morphologies a comparable absorption onset of ~ 539 nm was estimated. This is reasonable as addition of morphology directing polymer to the synthesis solution should not have any influence on the intrinsic material properties after calcination. In Figure 8-24b, a comparison between worm-like $BiVO_4$ and Mo:$BiVO_4$ is shown. Efficient light absorption can be observed for all samples. With increasing amount of Mo content the absorbance is increased drastically. As the measurements were carried out in transmission mode, most probably a big portion of the incident light was scattered and did not reach the detector. This is a result of increased particle size with increasing Mo content (vide infra) and is not related to a smaller band gap.

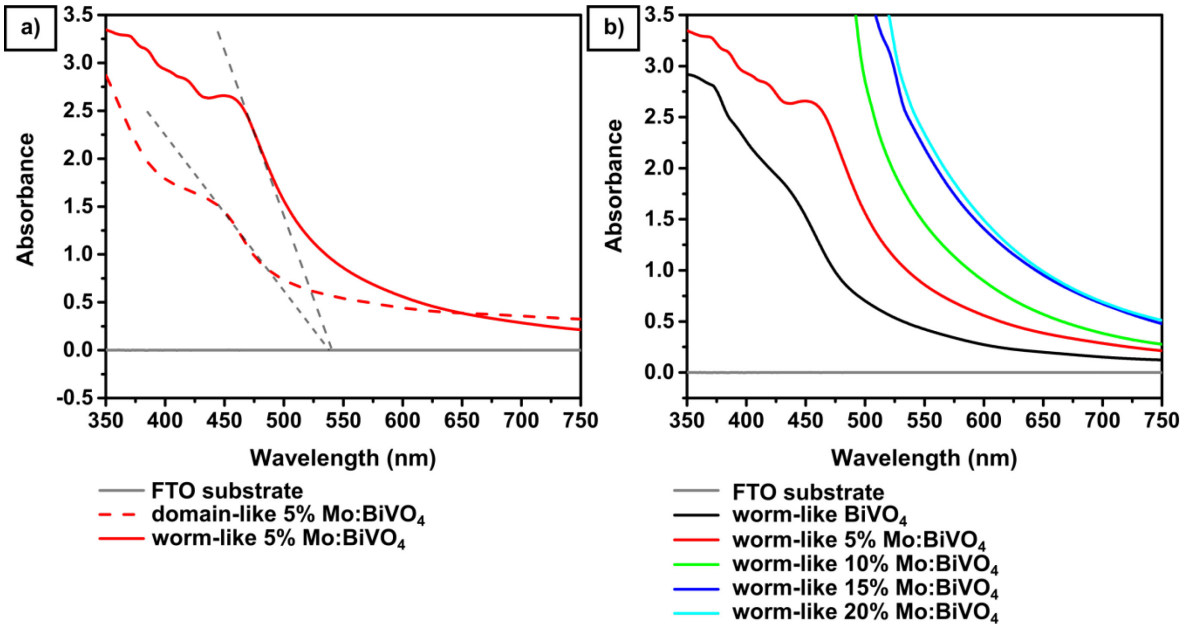

Figure 8-24. UV/Vis spectra of worm-like $BiVO_4$ and Mo:$BiVO_4$ thin films on FTO. a) comparison of a 5% Mo:$BiVO_4$ thin film with worm-like and domain-like morphology and b) comparison of worm-like $BiVO_4$ and Mo:$BiVO_4$ thin films.

The thin film morphology and composition has been investigated by SEM/EDX. SEM images of 10% Mo:$BiVO_4$ thin films FTO with and without F127 added to the precursor solution are shown in Figure 8-25. The structuration effect of the addition of the polymer is evident. As can be seen, the domain-like morphology (see chapter 8.2.2 and 8.3.3) of the thin films is changed to an open porous, particulate morphology upon addition of the F127 polymer. The addition of F127 results in thin films comprised of one-dimensionally elongated particles (worm-like). This worm-like morphology indicates evaporation-induced self-assembly of the Bi, V and Mo compounds during dip coating which in turn most probably is a consequence of phase segregation induced by the polymer.

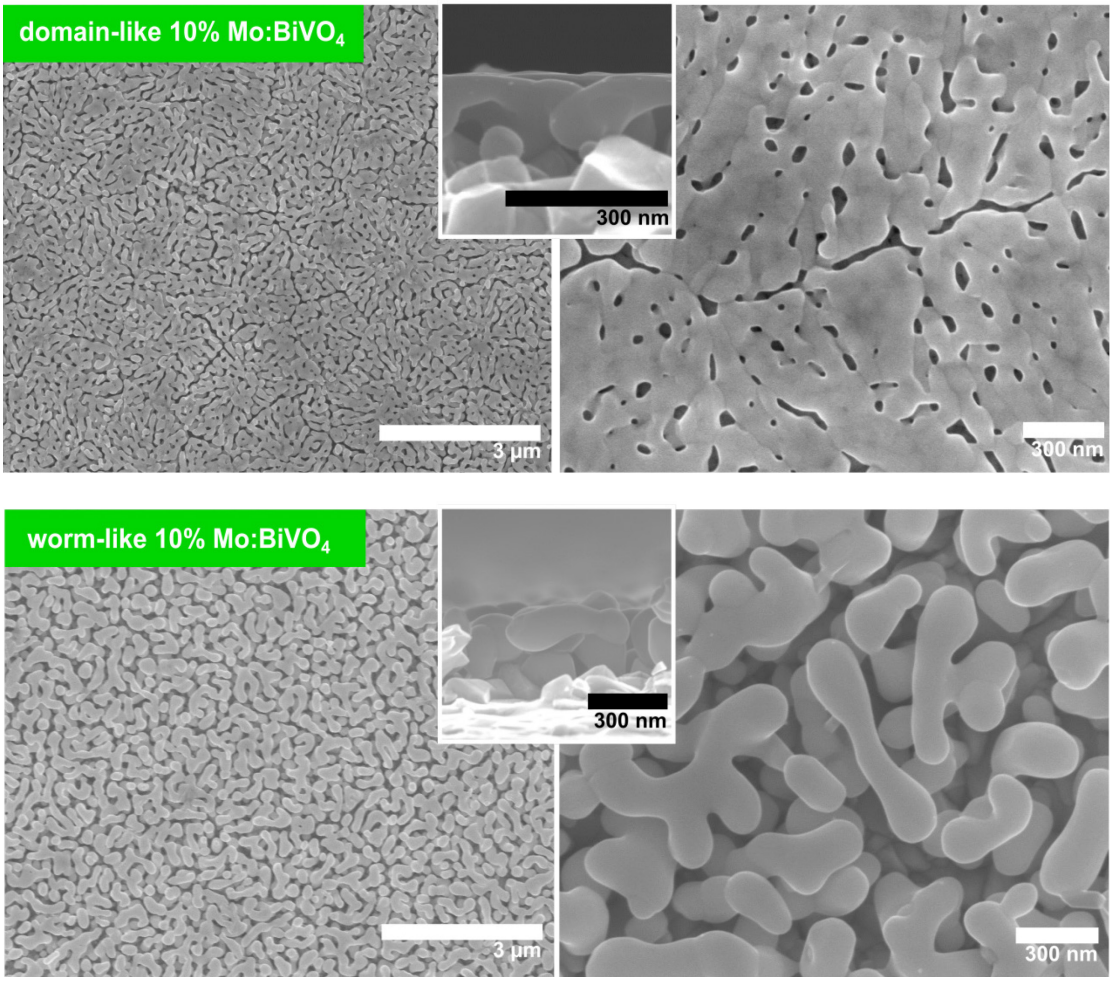

Figure 8-25. SEM images comparing the morphology of domain-like 10% Mo:$BiVO_4$ thin films and worm-like 10% Mo:$BiVO_4$ thin films.

Top view and cross section images together with EDX spectra of worm-like $BiVO_4$ and different Mo:$BiVO_4$ thin films on FTO are shown in Figure 8-26. A summary of all analyzed thin film features is given in Table 8-7. The structuration effect of the addition of the polymer is evident. All thin films exhibit the worm-like morphology. The morphology changes with increasing Mo content in terms of particle sizes and pore sizes.

Due to the irregular and inhomogeneous shape of the thin film particles and pores, determination of average particle diameter and pore diameter is not possible. However, to gather information about the particle sizes and pore sizes, the average geometrical area of particles and pores was determined by top-view SEM. Corresponding particle sizes and pore sizes, respectively, therefore are given as area units µm².

The pristine, worm-like $BiVO_4$ thin film is comprised particles of a geometrical size of about $0.5 \cdot 10^{-3}$ µm². This morphology gives rise to small pores of $3 \pm 2 \cdot 10^{-3}$ µm². With increasing Mo content, particle sizes as well as pore sizes increase. Only a slight increase in particle sizes is observed for the 5% Mo:$BiVO_4$, 10% Mo:$BiVO_4$ and 15% Mo:$BiVO_4$ thin films accounting for $2 \pm 1 \cdot 10^{-3}$ µm², $5 \pm 4 \cdot 10^{-3}$ µm² and $6 \pm 4 \cdot 10^{-3}$ µm², respectively. The particle size is largely increased for the 20% Mo:$BiVO_4$ thin film accounting for an average particle size of $19 \pm 16 \cdot 10^{-3}$ µm². As already elucidated in 8.3.3 and also reported in literature[67], average particle sizes/streak sizes increase with increasing Mo content. This trend is also observed for the worm-like structured $BiVO_4$ and Mo:$BiVO_4$ thin films. As average particles sizes increase, the pore sizes are enlarged with increasing Mo content as well, accounting for $3 \pm 2 \cdot 10^{-3}$ µm², $5 \pm 3 \cdot 10^{-3}$ µm², $7 \pm 6 \cdot 10^{-3}$ µm² and $63 \pm 45 \cdot 10^{-3}$ µm² for the worm-like 5% Mo:$BiVO_4$, 10% Mo:$BiVO_4$, 15% Mo:$BiVO_4$ and 20% Mo:$BiVO_4$, respectively.

The cross section images shown in Figure 8-26 confirm the particulate character of all thin films. As can be seen, all thin films are comprised of randomly deposited particles. Single particles are partially interconnected. This most probably is a consequence of sintering/material densification. Film thicknesses of the worm-like $BiVO_4$ and Mo:$BiVO_4$ thin films vary between ~320 nm for the 15% Mo:$BiVO_4$ sample and ~432 nm for the 5% Mo:$BiVO_4$ sample. Additionally, the cross section images show that particles sizes of

the 10% Mo:$BiVO_4$, the 15% Mo:$BiVO_4$ and the 20% Mo:$BiVO_4$ are in the range of the film thickness. That means, a single particle reaches from the FTO substrate to the thin film surface. EDX analysis proves all thin films to consist of Bi, V and Mo, respectively. Furthermore, only a very little carbon peak is observed for all samples which proves all organic compounds being successfully removed by calcination.

Table 8-7. Overview of particle and pore sizes and film thicknesses of worm-like $BiVO_4$ and Mo:$BiVO_4$ thin films on FTO substrate.

samples	**Particle size (10^{-3} µm²)** (geometrical particle area determined by top view images)	**Pore size (10^{-3} µm²)** (geometrical pore area determined by top view images)	**Film thickness (nm)** (determined by cross section images)
Worm-like $BiVO_4$	0.5 ±0.3	3 ±2	~352
Worm-like 5% Mo:$BiVO_4$	2 ±1	5 ±3	~432
Worm-like 10% Mo:$BiVO_4$	5 ±4	7 ±6	~368
Worm-like 15% Mo:$BiVO_4$	6 ±4	8 ±6	~320
Worm-like 20% Mo:$BiVO_4$	19 ±16	63 ±45	~358

TEM measurements were performed to investigate the microstructure of the worm-like $BiVO_4$ thin films. Due to the drastically increasing particle size with increasing Mo-content, only the undoped worm-like $BiVO_4$ sample was suitable for TEM measurements; results are shown in Figure 8-27. As can be seen by the overview image (Figure 8-27a) the worm-like morphology of the thin film material is confirmed by TEM investigations. The lattice fringes which can be seen in the high resolution image in Figure 8-27b further prove the thin film material to be highly crystalline. The FFT pattern of the fringes (Figure 8-27, inset) is comprised of only two signals corresponding to the (101) plane of $BiVO_4$ in the monoclinic scheelite phase. Additionally, SAED experiments were carried out; results are shown in Figure 8-27c. A ring-shaped diffraction pattern typical for polycrystalline samples was obtained. All reflections could be assigned to $BiVO_4$ in the monoclinic scheelite phase according to PDF 01-083-1698.

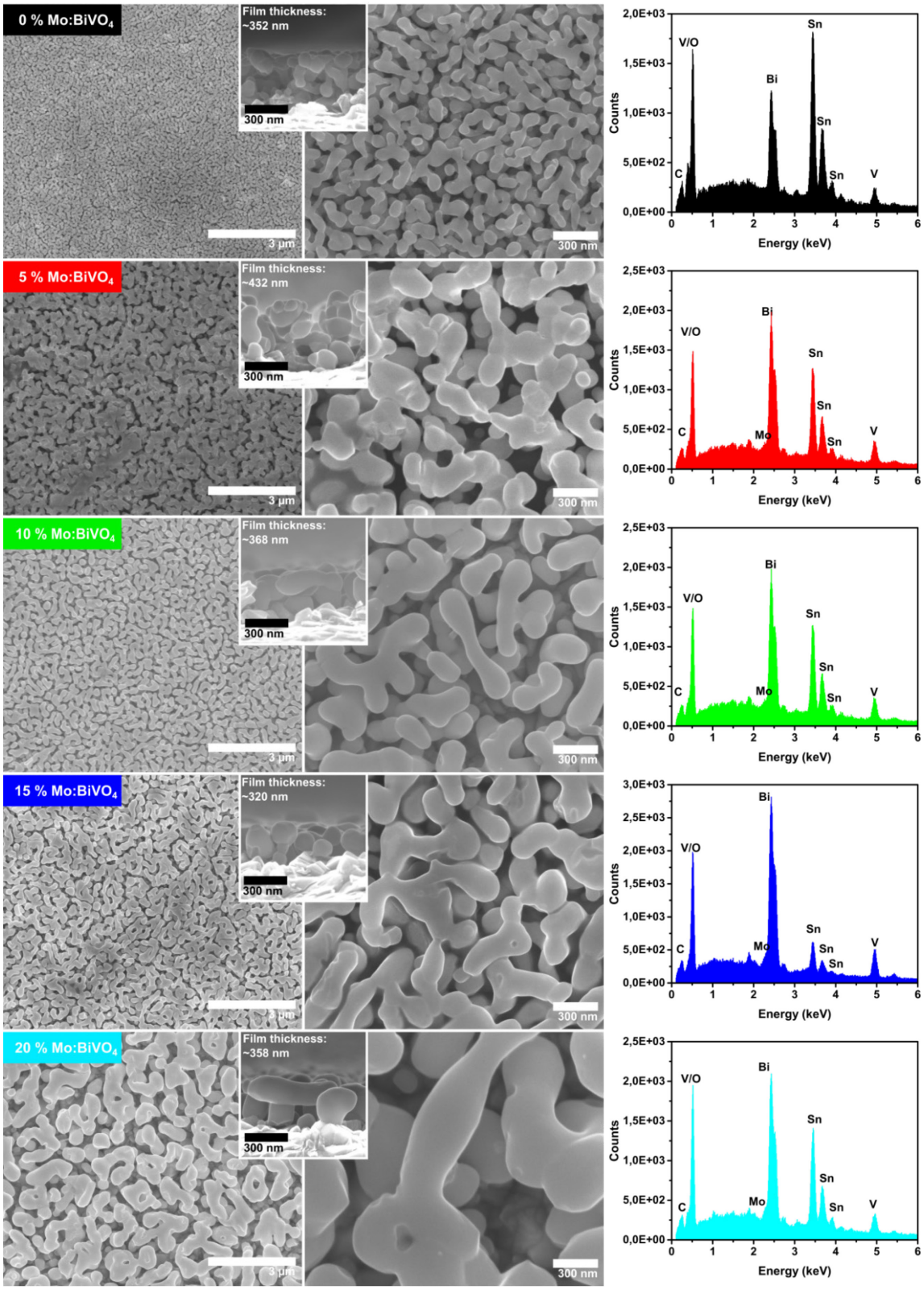

Figure 8-26 SEM investigations of worm-like F127 templated $BiVO_4$ and Mo:$BiVO_4$ thin films on FTO calcined at 450 °C and EDX spectra. The Mo-L peak overlaps with the Bi-M peak at 2.3 keV.

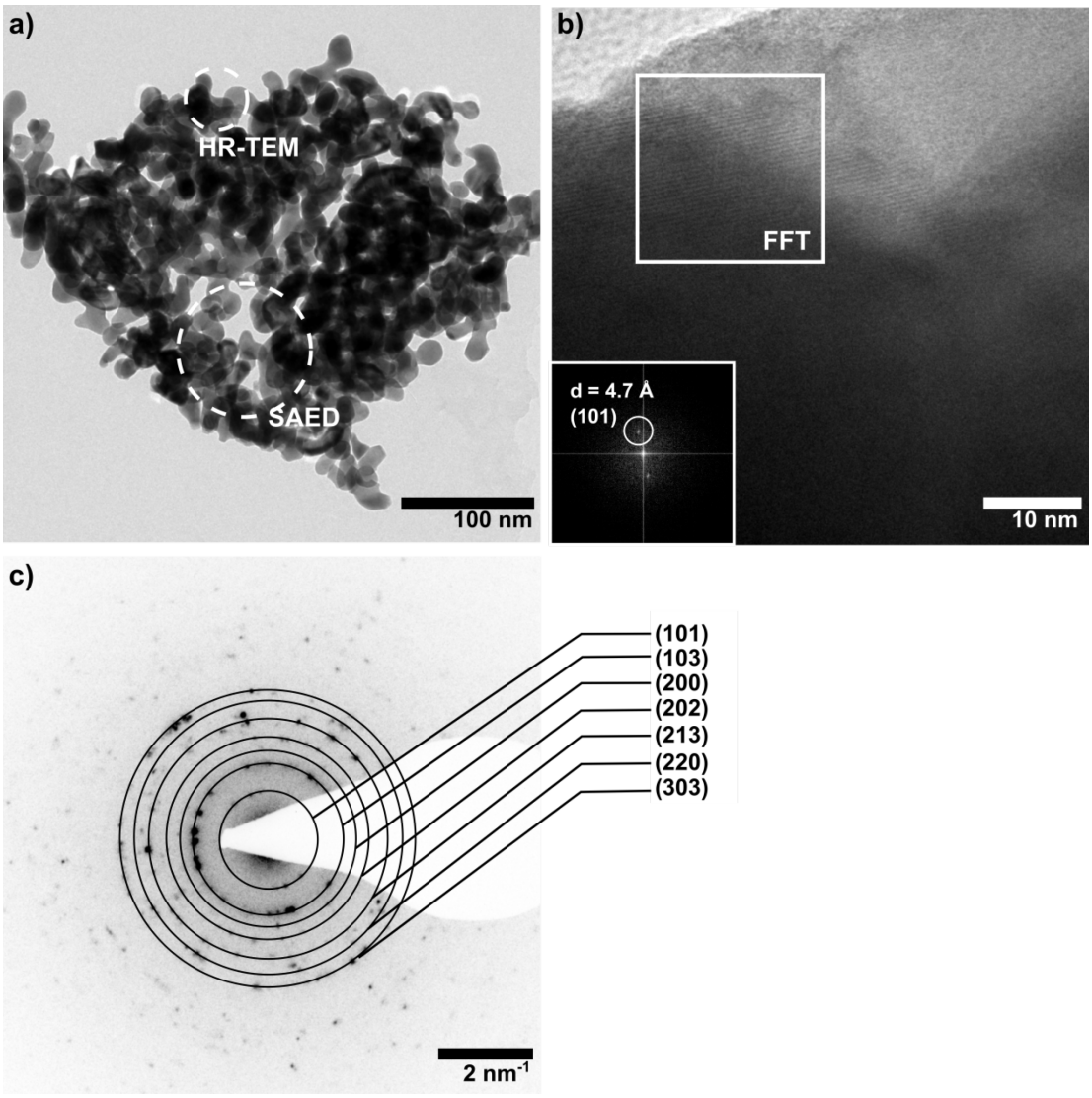

Figure 8-27. TEM/SAED investigations of a worm-like $BiVO_4$ thin film. a) overview image, b) HR-TEM image with corresponding FFT (inset) and c) SAED pattern with indexed reflections acc. to $BiVO_4$ in momoclinic scheelite phase (PDF 01-083-1698).

Photoelectrochemical performance of the Mo:$BiVO_4$ thin films regarding water oxidation was investigated using a standard electrochemical cell equipped with the commonly used electrodes (RHE – reference, Pt-wire – counter electrode). Figure 8-28 shows obtained j-V curves for the worm-like $BiVO_4$ and Mo:$BiVO_4$ photoanodes with and without a layer of CoPi deposited acquired in frontside and backside illumination. A summary of yielded photocurrents at an applied potential of 1.23 V vs RHE for all measured photoanodes is given in Table 8-8 together with photocurrents obtained for corresponding domain-like $BiVO_4$ and Mo:$BiVO_4$ photoanodes (given in brackets). See Appendix, chapter 12.1.2.6 for comparing plots of frontside and backside illumination for all worm-like photoanodes.

As can be seen in Figure 8-28, for the undoped worm-like $BiVO_4$ sample only very low photocurrents were obtained accounting for 0.03 mA/cm² 1.23 V vs RHE in frontside illumination. Photocurrent densities obtained in backside illumination are twice as high as in frontside illumination accounting for 0.07 mA/cm² at 1.23 V vs RHE. This indicates that the photoelectrochemical performance of undoped $BiVO_4$ is limited by its poor charge transport properties within the material.

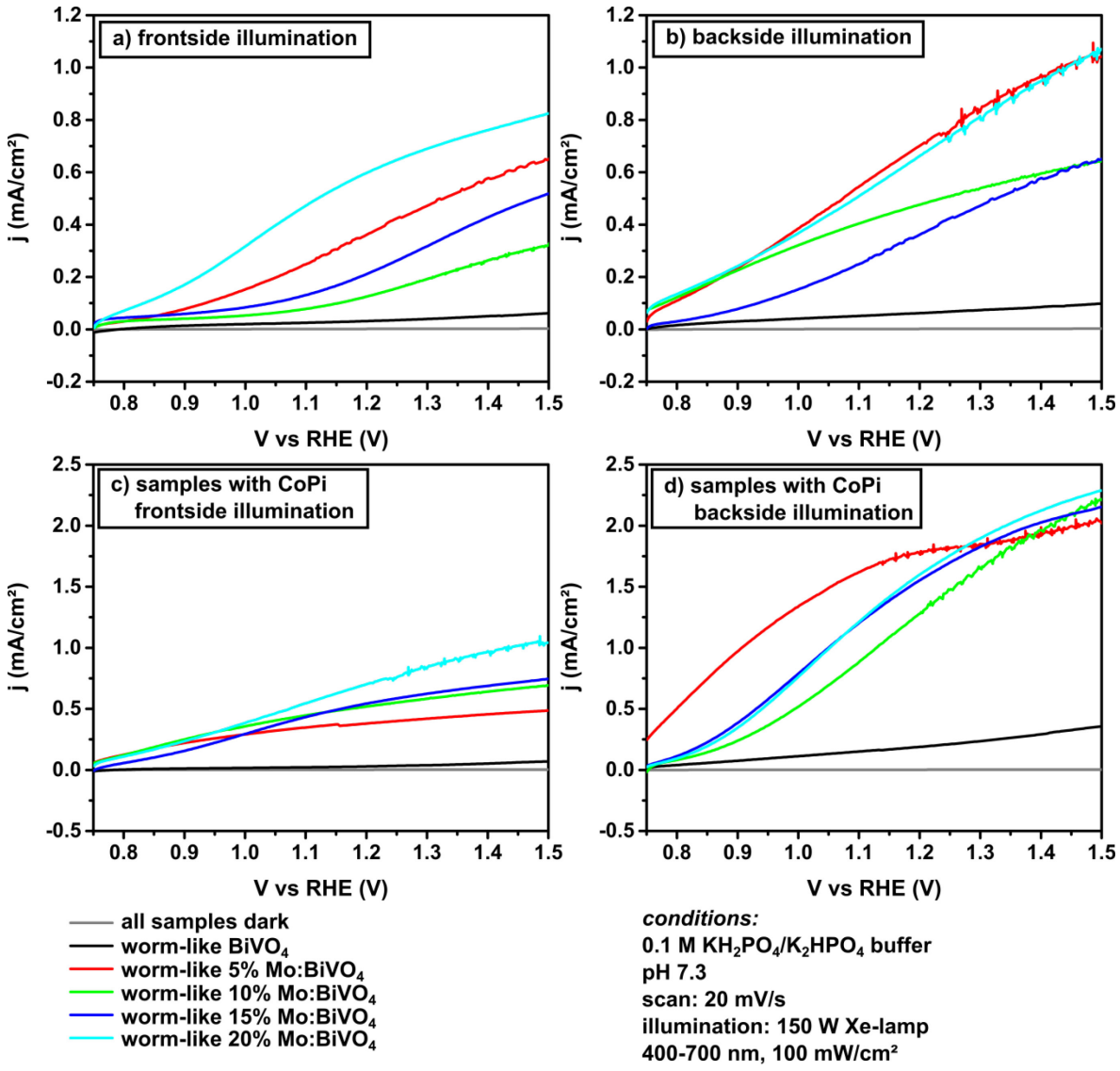

Figure 8-28. j-V-curves of worm-like $BiVO_4$ and Mo:$BiVO_4$ thin films on FTO substrate with and without CoPi deposited in frontside and backside illumination.

Additionally, as shown in Figure 8-29a, the observed photocurrents for the undoped, worm-like $BiVO_4$ are lower than for its domain-like counterparts. Particle sizes of the worm-like, undoped $BiVO_4$ photoanode can be estimated to be matching the hole diffusion length of 70-100 nm of $BiVO_4$. However, collection of the photo-generated charge carriers at the back-contact and electrolyte interfaces is aggravated due to the particulate morphology of the thin film. A high number of particle and grain boundaries promotes recombination and charge scattering of the migrating photo-generated charge carriers.

Hence, observed photocurrents are lower than for the undoped domain-like $BiVO_4$ photoanodes which consist of a barely porous, nearly dense material layer.

Mo doping generally enhances obtained photocurrent densities of the worm-like $BiVO_4$ thin film photoanodes leading to a maximum photocurrent density for the 20% Mo:$BiVO_4$ photoanode accounting for 0.63 mA/cm² and 0.71 mA/cm² at 1.23 V vs RHE in frontside and backside illumination, respectively.

However, although electron transport properties were improved by Mo doping, photocurrents obtained in backside illumination are higher than in frontside illumination in all cases. Furthermore, obtained photocurrents for the worm-like Mo:$BiVO_4$ photoanodes are considerably lower than for their domain-like structured counterparts, as shown exemplarily for the worm-like and domain-like 10% Mo:$BiVO_4$ photoanodes in Figure 8-29b. These findings can be traced back to two reasons: i) charge carriers migrating through the worm-like photoanode need to hurdle a higher number of particle boundaries to reach the back contact and the electrolyte, respectively, which, in consequence, increases the probability of recombination, and ii) particles sizes of the worm-like Mo:$BiVO_4$ photoanodes are much bigger than the hole diffusion length of $BiVO_4$ and also much bigger than material streaks of their domain-like analogues. This also enhances the probability of recombination and therefore aggravates efficient charge carrier collection at the surface.

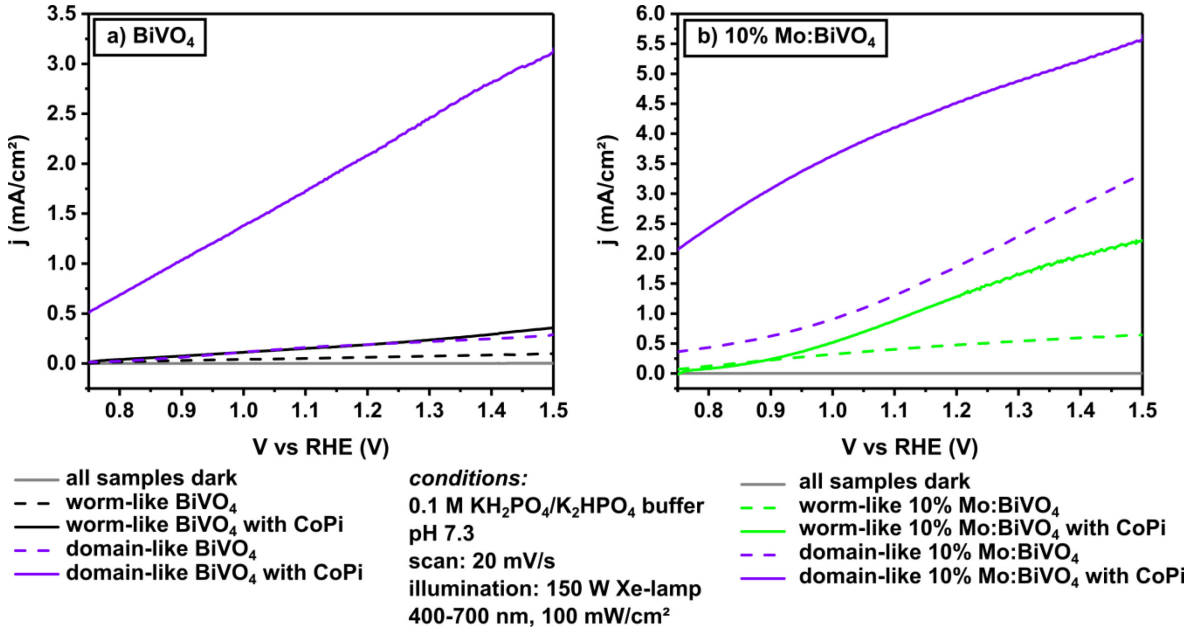

Figure 8-29. j-V curves of a) worm-like and domain-like $BiVO_4$ photoanodes and b) worm-like and domain-like 10% Mo:$BiVO_4$ photoanodes.

Table 8-8. Summary of yielded photocurrents at an applied potential of 1.23 V for worm-like $BiVO_4$ and Mo:$BiVO_4$ photoanodes with and without CoPi deposited in frontside and backside illumination. Corresponding photocurrents for domain-like $BiVO_4$ and Mo:$BiVO_4$ photoanodes given in brackets.

Sample	j at 1.23 V vs RHE (mA/cm²)			
	without CoPi		with CoPi	
	frontside illumination	backside illumination	frontside illumination	backside illumination
Worm-like $BiVO_4$	**0.03** (0.08)	**0.07** (0.20)	**0.04** (0.54)	**0.20** (2.19)
Worm-like 5% Mo:$BiVO_4$	**0.40** (1.75)	**0.75** (1.76)	**0.42** (4.02)	**1.81** (3.94)
Worm-like 10% Mo:$BiVO_4$	**0.15** (1.74)	**0.50** (1.93)	**0.54** (3.51)	**1.40** (4.64)
Worm-like 15% Mo:$BiVO_4$	**0.24** (1.13)	**0.40** (1.17)	**0.57** (4.00)	**1.64** (3.69)
Worm-like 20% Mo:$BiVO_4$	**0.63** (1.12)	**0.71** (1.02)	**0.75** (3.25)	**1.70** (2.91)

Deposition of CoPi water oxidation catalyst onto the photoanode surfaces improves observed photocurrent densities for all worm-like $BiVO_4$ and Mo:$BiVO_4$ samples by improvement of the water oxidation kinetics. When frontside illumination is applied, a maximum photocurrent accounting for 0.75 mA/cm² at an applied potential of 1.23 V vs RHE was observed for the worm-like 20% Mo:$BiVO_4$ photoanode. In backside illumination mode, a maximum photocurrent of 1.8 mA/cm² at 1.23 V vs RHE was obtained for the 5% Mo:$BiVO_4$ photoanode. Observed photocurrents for all CoPi-modified worm-like photoanodes are much lower compared to their domain-like structured counterparts. As surface recombination is reduced to a minimum by CoPi deposition, this further indicates the worm-like photoanode morphology to be rather disadvantageous for the PEC performance and therefore to be less favorable compared to the domain-like morphology (*vide infra*).

To further clarify the origin of the lowered PEC performance of the worm-like $BiVO_4$ and Mo:$BiVO_4$ photoanodes, photocurrent transient measurements were performed and analyzed according to the phenomenological approach explained in chapter 5.5.3.3. The photocurrent transients of the worm-like $BiVO_4$ and Mo:$BiVO_4$ photoanodes with and without CoPi deposited acquired using backside illumination are shown in Figure 8-30.

As can be seen in Figure 8-30a, there is only a very little photoresponse observable for the undoped, worm-like $BiVO_4$ photoanode. Depositing a layer of CoPi enhances the observed photocurrent density. For the CoPi-modified, undoped, worm-like sample a typical spike when light is switched on and overshoot when light is switched off is observed. The transient analysis reveals a surface recombination rate k_{rec} of 0.217 s^{-1} and a hole transfer rate k_{trans} of 0.171 s^{-1} after CoPi deposition which results in a low hole transfer efficiency $\eta_{transfer}$ of 0.440. As surface recombination should be reduced to a minimum by CoPi deposition, this photocurrent transient shape reveals the undoped, worm-like sample most probably to be highly suffering from slow charge transport through the electrode as photo-generated electrons are not sufficiently fast transported to the back contact and therefore rather recombine (see chapter 8.3.4).

For the worm-like 5% Mo:$BiVO_4$ the photocurrent transient shape is very similar different. When switching the light on, the photocurrent plateau is slowly building-up within a time

period of about 1 s. There is no initial photocurrent spike which decays fast after switching the light on. This is accompanied by a significant tailing of the photocurrent instead of the usual photocurrent overshoot when switching off the light. Both indicate a certain disorder within the electrode which can be assigned to trapping and detrapping processes of charge carriers within the space charge region due to unfavorable charge carrier transport.[154–156]

This most probably is a consequence of the hampered charge transport through the worm-like Mo:$BiVO_4$ nanostructures to the back contact and electrolyte, respectively, in combination with the sluggish water oxidation kinetics of the $BiVO_4$ surface. By improvement of water oxidation kinetics by CoPi deposition, the observed photocurrent transient for the worm-like 5% Mo:$BiVO_4$ photoanode reveals a small spike and overshoot indicating an improved photocurrent response. Analysis of the photocurrent transients reveals a low surface recombination rate k_{rec} of 0.034 s^{-1} and a hole transfer rate k_{trans} of 0.151 s^{-1} resulting in a high hole transfer efficiency $\eta_{transfer}$ of 0.818. This confirms the water oxidation kinetics at the surface to be improved by CoPi deposition. In turn, surface recombination is no longer a severe PEC performance limiting factor which further points to unfavorable charge transport through the anode's nanostructures.

The photocurrent transient shape of the 10% Mo:$BiVO_4$, the 15% Mo:$BiVO_4$ and the 20% Mo:$BiVO_4$ photoanodes is significantly different compared to the undoped $BiVO_4$ and 5% Mo:$BiVO_4$ sample. All samples without CoPi surface modification show pronounced spikes and overshoots when the light is switched on and off, respectively. The transient shape already indicates pronounced surface recombination for these samples. Indeed, photocurrent transient analysis reveals recombination rates k_{rec} of 0.254 s^{-1}, 0.271 s^{-1}, and 0.191 s^{-1} for the 10% Mo:$BiVO_4$, the 15% Mo:$BiVO_4$ and the 20% Mo:$BiVO_4$ samples, respectively. Hole transfer rates k_{trans} are in the range of the recombination rates accounting for 0.259 s^{-1}, 0.191 s^{-1}, and 0.162 s^{-1} for the the 10% Mo:$BiVO_4$, the 15% Mo:$BiVO_4$ and the 20% Mo:$BiVO_4$ samples, respectively. As a result, the hole transfer efficiencies $\eta_{transfer}$ are quite similar for the samples, accounting for 0.505, 0.414, and 0.458 for the 10% Mo:$BiVO_4$, the 15% Mo:$BiVO_4$ and the 20% Mo:$BiVO_4$ samples without CoPi surface functionalization, respectively.

The different transient shape for the worm-like 10%-20% Mo:$BiVO_4$ samples in terms of photocurrent spikes and overshoots instead of slow photocurrent build-ups and tailing as observed for the undoped $BiVO_4$ and the 5% Mo:$BiVO_4$ sample is a consequence of the different thin film morphology of the samples. The increased particle size of the 10%-20% Mo:$BiVO_4$ samples leads to less grain boundaries and less charge scattering and recombination sites, respectively, between the FTO-Mo:$BiVO_4$ interface and the $BiVO_4$-electrolyte interface for these samples (see cross section images in Figure 8-26). Therefore, charge transport through these electrodes is facilitated compared to the undoped and the 5% Mo:$BiVO_4$ sample.

After CoPi functionalization of the surface of the 10%-20% Mo:$BiVO_4$ samples, photocurrent spikes and overshoots are reduced to a minimum. Accordingly, analysis of the photocurrent transients reveals only very little surface recombination rates k_{rec} of 0.014 s^{-1}, 0.017 s^{-1}, and 0.025 s^{-1} and hole transfer rates k_{trans} of 0.246 s^{-1}, 0.153 s^{-1}, and 0.241 s^{-1} for the 10% Mo:$BiVO_4$, the 15% Mo:$BiVO_4$ and the 20% Mo:$BiVO_4$ samples, respectively. As a result the hole transfer efficiency $\eta_{transfer}$ is high for those samples after CoPi deposition accounting for 0.947, 0.899, and 0.906 for the 10% Mo:$BiVO_4$, the 15% Mo:$BiVO_4$ and the 20% Mo:$BiVO_4$ photoanodes, respectively.

Transient analysis reveals that the 10%-20% Mo:$BiVO_4$ samples do not suffer from surface hole recombination after CoPi deposition, i.e. the kinetics of water oxidation at the surface of the electrodes are no longer a PEC performance limiting factor. However, the morphology of the worm-like 10-20% Mo:$BiVO_4$ photoanodes in terms of big particle sizes and big film thickness is disadvantageous for photoelectrochemical applications.

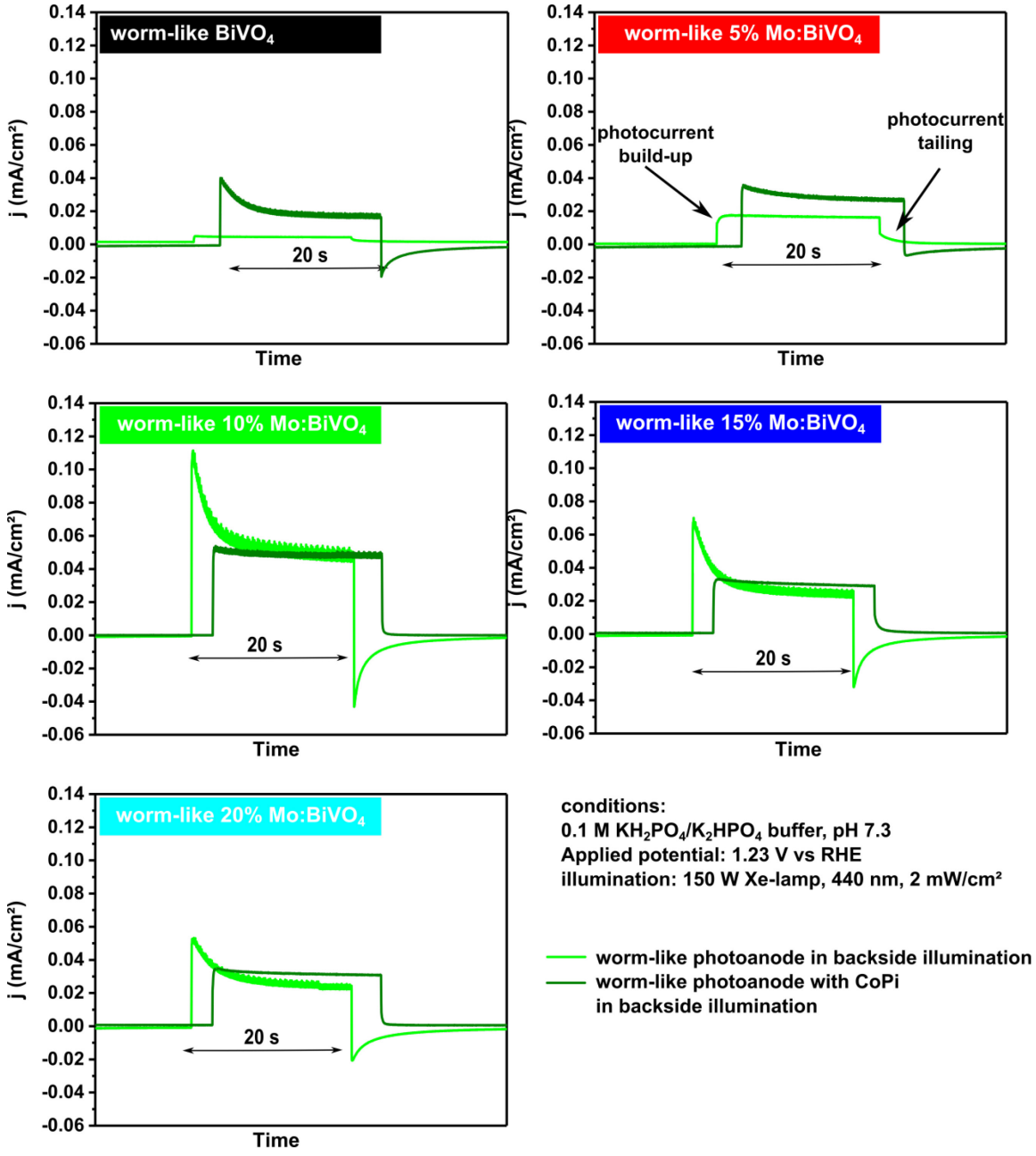

Figure 8-30. Photocurrent transients for a worm-like $BiVO_4$ (a) and a worm-like 5% Mi:$BiVO_4$ (b) photoanode with an without CoPi deposited. Measurements were performed using backside illumination.

Table 8-9. Summary of photocurrent transient analysis for pristine and Mo-doped $BiVO_4$ samples. Transients acquired at 1.23 V vs RHE with 2 mW/cm² of 440 nm light in backside illumination.

Sample	with or w/o CoPi	current densities (mA/cm²)	$\eta_{transfer}$	rate constants (s^{-1})
worm-like $BiVO_4$	without CoPi	n/a	n/a	n/a
		n/a		n/a
	with CoPi	j_{ini} = 0.040 mA/cm²	0.440	k_{trans} = 0.171
		j_{ss} = 0.018 mA/cm²		k_{rec} = 0.217
worm-like 5% Mo:$BiVO_4$	without CoPi	n/a	n/a	n/a
		n/a		n/a
	with CoPi	j_{ini} = 0.035 mA/cm²	0.818	k_{trans} = 0.151
		j_{ss} = 0.028 mA/cm²		k_{rec} = 0.034
worm-like 10% Mo:$BiVO_4$	without CoPi	j_{ini} = 0.111 mA/cm²	0.505	k_{trans} = 0.259
		j_{ss} = 0.056 mA/cm²		k_{rec} = 0.254
	with CoPi	j_{ini} = 0.052 mA/cm²	0.947	k_{trans} = 0.246
		j_{ss} = 0.049 mA/cm²		k_{rec} = 0.014
worm-like 15% Mo:$BiVO_4$	without CoPi	j_{ini} = 0.065 mA/cm²	0.414	k_{trans} = 0.191
		j_{ss} = 0.056 mA/cm²		k_{rec} = 0271
	with CoPi	j_{ini} = 0.052 mA/cm²	0.899	k_{trans} = 0.153
		j_{ss} = 0.049 mA/cm²		k_{rec} = 0.017
worm-like 20% Mo:$BiVO_4$	without CoPi	j_{ini} = 0.053 mA/cm²	0.458	k_{trans} = 0.233
		j_{ss} = 0.024 mA/cm²		k_{rec} = 0.208
	with CoPi	j_{ini} = 0.035 mA/cm²	0.906	k_{trans} = 0.386
		j_{ss} = 0.031 mA/cm²		k_{rec} = 0.176

In summary, synthesis of worm-like $BiVO_4$ and Mo:$BiVO_4$ thin films by modifying the bottom-up synthesis approach by addition of a structure directing polymer (F127) was successful. While no influence of addition of the polymer on the crystal structure was observed, light absorption properties and morphology were changed significantly. UV/Vis spectroscopy proved enhanced light absorption properties whereas electron microscopy revealed the single-crystalline, domain-like morphology to be replaced by a polycrystalline worm-like morphology. The influence of the morphology change on the photoelectrochemical performance regarding water oxidation was investigated. It was figured out that the PEC performance was considerably lower for the worm-like $BiVO_4$ and

Mo:$BiVO_4$ photoanodes compared to their domain-like structured counterparts. As revealed by photocurrent transient analysis, the particulate character of the worm-like photoanodes severely impeded charge carrier transport through the electrode. Hence, recombination of photo-generated charge carriers is promoted resulting in a significantly lower PEC performance for the worm-like $BiVO_4$ and Mo:$BiVO_4$ photoanodes compared to their domain-like structured counterparts.

These findings show: When tackling the problem of low charge carrier transport in $BiVO_4$, thin film morphologies posing hurdles in the migration pathway for the photo-generated charge carriers in terms of recombination and charge scattering sites should be avoided as far as possible. Furthermore, morphologies beneficial for migration of charge carriers like single-crystalline domains are highly beneficial for the PEC performance of $BiVO_4$-based photoanodes.

8.4.3. Calcination temperature

Calcination, i.e. heat treatment of the as-deposited Bi- and V- and Mo- containing, amorphous thin films in air, is the final synthesis step within the synthesis protocol for the direct deposition of $BiVO_4$ and Mo:$BiVO_4$ thin films. From a PEC point of view its importance must not be underestimated as the calcination procedure not only assures the removal of remaining organic compounds and solvent. It also directly affects materials properties like crystal structure and crystallinity as well as the thin film morphology due to sintering effects; parameters which in turn directly affect the PEC performance. For this reason a closer look at the calcination temperature is worth efforts.

Experimentally, 10% Mo:$BiVO_4$ thin films were synthesized according to the new bottom-up synthesis approach described in chapter 8.3 but the calcination procedure was adjusted in the following way: The aging time and temperature of 12 h at 100 °C remained unchanged. The maximum calcination temperature was varied from 350 °C to 550 °C in steps of 50 K. All samples were kept for 2 h at the final (maximum) temperature. Note: The heating ramp was constant for all experiments at 0.5 K/min which leads to an increased calcination time for samples treated at higher temperatures.

To gather information about the influence of the calcination temperature variation on the crystal structure of the resulting Mo:$BiVO_4$, XRD experiments were carried out. Due to the inhomogeneous substrate coverage of Mo:$BiVO_4$ thin films calcined at temperatures higher than 450 °C (*vide infra*), XRD experiments using gracing incidence of the x-ray beam did not provide reasonable results due to intense substrate (FTO) reflections. For this reason corresponding powder samples were prepared. Resulting XRD patterns are shown in Figure 8-31a.

All samples are confirmed to be isotropic and polycrystalline. For all samples calcined at temperatures of 400 °C and higher, the observed reflections can be assigned to the monoclinic scheelite crystal structure according to PDF 01-083-1698. As can be seen in Figure 8-31b, for the 350 °C sample, only a single reflection at ~35° is obtained which corresponds to the (200) plane of the tetragonal scheelite structure. The single reflection splits up into two reflections corresponding to the (200) and the (020) planes with increasing calcination temperature. This can be assigned to the transformation of the tetragonal scheelite structure which is obtained for the sample calcined at 350 °C into the monoclinic scheelite structure which is obtained for the samples calcined at 400 °C and higher.

No side phases could be traced within the detection limit of the equipment. Fitting of the reflection corresponding to the (004) plane at 30.57 ° to a Pseudo Voigt profile and analyzing the full width at half maximum (FWHM) of the resulting fit function reveals decreasing width of the reflections with increasing calcination temperature. Consequently, application of the Scherrer equation (see Equation 8-2) reveals an increase of crystallite sizes *L* with increasing calcination temperature accounting for an estimated crystallite size of 44.5 nm for the sample calcined at 350 °C up to 73.5 nm for the sample calcined at 550 °C (see Table 8-10). These findings indicate an enhancement of crystallinity with increasing calcination temperature.

Equation 8-2. Scherrer equation with K the structure factor, λ the wavelength of the x-ray irradiation, L the crystallite size and cos(θ) the Bragg angle.

$$FWHM = \frac{K \cdot \lambda}{L \cdot \cos\theta}$$

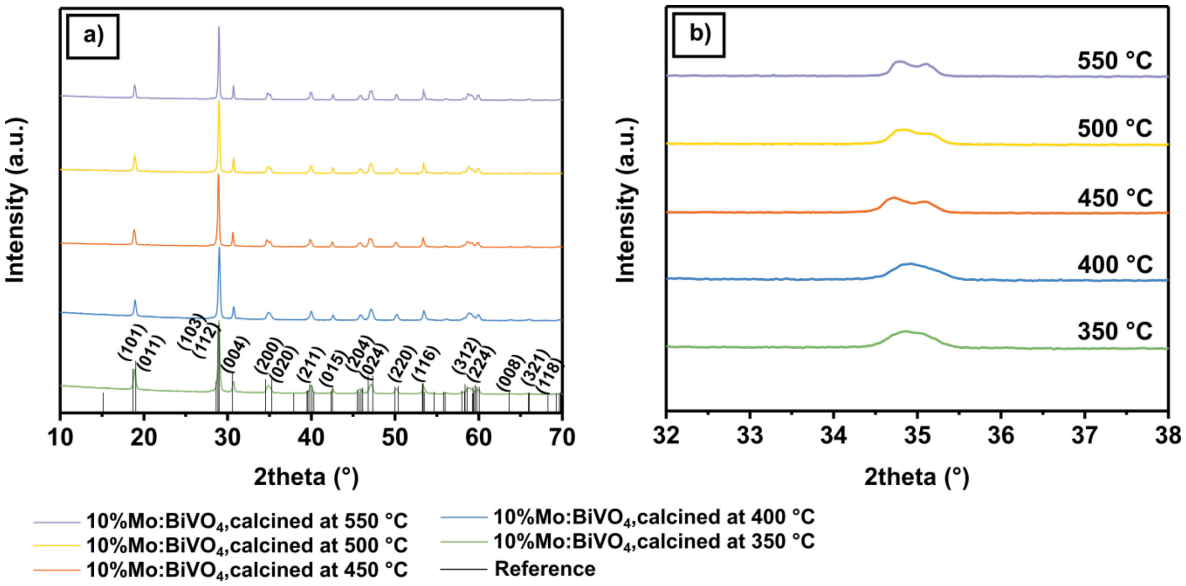

Figure 8-31. a) XRD patterns of 10% Mo:$BiVO_4$ powder samples calcined at different temperatures together with reference reflections acc. to PDF 01-083-1698 (monoclinic scheelite structure), b) magniefied view on the reflections at ~35°.

Table 8-10. FWHM of the (004) reflections at 30.57 ° and crystallite sizes *L* determined using the Scherrer equation with K = 1 and λ = 0.154056 nm for 10% Mo:$BiVO_4$ powder samples calcined at different temperatures.

Calcination temperature (°C)	FWHM at 30.6 ° 2θ (°)	L (nm)
350	0.23	44.5
400	0.21	49.0
450	0.16	63.4
500	0.15	68.5
550	0.14	73.5

The morphology of the 10% Mo:$BiVO_4$ thin films calcined at different temperatures was investigated by SEM. Top view images are shown in Figure 8-32; analyzed morphological thin film features are summarized in Table 8-11. As can be seen in Figure 8-32, the sample calcined at 350 °C exhibits a porous morphology of elongated thin film material. An average material streak size of 48 ±11 nm was determined. The average geometrical domain size of the 10% Mo:$BiVO_4$ calcined at 350 °C cannot be determined properly as the size of the thin grooves separating the domains from each other is in the order of the pore sizes. Raising the calcination temperature to 400 °C leads to a 10% Mo:$BiVO_4$ thin film with clearly separated domains of an average geometrical domain size of 3.2 ±1.7 µm² and an average material streak size of 71 ±19 nm. Increasing the calcination temperature to 450 °C only has little impact on the morphology accounting for a slightly decreased average domain size of 2.8 ±1.7 µm and a slightly increased material streak size of 84 ±9 nm. Further raising of the calcination temperature to 500 °C and 550 °C results in the collapse of the domain morphology. Due to strong sintering of the material, the 10% Mo:$BiVO_4$ thin films calcined at 500 °C and 550 °C consist of big, non-porous, sintered particles which inhomogeneously cover the substrate. This densification of the thin film material leads to a strong shrinkage of the average domain size (i.e. geometrical particle area) accounting for 0.2 ±0.2 µm² for the sample calcined at 500 °C. Due to advanced sintering, the domain/particle size of the thin film calcined at 550 °C is further increased accounting for 0.5 ±0.3 µm². These findings highlight the huge impact of the calcination procedure on the morphology of the 10% Mo:$BiVO_4$ thin films. Increasing the calcination temperature leads to sintering of the thin film material. Temperatures higher than 450 °C result in a collapsed thin film morphology and in sintered particles, respectively.

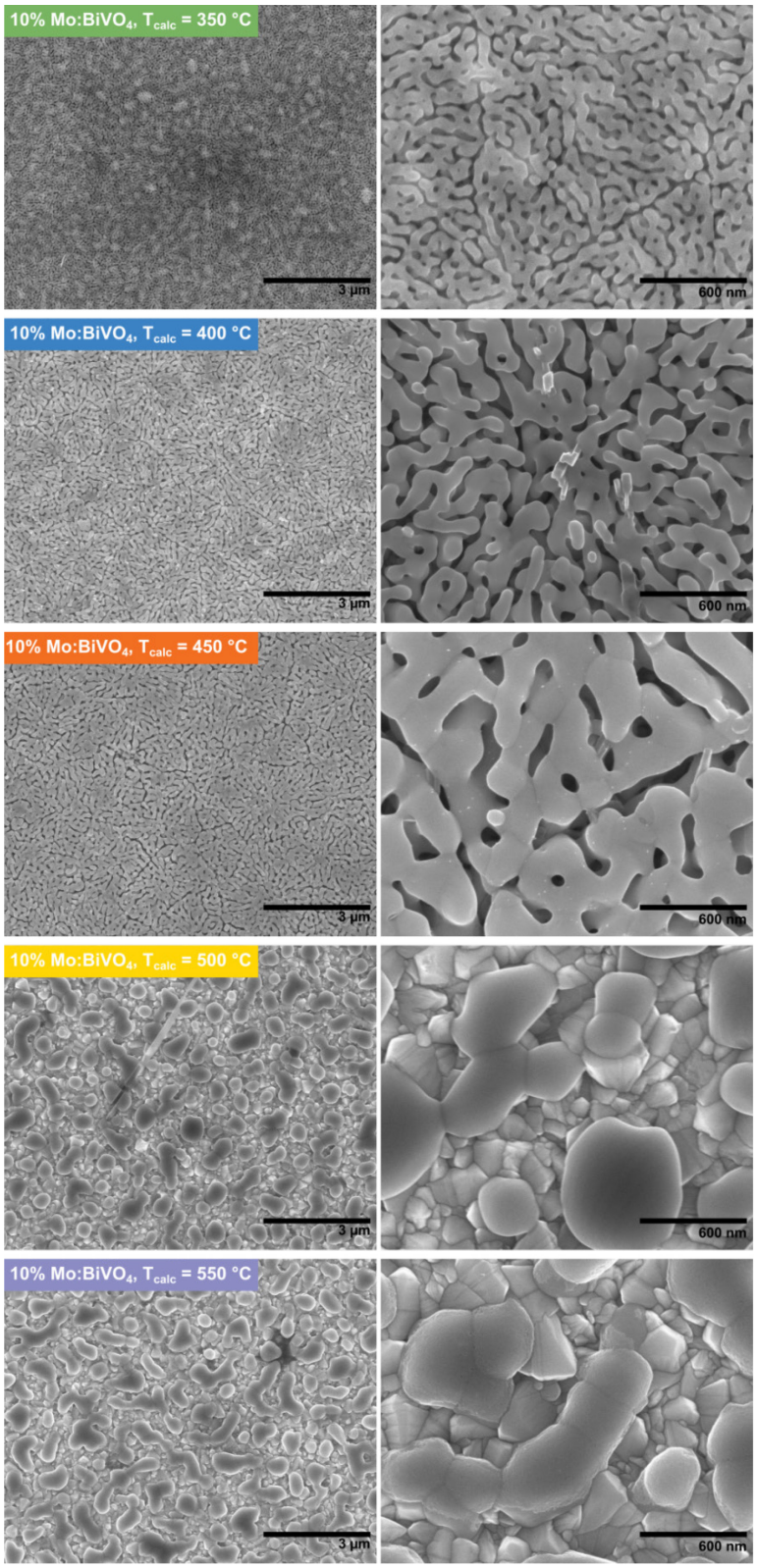

Figure 8-32. SEM top view images of 10% Mo:$BiVO_4$ thin films on FTO substrate calcined at different temperatures.

Table 8-11. Summary of analyzed morphological thin film features of 10% Mo:$BiVO_4$ thin films calcined at different temperatures.

Calcination temperature (°C)	Average geometrical domain size (µm²)	Average inner domain material streak size (nm)
350	n/a	48 ±11
400	3.2 ±1.7	71 ±19
450	2.8 ±1.7	84 ±9
500	0.2 ±0.2	n/a
550	0.5 ±0.3	n/a

In addition to SEM investigations, the 10% Mo:$BiVO_4$ thin films calcined at different temperatures were analyzed by TEM/SAED. Samples were scraped off the FTO substrate and were transferred to a TEM grid. Results are shown in Figure 8-33. The overview images reveal the particles/thin film material to be increasing in size and thickness respectively with increasing calcination temperature. This is in good agreement with the trend observed by SEM investigations. For all samples, observed spatial frequencies due to the lattice fringes indicate a good crystallinity. FFT patterns of each sample show only one set of reflections which can be assigned to the monoclinic scheelite or the tetragonal scheelite structure, respectively, in all cases. The results are in good agreement with XRD investigations (see Figure 8-31) of corresponding powder samples revealing monoclinic scheelite structure for the 10% Mo:$BiVO_4$ samples of each calcination temperature. Furthermore, the HR-TEM investigations reveal the material to undergo morphological changing upon irradiation of the electron beam. Little knobs are popping out of the surface of the material. This process occurs rapidly for samples calcined at temperatures lower than 450 °C and slowly for samples calcined at temperatures of 450 °C and higher. This indicates a dependence of the beam damage on the crystallinity of the material.

Additionally, SAED experiments yielded dot patterns for all samples pointing towards broad single-crystalline domains. The reflections of the obtained patterns can be assigned to certain d-spacing values matching the monoclinic scheelite structure and tetragonal scheelite structure, respectively, for all samples. In case of the sample calcined at 350 °C, various side reflections are present which most probably can be assigned to the knobs popping out of the material during the acquirement of the pattern.

The phenomenon of beam damage of the 10% Mo:$BiVO_4$ samples calcined at different temperatures was investigated extensively by HR-STEM/EDX in cooperation with Dr. Siyuan Zhang from the group of Prof. Dr. Christina Scheu from Max-Planck-Institut für Eisenforschung in Düsseldorf. A TEM lamella was cut out of the 10% Mo:$BiVO_4$ sample calcined at 450 °C and was investigated by an aberration-corrected 300 kV STEM by FEI Titan Themis equipped with a QUANTAX FlatQUAD EDX detector by Bruker.

First, the material of the lamella was damaged on purpose by irradiation with the electron beam for a time period of 30 s. Subsequently, a short time EDX mapping using a lowered acceleration voltage of 100 kV was acquired from a small area of the damaged material. Results are shown in Figure 8-34. The thin film material before and after irradiation of the electron beam is shown in Figure 8-34a. As can be seen, electron irradiation causes strong damaging of the material resulting in differently sized knobs at the material surface. Diameters of the knobs range from less than 1 nm up to about 10 nm. Results of the EDX mapping are shown in Figure 8-34b. As can be seen by the map and its corresponding single element maps, bismuth is predominantly traced at the knobs at the surface of the material. Vanadium principally is found at areas between the knobs. Point analysis of the knobs (red) and the material between the knobs (green) further confirms the knobs to be bismuth rich and the material areas between the knobs to be vanadium rich (spectra given in Figure 8-34c). These findings indicate the knobs popping out of the surface to be the result of electron beam-induced phase segregation. A Bi-rich phase is formed at the surface in form of knobs. The thin film material between the knobs remains in a V-rich state at the surface.

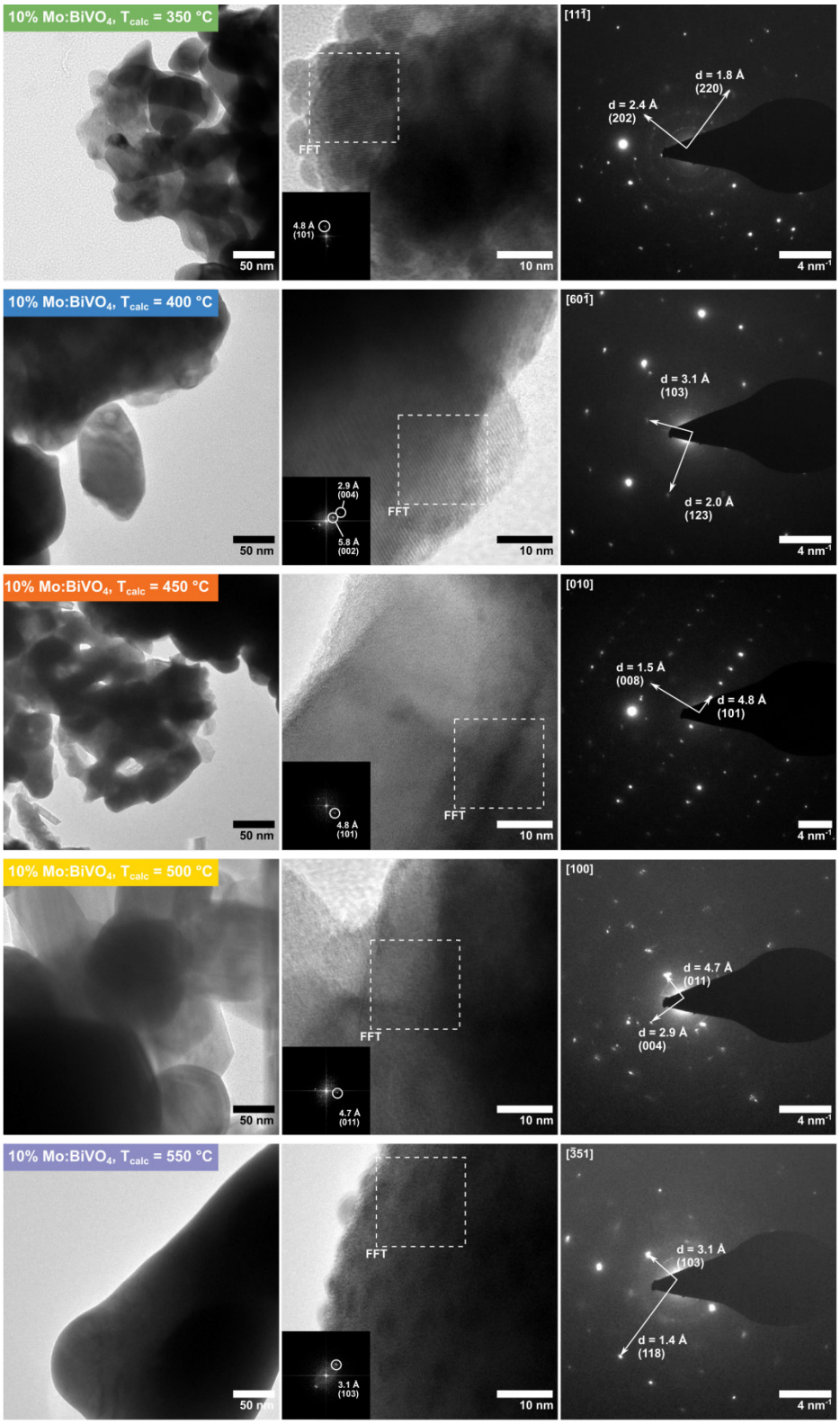

Figure 8-33. Results of TEM/SAED investigations of 10% Mo:$BiVO_4$ thin films on FTO substrate calcined at temperatures from 350 °C to 550 °C: overview images, HR-TEM images with corresponding FFT pattern given as inset and SAED patterns are shown.

This phenomenon occurs slowly for samples calcined at temperatures of 450 °C and higher (long electron beam irradiation time) and readily and rapidly for samples calcined at temperatures lower than 450 °C (rather short irradiation time). This can be explained as follows: In first approach, diffusion in solids proceeds by atom movement mediated by interstitial sites and vacancies within the lattice.[157–160] Diffusion in solids and phase segregation, respectively, is therefore promoted and facilitated by crystal structures exhibiting a high number of interstitials and vacancies. By XRD experiments the 10% Mo:$BiVO_4$ samples (*vide supra*) it was shown that crystallinity increases with increasing calcination temperature. The sample calcined at 350 °C exhibits a lower degree of crystallinity and therefore diffusion within the solid is facilitated. Hence, the fast and eager phase segregation results in the rapid formation of knobs upon short-time irradiation of the electron beam.

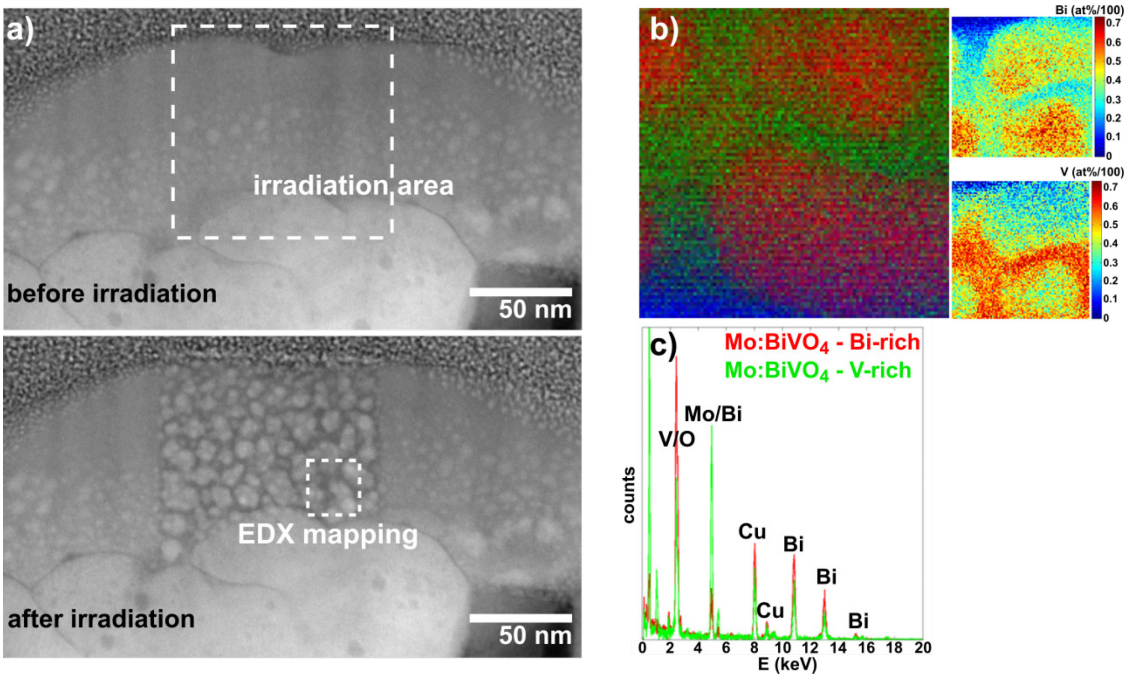

Figure 8-34. Results of STEM/EDX mapping of lamella cut out of a 10% Mo:$BiVO_4$ thin film calcined at 450 °C. a) overview images of the lamella before and after irradiation of the electron beam and b) EDX mapping with corresponding single element maps and c) EDX point analysis spectra of thin film material (green) and knob material (red).

To gather information about the influence of the changes of crystallinity and morphology induced by variation of the calcination temperature on the PEC performance of the 10% Mo:$BiVO_4$ thin films regarding water oxidation, (photo-)electrochemical investigations using a standard electrochemical cell equipped with the commonly used electrodes (RHE – reference electrode, Pt-wire – counter electrode) were carried out. j-V curves acquired using backside illumination together with ABPE curves calculated from the j-V data are shown in Figure 8-35 and summarized in Table 8-12. Corresponding curves obtained in frontside illumination mode are shown in the Appendix, chapter 12.1.2.7.

As can be seen in Figure 8-35a, among all samples the 10% Mo:$BiVO_4$ photoanode calcined at 400 °C not only yielded the highest photocurrent densities of 2.13 mA/cm² at an applied potential of 1.23V vs RHE but also showed highest PEC performance for lower applied potentials (E < 1.0 V vs RHE). The samples calcined at 450 °C and 500 °C yielded slightly lower photocurrents especially in the low potential range and slightly lower photocurrents at 1.23 V vs RHE accounting for 1.94 mA/cm² for the 450 °C sample and 1.71 mA/cm² for the 500 °C sample, respectively. The 10% Mo:$BiVO_4$ samples calcined at 350 °C and 550 °C yielded low photocurrents at an applied potential of 1.23 V vs RHE accounting for 0.74 mA/cm² for the 350 °C sample and 0.60 mA/cm² for the sample calcined at 550 °C. Noticeably, the sample calcined at 350 °C yields higher photocurrents in the low potential range.

In addition to the j-V curves, the ABPE curves are shown in Figure 8-35c. Among all samples the 10% Mo:$BiVO_4$ photoanode calcined at 400 °C shows the highest ABPE maximum of 0.40% at an applied potential of 0.88 V vs RHE followed by the samples calcined at 450 °C and 500 °C accounting for a maximum ABPE values of 0.21% and 0.14% at applied potentials of 0.95 V vs RHE and 1.05 V vs RHE. For the sample calcined at 350 °C, a maximum ABPE of 0.12% is obtained at an applied potential of only 0.86 V vs RHE. The sample calcined at 550 °C yields only a small maximum ABPE of 0.05 % at a potential of 1.05 V vs RHE. The ABPE curves confirm the information gathered by the j-V curves revealing the sample calcined at 400 °C to yield the highest ABPE at lowest applied potentials.

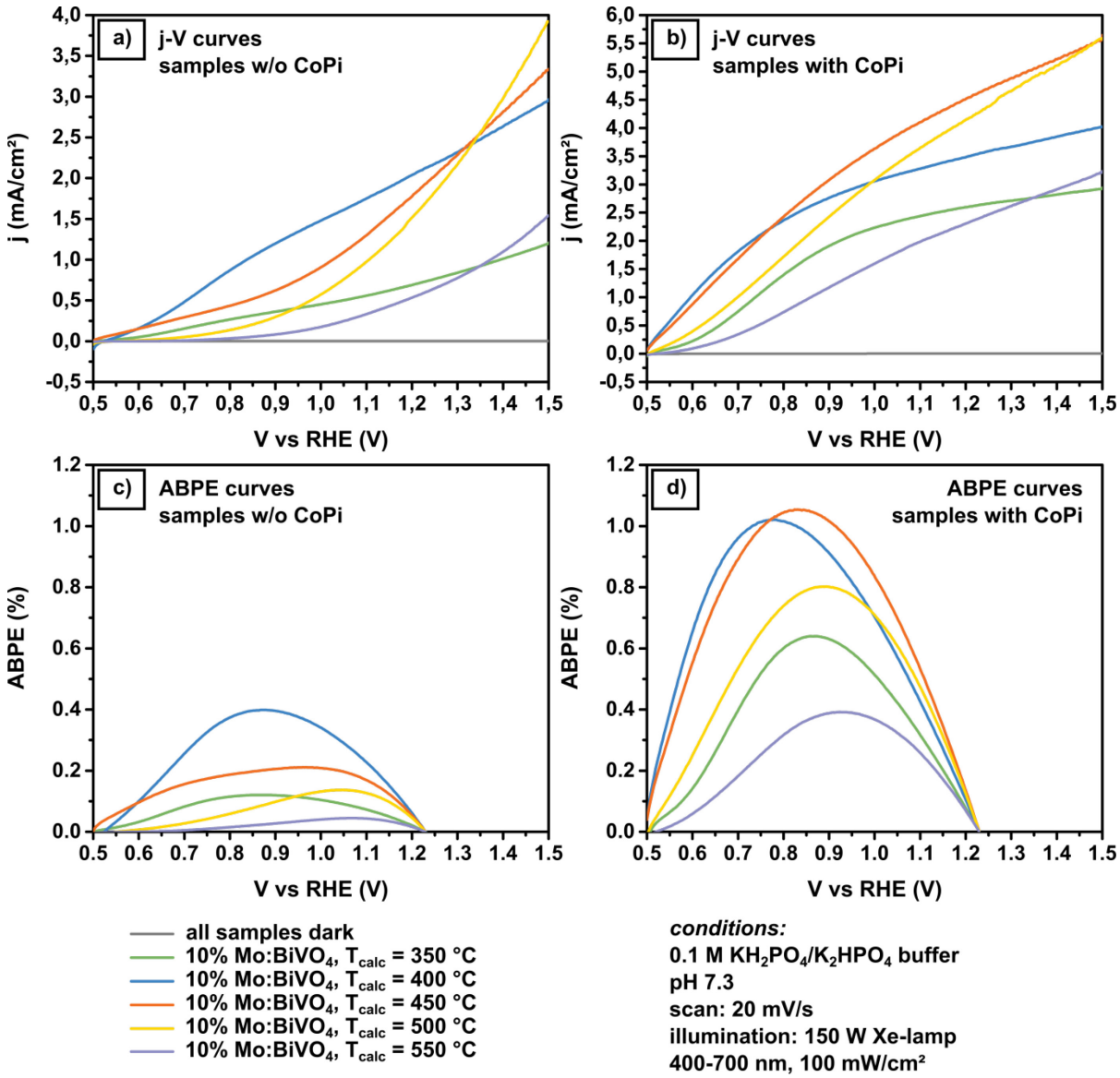

Figure 8-35. j-V curves and corresponding ABPE curves of 10% Mo:$BiVO_4$ thin films calcined at different temperatures: a and c) without CoPi water oxidation catalyst and b) and d) with CoPi catalyst deposited onto the surface.

Deposition of a layer of CoPi water oxidation catalyst onto the surface of the electrodes affects the overall PEC performance of all 10% Mo:$BiVO_4$ photoanodes positively. As can be seen in Figure 8-35b, yielded photocurrents for all samples were enhanced by CoPi deposition. The samples calcined at 350 °C and 550 °C yielded lowest photocurrents at an applied potential of 1.23 V vs RHE accounting for 2.64 mA/cm² and 2.40 mA/cm², respectively. The sample calcined at 350 °C again exhibits better PEC performance in the

lower potential range. For the 10% Mo:$BiVO_4$ photoanodes calcined at 400 °C to 500 °C, higher photocurrents were obtained at an applied potential of 1.23 V vs RHE. Best PEC performance was obtained for the sample calcined at 450 °C accounting for 4.64 mA/cm, followed by the 500 °C sample with photocurrents as high as 4.28 mA/cm² and the sample calcined at 400 °C yielding photocurrents of 3.55 mA/cm². Remarkably, the 400 °C sample shows comparable PEC performance to the 450 °C in the lower potential range.

The ABPE curves shown in Figure 8-35d confirm the trends derived from the j-V curves. As the photocurrents and PEC performance, respectively, was enhanced by CoPi deposition, the ABPE maxima are enhanced as well. The 10% Mo:$BiVO_4$ photoanodes calcined at 350 °C and 550 °C exhibit comparatively low ABPE maxima of 0.64% for the 350 °C sample and 0.39% for the 550 °C sample at comparatively high potentials of 0.86 V vs RHE and 0.92 V vs RHE, respectively. In agreement with the high PEC performance of the 10% Mo:$BiVO_4$ photoanode calcined at 400 °C, the ABPE maximum of 1.02% is located at an applied potential as low as 0.76 V vs RHE. The ABPE maximum of the 450°C sample of 1.05% occurs at slightly more anodic potentials of 0.83 V vs RHE. The ABPE of the sample calcined at 500 °C is lower and located at higher potentials accounting for 0.80% at 0.89 V vs RHE.

These findings reveal principally two relationships: i) by CoPi deposition the ABPE maxima are enhanced and shifted cathodically in all cases, i.e. by CoPi deposition the possible power gain is enhanced while lower bias potentials are necessary and ii) CoPi deposition has stronger impacts on the PEC performance of the 10% Mo:$BiVO_4$ photoanodes calcined at temperatures of 450 °C and higher than for the samples calcined at 350 °C and 400 °C. This indicates a lower influence of surface recombination for the samples calcined at 350 °C and 400 °C.

Table 8-12. Summary of obtained photocurrents at 1.23 V vs RHE with and without CoPi for 10% Mo:$BiVO_4$ samples calcined at different temperatures togehter with ABPE maxima and ABPE maxima position with and without CoPi deposited. All values given for illumination from the backside.

Calcination temperature (°C)	j (mA/cm²)		ABPE without CoPi		ABPE with CoPi	
	Without CoPi	With CoPi	E vs RHE (V)	Maximum ABPE (%)	E vs RHE (V)	Maximum ABPE (%)
350	0.74	2.64	0.87	0.12	0.86	0.64
400	2.13	3.55	0.88	0.40	0.76	1.02
450	1.94	4.64	0.95	0.21	0.83	1.05
500	1.71	4.28	1.05	0.14	0.89	0.80
550	0.60	2.40	1.07	0.05	0.92	0.39

To further clarify the different PEC performance of the 10% Mo:$BiVO_4$ photoanodes calcined at different temperatures, photocurrent transients were measured and analyzed using the phenomenological approach elucidated in chapter 5.5.3.3. Photocurrent transient curves acquired in backside illumination mode with blue light (440 nm, 2 mW/cm²) are shown in Figure 8-36; results of the corresponding transient analysis are summarized in Table 8-13. Photocurrent transients obtained in frontside illumination and corresponding analysis do not differ significantly from the results obtained in backside illumination mode and therefore are given in the Appendix, chapter 12.1.2.7.

As can be seen by the photocurrent spikes when switching the light on, all 10% Mo:$BiVO_4$ photoanodes suffer from surface recombination to different extents. The photocurrent spikes become more pronounced with increasing calcination temperature. Analysis of the occurring photocurrent transients reveals decreasing hole transfer rates k_{trans} with increasing calcination temperature accounting for 0.173 s^{-1} for the sample calcined at 350 °C to 0.103 s^{-1} for the sample calcined at 550 °C. Furthermore, the surface hole recombination rates k_{rec} increase with increasing calcination temperature accounting for 0.043 s^{-1} for the 350 °C sample up to 0.174 s^{-1} for the sample calcined at 550 °C. In consequence, hole transfer efficiencies $\eta_{transfer}$ are already high for the 10% Mo:$BiVO_4$ photoanodes calcined at 350 °C and 400 °C accounting for 0.789 and 0.795, respectively. With increasing calcination temperature, hole transfer efficiencies decrease significantly

accounting for $\eta_{transfer}$ of 0.371 for the sample calcined at 550 °C. That means most holes reaching the surface of a photoanode calcined at 350 °C or 400 °C will be transferred to the electrolyte whereas the probability of surface recombination is severely increased for photoanodes treated at higher temperatures.

Deposition of CoPi affects the water oxidation kinetics of the 10% Mo:$BiVO_4$ photoanodes to different extents. For the samples calcined at 350 °C and 400 °C, the hole transfer rates remain nearly constant compared to the pristine photoanodes. The already very small surface hole recombination rates are further decreased by CoPi deposition accounting for 0.031 s^{-1} and 0.014 s^{-1} for the 350 °C sample and the 400 °C sample, respectively. For samples calcined at temperatures of 450 °C up to 550 °C, k_{trans} is enhanced significantly; in all cases it is approximately doubled. Furthermore, for these samples, k_{rec} is lowered remarkably accounting for 0.042 s^{-1}, 0.045 s^{-1} and 0.031 s^{-1} for the 450 °C sample, the 500 °C sample and the 550 °C sample, respectively. As a consequence, hole transfer efficiencies are slightly enhanced for the photoanodes calcined at 350 °C and 400 °C, whereas $\eta_{transfer}$ is roughly doubled for the samples calcined at 450 °C to 550 °C.

These findings point towards only a little influence of CoPi deposition on the water oxidation kinetics of the samples calcined at 350 °C and 400 °C which in turn indicates surface recombination not being the PEC performance limiting factor for these samples. Furthermore, a strong positive influence of CoPi deposition on the electrode kinetics of the samples calcined at 450 °C to 550 °C is revealed which indicates a more important role of surface recombination for the samples treated at higher calcination temperatures.

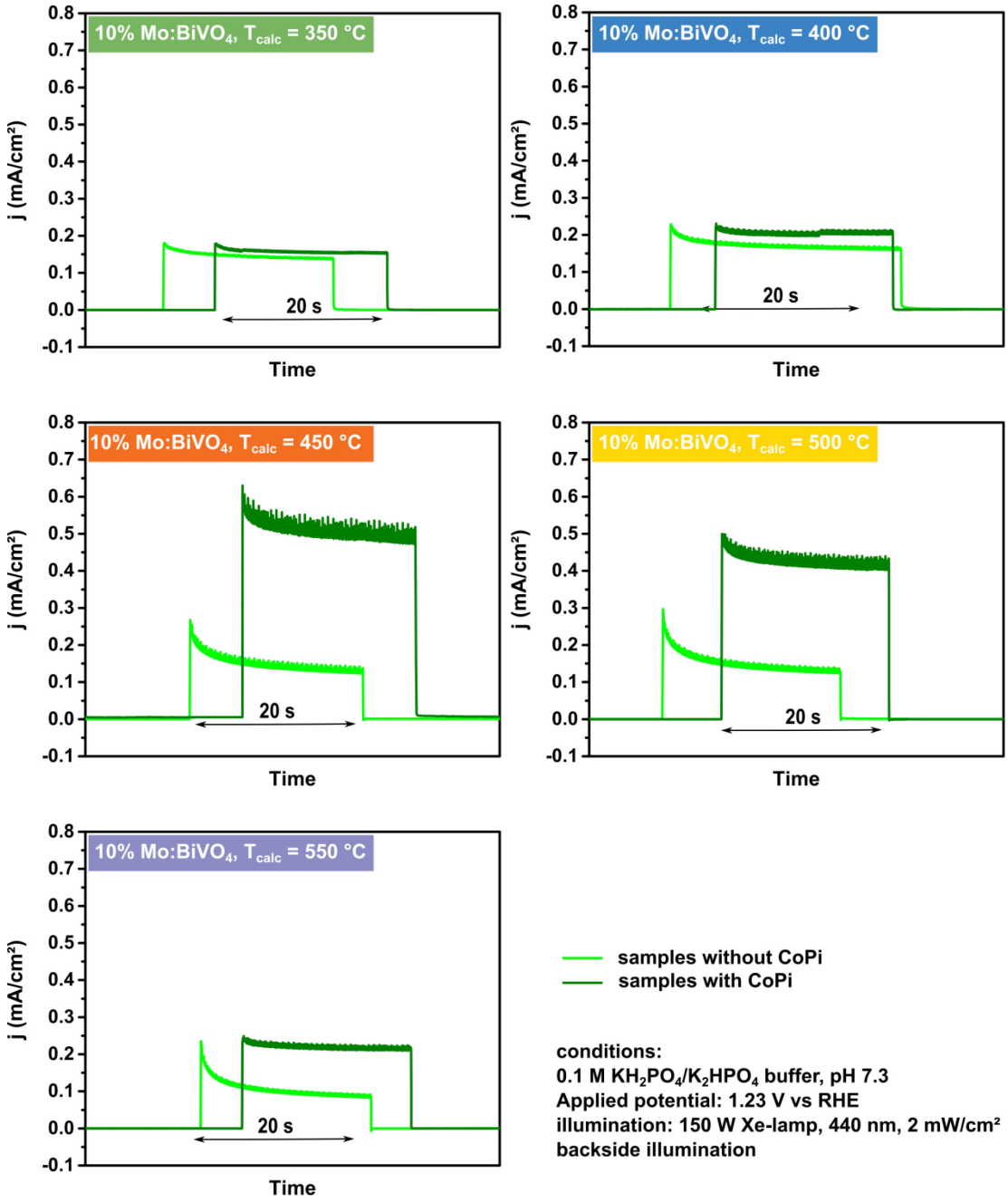

Figure 8-36. Photocurrent transients of 10% Mo:$BiVO_4$ photoanodes calcined at different temperatures. Transients were acquired at an applied potential of 1.23 V vs RHE using backside illumination of blue light (440 nm, 2 mW/cm²).

Table 8-13. Summary of analyzed photocurrent transients of 10% Mo:$BiVO_4$ photoanodes calcined at different temperatures. Values given correspond to transients measured in backside illumination mode.

calcination temperature (°C)	with or w/o CoPi	current densities (mA/cm²)	$\eta_{transfer}$	rate constants (s^{-1})
350	Without CoPi	j_{ini} = 0.178	0.789	k_{trans} = 0.173
		j_{ss} = 0.140		k_{rec} = 0.046
	With CoPi	j_{ini} = 0.179	0.860	k_{trans} = 0.193
		j_{ss} = 0.140		k_{rec} = 0.031
400	Without CoPi	j_{ini} = 0.207	0.795	k_{trans} = 0.189
		j_{ss} = 0.165		k_{rec} = 0.049
	With CoPi	j_{ini} = 0.179	0.926	k_{trans} = 0.176
		j_{ss} = 0.140		k_{rec} = 0.014
450	Without CoPi	j_{ini} = 0.267	0.477	k_{trans} = 0.170
		j_{ss} = 0.127		k_{rec} = 0.186
	With CoPi	j_{ini} = 0.563	0.877	k_{trans} = 0.302
		j_{ss} = 0.494		k_{rec} = 0.042
500	Without CoPi	j_{ini} = 0.295	0.440	k_{trans} = 0.096
		j_{ss} = 0.130		k_{rec} = 0.122
	With CoPi	j_{ini} = 0.489	0.831	k_{trans} = 0.211
		j_{ss} = 0.407		k_{rec} = 0.045
550	Without CoPi	j_{ini} = 0.229	0.371	k_{trans} = 0.103
		j_{ss} = 0.085		k_{rec} = 0.174
	With CoPi	j_{ini} = 0.242	0.867	k_{trans} = 0.201
		j_{ss} = 0.210		k_{rec} = 0.031

From these results which are briefly summarized in Figure 8-37, an explanation for the different PEC performance of the 10% Mo:$BiVO_4$ photoanodes calcined at different temperatures can be derived. Thin film morphologies with material streak sizes in the range of the diffusion length are beneficial for separation and collection of photo-generated charge carriers (Figure 8-37a). PEC performance of such a Mo:$BiVO_4$ photoanode is enhanced because of an increased number of surface reaching holes. Furthermore, a high degree of crystallinity facilitates charge transport through the material and reduces the

probability of recombination because of a lower number of defects acting as recombination sites (Figure 8-37a).

Variation of the calcination temperature affects the thin film morphology and the thin film crystallinity. As shown in this chapter, the degree of crystallinity increases with increasing calcination temperature whereas the morphology is changed towards bigger material streak sizes and thin film collapse due to advanced sintering/material densification. For the 10% Mo:$BiVO_4$ photoanode calcined at 450 °C, highest PEC performance after CoPi deposition is yielded amongst all samples (Figure 8-37b). In the context of the interplay of crystallinity and thin film morphology, the resulting thin film morphology and degree of crystallinity obtained by application of 450 °C calcination temperature can be assumed to be optimal. For samples calcined at lower temperatures, charge transport and electron-hole separation, respectively, is hampered because of a lower degree of crystallinity. As a consequence, few holes reach the electrode surface. This is in good agreement with the photocurrent transient analysis for photoanodes calcined at these temperatures (Figure 8-37b). For the photoanodes calcined at 350 °C and 400 °C only a slight impact of surface recombination on the PEC performance was revealed which excludes hole accumulation at the surface. For photoanodes calcined at temperatures higher than 450 °C, charge transport and electron-hole separation, respectively, is facilitated by a higher degree of crystallinity. However, the thin film morphology and material streaks become much bigger than the hole diffusion length of $BiVO_4$ (Figure 8-37a). This in turn is detrimental for the PEC performance. This is further confirmed by photocurrent transient analysis revealing a big influence of surface recombination on the PEC performance and decreasing photocurrents.

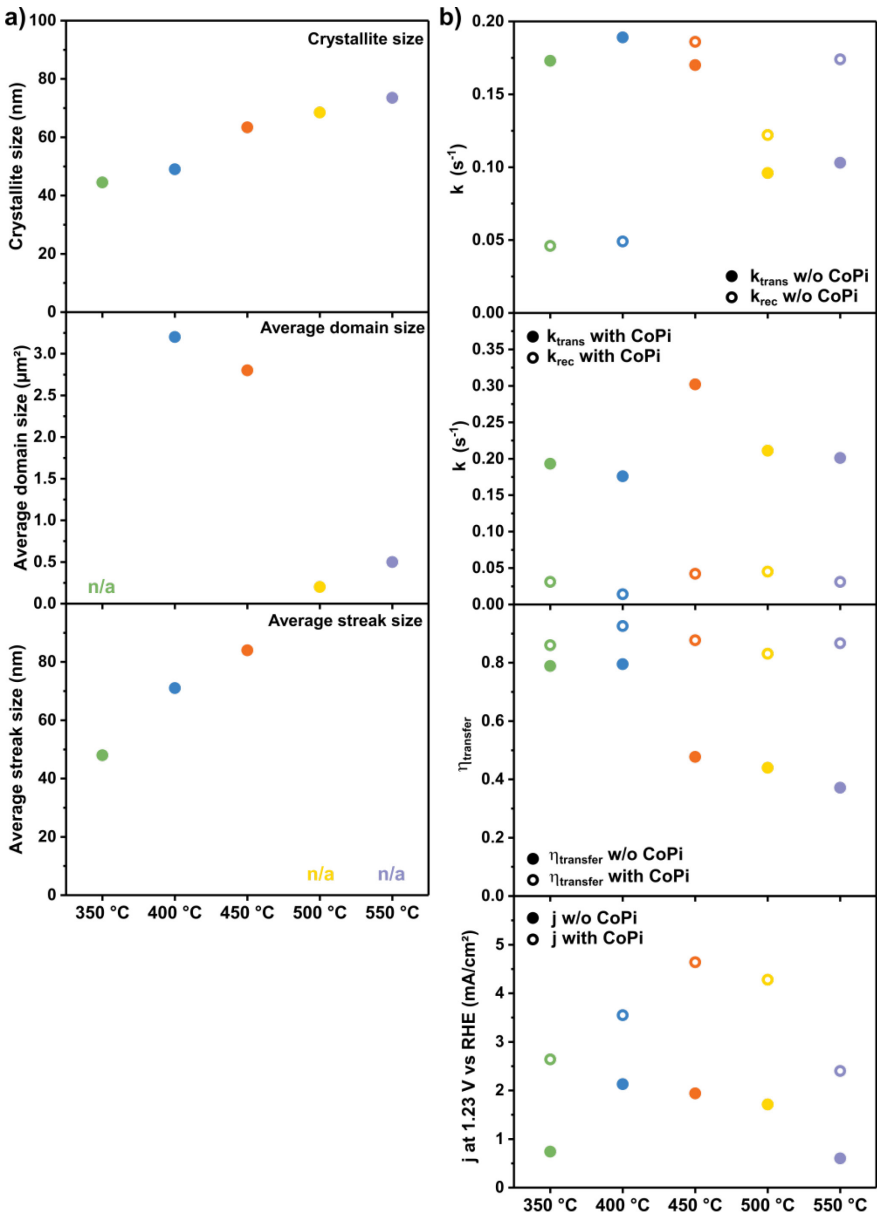

Figure 8-37. Comparison of 10% Mo:$BiVO_4$ samples calcined at different temperatures. a) morphology features and b) kinetics at the electrodes' surfaces and PEC performance (illumination: 400-700 nm, 100 mW/cm²) regarding water oxidation.

To sum-up briefly, in this chapter the influence of variation of the calcination temperature from 350 °C to 550 °C on the PEC performance of 10% Mo:$BiVO_4$ thin film photoanodes was investigated. XRD experiments using corresponding powder samples revealed increasing crystallinity with increasing calcination temperature whereas for the tetragonal crystal structure is obtained for the sample calcined at 350°C and the monoclinic scheelite

structure was obtained for samples calcined at 400 °C and higher. Electron microscopy showed the thin film morphology to be changing by application of different calcination temperatures. Material streak sizes increase with increasing calcination temperature. Domain-like morphology collapses at temperatures of 500 °C and higher forming particles and sintered particle agglomerates instead of a substrate-covering thin film. PEC performance of the differently calcined photoanodes was investigated by means of photoelectrochemistry and turns out to be strongly dependent on the calcination procedure. A calcination temperature of 450 °C was figured out to be an optimal compromise between thin film morphology and crystallinity as the PEC performance and ABPE turned-out to be the highest after CoPi surface modification.

8.4.4. CoPi deposition

8.4.4.1. Introduction

Photoelectrochemical water oxidation generally occurs at significant overpotentials as it involves removal of a total of four electrons and four protons from two water molecules to form one O_2 molecule (see chapter 5.1.2, Equation 5-1 – Equation 5-4). Aiming at improvement of the photoelectrochemical performance of a semiconductor photoanode regarding water oxidation, i.e. reduction of the overpotential required for water oxidation, the integration of an effective water oxidation (or oxygen evolving) electrocatalyst becomes essential. Several effective water oxidation catalysts (WOC) have been reported in literature. Among others, IrO_x-based catalysts have been shown to be effective WOCs for acidic electrolytes.[47–49,161,162] Working in alkaline media, for instance NiO_x-based catalysts have attracted a lot of attention and have been confirmed to be powerful WOCs.[53–55,163,164] The disadvantages of working either in highly alkaline or acidic environments was overcome by the breakthrough discovery of Kanan and Nocera in 2009, introducing “CoPi”, an amorphous cobalt phosphate species, as an efficient water oxidation catalyst working at neutral pH.[51,52]

Since its discovery as a water oxidation catalyst, CoPi has been in the focus of extensive investigations. Light was shed especially on the clarification of the origin of the tremendous water oxidation properties. A general approximation of the water oxidation mechanism at a CoPi-modified semiconductor photoanode was reported by Jeon, Choi and Park in 2011 which is illustrated schematically in Figure 8-38.[165] The initial state shown in Figure 8-38a consists of μ-oxo-bridged cobalt(II) and cobalt(III) phosphate groups. As shown in Figure 8-38b, the catalyst becomes partially oxidized by abstraction of a photo-generated hole which was produced by excitation of the photoactive semiconductor. After further irradiation and hole abstraction, respectively, the CoPi catalyst is fully oxidized (Figure 8-38c) resulting in O_2-release and recovery of the initial state of the catalyst by addition of water from the electrolyte. (Note: photo-generated electrons are transported to the outer circuit leading to H_2 evolution at the counter electrode.) However, it is still not fully understood how improvement of water oxidation is achieved by the CoPi WOC. Despite early work assuming CoPi to work as an electrocatalyst,[166,167] recent studies,[126,168] particularly by the group of James Durrant at the Imperial College London,[102,169,170] demonstrated the enhanced activity regarding water oxidation of CoPi to be resulting from optimization of the water oxidation kinetics and retardation of recombination kinetics, respectively. Especially suppression of back-electron-hole recombination across the space charge layer of the photoactive material has been proposed to play the key role in the water oxidation functionality of CoPi.

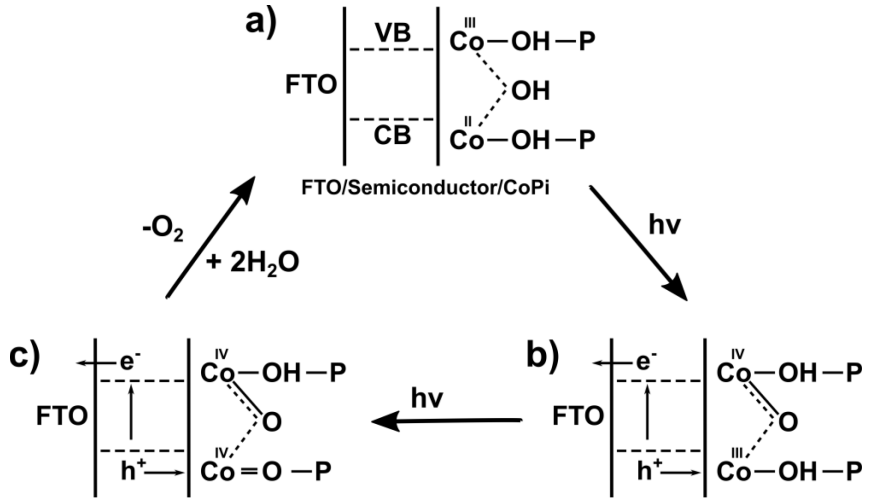

Figure 8-38. Schematic illustration of a water oxidation cycle at a CoPi-modified semiconductor photoanode on an FTO substrate: a) as deposited, b) partially oxidized and c) fully oxidized. Mecahnism adapted from Jeon et al.[165]

Despite its high activity regarding water oxidation at neutral pH, CoPi is characterized by numerous beneficial properties like its earth-abundance, its low-cost and its availability for straightforward deposition techniques onto various substrates. For this reason, CoPi has been proven to be a working water oxidation catalyst in combination with diverse semiconductor photoanodes for example in combination with Fe_2O_3[171,172], ZnO[173–175] and $BiVO_4$[32,35], respectively.

Three different basic CoPi deposition methods have been reported in literature. The group of Nocera and other groups used an electrodeposition method. By application of potentials more anodic with respect to the oxidation potential of Co^{2+} to Co^{3+} (E^0 = 1.81 V vs RHE[143]), Co^{2+} is partially oxidized to Co^{3+} resulting in deposition of the CoPi catalyst onto the electrode surface.[176]

The group of Choi introduced in 2009 the concept of photochemical deposition of Co-based water oxidation catalysts like CoPi.[175]By simple irradiation of light providing enough energy to excite electron-hole pairs within the semiconductor anode, Co^{2+} is oxidized to Co^{3+} by photo-generated holes at the semiconductor surface. An indispensable prerequisite for this method is a suitable band alignment of the semiconductor, i.e. the valence band has to be located more anodically with respect to the $Co^{2+/}Co^{3+}$ redox level at

$E^0(Co^{2+}/Co^{3+})$ = 1.92 V vs RHE. As shown in Figure 8-39. the valence band of $BiVO_4$ is positioned significantly more anodic with respect to $E^0(Co^{2+}/Co^{3+})$ at about 2.47 V vs RHE which matches band alignment criteria for the feasibility of photochemical CoPi deposition. Photochemical deposition provides an efficient way to couple the CoPi oxygen evolution catalysts with photoanodes by naturally placing catalysts at the locations where the holes are most readily available. A big advantage of this method is the applicability to porous semiconductor electrodes, as the catalyst is selectively deposited onto the anode material without deposition onto the usually more conductive FTO substrate.

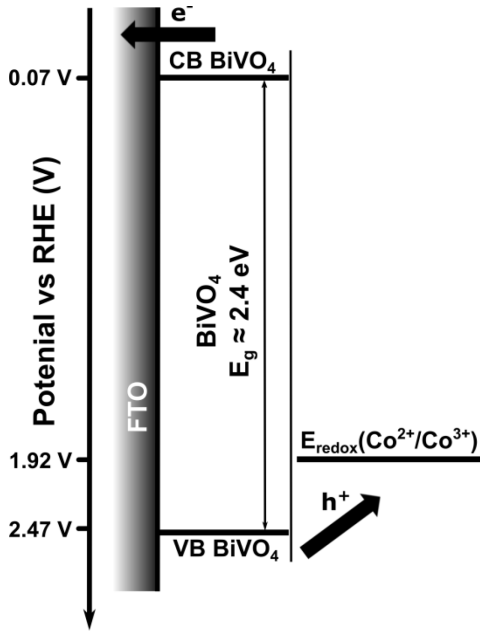

Figure 8-39. Band diagram illustrating the band positions of $BiVO_4$ and the redox potential of Co^{2+}/Co^{3+}.

Both deposition concepts were combined to the photo-assisted electrodeposition method.[101,106,177] By application of potentials more cathodic with respect to the redox potential of Co^{2+}/Co^{3+} and additional irradiation of light, uniformly spread CoPi layers can thereby be formed onto the photoactive anode material.

In the following section, results of the investigation of the influence of the applied CoPi deposition technique on the PEC performance regarding water oxidation of the Mo-doped $BiVO_4$ thin film photoanodes are presented. For this purpose, electrodeposition, photochemical deposition and photo-assisted electrodeposition of CoPi water oxidation catalyst were carried-out to spread CoPi catalyst onto the surface of 10% Mo:$BiVO_4$ thin film photoanodes. The CoPi-modified 10% Mo:$BiVO_4$ photoanodes were investigated photoelectrochemically and by electron microscopy methods.

8.4.4.2. Electrodeposition (ED)

The electrodeposition (ED) procedure applied to fabricate CoPi-modified 10% Mo:$BiVO_4$ photoanodes is based on the work of Kanan and Nocera.[52] Briefly explained, an electrochemical cell equipped with RHE reference electrode, Pt counter electrode and the 10% Mo:$BiVO_4$ thin film as working electrode was filled with 20 ml of 0.1 M potassium phosphate solution containing 0.5 mM $Co(NO_3)_2$. The deposition was carried out at an applied potential of 1.9 V vs RHE in the dark without stirring and without IR-correction and was stopped after a certain amount of charge Q_{trans} was transferred. Q_{trans} was calculated on-line according to Equation 8-3a. The transferred charge Q_{trans} correlates directly with the amount of deposited CoPi as one electron is transferred per Co^{+3} cation deposited onto the 10% Mo:$BiVO_4$ surface according to Equation 8-3b.

Equation 8-3. a) Transferred charge Q_{trans} during CoPi electrodeposition, b) oxidation reaction occuring during electrodeposition.

a) $Q_{trans} = \int I \, dt$ b) $Co^{2+} \rightarrow Co^{3+} + e^-$

Following this procedure, different amounts of CoPi were deposited onto the 10% Mo:$BiVO_4$ photoanode ranging from 2.5 mC to 30 mC. In the following, all samples are referred according to their corresponding Q_{trans} values.

Resulting samples were investigated by means of photoelectrochemistry. j-V curves are shown in Figure 8-40; maximum photocurrents yielded at an applied potential of 1.23 V vs RHE are summarized in Table 8-14 for all samples (Note: j-V curves measured in the dark were left out for clarity reason; j-V curves including the dark measurements can be found in the Appendix, chapter 12.1.2.8.). As can be seen in Figure 8-40a and b, the obtained photocurrents are different and dependent on the transferred charge and electrodeposited amount of CoPi, respectively. In frontside illumination mode the 5 mC sample yielded the highest photocurrents accounting for 3.25 mA/cm² whereas the for the 30 mC sample lowest photocurrents accounting for 0.40 mA/cm² were obtained; both values given for an applied potential of 1.23 V vs RHE and an illumination of white light (400-700 nm) at an intensity 100 mW/cm². In backside illumination mode maximum photocurrents accounting for 3.03 mA/cm² at 1.23 V vs RHE were obtained for the 15 mC sample whereas for the 30 mC sample lowest photocurrents were yielded accounting for 1.14 mA/cm² at 1.23 V vs RHE under similar illumination conditions.

For photoelectrochemical applications a too big amount of CoPi reduces obtained photocurrents. This can be attributed to a thick CoPi overlayer which limits the photon penetration to the underlying Mo:$BiVO_4$.[165]

Depending on the illumination mode, different PEC performance is observed for different amounts of deposited CoPi. For smaller CoPi amounts, higher photocurrent densities are yielded in frontside illumination mode. Related to the absorption of CoPi itself, a smaller amount of CoPi is favorable in frontside illumination mode, as the light needs to be transmitted through the CoPi layer. The less CoPi is deposited onto the surface, the more photons reach the underlying Mo:$BiVO_4$. In contrast, in backside illumination a bigger amount of deposited CoPi yields best photocurrents as the photons are not affected by the CoPi overlayer.

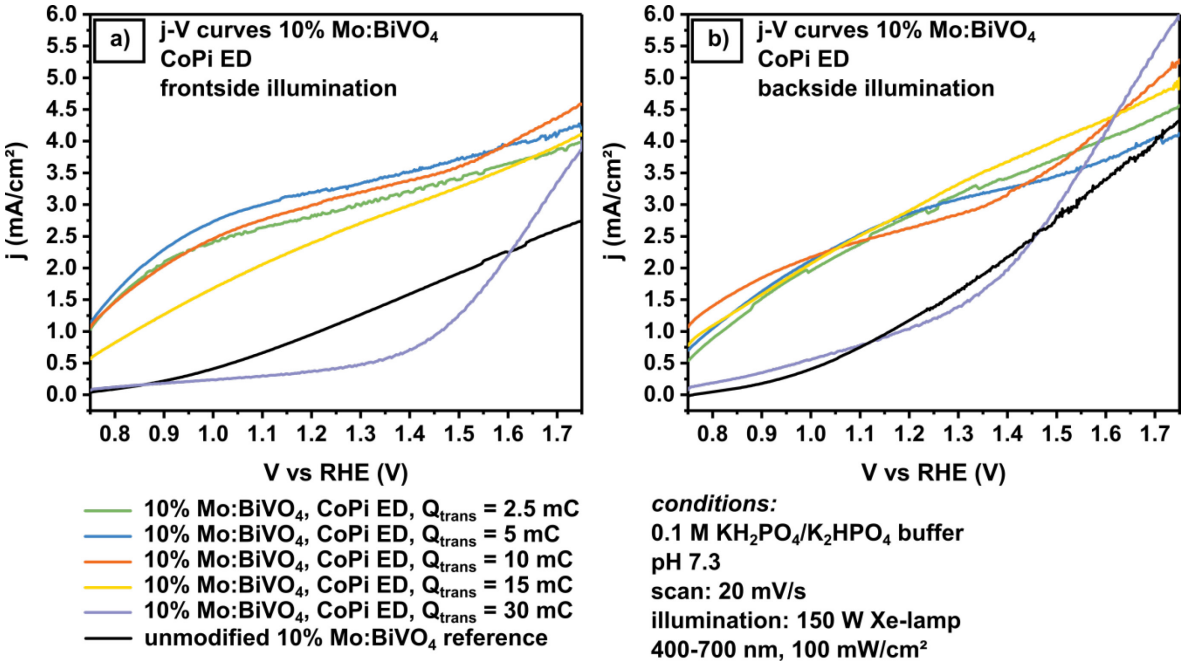

Figure 8-40. j-V curves of CoPi-modified 10% Mo:$BiVO_4$ photoanodes obtained in a) frontside illumination and b) backside illumination. Electrodeposition (ED) method was applied. j-V curves of all samples in the dark are not shown.

Table 8-14. Summary of photocurrents yielded at an applied potential of 1.23 V vs RHE are for CoPi-modified 10% Mo:$BiVO_4$ photoanodes. Electrodeposition (ED) method was applied.

ED - Q_{trans} (mC)	j at 1.23 V vs RHE (mA/cm²)	
	frontside illumination	backside illumination
2.5	2.86	2.92
5	3.25	2.93
10	3.07	2.69
15	2.49	3.03
30	0.40	1.14

Figure 8-41 shows a comparison of the j-V curves of the 10% Mo:$BiVO_4$ sample modified by an electrodeposited CoPi layer (15 mC) and its non-functionalized 10% Mo:$BiVO_4$ counterpart. As can be seen, the photocurrent of the 10% Mo:$BiVO_4$ photoanode obtained in frontside illumination was increased by a factor of ~2.5 from 1.04 mA/cm² to 2.48 mA/cm² by the CoPi electrodeposition, values given for a applied potential of 1.23 V vs RHE under white light illumination (400-700 nm) at an intensity of 100 mW/cm². The photocurrents yielded in backside illumination were increased by a factor of ~2.3 upon CoPi deposition from 1.31 mA/cm² at 1.23 V vs RHE to 3.03 mA/cm² at 1.23 V vs RHE and similar illumination intensity. The observed enhancement of the PEC performance for electrodeposited CoPi on doped $BiVO_4$ photoanodes is in good agreement with comparable studies in literature.[165,177]

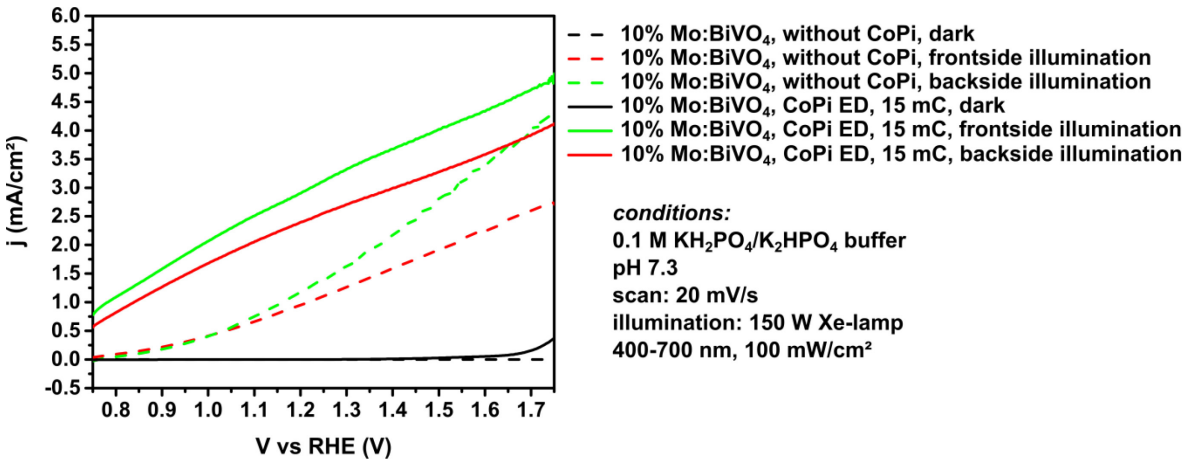

Figure 8-41. j-V curves of 10% Mo:$BiVO_4$ without CoPi and with electrodeposited CoPi (15 mC).

To gain insights into the kinetic background of the electrodeposited CoPi on 10% Mo:$BiVO_4$ photoanodes, photocurrent transients were measured for the samples yielding the highest photocurrents in frontside and backside illumination and results were analyzed using the phenomenological approach described in chapter 5.5.3.3. Photocurrent transients are shown in Figure 8-42; the corresponding analysis is summarized in Table 8-15.

As can be seen in Figure 8-42c, the reference 10% Mo:$BiVO_4$ sample without surface functionalization by the CoPi water oxidation catalyst exhibits a typical photocurrent spike when switching-on the light. This spike can be assigned to displacement of the photo-generated holes. Initially photo-generated holes undergo recombination at the surface. For this reason the initial photocurrent decreases to a steady-state photocurrent (photocurrent plateau) which is a consequence of the interplay between holes arriving at the surface, surface recombination and successfully transferred holes at the electrode/electrolyte interface. When switching-off the light no photocurrent overshoot is observed, i.e. no holes are accumulated at the anode surface which is a result of Mo-doping, as doping decreases the width of the space charge region and removes surface states (see PEC investigations of $BiVO_4$ and Mo:$BiVO_4$ thin film photoanodes in the chapters 8.2.3 and 8.3.4). As can be seen in Table 8-15, for the non-functionalized 10% Mo:$BiVO_4$ sample, hole transfer rates and surface hole recombination rates are approximately balanced around 0.5 s^{-1} which in turn leads to hole transfer efficiencies $\eta_{transfer}$ of ~ 0.5 in both illumination modes. That confirms the non-functionalized reference sample to suffer from surface recombination.

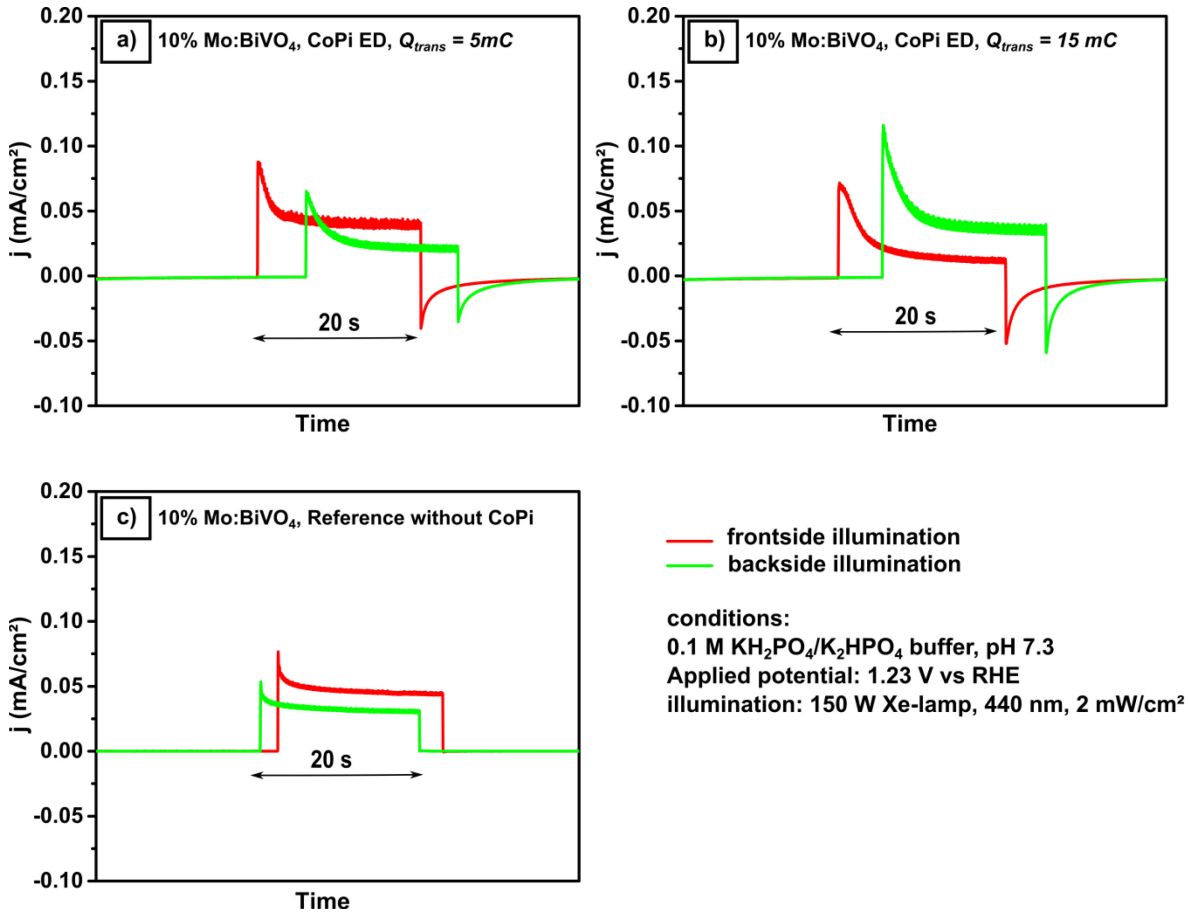

Figure 8-42. Photocurrent transients of 10% Mo:$BiVO_4$ photoanodes with electrodeposited CoPi. a) Q_{trans} = 5 mC, b) Q_{trans} = 15 mC and c) reference sample without CoPi.

Using the electrodeposition method to functionalize the 10% Mo:$BiVO_4$ electrode surface with CoPi and having a look at the corresponding photocurrent transients turns out to be very interesting. As can be seen in Figure 8-42a and b, in contrast to the non-functionalized reference, both 10% Mo:$BiVO_4$ electrodes with an electrodeposited layer of CoPi show an increase of the photocurrent spike and a significant overshoot when the light is switched off. That means electrodepositing CoPi onto the 10% Mo:$BiVO_4$ electrode surface induces hole accumulation, most probably by creation of surface states at the interfacial region between the 10% Mo:$BiVO_4$ and CoPi.[178] This is also expressed by small hole transfer rates k_{trans} accounting for 0.432 s^{-1} and 0.160 s^{-1} for the Q_{trans} = 5 mC sample in frontside and backside illumination, respectively, as well as by nearly unchanged surface hole recombination rates k_{rec} accounting for 0.318 s^{-1} and 0.343 s^{-1} and for the for the

Q_{trans} = 5 mC sample in frontside and backside illumination, respectively. As a result, the hole transfer efficiency $\eta_{transfer}$ is at the same level as the unmodified reference sample in frontside illumination and even smaller in backside illumination. Same trend is observed for the Q_{trans} = 15 mC sample. Small k_{trans} of 0.055 s^{-1} and 0.143 s^{-1} and comparatively high k_{rec} values of 0.322 s^{-1} and 0.319 s^{-1} are observed in frontside and backside illumination, respectively. This also results in small hole transfer efficiencies accounting for 0.146 in frontside illumination and 0.310 in backside illumination.

These results are in good agreement with photocurrent measurements (*vide supra*) revealing increased photocurrents for the Q_{trans} = 5 mC and for the Q_{trans} = 15 mC sample. Compared to the unmodified reference sample, hole transfer rates are smaller after CoPi deposition and surface hole recombination rates are only slightly decreased. Water oxidation kinetics are influenced negatively by electrodeposition of CoPi. Nevertheless, obtained photocurrents are increased, while the extent of enhancement depends on the CoPi layer thickness and the illumination mode. As a reason for these in first approach contradicting results Park et al. proposed that electrodeposited CoPi acts as a hole-conducting electrocatalyst making the photo-generated electrons more mobile and, consequently, increasing conductivity.[165] Hence, PEC water oxidation performance of Mo:$BiVO_4$ is enhanced.

Table 8-15. Summary of photocurrent transient analysis of a pristine 10% Mo:$BiVO_4$ photoanode and two 10% Mo:$BiVO_4$ photoanodes with electrodeposited CoPi, Q_{trans} = 5 mC and Q_{trans} = 15 mC.

Sample/ Q_{trans}	Illumination mode	current densities (mA/cm²)	$\eta_{transfer}$	rate constants (s^{-1})
Reference without CoPi	frontside	j_{ini} = 0.077	0.571	k_{trans} = 0.638
		j_{ss} = 0.044		k_{rec} = 0.480
	backside	j_{ini} = 0.053	0.566	k_{trans} = 0.477
		j_{ss} = 0.030		k_{rec} = 0.366
ED - Q_{trans} = 5 mC	frontside	j_{ini} = 0.076	0.577	k_{trans} = 0.432
		j_{ss} = 0.044		k_{rec} = 0.318
	backside	j_{ini} = 0.063	0.319	k_{trans} = 0.160
		j_{ss} = 0.020		k_{rec} = 0.343
ED - Q_{trans} = 15 mC	frontside	j_{ini} = 0.070	0.146	k_{trans} = 0.055
		j_{ss} = 0.010		k_{rec} = 0.322
	backside	j_{ini} = 0.112	0.310	k_{trans} = 0.143
		j_{ss} = 0.035		k_{rec} = 0.319

In addition to the photoelectrochemical investigations the quality of electrodeposited CoPi was investigated by means of SEM/EDX. Corresponding SEM images and EDX spectra are shown in Figure 8-43. As can be seen by the lower magnification image in Figure 8-43a, the applied electrodeposition method results in inhomogeneous distribution of CoPi at the surface of the 10% Mo:$BiVO_4$ photoanode. Large areas of the electrode surface have not been affected by the CoPi deposition procedure, as there is no or only a very low amount of CoPi traceable on the Mo:$BiVO_4$ surface. Additionally, CoPi has been deposited in a more concentrated manner at certain electrode surface spots. As can be seen in Figure 8-43b, the concentrated CoPi deposition most likely occurs at pore walls in form of spread area-like deposition and at small nodules or the like of the Mo:$BiVO_4$ electrode in form of dot-like depositions. In consideration of the deposition technique which includes application of high anodic potentials to achieve oxidation of Co^{2+} and subsequent deposition of Co^{3+} species, the resulting morphology of the CoPi depositions is reasonable as the oxidation proceeds preferably at sites where electron transport to the conductive back contact is facilitated, e.g. along pore walls.

Additionally, the EDX spectrum (Figure 8-43c) is comprised of the typical peaks for Bi, V, O and Mo. Furthermore, EDX investigations confirm the deposition of phosphorus; the presence of cobalt (Lα at 0.776 keV[179]) cannot be confirmed free of doubt by EDX. This is most probably a consequence of the low amount of deposited CoPi leading to Co amounts which are lower than the detection limit of the equipment

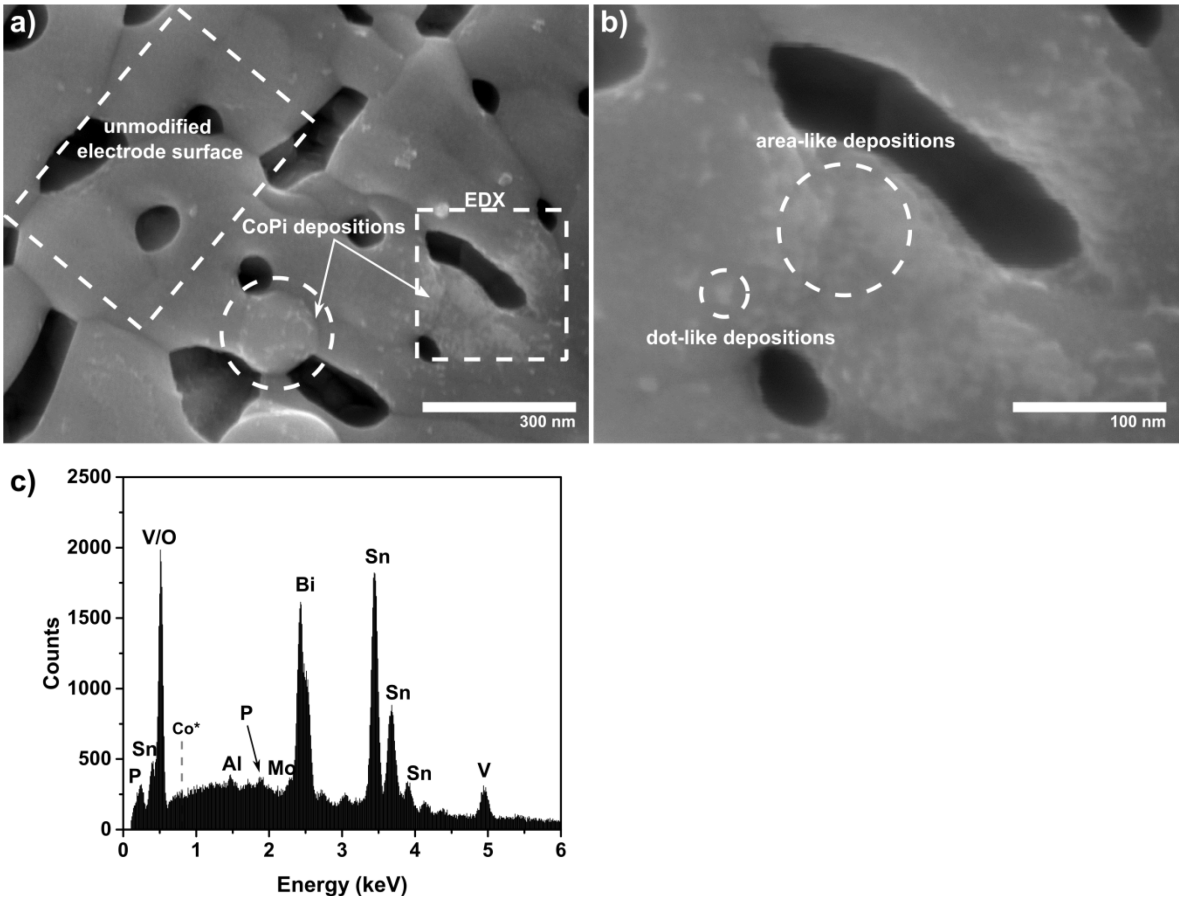

Figure 8-43. SEM/EDX investigations of electrodeposited CoPi (15 mC) at a 10% Mo:$BiVO_4$ photoanode. a) lower magnification image showing unmodified areas and areas with concentrated CoPi depositions, b) higher magnification image highlighting area-like and dot-like CoPi depositions and c) EDX spectrum of CoPi-modified 10% Mo:$BiVO_4$ photoanode. Al-peak within EDX spectrum belongs to the sample holder. Theoretical position of Co-K peak is given as Co*.

8.4.4.3. Photochemical deposition (PD)

Based on the work of Steinmiller and Choi,[175] 10% Mo:$BiVO_4$ photoanodes were modified by photochemically deposited CoPi. Briefly explained, an electrochemical cell equipped with RHE reference electrode, Pt counter electrode and the 10% Mo:$BiVO_4$ thin film as working electrode was filled with 20 ml of 0.1 M potassium phosphate solution containing 0.5 mM $Co(NO_3)_2$. Without application of any bias potential, the working electrode was irradiated by white light (400-700 nm) of an intensity of 100 mW/cm² in frontside mode (further referred to as frontside photochemical deposition, *frontside* PD) or in backside mode (referred to as backside photochemical deposition, *backside* PD). Photo-generated holes of the valence band of the Mo:$BiVO_4$ electrode were consumed by the oxidation of Co^{2+} to Co^{3+} which was subsequently deposited at the electrode surface. The corresponding electrons traveled to the counter electrode and were used for water reduction. This experimental setup ("short-circuited" with counter electrode) separates the photo-oxidation reaction from the photo-reduction reaction, which should result in a significant increase of the density and the amount of the CoPi depositions.[180,181] According to this procedure different amounts of CoPi were photochemically deposited by simple variation of the irradiation time. Furthermore, the influence of the illumination mode used for PD was investigated.

Resulting CoPi-modified 10% Mo:$BiVO_4$ were investigated photoelectrochemically. Obtained j-V-curves of samples modified by *frontside* PD are shown in Figure 8-44a and b. As can be seen, for all 10% Mo:$BiVO_4$ samples modified by different *frontside* PD times in the range of 20 min to 40 min, highest photocurrents were yielded by application of frontside illumination during the measurements of the j-V curves. The best PEC performance was achieved by the sample modified by a PD time of 30 min accounting for 3.86 mA/cm² and 2.43 mA/cm² at an applied potential of 1.23 V vs RHE in frontside illumination and backside illumination, respectively.

Obtained j-V-curves of 10% Mo:$BiVO_4$ photoanodes modified by *backside* PD are shown in Figure 8-44c and d. As can be seen, for the samples with shortest and longest PD times and smallest and biggest amounts of deposited CoPi, respectively, significantly higher photocurrents were obtained by measuring the j-V curves using frontside illumination. For

PD times of 25, 30 and 35 min higher photocurrents were obtained measuring in backside illumination mode. The sample modified by a PD time of 35 min yields highest photocurrent of 3.60 mA/cm² at 1.23 V vs RHE. All obtained photocurrents at the reference potential of 1.23 V vs RHE for electrodes modified by *frontside* and *backside* PD are summarized in Table 8-16.

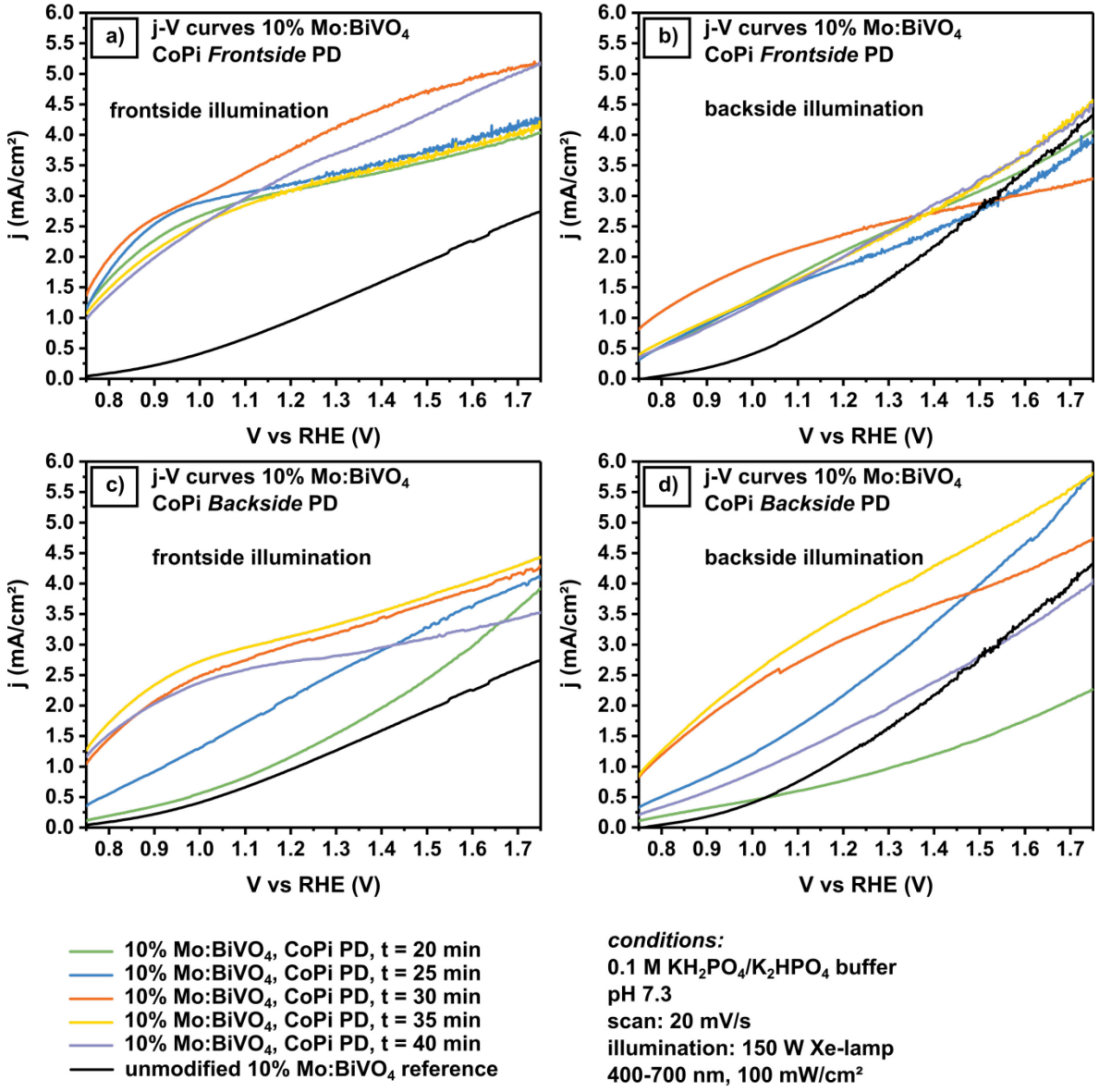

Figure 8-44. j-V-curves of 10% Mo:$BiVO_4$ photoanodes modified with CoPi deposited by *frontside* PD and *backside* PD. j-V curves of all samples in the dark are not shown.

Table 8-16. Summary of photocurrents yielded at an applied potential of 1.23 V vs RHE are for CoPi modified 10% Mo:$BiVO_4$ photoanodes. CoPi was deposited by *frontside* PD and *backside* PD.

Frontside illumination - photochemical deposition		
Irradiation time (min)	j at 1.23 V vs RHE (mA/cm²)	
	frontside illumination	backside illumination
20	3.13	2.19
25	3.23	1.92
30	3.86	2.43
35	3.17	2.10
40	3.48	2.13
Backside illumination - photochemical deposition		
Irradiation time (min)	j at 1.23 V vs RHE (mA/cm²)	
	frontside illumination	backside illumination
20	1.26	0.83
25	2.26	2.33
30	3.06	3.18
35	3.19	3.60
40	2.75	1.70

Like already elucidated for CoPi functionalization by electrodeposition (*vide supra*), depending on the illumination mode when measuring the photocurrents, different CoPi deposition parameters need to be applied to yield maximum PEC performance. For the usage of frontside illumination smaller photochemical deposition times and smaller amounts of deposited CoPi, respectively, are favorable. For application of backside illumination slightly longer deposition times and slightly bigger CoPi amounts, respectively, are beneficial for resulting PEC performance. In accordance with the information gained for electrodeposited CoPi, these findings most probably can be attributed to light harvesting reasons. The less CoPi is deposited onto the surface, the more photons are transmitted to the underlying Mo:$BiVO_4$ when frontside illumination is used. In backside illumination mode slightly bigger amounts of deposited CoPi yield best photocurrents as the light beam is not affected by the CoPi overlayer.

Additionally, the illumination mode during the photochemical deposition procedure plays a key role. Using backside illumination during the PD (*backside* PD) in turn yields best PEC

performance in backside illumination mode. Vice versa, application of frontside illumination (*frontside* PD) yields highest PEC performance when frontside illumination is applied for PEC measurements. A beneficial feature of photochemical deposition is the selective CoPi deposition at sites at the anode surface where photo-generated holes most-likely reach the surface. That means CoPi is deposited at sites which are preferentially used for water oxidation reaction.

In Figure 8-46, photochemically CoPi-modified 10% Mo:$BiVO_4$ electrodes with the highest PEC performance obtained in this study are shown in comparison with the unmodified 10% Mo:$BiVO_4$ sample. As can be seen in Figure 8-46a, the obtained photocurrents for the *frontside* PD-modified sample are dramatically increased in frontside illumination. Corresponding photocurrents of 1.04 mA/cm² at 1.23 V vs RHE for the unmodified sample are increased by a factor of 3.70 to 3.86 mA/cm² at 1.23V vs RHE. The PEC performance of the *backside* PD sample measured in backside illumination is increased by factor of 3.4 from corresponding photocurrents of 1.31 mA/cm² for the unmodified sample to 3.60 mA/cm² for the CoPi-modified sample at a reference potential of 1.23 V vs RHE. The observed enhancement of the PEC performance for photochemical deposition of CoPi on doped $BiVO_4$ photoanodes is nearly reaching the maximum enhancement factor of 4 reported by Park et al.[165] for *frontside* PD and frontside illumination during acquirement of the j-V curves.

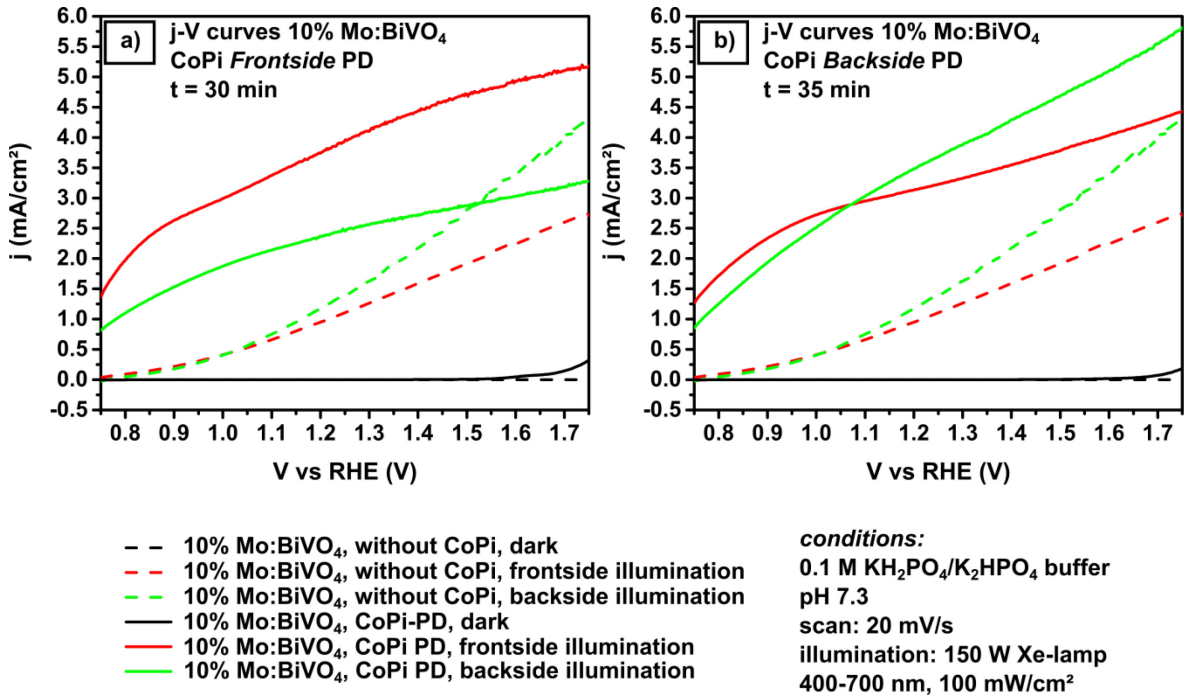

Figure 8-45. j-V curves of unmodified 10% Mo:$BiVO_4$ reference sample and 10% Mo:$BiVO_4$ anodes modified by frontside PD (30 min) and backside PD (35 min).

To gather information about the kinetic background of photochemical deposited CoPi on 10% Mo:$BiVO_4$ photoanodes, photocurrent transients were measured for the *frontside* PD (30 min) and the *backside* PD (35 min) samples which yielded the highest photocurrents. Again, results were analyzed using the phenomenological approach described in chapter 5.5.3.3. Corresponding photocurrent transients are shown in Figure 8-46 along with the transients of an unmodified reference sample. The analysis of the photocurrent transients is summarized in Table 8-17.

As can be seen in Figure 8-46a, the photocurrent transients of the *frontside* PD-modified 10% Mo:$BiVO_4$ exhibit only a very little photocurrent spike when the light is switched on. In consequence, only very little decay of photocurrent occurs over the measurement time of 20 s. Furthermore, no cathodic photocurrent overshoot is observed when switching-off the light. In a first approximation, by having a look at the photocurrent transient shape of the *frontside* PD-modified sample, surface recombination can be assumed to be reduced to a minimum. Indeed, comparison of the surface hole recombination rates k_{rec} of the frontside

PD sample in frontside and backside illumination (accounting for 0.011 s^{-1} and 0.054 s^{-1}, respectively), with the k_{rec} values of the unmodified sample (accounting for 0.480 s^{-1} and 0.366 s^{-1} in frontside and backside illumination, respectively), reveals surface recombination to be drastically minimized by photochemical CoPi deposition. Hole transfer rates k_{trans} of the *frontside* PD sample accounting for 0.272 s^{-1} in frontside illumination and 0.326 s^{-1} in backside illumination, respectively, are slightly smaller in comparison to the k_{trans} values of the unmodified sample. As a consequence, high hole transfer efficiencies $\eta_{transfer}$ of 0.962 and 0.858 are obtained in frontside and backside illumination, respectively; results which are in excellent agreement with obtained photocurrents for these samples.

Principally, same trends are observed for the *backside* PD sample (Figure 8-46 b). Again only very little photocurrent spikes and no photocurrent overshoot is observed. Surface hole recombination rates are decreased to a minimum and k_{trans} values are only slightly smaller compared to the unmodified sample which results in high hole transfer efficiencies. In case of the *backside* PD sample $\eta_{transfer}$ is slightly higher for the backside illuminated sample which is in good agreement with j-V measurements.

In contrast to electrodeposited CoPi, the results reveal a tremendous influence of photochemical deposited CoPi at the electrode surface of a 10% Mo:$BiVO_4$ photoanode on the water oxidation kinetics. Surface recombination is reduced to a minimum by photochemical deposition. As a consequence the overall PEC performance of photochemical CoPi-modified 10% Mo:$BiVO_4$ photoanodes is significantly enhanced.

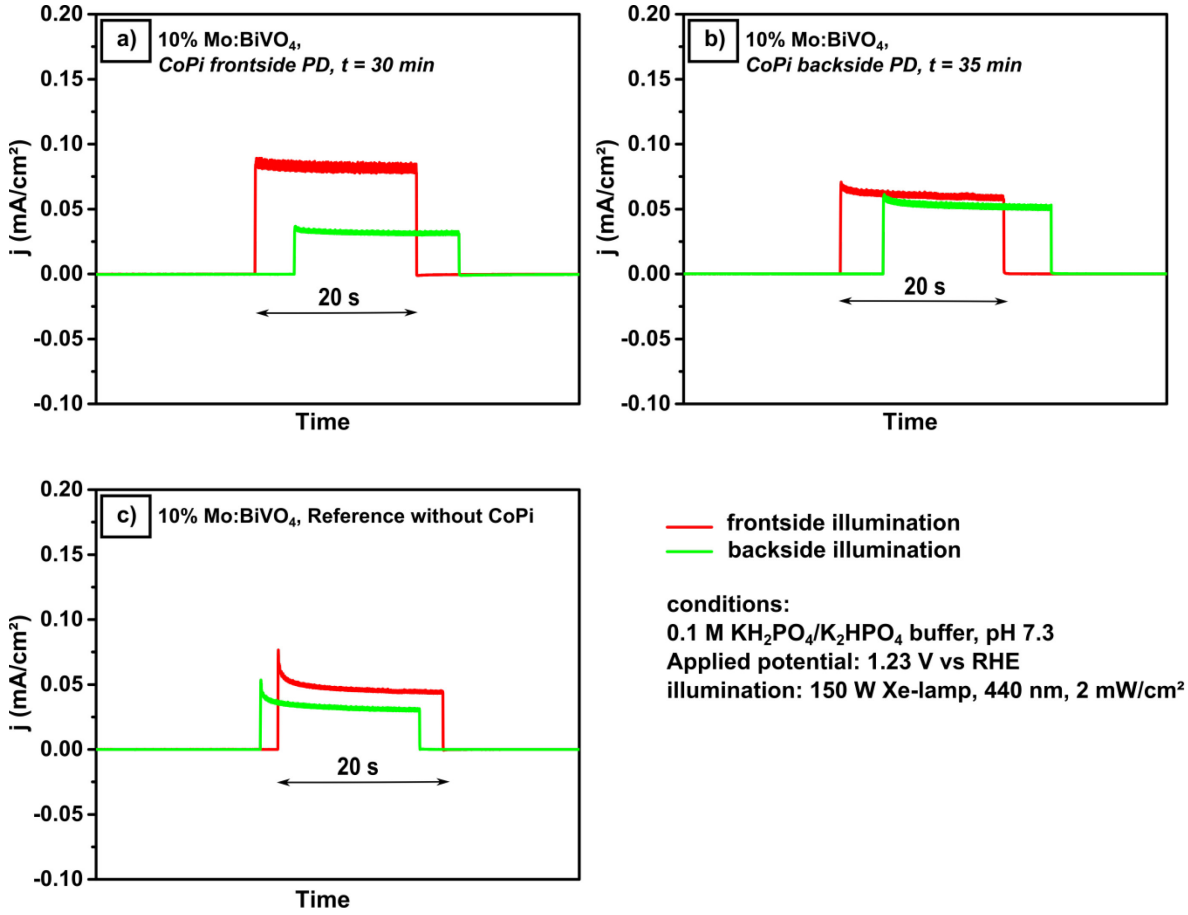

Figure 8-46. Photocurrent transients of a) 10% Mo:$BiVO_4$ modified by frontside PD (30 min), b) 10% Mo:$BiVO_4$ modified by backside PD (35 min) and c) unmodified 10% Mo:$BiVO_4$ reference sample.

Table 8-17. Summary of photocurrent transient analysis of an unmodified 10% Mo:$BiVO_4$ photoanode and two CoPi-modified 10% Mo:$BiVO_4$ photoanodes by frontside PD (30 min) and backside PD (35 min).

Deposition mode and time	Illumination mode	current densities (mA/cm²)	$\eta_{transfer}$	rate constants (s^{-1})
Reference without CoPi	frontside	j_{ini} = 0.077	0.571	k_{trans} = 0.638
		j_{ss} = 0.044		k_{rec} = 0.480
	backside	j_{ini} = 0.053	0.566	k_{trans} = 0.477
		j_{ss} = 0.030		k_{rec} = 0.366
Frontside PD 30 min	frontside	j_{ini} = 0.085	0.962	k_{trans} = 0.272
		j_{ss} = 0.082		k_{rec} = 0.011
	backside	j_{ini} = 0.036	0.858	k_{trans} = 0.326
		j_{ss} = 0.031		k_{rec} = 0.054
Backside PD 35 min	frontside	j_{ini} = 0.069	0.873	k_{trans} = 0.361
		j_{ss} = 0.060		k_{rec} = 0.052
	backside	j_{ini} = 0.060	0.882	k_{trans} = 0.410
		j_{ss} = 0.053		k_{rec} = 0.055

As water oxidation kinetics have been improved by photochemical CoPi deposition, changes in the morphology of the CoPi depositions at the Mo:$BiVO_4$ surface are expected. Hence, the frontside PD (30 min) sample was investigated by SEM/EDX; results are shown in Figure 8-47. As can be seen in the lower magnification image (Figure 8-47a), CoPi is deposited much more homogeneously on the Mo:$BiVO_4$ surface compared to electrodeposited CoPi. Apparently, photochemical deposition results in only small areas of unmodified electrode surface. In consideration of the deposition mechanism, probably no photo-generated holes reached the electrode surface during the PD at the unmodified areas. Hence, no oxidation of Co^{2+} and subsequent Co^{3+} deposition occurred. Additionally, as can be seen in Figure 8-47a und b, despite wide-spread CoPi deposition domains nicely covering the electrode surface, CoPi is also deposited in dot-like and concentrated, pile-like morphologies; the latter forming CoPi nodules. Furthermore, despite the common Bi, V, Mo and O peaks, EDX investigations (Figure 8-47c) confirm the deposition of a species containing Co and P, both elements traced in amounts slightly above the detection limit of the equipment.

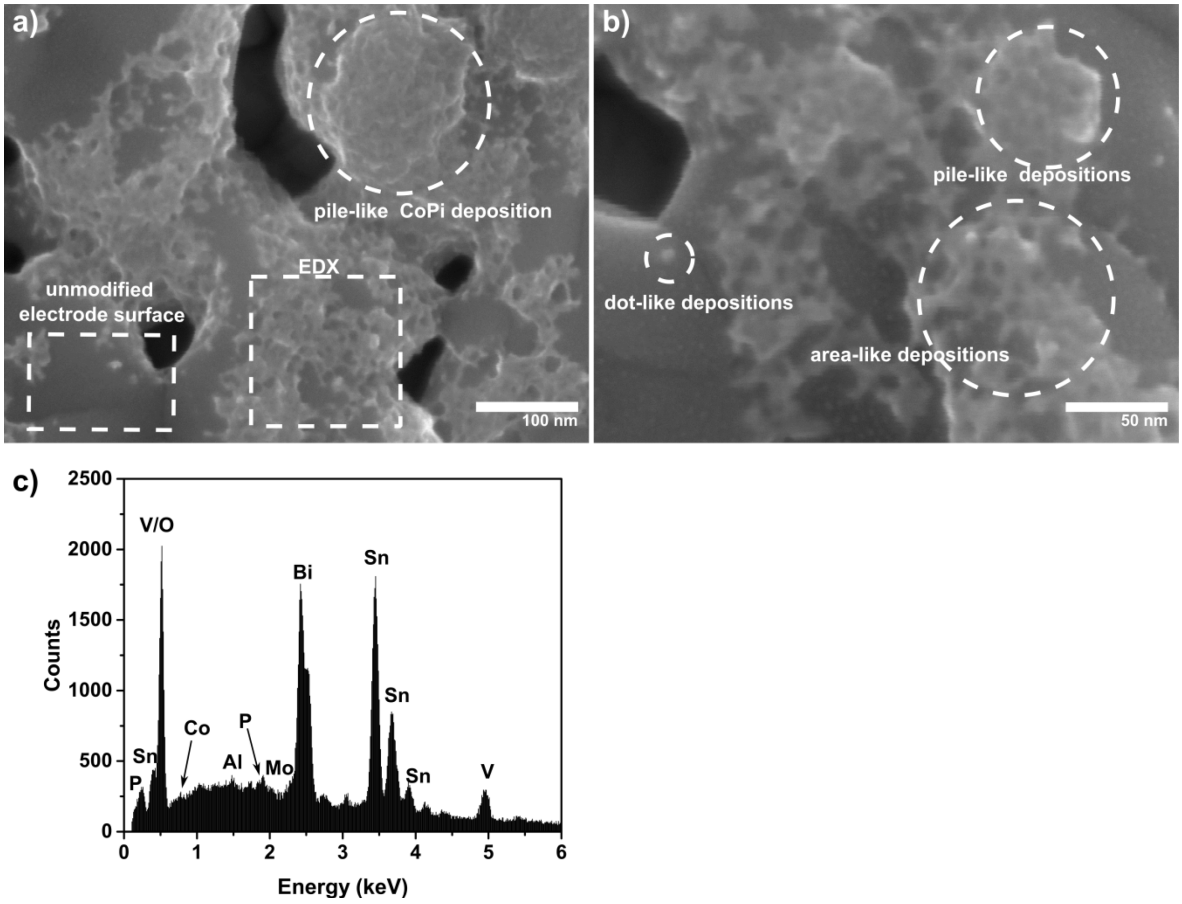

Figure 8-47. SEM/EDX investigations of photochemically deposited CoPi (*frontside* PD, 30 min) at a 10% Mo:$BiVO_4$ photoanode. a) lower magnification image showing nicely CoPi-covered areas and small areas without CoPi depositions, b) higher magnification image highlighting showing different CoPi morphologies deposited and c) EDX spectrum of CoPi-modified 10% Mo:$BiVO_4$ photoanode. Al peak belongs to the sample holder.

8.4.4.4. Photo-assisted electrodeposition (PED)

For photo-assisted electrodeposition, photochemical deposition of CoPi is supplemented by the application of bias voltage. Instead of solely irradiating the 10% Mo:$BiVO_4$ photoanode in Co-containing phosphate buffer and consequently deposit CoPi only at sites where photo-generated holes reach the electrode surface, an additional bias voltage is applied to increase band bending at the semiconductor/electrolyte interface and therefore make more holes reach the surface. In principal, a more homogeneous CoPi-coverage than obtained

with the techniques decribed previously (electrodeposition, photochemical deposition) should be achieved using this technique.

A slightly modified PED method based on previous reports by Gamelin and Grätzel[101] as well as by Ma and Durrant[102] was performed to functionalize 10% Mo:$BiVO_4$ photoanodes by CoPi. In brief, the same electrochemical setup as used for the photochemical CoPi deposition was used. While the 10% Mo:$BiVO_4$ working electrode was irradiated by white light (400-700 nm) of an intensity of 100 mW/cm² in frontside illumination mode, an additional bias potential of 1.2 V vs RHE was applied. The deposition was carried out without stirring and was stopped after a certain amount of charge was transferred which was calculated on-line according to Equation 8-3. (Note: no IR correction was applied for PED CoPi deposition). The transferred charge Q_{trans} directly correlates with the amount of deposited CoPi and therefore is used as variation parameter. Note: At applied potentials of 1.2 V vs RHE under irradiation of light of the above mentioned intensity, water oxidation reaction occurs concomitantly, i.e. in case of PED Q_{trans} is not a direct measure for the deposited amount of CoPi but is directly proportional to it.

According to this method, 10% Mo:$BiVO_4$ photoanodes were functionalized and their photoelectrochemical properties were investigated. In Figure 8-48, j-V curves of samples modified by different amounts of CoPi (i.e. with different Q_{trans} flown) are shown, obtained photocurrents at a reference potential of 1.23 V vs RHE are summarized in Table 8-18. As can be seen, the obtained photocurrents are dependent of the transferred charge Q_{trans} and the amount of deposited CoPi, respectively, and the illumination mode during PEC measurements. Smaller amounts of CoPi are beneficial for frontside illumination PEC measurements for instance for the Q_{trans} = 75 mC sample yielding photocurrents as high as 3.22 mA/cm² at 1.23 V vs RHE in frontside illumination and 2.68 mA/cm² at 1.23 V vs RHE in backside illumination, respectively. With increasing Q_{trans}, photocurrents obtained in frontside and backside illumination become nearly equal as can be seen for the Q_{trans} = 125 mC sample where frontside and backside illuminations photocurrent densities account for 3.31 mA/cm² in frontside illumination and 3.28 mA/cm² in backside illumination, respectively (given for the reference potential of 1.23 V vs RHE). With

further increasing Q_{trans}, backside illumination affects higher photocurrents as revealed by the Q_{trans} = 150 mC sample and the Q_{trans} = 200 mC sample. These findings are in good agreement with the previous investigations of the influence of different amounts of deposited CoPi by ED and PD revealing better PEC performance of samples with low amounts of deposited CoPi in frontside illumination and better PEC performance for samples with big amounts of CoPi in backside illumination mode. Highest photocurrents in frontside illumination as well as in backside illumination were obtained for the Q_{trans} = 150 mC sample accounting for 3.78 mA/cm² and 4.36 mA/cm² at 1.23 V vs RHE, respectively.

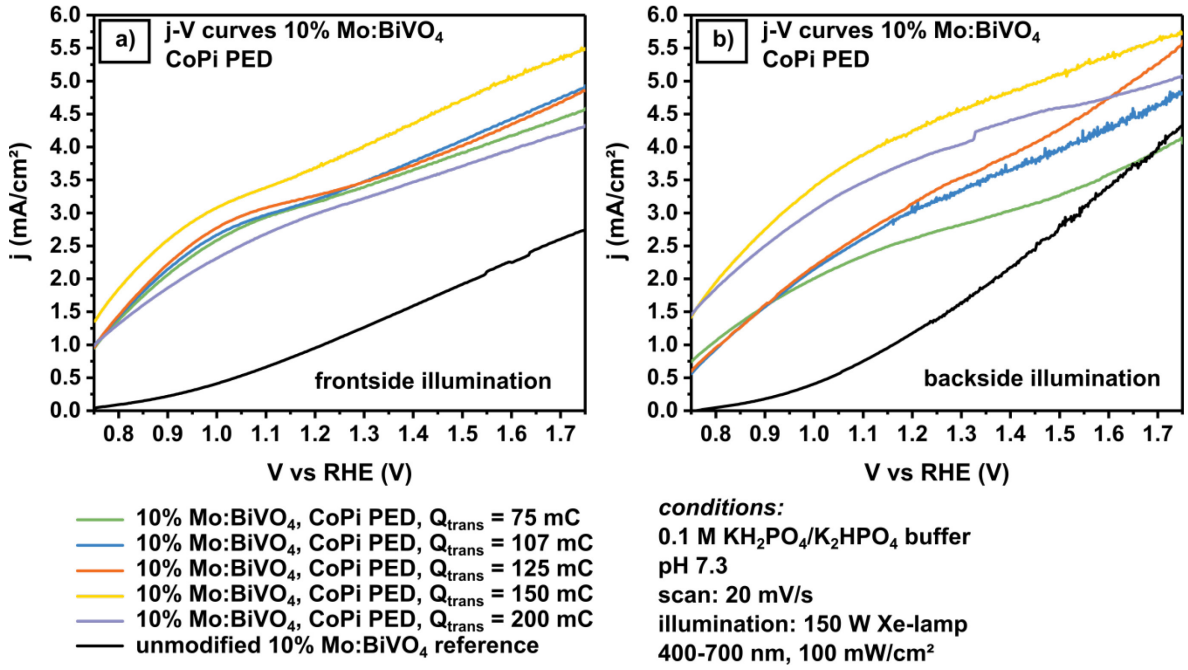

Figure 8-48. j-V curves of CoPi-modified 10% Mo:$BiVO_4$ photoanodes obtained in a) frontside illumination and b) backside illumination. Photo-assisted electrodeposition (PED) method was applied for CoPi deposition. j-V curves of all samples in the dark are not shown for clarity.

Table 8-18. Summary of photocurrents yielded at an applied potential of 1.23 V vs RHE are for CoPi modified 10% Mo:$BiVO_4$ photoanodes. Photo-assisted electrodeposition (PED) method was applied.

PED - Q_{trans} (mC)	j at 1.23 V vs RHE (mA/cm²)	
	frontside illumination	backside illumination
75	3.22	2.68
107	3.27	3.11
125	3.31	3.28
150	3.78	4.36
200	3.06	3.88

In Figure 8-49, the Q_{trans} = 150 mC CoPi-modified 10% Mo:$BiVO_4$ electrodes using photo-assisted electrodeposition method which yielded highest PEC performance is shown in comparison to the unmodified 10% Mo:$BiVO_4$ sample. The photocurrents without CoPi modification accounting for 1.04 mA/cm² in frontside illumination and 1.31 mA/cm² in backside illumination, respectively, are drastically enhanced by CoPi deposition to yield photocurrents as high as 3.78 mA/cm² and 4.36 mA/cm² in frontside and backside illumination, respectively (all values given for an applied potential of 1.23 V vs RHE). Thus, photocurrents obtained using frontside illumination are enhanced significantly by a factor of 3.7 and corresponding photocurrents obtained in backside illumination mode are enhanced by a factor of 3.4 which is in good agreement with literature reports.[101,102,169,170,177]

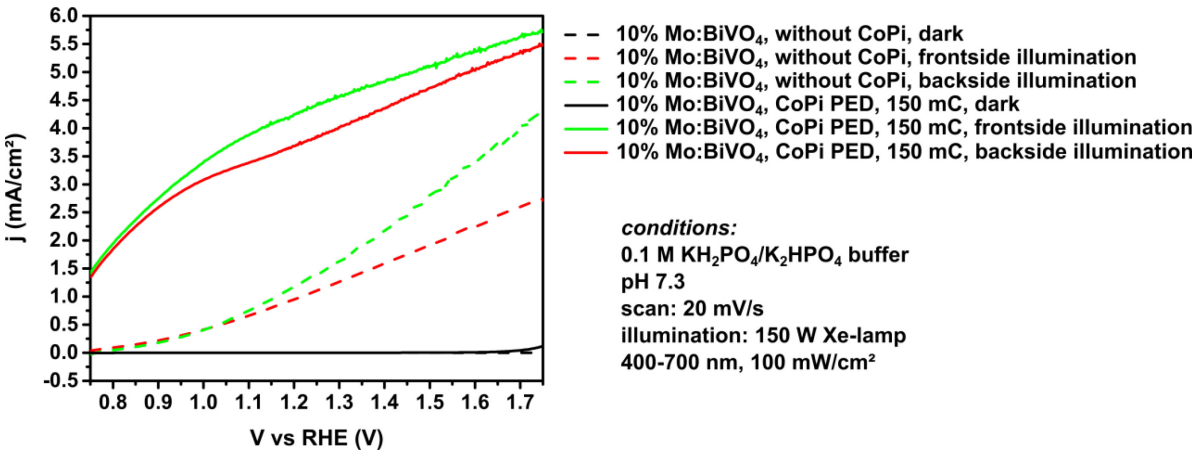

Figure 8-49. j-V curves of unmodified 10% Mo:$BiVO_4$ reference sample and 10% Mo:$BiVO_4$ anode modified by PED, Q_{trans} = 150 mC.

As PEC performance regarding water oxidation was impressively improved by CoPi functionalization according to the PED method, a look at the corresponding water oxidation kinetics is worth the effort. For this purpose, photocurrent transients were measured and again analyzed following the phenomenological approach explained in chapter 5.5.3.3. Resulting photocurrent transients of the 150 mC 10% Mo:$BiVO_4$ sample which showed the highest PEC performance is presented in Figure 8-50 along with the transients of an unmodified 10% Mo:$BiVO_4$ reference sample. Corresponding results of the transient analysis are summarized in Table 8-19.

As can be seen, the 10% Mo:$BiVO_4$ sample modified by CoPi according to the PED procedure (Q_{trans} = 150 mC) exhibits nearly ideal behavior when light is switched on/off. Neither in frontside illumination nor in backside illumination a significant photocurrent spike and subsequent decay of photocurrent over time and/or cathodic photocurrent overshoot is observed. That means hole accumulation at the surface seems to be reduced. This is confirmed by the photocurrent transient analysis. In comparison to the unmodified reference sample (Figure 8-50b), surface hole recombination rates k_{rec} are reduced to a minimum of 0.046 s^{-1} and 0.007 s^{-1} in frontside and backside illumination, respectively. In addition, hole transfer rates k_{trans} are significantly enhanced from 0.638 s^{-1} and 0.477 s^{-1} in frontside and backside illumination for the unmodified 10% Mo:$BiVO_4$ reference sample, respectively, to hole transfer rates of 0.725 s^{-1} and 0.591 s^{-1} in frontside and backside illumination, respectively, for the CoPi-functionalized sample; both effects resulting in tremendous hole transfer efficiencies $\eta_{transfer}$ of 0.940 and 0.980 in frontside and backside illumination, respectively.

To summarize, the water oxidation kinetics of the 10% Mo:$BiVO_4$ photoanodes were influenced positively by CoPi-functionalization. From a kinetic point of view, the resulting hole transfer efficiencies of nearly 1 reveal the PED method to be a very promising procedure to functionalize photoanodes for water oxidation.

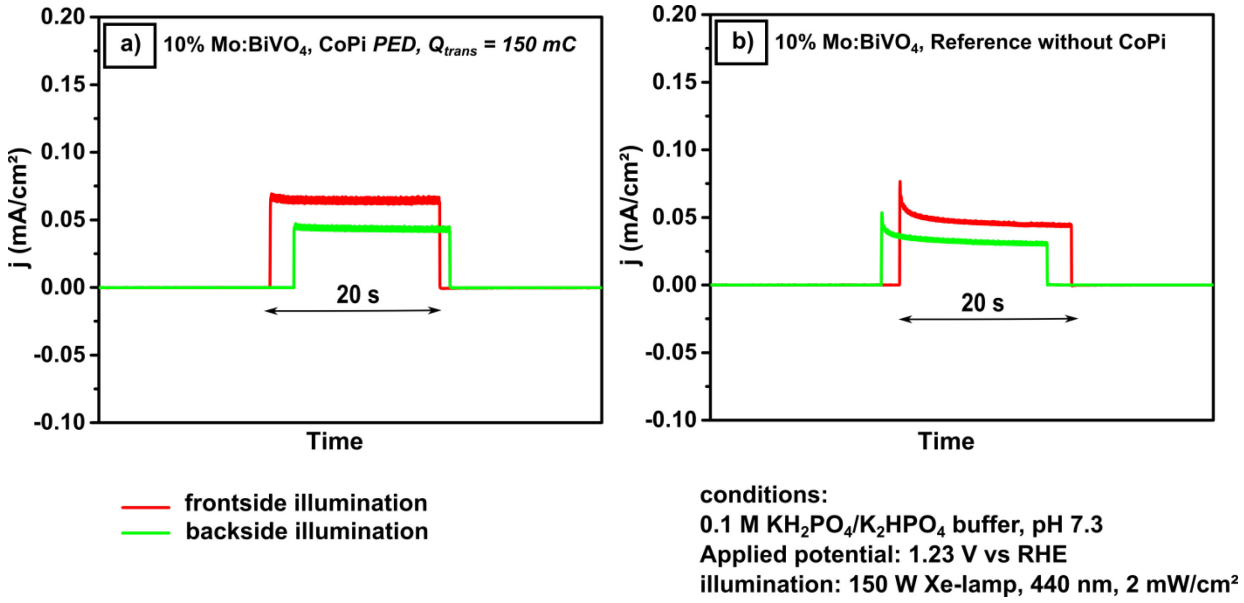

Figure 8-50. Photocurrent transients of a) 10% Mo:$BiVO_4$ modified by PED of CoPi, Q_{trans} = 150 mC and b) unmodified 10% Mo:$BiVO_4$ reference sample.

Table 8-19. Summary of photocurrent transient analysis of an unmodified 10% Mo:$BiVO_4$ photoanode and the Q_{trans} = 150 mC CoPi-modified 10% Mo:$BiVO_4$ photoanodes by usage of the PED method.

Deposition mode and time	Illumination mode	current densities (mA/cm²)	$\eta_{transfer}$	rate constants (s^{-1})
Reference without CoPi	frontside	j_{ini} = 0.077	0.571	k_{trans} = 0.638
		j_{ss} = 0.044		k_{rec} = 0.480
	backside	j_{ini} = 0.053	0.566	k_{trans} = 0.477
		j_{ss} = 0.030		k_{rec} = 0.366
PED Q_{trans} = 150 mC	frontside	j_{ini} = 0.067	0.940	k_{trans} = 0.725
		j_{ss} = 0.063		k_{rec} = 0.046
	backside	j_{ini} = 0.043	0.988	k_{trans} = 0.591
		j_{ss} = 0.043		k_{rec} = 0.007

In addition to the photocurrent transient analysis, SEM/EDX investigations of the CoPi morphology at the surface of the 10% Mo:$BiVO_4$ photoanode surface were performed. As can be seen in Figure 8-51a and b, the whole photoanode material surface is homogeneously covered by a wide-spread, thin layer of CoPi. As can be seen in contrast to the other deposition methods, no CoPi artefacts like piles, nodules or dot like-depositions were found in the analyzed areas. In comparison with the surface of an unmodified

10% Mo:$BiVO_4$ sample (Figure 8-51d), the surface of the PED-CoPi-modified sample is significantly roughened which proves the modification of the surface. Additionally, the EDX spectrum (Figure 8-51c) reveals the common Bi, V, O and Mo peaks of the Mo:$BiVO_4$. In addition, the presence of Co and P is confirmed within the analyzed sample in amounts close to the detection limit of the equipment. In agreement with the improved PEC performance of the PED-CoPi-modified photoanodes, the morphology of the CoPi at the Mo:$BiVO_4$ surface is significantly improved when compared to the photochemically and electrochemically CoPi-modified analogues.

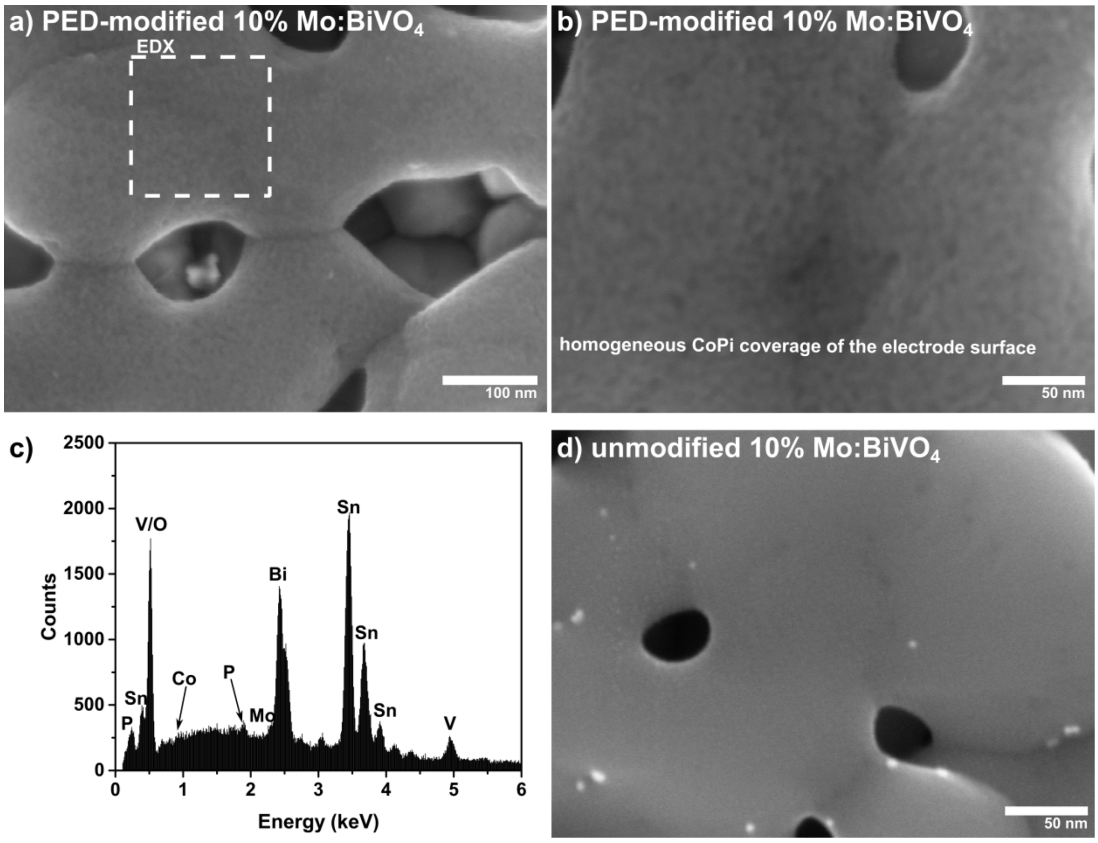

Figure 8-51. SEM/EDX investigations of a 10% Mo:$BiVO_4$ photoanode modified by CoPi according to the PED method, Q_{trans} = 150 mC. a) lower magnification image showing nicely CoPi-covered photoanode material, b) higher magnification revealing a roughened surface of the electrode material proofing CoPi deposition, c) EDX spectrum of CoPi-modified 10% Mo:$BiVO_4$ photoanode, d) image of an unmodified 10% Mo:$BiVO_4$ sample.

8.4.4.5. Conclusion

In summary, the PEC performance regarding water oxidation of Mo:$BiVO_4$ photoanodes can be influenced by deposition of the cobalt phosphate water oxidation catalyst CoPi. The CoPi deposition method plays a key role as it directly affects the morphology of the CoPi depositions at the photoanode surface and, hence, also directly influences the PEC performance.

Application of the electrodeposition method results in pile-like and dot-like CoPi depositions, i.e. inhomogeneous surface coverage of the photoanode material. Moreover, instead of being deposited at anode sites which are eager for performing the water oxidation reaction, CoPi is deposited at anode sites which are favorable for electron transport through the photoanode material to the conductive substrate. This disadvantageous morphology of the water oxidation catalyst results in worsened water oxidation kinetics and reduced hole transfer rates (k_{trans}), respectively, when compared to the non-functionalized 10% Mo:$BiVO_4$ photoanode. Only a slight increase of the PEC performance was observed, most probably as a consequence of improved electron mobility/charge separation induced by CoPi.

Photochemical deposition of CoPi results in much more homogeneous CoPi deposition at the photoanode surface. Only few, small non-functionalized areas and some pile-like CoPi nodules were observed. Due to the deposition procedure, CoPi is deposited at photoanode sites at which photo-generated holes readily oxidize the Co^{+2} species. As a consequence, CoPi depositions are located at sites which are probably also used during water oxidation. This results in enhanced water oxidation kinetics. Hence, much higher PEC performance was yielded.

Combination of electrodeposition and photochemical deposition was demonstrated to be a very powerful CoPi deposition method. By photo-assisted electrodeposition a wide-spread, thin layer of CoPi homogeneously and completely covering the photoanode surface is obtained. Perfecting the CoPi morphology yields a tremendous improvement of the water oxidation kinetics expressed by hole transfer efficiencies near to 1 (~0.50 for the ED-

samples and ~0.85 for the PD samples). As a consequence, the PEC performance is largely enhanced.

To sum-up, the j-V-curves of the best-performing 10% Mo:$BiVO_4$ photoanodes functionalized by the mentioned CoPi deposition methods shown in Figure 8-52a and b. Independent of the illumination direction, the Mo:$BiVO_4$ photoanodes modified by the PED method yield highest photocurrents when compared to the best performing ED and PD samples. This is directly translated into highest ABPE maxima (applied-bias to photon efficiency), as illustrated in Figure 8-52c and d. As can be seen, the location/potential of the ABPE maximum is for all deposition methods approximately the same. The highest ABPE of about 0.93 % can be derived from the photoanodes modified by the PED procedure which additionally confirms this method to be the most favorable one.

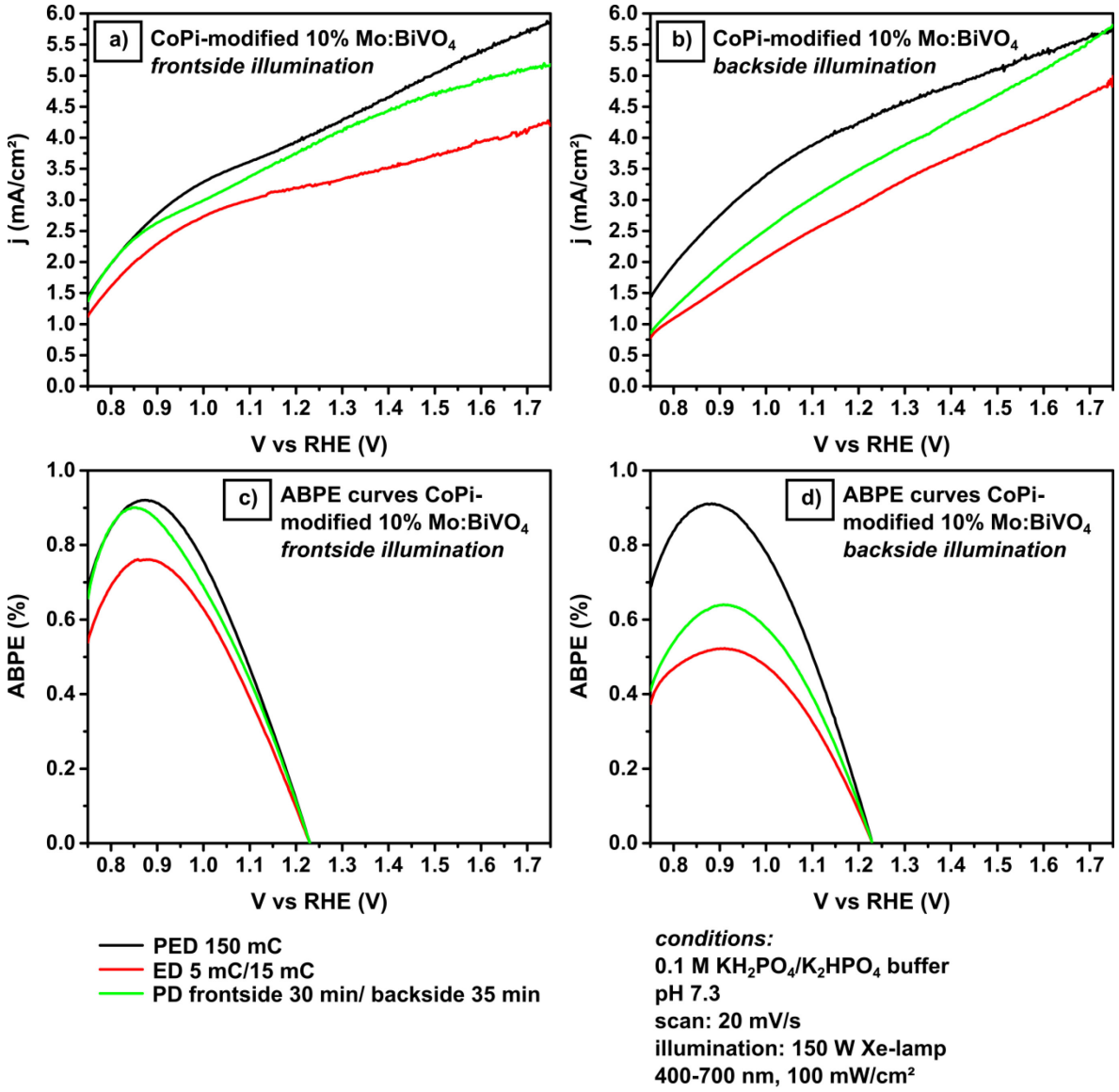

Figure 8-52 j-V curves of best-performing 10% Mo:$BiVO_4$ photoanodes, CoPi-modified by ED, PD and PED in a) frontside illumination and b) backside illumination along with the corresponding ABPE curves calculated from the j-V curves yielded in c) frontside illumination and d) backside illumination.

9. F:$BiVO_4$ and F/Mo:$BiVO_4$ thin film photoanodes

9.1. Introduction

In the previous sections, the main PEC performance limiting factor for $BiVO_4$ – the slow electron transport – was addressed by cation doping with molybdenum. Additionally, in chapter 7 the concept of anion doping in terms of partial O/F substitution was developed and applied to $BiVO_4$ powder samples and turned out to be a valuable tool to enhance the PEC performance of $BiVO_4$ EPD-photoanodes regarding water oxidation. In this section the concept of anion doping is applied to $BiVO_4$ thin film photoanodes. Additionally, Mo:$BiVO_4$ thin films are co-doped with fluorine. The influence of fluorination on the thin film properties as well as on their PEC performance regarding water oxidation is studied.

9.2. Partial O/F substituted $BiVO_4$ thin films

To put this aim into practice, $BiVO_4$ thin films on FTO-coated glass slides were prepared by the wet chemical synthesis method presented in chapter 8.2. The obtained $BiVO_4$ thin films were then fluorinated by the soft solid-vapor reaction using the indirect gas flow apparatus illustrated an explained in chapter 7.2. A maximum of two $BiVO_4$ thin film samples per heating procedure were loaded in a small corundum boat which in turn was placed inside a larger corundum boat containing varying amounts of PVDF. The nested boats were then placed inside a corundum tube with one closed end and then put in a horizontal tube furnace with a low nitrogen gas flow of 5 l/h. The reaction conditions of the fluorination procedure needed to be adjusted for two reasons: i) the amount of $BiVO_4$ in the thin films was by far smaller than the amount of powdered $BiVO_4$ and ii) the FTO-coated glass substrate corrodes by too harsh fluorination conditions leading to delamination of the thin films. Both problems can be overcome by adjustment of the HF concentration inside

the reaction tube which in turn can be tuned by variation of the reaction temperature and the amount of the HF-releasing polymer PVDF.

Applied reaction parameters together with photocurrents yielded for the corresponding fluorinated $BiVO_4$ photoanodes are summarized in Table 9-1 (j-V curves are shown in the appendix, chapter 12.1.3.1). Having a look at the conditions 1-3, an amount of 2 g of PVDF was found to result in the best performing $BiVO_4$ thin film photoanodes while the reaction temperature was kept constant at 400 °C. Additional variation of the reaction temperature resulted in the optimal reaction conditions (condition 5, 2 g of PVDF, 370 °C) leading to fluorinated $BiVO_4$ thin films with best PEC performance.

Table 9-1. Summary of fluorination reaction conditions in line with obtained photocurrents at an applied potential of 1.23 V vs RHE (0.1 M KPi buffer, pH = 7.3, light: 400-700 nm at 100 mW/cm²). For all fluorination reactions undoped $BiVO_4$ thin films were used.

condition	m(PVDF) (g)	T (°C)	t (h)	j at 1.23 V vs. RHE (mA/cm²)			
				without CoPi		with CoPi	
				Frontside illumination	Backside illumination	Frontside illumination	Backside illumination
ref	-	-	-	0.08	0.20	0.54	2.19
1	1	400	2	0.41	0.57	0.59	0.97
2	2	400	2	0.45	0.82	0.50	1.70
3	3	400	2	0.23	1.02	0.16	1.11
4	2	350	2	0.44	0.40	1.12	1.72
5	2	370	2	0.69	1.01	1.28	2.65

$BiVO_4$ thin films treated according to the optimized fluorination conditions were characterized by XRD in gracing incidence mode of the x-ray beam. The obtained diffraction pattern together with the pattern obtained for a pristine $BiVO_4$ thin film is shown in Figure 9-1. As already elucidated in chapter 7.2, the diffraction patterns of $BiVO_4$ and F:$BiVO_4$ are quite similar as the positional parameters (derived by Rietveld refinement of powder XRD data, see chapter 7.2) are more or less identical. Furthermore, the elements oxygen and fluorine cannot be distinguished using X-ray diffraction techniques. For this reason, the thin film diffraction pattern obtained by GI-XRD can only be used to gain qualitative information about the thin film material after having passed the fluorination procedure because of the insufficient quality of diffraction data. For the fluorinated sample, an isotropic, polycrystalline crystal structure is revealed by XRD in gracing incidence mode. All obtained reflections can be assigned to the scheelite-structure, while it cannot be distinguished between monoclinic and tetragonal scheelite phase based on GI-XRD data. The results are in good agreement with the pattern of the pristine $BiVO_4$ and based on powder XRD data (see chapter 7.2) the structure type can be assumed to remain unchanged upon fluorine incorporation.

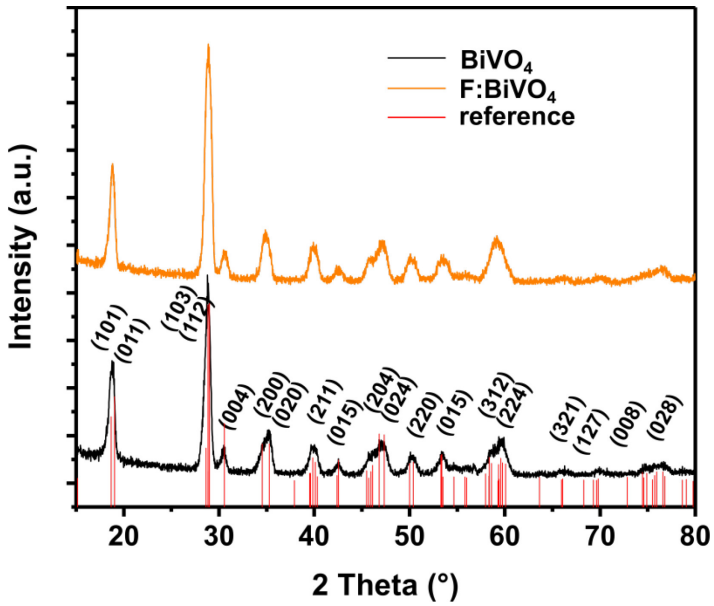

Figure 9-1. XRD pattern (gracing incidence) for pristine $BiVO_4$ thin films and fluorinated $BiVO_4$ thin films in line with the reference reflections acc. to PDF 01-083-1698.

As shown in chapter 7.2, fluorine incorporation directly influences the optical absorption properties of $BiVO_4$ powder samples. By UV/Vis investigations in diffuse reflectance mode, a small decrease of the band gap from 2.45 eV for the pristine $BiVO_4$ powder sample to 2.38 eV for the fluorinated powder sample was estimated by extrapolation of the linear part of the absorption spectrum using the Tauc method. UV/Vis spectra obtained in transmission mode for an F:$BiVO_4$ thin film in comparison to a pristine $BiVO_4$ thin film sample are shown in Figure 9-2. By extrapolation of the linear part of the spectrum the absorption onset can be estimated to 510 nm for the fluorinated thin film and 508 nm for the pristine thin film. This corresponds to band gaps of 2.43 eV and 2.44 eV for the fluorinated $BiVO_4$ and the pristine $BiVO_4$ thin film samples, respectively. The difference between the band gaps of both thin film samples is not as significant as for the corresponding powder samples. However, the decrease of the optical band gap upon fluorination is also observed for the thin films.

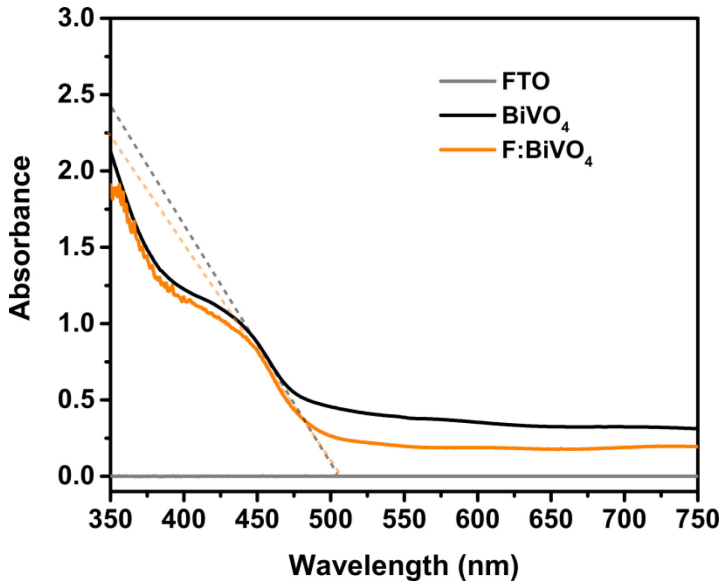

Figure 9-2. UV/Vis spectrum of fluorinated and pristine $BiVO_4$ thin films, measurements carried out in transmission mode.

As elucidated in chapter 8.4.3, thermal treatment has a significant impact on the thin films' morphology and therefore on their PEC performance regarding water oxidation. For this reason the fluorinated $BiVO_4$ thin films were investigated by SEM. Results are shown in Figure 9-3, which illustrates the morphologies of pristine $BiVO_4$ thin films and fluorinated thin films on FTO substrates. As can be seen by the top view images at different magnifications, the thin film morphology is changed by the fluorination procedure. The pristine $BiVO_4$ sample consists of domains of an average geometrical size of 7.2 ±3.3 µm² with inner domain material streaks of an average thickness of 68 ±7 nm. The average domain size of the fluorinated $BiVO_4$ thin films is very similar a(accounting for 6.9 ±3.3 µm²). The fluorination procedure affects sintering of the thin film material. Hence, no single material streaks are present in the F:$BiVO_4$ thin film. Instead, the F:$BiVO_4$ thin film exhibits a more dense morphology with elliptical pores of an average geometrical pore area of 275 ±260 nm². The more dense character of the fluorinated thin film is further confirmed by SEM images of cross sections of the pristine and fluorinated $BiVO_4$ samples, revealing a more dense thin film character in case of the fluorinated sample. In good agreement with these data, the film thickness is slightly decreased from ~269 nm for the pristine $BiVO_4$ thin film to ~258 nm for the fluorinated thin films. The change in morphology is induced by the additional thermal treatment which is proven by SEM investigations of a reference sample (see Figure 9-3) which was treated according to the fluorination procedure but leaving out the HF releasing PVDF.

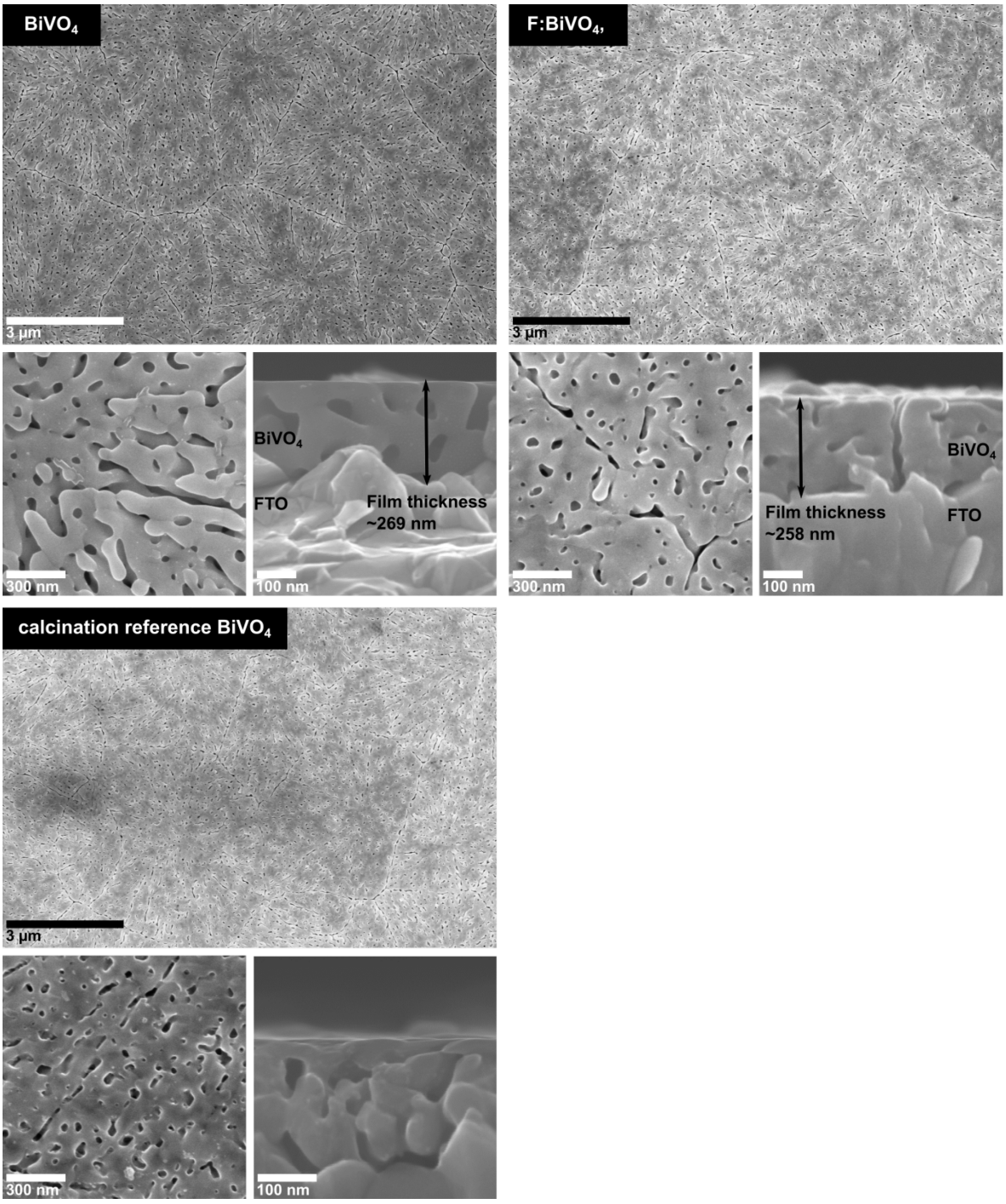

Figure 9-3. SEM top view and cross sectional images of $BiVO_4$ (left) and fluorinated $BiVO_4$ (right) thin films on FTO substrate and a calcination reference which was calcined in similar manner but leaving out the PVDF. Fluorination temperature: 370 °C, post-calcination temperature: 400 °C.

To gather information about a possible impact of the fluorination procedure on the microstructure and crystal orientation of the thin film domains, TEM investigations were carried out. Results are shown in Figure 9-4. As can be seen by the overview image in Figure 9-4a, the more dense thin film morphology with small elliptical pores is confirmed by TEM investigations. By SAED measurements at two different spots along one domain similar dot diffraction patterns were obtained. The reflections correspond to the (011) and the (101) planes of $BiVO_4$ in the scheelite structure in both cases. That means the single-crystalline character of the thin film domains is preserved after the fluorination procedure. The crystalline character of the sample is also confirmed by HR-TEM (Figure 9-4b). FFT reveals spatial frequencies due to the lattice fringes which can be assigned to the (011) and the (101) plane of the monoclinic scheelite structure. EDX analysis was carried out using TEM to assure no influence of the FTO substrate. As can be seen in Figure 9-4c, the EDX spectrum of the fluorinated thin film consists of the typical peaks for Bi, V, O and Cu (due to the copper TEM grid) and an additional peak for fluorine at 0.677 keV (F K_α) which is more clearly visible in the inset. Due to the low amount of fluorine within the sample (near the detection limit of the equipment) fluorine quantification was not possible and the EDX analysis only provides a qualitative proof of the fluorine incorporation into the $BiVO_4$ thin film material.

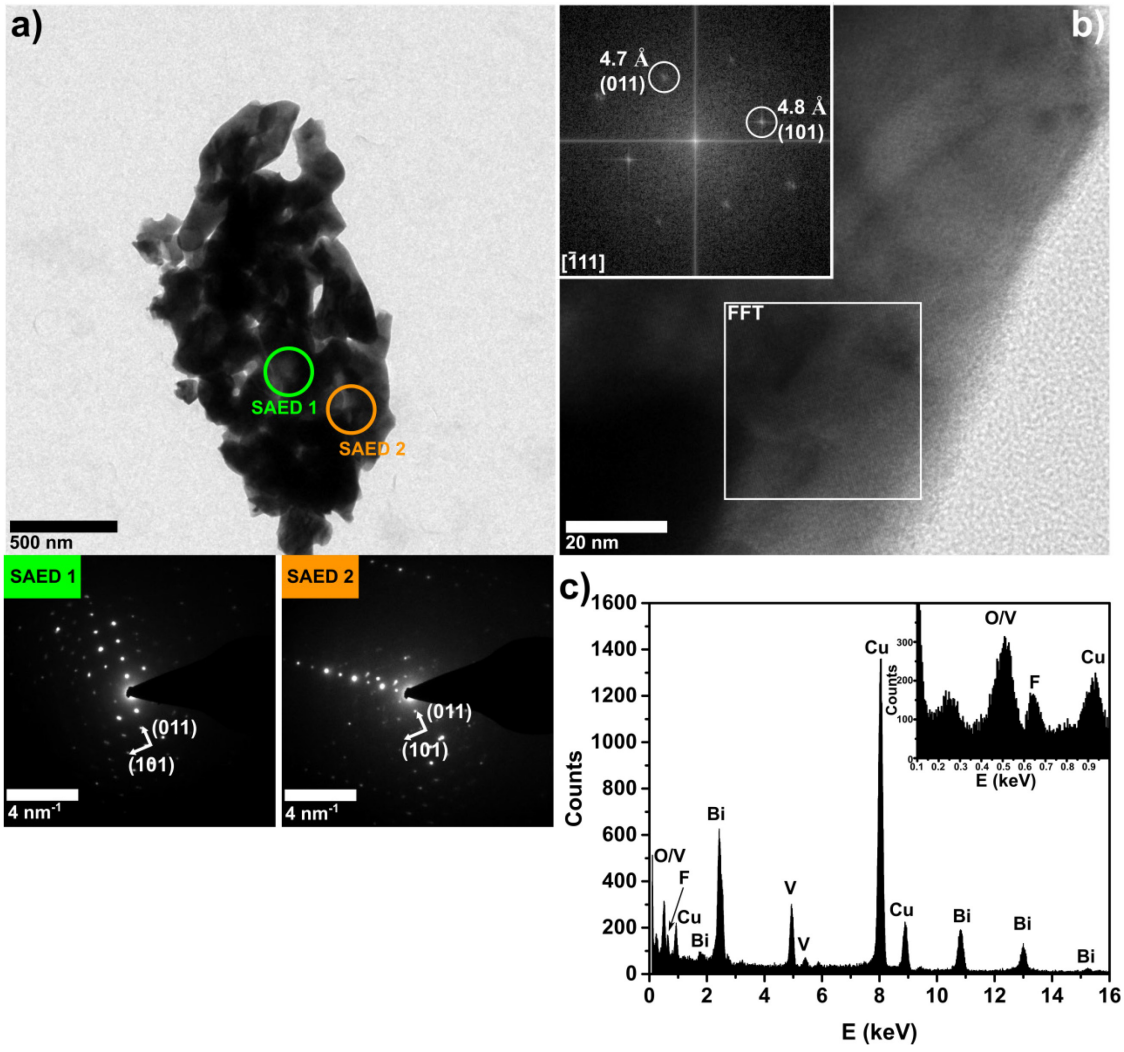

Figure 9-4. TEM investigations of fluorinated $BiVO_4$, a) overview image and corresponding SAED pattern, b) HR-TEM image with corresponding FFT pattern (inset) and c) EDX spectrum with a zoomed view on the fluorine peak. Sample was scraped-off the FTO substrate.

Characterization of the fluorinated $BiVO_4$ thin films revealed a slight influence of the fluorination on the structural, optical and morphological properties of the thin film. While the structure type remains the same, the optical band gap is slightly decreased. The morphology is changed due to sintering effects whereas the single-crystalline character of the domains remains unchanged. Fluorine was traced qualitatively within the thin film material by EDX. How these changes of the thin film properties affect the water oxidation

properties was investigated by means of photoelectrochemistry. Figure 9-5 shows j-V curves of pristine $BiVO_4$ thin film photoanodes and the fluorinated counterparts with and without CoPi under constant and under chopped illumination in frontside and backside mode. Obtained photocurrents at an applied potential of 1.23 V vs RHE are summarized in Table 9-2. As can be seen for the samples without CoPi deposited onto the surface (Figure 9-5a), the photocurrents are slightly higher for the fluorinated samples. Photocurrents obtained in frontside illumination vary only little accounting for 0.08 mA/cm² and 0.09 mA/cm² at 1.23 V vs RHE for the pristine and the fluorinated $BiVO_4$ thin films, respectively. Using backside illumination results in higher photocurrents and a bigger difference between the pristine $BiVO_4$ and its fluorinated counterpart accounting for 0.20 mA/cm² and 0.28 mA/cm² at 1.23 V vs RHE, respectively. Same trend is observed when chopped illumination is applied. As can be seen in Figure 9-5c, higher photocurrents are yielded for the F:$BiVO_4$ photoanodes. Furthermore, significant spikes are recorded for both samples which are most pronounced when backside illumination was used. This indicates both samples severely suffering from surface recombination. Additionally, different photocurrents in dependence of the illumination direction (higher photocurrents in backside illumination mode) point to bad electronic conductivity.

After deposition of a thin layer of CoPi, generally the same trend is observed. Nearly similar photocurrents are observed when frontside illumination is used accounting for 0.52 mA/cm² and 0.48 mA/cm² at 1.23 V vs RHE for the pristine $BiVO_4$ and the fluorinated $BiVO_4$, respectively. Application of backside illumination results in higher photocurrents. The fluorinated sample yields a maximum photocurrent of 3.03 mA/cm² at 1.23 V vs RHE which is 0.8 mA/cm² higher than its pristine counterpart, which only yields 2.20 mA/cm² at 1.23 V vs RHE. The big difference in observed photocurrents depending on the illumination mode remains upon CoPi deposition.

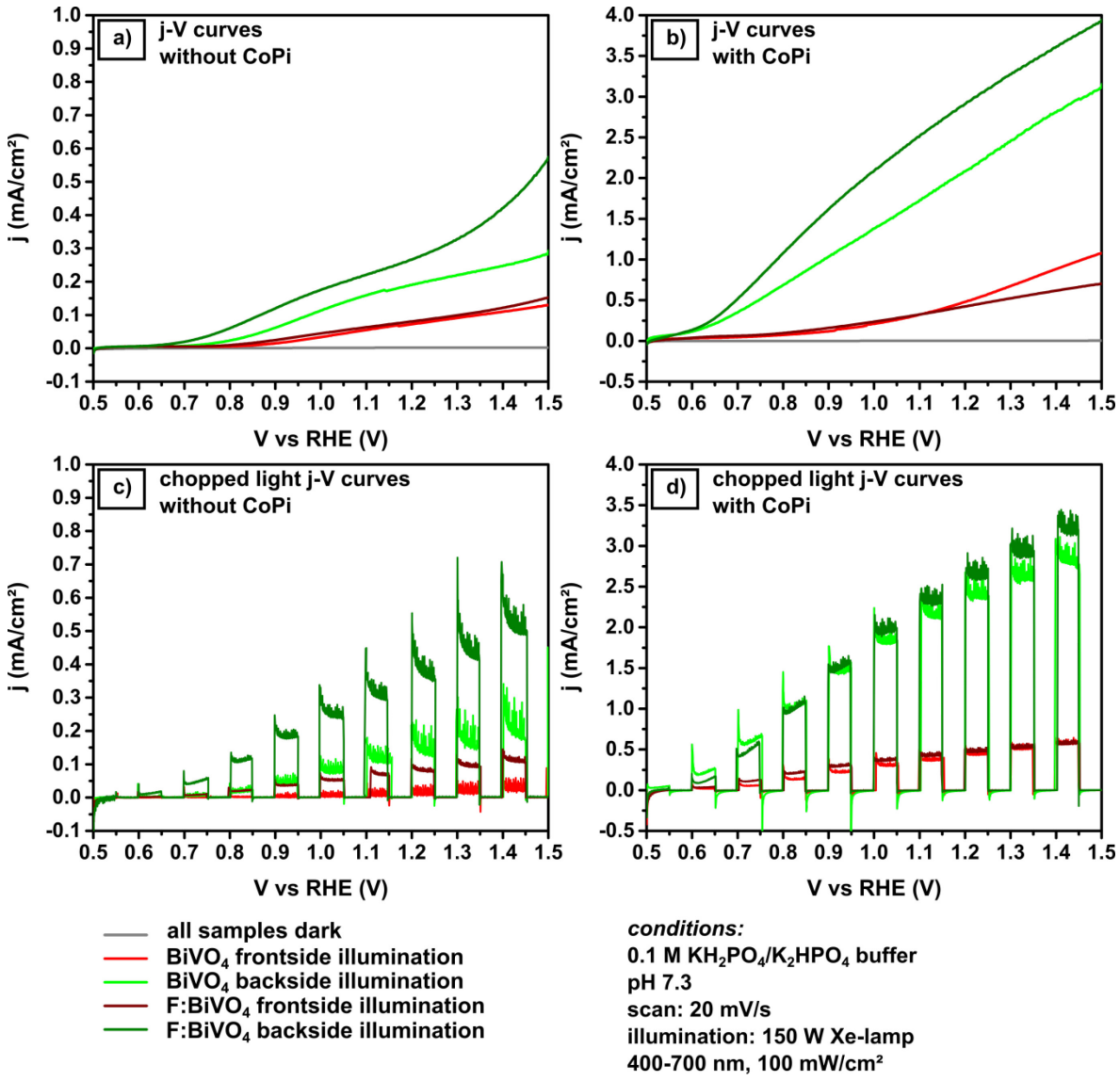

Figure 9-5. j-V curves of $BiVO_4$ and fluorinated $BiVO_4$ thin film photoanodes. a) j-V curves without CoPi deposited in constant illumination, b) j-V curves with CoPi deposited in constant illumination, c) j-V curves without CoPi deposited in chopped illumination and d) j-V curves with CoPi deposited in chopped illumination.

For chopped illumination (Figure 9-5d) the same trend is observed, i.e. higher photocurrents in backside illumination for the pristine and the fluorinated $BiVO_4$ thin film and maximum photocurrent for the fluorinated $BiVO_4$ thin film photoanode. Photocurrent spikes are significantly reduced for both samples pointing in first approximation to reduced surface hole recombination.

Note: Reference samples which have been treated according to the fluorination procedure but leaving out the PVDF revealed decreased photocurrents in comparison to the pristine $BiVO_4$ thin film photoanodes. Whereas the thin film morphology of the reference sample is similar to the morphology of the fluorinated samples (SEM and PEC data are shown in the Appendix, chapter 12.1.3.2). The improvement of the PEC performance due to the additional heat treatment can therefore be excluded.

Table 9-2. Summary of obtained photocurrents at 1.23 V vs RHE for $BiVO_4$ and F:$BiVO_4$ in frontside and backside illumination.

sample	j at 1.23 V vs RHE (mA/cm²)			
	Without CoPi		With CoPi	
	frontside illumination	backside illumination	frontside illumination	backside illumination
$BiVO_4$	0.08	0.20	0.54	2.20
F:$BiVO_4$	0.09	0.28	0.46	3.03

To gain information about the origin of the improved PEC performance upon fluorine incorporation, photocurrent transients were recorded and analyzed according to the phenomenological approach elucidated in chapter 8.3. Photocurrent transients are shown in Figure 9-6 and results of the transient analysis are summarized in Table 9-3.

As can be seen in Figure 9-6a, both samples show significant spikes when switching-on the light. Only very little overshoots are observed for the fluorinated sample. Overshoots are more pronounced for the pristine $BiVO_4$ sample. Analysis of the photocurrent transients reveals the pristine $BiVO_4$ photoanode to be drastically suffering from surface hole recombination accounting for recombination rates k_{rec} as high as 0.957 s^{-1} in frontside illumination and 0.940 s^{-1} in backside illumination whereas the hole transfer rates k_{trans} are very small accounting for 0.026 s^{-1} and 0.040 s^{-1} in frontside and backside illumination, respectively. In consequence, the hole transfer efficiency $\eta_{transfer}$ is low accounting for 0.026 and 0.046 in frontside and backside illumination, respectively.

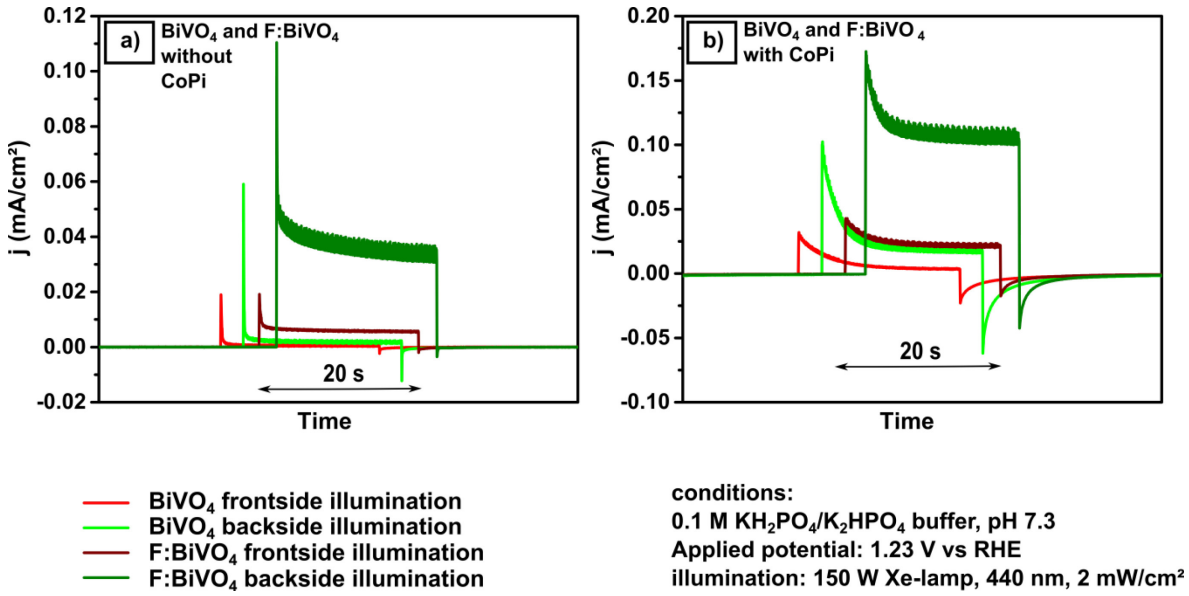

Figure 9-6. Photocurrent transients of $BiVO_4$ and F:$BiVO_4$ thin film photoanodes without (a) and with (b) a layer of CoPi deposited, obtained in frontside and backside illumination mode.

In agreement with the results obtained for powdered F:$BiVO_4$ (see chapter 7.3), transient analysis for the fluorinated $BiVO_4$ thin films reveals considerably smaller surface hole recombination rates in frontside and backside illumination accounting for 0.536 s^{-1} and 0.537 s^{-1} and enhanced hole transfer rates accounting for 0.353 s^{-1} and 0.251 s^{-1} in frontside and backside illumination when compared with the pristine $BiVO_4$ thin film sample,. As a result, the hole transfer efficiency is enhanced to 0.396 and 0.319, respectively by a factor of ~15 compared to the pristine counterpart. According to these results, fluorine incorporation considered as n-type doping affects an increase in electronic conductivity. Therefore hole transfer rates are enhanced as a bigger number of photo-generated holes reach the electrode surface. Furthermore, as suggested by Li et al.,[115] fluorine at the surface of the electrode induces electron traps which are responsible for restrained recombination of photo-generated electron–hole pairs at the surface.

After CoPi deposition (Figure 9-6b) all samples show spikes when switching-on the light. Transient analysis reveals decreased k_{rec} values for all samples upon CoPi deposition. In turn, all hole transfer efficiencies are enhanced too. When the light is switched off, an overshoot is observed for all samples after CoPi deposition. The overshoot is more

pronounced for the pristine $BiVO_4$ samples. As CoPi enhances water oxidation kinetics, surface reaching holes are rapidly transferred to the electrolyte and used for the water oxidation, respectively. Due to the bad conductivity of the material, electron transport to the back contact is not fast enough which results in a high number of electrons within the space charge region impeding further holes being transferred to the electrolyte and used for water oxidation. As a consequence, holes accumulate at the electrode surface and the CoPi layer. When the light is switched off, photo-generated electrons drift back to the surface to recombine with surface-accumulated holes. This causes the cathodic overshoot. As the overshoot of the fluorinated $BiVO_4$ sample is less pronounced compared to its undoped counterpart, this clearly indicates a lower amount of surface accumulated holes and enhanced electron transport upon fluorination of the $BiVO_4$ thin film photoanode.

Note: It was not possible, to carry out electrochemical impedance spectroscopy (EIS) and Mott-Schottky analysis with the fluorinated $BiVO_4$ thin film electrodes. Obtained flat band potentials were highly frequency-dependent which indicates the electrodes to behave like non-ideal capacitor. In turn, analysis of the EIS data according to the Mott-Schottky equation is not appropriate. Most probably, the electrochemical properties of FTO-substrate have been changed due to the fluorination which impedes reliable Mott-Schottky analysis.

Table 9-3. Summary of photocurrent transient analysis of $BiVO_4$ and F:$BiVO_4$ thin film photoanodes with and without CoPi in frontside and backside illumination.

sample	Illumination mode	current densities (mA/cm²)	$\eta_{transfer}$	rate constants (s^{-1})
$BiVO_4$	Frontside	j_{ini} = 0.018	0.026	k_{trans} = 0.026
		j_{ss} = 0.001		k_{rec} = 0.957
	Backside	j_{ini} = 0.049	0.046	k_{trans} = 0.040
		j_{ss} = 0.002		k_{rec} = 0.940
F:$BiVO_4$	Frontside	j_{ini} = 0.015	0.396	k_{trans} = 0.353
		j_{ss} = 0.006		k_{rec} = 0.537
	Backside	j_{ini} = 0.109	0.319	k_{trans} = 0.251
		j_{ss} = 0.035		k_{rec} = 0.536
$BiVO_4$ with CoPi	Frontside	j_{ini} = 0.031	0.122	k_{trans} = 0.035
		j_{ss} = 0.004		k_{rec} = 0.250
	Backside	j_{ini} = 0.097	0.173	k_{trans} = 0.088
		j_{ss} = 0.017		k_{rec} = 0.420
F:$BiVO_4$ with CoPi	Frontside	j_{ini} = 0.041	0.512	k_{trans} = 0.206
		j_{ss} = 0.021		k_{rec} = 0.196
	Backside	j_{ini} = 0.166	0.638	k_{trans} = 0.387
		j_{ss} = 0.106		k_{rec} = 0.220

9.3. Partial O/F substituted 10% Mo:$BiVO_4$ thin films

In the previous section it was shown that the soft fluorination method allows fluorine incorporation into $BiVO_4$ thin films. PEC performance regarding water oxidation was slightly enhanced upon fluorination whereas the thin film morphology underwent sintering and the optical band gap was decreased slightly. Photocurrent transient analysis gave hints that fluorination improves the electron transport properties of the $BiVO_4$ thin film material. However, PEC performance was still limited by insufficiently fast electron transport through the thin film material to the back contact. To overcome this problem, the 10% Mo:$BiVO_4$ thin film photoanodes which showed superior PEC performance regarding water oxidation due a drastically enhanced number of free charge carriers (see chapter 8.3) was fluorinated. For this approach, 10% Mo:$BiVO_4$ thin films were synthesized according to the wet chemical synthesis method applied in chapter 8.3 and were subsequently fluorinated by the soft solid-vapor reaction. Optimized fluorination conditions (2 g PVDF, 370 °C, 2 h) obtained by variation of reaction parameters (see previous section) were used for fluorination of the thin films. Obtained co-doped F/10% Mo:$BiVO_4$ thin film photoanodes were characterized structurally and by means of photoelectrochemistry.

The F/10 %Mo:$BiVO_4$ were investigated by XRD using gracing incidence of the X-ray beam. Resulting XRD pattern are shown in Figure 9-7 along with the diffraction pattern of an unmodified 10% Mo:$BiVO_4$ for comparison and the reference reflections for the monoclinic scheelite structure (PDF 01-083-1698). All reflections can be assigned to $BiVO_4$ in the scheelite structure. Due to the low resolution of the diffraction data obtained in gracing incidence mode of the X-ray beam, it cannot be distinguished between monoclinic and tetragonal scheelite structure without a doubt. The F/10% Mo:$BiVO_4$ sample is polycrystalline and of isotropic character. As already mentioned in the previous section, the positional parameters of $BiVO_4$ and partially O/F substituted $BiVO_4$ are more or less identical (see also chapter 7.2). For this reason the diffraction patterns of both samples are identical too. GI-XRD investigations reveal the scheelite crystal structure to remain unchanged upon the fluorination procedure.

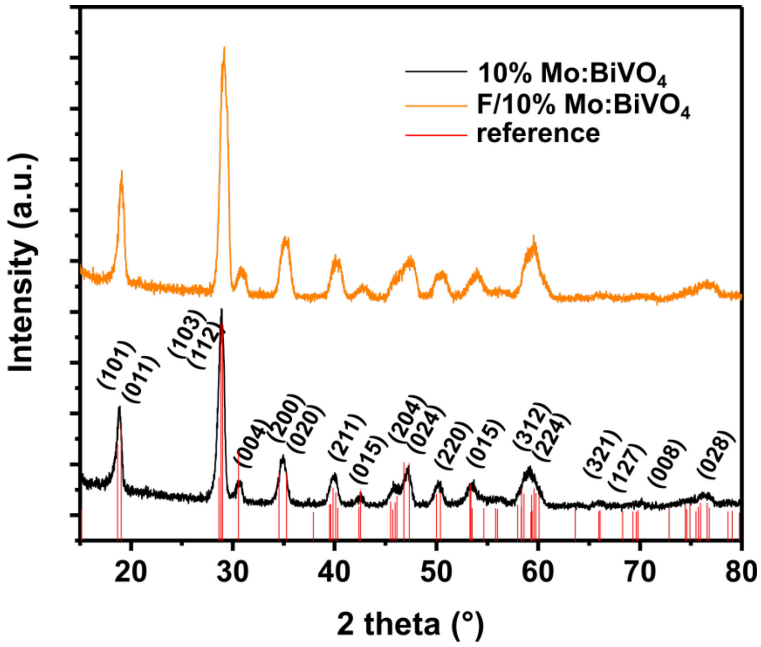

Figure 9-7. XRD pattern (gracing incidence) for a 10% Mo:$BiVO_4$ thin film and a F/10% Mo:$BiVO_4$ thin film in line with the reference reflections acc. to PDF 01-083-1698 for monoclinic scheelite structure.

The influence of fluorine incorporation on the light absorption properties of the 10% Mo:$BiVO_4$ was investigated by UV/Vis spectroscopy. Corresponding spectra of the unmodified and fluorinated 10% Mo:$BiVO_4$ samples are shown in Figure 9-8. By extrapolation of the linear part of the absorption curve, the absorption onset can be estimated to wavelengths of 516 nm for the 10% Mo:$BiVO_4$ sample and to 525 nm for the F/10% Mo:$BiVO_4$ sample which can be translated into an optical band gaps of 2.40 eV and 2.37 eV for the unmodified and the fluorinated 10% Mo:$BiVO_4$ sample, respectively. The absorption onset is slightly shifted to bigger wavelengths upon fluorination, i.e. a bigger portion of visible light can be used for photoelectrochemical applications.

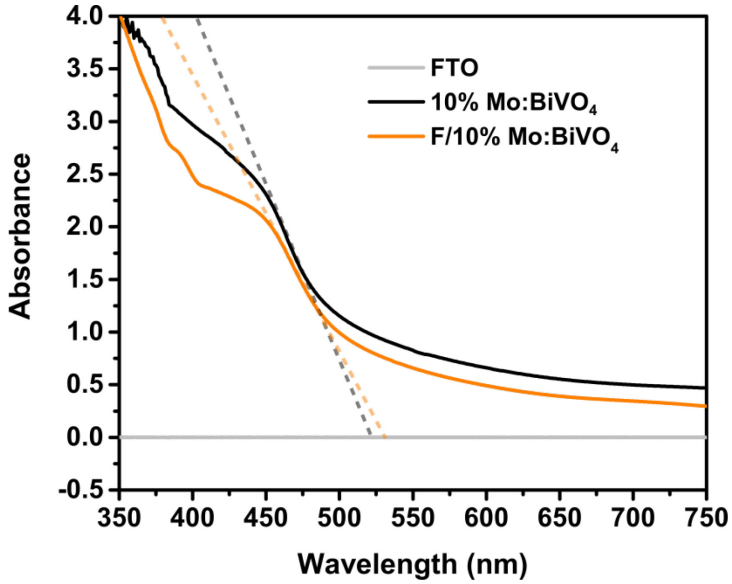

Figure 9-8. UV/Vis spectrum of fluorinated and unmodified 10% Mo:$BiVO_4$ thin films, measurements carried out in transmission mode.

As presented in the previous section, the thin film morphology is affected by the fluorination procedure/the additional heat treatment. The morphology of the undoped $BiVO_4$ thin films underwent sintering upon fluorination. For this reason, the morphology of the 10% Mo:$BiVO_4$ and the F/10% Mo:$BiVO_4$ thin films was investigated by means of SEM as well. Results are shown in Figure 9-9. As can be seen by the top view images, the 10% Mo:$BiVO_4$ samples sinter as well due to the additional heat treatment that comes along with the fluorination procedure. As shown by the lower magnification images, the 10% Mo:$BiVO_4$ sample before fluorination exhibits the domain-like morphology with average geometrical domain sizes of 3.0 ±2.0 µm². Due to sintering of the thin film material, discrete thin film domains are not distinguishable for the F/10% Mo:$BiVO_4$ sample. Additionally, the higher magnification images reveal thicker inner domain material streak sizes after the fluorination procedure accounting for 84 ±9 nm before and 160 ±19 nm after fluorination. In turn the geometrical pore sizes increase as well from 0.002 ±0.002 µm² before fluorination to 0.014 ±0.007 µm² after fluorination. As can be seen by the cross-sectional images, the film thickness remains nearly unaffected by the fluorination procedure accounting for a small decrease from 218 nm to 211 nm upon fluorination. SEM investigations proof that the morphology of the 10% Mo:$BiVO_4$ thin

films is directly affected in terms of sintering and material densification, respectively, by the additional heat treatment associated with the fluorination procedure.

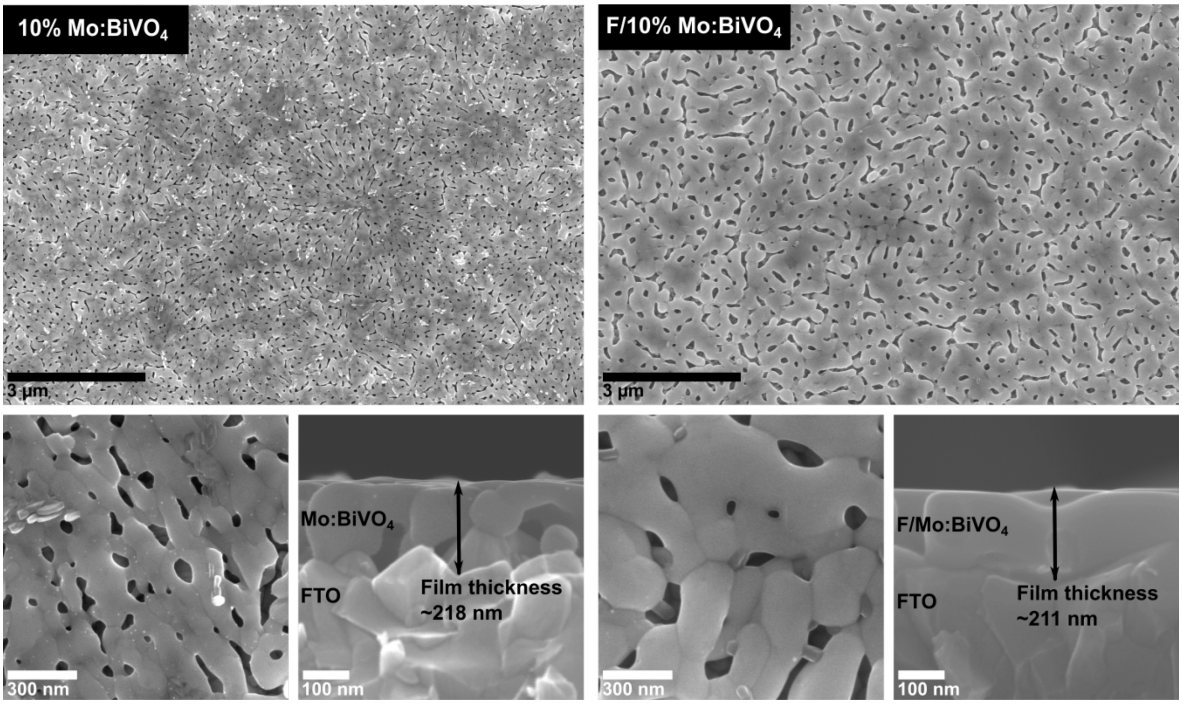

Figure 9-9. SEM top view and cross sectional images of 10% Mo:$BiVO_4$ (left) and F/10% Mo:$BiVO_4$ (right) thin films on FTO substrate.

To gather information about the impact of the fluorination on the microstructure and crystallinity, the F/10% Mo:$BiVO_4$ thin film material was scraped-off the FTO substrate and analyzed by means of TEM/SAED and EDX. Results are shown in Figure 9-10. The overview image (Figure 9-10a) confirms the sintered thin film morphology revealed by SEM. SAED investigations delivered dot patterns. The reflections can be assigned to the (103) plane and the (008) plane of the monoclinic scheelite structure for two investigated spots along one thin film fragment. This indicates the wide-spread single-crystalline character of the thin film material even though no discrete domains were observed by SEM due to advanced sintering. Furthermore, the high resolution image (Figure 10-1b) reveals spatial frequencies due to the lattice fringes. Corresponding FFT pattern contains only one set of reflections which can be assigned to the (011) plane. EDX investigations (Figure

9-10) prove the thin film to consist of Bi, V, O and Mo (Cu peaks belong to the sample grid). Additionally, a small peak which can be assigned to fluorine (F K_α) occurs at 0.68 keV, i.e. the presence of fluorine within the 10% Mo:$BiVO_4$ thin film material can be confirmed qualitatively by EDX.

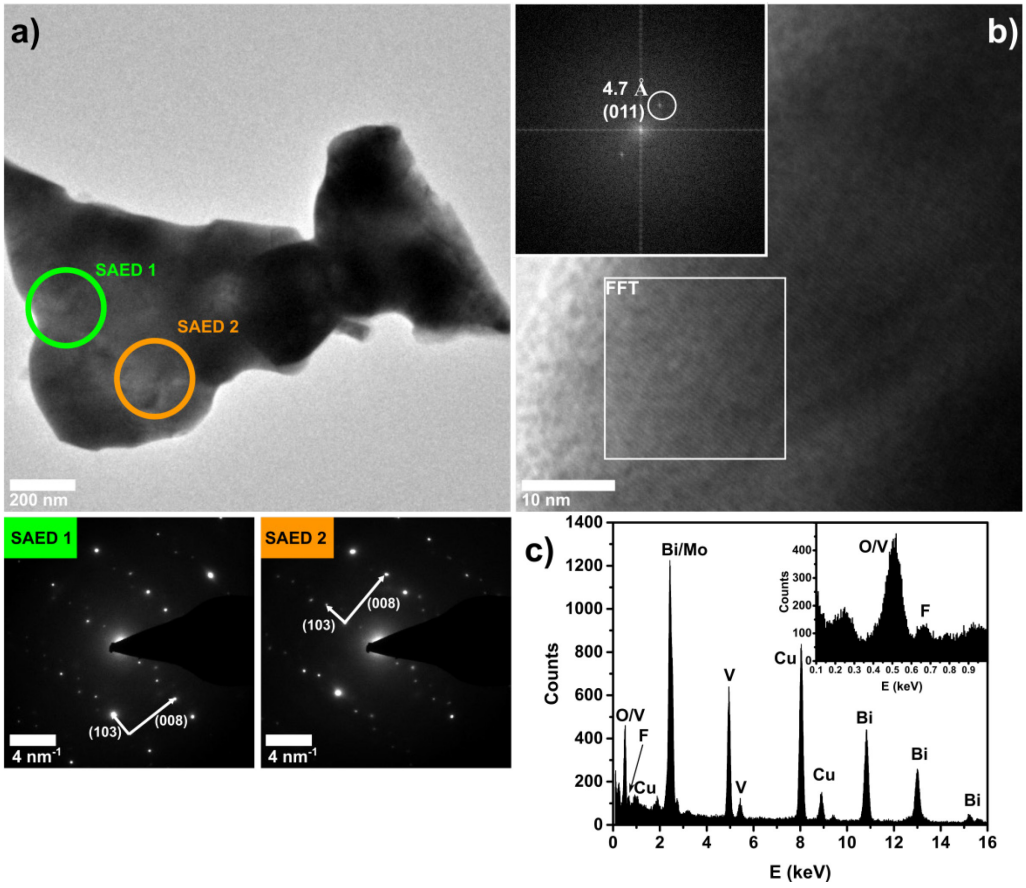

Figure 9-10. TEM investigations of F/10% Mo:$BiVO_4$, a) overview image and corresponding SAED pattern, b) HR-TEM image with corresponding FFT pattern (inset) and c) EDX spectrum with a zoomed view on the fluorine peak. Sample was scraped-off the FTO substrate.

In the previous section, an enhancement of PEC performance regarding water oxidation was revealed by fluorination of $BiVO_4$ thin film photoanodes. The impact of fluorine incorporation on the PEC water oxidation properties of the 10% Mo:$BiVO_4$ thin film photoanodes was also investigated by means of photoelectrochemistry. j-V curves in constant and chopped illumination are shown in Figure 9-11, obtained photocurrents at an

applied potential of 1.23 V vs RHE are summarized in Table 9-4. As can be seen in Figure 9-11a, the obtained photocurrents of the 10% Mo:$BiVO_4$ sample accounting for 0.99 mA/cm² and 1.19 mA/cm² at 1.23 V vs RHE in frontside and backside illumination, respectively, are enhanced by fluorine incorporation resulting in photocurrents of 1.19 mA/cm² and 1.45 mA/cm² at 1.23 V vs RHE in frontside and backside illumination, respectively. As can be seen by the j-V-curves under chopped illumination, only small spikes and no overshoots are observed for the unmodified and the fluorinated samples which indicates only a little influence of surface recombination for these samples.

Depositing a layer of CoPi water oxidation catalyst onto the photoanode surfaces leads to an increase of all observed photocurrents as can be seen in Figure 9-11c and d. Photocurrents of 3.52 mA/cm² and 4.48 mA/cm² at an applied potential of 1.23 V vs RHE were yielded for the 10% Mo:$BiVO_4$ photoanode in frontside and backside illumination, respectively. After fluorination, PEC performance was further enhanced accounting for photocurrents as high as 4.78 mA/cm² and 5.43 mA/cm² at 1.23 V vs RHE in frontside and backside illumination, respectively. The obtained photocurrents for the F/10% Mo:$BiVO_4$ sample are to the best of my knowledge the highest photocurrents reported for a CoPi-modified, doped $BiVO_4$ photoanode for water oxidation (see Table 8-3 on page 106).

Table 9-4. Summary of obtained photocurrents at 1.23 V vs RHE for 10% Mo:$BiVO_4$ and F/10% Mo:$BiVO_4$ in frontside and backside illumination.

sample	j at 1.23 V vs RHE (mA/cm²)			
	Without CoPi		With CoPi	
	frontside illumination	backside illumination	frontside illumination	backside illumination
10% Mo:$BiVO_4$	0.99	1.19	3.52	4.48
F/10% Mo:$BiVO_4$	1.19	1.45	4.78	5.43

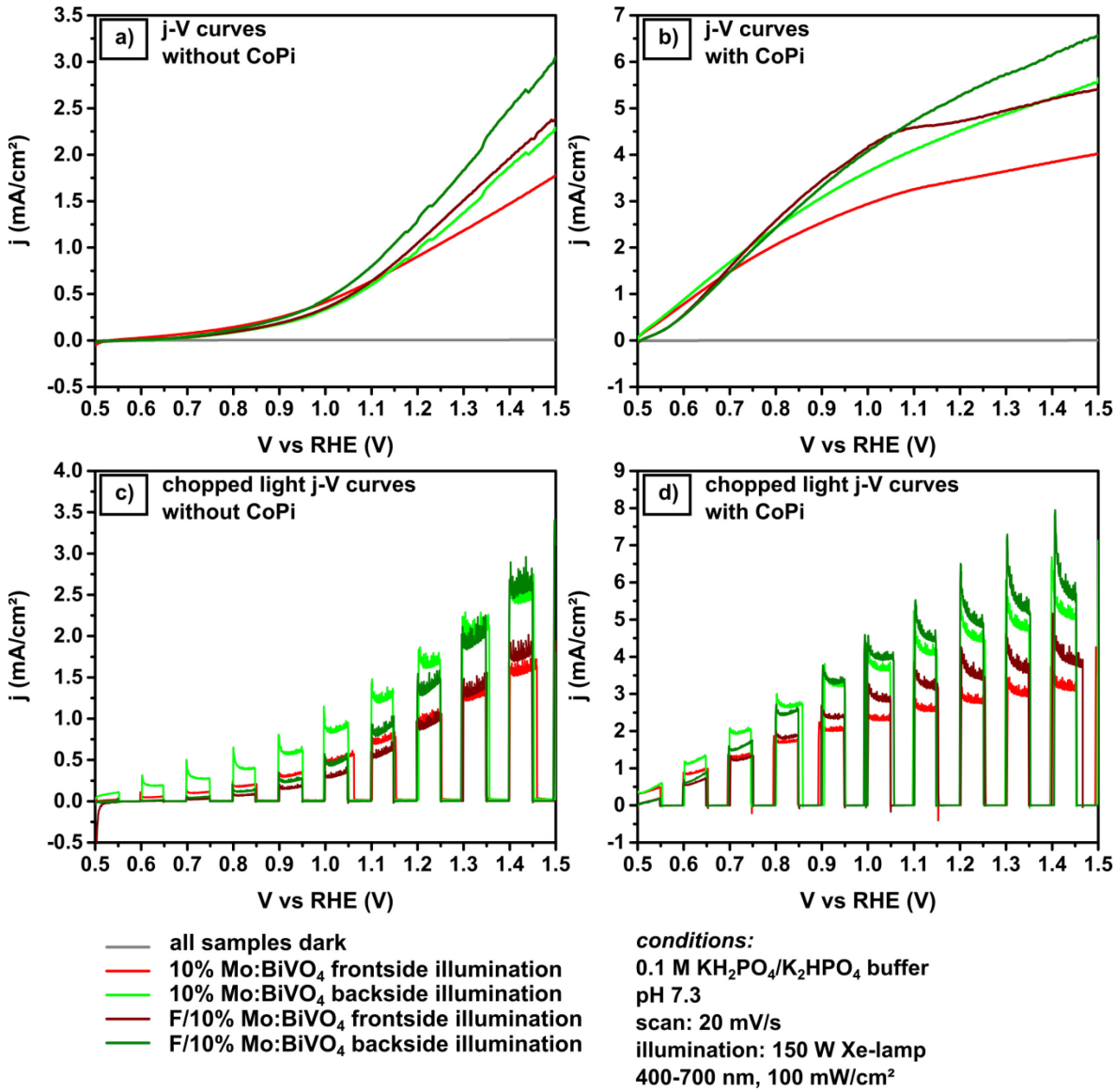

Figure 9-11. j-V curves of 10% Mo:$BiVO_4$ and F/10% Mo:$BiVO_4$ thin film photoanodes. a) j-V curves without CoPi deposited in constant illumination, b) j-V curves with CoPi deposited in constant illumination, c) j-V curves without CoPi deposited in chopped illumination and d) j-V curves with CoPi deposited in chopped illumination.

j-V curves recorded in chopped illumination mode (Figure 9-11c and d) revealed small photocurrent spikes occurring for all samples, especially at applied potentials higher than 1.1 V vs RHE. To gain further insights into the origin of PEC performance enhancement, photocurrent transients were recorded and analyzed according to the phenomenological approach described in chapter 5.5.3.3. Obtained photocurrent transients are shown in Figure 9-12; corresponding transient analysis results are summarized in Table 9-5.

As can be seen in Figure 9-12a, the 10% Mo:$BiVO_4$ thin film photoanode and its fluorinated counterpart exhibit photocurrent spikes when the light is switched on indicating both samples to be suffering from surface recombination. No cathodic overshoots are observed for both samples when the light is switched off. The shape of the photocurrent transients obtained in frontside and backside illumination is very similar for both samples. Analysis of the photocurrent transients reveals a similar trend. For the 10% Mo:$BiVO_4$ and the F/10% Mo:$BiVO_4$ photoanodes the hole transfer efficiencies are nearly identical accounting for 0.462 and 0.461 for the unmodified and the fluorinated 10% Mo:$BiVO_4$ samples in frontside illumination and 0.551 and 0.547 in backside illumination, respectively. This is in good agreement with obtained photocurrents which are only slightly different for both samples before CoPi deposition.

After CoPi modification of the 10% Mo:$BiVO_4$ and the F/10% Mo:$BiVO_4$ samples surfaces, hole recombination rates k_{rec} are decreased for both samples. Surface hole recombination rates of 0.074 s^{-1} and 0.061 s^{-1} were determined for the 10% Mo:$BiVO_4$ sample in frontside and backside illumination, respectively. For the F/10% Mo:$BiVO_4$ sample k_{rec} values are even lower accounting for 0.016 s^{-1} and 0.030 s^{-1}. k_{trans} values are slightly enhanced or remain nearly constant after CoPi functionalization. This results in high hole transfer efficiencies $\eta_{transfer}$ accounting for 0.824 and 0.832 for the 10% Mo:$BiVO_4$ sample and 0.954 and 0.896 for the F/10% Mo:$BiVO_4$ sample in frontside and backside illumination, respectively. These findings are in good agreement with observed photocurrents which were higher for the fluorinated 10% Mo:$BiVO_4$.

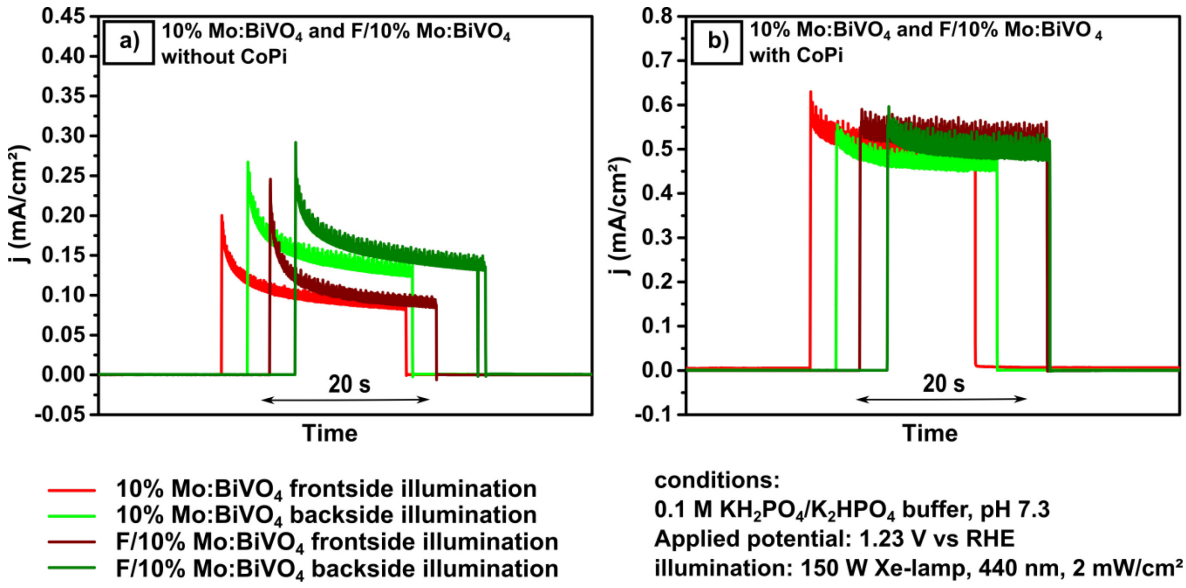

Figure 9-12. Photocurrent transients of 10% Mo:$BiVO_4$ and F/10% Mo:$BiVO_4$ thin film photoanodes without (a) and with (b) a layer of CoPi deposited, obtained in frontside and backside illumination mode.

The reduction of surface recombination yielded by CoPi deposition is more pronounced for the fluorinated sample. This most probably is a consequence of a further enhanced number of free charge carriers and better charge carrier separation which was predicted by DFT calculations on F:$BiVO_4$ by Wen et al.[132] As k_{rec} values for F/10% Mo:$BiVO_4$ photoanodes are also smaller before CoPi deposition compared to k_{rec} values of 10% Mo:$BiVO_4$ sample, fluorine-induced electron traps most probably restrain recombination of photo-generated electron–hole pairs at the surface. This probably also contributes to improved water oxidation kinetics of the F/10%Mo:$BiVO_4$ photoanode.

An additional explanation can be derived based on the work of Bard and Mullins.[182] The valence band edge of $BiVO_4$ is comprised of O 2p orbitals.[23] Probably the valence band of F/Mo:$BiVO_4$ consists of a mixture of O 2p orbitals and F 2p orbitals. This could result in less anodic potential of the valence band leading to less needed bias to transfer photo-generated holes to the CoPi covered surface. For further clarification of the origin of improved photoelectrochemical performance of F/Mo co-doped $BiVO_4$ thin film photoanodes further investigations, e.g. DFT studies, are desirable.

Table 9-5. Summary of photocurrent transient analysis of 10% Mo:$BiVO_4$ and F/10% Mo:$BiVO_4$ thin film photoanodes with and without CoPi in frontside and backside illumination.

sample	Illumination mode	current densities (mA/cm²)	$\eta_{transfer}$	rate constants (s^{-1})
10% Mo:$BiVO_4$	Frontside	j_{ini} = 0.191	0.462	k_{trans} = 0.276
		j_{ss} = 0.088		k_{rec} = 0.321
	Backside	j_{ini} = 0.247	0.551	k_{trans} = 0.347
		j_{ss} = 0.136		k_{rec} = 0.283
F/10% Mo:$BiVO_4$	Frontside	j_{ini} = 0.215	0.461	k_{trans} = 0.247
		j_{ss} = 0.099		k_{rec} = 0.288
	Backside	j_{ini} = 0.274	0.547	k_{trans} = 0.253
		j_{ss} = 0.150		k_{rec} = 0.210
10% Mo:$BiVO_4$ with CoPi	Frontside	j_{ini} = 0.603	0.824	k_{trans} = 0.348
		j_{ss} = 0.497		k_{rec} = 0.074
	Backside	j_{ini} = 0.552	0.832	k_{trans} = 0.305
		j_{ss} = 0.4595		k_{rec} = 0.061
F/10% Mo:$BiVO_4$with CoPi	Frontside	j_{ini} = 0.548	0.954	k_{trans} = 0.325
		j_{ss} = 0.522		k_{rec} = 0.016
	Backside	j_{ini} = 0.549	0.896	k_{trans} = 0.257
		j_{ss} = 0.492		k_{rec} = 0.030

9.4. Conclusion

In this chapter the soft fluorination method used to partially substitute O by F in powdered $BiVO_4$ samples was applied to $BiVO_4$ and Mo:$BiVO_4$ thin film photoanodes. After adjustment of reaction parameters the fluorination was first accomplished for $BiVO_4$ thin film photoanodes. Resulting F:$BiVO_4$ thin films exhibited improved light absorption properties and a slightly smaller band gap, respectively. The monoclinic scheelite structure was retained upon fluorination. The thin film morphology underwent sintering due to the additional heat treatment. However, the single-crystalline character of the domains is preserved upon fluorination. PEC performance of the F:$BiVO_4$ photoanodes was investigated and reveled enhanced photocurrents in comparison with its unmodified counterpart. Photocurrent transient analysis revealed reduction of surface hole recombination upon fluorination which most probably comes from an enhanced number of

free charge carriers improving the separation of the photo-generated electron-hole-pairs and due to beneficial electron trapping at the electrode's surface. PEC performance of $BiVO_4$ thin film photoanodes is improved by fluorine incorporation. However, it is still limited by unfavorable electron transport properties. For this reason the fluorination procedure was applied to 10% Mo:$BiVO_4$ thin film photoanodes which offer improved electron transport properties. Resulting co-doped F/10% Mo:$BiVO_4$ photoanodes showed also exhibited the monoclinic scheelite structure as well as slightly improved light absorption properties and smaller optical band gap, respectively. Thin film morphology investigations of the F/10% Mo:$BiVO_4$ thin films revealed material densification due to sintering as well as retained wide-spread single-crystalline areas. PEC investigations of the F/10% Mo:$BiVO_4$ thin films regarding water oxidation revealed slightly enhanced photocurrents and more pronounced improvement of yielded photocurrents after CoPi deposition compared to its non-fluorinated counterpart. Maximum photocurrents of 5.43 mA/cm² at an applied potential of 1.23V vs RHE were yielded and to the best of my knowledge are the highest photocurrent reported for a doped $BiVO_4$ thin film photoanode with CoPi functionalization. Photocurrent transient analysis revealed nearly identical kinetics for the 10% Mo:$BiVO_4$ and the F/10% Mo:$BiVO_4$ samples. CoPi deposition has a bigger influence on the fluorinated sample in terms of surface hole recombination which is expressed by small surface hole recombination rates and therefore high hole transfer efficiencies. This most probably can be assigned to a further increase of free charge carriers and charge carrier separation, respectively.

All in all, fluorination of $BiVO_4$ and Mo:$BiVO_4$ thin film photoanodes turns out to be a viable way to improve the photoelectrochemical properties. Application of fluorine doping and anion-cation co-doping can in principle also be applied to other oxide-based n-type electrode materials.

10. WO_3/Mo:$BiVO_4$ heterojunction photoanodes

10.1. Introduction

The interface that arises when two dissimilar materials are brought into contact is called heterojunction. A semiconductor heterojunction is characterized by different band gaps and band positions of the conduction and valence bands of both materials. Depending on the nature of the semiconductors, the heterojunction can be classified into three different types according to the alignment of the bands and bands electron affinity, respectively.[183] The three types are illustrated schematically in Figure 10-1a.

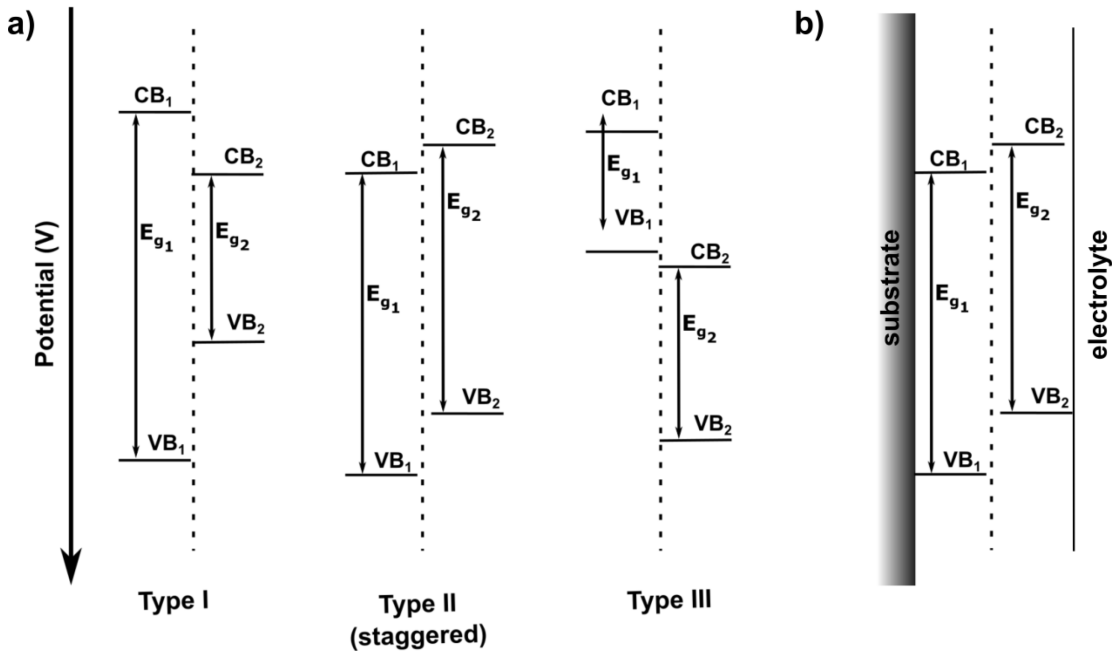

Figure 10-1. a) Schematic illustration of different heterojunction types, b) staggered type heterojunction photoanode.

In Type I heterojunctions, the band positions and band gap of one material entirely straddles the band positions and band gap of the other one. In Type II heterojunctions (also called staggered gap type) conduction band edge and valence band edge positions of one material are lower than the corresponding band edges of the other material leading to confinement of electrons in the material with more anodic band positions whereas holes are confined in the other material with more cathodic band positions. For Type III heterojunctions band gaps and band positions, respectively, do not overlap at all.

With respect to photoelectrochemical water oxidation the Type II band alignment which is illustrated in Figure 10-1b is most appealing. A well-studied example of an effective heterojunction composite electrode matching this band alignment is $WO_3/BiVO_4$. This heterojunction does not only fulfill the desired band alignment but also combines the merits of both semiconductor materials, i.e. excellent charge transport properties of WO_3 and efficient light absorption of $BiVO_4$.[184] The valence and conduction bands of WO_3 are more anodic than those of $BiVO_4$, respectively. This relative potential energy level configuration will allow the photo-generated holes to migrate to the $BiVO_4$ layer, whereas the photo-generated electrons migrate to the WO_3 layer; process which is induced by the gradient in charge-carrier concentration at the interface of the WO_3 and the $BiVO_4$ layer. (diffusion current). Additionally, the band gap of WO_3 is ~0.3 eV wider than the band gap of $BiVO_4$. Assuming that all photons of wavelengths smaller than ~440 nm are absorbed by the WO_3 layer, the $BiVO_4$ layer absorbs photons of wavelengths of $\sim 440\ nm < \lambda < \sim 525\ nm$ (in backside illumination).

To the best of my knowledge the first work on $WO_3/BiVO_4$ heterojunctions used as photoanode for photoelectrochemical water oxidation was reported by Hong et al. in 2011.[37] They fabricated $WO_3/BiVO_4$ composite electrodes by layer-by-layer deposition on FTO and yielded photocurrents of 1.6 mA/cm² at 1.23 V vs RHE in 0.5 M Na_2SO_4 (pH = 7) electrolyte under irradiation of simulated solar light.

A different synthesis approach was reported by Zhang et al. in 2012.[38] Dropcasting and subsequent drying of H_2WO_4 solution followed by deposition of hydrothermally pre-synthesized $BiVO_4$ and Mo:$BiVO_4$ crystals onto the WO_3 matrix and subsequent calcination yielded layered $WO_3/BiVO_4$ and WO_3/Mo:$BiVO_4$ composite electrodes. For

this type of WO_3/Mo:$BiVO_4$ electrodes photocurrents up to 2.0 mA/cm² at 1.23 V vs RHE were obtained (0.5 Na_2SO_4, pH = 7).

In 2013 Jeong et al. used spin coating to fabricate a WO_3 layer on an FTO substrate and further spin coated a Mo-doped $BiVO_4$ layer onto it to fabricate layered heterojunction electrode.[185] By additional (electro-)deposition of CoPi onto the surface they further increased the photoelectrochemical performance of the heterojunction and yielded photocurrents up to 2.4 mA/cm² at 1.23 V vs RHE under illumination of simulated sunlight (0.1 M KH_2PO_4/K_2HPO_4, pH = 7).

A hetero junction design approach which is significantly different from the layerered design was introduced by Pilli et al.[186] They synthesized WO_3 nanorods by a polymer-assisted decomposition method, spray deposited a layer of $BiVO_4$ onto the WO_3 nanorods followed by a photo-assisted electrodeposition of CoPi water oxidation catalyst. The $BiVO_4$-coated one-dimensional WO_3 nanorods yielded photocurrents of 2.5 mA/cm² at 1.23 V at neutral pH and under irradiation of simulated sunlight (0.5 M Na_2SO_4, pH = 7).

The concept of $BiVO_4$-coated WO_3 nanorods was further expanded by various groups.[187,188] Greatest progress was made by Pihosh et al. who published in 2014 a fully developed and uniform 1D core-shell WO_3/$BiVO_4$ photoanode fabricated by Glancing Angle Deposition.[36] After additional deposition of CoPi water oxidation catalyst photocurrents of 3.2 mA/cm² at 1.23 V vs RHE under simulated sunlight were yielded (0.1 M KH_2PO_4/K_2HPO_4, pH = 7). By optimization of the WO_3/$BiVO_4$ nanostructures in terms of length and thickness of the WO_3 rods and reducing the $BiVO_4$ layer thickness to only 25 nm they could further increase photoelectrochemical performance and yielded photocurrents of 6.72 mA/cm² at 1.23 V vs RHE which is the highest reported value so far.[35]

Best photoelectrochemically performing WO_3/$BiVO_4$ composite photoanodes follow the $BiVO_4$-coated WO_3 nanorod design scheme. The idea behind this scheme is the use of extremely thin $BiVO_4$ layers of thicknesses smaller than its hole diffusion length of 70-100 nm[22,74,75]. The objective of using these thin layers is the reduction of the recombination rate of photo-generated charge carriers because of the poor charge carrier

transport properties of $BiVO_4$. Unfortunately, these small layer thicknesses are not sufficient for efficient light absorption. To resolve this issue, thin $BiVO_4$ layers are coated onto vertically aligned WO_3 nanorods in form of a core-shell heterojunction. This design allows the deposition of the desired extremely thin $BiVO_4$ layers while its optical thickness is reestablished by light trapping in high aspect ratio nanostructures.

The optimized $BiVO_4$ and Mo:$BiVO_4$ thin film photoanodes described in the previous sections address improvement of charge carrier transport properties and photoelectrochemical performance by Mo-doping and an optimized morphology consisting of single-crystalline domains and material streak sizes in the range of the hole diffusion length (see chapter 8.2 and 8.3). Usage of these $BiVO_4$ and Mo:$BiVO_4$ thin films in a WO_3/$BiVO_4$ and WO_3/Mo:$BiVO_4$ heterojunction should lead to increased photoelectrochemical performance due to the heterojunctions' positive impact on charge carrier separation.

In principal, there is no need for advanced nanostructures in terms of vertically aligned 1D WO_3 nanorods because the optimized $BiVO_4$ and Mo:$BiVO_4$ thin films can be deposited in sufficient thicknesses providing good light absorption. In the upcoming section, this idea is translated into practice. WO_3 thin films were fabricated by dip coating FTO substrates with a WO_3 sol. After calcination FTO/WO_3 electrodes were used as substrates for the deposition of $BiVO_4$ and Mo:$BiVO_4$, respectively according to the previously described procedure. Synthesis, characterization, (photo-)electrochemical investigation and further optimization of the FTO/WO_3, the FTO/WO_3/$BiVO_4$, and FTO/WO_3/Mo:$BiVO_4$ composite electrodes are elucidated in the following sections.

10.2. Synthesis and Characterization of WO_3 thin films

To fabricate WO_3 thin films on FTO substrates a sol-gel-approach was used according to a method reported by Brezesinski et al.[103] The synthesis method is illustrated in Figure 10-2. WCl_6 was chosen as tungsten precursor and ethanol as solvent to synthesize a deep-blue WO_3 sol (the blue color is a result of a small fraction of W^{6+} being reduced to W^{5+}) (Figure 10-2a). After 4 h of stirring, the WO_3 sol was used for dip coating of FTO

substrates under controlled conditions (200 mm/min, 55% relative humidity, room temperature, 2 s dwell time) (Figure 10-2b). After a heating procedure comprised of a film aging step at 100 °C for 12 h and a subsequent calcination in air at 550 °C for 30 min crystalline WO_3 thin films were obtained (Figure 10-2c).

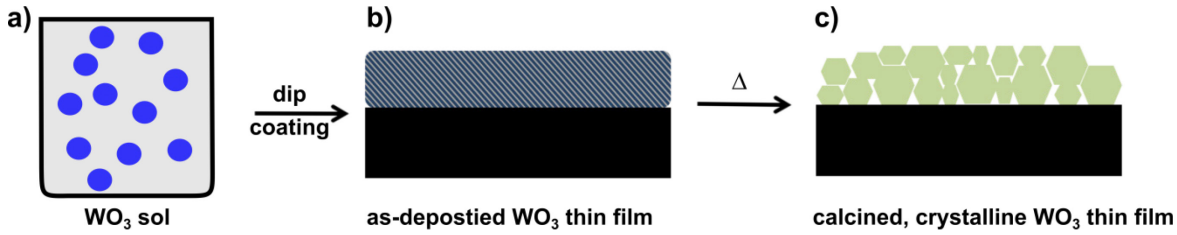

Figure 10-2. Illustration of WO_3 thin film synthesis a) WO_3 sol, b) as-prepared WO_3 thin film and c) WO_3 thin film after calcination.

The crystal structure of WO_3 can be described as a three-dimensional network of corner-sharing WO_6 octahedra which, in principal, is identical to the cubic ReO_3 structure. However, due to tilting of WO_6 octahedra and displacement of tungsten from the octahedron center the symmetry of WO_3 is lowered compared to the ideal ReO_3 structure. Variations of these two forms of distortion result in several phase transitions. WO_3 comprises five different crystallographic modifications between 0 K and 1973 K, its melting point,[189] as summarized in Table 10-1. Most common modification at room temperature is the monoclinic γ-WO_3 with space group $P2_1/n$.[190]

Table 10-1. Phase transitions of WO_3.

Phase	Symmetry	Space group	Temperature range (K)	Reference
ε-WO_3	monoclinic	P_c	0-230	Salje[191]
δ-WO_3	triclinic	$P\bar{1}$	230-290	Diehl et al.[192]
γ-WO_3	monoclinic	$P2_1/n$	290-600	Loopstra and Rietveld[193]
β-WO_3	orthorhombic	$Pmnb$	600-1170	Salje[194]
α-WO_3	tetragonal	$P4/nmm$	1010-1170	Kehl et al.[195]

For structural characterization, WO_3 thin films and corresponding powder samples obtained by drying and calcinination of the WO_3-sol were used. The crystal structure of the WO_3 thin films and WO_3 powder samples was analyzed by GI-XRD and P-XRD, respectively. The corresponding patterns are shown in Figure 10-3. The sharp reflections of both patterns could be assigned to γ-WO_3 in the monoclinic phase according to JCPDS 71-2141. The GI-XRD pattern (Figure 10-3a) reveals a strong pronunciation of the reflection at 24.4 ° corresponding to the (200) plane which indicates a preferential orientation/texture of the WO_3 thin film. Similar increased intensity of the reflection corresponding to the (200) plane is observed in the P-XRD pattern; however, it is by far less pronounced (Figure 10-3b). This indicates a substrate-dependent preferential growth orientation. As proposed by Ramana et al.[196–198] preferred orientation and the extent of texture in crystalline oxide thin films on specific substrates occur to minimize the internal strain energy within the film. Strain energy densities are different for different crystallographic orientations of the thin film on the substrate. Those orientations with low strain energy densities with respect to the substrate are favored growth directions resulting in anisotropic, textured thin films. The preferred (200) orientation of WO_3 thin films on various substrates is well known and has already been reported by several other groups.[199–204]

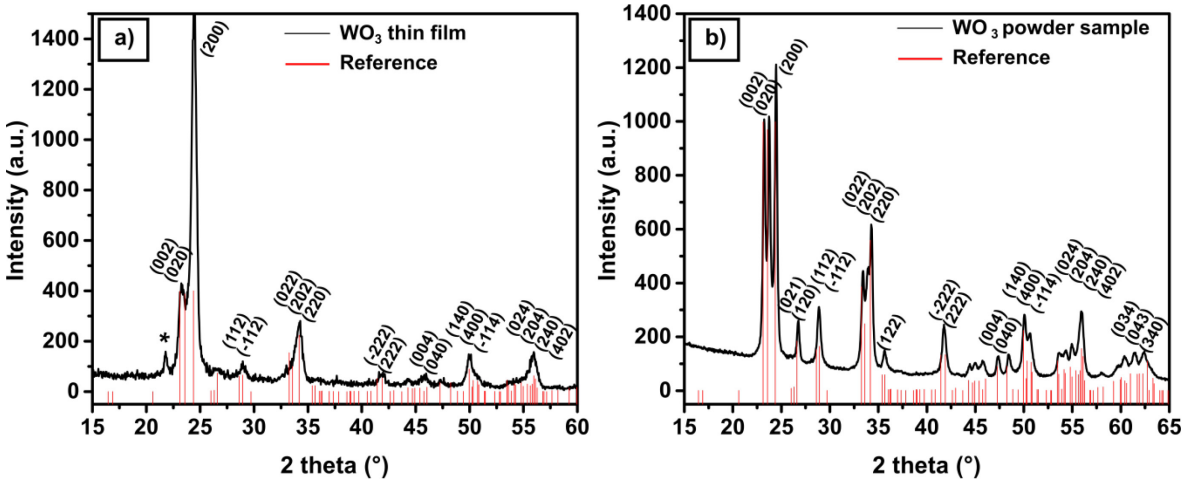

Figure 10-3. a) GI-XRD of WO_3 thin film on FTO substrate and (reflection marked with a * belongs to the sample holder) b) powder XRD of WO_3 powder sample obtained by drying and calcination of the WO_3-sol used for dip coating, Reference pattern γ-WO_3 (JCPDS 71-2141).

The light absorption properties of the WO_3 thin films were studied by UV/Vis spectroscopy, results are shown in Figure 10-4a. Light of wavelengths smaller than about 450 nm is absorbed by the WO_3 thin film; result which is in good agreement with literature reports.[205–207] Based on the absorption onset, a band gap of about 2.8 eV can be estimated. The overall absorption is low accounting for a maximum absorbance of 0.4 at a wavelength of 350 nm which is additionally illustrated by the photograph of the FTO substrate and the WO_3 thin film deposited on FTO in Figure 10-4b.

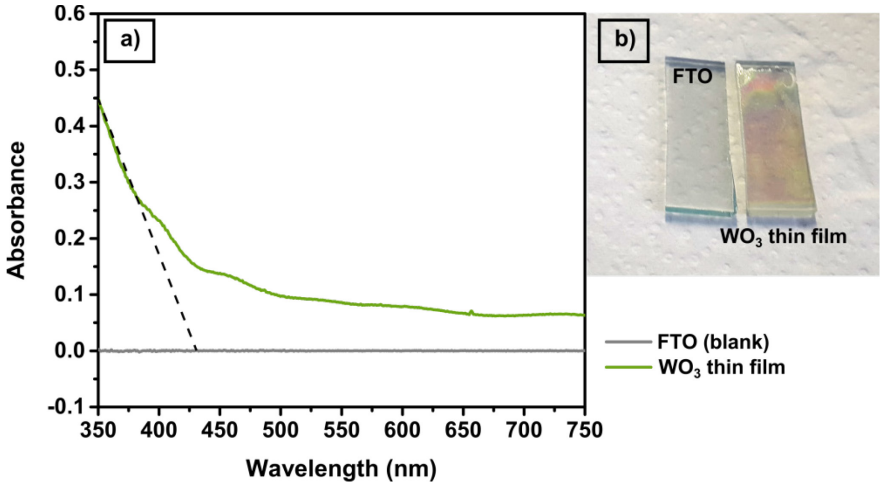

Figure 10-4. a) UV/Vis spectrum of WO_3 thin film on FTO substrate and b) photograph of WO_3 thin film on FTO substrate next to bare FTO sample.

The morphology and elemental composition of the WO_3 thin films was studied using SEM and EDX analysis. Top-view and cross section images as well as an EDX spectrum of a WO_3 thin film deposited onto an FTO substrate are shown in Figure 10-5. The lower magnification image (Figure 10-5a) proves the thin film to be homogeneously covering the FTO substrate. The thin film exhibits an open porous morphology comprised of single WO_3 particles and sintered agglomerates. Because of the sintered agglomerates, the size distribution is rather broad accounting for an average particle size of $1.70 \cdot 10^{-2} \pm 0.52 \cdot 10^{-2}$ µm² (geometrical particle area determined by top-view images). An average pore size (pore area determined by top-view images) of $7.42 \cdot 10^{-3} \pm 3.91 \cdot 10^{-3}$ µm² was determined. By the cross section image (Figure 10-5c) an average film thickness of

230 ±11 nm was estimated. EDX analysis (Figure 10-5d) reveals the thin films to consist of W and O. Furthermore, no significant C peak is observed which indicates that all organic solvent components were removed by the calcination procedure. The EDX spectrum was quantified yielding an amount of 19 at% of W and 81 at% of O. The deviation from the ideal atomic ratios of 25 at% of W and 75 at% of O is assigned to peaks of the FTO substrate enlarging the amount of determined oxygen.

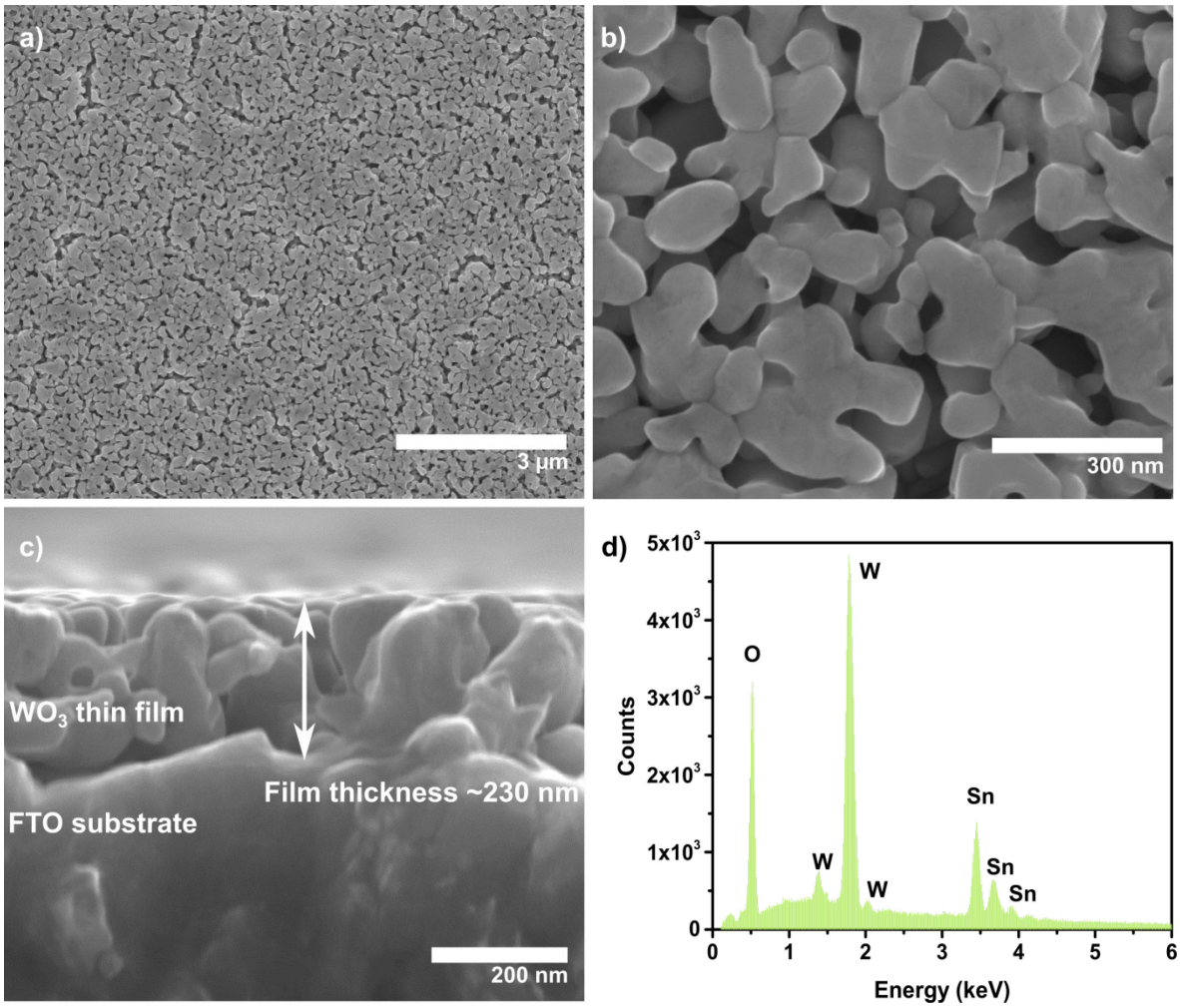

Figure 10-5. SEM/EDX investigations on WO_3 thin film deposited on FTO substrates. a+b) top view images, c) cross section image d) EDX spectrum (Sn peaks assigned to FTO substrate).

Furthermore, the WO_3 thin films were investigated by TEM/SAED. Results are shown in Figure 10-6. The particulate character of the WO_3 thin films is further confirmed by the overview image (Figure 10-6a) showing single particles and a sintered agglomerates. As shown by the HR-TEM (Figure 10-6b) the WO_3 particles are highly crystalline. This is illustrated more clearly by the FFT pattern revealing spatial frequencies corresponding to the (011), (101), and (002) planes of γ-WO_3 in the monoclinic phase according to JCPDS 71-2141. SAED measurements of the agglomerated particles show a diffraction pattern which is typical for polycrystalline samples (Figure 10-6c). Again, all reflections could be assigned to monoclinic γ-WO_3 according to JCPDS 71-2141.

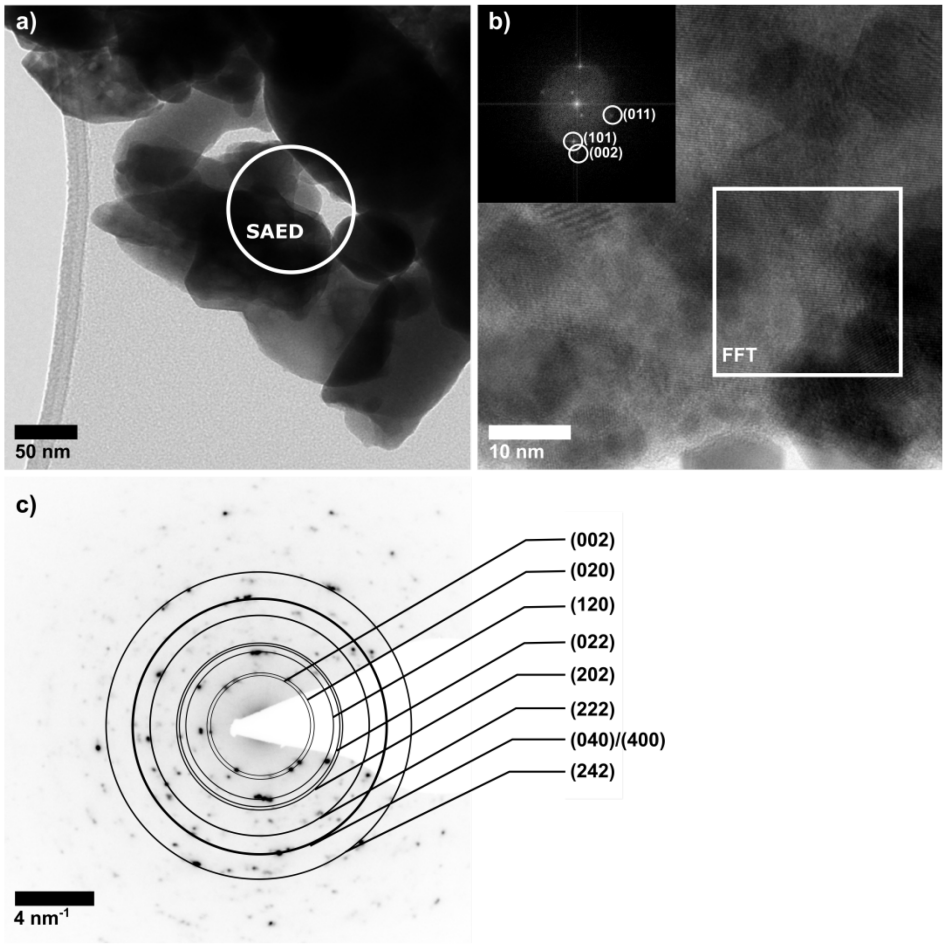

Figure 10-6. TEM/SAED investigations of a WO_3 thin film a) TEM overview image, b) HR-TEM image with corresponding FFT pattern and c) inverted SAED pattern with reflcetions assigned to monoclinic γ-WO_3 (JCPDS 71-2141).

Finally, the photoelectrochemical performance of the WO_3 thin films concerning water oxidation was investigated. In Figure 10-7a j-V-curves for WO_3 thin films with and without CoPi deposited onto the surface in frontside and backside illumination are shown. Photocurrents of 0.2 mA/cm² in frontside illumination and 0.7 mA/cm² in backside illumination, respectively, were yielded for WO_3 thin films without CoPi (given for an applied potential of 1.23 V vs RHE). Higher photoelectrochemical performance by usage of backside illumination can be explained by the dependence of the photocurrent on the distance of the electron-hole-pair generation from the back contact. Charge separation is most efficient close to the conductive FTO back contact. The probability of recombination during electron transport through the thin film increases with increasing distance of the generation of the electron-hole-pair from the back contact. The WO_3 thin film morphology exhibiting a high number of particle boundaries which potentially act as recombination sites additionally promotes recombination of the electron traveling through the thin film to the back contact.

Previous studies on n-type WO_3 photoanodes reported that the oxidation of water to O_2 is not the only photo-oxidation occurring at the WO_3 anode surface upon illumination. Due to the poor kinetics of the WO_3 surface for the O_2 evolution reaction, incomplete oxidation of water to peroxide species can also occur and cause considerable photocurrents even though it is thermodynamically unfavorable (see Equation 10-1).[178,208,209] In order to avoid the competing peroxide formation reaction, CoPi water oxidation catalyst was deposited onto the WO_3 photoanode surface to increase kinetics of water oxidation to oxygen.

Equation 10-1. competing reactions occuring at the WO_3 photoanode surface under illumination with corresponding thermodynamic standard potentials given acc. to Izgorodin et al.[209] Reactions stated for pH = 0, E^0 given vs NHE.

$$2\,H_2O \rightarrow 4H^+ + O_2 + 4e^- \quad E^0 = 1.23\,V \qquad (1)$$

$$H_2O \rightarrow 2H^+ + H_2O_2 + 2e^- \quad E^0 = 1.78\,V \qquad (2)$$

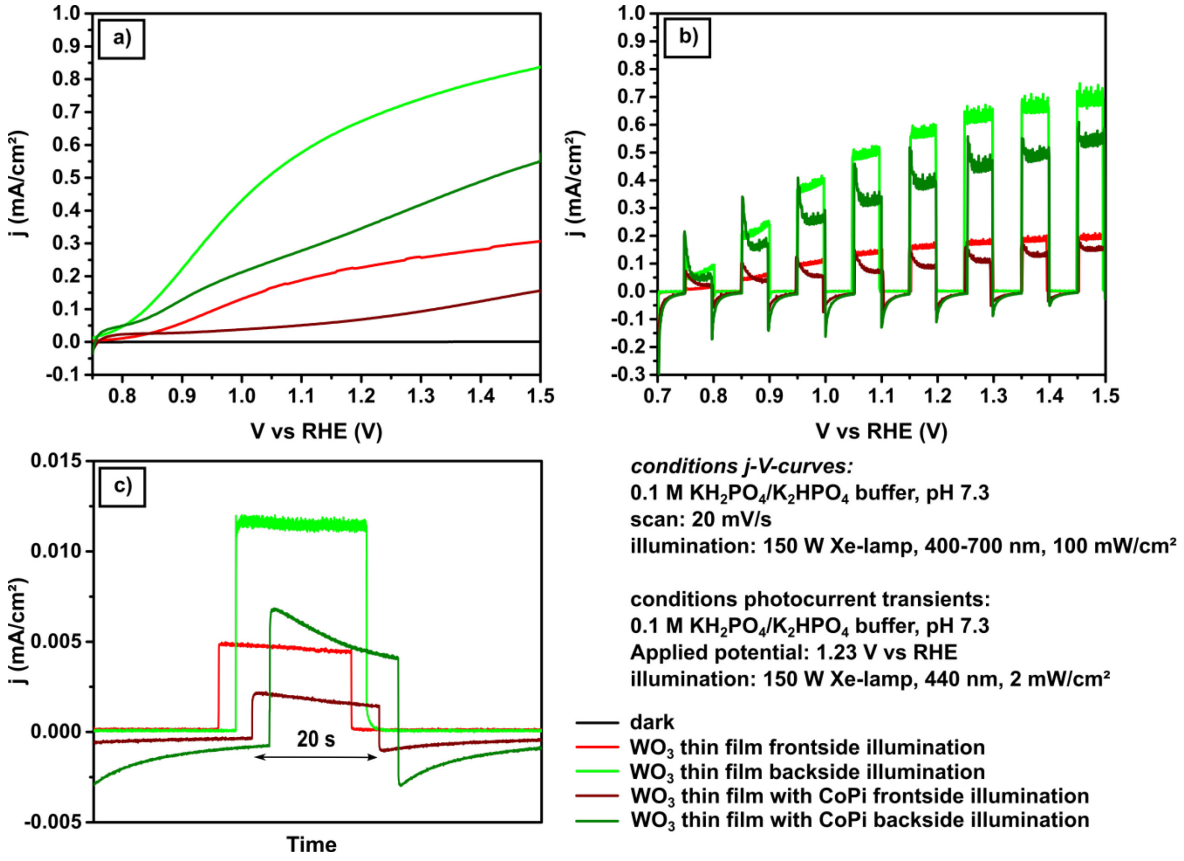

Figure 10-7. a) j-V-curves of WO_3 thin films with and without CoPi deposited onto the surface, b) j-V-curves of WO_3 thin films with and without CoPi deposited onto the surface in light on/off mode and c) photocurrent transients of pristine and CoPi-decorated WO_3 photoanodes.

Photocurrents measured for CoPi-decorated WO_3 photoanodes are significantly lower than for their unmodified counterparts accounting for 0.1 mA/cm² in frontside illumination and 0.4 mA/cm² in backside illumination, respectively (Figure 10-7a). In first approach, this indicates an unfavorable photoelectrochemical behavior of the CoPi-decorated WO_3 photoanodes with respect to water oxidation. Indeed, as shown in Figure 10-7b by photocurrent measurements in light on/off mode, throughout the whole measured potential range of 0.75 V to 1.5 V vs RHE, photocurrent spikes and overshoots can be observed when switching the light on and off for the CoPi-modified WO_3 photoanodes. This indicates enhanced recombination induced by decorating the surface of the WO_3 photoanode with CoPi. Analysis of the photocurrent transients according to the phenomenological approach explained in chapter 5.5.3.3 further confirms this assumption.

As shown in Figure 10-7c and summarized in Table 10-2, independent of the illumination direction, unmodified WO_3 photoanodes do not show any significant decay of photocurrent after switching the light on, i.e. the hole transfer efficiency $\eta_{transfer}$ is assumed to be 1. In case of the CoPi modified WO_3 electrodes values as low as 0.655 in case of frontside illumination and 0.574 in case of backside illumination are yielded for the hole transfer efficiency $\eta_{transfer}$ due to increased rate constants for surface recombination of photo-generated holes k_{rec}.

Table 10-2. Summary of results of photocurrent transient analysis for CoPi modified WO_3 photoanodes. Transients were measured at an applied potential of 1.23 V vs RHE under illumination of blue light 440 nm at an intensity of 2 mW/cm²)

CoPi-modified WO_3 thin films	frontside illumination	j_{ini} = 0.0022 mA/cm²	$\eta_{transfer}$ = 0.655	k_{trans} = 0.020
		j_{ss} = 0.0014 mA/cm²		k_{rec} = 0.010
	backside illumination	j_{ini} = 0.0071 mA/cm²	$\eta_{transfer}$ = 0.574	k_{trans} = 0.034
		j_{ss} = 0.0041 mA/cm²		k_{rec} = 0.026

This phenomenom was studied extensively by Seabold and Choi.[178] They demonstrated that the deposition of CoPi water oxidation catalyst onto a WO_3 photoanode increases the observed photocurrents by reducing the electron-hole recombination only for applied potentials near the flat band potential V_{fb}. They figured out that Co ions of the CoPi create surface states at the WO_3/CoPi junction. Judging from the fact that the CoPi water oxidation catalyst reduces recombination near the flat band potential, Seabold and Choi assumed these states to be located a few hundred millivolts more positive with respect to the flat band potential of the WO_3. Moving the applied potential anodically beyond the level of the surface states results in an excess of positive charges accumulated at these states and at the surface, respectively. Hence, electron-hole recombination is increased due to the excess of positive charges. Furthermore, this results in a lower degree of band bending in the WO_3/Co-Pi electrode than in the bare WO_3 photoanode at potentials more anodic with respect to the surface states. As a consequence, less photocurrent is generated by the CoPi-modified WO_3 photoanode compared to the bare WO_3 electrode.

To approve the applied potentials to be more anodic with respect to the flat band potential, Mott-Schottky-type electrochemical impedance spectroscopy was carried out to determine the flat band potential V_{fb} of the WO_3 photoanodes. Mott-Schottky-plots for two different frequencies are shown in Figure 10-8. It is shown, that extrapolation of the linear region of the Mott-Schottky-plots for both applied frequencies reveal nearly similar values for V_{fb}. The flat band potential was determined to be ~0.33 V vs RHE which is in good agreement with V_{fb} values reported in literature.[178,210–212] As applied potentials of the photoelectrochemical investigations in Figure 10-7 are significantly above the V_{fb}, the explanation given by Seabold and Choi agrees well for the observed j-V characteristics.

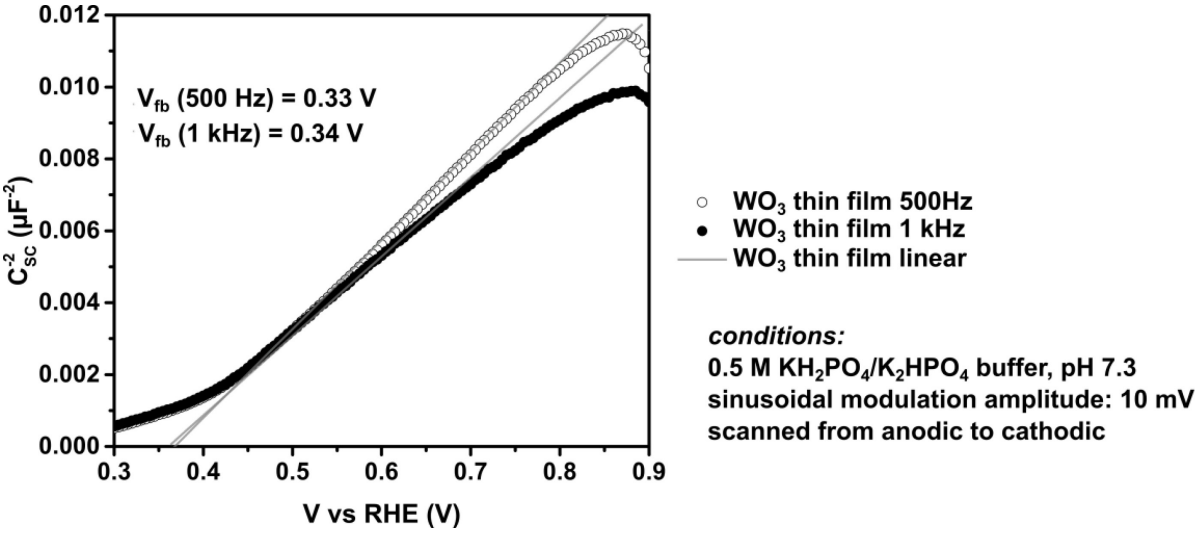

Figure 10-8. Mott-Schottky-Plots of a WO_3 thin film at frequencies of 500 Hz and 1 kHz.

To sum up shortly, WO_3 thin films were prepared using a sol-gel approach to synthesize a WO_3 sol used for dip coating of FTO substrates followed by calcination procedure. WO_3 thin films crystallize textured in monoclinic structure with preferred (002) orientation. Based on UV/Vis spectroscopy, a band gap of about 2.8 eV was estimated for the WO_3 thin films. Electron microscopy reveals the thin films to be comprised of highly crystalline particles and sintered particle agglomerates. A film thickness of about 230 nm was estimated. By photoelectrochemical investigations photocurrent densities of 0.7 mA/cm² at

1.23 V vs RHE were determined. However, as also the formation of peroxide species is a competing reaction to oxygen evolution, it is uncertain to which extend the obtained photocurrents can be associated to the oxygen evolution. A flat band potential of ~0.33 V was determined for WO_3 thin films by Mott-Schottky-analysis.

In the upcoming section, the WO_3 thin films on FTO were used as substrates for $BiVO_4$ and Mo:$BiVO_4$ thin film deposition according to the previously described thin film synthesis method to form WO_3/$BiVO_4$ and WO_3/Mo:$BiVO_4$ composite photoanodes for water oxidation.

10.3. Synthesis and Characterization of WO_3/Mo:$BiVO_4$ heterojunction

In the previous section the synthesis of WO_3 thin films on FTO substrate was elucidated and obtained WO_3 thin films were characterized profoundly. Using the knowledge gained about both semiconductors, it is possible to develop the potential energy diagram of the heterojunction when bringing both materials into contact. For this purpose, the band gaps and flat band potentials of each material are necessary to figure out the relative band positions within the WO_3/$BiVO_4$ composite. Based on UV/Vis spectroscopy for both materials optical band gaps of 2.8 eV for WO_3 and ~2.4 eV for Mo:$BiVO_4$ and $BiVO_4$, respectively, were estimated. Flat band potentials for both types of materials were measured by means of Mott-Schottky analysis. Assuming the gap between flat band potential V_{fb} and the bottom edge of the conduction band (CB) to be negligible for n-type semiconductors, the conduction band position can be estimated to be equal to the flat band potential. Using the optical band gap energy E_g, the upper edge of the valence band (VB) can be estimated.[37,213] Based on these assumptions the potential energy diagram can be constructed and is shown in Figure 10-9 (summary of valence band positions, conduction band positions and band gap energies can be found in the Appendix, chapter 12.1.4.1).

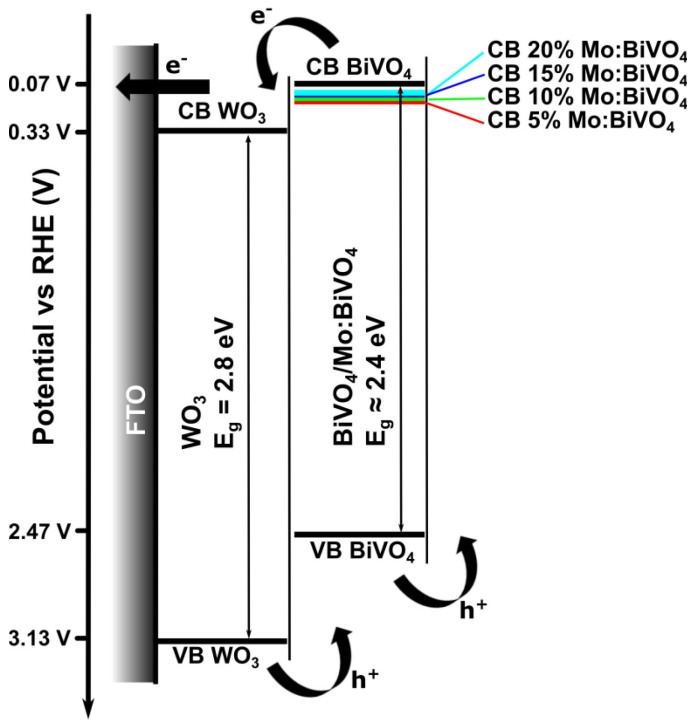

Figure 10-9. Schematic potential energy diagramm of $WO_3/BiVO_4$ heterojunctions.

As expected, the band alignment of the $WO_3/BiVO_4$ and WO_3/Mo:$BiVO_4$ heterojunctions match the Type II band alignment with staggered band gaps. The conduction band and valence band of $BiVO_4$ are more cathodic than the corresponding bands of WO_3. This thermodynamic condition favors the injection of electrons of the $BiVO_4$ conduction band to the conduction band of WO_3. On the other hand photo-generated holes migrate to the semiconductor/electrolyte junction either directly within the $BiVO_4$ layer or after being injected from the WO_3 valence band to the $BiVO_4$ valence band. The facile electron transfer to the back contact and the enhanced migration of holes to the semiconductor/electrolyte junction affect an improved charge separation and reduced recombination, respectively, which should result in improved photoelectrochemical performance regarding water oxidation.

The WO_3 thin films on FTO substrates synthesized by a common sol-gel-approach (*vide supra*) are used as substrates for the fabrication of the FTO/$WO_3/BiVO_4$ and FTO/WO_3/Mo:$BiVO_4$ composite heterojunction electrodes, respectively. Synthesis

procedure of the $BiVO_4$ layers remained unchanged and was conducted similar to the already described methods (see chapter 8.2 and 8.3).

Keeping the synthesis protocols of WO_3 and $BiVO_4$ or Mo:$BiVO_4$ thin films unchanged should result in a thin film composite electrode comprised of the individual extensively characterized electrode materials. To assure this assumption is valid, the crystal structure of a WO_3/10% Mo:$BiVO_4$ composite electrode was investigated. Results of x-ray diffraction in gracing incidence of the x-ray beam are shown in Figure 10-10 together with reference patterns of monoclinic γ-WO_3 and $BiVO_4$ in the monoclinic scheelite phase. All observed reflections could be assigned to either WO_3 or $BiVO_4$. The preferred orientation of the (002) plane of WO_3 (*vide infra*) can also be observed within the diffraction pattern of the WO_3/10% Mo:$BiVO_4$ composite electrode. The reflections assigned to Mo:$BiVO_4$ prove the Mo:$BiVO_4$ layer to exhibit polycrystalline, isotropic character.

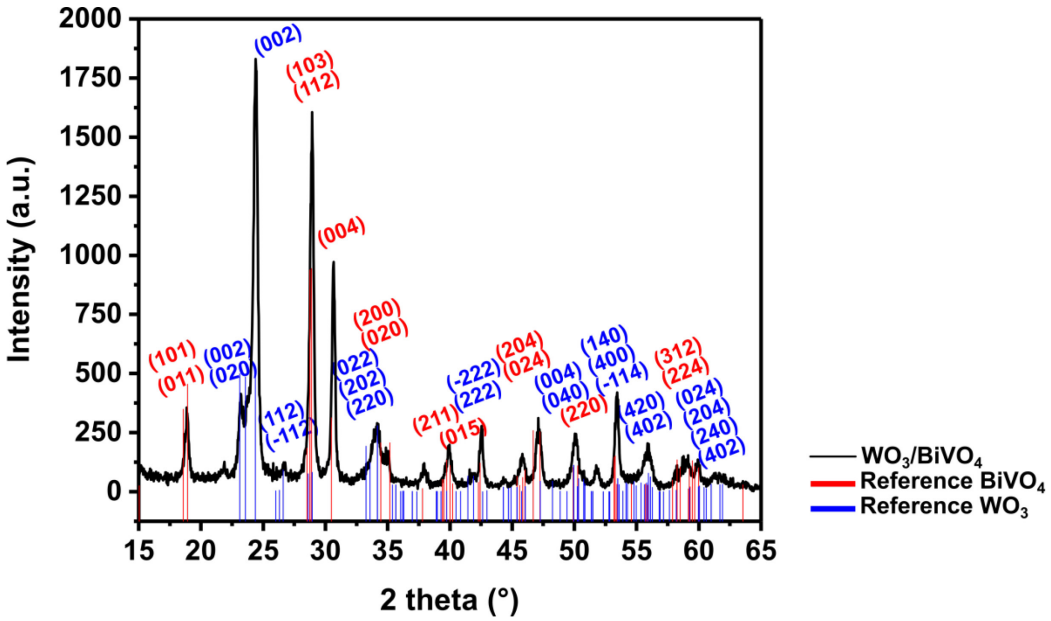

Figure 10-10. Gracing incidence XRD pattern of WO_3/10% Mo:$BiVO_4$ composite electrodes with reference patterns of monoclinc γ-WO_3 (JCPDS 71-2141) and monoclinic scheelite $BiVO_4$ (PDF 01-083-1698).

Light absorption properties of the $WO_3/BiVO_4$ and WO_3/Mo:$BiVO_4$ electrodes were investigated by UV/Vis spectroscopy. Results are shown in Figure 10-11. Exemplarily, in Figure 10-11a the absorption properties for a WO_3/5% Mo:$BiVO_4$ composite electrode is shown in comparison to the spectra of songle WO_3 and 5% Mo:$BiVO_4$ thin films, respectively. The absorbance is slightly enhanced for the WO_3/5% Mo:$BiVO_4$ composite compared to the 5% Mo:$BiVO_4$ thin film. This seems reasonable as the WO_3 layer contributes to the overall absorbance. As can be seen in Figure 10-11b, the light absorption properties of all $WO_3/BiVO_4$ and WO_3/Mo:$BiVO_4$ electrodes and the estimated onset of light absorption of 525 nm which corresponds to a band gap energy of ≈ 2.37 eV is comparable and in good agreement with literature.[36,187]

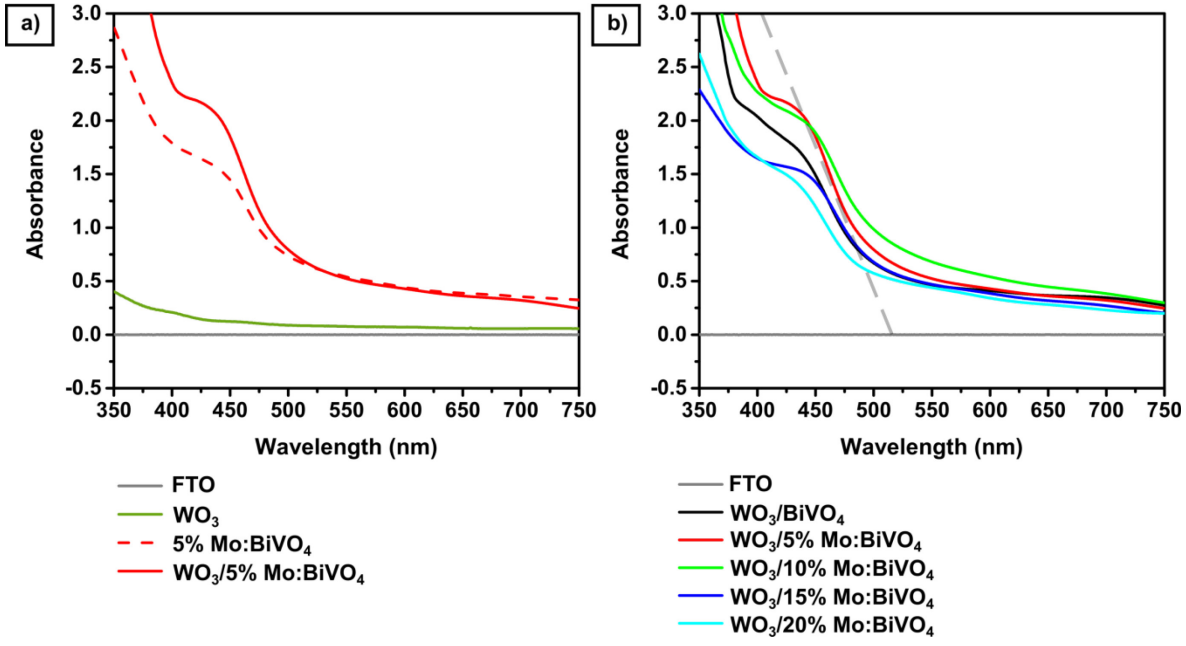

Figure 10-11. UV/Vis spectroscopy on $WO_3/BiVO_4$ and WO_3/Mo:$BiVO_4$ composite electrodes. a) Comparison of WO_3, 5% Mo:$BiVO_4$ and the junction WO_3/5% Mo:$BiVO_4$ on FTO substrates, b) results for different $WO_3/BiVO_4$ and WO_3/Mo:$BiVO_4$ junctions on FTO.

Composite electrode morphology was further investigated by electron microscopy. SEM top view images and corresponding EDX spectra are shown in Figure 10-12. Obtained EDX spectra are homogeneous for all samples and qualitatively prove the composite thin films to consist of W, Bi, V, O and Mo. The domain-like morphology of the $BiVO_4$ layer and Mo:$BiVO_4$ layer, respectively, described in chapter 8.2 and 8.3 is also observed for the composite electrodes. However, domain size and inner domain streak size have changed significantly. For the WO_3/$BiVO_4$ electrode an average geometrical domain size of 7.0 ±2.8 µm² and an average inner domain material streak size of 131 ±19 nm were determined. For the WO_3/Mo:$BiVO_4$ composite electrodes smaller domain sizes were determined accounting for 6.7 ±3.7 µm², 4.4 ±2.7 µm² and 4.1 ±1.5 µm² for the WO_3/5% Mo:$BiVO_4$, the WO_3/10% Mo:$BiVO_4$ and the WO_3/15% Mo:$BiVO_4$ electrodes, respectively. The average domain size of the WO_3/20% Mo:$BiVO_4$ could not be determined due to advanced sintering of the thin film material leading to indistinguishable single domains. The average inner domain streak sizes increase with increasing Mo-content of the different WO_3/Mo:$BiVO_4$ composite electrodes accounting for 186 ±76 nm, 190 ±51 nm, 203 ±84 nm and 207 ±74 nm for the WO_3/5% Mo:$BiVO_4$, WO_3/10% Mo:$BiVO_4$, WO_3/15% Mo:$BiVO_4$ and WO_3/20% Mo:$BiVO_4$ electrodes, respectively. A summary of the analyzed average geometrical domain size and average inner domain material streak size for WO_3/$BiVO_4$, WO_3/Mo:$BiVO_4$ double layers on FTO in comparison with $BiVO_4$ and Mo:$BiVO_4$ monolayers on FTO is given in Table 10-3.

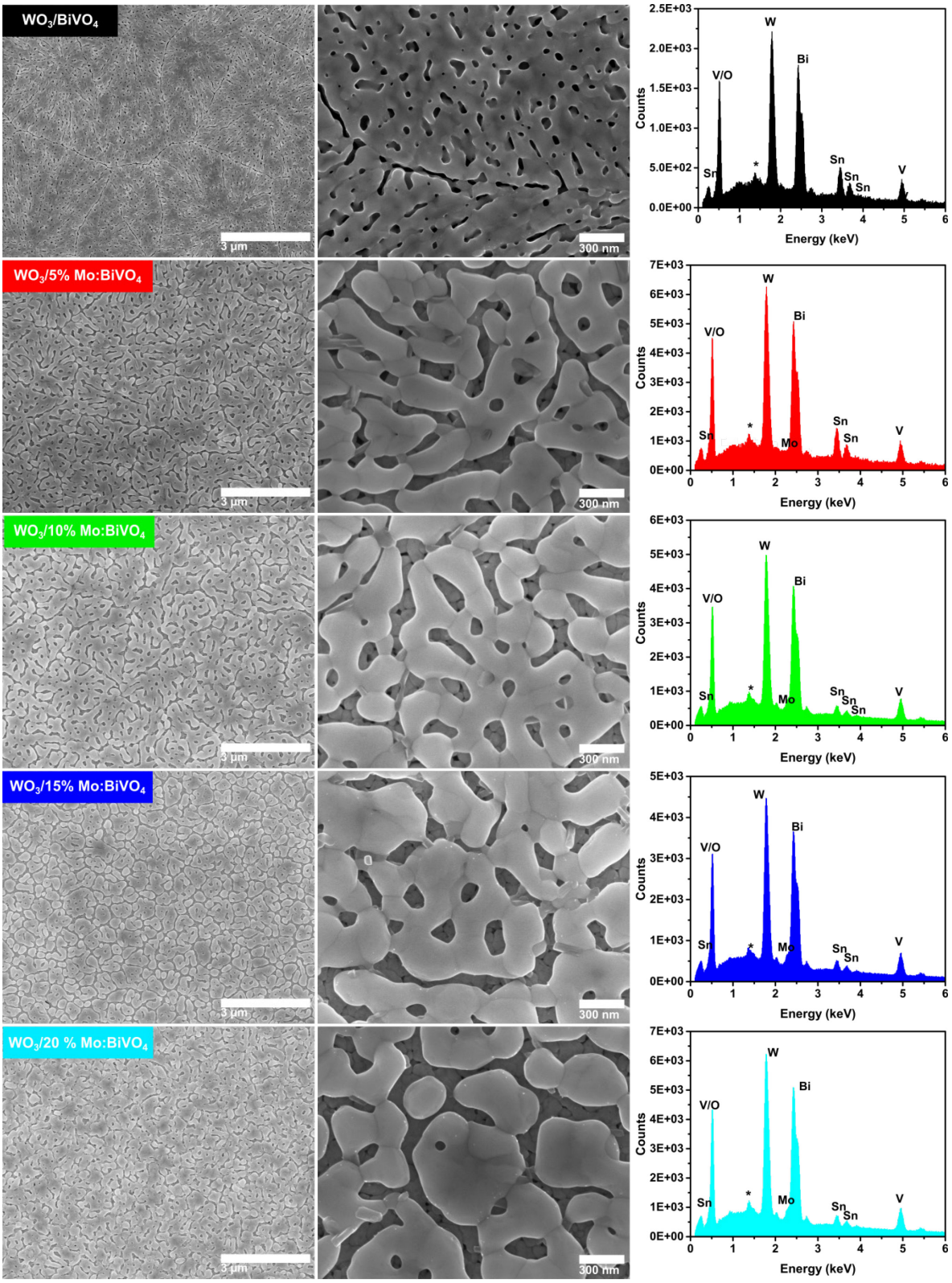

Figure 10-12. SEM top view images of $WO_3/BiVO_4$ and WO_3/Mo:$BiVO_4$ thin films on FTO substrate together with corresponding EDX spectra. The Mo-L peak overlaps with the Bi-M peak at 2.3 keV.

In comparison with the monolayers of $BiVO_4$ and Mo:$BiVO_4$ on FTO the morphological properties of the $BiVO_4$ and Mo:$BiVO_4$ layers of the composite electrodes have significantly changed. In case of undoped $BiVO_4$ thin films, the average geometrical domain sizes of 7.0 ±2.8 µm² and 7.2 ±3.3 µm² are comparable for the composite electrodes and the monolayer electrodes, respectively. However, average inner domain material streak sizes are increased by a factor of 2 when deposited onto a FTO/WO_3 substrate instead of depositing onto bare FTO. For the Mo-doped $BiVO_4$ thin films on FTO/WO_3 and bare FTO average domain sizes decrease with increasing Mo content whereas inner domain material streak sizes increase with increasing Mo content. In case of depositing the Mo:$BiVO_4$ layer onto the FTO/WO_3 substrate domain sizes and inner domain material streak sizes are significantly bigger compared to the Mo:$BiVO_4$ thin films on bare FTO.

Table 10-3. Summary of analyzed average geometrical domain size and average inner domain material streak size for WO_3/$BiVO_4$, WO_3/Mo:$BiVO_4$ double layers on FTO in comparison with $BiVO_4$ and Mo:$BiVO_4$ monolayers on FTO.

sample	WO_3/$BiVO_4$ and WO_3/Mo:$BiVO_4$ composite layers		$BiVO_4$ and Mo:$BiVO_4$ single layers	
	Average geometrical domain size by SEM (µm²)	Average inner domain streak size (nm)	Average geometrical domain size by SEM (µm²)	Average inner domain streak size (nm)
$BiVO_4$	7.0 ±2.8	131 ±19	7.2 ±3.3	68 ±7
5% Mo:$BiVO_4$	6.7 ±3.7	186 ±76	6.4 ±2.4	80 ±7
10% Mo:$BiVO_4$	4.4 ±2.7	190 ±51	2.8 ±1.7	84 ±9
15% Mo:$BiVO_4$	4.1 ±1.5	203 ±84	1.7 ±1.1	105 ±9
20% Mo:$BiVO_4$	--	207 ±74	<1	139 ±8

Despite the substrate, all synthesis parameters were kept constant for the deposition and calcination of the $BiVO_4$ and Mo:$BiVO_4$ thin films. For this reason the origin of the different morphologies of the $BiVO_4$ and Mo:$BiVO_4$ thin films most probably can be found in the different sintering behavior of the thin films in dependence of the substrate. Sintering of thin films deposited on rigid substrates has been described first by Scherer and Garino[214] and has been supplemented by various other groups.[215–218] Briefly explained, the developed models to describe sintering of thin films on rigid substrates presuppose two requirements: i) the rigidity of the substrate upon sintering conditions and ii) ideal (i.e. strong) adhesion of the thin film on the substrate. If both requirements are fulfilled, a tension rises in the x-y-plane of the thin film upon sintering conditions which counteracts the densification of the thin film material. As a consequence, densification rates in x-y-plane of the thin films equal zero and the thin film is only densified perpendicular to the substrate and in z-direction, respectively (see Figure 10-13 for illustration).

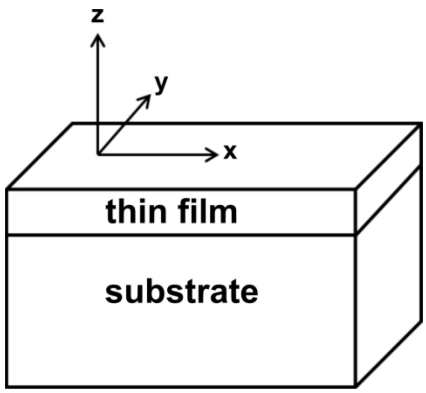

Figure 10-13. Schematic illustration of a thin film on a igid substrate. Coordinates are defined by x, y and z vectors.

Assuming the substrate to be rigid and the adhesion of the $BiVO_4$ and Mo:$BiVO_4$ thin films to be non-ideal and particularly weaker on WO_3 than on FTO, sintering is facilitated for the $BiVO_4$ and Mo:$BiVO_4$ films deposited onto the FTO/WO_3 substrates. Hence, bigger domain sizes and bigger inner domain material streak sizes are observed for the $BiVO_4$ and

Mo:$BiVO_4$ thin films deposited onto FTO/WO_3 substrates compared to same thin films deposited onto bare FTO.

The assumption of weak adhesion of the $BiVO_4$ and Mo:$BiVO_4$ thin films on the WO_3 layer is further supported by investigation of the cross section of the composite electrodes. In Figure 10-14 cross section images of a WO_3/10% Mo:$BiVO_4$ composite electrode is shown exemplarily for all samples. As highlighted in Figure 10-14, there are several voids at the WO_3/Mo:$BiVO_4$ interface. A high number of voids results in a lower degree of adhesion of the WO_3 and Mo:$BiVO_4$ thin films. Additionally, there are several voids at the FTO/WO_3 interface. Thin film thicknesses of the compartments of the composite electrodes accounting for ~233 nm for the Mo:$BiVO_4$ thin film and ~235 nm for the WO_3 thin film are in line with the film thicknesses determined for the monolayer thin films of each material on FTO ($d_{10\%\ Mo:BiVO_4}$ = 238 nm, d_{WO_3} = 230 nm, *vide supra*).

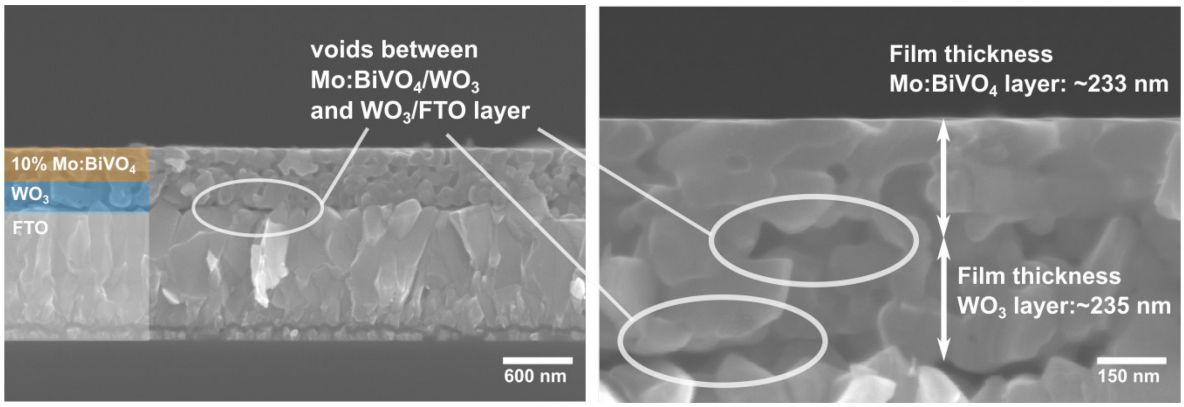

Figure 10-14. SEM cross section images of a WO_3/10% Mo:$BiVO_4$ composite electrode with marked voids at the FTO/WO_3 and the WO_3/Mo:$BiVO_4$ interfaces.

Exemplarily for all samples, a WO_3/10% Mo:$BiVO_4$ composite electrode was further investigated by HR-STEM. For this purpose a lamella was cut out of the thin film by FIB-SEM, operated by Dr. Dirk Berger from ZELMI/TU Berlin. STEM measurements were carried out by Dr. Siyuan Zhang and supervised by Prof. Dr. Christina Scheu from Max-Planck-Institut für Eisenforschung. A HR-STEM image focusing on the WO_3/Mo:$BiVO_4$ interface is shown in Figure 10-15a along with the corresponding FFT

patterns of the WO_3 layer, the Mo:$BiVO_4$ layer and the interfacial region. Both layers are highly crystalline as can be seen by the lattice fringes and the frequencies within the FFT patterns of the single layers. The FFT pattern of the Mo:$BiVO_4$ layer (framed red) exhibits two reflections corresponding to the (103) plane and the (020) plane of the monoclinic scheelite phase ([$\bar{3}$01] zone axis). The FFT pattern of the WO_3 layer only exhibits one set of reflections corresponding to the (202) plane. The FFT pattern of the interfacial region exhibits reflections of both components revealing the contact between WO_3 and Mo:$BiVO_4$ thin films to be highly crystalline which is favorable for fast charge carrier transport. Additionally, the EDX map shown in Figure 10-15b, proves the composite electrode to consist of separated layers of WO_3 and Mo:$BiVO_4$. No mingling or interpenetration of the two layers could be observed.

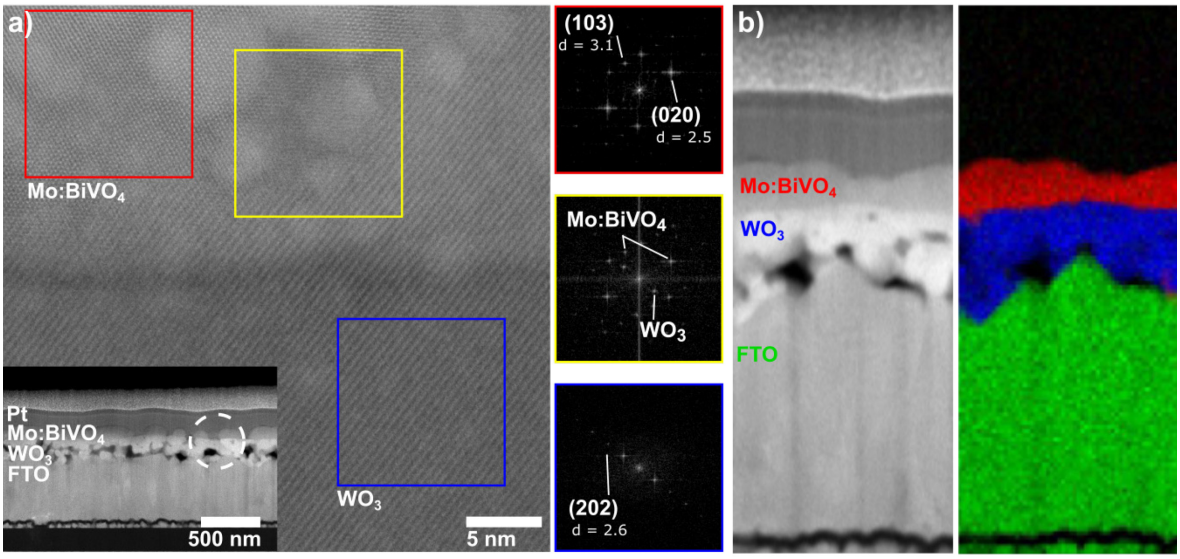

Figure 10-15. a) HR-STEM investigations of a FIB lamella focusing on the WO_3/Mo:$BiVO_4$ interface. Corresponding FFT patterns are given for the WO_3 (blue), Mo:$BiVO_4$ (red) and the interface region (yellow) and b) STEM-EDX-Map of the WO_3/Mo:$BiVO_4$ composite electrode.

The photoelectrochemical performance regarding water oxidation of the prepared WO_3/$BiVO_4$ and WO_3/Mo:$BiVO_4$ composite electrodes were investigated briefly. Respective j-V-curves with and without CoPi water oxidation catalyst deposited onto the surface, illuminated in frontside and the backside mode are shown in Figure 10-16.

Obtained photocurrents at an applied potential of 1.23 V vs RHE are summarized in Table 10-4 together with obtained photocurrents for the $BiVO_4$ and Mo:$BiVO_4$ single layer photoanodes (see chapter 8.3, Table 8-2). Comparative j-V-curves obtained in frontside and backside illumination for each sample are given in the Appendix, chapter 12.1.4.2.

For the WO_3/$BiVO_4$ composite electrode comparable photocurrents were yielded in frontside and backside illumination accounting for 1.67 mA/cm² and 1.47 mA/cm² at 1.23 V vs RHE, respectively. In comparison with the single layer photoanodes, for which drastically higher photocurrents were observed when backside illumination was used, this result indicates the separation of photo-generated charge carriers to be dramatically increased by the creation of the WO_3/$BiVO_4$ heterojunction. (Note: photocurrents for the pristine $BiVO_4$ monolayer on FTO obtained in frontside and backside illumination were much lower (0.08 mA/cm² and 0.20 mA/cm² at 1.23 V vs RHE in frontside and backside illuminaton) and limited by poor charge transport properties (see chapter 8.3)). For the WO_3/Mo:$BiVO_4$ heterojunction photoanode yielded photocurrents increase with increasing Mo-content of the $BiVO_4$ layer accounting for 2.64 mA/cm² at 1.23 V vs RHE for the WO_3/5% Mo:$BiVO_4$ electrode up to 3.37 mA/cm² at 1.23 V vs RHE for the WO_3/20% Mo:$BiVO_4$ electrode in frontside illumination, respectively and from 2.03 mA/cm² at 1.23 V vs RHE for the 5% Mo:$BiVO_4$ sample to 3.22 mA/cm² for the 15% Mo:$BiVO_4$ sample in backside illumination, respectively. The morphology of all Mo-doped $BiVO_4$ layers of the composite electrodes are exceeding the hole diffusion length of $BiVO_4$ (70-100 nm[22,74,75]) in terms of inner domain material streak size. Hence, the origin of the observed photocurrent trend with increasing Mo content most probably is not a consequence of the thin film morphology but most probably can be derived from the position of the respective conduction bands. As shown previously (see Figure 10-9, schematic potential energy diagram), the higher the Mo content of the Mo:$BiVO_4$ layer, the more cathodic is the conduction band with respect to the conduction band of the WO_3. The higher the difference in the position of the conduction bands in the WO_3/Mo:$BiVO_4$ heterojunction, the stronger is the induced electron attraction of the WO_3 conduction band within the junction which results in increased charge carrier separation and higher photocurrents, respectively.

Depositing a layer of CoPi water oxidation catalyst onto the surface of the $WO_3/BiVO_4$ and $WO_3/Mo:BiVO_4$ composite electrodes further enhances the photoelectrochemical performance and obtained photocurrents, respectively, accounting for 3.79 mA/cm² at 1.23 V vs RHE for the $WO_3/BiVO_4$ electrode up to 4.91 mA/cm² for the WO_3/20% $Mo:BiVO_4$ electrode, respectively; all values obtained in frontside illumination. With increasing Mo content of the $Mo:BiVO_4$ layers the photocurrents obtained in backside illumination surpass respective photocurrents obtained in frontside illumination accounting for 4.79 mA/cm² at 1.23 V vs RHE for the WO_3/10% $Mo:BiVO_4$ electrode up to maximum photocurrents of 5.41 mA/cm² at 1.23 V vs RHE for the WO_3/20% $Mo:BiVO_4$ electrode. For all samples significantly higher photocurrents were observed with respect to the yielded photocurrents for the $BiVO_4$ and $Mo:BiVO_4$ monolayer photoanodes. This clearly indicates the positive impact of the WO_3 interlayer on the photoelectrochemical performance regarding water oxidation.

Table 10-4. Summary of obtained photocurrents at an applied potential of 1.23 V vs RHE of the $WO_3/BiVO_4$ and $WO_3/Mo:BiVO_4$ composite electrodes with and without CoPi water oxidation catalyst deposited onto the surface in frontside and backside illumination. Values given in brackets are respective photocurrents for the $BiVO_4$ and $Mo:BiVO_4$ monolayer photoanodes.

Sample	j at 1.23 V vs RHE (mA/cm²)			
	without CoPi		with CoPi	
	frontside illumination	backside illumination	frontside illumination	backside illumination
$WO_3/BiVO_4$	**1.67** (0.08)	**1.47** (0.20)	**3.79** (0.54)	**3.36** (2.19)
WO_3/5% $Mo:BiVO_4$	**2.64** (1.75)	**2.03** (1.76)	**4.34** (4.02)	**4.33** (3.94)
WO_3/10% $Mo:BiVO_4$	**2.87** (1.74)	**2.86** (1.93)	**4.09** (3.51)	**4.79** (4.64)
WO_3/15% $Mo:BiVO_4$	**3.34** (1.13)	**3.22** (1.17)	**4.77** (4.00)	**5.22** (3.69)
WO_3/20% $Mo:BiVO_4$	**3.37** (1.12)	**3.11** (1.02)	**4.91** (3.25)	**5.41** (2.91)

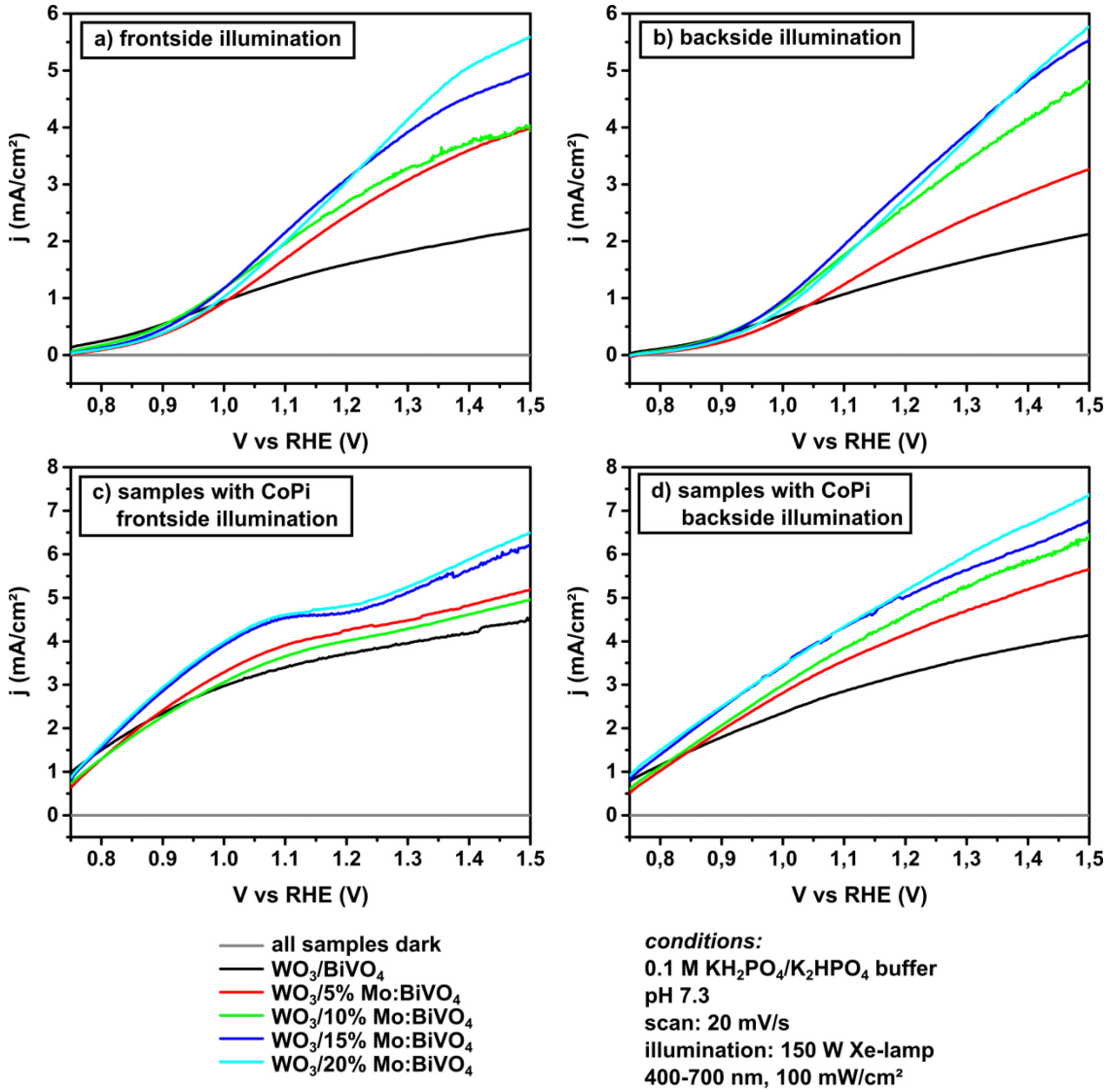

Figure 10-16. j-V-curves obtained for the $WO_3/BiVO_4$ and WO_3/Mo:$BiVO_4$ composite electrodes with and without CoPi deposited onto the surface in frontside and backside illumination.

To summarize briefly, the synthesis of heterojunction electrodes consisting of WO_3 and $BiVO_4$ and Mo:$BiVO_4$, respectively, was successful. Analysis of the crystal structure revealed both layers to be isotropic and highly crystalline. Light absorption properties were slightly improved for the heterojunctions compared to the $BiVO_4$ and Mo:$BiVO_4$ monolayers, respectively, due to the contribution of the WO_3 interlayer to the overall absorbance. By SEM investigations a morphology change of the $BiVO_4$ and Mo:$BiVO_4$ layers could be observed which is most probably a consequence of advanced sintering.

Investigation of the cross section of a FTO/WO_3/10% Mo:$BiVO_4$ electrode revealed a high number of voids and missing contact between the single layers and the substrate, respectively. HR-STEM investigations of the WO_3/Mo:$BiVO_4$ interface proved the interface to be highly crystalline and interpenetration of both phases could be excluded by EDX mapping. Photoelectrochemical investigations of the synthesized composite electrodes confirmed the concept of charge carrier separation improvement by the creation of a heterojunction to be functioning. Improved photoelectrochemical performance for all analyzed WO_3/$BiVO_4$ and WO_3/Mo:$BiVO_4$ samples was observed with and without CoPi water oxidation catalyst deposited onto the surface in comparison to the $BiVO_4$ and Mo:$BiVO_4$ monolayer photoanodes. A maximum photocurrent of 5.41 mA/cm² at 1.23 V vs RHE was observed for the WO_3/20% Mo:$BiVO_4$ electrode, a photocurrent which is significantly higher than reported results for comparable layered electrode morphologies.[37,38,185] However, the WO_3/Mo:$BiVO_4$ electrodes of the present work so far do not keep up with the highest reported photocurrents for WO_3/$BiVO_4$/CoPi heterojunctions which consist of vertically aligned WO_3 nanorods coated with a thin layer of $BiVO_4$ and additionally coated with CoPi water oxidation catalyst.[35] An overview of highest reported photocurrents for WO_3/(doped)$BiVO_4$/catalyst heterojunctions under illumination of 100 mW/cm² and at neutral pH is given in Table 10-5.

Photoelectrochemical performance regarding water oxidation of the composite electrodes has already been improved significantly compared to the $BiVO_4$ and Mo:$BiVO_4$ monolayers on FTO. However, morphological characterization of the composite electrodes revealed room for improvement of the electrode design.

The WO_3 layer is comprised of highly crystalline particles and sintered particle agglomerates. Due to this morphology a high number of particle boundaries and grain boundaries are present within the migration pathway of the charge carriers which act as recombination sites and promote charge scattering. Hence, recombination of photo-generated charge carriers is enhanced and charge carrier transport through this particulate layer is aggravated. To resolve this issue a WO_3 thin film exhibiting less particulate character and a smaller number of particle and grain boundaries in the migration pathway of the charge carriers is desirable.

Additionally, a high number of voids at the interfaces between the FTO/WO_3 and WO_3/$BiVO_4$ layers were observed in the previous section. To enhance charge carrier transport across the interfaces and reduce recombination of photo-generated charge carriers, homogeneous coverage of the layers' surfaces and compact interfaces are desirable.

In the upcoming section, strategies to achieve the goal of optimized composite electrode morphology are explained and results of investigations of the photoelectrochemical performance regarding water oxidation are presented.

Table 10-5. Overview of highest reported photocurrents for WO_3/(doped)$BiVO_4$/catalyst heterojunctions at neutral pH and under illumination of 100 mW/cm².

Anode	Morphology	j at 1.23 V vs RHE (mA/cm²)	Authors	Publication year
WO_3/$BiVO_4$	layered	1.6	Hong et al.[37]	2011
WO_3/Mo:$BiVO_4$	layered	~2	Zhang et al.[38]	2012
WO_3/Mo:$BiVO_4$/CoPi	layered	2.4	Jeong et al.[185]	2013
WO_3/$BiVO_4$/CoPi	$BiVO_4$-coated WO_3 nanorods	2.5	Pilli et al.[186]	2013
WO_3/W:$BiVO_4$	$BiVO_4$-coated WO_3 nanorods	3.1	Rao et al.[187]	2014
WO_3/$BiVO_4$/CoPi	$BiVO_4$-coated WO_3 nanorods	3.2	Pihosh et al.[36]	2014
WO_3/(W,Mo):$BiVO_4$/FeOOH/NiOOH	$BiVO_4$-coated WO_3 nanohelices	5.4	Shi et al.[188]	2014
WO_3/$BiVO_4$/CoPi	$BiVO_4$-coated WO_3 nanorods	6.7	Pihosh et al.[35]	2015

10.4. Optimization of composite electrode design

10.4.1. Introduction

Morphological optimization objectives ruled out in the previous section namely: i) preparation of a WO_3 thin film exhibiting less particulate character and a smaller number of particle and grain boundaries and ii) homogeneous coverage of the layers' surfaces and compact interfaces are addressed by slight adjustment of the synthesis parameters of the WO_3 layer and the $BiVO_4$ and Mo:$BiVO_4$ layers, respectively. To improve wetting of the FTO substrate by the WO_3 sol, 2 w% of the block-copolymer F127 (PEO_{101}-PPO_{56}-PEO_{101}) were added to the sol (w% with respect to the amount of WO_3 formed in the sol). Additionally, the dwell time of the FTO substrate inside the WO_3 sol was prolonged from 2 s to 8 s to ensure an improved wetting of the rough FTO substrate surface. Furthermore, for the WO_3 thin films the environmental conditions during dip coating were changed from room temperature to 30 °C and a lower relative humidity of 25% instead of 55% was used; first promotes faster evaporation of the solvent and latter reduces hydrolysis water present during the dip coating procedure. This in turn is beneficial for heterogeneous nucleation of WO_3 at the FTO surface which is useful for improved FTO-coverage.[93,94] Furthermore, the withdrawal speed was reduced from 200 mm/min to 100 mm/min to avoid exfoliation and peeling of the thin film after calcination. Finally, 2 w% of the block-copolymer F127 (PEO_{101}-PPO_{56}-PEO_{101}) were added to the $BiVO_4$ and Mo:$BiVO_4$ synthesis solutions to improve wetting of the FTO/WO_3-substrate surface during dip coating as well.

Application of these optimized synthesis parameters results in a different morphology of the WO_3 thin films and of the WO_3/$BiVO_4$ and WO_3/Mo:$BiVO_4$ composite electrodes, respectively. Structural and morphological characterization as well as investigations of the photoelectrochemical performance regarding water oxidation is presented in the following section.

10.4.2. Optimization of WO_3 thin films

The influence of the adjustment of the synthesis parameters on the crystal structure of the optimized WO_3 thin films was not investigated exclusively for pure WO_3 thin films but for

already $BiVO_4$-coated electrodes. Results are shown in Figure 10-22 (chapter 10.4.3). The adjustment of the synthesis parameters does not have any significant impact on the crystal structure of the WO_3 thin films. Besides the reflections for $BiVO_4$, all reflections can be assigned to monoclinic γ-WO_3. The preferred orientation of the WO_3 particles along the (002) plane remains in the optimized WO_3 thin films. This is reasonable as the occurrence of texture was figured out to be a substrate-induced energetic phenomenon (see chapter 10.1).

Light absorption properties were investigated by UV/Vis spectroscopy. A comparison between an optimized and a non-optimized WO_3 thin film on FTO substrate is shown in Figure 10-17. As can be seen, the light absorption was slightly enhanced over the whole measured wavelength range by optimization of the WO_3 thin film synthesis protocol. Most probably this is a consequence of a denser layer of particles leading to increased light absorption.

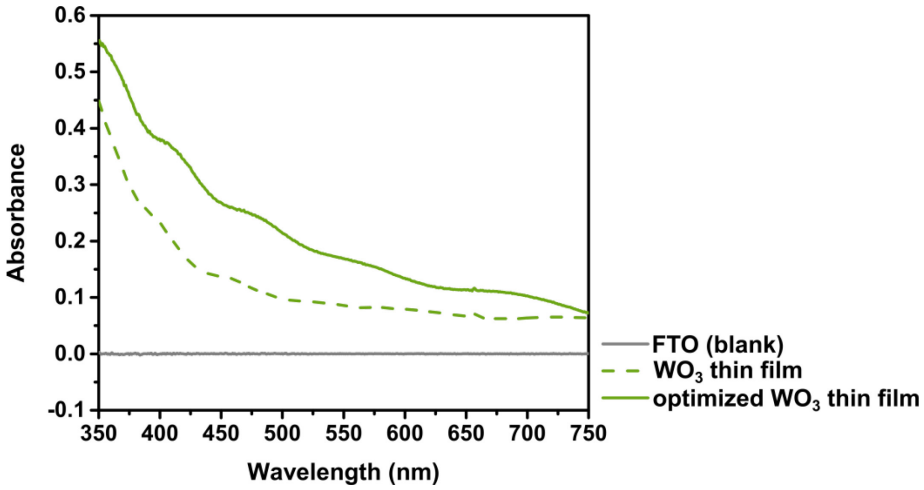

Figure 10-17. UV/Vis spectrum of an optimized WO_3 thin film in comparison to a non-optimzed WO_3 thin film.

The assumption of a denser layer of particles was confirmed by SEM investigations of the WO_3 thin films on FTO substrate. Respective top view and cross section images along with EDX analysis are shown in Figure 10-18. As can be seen in Figure 10-18a and b, the

optimized WO_3 thin film is comprised of particles/flakes of an average size of $0.89 \cdot 10^{-2}$ $\pm 0.38 \cdot 10^{-2}$ µm² (geometrical area determined by top view images). The particles are sintered to a dense WO_3 layer exhibiting only few pores of an average size of $2.3 \cdot 10^{-4}$ $\pm 2.2 \cdot 10^{-4}$ µm² (geometrical area determined by top view images). By the cross section image (Figure 10-18c) the dense character of the thin film is further confirmed and moreover it can be seen that the optimized WO_3 thin film is comprised of a monolayer of interconnected particles which results in an average film thickness of 112 ±9 nm. The cross section image further proves the WO_3 thin film to be homogeneously covering the rough FTO surface and therefore exhibiting only very few voids at the interface. Furthermore, EDX analysis proves the thin film to solely consist of W and O, nearly no C could be traced revealing the whole organic solvent as well as the F127 polymer to be removed by calcination.

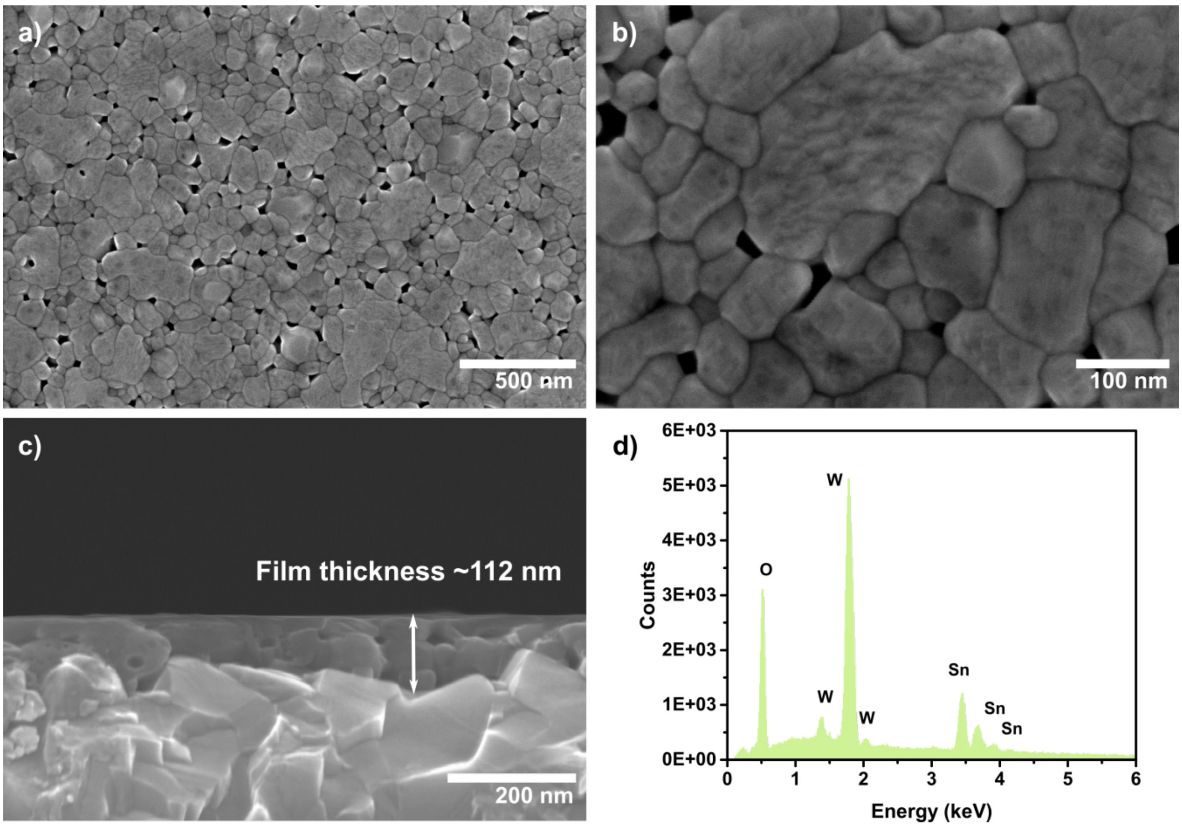

Figure 10-18. SEM investigations of optimized WO_3 thin films on FTO substrate: a and b) top view images, c) cross section image and d) EDX spectrum.

In comparison to the non-optimized WO_3 thin films, the morphology has changed significantly. A summarizing comparison of the analyzed WO_3 thin film features before and after optimization is given in Table 10-6. The average particle size of the optimized WO_3 thin film is decreased to about half of the size of the particles of the non-optimized thin films. The average pore size of the optimized WO_3 thin films has decreased dramatically by a factor of ~30. Both, reduced particle size and pore size lead to better substrate coverage and less voids at the interface, respectively. Furthermore the film thickness of the optimized WO_3 thin film is halved compared to its non-optimized counterpart. Most probably, this is a consequence of the adjusted withdrawal speed as well as of the reduced porosity of the optimized WO_3 thin films.

Table 10-6. Comparison of morphological thin film features of optimized WO_3 thin films and non-optimized WO_3 thin films.

	optimized WO_3 thin film	WO_3 thin film (non-optimized)
Particle size in µm² (geometrical particle area determined by top view images)	$0.89 \cdot 10^{-2} \pm 0.38 \cdot 10^{-2}$	$1.70 \cdot 10^{-2} \pm 0.52 \cdot 10^{-2}$
Pore size in µm² (geometrical pore area determined by top view images)	$2.3 \cdot 10^{-4} \pm 2.2 \cdot 10^{-4}$	$7.42 \cdot 10^{-3} \pm 3.91 \cdot 10^{-3}$
Film thickness in nm (determined by cross section images)	112 ±9	230 ±11

The optimized WO_3 thin films were further investigated by TEM/SAED, results are shown in Figure 10-19. As can be seen in Figure 10-19a and b, particle size and shape observed in the SEM images can generally be confirmed by TEM. Furthermore, the high resolution image proves the thin film particles to be highly crystalline. FFT analysis of a selected area exhibits two sets of reflections matching the d-spacing of the (222) and (022) plane ([011] zone axis), respectively, which corresponds to monoclinic γ-WO_3. Additional SAED investigations were carried out; results are shown in Figure 10-19c. Electron diffraction at three different spots along one larger WO_3 flake results in three similar dot patterns which contain reflections of the (-112) and (032) planes. According to SAED experiments the

WO_3 flakes exhibit single-crystalline character. Unfortunately, it was not possible to obtain reliable results by electron backscatter diffraction investigations (EBSD) of the WO_3 thin films because the resolution limit of the available equipment was not sufficient for the small WO_3 particles. Hence, it remains uncertain how and to which extent the single-crystalline character of the WO_3 flakes/particles is translated into the thin film morphology.

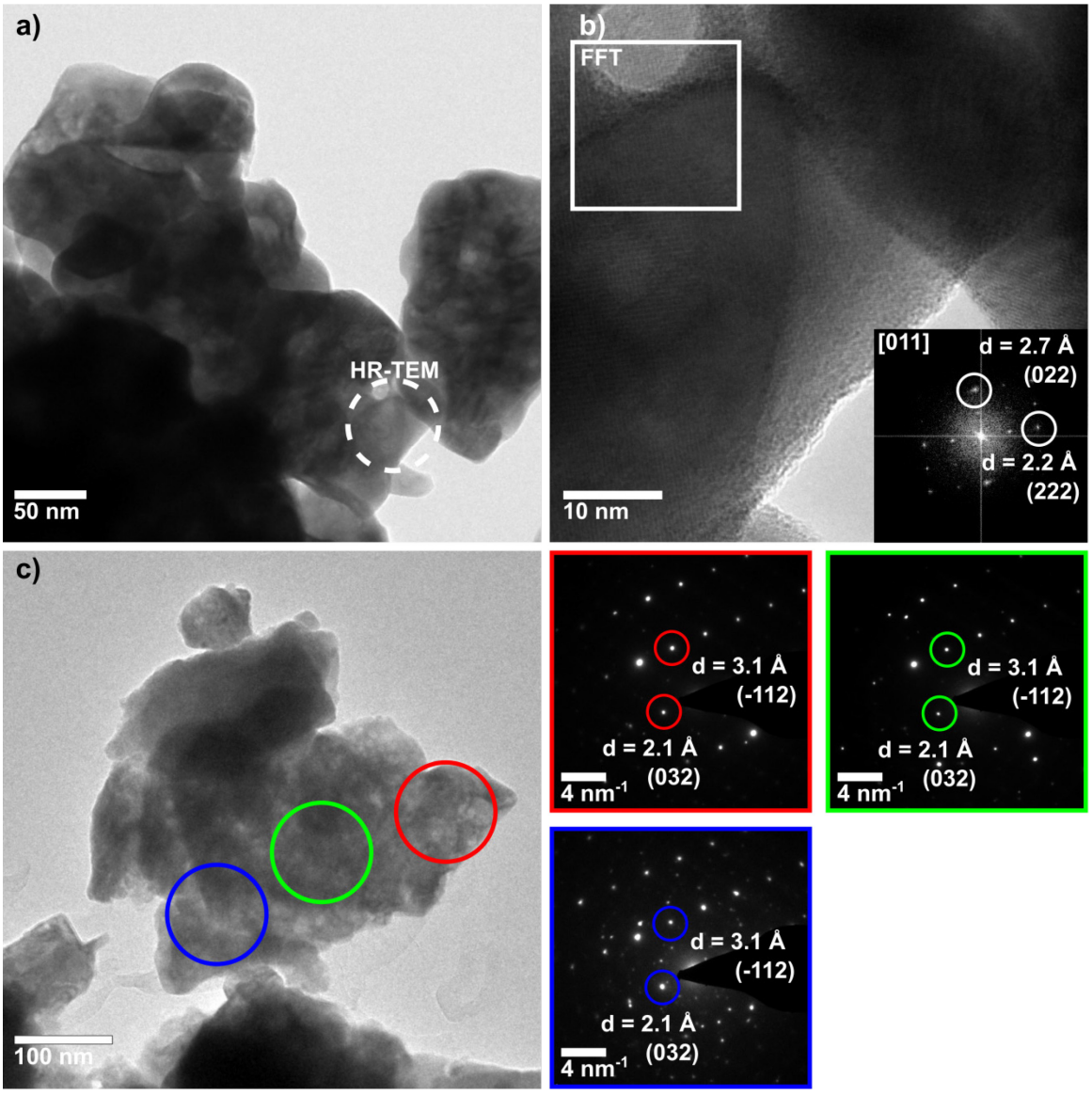

Figure 10-19. TEM/SAED investigations of optimized WO_3 thin films. a) Overview image, b) HR-TEM image with FFT illustrating crystallinity, c) SAED investigations of three different spots along one WO_3 flake.

Finally, the optimized WO_3 thin films' photoelectrochemical performance regarding water oxidation was investigated. Results in comparison with the results of the photoelectrochemical investigations of the non-optimized WO_3 thin films are shown in Figure 10-20. As shown in Figure 10-20a and summarized in Table 10-7, the photocurrents of the optimized WO_3 thin film photoanodes are enhanced in comparison with the non-optimized WO_3 photoanodes accounting for 0.47 mA/cm² in frontside illumination and 0.86 mA/cm² in backside illumination at an applied potential of 1.23 V vs RHE, respectively. This probably results from the interplay of slightly enhanced light absorption properties and the improved FTO/WO_3 interface. Photocurrents obtained in frontside illumination are remarkably improved by a factor of ~8 for the optimized WO_3 thin films which most probably is a consequence of the dense, barely porous thin film morphology and the reduced number of grain and particle boundaries in the migration pathway of the photo-generated charge carriers, respectively. As can be seen in Figure 10-20b, the j-V curves obtained in light on/off mode show the same trend. Independent of the illumination direction, photocurrents of the optimized WO_3 thin films are higher. Additionally, only small spikes and overshoots at lower potentials (0.75 – 1.00 V) are observed for both WO_3 photoanodes. At higher potentials no significant spikes and overshoots can be traced. This is further confirmed by having a closer look at the photocurrent transients shown in Figure 10-20c. No spikes and overshoots can be traced which proves surface recombination to be negligible. This nearly ideal photoresponse can be assigned to the possibility of the incomplete water oxidation to peroxide species, a competing reaction to water oxidation to O_2, which is kinetically favored. This has been reported in literature[178,208,209] and was explained in a previous section of this chapter (see chapter 10.1). To verify this, quantitative O_2 detection measurements would be desirable.

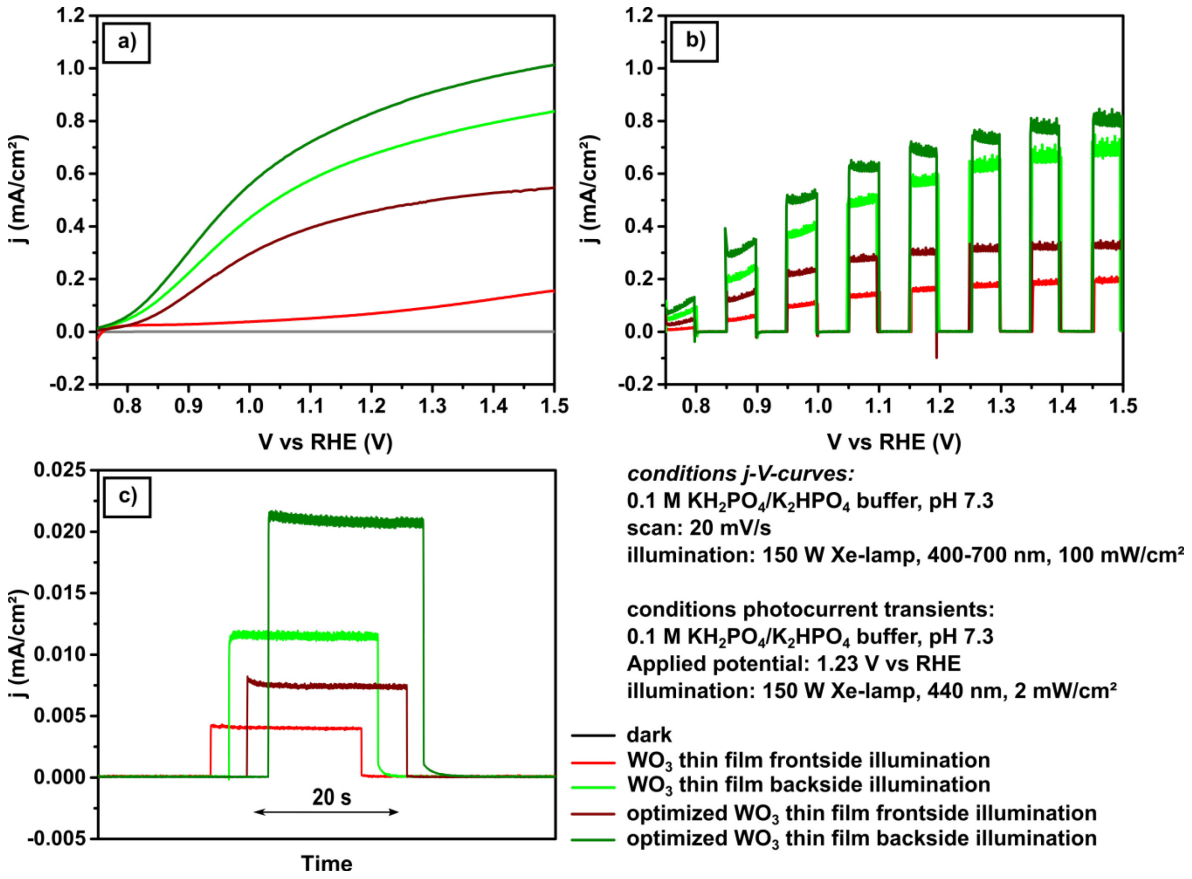

Figure 10-20. Comparison of photoelectrochemical performance of WO_3 thin films before and after optimization. a) j-V curves obtained in frontside and backside illumination, b) j-V-curves in light on/off mode obtained in frontside and backside illumination and c) photocurrent transient measurements obtained in frontside and backside illumination.

Table 10-7. Summarizing comparison of yielded photocurrents at 1.23 V vs RHE of the optimized and non-optimized WO_3 thin films in frontside and backside illumination.

	j at 1.23 V vs RHE (mA/cm²)	
	Frontside illumination	Backside illumination
optimized WO_3 thin film	0.47	0.86
WO_3 thin film (non-optimized)	0.08	0.70

Finally, Mott-Schottky-type PEIS measurements were carried out for the optimized WO_3 thin films. As shown in Figure 10-21a, extrapolation of the linear part of the graphs reveals nearly the same flat band potential for both applied frequencies which proves the results to be reliable. Flat band potentials of 0.35 V vs RHE and 0.32 V vs RHE could be determined for applied frequencies of 500 Hz and 1 kHz, respectively. These results are in excellent agreement with the flat band potentials determined for the non-optimized WO_3 thin film photoanodes (0.35 V vs RHE at 500 Hz and 0.32 V vs RHE at 1 kHz). As shown in Figure 10-21b, the slope of the Mott-Schottky-plot of the optimized WO_3 photoanodes is much smaller compared to the non-optimized WO_3 thin film. Generally, a lowered slope of the linear region of the Mott-Schottky plot is assigned to a higher number of free charge carriers within the electrode material. However, as there is no compositional change in both photoanode materials (no doping or the like) there also should not be a change in the intrinsic number of free charge carriers. Hence, the lower slope of the Mott-Schottky-plot most probably has its origin in the improved substrate coverage of the optimized WO_3 thin film and the denser thin film character which leads to a higher number of electrochemically addressable free charge carriers.

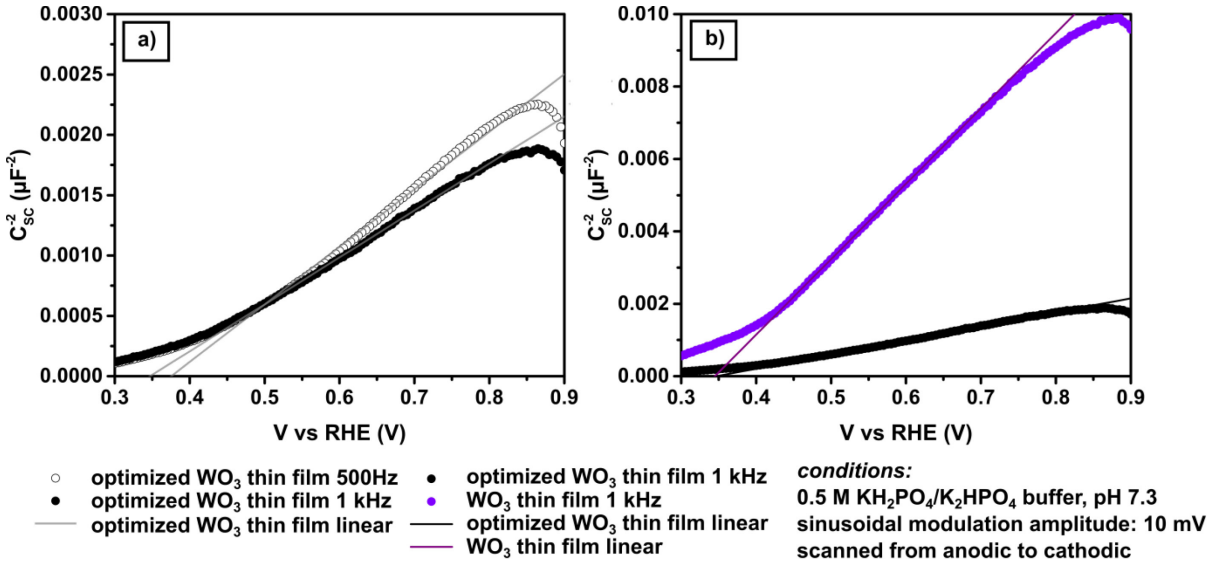

Figure 10-21. a) Mott-Schottky-Plot of the optimized WO_3 thin film photoanodes at frequencies of 500 Hz and 1 kHz and b) comparison of Mott-Schottky-plots of optimized and non-optimized WO_3 thin film photoanodes obtained at a frequency of 1 kHz.

To summarize briefly, the adjustment of the synthesis parameters of the WO_3 thin film deposition has a remarkable influence on the thin film properties. Whereas crystal structure (XRD) and composition (EDX) remain unaffected, the morphology and the (photo-)electrochemical properties of the WO_3 thin films have improved significantly. The FTO substrate is covered homogeneously by the optimized WO_3 thin film, only exhibiting very few voids. The particles of the optimized WO_3 thin films are smaller but very well connected with each other resulting in a homogeneous, continuous WO_3 layer. By reduction of the thin film thickness it was ensured that the WO_3 thin films do not exfoliate. Moreover, the smaller film thickness affects that the whole thin film is comprised of a monolayer of particles. Moreover, by TEM/SAED investigations it was shown that the single WO_3 particles exhibit single-crystalline character. (Photo-)electrochemical investigations of the optimized WO_3 thin films revealed significant improvement of the photoelectrochemical properties. In the following section the optimized WO_3 thin films on FTO substrate are applied in the FTO/WO_3/$BiVO_4$ and FTO/WO_3/Mo:$BiVO_4$ composite electrode system.

10.4.3. Application of optimized WO_3 thin films in WO_3/$BiVO_4$ composite electrodes

The optimized WO_3 thin films on FTO were used as substrates for $BiVO_4$ and Mo:$BiVO_4$ deposition. The parameters for this synthesis step were kept constant except for a small amount of F127 polymer added to the Bi, V and Mo containing synthesis solutions in order to increase wetting of the WO_3 thin film by the $BiVO_4$ synthesis solution.

The influence of the adjustments of the synthesis parameters on the crystal structure of the compartments of the composite photoanodes was investigated. Exemplarily for all synthesized composite electrodes a WO_3/$BiVO_4$ photoanode was investigated by GI-XRD. Resulting diffraction pattern is shown in Figure 10-22. All reflections can either be assigned to monoclinic γ-WO_3 or to monoclinic scheelite $BiVO_4$. As already mentioned in section 10.4.2, the preferred orientation of the WO_3 thin films on the FTO substrate remains after optimization of the synthesis parameters. The $BiVO_4$ thin film is revealed to be isotropic and polycrystalline. The change of the synthesis parameters does not have any influence on the crystal structure of the WO_3 or $BiVO_4$ compartments of the composite

electrode. (Note: The reflections of the WO_3 thin film are by far less pronounced than the reflections of the $BiVO_4$ layer which is a consequence of the incidence angle of the x-ray beam chosen to avoid reflections of the FTO substrate.)

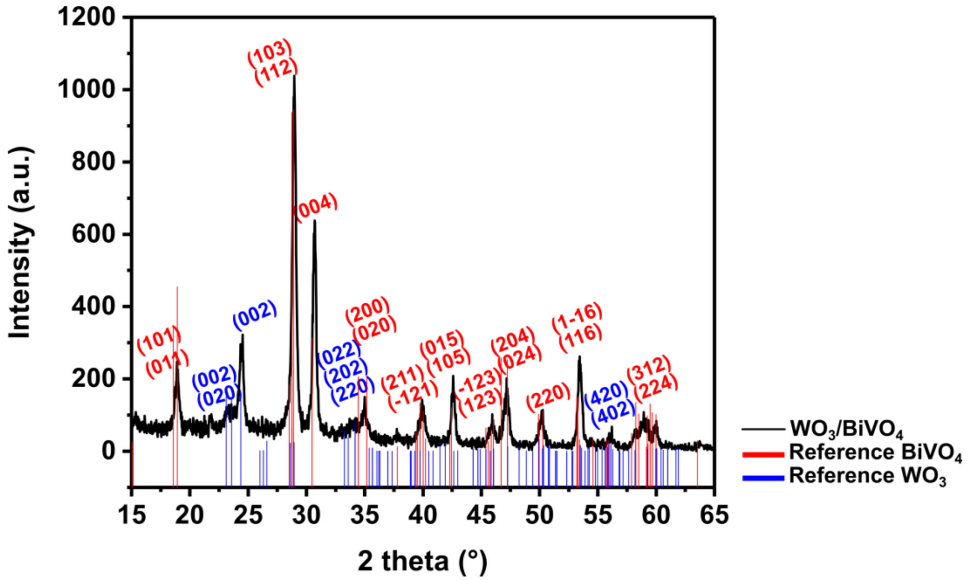

Figure 10-22. XRD pattern (gracing incidence) of optimized $WO_3/BiVO_4$ thin film on FTO substrate along with reference reflections acc. to JCPDS 71-2141 (γ-WO_3) and PDF 01-083-1698 ($BiVO_4$, monoclinic scheelite phase).

Light absorption properties of the optimized $WO_3/BiVO_4$ and WO_3/Mo:$BiVO_4$ composite electrodes were investigated by UV/Vis spectroscopy. Figure 10-23a shows a comparison between the non-optimized and optimized WO_3/5% Mo:$BiVO_4$ composite electrode along with the spectra of the WO_3 and 5% Mo:$BiVO_4$ single layers on FTO. The light absorption of the optimized composite electrode is very slightly enhanced compared to its non-optimized counterpart. This most probably is a consequence of the slightly enhanced light absorption of the optimized WO_3 thin film contributing to the overall absorbance of the WO_3/5% Mo:$BiVO_4$ composite electrode. Figure 10-23b shows a comparison of the light absorption properties of the $WO_3/BiVO_4$ and WO_3/Mo:$BiVO_4$ composite electrodes. The $WO_3/BiVO_4$, WO_3/5%Mo:$BiVO_4$ and WO_3/10% Mo:$BiVO_4$ electrodes show very similar absorption properties. Absorbances of the WO_3/15% Mo:$BiVO_4$ and WO_3/20% Mo:$BiVO_4$

are increased which probably is a result of enhanced light scattering because of bigger Mo:$BiVO_4$ compartments at higher Mo contents.

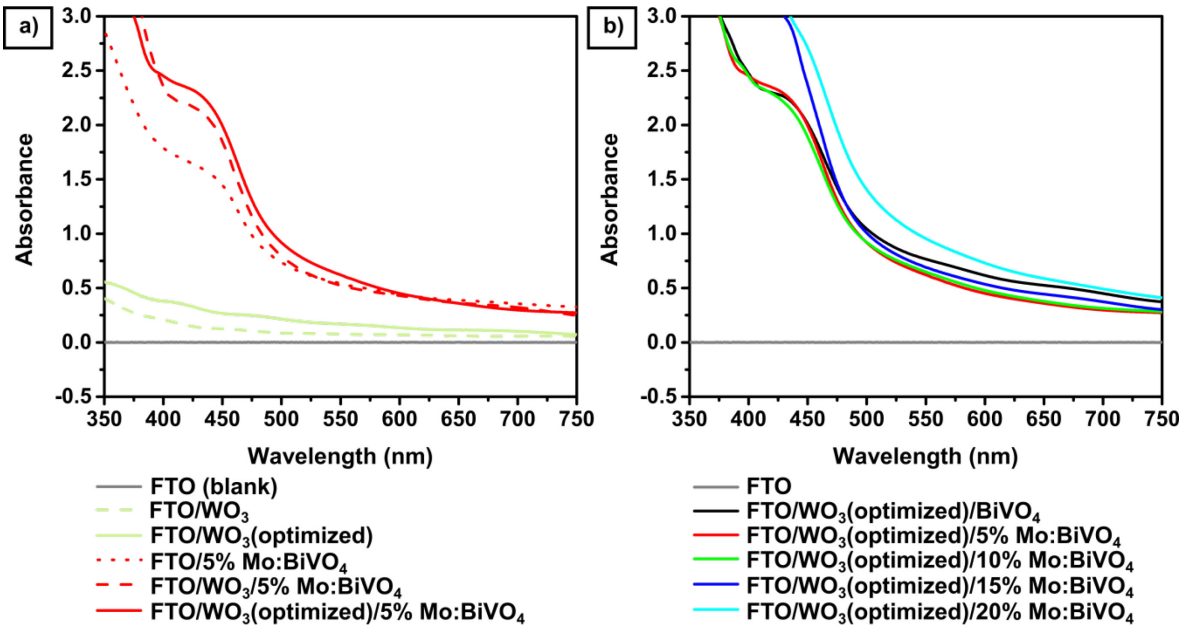

Figure 10-23. UV/Vis spectra of optimized composite electrodes. a) comparison of optimized and non-optimized WO_3/5% Mo:$BiVO_4$ composite electrodes along with single layer spectra of WO_3 and 5% Mo:$BiVO_4$ and b) comparison of UV/Vis spectra of all optimized WO_3/$BiVO_4$ and WO_3/Mo:$BiVO_4$ composite electrodes.

The morphology of the optimized WO_3/$BiVO_4$ and WO_3/Mo:$BiVO_4$ electrodes was investigated by SEM. Top view and cross section images are shown in Figure 10-24. The $BiVO_4$ and Mo:$BiVO_4$ layers of the composite electrodes again exhibit the typical domain-like morphology. Morphological features of the thin films are significantly different to $BiVO_4$ and Mo:$BiVO_4$ single layers on FTO. However, they are quiet similar to the previously described non-optimized composite electrode analogues (see chapter 10.3). For the optimized WO_3/$BiVO_4$ composite electrode an average domain size of 7.4 ±2.3 µm² and an average inner domain material streak size of 121 ±21 nm were determined. Same trend of decreasing average domain sizes and increasing average inner material streak sizes was observed for the WO_3/Mo:$BiVO_4$ electrodes. Average domain sizes of 6.7 ±2.6 µm², 5.0 ±3.0 µm² and 4.2 ±2.1 µm² for the WO_3/5% Mo:$BiVO_4$, WO_3/10% Mo:$BiVO_4$, and

WO_3/15% Mo:$BiVO_4$ composite electrodes were determined. Due to advanced sintering it is not possible to distinguish between single domains for the WO_3/20% Mo:$BiVO_4$ electrode. An average inner domain material streak size of 176 ±45 nm was determined for the WO_3/5% Mo:$BiVO_4$ sample. Inner domain material streaks sizes are increasing with increasing Mo content accounting for 201 ±51 nm for the WO_3/20% Mo:$BiVO_4$ electrode. An overview of all analyzed $BiVO_4$ thin film features of the optimized WO_3/$BiVO_4$ and WO_3/Mo:$BiVO_4$ composite electrodes is given in Table 10-8 along with similar analyzed features for the non-optimized counterparts for comparison.

By the cross section images a reproducible WO_3 layer thickness of ~108 ±4 nm is revealed for all samples. The average layer thickness and its standard deviation is somewhat bigger for the $BiVO_4$ and the Mo:$BiVO_4$ layers accounting for 147 ±15 nm. Additionally, the cross section images reveal a very homogeneous coverage of the rough FTO surface by the WO_3 layer resulting in an impressive reduction of voids at the interface. Furthermore, the WO_3 surface is noticeably flat compared to the non-optimized WO_3 surface (see chapter 10.3, Figure 10-14). For this reason it can be evenly wetted by the $BiVO_4$ and Mo:$BiVO_4$ synthesis solutions, respectively, leading to a remarkable reduction of voids at the interface between the WO_3 layer and the $BiVO_4$ and or Mo:$BiVO_4$ layer, respectively.

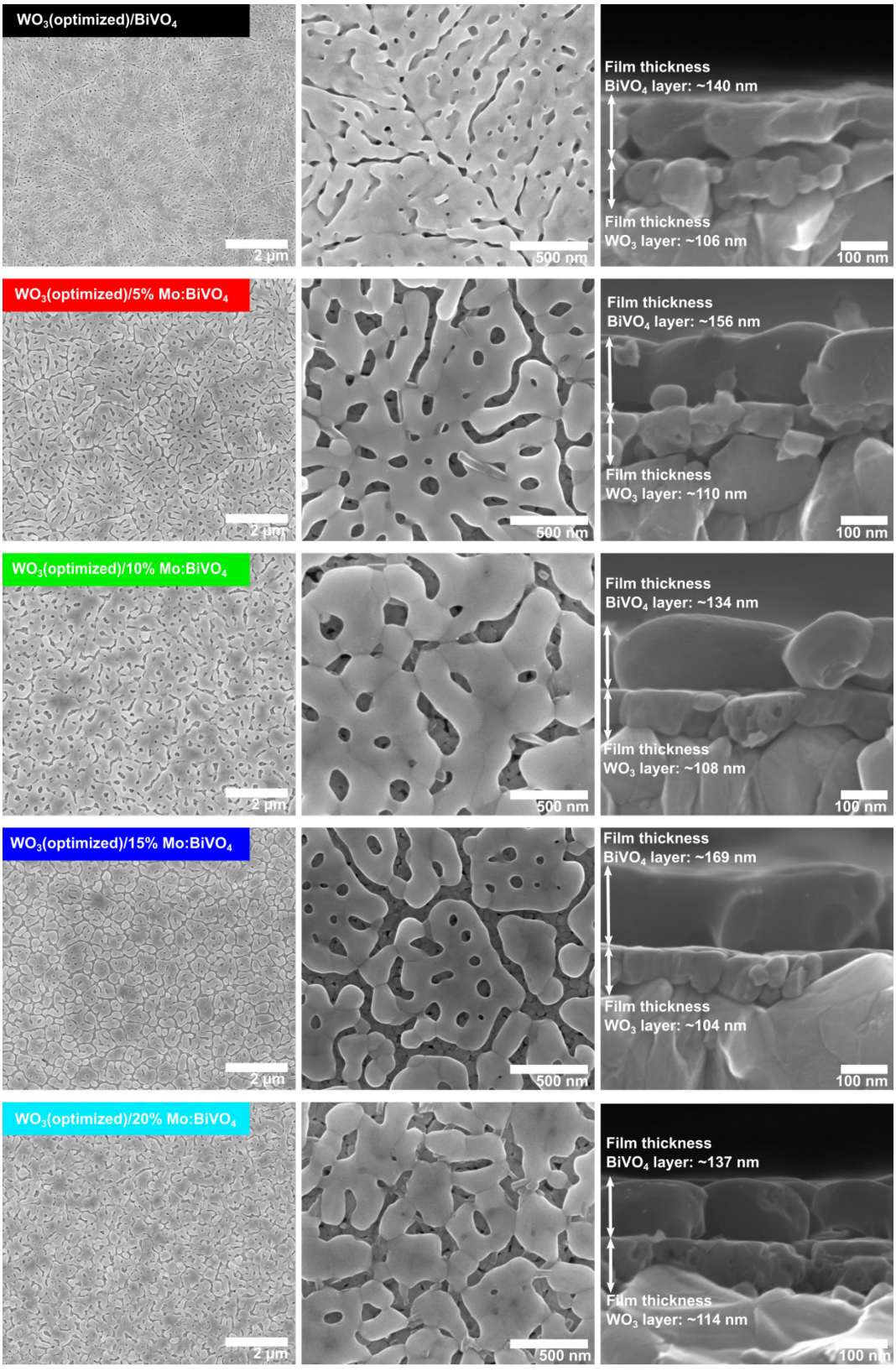

Figure 10-24. SEM investigations (top view and cross section images) of the optimized $WO_3/BiVO_4$ and WO_3/Mo:$BiVO_4$ composite electrodes on FTO substrate.

Table 10-8. Overview on analyzed morphology features of the $BiVO_4$ and Mo:$BiVO_4$ layers of the optimized and non-optimized composite electrodes.

	Optimized composite electrodes		Non-optimized composite electrodes	
Sample	Average domain size (µm²)	Average inner domain material streak size (nm)	Average domain size (µm²)	Average inner domain material streak size (nm)
$WO_3/BiVO_4$	7.4 ±2.3	121 ±21	7.0 ±2.8	131 ±19
WO_3/5% Mo:$BiVO_4$	6.7 ±2.6	176 ±45	6.7 ±3.7	186 ±76
WO_3/10% Mo:$BiVO_4$	5.0 ±3.0	181 ±51	4.4 ±2.7	190 ±51
WO_3/15% Mo:$BiVO_4$	4.2 ±2.1	193 ±66	4.1 ±1.5	203 ±84
WO_3/20% Mo:$BiVO_4$	--	201 ±51	--	207 ±74

To have a closer look at the microstructure of the optimized composite electrodes HR-TEM and SAED analysis were applied. Representative for all samples, the $WO_3/BiVO_4$ composite electrode was investigated by means of TEM. Results are shown in Figure 10-25. As can be seen by the overview image (Figure 10-25a) the general composition of the composite electrode in terms of small WO_3 compartments covered by a large $BiVO_4$ domain can be confirmed by TEM investigations. This is further proved by HR-TEM investigations and corresponding FFT analysis (Figure 10-25c). The high degree of crystallinity of the single layers of the composite electrode results in various lattice fringes which can be analyzed by FFT. The FFT pattern obtained at a bright spot of the image (surrounded in red) reveals only one set of signals which can be assigned to the (011) plane of the $BiVO_4$ layer. The FFT pattern received by analyzing the lattice fringes at a darker spot of the image (surrounded in green) reveals three different signals which can either be assigned to the (011) plane of the $BiVO_4$ layer or to the (022) and (002) planes of the WO_3 layer.

The single-crystalline character of the WO_3 flakes/particles and the $BiVO_4$ domains is further confirmed by TEM/SAED analysis shown in Figure 10-25b. The diffraction pattern obtained by selecting a small and thin material area indexed in Figure 10-25a mainly consists of two overlaid dot patterns. One set of reflections can be assigned to the (011) and the (101) planes of the $BiVO_4$ layer. Another part of the dot pattern matches the d-spacing of the (032) and the (112) planes of the WO_3 layer. These findings confirm the single-

crystalline character of the WO_3 and $BiVO_4$ thin film compartments (see chapter 8.2.2 and 10.4.2) of the composite electrodes.

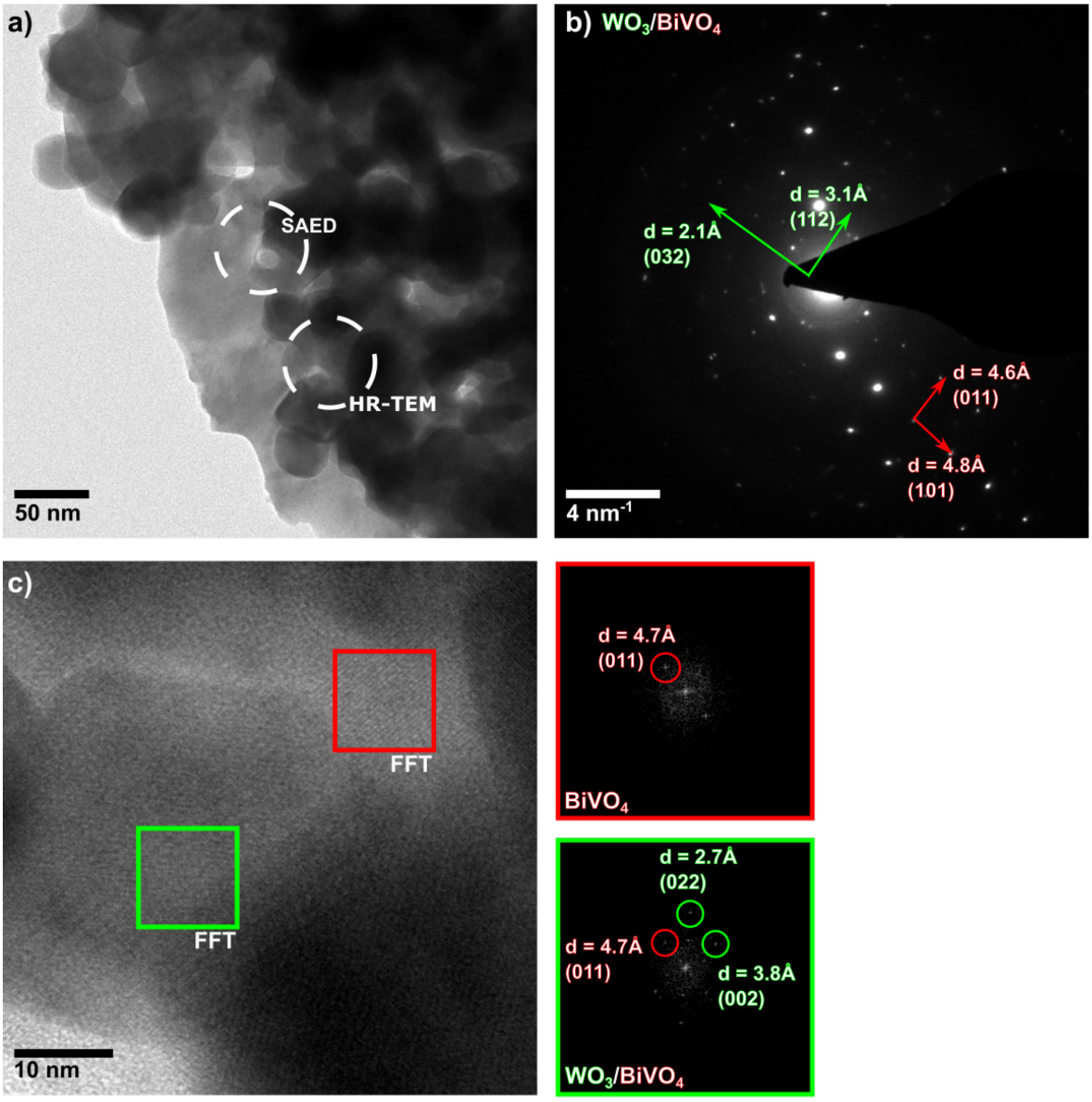

Figure 10-25. TEM investigations of an optimized $WO_3/BiVO_4$ composite electrode. a) overview image, b) corresponding SAED pattern and c) HR-TEM image with corresponding FFT patterns.

The influence of the optimized design of the $WO_3/BiVO_4$ and WO_3/Mo:$BiVO_4$ composite electrodes on the photoelectrochemical performance regarding water oxidation was investigated. Figure 10-26 shows j-V curves of the optimized composite electrodes in frontside and backside illumination (illumination of white light, 400-700 nm at an intentsity of 100 mW/cm²) with and without a layer of CoPi water oxidation catalyst deposited onto the surface. Table 10-9 provides an overview of the yielded photocurrents at an applied potential of 1.23 V vs RHE. Comparative j-V-curves of all single samples are given in the Appendix, chapter 12.1.4.2.

Without CoPi water oxidation catalyst comparable photocurrents of ~3.80 mA/cm² at a potential of 1.23 V vs RHE were obtained for all samples in frontside illumination. Highest photocurrent accounting for 3.91 mA/cm² at 1.23 V vs RHE was observed for the WO_3/10% Mo:$BiVO_4$ electrode. When backside illumination was used, higher photocurrents were yielded accounting for 3.44 mA/cm² for the WO_3/20% Mo:$BiVO_4$ electrode up to the highest photocurrent of 5.08 mA/cm² for the $WO_3/BiVO_4$ sample, both values given for an applied potential of 1.23 V vs RHE.

These findings can be connected to the materials properties of the $BiVO_4$ and Mo:$BiVO_4$ layer of the composite electrode. Generally, the observed photocurrents for the composite electrodes are much higher than for single layer electrodes on FTO. This proves the strong positive effect of the creation of the $WO_3/BiVO_4$ and WO_3/Mo:$BiVO_4$ heterojunction on the separation of photo-generated charge carriers and yielded photocurrents, respectively. Regarding the $WO_3/BiVO_4$ electrode photocurrents yielded in backside illumination are significantly higher than corresponding measurements in frontside illumination. That makes sense as the $BiVO_4$ layer thickness of ~140 nm exceeds the hole diffusion length of 70-100 nm[22,74,75] of the material. Without improvement of the electron transport properties of the material, bulk recombination limits the photoelectrochemical performance in frontside illumination. Hence, backside illumination yields higher photocurrents as the electron-hole pairs are excited only short distance apart from the well-conductive WO_3 backcontact. Enhancing electron transport properties by Mo-doping of the $BiVO_4$ layer of the composite electrode results in comparable photocurrents obtained in frontside and backside illumination. However, yielded photocurrents for all WO_3/Mo:$BiVO_4$ composite

electrodes are lower than for the undoped analogue, basically for two reasons: i) the inner domain material streak size and film thickness of the Mo:$BiVO_4$ layers exceed the hole diffusion length of $BiVO_4$ by far and ii) according to the potential energy diagram shown in chapter 10.3, Figure 10-9, the electron withdrawal is the strongest for the junction between WO_3 and the undoped $BiVO_4$ because of the biggest difference in the potential energies of the materials' conduction bands. Optimization of the composite electrode design results in better interfacial contact between WO_3 and $BiVO_4$ layers allowing the heterojunctions electron withdrawal effect to be more powerful.

Depositing a thin layer of CoPi water oxidation catalyst improves water oxidation kinetics at the $BiVO_4$ surface and therefore further enhances yielded photocurrents. Same trends of yielded photocurrents are observed for the CoPi modified composite electrodes. In frontside illumination for WO_3/10% Mo:$BiVO_4$ composite electrode the highest photocurrents accounting for 5.70 mA/cm² at 1.23 V vs RHE are obtained. When backside illumination is used the WO_3/$BiVO_4$ composite electrode yields highest photocurrents accounting for 6.77 mA/cm² at 1.23 V vs RHE – a value which is in line with the highest values published by Pihosh et al. for a highly developed WO_3/$BiVO_4$ heterojunction comprised of WO_3 nanorods coated by a ultrathin layer of $BiVO_4$.[35]

Table 10-9. Summary of yielded photocurrents at 1.23 V vs RHE in frontside and backside illumination with and without a layer of CoPi for the optimized WO_3/$BiVO_4$ and WO_3/Mo:$BiVO_4$ composite electrodes.

Sample	j at 1.23 V vs RHE (mA/cm²)			
All samples after optimization of the electrode design	without CoPi		with CoPi	
	frontside illumination	backside illumination	frontside illumination	backside illumination
WO_3/$BiVO_4$	3.87	5.08	5.43	6.77
WO_3/5% Mo:$BiVO_4$	3.88	4.45	4.77	6.31
WO_3/10% Mo:$BiVO_4$	3.91	3.88	5.70	6.25
WO_3/15% Mo:$BiVO_4$	3.80	4.18	5.04	6.37
WO_3/20% Mo:$BiVO_4$	3.70	3.44	5.30	4.57

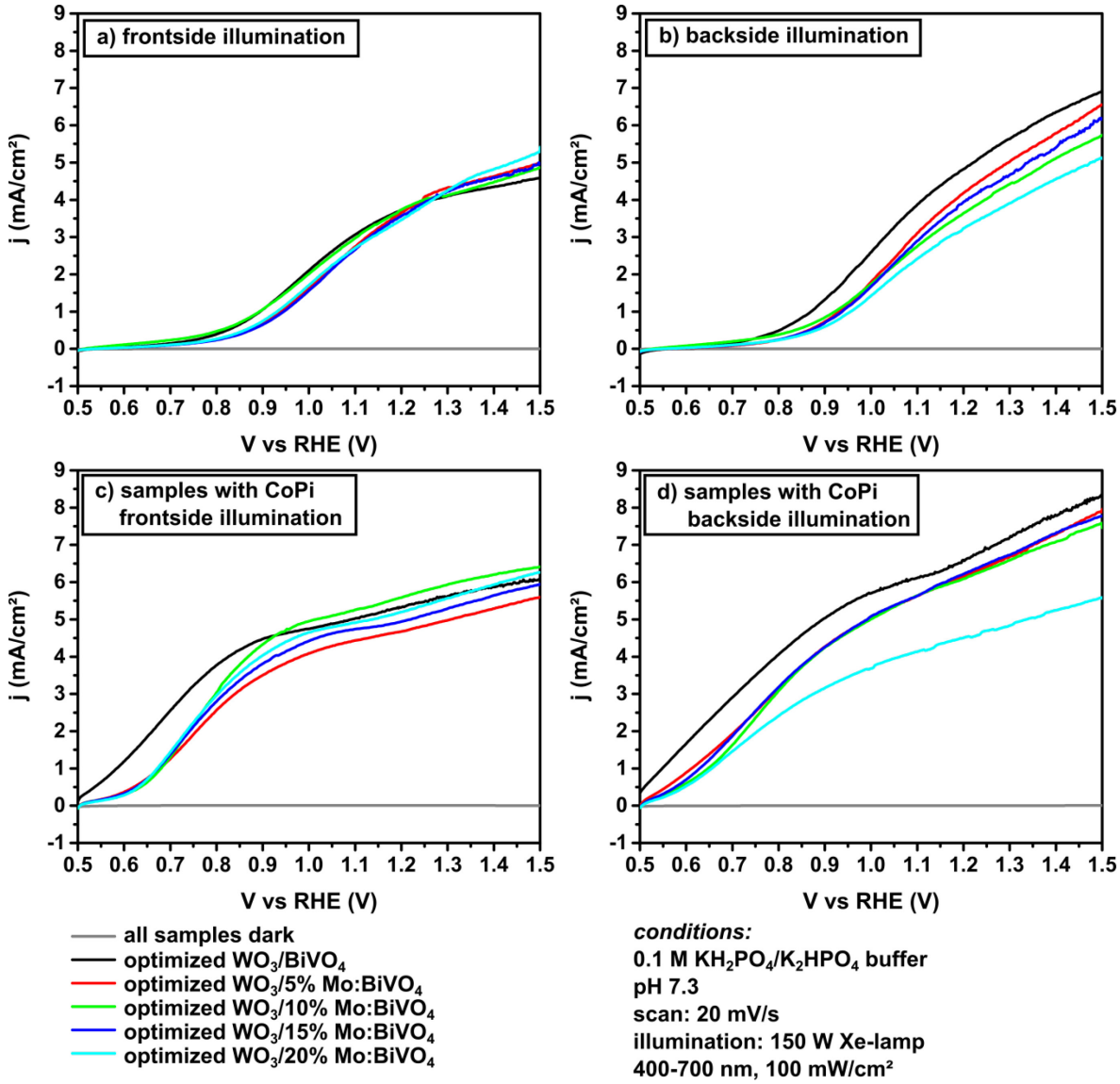

Figure 10-26. j-V curves of optimized $WO_3/BiVO_4$ and WO_3/Mo:$BiVO_4$ composite electrodes in frontside and backside illumination with and without CoPi deposited onto the surface.

To further investigate the origin of the tremendous photoelectrochemical performance of the composite electrodes regarding water oxidation, j-V measurements in light on/off mode and corresponding photocurrent transient measurements acquired at an applied potential of 1.23 V vs RHE were carried out. Exemplarily for all samples, results of the WO_3/10% Mo:$BiVO_4$ and the $WO_3/BiVO_4$ photoanodes, the two best performing electrodes in frontside and backside illumination, are shown in Figure 10-27. Results for the remaining samples are given in the Appendix, chapter 12.1.4.2.

In case of the undoped $BiVO_4$ material within the composite electrode j-V curves in light on/off mode reveal a nearly ideal electrode behavior when the light is switched on and off. Only very little spikes and overshoots can be observed up to applied voltages of ~1.0 V vs RHE. The near-ideal behavior is further confirmed by the photocurrent transient measurements. Only a very little decrease of photocurrent can be observed directly after switching the light on, independent of the CoPi deposition or illumination direction. This clearly indicates that surface recombination is not a severely limiting factor for the photoelectrochemical performance. Measurements of the photocurrent transients were carried out at low light intensities (2 mW/cm²). At low light intensities the photocurrents yielded with and without CoPi deposited onto the surface are comparable. This reveals the photoelectrochemical performance rather to be limited by the amount of surface-reaching holes whereas surface recombination becomes negligible. This finding is in good agreement with literature reports on the slow charge carrier transport properties of $BiVO_4$ being the bottleneck for its photoelectrochemical performance concerning water oxidation.[22,141]

In case of the WO_3/10% Mo:$BiVO_4$ composite electrode similar, nearly ideal electrode behavior is revealed by the j-V measurements in light on/off mode. Again only very little spikes and overshoots are observable at applied potentials up to ~1.0 V vs RHE. This is further confirmed by the photocurrent transient measurements for this electrode revealing only very low decrease of the yielded photocurrent directly after switching the light on. In contrast to the WO_3/$BiVO_4$ photoanode, the photoelectrochemical performance of the WO_3/10% Mo:$BiVO_4$ photoanode is strongly influenced by the deposition of CoPi for both illumination modes. Obtained photocurrents are enhanced significantly when CoPi was deposited onto the surface throughout the whole scanned potential range.

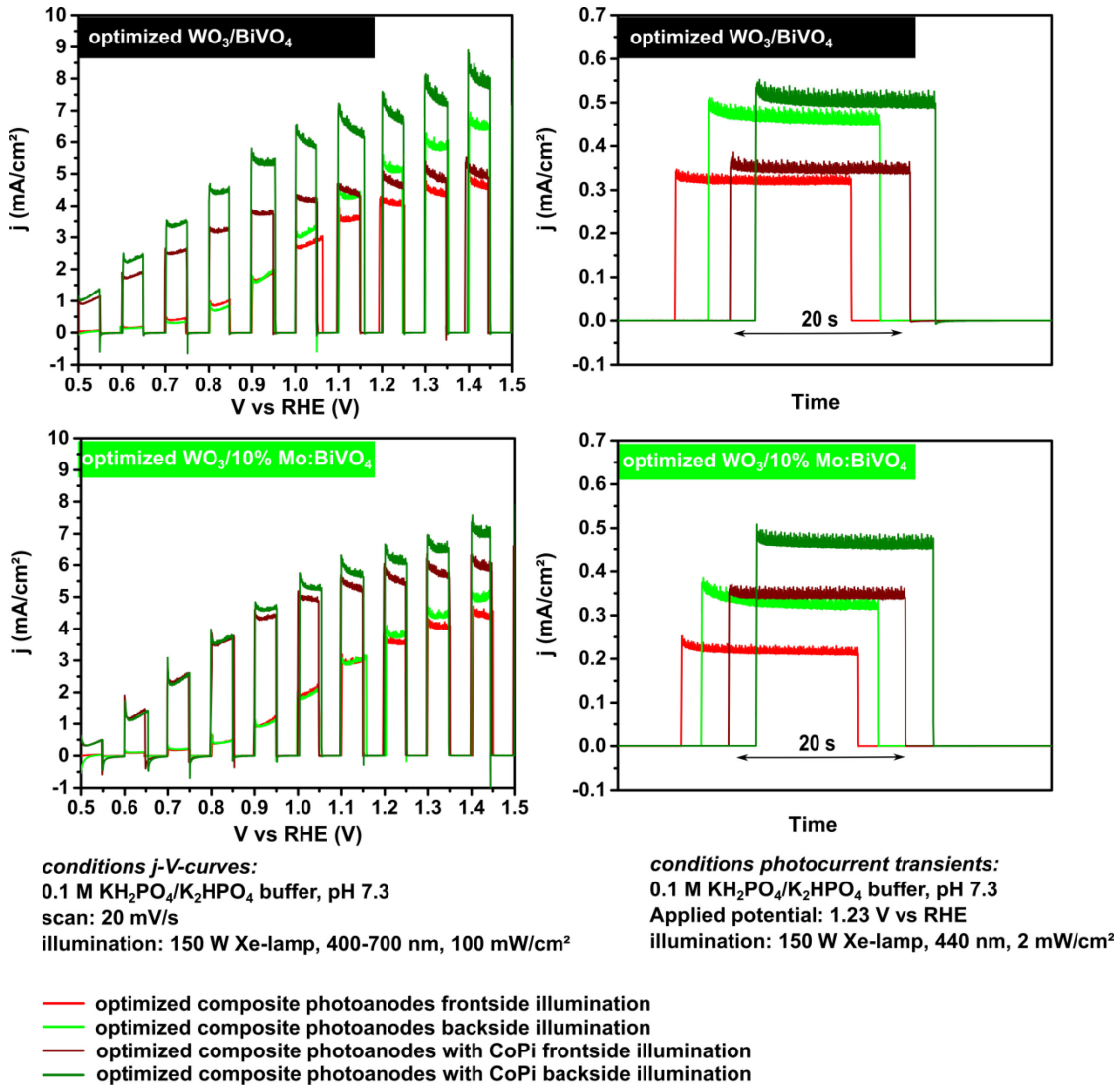

Figure 10-27. j-V curves and photocurrent transients of the $WO_3/BiVO_4$ and the WO_3/10% Mo:$BiVO_4$ composite electrodes. Measurements accomplished in frontside and backside illumination as well as with and without CoPi deposited.

As a consequence of the outstanding PEC performance and the near-ideal light response, very high ABPE is obtained for the composite electrodes. ABPE curves are shown in Figure 10-28; a summary of the ABPE maxima is given in Table 10-10. In accordance with the j-V curves, the $WO_3/BiVO_4$ composite electrode yields highest ABPE values of 1.63 % and 1.75 % in frontside and backside illumination; both maxima obtained at a potential of 0.81 V vs RHE.

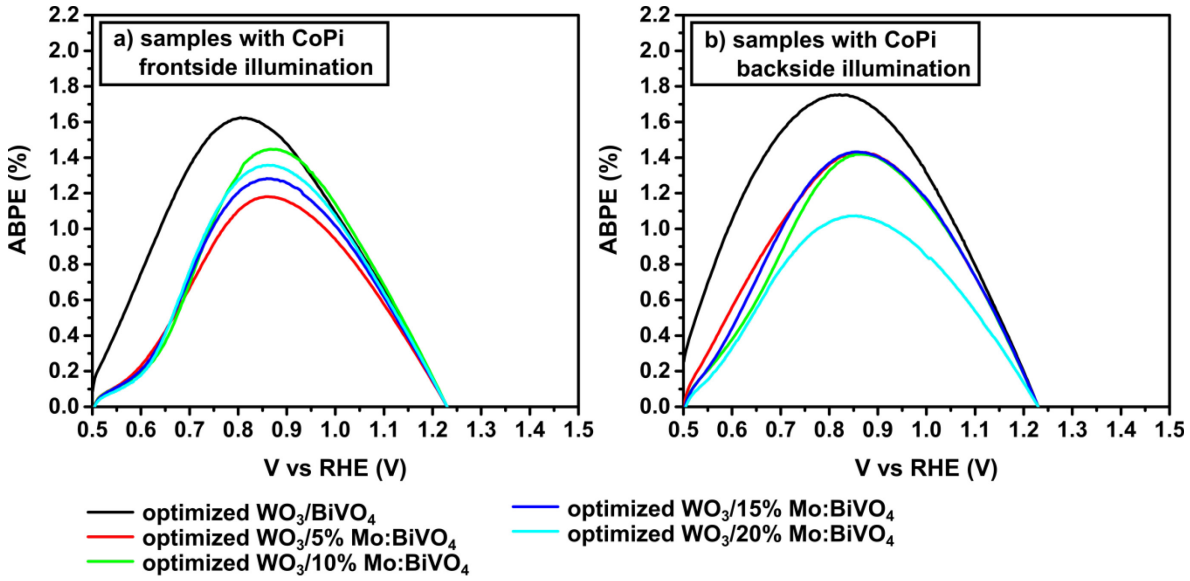

Figure 10-28. ABPE curves of the $WO_3/BiVO_4$ and the WO_3/ Mo:$BiVO_4$ composite electrodes with CoPi deposited in frontside and backside illumination. Curves were calculated based on j-V curves.

Table 10-10. Summary of ABPE maxima for $WO_3/BiVO_4$ and WO_3/Mo:$BiVO_4$ composite electrode.

Sample	ABPE maximum			
All samples after optimization of the electrode design	frontside illumination		backside illumination	
	V vs RHE (V)	ABPE (%)	V vs RHE (V)	ABPE (%)
$WO_3/BiVO_4$	0.81	1.63	0.81	1.75
WO_3/5% Mo:$BiVO_4$	0.85	1.18	0.86	1.43
WO_3/10% Mo:$BiVO_4$	0.87	1.45	0.86	1.42
WO_3/15% Mo:$BiVO_4$	0.86	1.28	0.86	1.43
WO_3/20% Mo:$BiVO_4$	0.86	1.36	0.85	1.07

Finally, the long-term stability of a CoPi decorated $WO_3/BiVO_4$ composite electrode was tested. Using a 3-electrode-configuration a potential of 1.2 V vs RHE was applied and the generated photocurrent was measured over a time period of 60 min. Results are shown in Figure 10-29. As can be seen, the initial photocurrent of about 5.5 mA/cm² decreases rapidly by half during the first 5 minutes. During the following 55 min the observed photocurrent is further decreased to only 1.2 mA/cm² after 60 min. The long-term decrease of the initial photocurrent is related to two factors: i) oxygen bubbles sticking to the electrode surface and therefore blocking it for further reaction with the electrolyte and ii) due to chemical instability of the $BiVO_4$ layer, corrosion occurs which degrades the photoelectrocatalytic activity of the photoanode.

This disadvantageous long-term behavior is known for $BiVO_4$-based photoanode systems. It is related to slow interfacial hole transfer kinetics which result in accumulation of holes at the $BiVO_4$ surface. The accumulated holes affect a destabilization of the $BiVO_4$ lattice. Unfortunately, predicted by computational methods, self-passivation by the formation of a chemically stable surface phase is kinetically hindered. That is the reason why protective layers need to be deposited onto the $BiVO_4$ surface to prevent it from chemical destabilization.[219,220]. Despite the use of ferrite-based compounds which not only act as protective layer but also enhance light absorption properties,[220,221] an auspicious research approach is the development of protective layers which also act as water oxidation catalyst like NiO_x-based compounds.[222,223] These topics are intensively investigated subjects of current research.

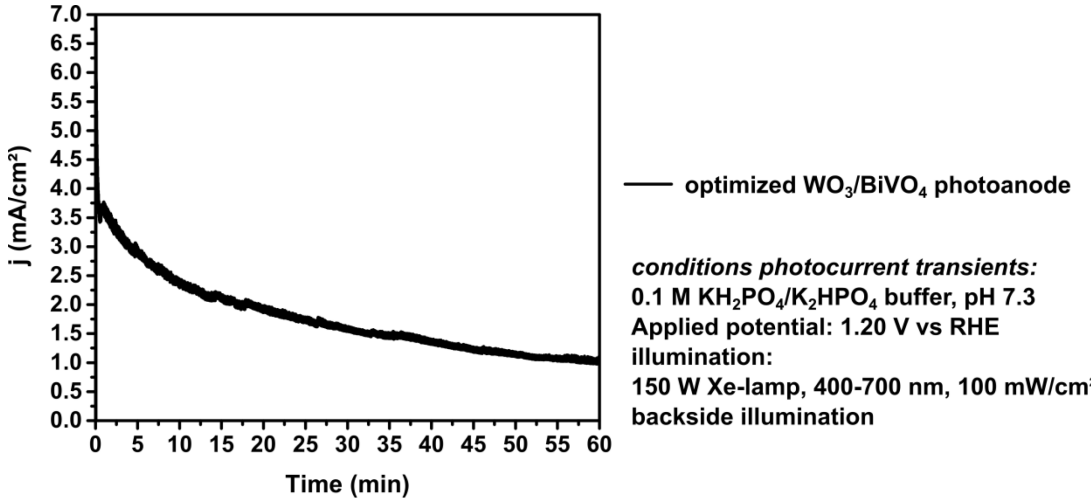

Figure 10-29. Long-term stabiltiy test of an optimized CoPi-decorated $WO_3/BiVO_4$ photoanode using a 3-electrode configuration.

10.4.4. Conclusion

In this chapter the application of the bottom-up synthesis approach for $BiVO_4$ and Mo:$BiVO_4$ thin films was applied to create a heterojunction $WO_3/BiVO_4$ thin film on FTO substrate. WO_3 thin films were fabricated by dip coating of FTO substrates with a WO_3 sol. After calcination FTO/WO_3 electrodes were used as substrates for further deposition of $BiVO_4$ and Mo:$BiVO_4$ thin films, respectively. Characterization and photoelectrochemical investigations of the as-prepared $WO_3/BiVO_4$ and WO_3/Mo:$BiVO_4$ proved the synthesis concept to be functioning. Maximum photocurrents of 5.41 mA/cm² at 1.23 V vs RHE were obtained for the WO_3/20% Mo:$BiVO_4$ sample. The yielded photocurrents are significantly higher than published values in literature for comparable photoanodes using the layered heterojunction electrode design. However, as the observed photoelectrochemical performance did not keep up with state-of-the-art $WO_3/BiVO_4$ photoanodes following the $BiVO_4$-coated WO_3 nanorod design scheme, optimization of the synthesis parameters and the photoanode design, respectively, was necessary.

The coverage of the FTO by the WO_3 layer was improved significantly, resulting in turn in a plane WO_3 surface which then again leads to improved wetting of the WO_3 layer by the

$BiVO_4$ and Mo:$BiVO_4$ synthesis solutions. The homogeneous coverage of each layer affects a tremendous reduction of voids and missing contact at the interfaces between the single layers and the substrate. As a consequence, photoelectrochemical performance regarding water oxidation was dramatically improved. Yielding photocurrents as high as 6.77 mA/cm² at 1.23 V vs RHE the optimized WO_3/$BiVO_4$ photoanode is able to compete with the highest reported value so far of 6.71 mA/cm² at 1.23 V vs RHE by Pihosh et al.[35]

These findings impressively show that the simple, robust and scalable method of dip coating an FTO substrate twice, first with WO_3 and second with $BiVO_4$, is a useful tool to synthesize highly photoelectrocatalytically active composite electrodes. It was shown, that there is no urgent need for advanced nanostructuring of the photoanode in terms of 1D vertically aligned WO_3 nanorods covered by an ultrathin layer of $BiVO_4$. Future work should focus on improvement of long-term stability and on effective strategies to prevent the photoanode material from corrosion, respectively.

11. Conclusion and Outlook

The main drawback concerning $BiVO_4$-based photoanodes with respect to solar water splitting was figured out to be its poor electron transport properties. This main PEC performance-limiting factor was addressed in this thesis and different strategies were applied to overcome this problem.

Partial O/F substitution in $BiVO_4$ was investigated regarding its influence of the materials properties with respect to PEC water splitting. In cooperation with the solid state chemistry group of Prof. Dr. Lerch from TU Berlin, a clean and facile synthesis route to F-doped $BiVO_4$ was developed. In addition to the extensive chemical and structural characterization of the powder samples, the (photo-)electrochemical characterization was enabled by the development of a straight-forward fabrication method for photoanodes out of the pre-synthesized powder samples which is comprised of an electrophoretic deposition method followed by heat treatment. With the $BiVO_4$ and F:$BiVO_4$ photoanodes in hands, it could be shown, that F-doping enhances the overall PEC performance expressed by higher photocurrents compared to undoped $BiVO_4$. Despite the smaller band gap of the F-doped $BiVO_4$ sample, the higher PEC performance could be assigned to a drastically enhanced number of free charge carriers as revealed by Mott-Schottky-type PEIS and to reduced surface recombination of photo-generated charge carriers. It is concluded, that anion doping is a viable tool for band gap engineering of semiconductors. Hence, also photoelectrochemical performance can be enhanced. Future investigations should focus on a deeper understanding of the impacts of partial O/F substitution in $BiVO_4$. The theoretical chemistry group of Prof. Dr. Bredow currently focusses on DFT-based calculations of F-doped $BiVO_4$ with respect to PEC water splitting. Another subject of interest could be the substitution of oxygen by other halogens as for example recently shown by Wang et al. who synthesized Br-doped TiO_2 which improved its PEC performances.[224]

Improvement of the design of the $BiVO_4$-based photoanodes was addressed by the development of a new bottom-up synthesis approach starting from molecular precursors and processing thin film electrodes by dip coating and subsequent calcination. This method allowed fine-tuning of nearly all electrode properties. Choosing suitable metal-organic precursors and implementing molybdenum as cationic n-type dopants, the Mo:$BiVO_4$ thin film photoanodes crystallized in differently sized, single-crystalline domains. Consequently, PEC performance regarding water oxidation was considerably improved, resulting in tremendous photocurrents, which were highest ever reported for doped $BiVO_4$-photoanodes in combination with CoPi water oxidation catalyst at that time. With this powerful synthesis method in hand, future investigations should basically focus two different aspects: i) application of the developed synthesis strategy to other electrode materials suffering from slow electron transport properties, e.g. MoS,[225] and ii) further improvement of the electrode design in terms of doping and orientation of the single-crystalline domains. As already demonstrated, PEC performance of $BiVO_4$ thin film photoanodes can be further improved by co-doping with Mo and F. As reported in literature and already predicted by preliminary results, cation co-doping also is a powerful tool to further improve the PEC performance of Mo:$BiVO_4$-based photoanodes.[226] Niobium and tantalum were revealed to be suitable candidates. For this purpose, adjustment of the synthesis route is necessary. Additionally, it was shown by several groups that different facets exhibit different properties concerning charge carrier separation and photoelectrochemical water oxidation.[227–232] Hence, gaining control of the orientation of the single-crystalline domains is another subject of prospective investigations. For instance, this could be achieved by depositing crystallization grains onto the FTO substrate prior to dip coating and calcination.

Finally, the usage of $BiVO_4$ and Mo:$BiVO_4$ thin films in combination with optimized sol-gel-based WO_3 thin films forming a staggered-type semiconductor heterojunction resulted in extraordinary photoelectrochemical performance. Obtained maximum photocurrents of 6.77 mA/cm² at an applied potential of 1.23 V vs RHE have not been reported for simple layered WO_3/$BiVO_4$ photoanodes, but only for highly sophisticated nanostructured pendants. These photocurrent represents already 92 % of the maximum photocurrent of 7.4 mA/cm² calculated on the basis of a possible solar-to-hydrogen efficiency of 9.1 % for

$BiVO_4$. Future investigations may focus the application of these heterojunction electrodes in a tandem-cell in combination with an efficient photocathode driving the water reduction reaction for efficient unbiased water splitting or for instance in combination with photovoltaics which provide external bias. Furthermore, as impressively shown by van de Krol and Lee,[233] combination of the efficient $WO_3/BiVO_4$ heterojunctions with a parallel-connected photoanode which absorbs the lower energetic range of the solar spectrum is an interesting point to start from for prospective investigations.

12. Appendix

12.1. Supplementary data

12.1.1. Supplementary data for chapter 7: Fluorine-doped $BiVO_4$

12.1.1.1. PEC investigations of $BiVO_4$ and F:$BiVO_4$ EPD electrodes.

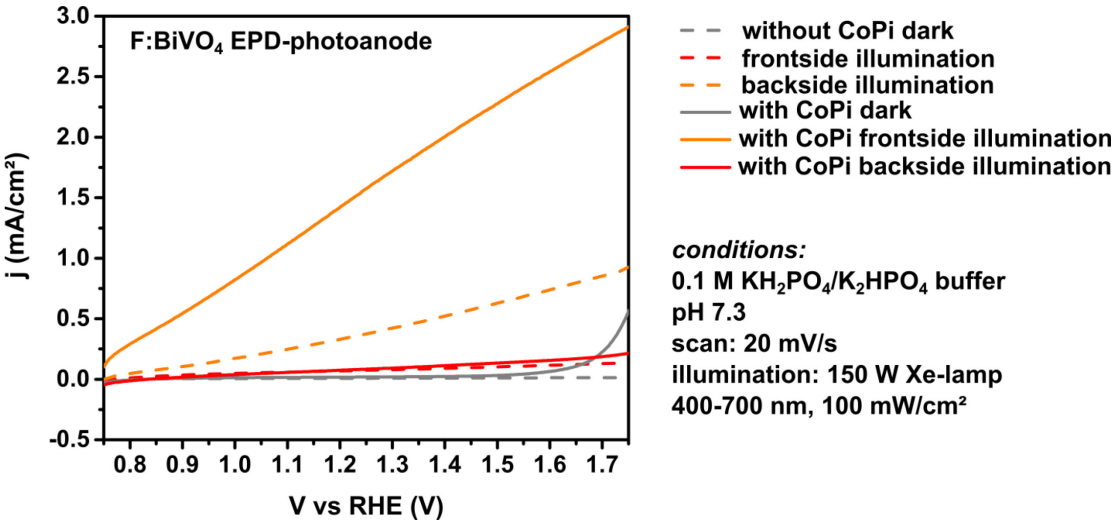

Figure 12-1. j-V curves of an F:$BiVO_4$ EPD electrode in frontside and backside illumination.

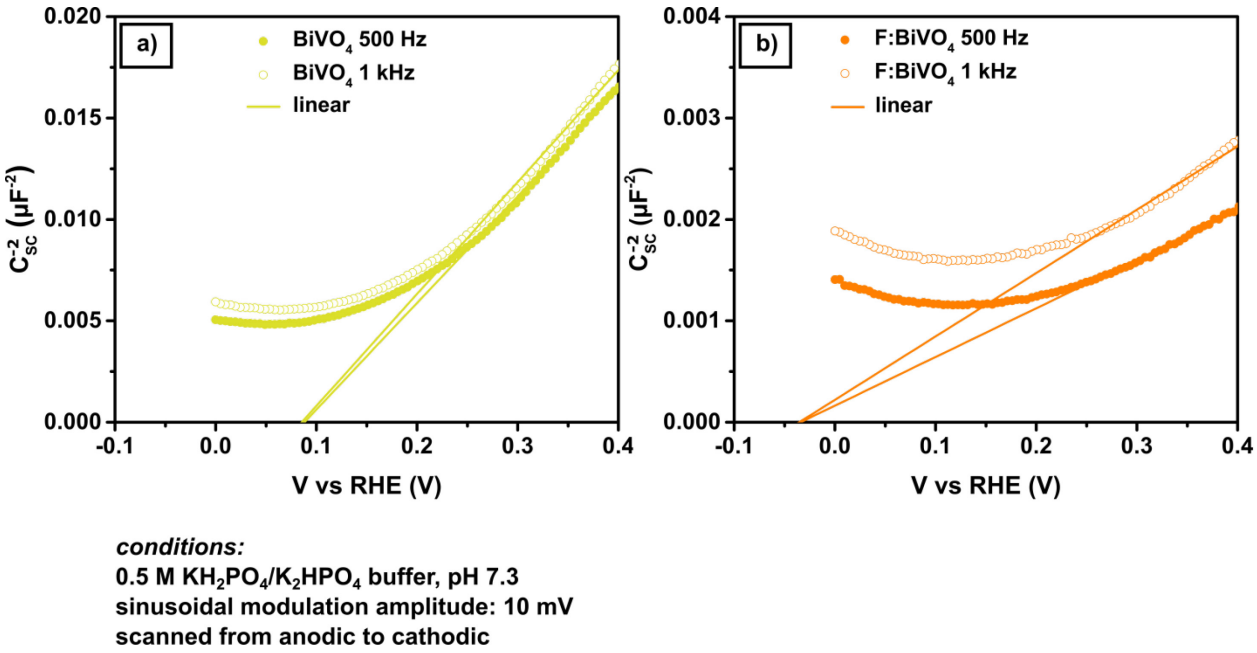

Figure 12-2. Mott-Schottky plots of $BiVO_4$ and F:$BiVO_4$ EPD electrodes calcined at 550 °C, electrochemical impedance spectroscopy was carried out at different frequencies.

12.1.2. Supplementary data for chapter 8: $BiVO_4$ and Mo:$BiVO_4$ thin film photoanodes

12.1.2.1. Additional powder XRD and Rietveld refinement data

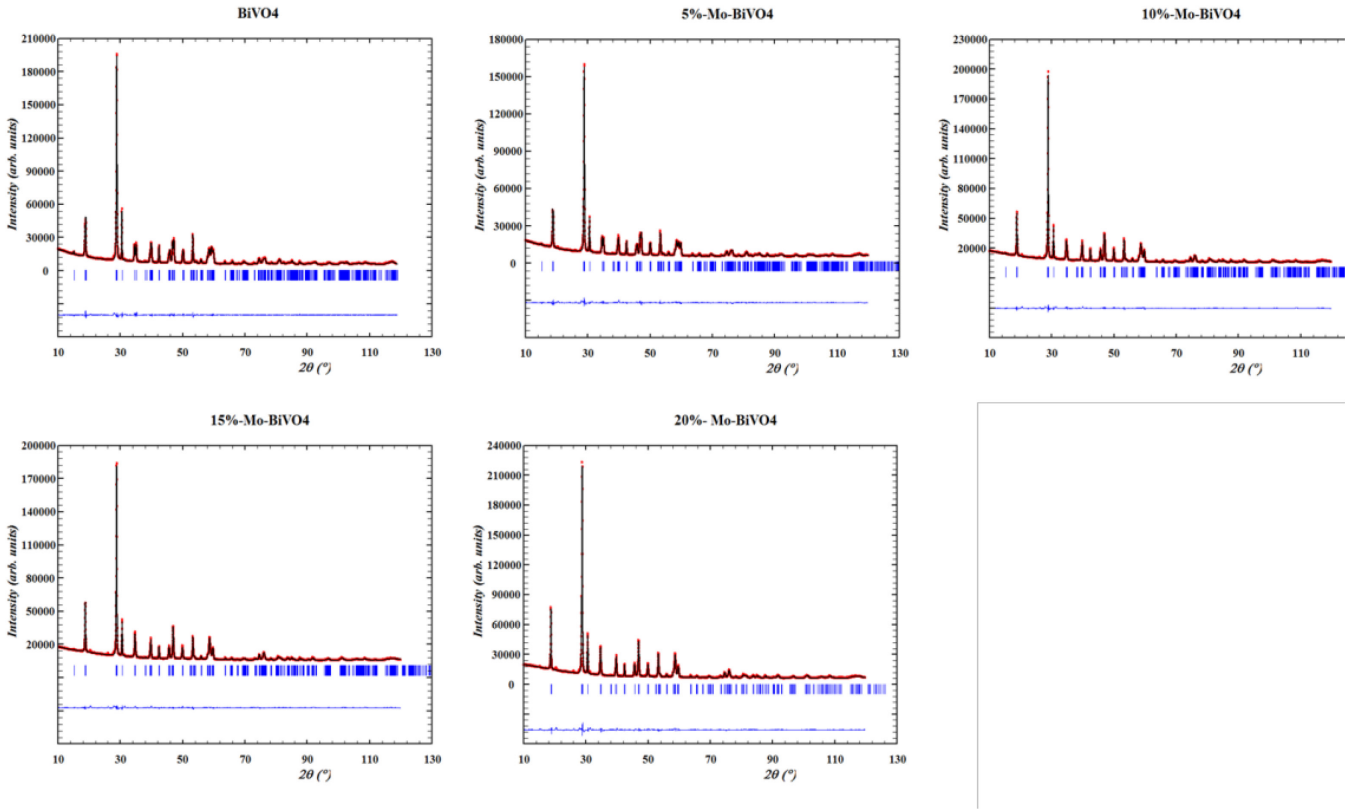

Figure 12-3. Powder-XRD pattern of $BiVO_4$ and Mo:$BiVO_4$ powder samples, obtained out of the corresponding synthesis solutions.

Table 12-1. Structural parameters for $BiVO_4$ and Mo:$BiVO_4$ powders obtained by Rietveld refinements.

Composition	$BiVO_4$	5% Mo:$BiVO_4$	10% Mo:$BiVO_4$	15% Mo:$BiVO_4$	20% Mo:$BiVO_4$
Crystal system Space group	monoclinic I2/b				tetragonal $I4_1/a$
Formular units	Z= 4				
Lattice parameters	a = 5.1930(6) Å b = 5.1019(6) Å c = 11.7028(3) Å γ = 90.333(2) °	a =5.1839(5) Å b = 5.1188(5) Å c = 11.6959(10) Å γ = 90.238(2) °	a =5.1741(4) Å b = 5.1412(4) Å c = 11.6917(9) Å γ = 90.144(3) °	a = 5.1673(4) Å b = 5.1532(4) Å c = 11.6855(8) Å γ = 90.094(4) °	a=b = 5.1634(2) Å c = 11.6825(3) Å γ = 90 °
Unit cell volume	V = 310.05(7) Å³	V = 310.35(5) Å³	V = 311.01(4) Å³	V = 311.16(4) Å³	V = 311.46(2) Å³
R_{wp}	0.0296	0.0263	0.0256	0.0240	0.0285
R_{Bragg}	0.0286	0.0302	0.0267	0.0278	0.0307
R_{exp}	0.0107	0.0105	0.0103	0.0103	0.0098
S	2.79	2.49	2.48	2.32	2.91

Table 12-2. Structural parameters for $BiVO_4$ and Mo:$BiVO_4$ powders (continuation).

$BiVO_4$	Site	*x*	*y*	*z*	s.o.f.
Bi	4*e*	0	¼	0.6339(2)	0.998(3)
V	4*e*	0	¼	0.1279(4)	1.004(3)
O1	8*f*	0.143(2)	0.4954(14)	0.2103(7)	1
O2	8*f*	0.2763(14)	0.370(2)	0.4462(7)	1
5 % Mo:$BiVO_4$	Site	*x*	*y*	*z*	s.o.f.
Bi	4*e*	0	¼	0.6291(11)	0.996(2)
V	4*e*	0	¼	0.1309(4)	0.930(4)
Mo	4*e*	0	¼	0.1309(4)	0.070(4)
O1	8*f*	0.1458(16)	0.4957(13)	0.2085(7)	1
O2	8*f*	0.2663(13)	0.3687(17)	0.4493(7)	1
10 % Mo:$BiVO_4$	Site	*x*	*y*	*z*	s.o.f.
Bi	4*e*	0	¼	0.6298(2)	0.964(3)
V	4*e*	0	¼	0.1314(5)	0.880(4)
Mo	4*e*	0	¼	0.1314(5)	0.120(4)
O1	8*f*	0.131(2)	0.479(2)	0.2076(9)	1
O2	8*f*	0.2541(16)	0.378(2)	0.4517(9)	1
15 % Mo:$BiVO_4$	Site	*x*	*y*	*z*	s.o.f.
Bi	4*e*	0	¼	0.63133(15)	0.950(3)
V	4*e*	0	¼	0.1216(4)	0.836(4)
Mo	4*e*	0	¼	0.1216(4)	0.164(4)
O1	8*f*	0.133(2)	0.478(2)	0.2069(12)	1
O2	8*f*	0.250(2)	0.382(3)	0.4498(11)	1
20 % Mo:$BiVO_4$	Site	*x*	*y*	*z*	s.o.f.
Bi	4*b*	0	¼	$^5/_8$	0.470(3)
V	4*a*	0	¼	$^1/_8$	0.400(3)

Mo	4*a*	0	¼	$^1/_8$	0.100(3)
O	*16f*	0.1408(9)	0.0043(7)	0.2044(4)	1

Table 12-3. Reasonable defect models for the substitution of V^{5+} by Mo^{6+} in $BiVO_4$ (formal defect equations, Kröger-Vink notation).

Formation of vanadium vacancies ($BiMo_{5x/6}V_{1-x}O_4$):

$$12\,V_V^x\ +\ 10\,MoO_3(sf)\ =\ 10\,Mo_V^\bullet\ +\ 2\,V_V''''''\ +\ 6\,V_2O_5(sf)$$

Formation of bismuth vacancies ($Bi_{1-x/3}Mo_xV_{1-x}O_4$):

$$Bi_{Bi}^x\ +\ 3\,V_V^x\ +3\,MoO_3(sf)\ =\ 3\,Mo_V^\bullet\ +\ V_{Bi}'''+\ BiVO_4(sf)\ +\ V_2O_5(sf)$$

Formation of bismuth and vanadium vacancies ($Bi_{1-x/9}Mo_{8x/9}V_{1-x}O_4$):

$$Bi_{Bi}^x\ +\ 9\,V_V^x\ +8\,MoO_3(sf)\ =\ 8\,Mo_V^\bullet\ +\ V_V''''''+V_{Bi}'''+\ BiVO_4(sf)\ +4\,V_2O_5(sf)$$

Oxygen on interstitial positions ($BiMo_xV_{1-x}O_{4+x/2}$):

$$2\,V_V^x\ +2\,MoO_3(sf)=\ 2\,Mo_V^\bullet\ +O_i''+V_2O_5(sf)$$

12.1.2.2. Kr-physisorption data

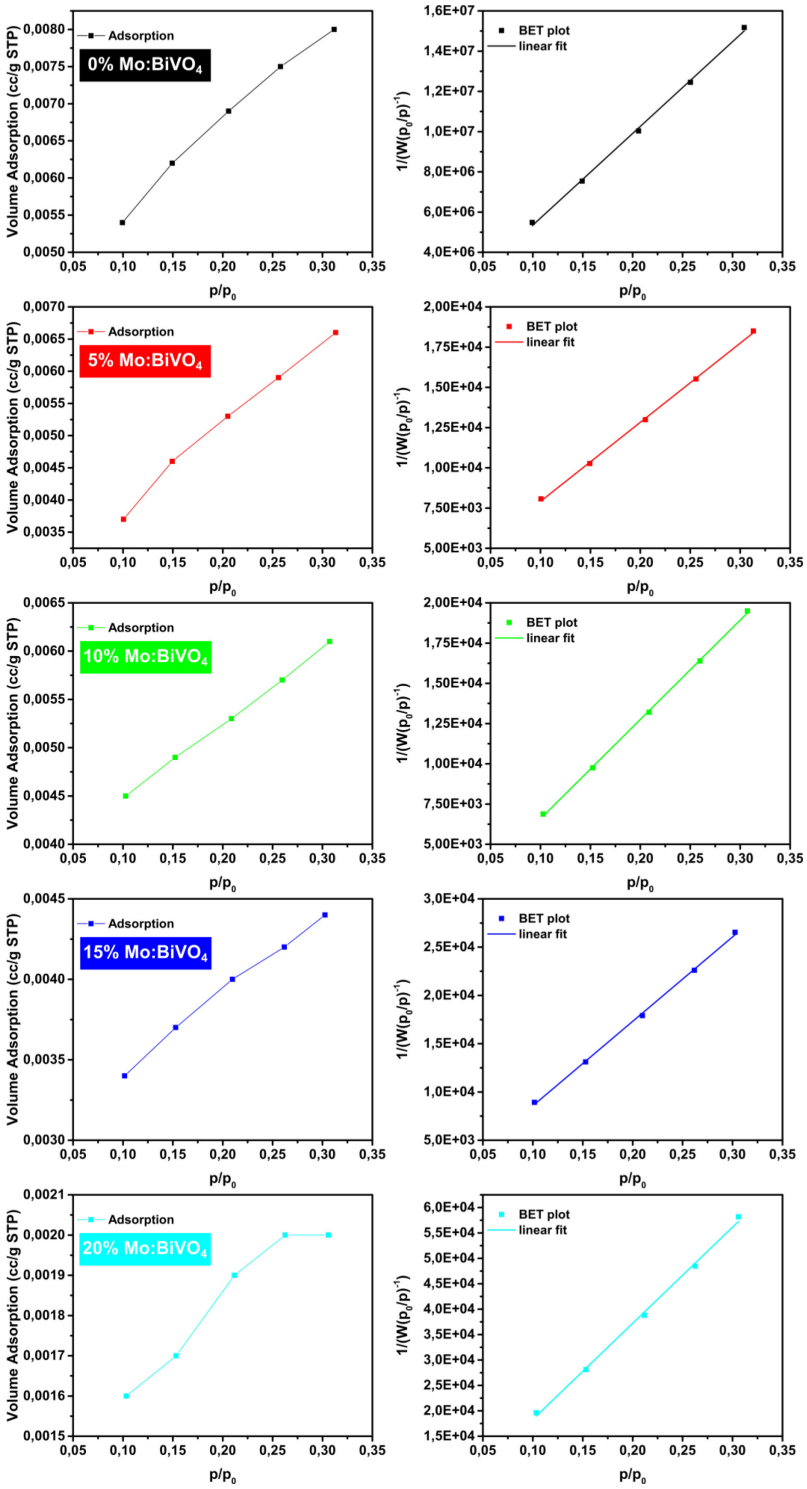

Figure 12-4. Kr-physisorption isotherms and BET plots of $BiVO_4$ and Mo:$BiVO_4$ thin films.

12.1.2.3. SEM investigations

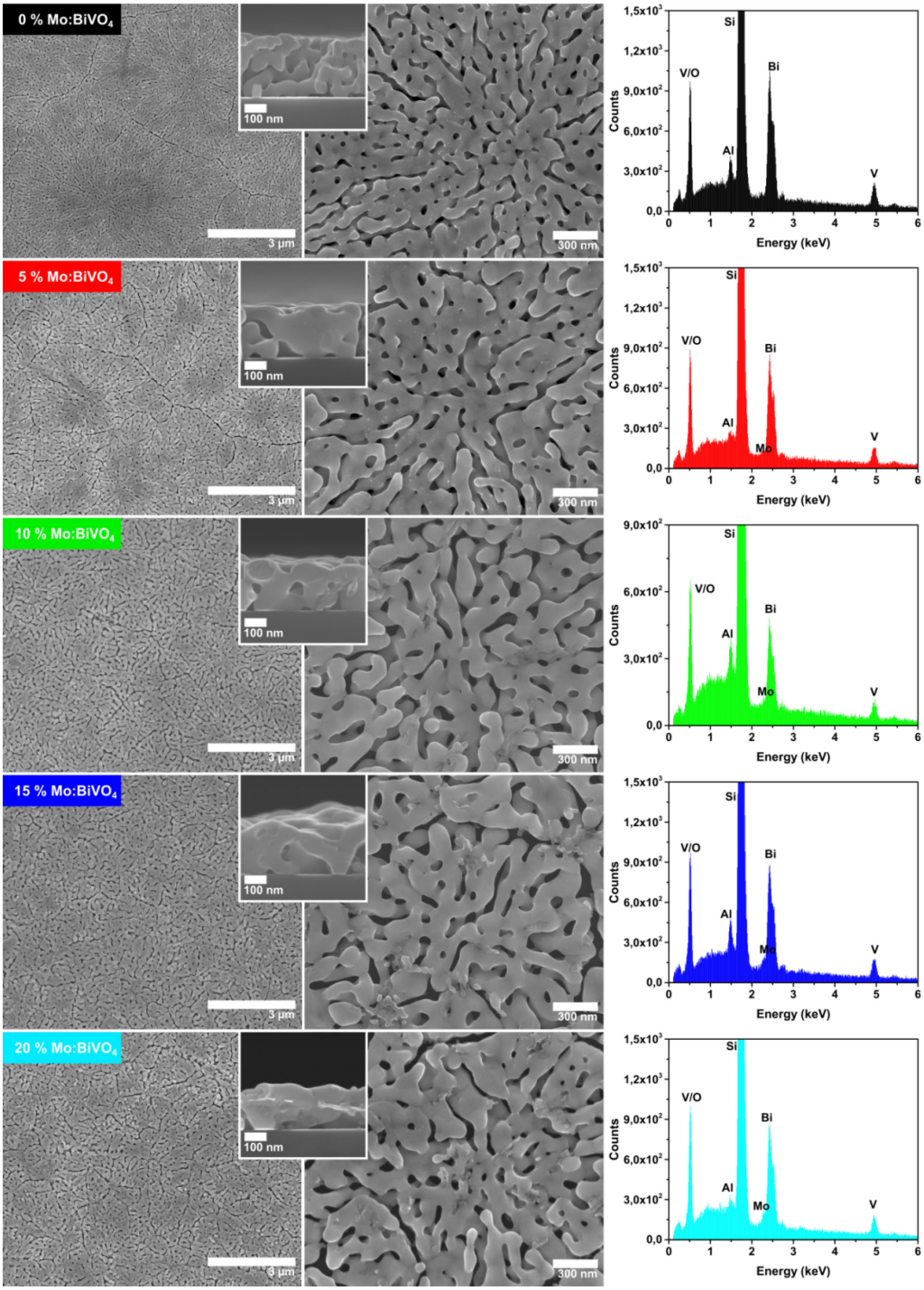

Figure 12-5. SEM and EDX investigations of $BiVO_4$ and Mo:$BiVO_4$ thin films deposited on Si substrate.

12.1.2.4. TEM/SAED investigations

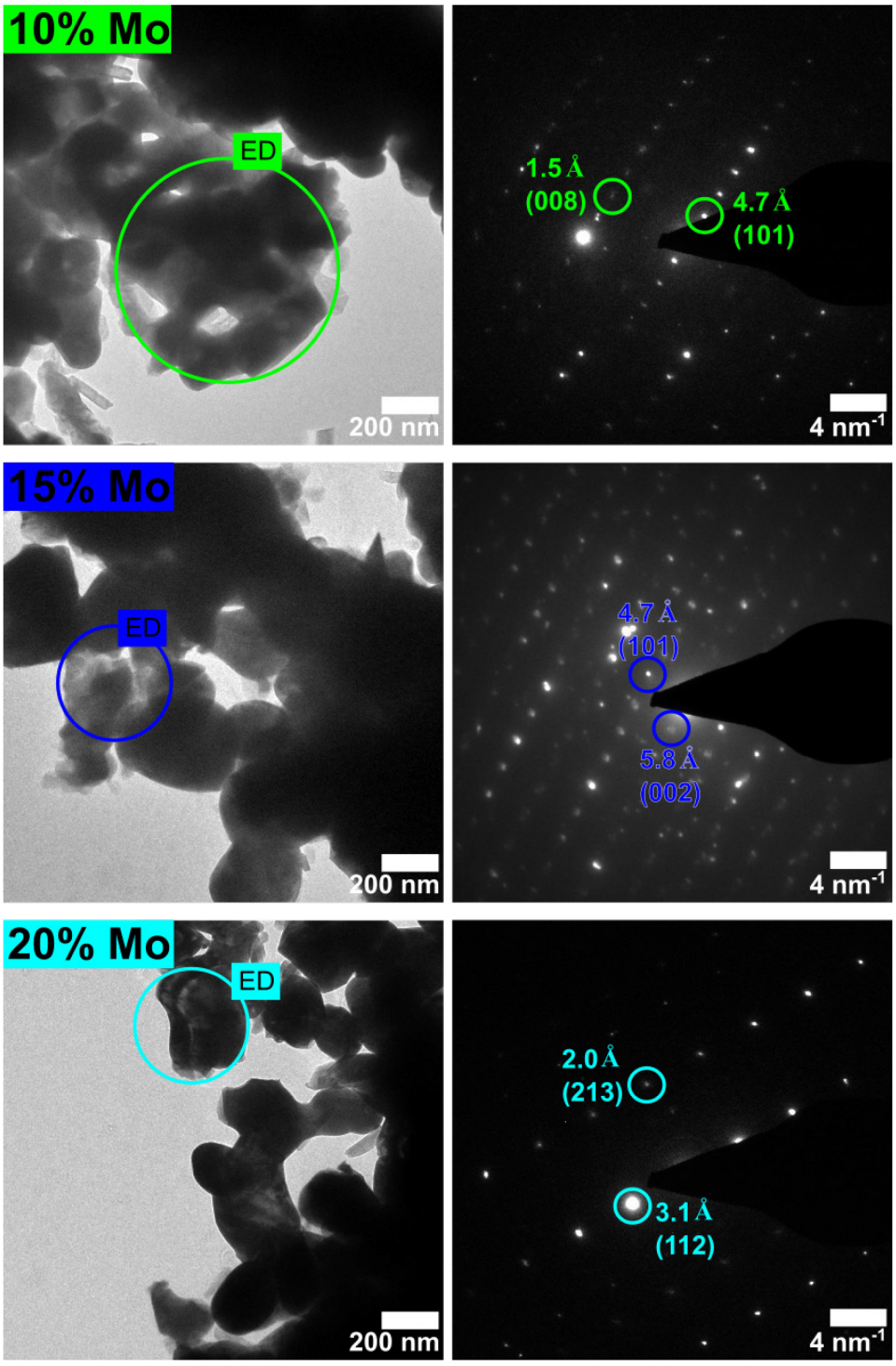

Figure 12-6. TEM/SAED investigations of Mo:$BiVO_4$ thin films. Samples were scraped-off the substrate and transferred to a TEM grid.

12.1.2.5. PEC investigations of $BiVO_4$ and Mo:$BiVO_4$ thin film photoanodes

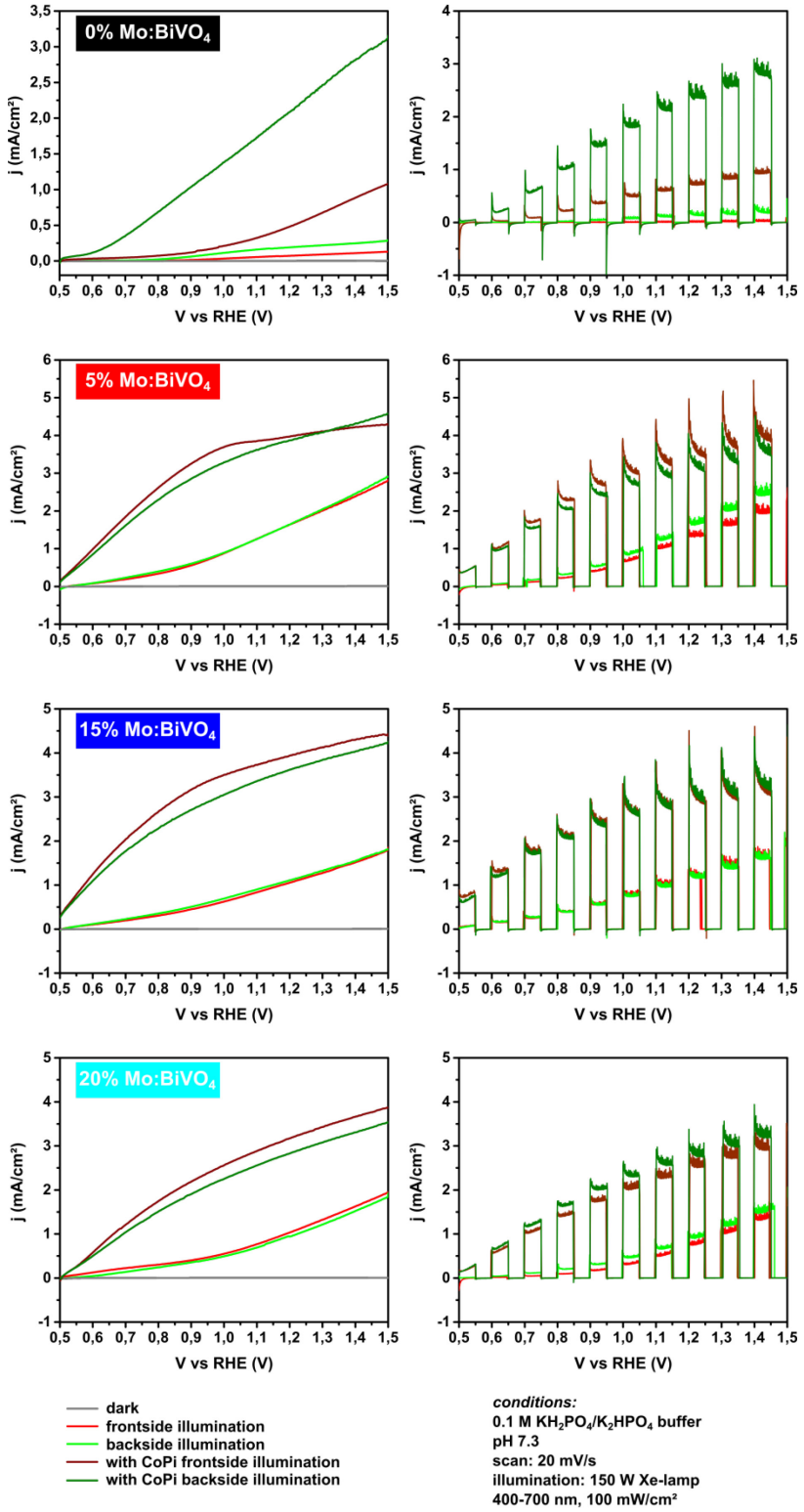

Figure 12-7. j-v curves of $BiVO_4$ and Mo:$BiVO_4$ thin film photoanodes in frontside and backside illumination mode using continuous and chopped illumination.

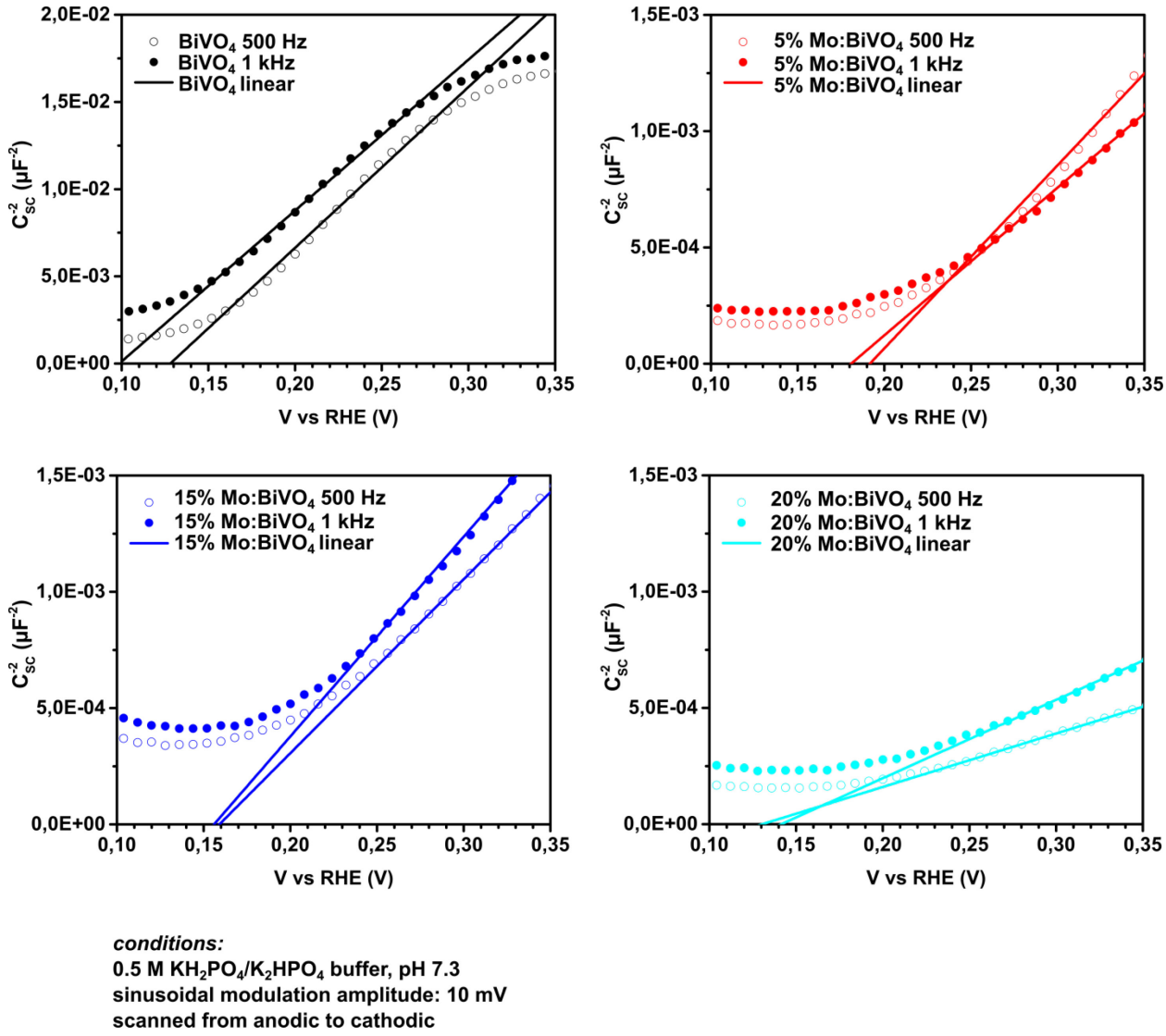

Figure 12-8. Mott-Schottky plots of $BiVO_4$ and Mo:$BiVO_4$ thin film photoanodes, carried-out at different frequencies.

12.1.2.6. PEC investigations of worm-like $BiVO_4$ and Mo:$BiVO_4$ thin film photoanodes

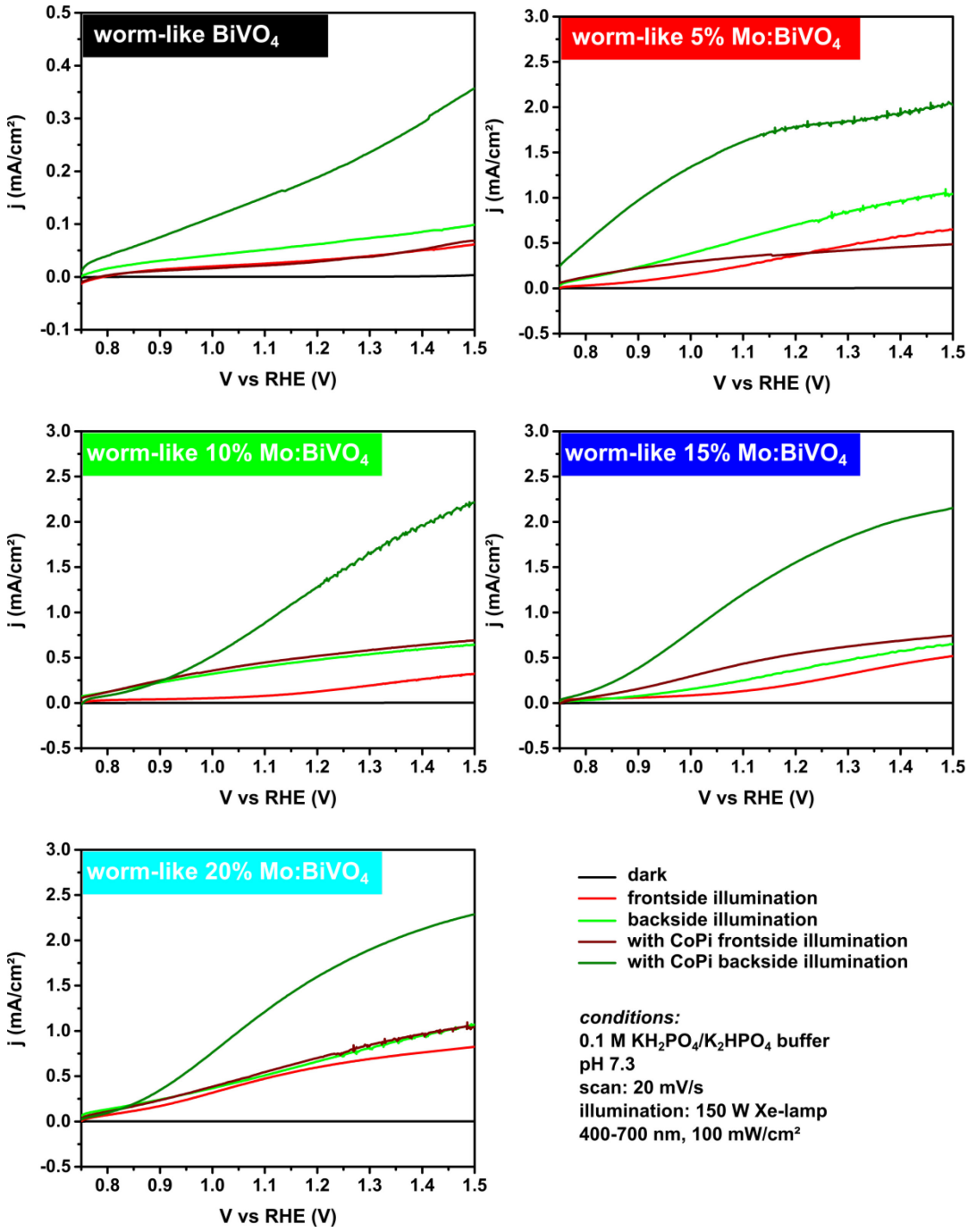

Figure 12-9. j-V curves of worm-like $BiVO_4$ and Mo:$BiVO_4$ thin film photoanodes with and without CoPi deposited in frontside and backside illumination.

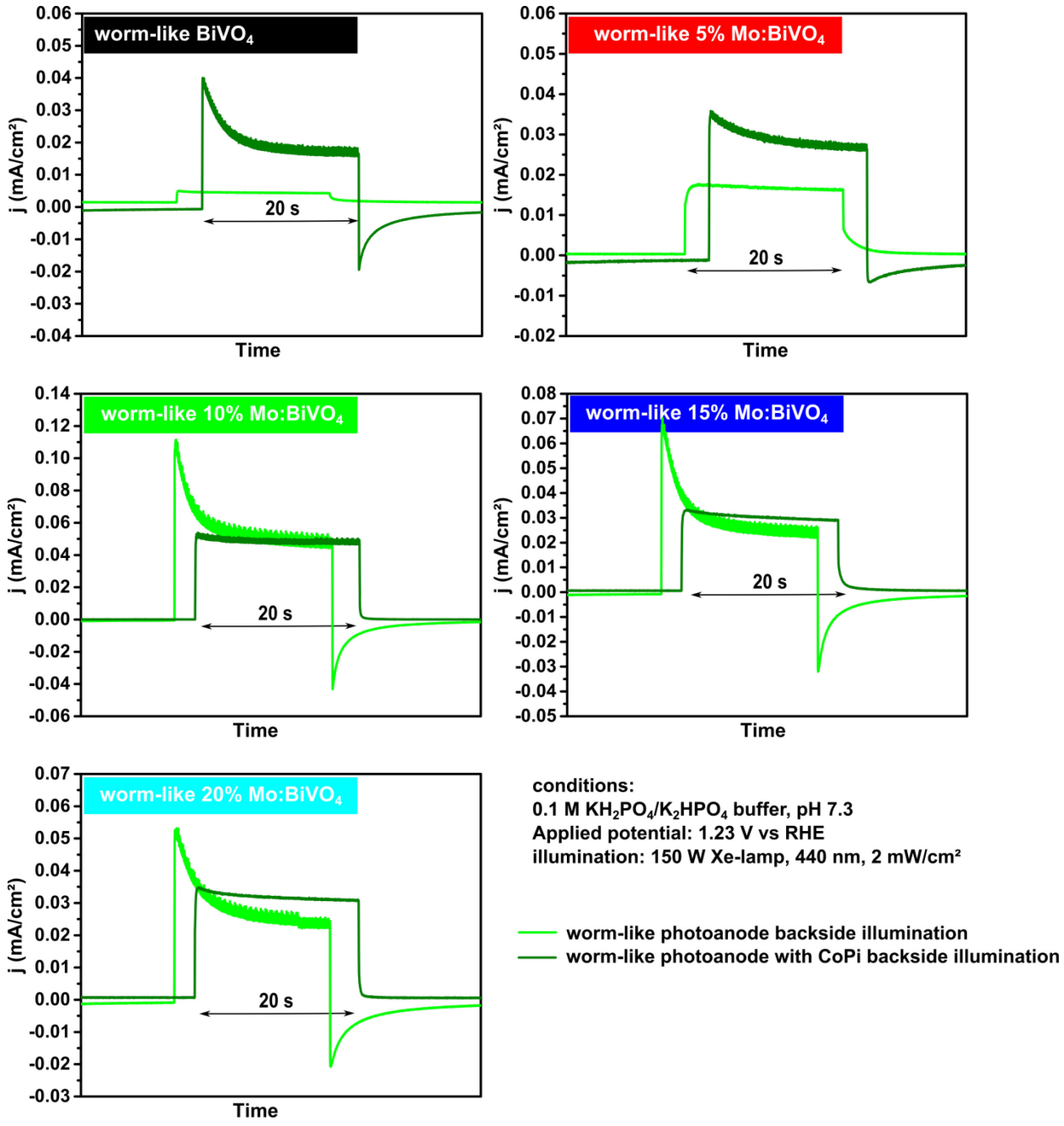

Figure 12-10. Photocurrent transients of worm-like $BiVO_4$ and Mo:$BiVO_4$ thin film photoanodes with and without CoPi deposited in backside illumination mode.

12.1.2.7. PEC investigations of 10% Mo:$BiVO_4$ thin film photoanodes calcined at different temperatures

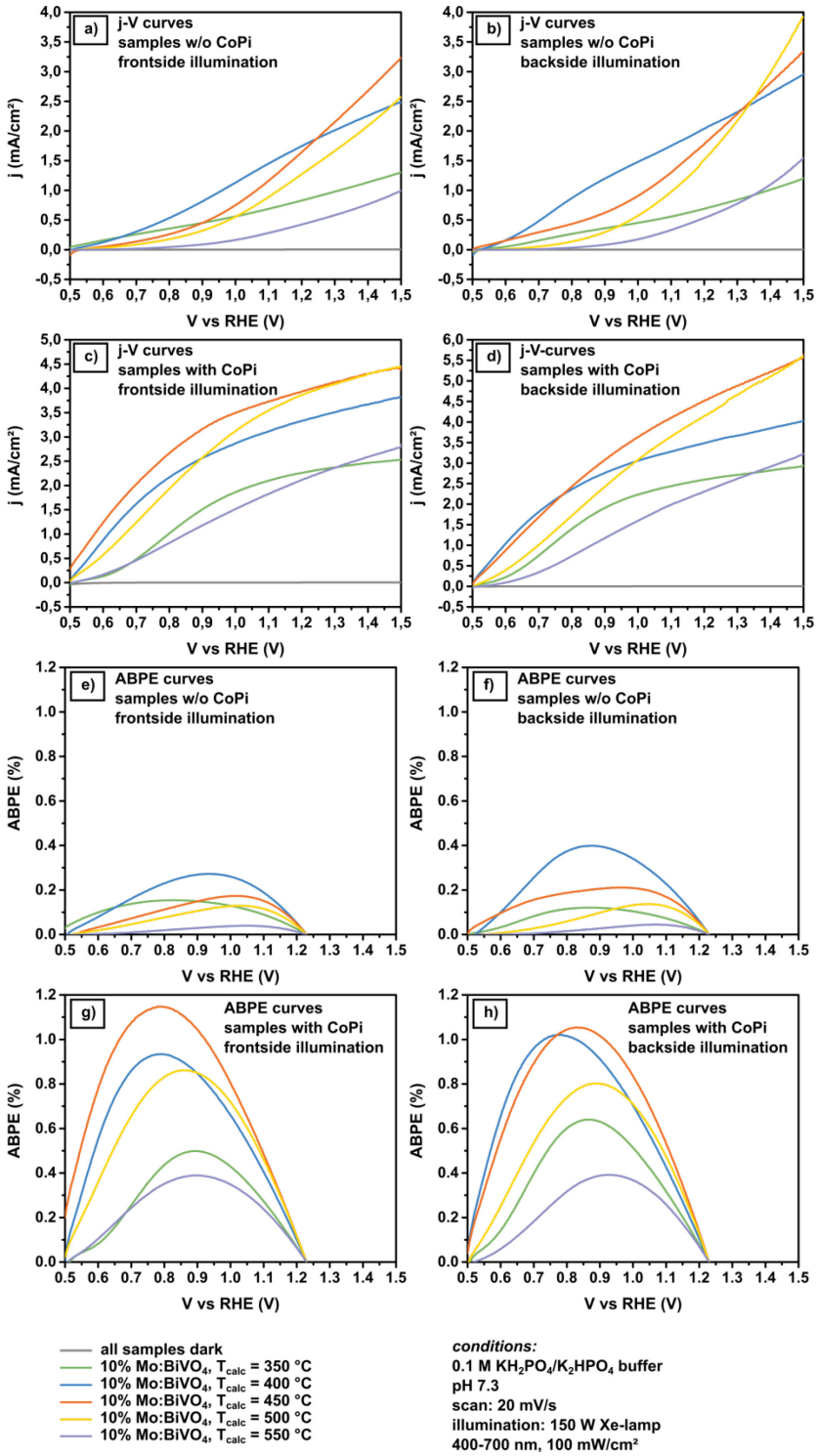

Figure 12-11. j-V curves and ABPE curves for 10% Mo:$BiVO_4$ thin film photoanodes calcined at different temperatures with and without CoPi deposited in frontside and backside illumination.

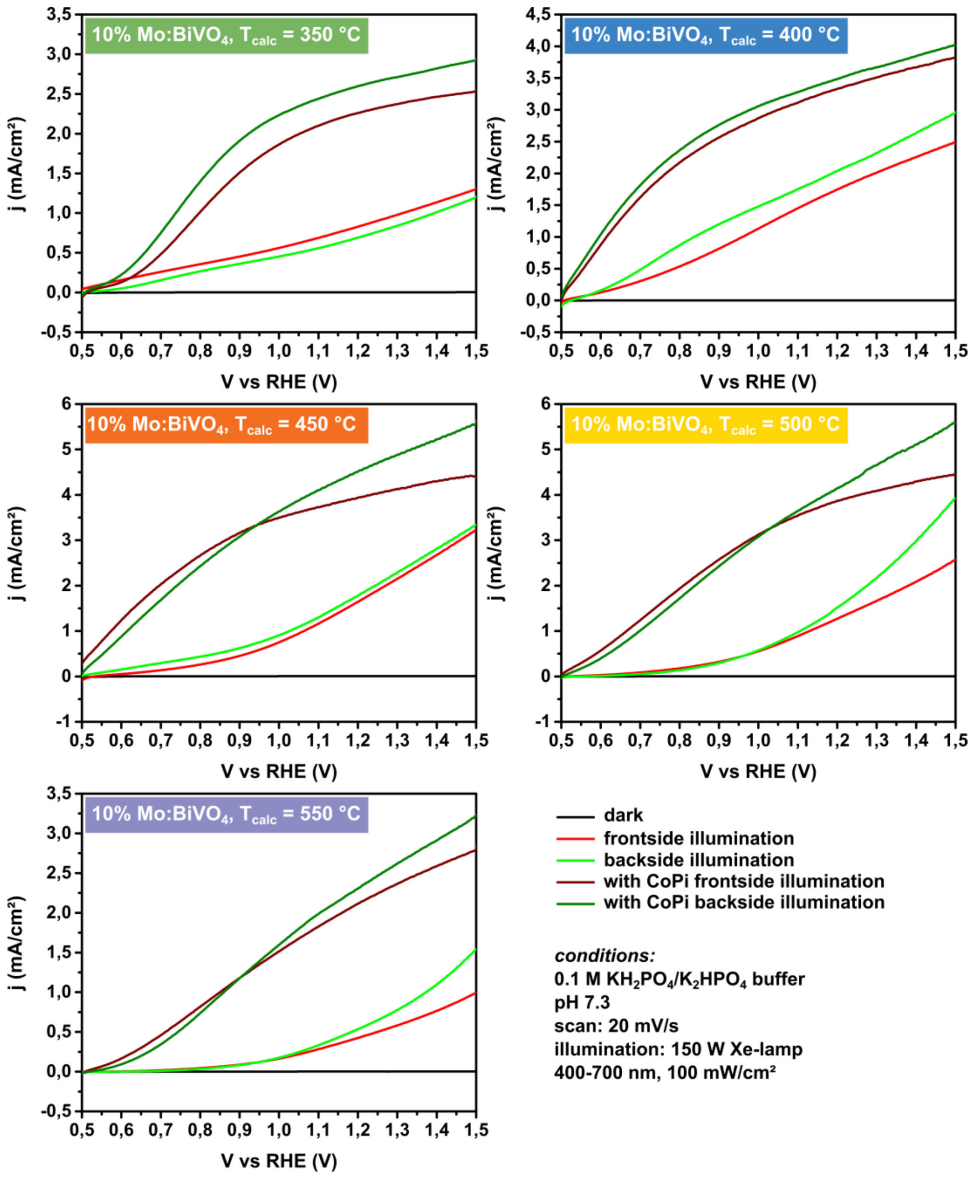

Figure 12-12. j-V curves of single 10% Mo:$BiVO_4$ thin film photoanodes calcined at different temperatures with and without CoPi deposited in frontside and backside illumination.

Table 12-4. Summary of obtained photocurrents and ABPE maxima for 10% Mo:$BiVO_4$ thin film photoanode obtained in *frontside illumination*.

Calcination temperature (°C)	j (mA/cm²)		ABPE without CoPi		ABPE with CoPi	
	Without CoPi	With CoPi	E vs RHE (V)	Maximum ABPE (%)	E vs RHE (V)	Maximum ABPE (%)
350	0.87	2.30	0.83	0.15	0.89	0.50
400	1.83	3.39	0.94	0.27	0.78	0.93
450	1.80	3.99	1.01	0.17	0.79	1.15
500	1.39	3.94	1.03	0.13	0.86	0.86
550	0.47	2.20	1.05	0.04	0.90	0.39

Table 12-5. Summary of obtained photocurrents and ABPE maxima for 10% Mo:$BiVO_4$ thin film photoanode obtained in *backside illumination*.

Calcination temperature (°C)	j (mA/cm²)		ABPE without CoPi		ABPE with CoPi	
	Without CoPi	With CoPi	E vs RHE (V)	Maximum ABPE (%)	E vs RHE (V)	Maximum ABPE (%)
350	0.74	2.64	0.87	0.12	0.86	0.64
400	2.13	3.55	0.88	0.40	0.76	1.02
450	1.94	4.64	0.95	0.21	0.83	1.05
500	1.71	4.28	1.05	0.14	0.89	0.80
550	0.60	2.40	1.07	0.05	0.92	0.39

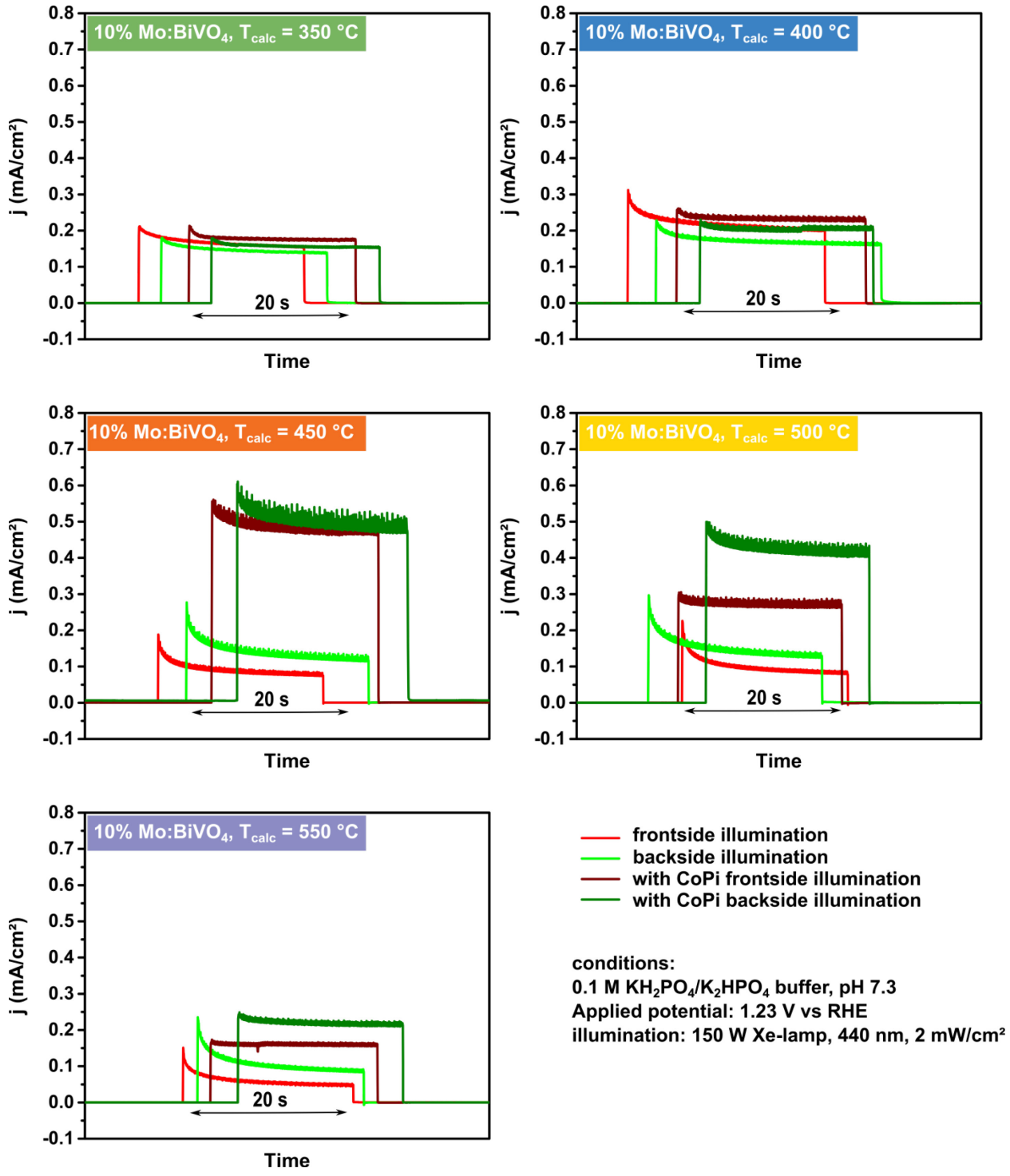

Figure 12-13. Photocurrent transients of 10% Mo:$BiVO_4$ thin film photoanodes calcined at different temperatures with and without CoPi deposited in frontside and backside illumination.

Table 12-6. Summary of photocurrent transient analysis results for 10% Mo:$BiVO_4$ thin film photoanodes calcined at different temperatures with and without CoPi deposited in frontside and backside illumination.

calcination temperature	with or w/o CoPi	illumination mode	current densities (mA/cm²)	$\eta_{transfer}$	rate constants (s^{-1})
350 °C	w/o CoPi	Frontside illumination	j_{ini} = 0.210	0.748	k_{trans} = 0.152
			j_{ss} = 0.157		k_{rec} = 0.051
		Backside illumination	j_{ini} = 0.178	0.789	k_{trans} = 0.173
			j_{ss} = 0.140		k_{rec} = 0.046
	with CoPi	Frontside illumination	j_{ini} = 0.211	0.846	k_{trans} = 0.267
			j_{ss} = 0.178		k_{rec} = 0.049
		Backside illumination	j_{ini} = 0.179	0.860	k_{trans} = 0.193
			j_{ss} = 0.140		k_{rec} = 0.031
400 °C	w/o CoPi	Frontside illumination	j_{ini} = 0.307	0.651	k_{trans} = 0.248
			j_{ss} = 0.200		k_{rec} = 0.133
		Backside illumination	j_{ini} = 0.207	0.795	k_{trans} = 0.189
			j_{ss} = 0.165		k_{rec} = 0.049
	with CoPi	Frontside illumination	j_{ini} = 0.258	0.885	k_{trans} = 0.176
			j_{ss} = 0.228		k_{rec} = 0.023
		Backside illumination	j_{ini} = 0.179	0.926	k_{trans} = 0.176
			j_{ss} = 0.140		k_{rec} = 0.014
450 °C	w/o CoPi	Frontside illumination	j_{ini} = 0.192	0.476	k_{trans} = 0.178
			j_{ss} = 0.091		k_{rec} = 0.196
		Backside illumination	j_{ini} = 0.267	0.477	k_{trans} = 0.170
			j_{ss} = 0.127		k_{rec} = 0.186
	with CoPi	Frontside illumination	j_{ini} = 0.627	0.832	k_{trans} = 0.265
			j_{ss} = 0.522		k_{rec} = 0.054
		Backside illumination	j_{ini} = 0.563	0.877	k_{trans} = 0.302
			j_{ss} = 0.494		k_{rec} = 0.042

500 °C	w/o CoPi	Frontside illumination	j_{ini} = 0.264	0.308	k_{trans} = 0.075
			j_{ss} = 0.081		k_{rec} = 0.168
		Backside illumination	j_{ini} = 0.295	0.440	k_{trans} = 0.096
			j_{ss} = 0.130		k_{rec} = 0.122
	with CoPi	Frontside illumination	j_{ini} = 0.288	0.956	k_{trans} = 0.277
			j_{ss} = 0.275		k_{rec} = 0.013
		Backside illumination	j_{ini} = 0.489	0.831	k_{trans} = 0.211
			j_{ss} = 0.407		k_{rec} = 0.045
550 °C	w/o CoPi	Frontside illumination	j_{ini} = 0.132	0.368	k_{trans} = 0.103
			j_{ss} = 0.049		k_{rec} = 0.176
		Backside illumination	j_{ini} = 0.229	0.371	k_{trans} = 0.103
			j_{ss} = 0.085		k_{rec} = 0.174
	with CoPi	Frontside illumination	j_{ini} = 0.166	0.958	k_{trans} = 0.437
			j_{ss} = 0.159		k_{rec} = 0.019
		Backside illumination	j_{ini} = 0.242	0.867	k_{trans} = 0.201
			j_{ss} = 0.210		k_{rec} = 0.031

12.1.2.8. PEC investigations of 10% Mo:$BiVO_4$ thin film photoanodes – CoPi deposition

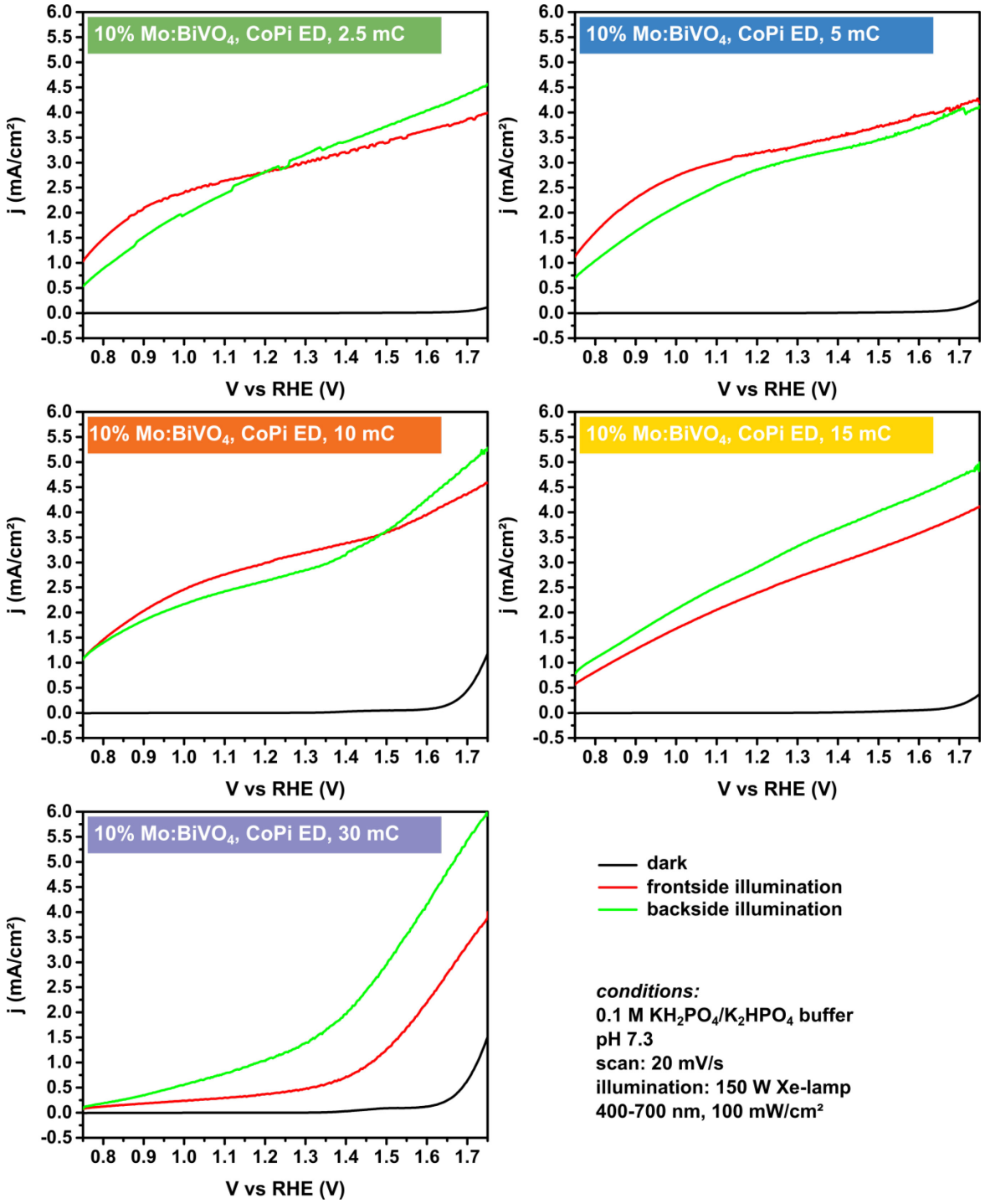

Figure 12-14. j-V curves of 10% Mo:$BiVO_4$ thin film photoanodes with different amounts of electrodeposited CoPi in frontside and backside illumination.

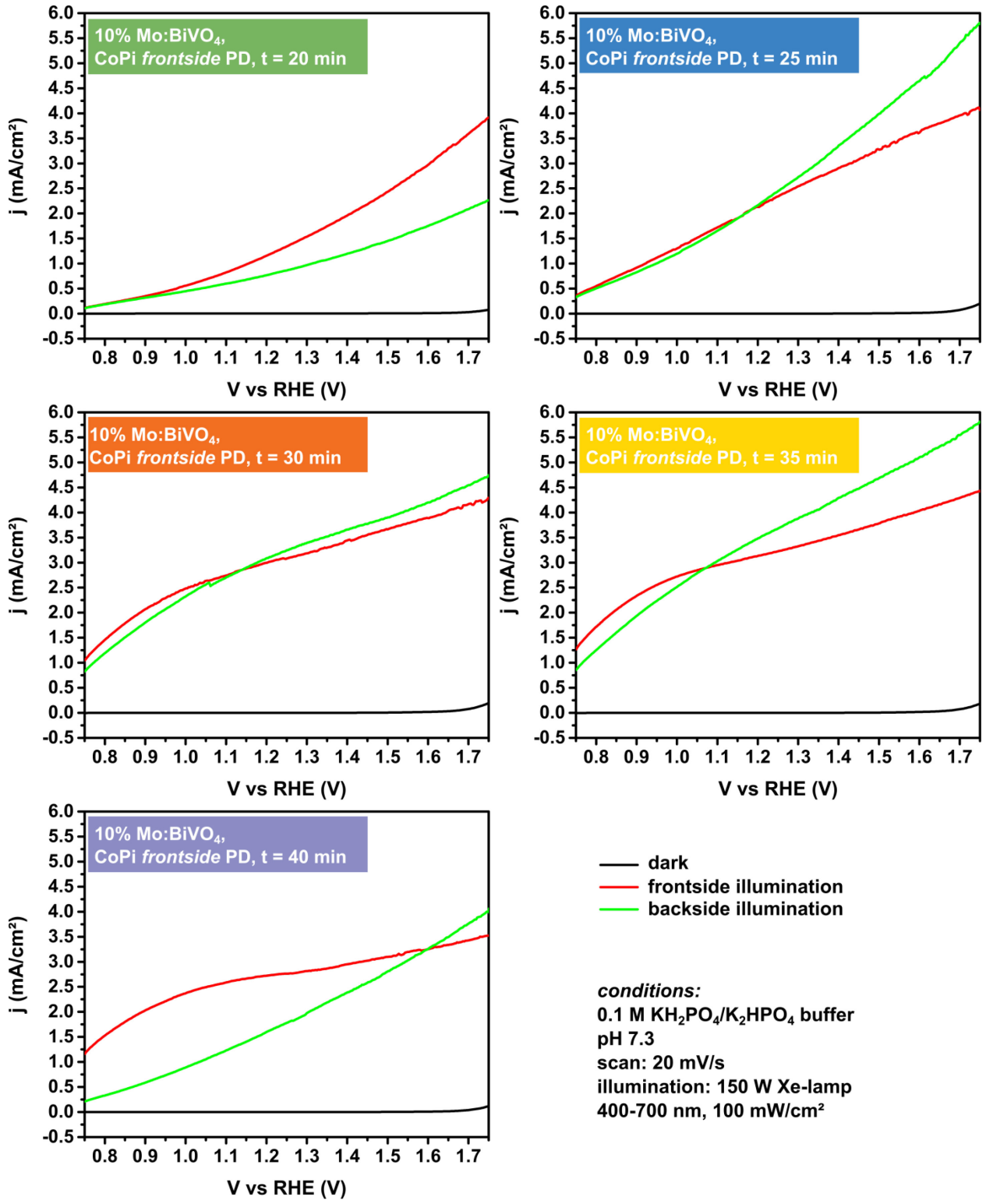

Figure 12-15. j-V curves of 10% Mo:$BiVO_4$ thin film photoanodes with different amounts of photochemically deposited CoPi (*frontside PD*) in frontside and backside illumination.

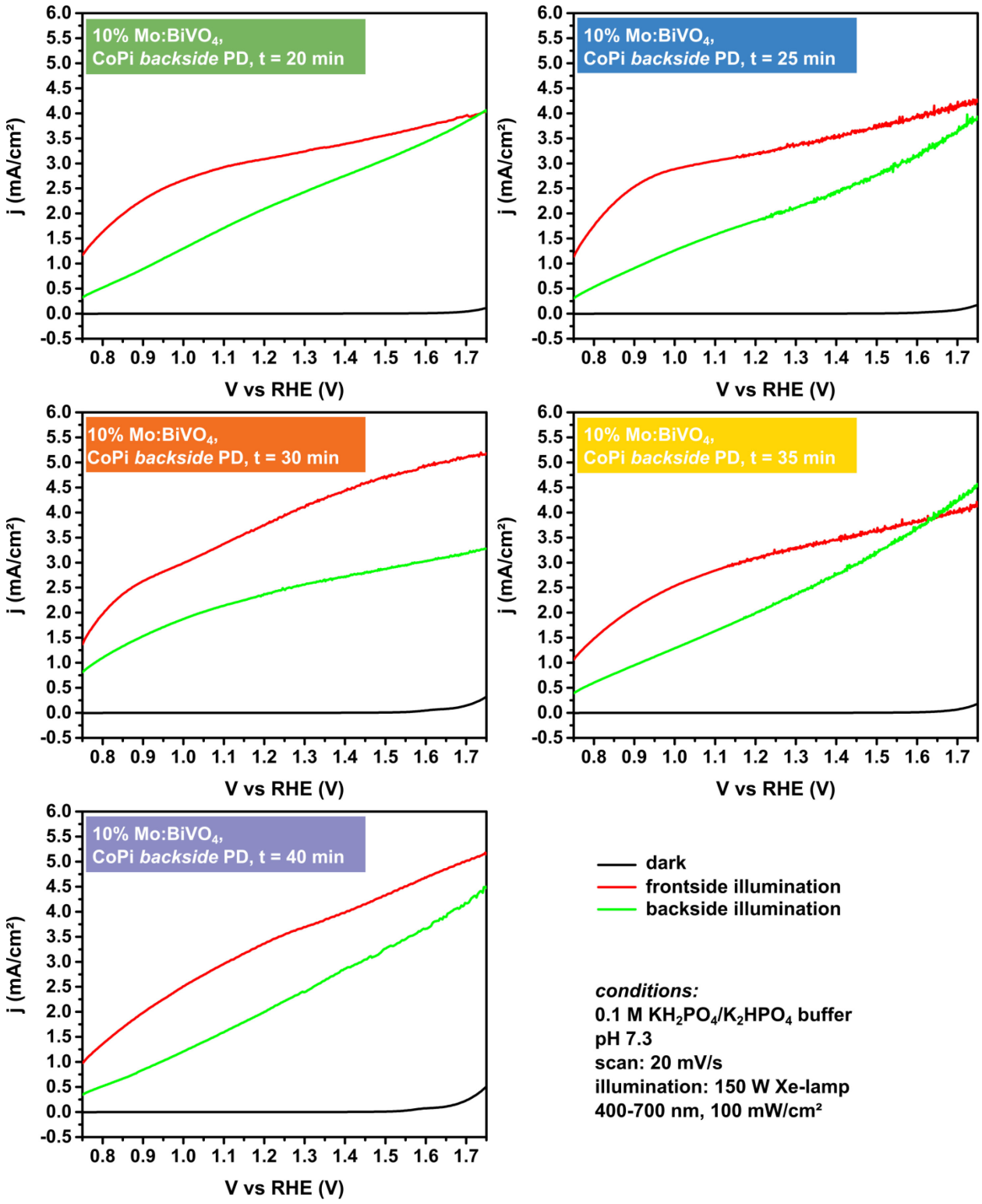

Figure 12-16. j-V curves of 10% Mo:$BiVO_4$ thin film photoanodes with different amounts of photochemically deposited CoPi (*backside PD*) in frontside and backside illumination.

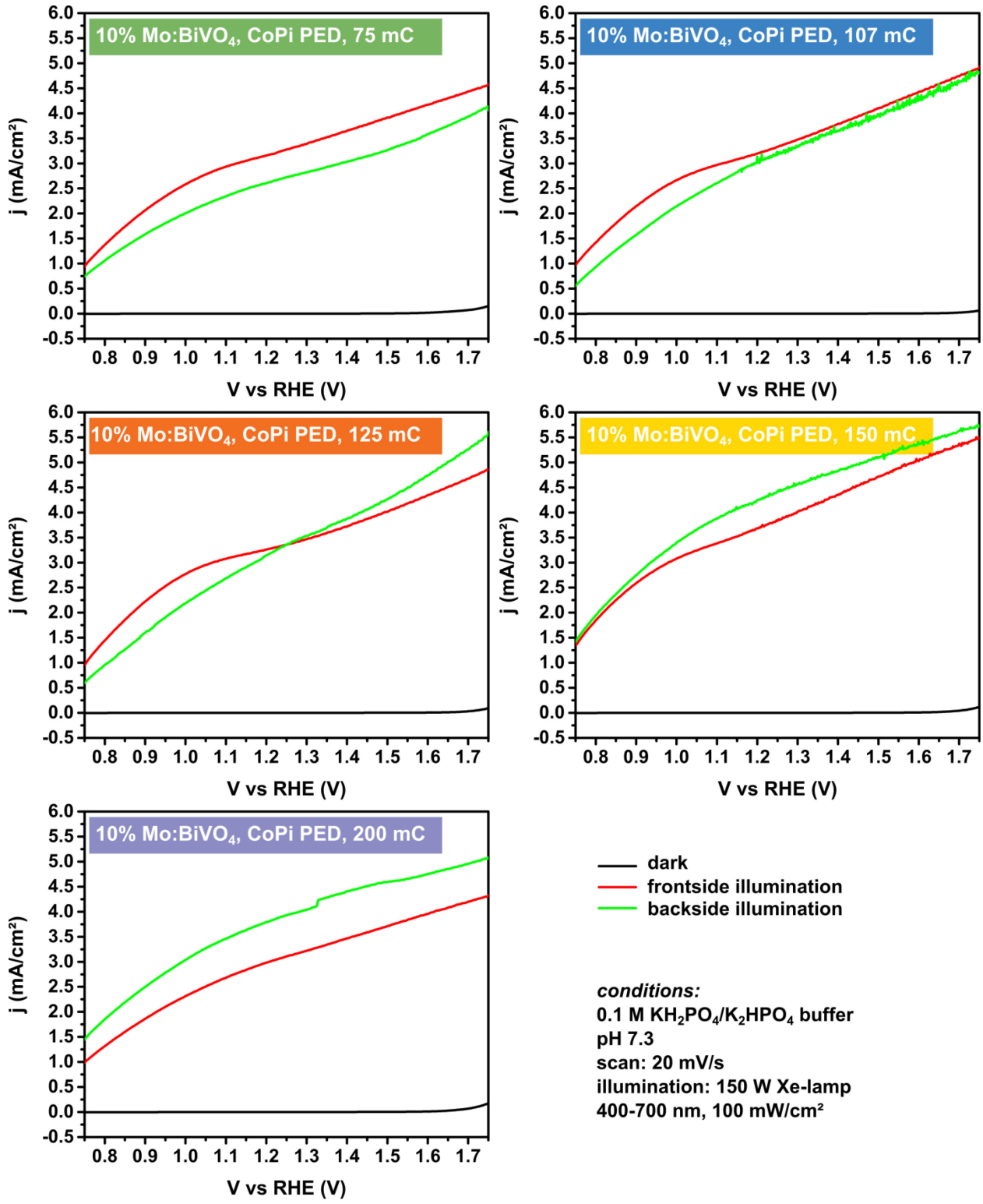

Figure 12-17. Figure 0 17. j-V curves of 10% Mo:$BiVO_4$ thin film photoanodes with different amounts of CoPi deposited by photo-assisted electrodeposition (PED) in frontside and backside illumination.

12.1.3. Supplementary data for chapter 9: $F:BiVO_4$ and $F/Mo:BiVO_4$ thin film photoanodes

12.1.3.1. Screening of synthesis parameters

Table 12-7. Summary of fluorination reaction conditions in line with obtained photocurrents at an applied potential of 1.23 V vs RHE (0.1 M KPi buffer, pH = 7.3, light: 400-700 nm at 100 mW/cm²).

condition	m(PVDF) (g)	T (°C)	t (h)	j at 1.23 V vs RHE (mA/cm²)			
				without CoPi		with CoPi	
				Frontside illumination	Backside illumination	Frontside illumination	Backside illumination
1	1	400	2	0.41	0.57	0.59	0.97
2	2	400	2	0.45	0.82	0.50	1.70
3	3	400	2	0.23	1.02	0.16	1.11
4	2	350	2	0.44	0.40	1.12	1.72
5	2	370	2	0.69	1.01	1.28	2.65

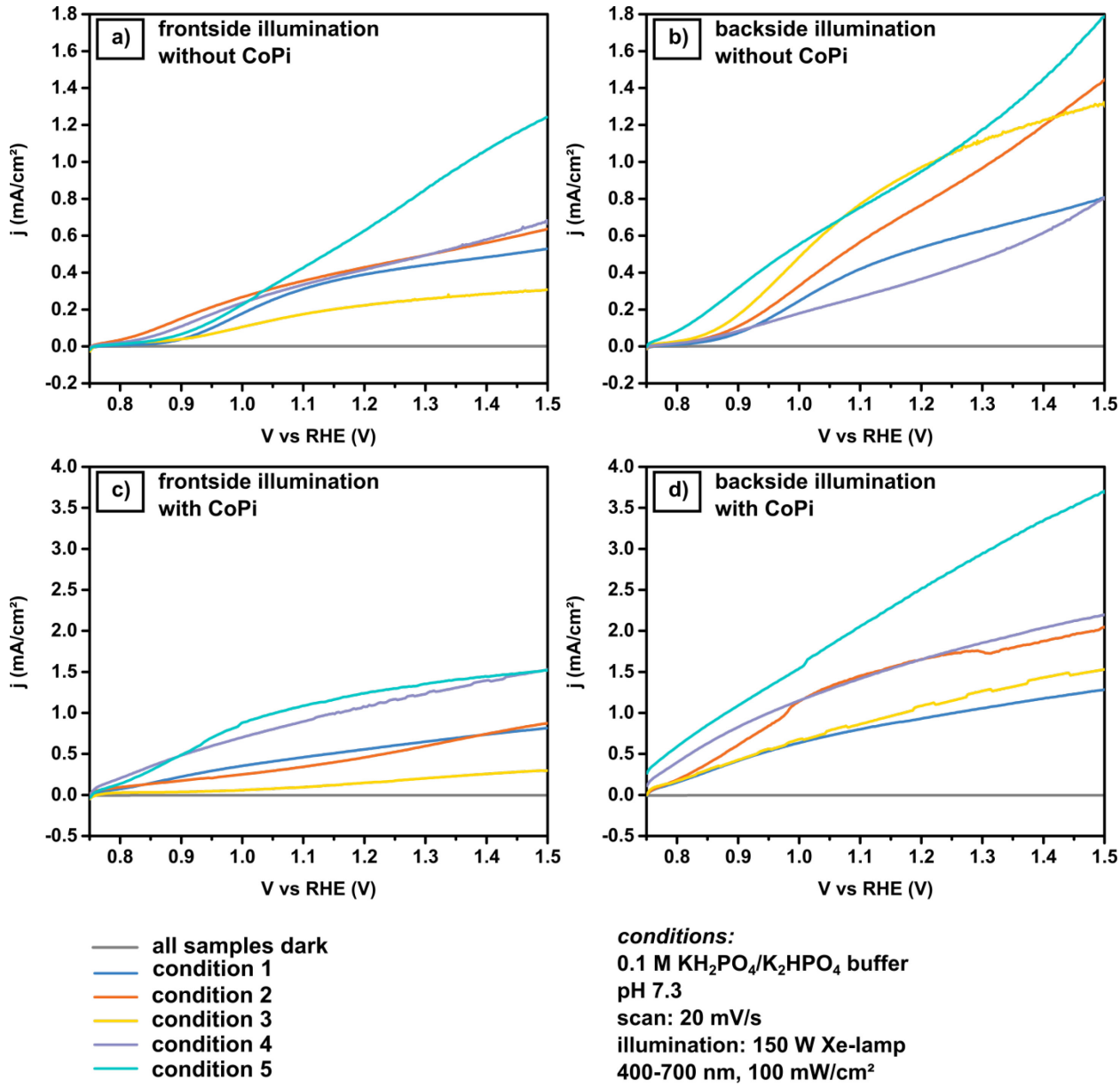

Figure 12-18. j-V curves of F:$BiVO_4$ thin film photoanodes fluorinated according to the conditions given in Table 12-7 with and without CoPi deposited in frontside and backside illumination.

12.1.3.2. Reference calcination without PVDF

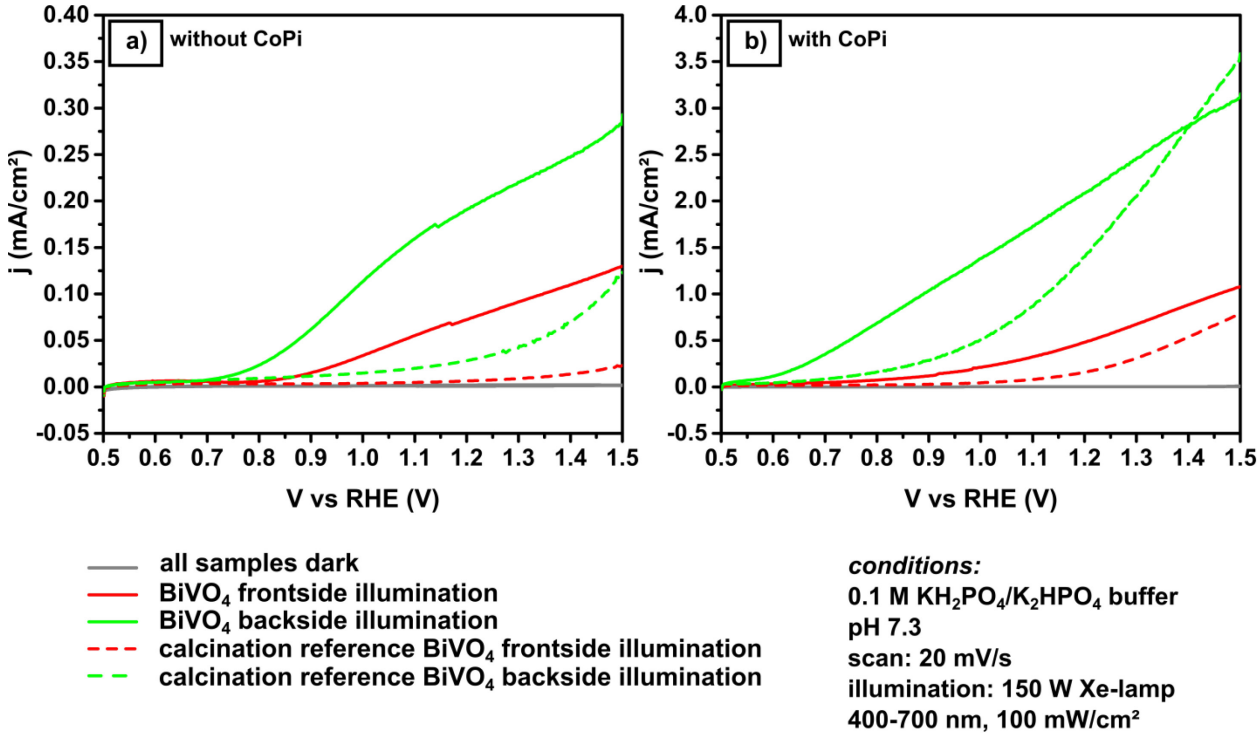

Figure 12-19. j-V curves of a $BiVO_4$ thin film photoanode and a twice-calcined $BiVO_4$ thin film photoanode according to the heat treatment involved in the fluorination procedure. Results of samples with and without CoPi in frontside and backside illumination are shown.

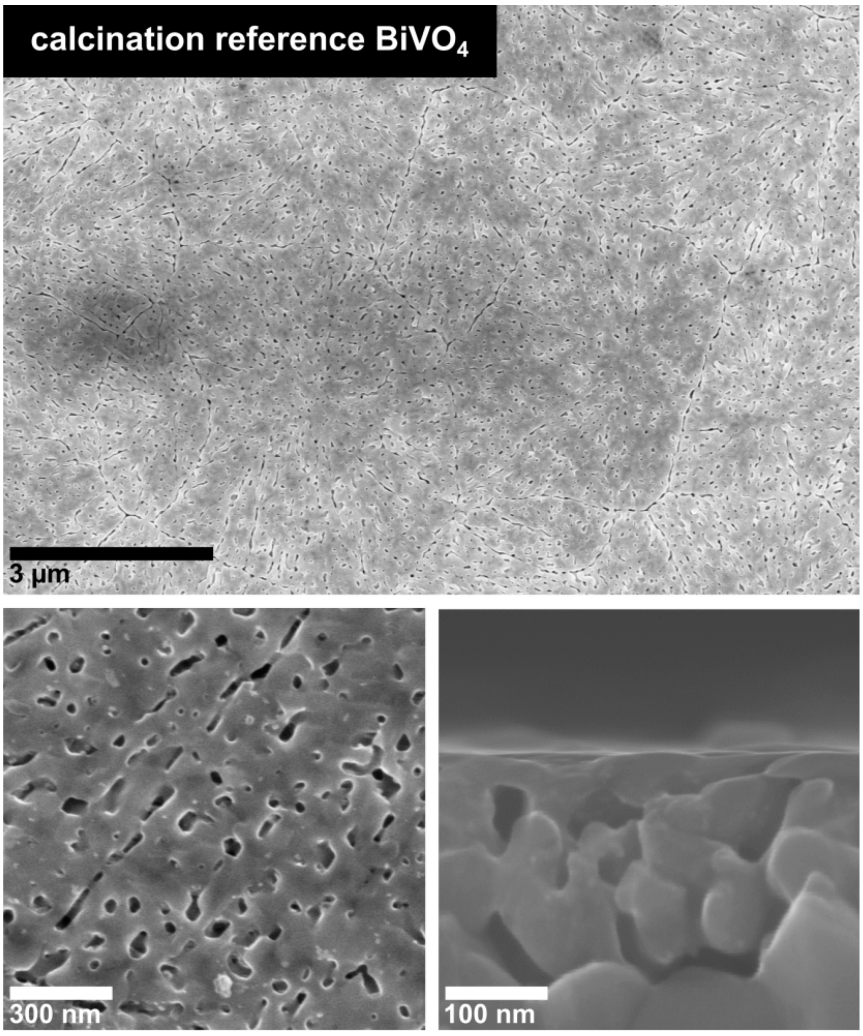

Figure 12-20. SEM investigations of a twice-calcined $BiVO_4$ thin film photoanode according to the heat treatment involved in the fluorination procedure.

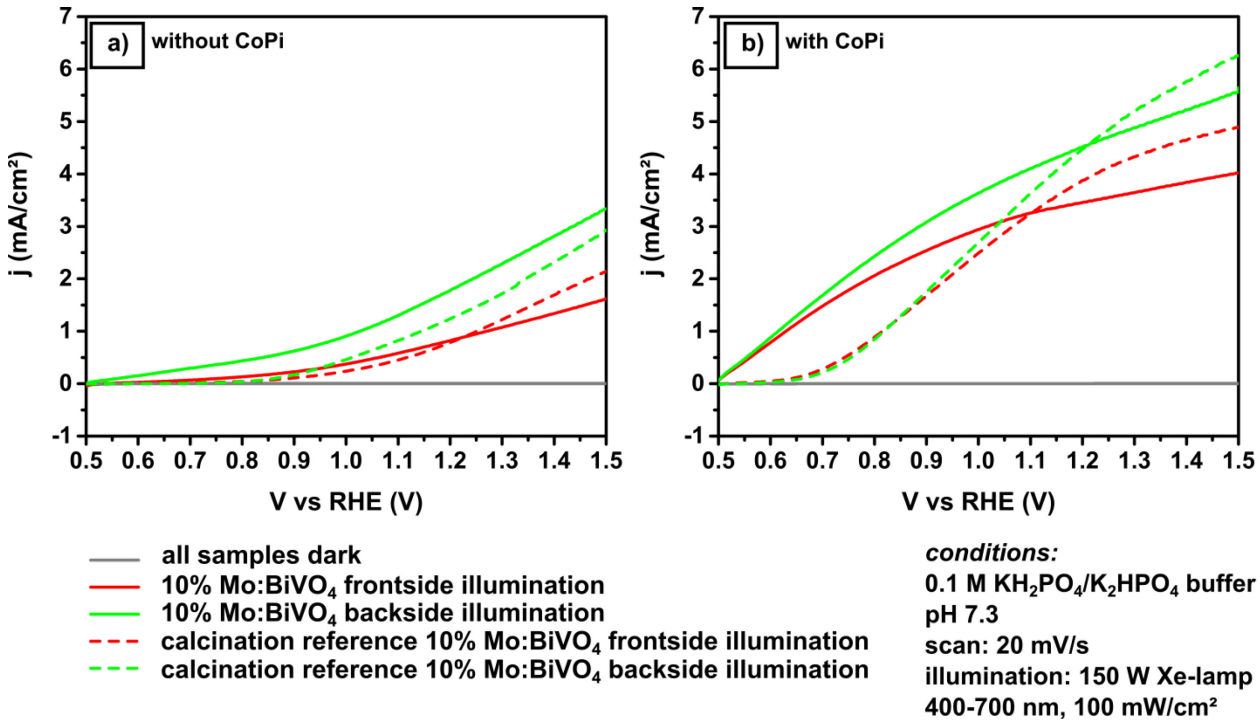

Figure 12-21. j-V curves of a 10% Mo:$BiVO_4$ thin film photoanode and a twice-calcined $BiVO_4$ thin film photoanode according to the heat treatment involved in the fluorination procedure. Results of samples with and without CoPi in frontside and backside illumination are shown.

12.1.4. Supplementary data for chapter 10: WO_3/Mo:$BiVO_4$ heterojunction photoanode

12.1.4.1. WO_3-$BiVO_4$-Potential energy diagram data

Table 12-8. Data used to plot the energy diagramm of a WO_3/$BiVO_4$ and WO_3/Mo:$BiVO_4$ heterojunctions.

compound	Band gap E_g (eV)	Conduction band edge positon (V vs RHE)	Valence band edge positon (V vs RHE)
WO_3	2.8	0.33	3.13
$BiVO_4$	2.4	0.07	2.47
5% Mo:$BiVO_4$	2.31	0.16	2.47
10% Mo:$BiVO_4$	2.32	0.15	2.47
15% Mo:$BiVO_4$	2.34	0.13	2.47
20% Mo:$BiVO_4$	2.35	0.12	2.47

12.1.4.2. PEC investigations of $WO_3/BiVO_4$ and WO_3/Mo:$BiVO_4$ heterojunction photoanodes

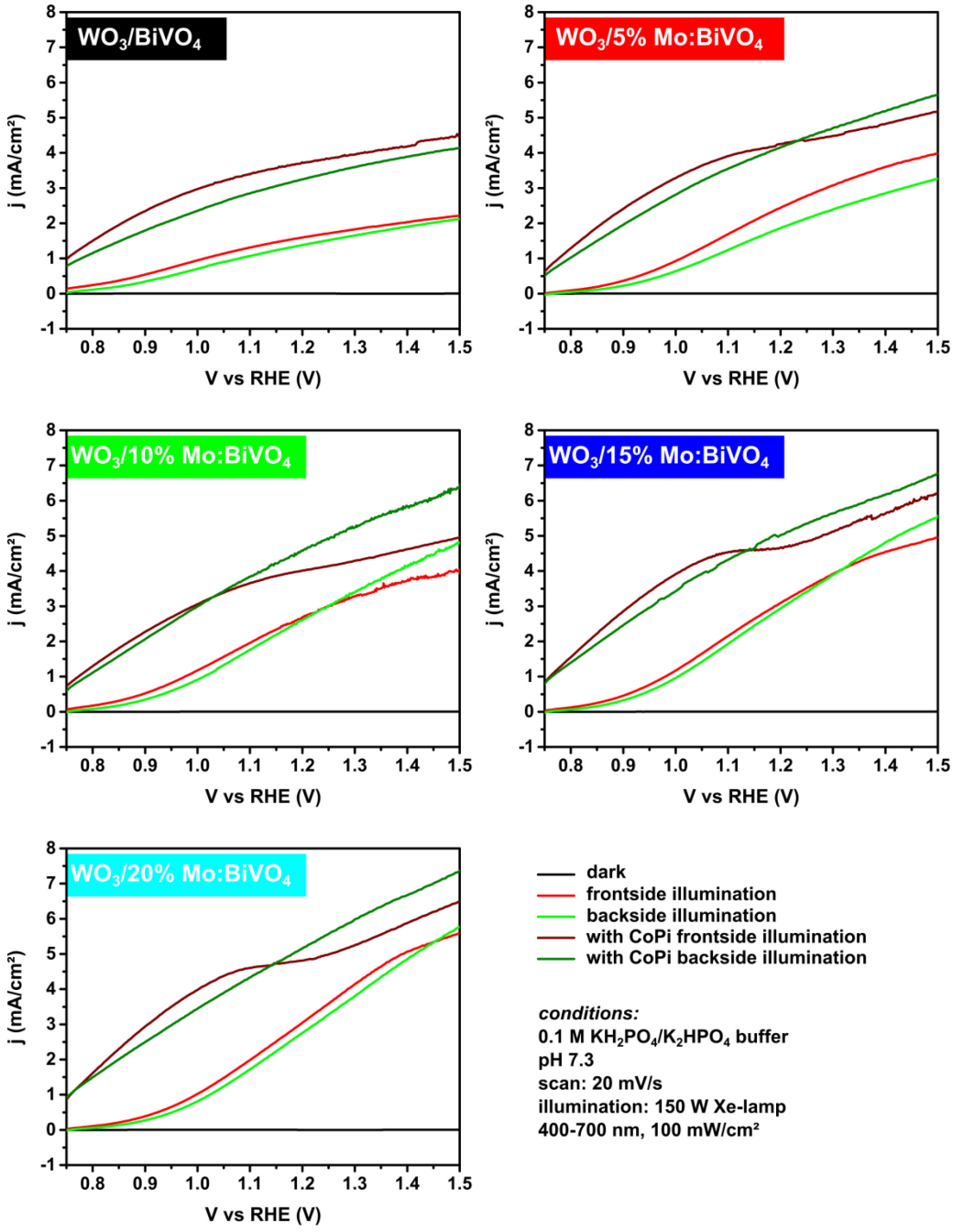

Figure 12-22. j-V curves of $WO_3/BiVO_4$ and WO_3/Mo:$BiVO_4$ heterojunction photoanodes with and without CoPi deposited in frontside and backside illumination.

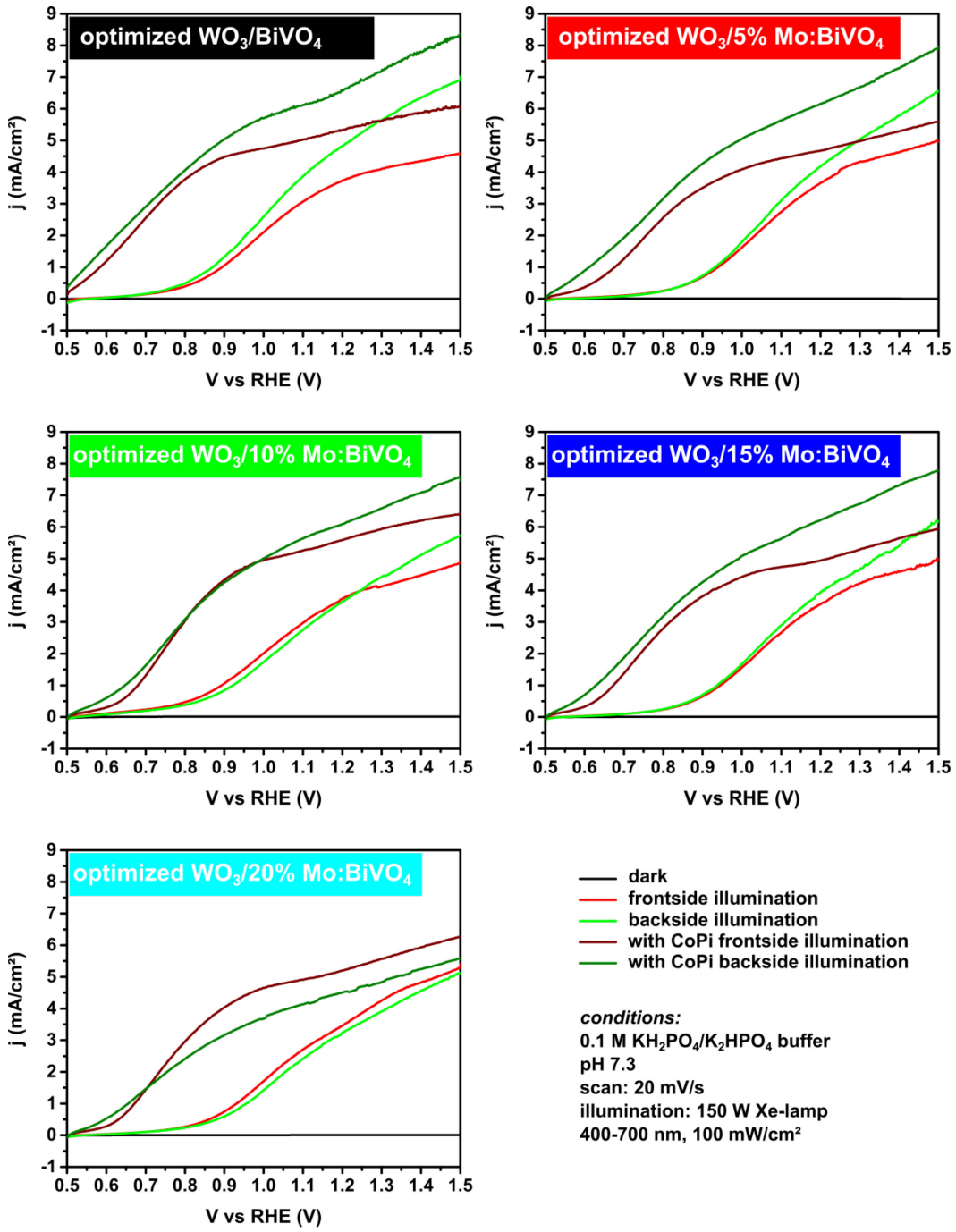

Figure 12-23. j-V curves of optimized $WO_3/BiVO_4$ and WO_3/Mo:$BiVO_4$ heterojunction photoanodes with and without CoPi deposited in frontside and backside illumination.

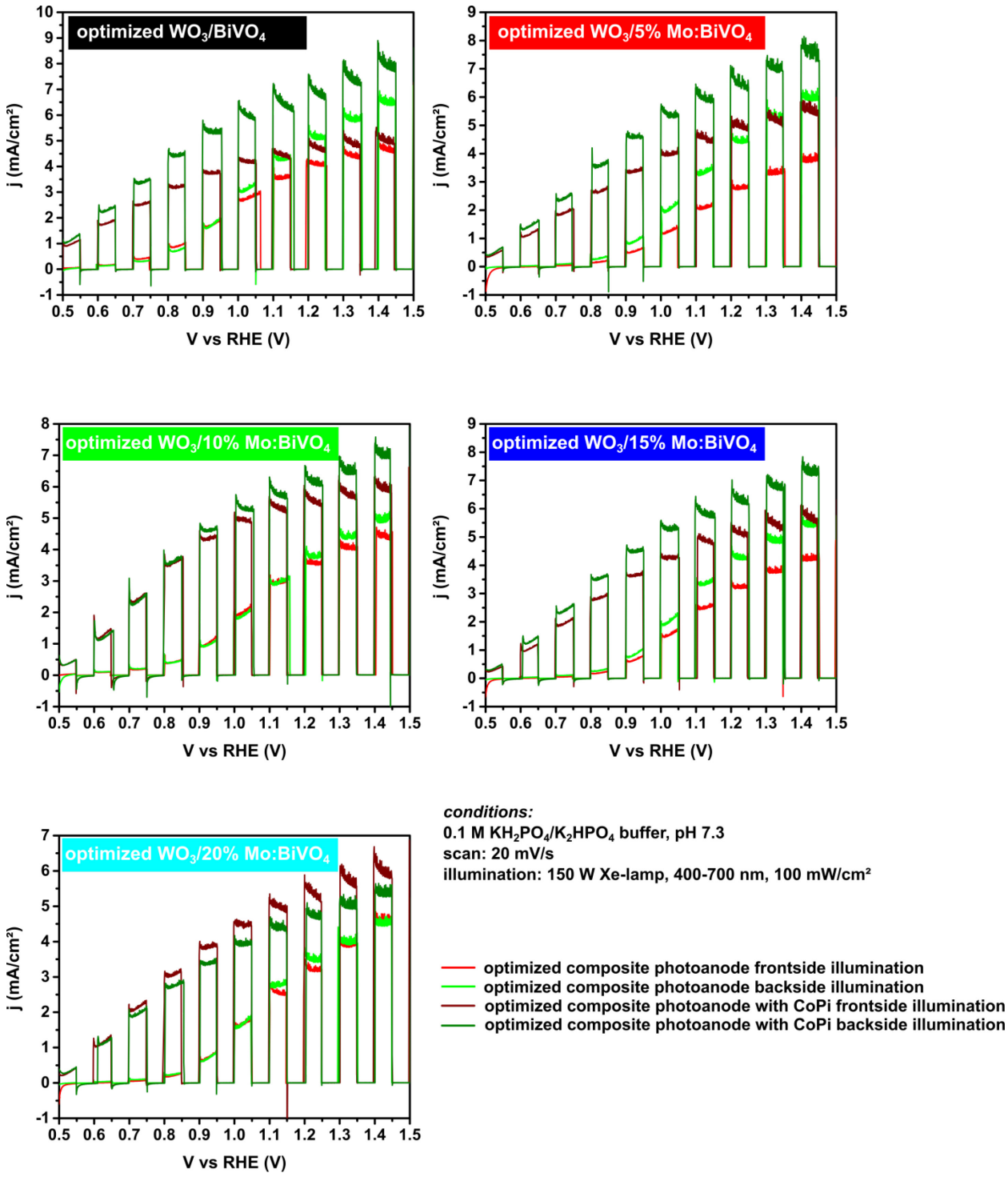

Figure 12-24. j-V curves of optimized $WO_3/BiVO_4$ and WO_3/Mo:$BiVO_4$ heterojunction photoanodes with and without CoPi deposited in chopped frontside and backside illumination.

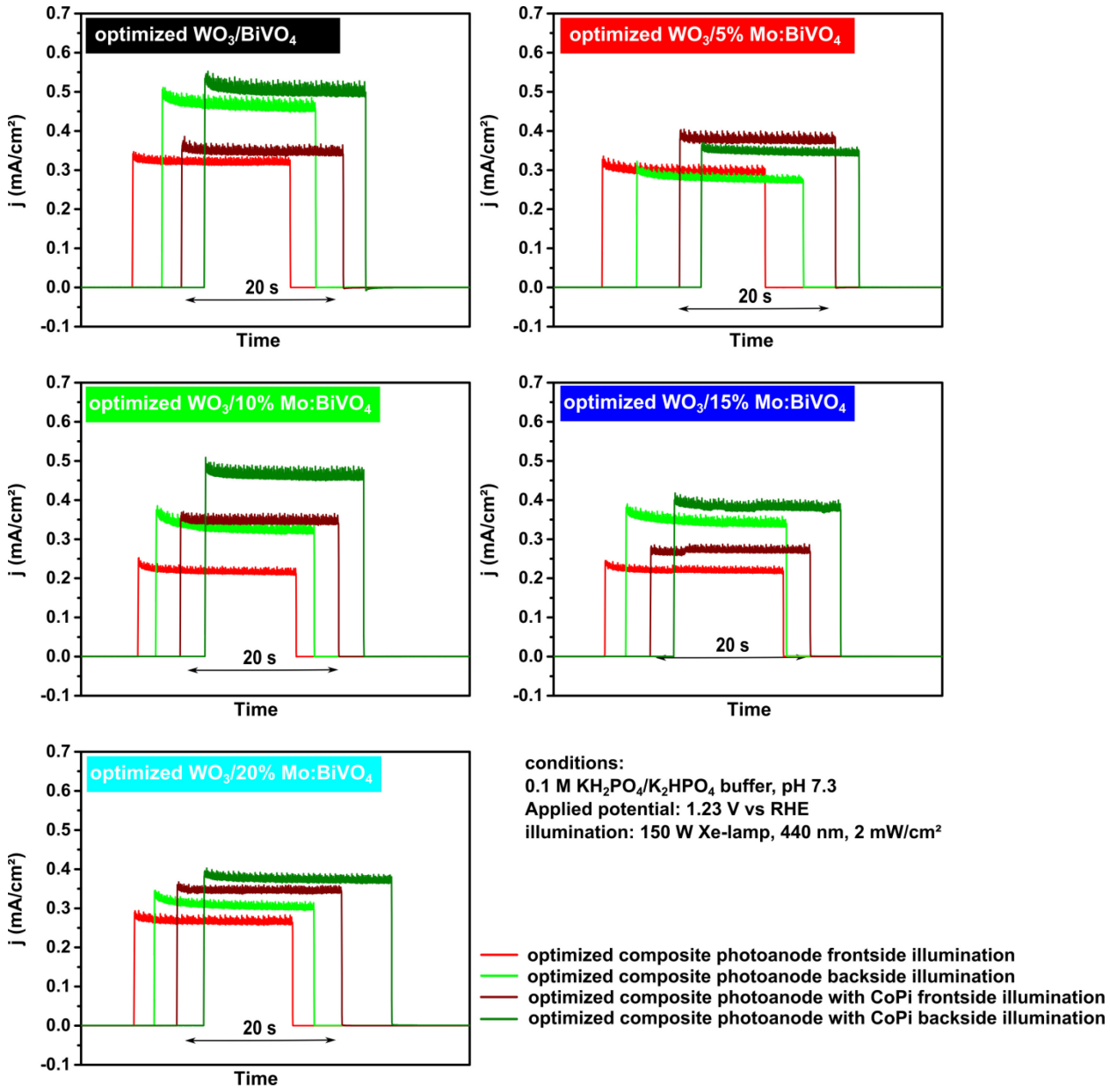

Figure 12-25. Photocurrent transients of optimized $WO_3/BiVO_4$ and WO_3/Mo:$BiVO_4$ heterojunction photoanodes with and without CoPi deposited in frontside and backside illumination.

12.2. List of publications

M. Rohloff, B. Anke, S. Zhang, U. Gernert, C. Scheu, M. Lerch, A. Fischer; "Mo-doped $BiVO_4$ Thin Films – High Photocatalytic Activity Achieved by Tailored Structure and Morphology", **accepted**

B. Anke, M. Rohloff, M.G. Willinger, W. Hetaba, A. Fischer, M. Lerch; "Improved photoelectrochemical performance of bismuth vanadate by partial O/F-substitution", *Solid State Sci.* **2017**, 63, 1–8**. [*]**

Sevilay Cosgun, Martin Rohloff, Caren Göbel, Ulrich Gernert, Anna Fischer, Martin Lerch; "Synthesis and Crystal Structure of Rutile-type $ScTa_2O_5N$", Z. Anorg. Allg. Chem. **2014**, *640*, 2771–2775.

S. Cosgun, M. Rohloff, M. Lublow, T. Lunkenbein, A. Senyshyn, S. Müller, A. Bartelt, M. Behrens, A. Fischer, M. Lerch; „Strukturelle Defekte in ß-TaON", Z. Anorg. Allg. Chem. **2014**, 640, 2383.

S. Cosgun, M. Rohloff, A. Fischer, M. Lerch; „Synthese und Kristallstruktur von ScTa2O5N", Z. Anorg. Allg. Chem. **2014**, 640, 2348.

S. Cosgun, M. Rohloff, M. Lublow, T. Lunkenbein, A. Senyshyn, S. Müller, A. Bartelt, A. Fischer, M. Lerch; „Structural Defects in ß-TaON", Proc. 22nd Annual Conference of the German Crystallographic Society (DGK), Berlin, **2014**, 91. (ISBN 978-3-981-6508-2-2).

S. Cosgun, M. Rohloff, M. Lublow, A. Fischer, M. Lerch; „Synthesis and Crystal Structure of ScTa2O5N", Proc. 22nd Annual Conference of the German Crystallographic Society (DGK), Berlin, **2014**, 92. (ISBN 978-3-981-6508-2-2).

M. Rohloff, B. Anke, M. Lerch, A. Fischer; "Enhancement of photoelectrochemical performance by partial O/F substitution in Mo:$BiVO_4$ thin film electrodes", **in preparation**.

M. Rohloff, S. Zhang, C. Scheu, A. Fischer; "WO_3/Mo:$BiVO_4$ heterojunctions for PEC water splitting – Simple layered design competes with advanced nanostructures", **in preparation**.

M. Rohloff, A. Fischer, M. Radtke, K. Rademann; "Functionalized γ-iron oxide for multipurpose wastewater treatment", **in preparation.**

M. Rohloff, S. Cosgun, T. Lunkenbein, C. Massue, A. Senyshyn, M. Lerch, A. Fischer, M. Behrens; "Structural defects in β-TaON and their effect on the photocatalytic properties", **in preparation.**

[*] - shared first authorship

13. References

[1] R. K. Pachauri, L. Mayer (Eds.) *Climate change 2014. Synthesis report*, Intergovernmental Panel on Climate Change, Geneva, Switzerland, **2015**.

[2] C. D. Thomas, A. Cameron, R. E. Green, M. Bakkenes, L. J. Beaumont, Y. C. Collingham, B. F. N. Erasmus, M. F. de Siqueira, A. Grainger, L. Hannah et al., *Nature* **2004**, *427*, 145–148.

[3] WWF, ECOFYS, OMA, *The Energy Report. 100% Renewable Energy By 2050*.

[4] Scripps Institution of Oceanography, UC San Diego, "The Keeling Curve", can be found under https://scripps.ucsd.edu/programs/keelingcurve/, **2017**.

[5] REN21, *REN21. 2016. Renewables 2016 Global Status Report*, **2016**, Paris.

[6] N. S. Lewis, D. G. Nocera, *Proc. Natl. Acad. Sci. USA* **2006**, *103*, 15729–15735.

[7] U.S. Energy Information Administration, *International Energy Outlook 2016*, **2016**, Washington DC.

[8] Z. Yang, J. Zhang, M. C. W. Kintner-Meyer, X. Lu, D. Choi, J. P. Lemmon, J. Liu, *Chem. Rev.* **2011**, *111*, 3577–3613.

[9] G. L. Soloveichik, *Annu. Rev. Chem. Biomol. Eng.* **2011**, *2*, 503–527.

[10] B. Dunn, H. Kamath, J.-M. Tarascon, *Science* **2011**, *334*, 928–935.

[11] H. Chen, T. N. Cong, W. Yang, C. Tan, Y. Li, Y. Ding, *Prog. Nat. Sci.* **2009**, *19*, 291–312.

[12] M. Beaudin, H. Zareipour, A. Schellenberglabe, W. Rosehart, *Energy Sustain. Dev.* **2010**, *14*, 302–314.

[13] L. Schlapbach, A. Zuttel, *Nature* **2001**, *414*, 353–358.

[14] M. G. Walter, E. L. Warren, J. R. McKone, S. W. Boettcher, Q. Mi, E. A. Santori, N. S. Lewis, *Chem. Rev.* **2010**, *110*, 6446–6473.

[15] J. Xu, G. F. Froment, *AIChE J.* **1989**, *35*, 88–96.

[16] J. Yoshihara, C. T. Campbell, *J. Catal.* **1996**, *161*, 776–782.

[17] F. Fischer, H. Tropsch, *Ber. dtsch. Chem. Ges. A/B* **1926**, *59*, 830–831.

[18] G. Zini, P. Tartarini, *Solar hydrogen energy systems*. *Science and technology for the hydrogen economy*, Springer-Verlag Italia, Milan, **2012**.

[19] Y. Tachibana, L. Vayssieres, J. R. Durrant, *Nature Photon* **2012**, *6*, 511–518.

[20] K. Rajeshwar, R. D. McConnell, S. Licht, *Solar hydrogen generation*. *Toward a renewable energy future*, Springer, New York, NY, **2008**.

[21] E. W. Justi, *A Solar-hydrogen Energy System*, Springer Verlag, **2011**.

[22] F. F. Abdi, T. J. Savenije, M. M. May, B. Dam, R. van de Krol, *J. Phys. Chem. Lett.* **2013**, *4*, 2752–2757.

[23] J. K. Cooper, S. Gul, F. M. Toma, Le Chen, P.-A. Glans, J. Guo, J. W. Ager, J. Yano, I. D. Sharp, *Chem. Mater.* **2014**, *26*, 5365–5373.

[24] T. W. Kim, Y. Ping, G. A. Galli, K.-S. Choi, *Nat. Commun.* **2015**, *6*, 8769.

[25] S. P. Berglund, A. J. E. Rettie, S. Hoang, C. B. Mullins, *Phys. Chem. Chem. Phys.* **2012**, *14*, 7065–7075.

[26] F. F. Abdi, L. Han, A. H. M. Smets, M. Zeman, B. Dam, R. van de Krol, *Nat. Commun.* **2013**, *4*, 2195.

[27] K. Ding, B. Chen, Z. Fang, Y. Zhang, Z. Chen, *Phys. Chem. Chem. Phys.* **2014**, *16*, 13465–13476.

[28] H. S. Park, K. E. Kweon, H. Ye, E. Paek, G. S. Hwang, A. J. Bard, *J. Phys. Chem. C* **2011**, *115*, 17870–17879.

[29] R. Asahi, T. Morikawa, T. Ohwaki, K. Aoki, Y. Taga, *Science* **2001**, *293*, 269–271.

[30] L. Junqi, W. Defang, L. Hui, H. Zuoli, Z. Zhenfeng, *Appl. Surf. Sci.* **2011**, *257*, 5879–5884.

[31] W.-J. Chun, A. Ishikawa, H. Fujisawa, T. Takata, J. N. Kondo, M. Hara, M. Kawai, Y. Matsumoto, K. Domen, *J. Phys. Chem. B* **2003**, *107*, 1798–1803.

[32] F. F. Abdi, N. Firet, R. van de Krol, *ChemCatChem* **2013**, *5*, 490–496.

[33] S. P. Berglund, D. W. Flaherty, N. T. Hahn, A. J. Bard, C. B. Mullins, *J. Phys. Chem. C* **2011**, *115*, 3794–3802.

[34] J. A. Seabold, K.-S. Choi, *J. Am. Chem. Soc.* **2012**, *134*, 2186–2192.

[35] Y. Pihosh, I. Turkevych, K. Mawatari, J. Uemura, Y. Kazoe, S. Kosar, K. Makita, T. Sugaya, T. Matsui, D. Fujita et al., *Sci. Rep.* **2015**, *5*, 11141.

[36] Y. Pihosh, I. Turkevych, K. Mawatari, T. Asai, T. Hisatomi, J. Uemura, M. Tosa, K. Shimamura, J. Kubota, K. Domen et al., *Small* **2014**, *10*, 3692–3699.

[37] S. J. Hong, S. Lee, J. S. Jang, J. S. Lee, *Energy Environ. Sci.* **2011**, *4*, 1781.

[38] K. Zhang, X.-J. Shi, J. K. Kim, J. H. Park, *Phys. Chem. Chem. Phys.* **2012**, *14*, 11119–11124.

[39] A. Fujishima, K. Honda, *Nature* **1972**, *238*, 37–38.

[40] A. J. Bard, L. R. Faulkner, *Electrochemical methods*. *Fundamentals and applications / Allen J. Bard, Larry R. Faulkner*, John Wiley, New York, Chichester, **2001**.

[41] R. Memming, *Semiconductor electrochemistry*, Wiley-VCH, Weinheim, Cambridge, **2000**.

[42] R. van de Krol, M. Grätzel, *Photoelectrochemical hydrogen production*, Springer, New York, London, **2012**.

[43] R. van de Krol, Y. Liang, J. Schoonman, *J. Mater. Chem.* **2008**, *18*, 2311.

[44] M. Weber, M. Dignam, *Int. J. Hydrogen Energy* **1986**, *11*, 225–232.

[45] M. Sterner, I. Stadler, *Energiespeicher - Bedarf, Technologien, Integration*, Springer Berlin, Berlin, **2014**.

[46] R. Marschall, *Adv. Funct. Mater.* **2014**, *24*, 2421–2440.

[47] R. D. L. Smith, B. Sporinova, R. D. Fagan, S. Trudel, C. P. Berlinguette, *Chem. Mater.* **2014**, *26*, 1654–1659.

[48] H. N. Nong, L. Gan, E. Willinger, D. Teschner, P. Strasser, *Chem. Sci.* **2014**, *5*, 2955.

[49] B. Mei, B. Seger, T. Pedersen, M. Malizia, O. Hansen, I. Chorkendorff, P. C. K. Vesborg, *J. Phys. Chem. Lett.* **2014**, *5*, 1948–1952.

[50] Y. Ma, A. Kafizas, S. R. Pendlebury, F. Le Formal, J. R. Durrant, *Adv. Funct. Mater.* **2016**, *26*, 4951–4960.

[51] M. W. Kanan, Y. Surendranath, D. G. Nocera, *Chem. Soc. Rev.* **2009**, *38*, 109–114.

[52] M. W. Kanan, D. G. Nocera, *Science* **2008**, *321*, 1072–1075.

[53] K. Sun, S. Shen, J. S. Cheung, X. Pang, N. Park, J. Zhou, Y. Hu, Z. Sun, S. Y. Noh, C. T. Riley et al., *Phys. Chem. Chem. Phys.* **2014**, *16*, 4612–4625.

[54] Y. Qiu, Le Xin, W. Li, *Langmuir* **2014**, *30*, 7893–7901.

[55] M. Gao, W. Sheng, Z. Zhuang, Q. Fang, S. Gu, J. Jiang, Y. Yan, *J. Am. Chem. Soc.* **2014**, *136*, 7077–7084.

[56] A. Kudo, K. Ueda, H. Kato, I. Mikami, *Catal. Lett.* **1998**, *53*, 229–230.

[57] C. Martinez Suarez, S. Hernández, N. Russo, *Appl. Catal., A.* **2015**, *504*, 158–170.

[58] B. Liu, Y. Fang, Z. Li, S. Xu, *J. Nanosci. Nanotechnol.* **2015**, *15*, 889–920.

[59] J. H. Kim, J. S. Lee, *Energy Environ. Focus.* **2014**, *3*, 339–353.

[60] Z.-F. Huang, L. Pan, J.-J. Zou, X. Zhang, L. Wang, *Nanoscale* **2014**, *6*, 14044–14063.

[61] Y. H. Xu, C. J. Liu, M. J. Chen, Y. Q. Liu, *IJNP* **2011**, *4*, 268.

[62] J. Granzin, D. Pohl, *Z. Kristallog.* **1984**, *169*, 289–294.

[63] M. M. Qurashi, W. H. Barnes, *Am. Mineral.* **1957**, *37*, 423–427.

[64] G. Dreyer, E. Tillmanns, *Neu. Jb. Mineral., Mh.* **1981**, 151–154.

[65] B. Anke, M. Rohloff, M. G. Willinger, W. Hetaba, A. Fischer, M. Lerch, *Solid State Sci.* **2017**, *63*, 1–8.

[66] J. D. Bierlein, A. W. Sleight, *Solid State Commun.* **1975**, *16*, 69–70.

[67] S. Tokunaga, H. Kato, A. Kudo, *Chem. Mater.* **2001**, *13*, 4624–4628.

[68] A. K. Bhattacharya, K. K. Mallick, A. Hartridge, *Mater. Lett.* **1997**, *30*, 7–13.

[69] A. R. Lim, S. H. Choh, M. S. Jang, *J. Phys.: Condens. Matter* **1989**, *1*, 1571–1576.

[70] P. Wood, F.P. Glasser, *Ceram. Int.* **2004**, *30*, 875–882.

[71] A. Kudo, K. Omori, H. Kato, *J. Am. Chem. Soc.* **1999**, *121*, 11459–11467.

[72] F. M. Toma, J. K. Cooper, V. Kunzelmann, M. T. McDowell, J. Yu, D. M. Larson, N. J. Borys, C. Abelyan, J. W. Beeman, K. M. Yu et al., *Nat. Commun.* **2016**, *7*, 12012.

[73] M. Zhou, J. Bao, Y. Xu, J. Zhang, J. Xie, M. Guan, C. Wang, L. Wen, Y. Lei, Y. Xie, *ACS nano* **2014**, *8*, 7088–7098.

[74] A. J. E. Rettie, H. C. Lee, L. G. Marshall, J.-F. Lin, C. Capan, J. Lindemuth, J. S. McCloy, J. Zhou, A. J. Bard, C. B. Mullins, *J. Am. Chem. Soc.* **2013**, *135*, 11389–11396.

[75] D. K. Zhong, S. Choi, D. R. Gamelin, *J. Am. Chem. Soc.* **2011**, *133*, 18370–18377.

[76] K. Tolod, S. Hernández, N. Russo, *Catalysts* **2017**, *7*, 13.

[77] K. Ding, B. Chen, Y. Li, Y. Zhang, Z. Chen, *J. Mater. Chem. A* **2014**, *2*, 8294.

[78] T. Liu, X. Zhou, M. Dupuis, C. Li, *Phys. Chem. Chem. Phys.* **2015**, *17*, 23503–23510.

[79] R. Munprom, P. A. Salvador, G. S. Rohrer, *J. Mater. Chem. A* **2015**, *3*, 2370–2377.

[80] V. Nair, C. L. Perkins, Q. Lin, M. Law, *Energy Environ. Sci.* **2016**, *9*, 1412–1429.

[81] J. Zhu, F. Fan, R. Chen, H. An, Z. Feng, C. Li, *Angew. Chem.* **2015**, *127*, 9239–9242.

[82] S. R. Taylor, *Geochim. Cosmochim. Acta* **1964**, *28*, 1273–1285.

[83] C. R. Brundle, C. A. Evans, S. Wilson, *Encyclopedia of materials characterization*. *Surfaces, interfaces, thin films*, **1992**.

[84] H. Czichos, T. Saito, L. R. Smith, *Springer Handbook Of Materials Measurement Methods*, Springer, New York, **2006**.

[85] H. S. Nalwa, *Deposition And Processing Of Thin Films*, Harcourt Academic, San Diego, Calif., London, **2002**.

[86] M. Ohring, *Materials science of thin films*, Academic Press, San Diego, CA, **2002**.

[87] L. Reimer, *Transmission electron microscopy*. *Physics of image formation and microanalysis*, Springer-Verlag, Berlin, New York, **1984**.

[88] I. M. Watt, *The principles and practice of electron microscopy*, Cambridge University Press, Cambridge, **1997**.

[89] D. B. Williams, C. B. Carter, *Transmission electron microscopy*. *A textbook for materials science*, Springer, New York, London, **2009**.

[90] S. Zhang, L. Li, A. Kumar, *Materials Characterization Techniques*, CRC Press, Hoboken, **2008**.

[91] C. J. Brinker, G. W. Scherer, *Sol-gel science*. *The physics and chemistry of sol-gel processing*, Academic Press, Boston, **1990**.

[92] C. J. Brinker, G. C. Frye, A. J. Hurd, C. S. Ashley, *Thin Solid Films* **1991**, *201*, 97–108.

[93] C. J. Brinker in *Chemical Solution Deposition of Functional Oxide Thin Films* (Eds.: T. Schneller, R. Waser, M. Kosec, D. Payne), Springer Vienna, Vienna, **2013**.

[94] D. Grosso, F. Cagnol, Soler-Illia, G. J. de A. A., E. L. Crepaldi, H. Amenitsch, A. Brunet-Bruneau, A. Bourgeois, C. Sanchez, *Adv. Funct. Mater.* **2004**, *14*, 309–322.

[95] F. Cagnol, D. Grosso, Soler-Illia, Galo J.de A. A., E. L. Crepaldi, F. Babonneau, H. Amenitsch, C.??m. Sanchez, *J. Mater. Chem.* **2003**, *13*, 61–66.

[96] R. Abe, M. Higashi, K. Domen, *J. Am. Chem. Soc.* **2010**, *132*, 11828–11829.

[97] Z. Chen, H. N. Dinh, E. Miller, *Photoelectrochemical Water Splitting*. *Standards, Experimental Methods, And Protocols*, Springer, New York, **2013**.

[98] L. M. Peter, J. Li, R. Peat, *J. Electroanal. Chem.* **1984**, *165*, 29–40.

[99] L. M. Peter, *J. Solid State Electrochem.* **2013**, *17*, 315–326.

[100] L. M. Peter, *Electroanalysis* **2015**, *27*, 864–871.

[101] D. K. Zhong, M. Cornuz, K. Sivula, M. Grätzel, D. R. Gamelin, *Energy Environ. Sci.* **2011**, *4*, 1759.

[102] Y. Ma, F. Le Formal, A. Kafizas, S. R. Pendlebury, J. R. Durrant, *J. Mater. Chem. A. Mater. Energy Sustain.* **2015**, *3*, 20649–20657.

[103] T. Brezesinski, D. F. Rohlfing, S. Sallard, M. Antonietti, B. M. Smarsly, *Small* **2006**, *2*, 1203–1211.

[104] *Abstracts of the Satellite Meeting on Powder Diffraction of the XV Congress of the IUCr*, **1990**.

[105] J. Rodriguez-Carvajal in *Abstracts of the Satellite Meeting on Powder Diffraction of the XV Congress of the IUCr*, **1990**.

[106] S. K. Pilli, T. E. Furtak, L. D. Brown, T. G. Deutsch, J. A. Turner, A. M. Herring, *Energy Environ. Sci.* **2011**, *4*, 5028.

[107] E. J. Joo, G. Park, J. S. Gwak, J. H. Seo, K. Y. Jang, K. H. Oh, K. M. Nam, *J. Nanomater.* **2016**, *2016*, 1–7.

[108] K. P. S. Parmar, H. J. Kang, A. Bist, P. Dua, J. S. Jang, J. S. Lee, *ChemSusChem* **2012**, *5*, 1926–1934.

[109] W. Yao, H. Iwai, J. Ye, *Dalton Trans.* **2008**, 1426–1430.

[110] J. L. Gole, J. D. Stout, C. Burda, Y. Lou, X. Chen, *J. Phys. Chem. B* **2004**, *108*, 1230–1240.

[111] F. Tian, C. Liu, *J. Phys. Chem. B* **2006**, *110*, 17866–17871.

[112] H. Park, W. Choi, *J. Phys. Chem. B* **2004**, *108*, 4086–4093.

[113] R. Shi, G. Huang, J. Lin, Y. Zhu, *J. Phys. Chem. C* **2009**, *113*, 19633–19638.

[114] H. Fu, S. Zhang, T. Xu, Y. Zhu, J. Chen, *Environ. Sci. Technol.* **2008**, *42*, 2085–2091.

[115] J.-Q. Li, Z.-Y. Guo, H. Liu, J. Du, Z.-F. Zhu, *J. Alloys Compd.* **2013**, *581*, 40–45.

[116] P. R. Slater, *J. Fluor. Chem.* **2002**, *117*, 43–45.

[117] A. W. Sleight, H.-y. Chen, A. Ferretti, D. E. Cox, *Mater. Res. Bull.* **1979**, *14*, 1571–1581.

[118] G. Tobias, D. Beltran-Porter, O. I. Lebedev, G. van Tendeloo, J. Rodriguez-Carvajal, A. Fuertes, *Inorg. Chem.* **2004**, *43*, 8010–8017.

[119] F. A. Kröger, H. J. Vink in *Solid State Physics*, Elsevier, **1956**.

[120] M. Cesari, G. Perego, A. Zazzetta, G. Manara, B. Notari, *J. Inorg. Nucl. Chem.* **1971**, *33*, 3595–3597.

[121] J. Tauc, *Mater. Res. Bull.* **1968**, *3*, 37–46.

[122] Y. Izumi, T. Itoi, S. Peng, K. Oka, Y. Shibata, *J. Phys. Chem. C* **2009**, *113*, 6706–6718.

[123] M. W. Stoltzfus, P. M. Woodward, R. Seshadri, J.-H. Klepeis, B. Bursten, *Inorg. Chem.* **2007**, *46*, 3839–3850.

[124] A. Walsh, Y. Yan, M. N. Huda, M. M. Al-Jassim, S.-H. Wei, *Chem. Mater.* **2009**, *21*, 547–551.

[125] A. Dolgonos, T. O. Mason, K. R. Poeppelmeier, *J. Solid State Chem.* **2016**, *240*, 43–48.

[126] D. K. Zhong, S. Choi, D. R. Gamelin, *J. Am. Chem. Soc.* **2011**, *133*, 18370–18377.

[127] S. Xiao, H. Chen, Z. Yang, X. Long, Z. Wang, Z. Zhu, Y. Qu, S. Yang, *J. Phys. Chem. C* **2015**, *119*, 23350–23357.

[128] M. Zhong, T. Hisatomi, Y. Kuang, J. Zhao, M. Liu, A. Iwase, Q. Jia, H. Nishiyama, T. Minegishi, M. Nakabayashi et al., *J. Am. Chem. Soc.* **2015**, *137*, 5053–5060.

[129] W. Luo, Z. Yang, Z. Li, J. Zhang, J. Liu, Z. Zhao, Z. Wang, S. Yan, T. Yu, Z. Zou, *Energy Environ. Sci.* **2011**, *4*, 4046.

[130] D. Wang, R. Li, J. Zhu, J. Shi, J. Han, X. Zong, C. Li, *J. Phys. Chem. C* **2012**, *116*, 5082–5089.

[131] W. J. Jo, J.-W. Jang, K.-j. Kong, H. J. Kang, J. Y. Kim, H. Jun, K. P. S. Parmar, J. S. Lee, *Angew. Chem. Int. Ed. Engl.* **2012**, *51*, 3147–3151.

[132] L. Wen, K. Ding, S. Huang, Y. Zhang, Y. Li, W. Chen, *New J. Chem.* **2017**, *41*, 1094–1102.

[133] M. Zhou, J. Bao, W. Bi, Y. Zeng, R. Zhu, M. Tao, Y. Xie, *ChemSusChem* **2012**, *5*, 1420–1425.

[134] Lange, *Science* **1996**, *273*, 903–909.

[135] T. W. Kim, K.-S. Choi, *Science* **2014**, *343*, 990–994.

[136] J. V. Mantese, A. L. Micheli, A. H. Hamdi, R. W. Vest, *MRS Bull.* **1989**, *14*, 48–53.

[137] D. K. Leung, C.-J. Chan, M. Ruhle, F. F. Lange, *J. Am. Ceram. Soc.* **1991**, *74*, 2786–2792.

[138] H.-q. Jiang, H. Endo, H. Natori, M. Nagai, K. Kobayashi, *J. Europ. Ceram. Soc.* **2008**, *28*, 2955–2962.

[139] J. Yu, A. Kudo, *Adv. Funct. Mater.* **2006**, *16*, 2163–2169.

[140] C. V. Thompson, *Annu. Rev. Mater. Sci.* **1990**, *20*, 245–268.

[141] F. F. Abdi, R. van de Krol, *J. Phys. Chem. C* **2012**, *116*, 9398–9404.

[142] T. H. Jeon, W. Choi, H. Park, *Phys. Chem. Chem. Phys.* **2011**, *13*, 21392–21401.

[143] M. Pourbaix, *Atlas of electrochemical equilibria in aqueous solutions*, Nat'L Assoc. Of Corrosion Engineers, Housten, Texas, USA, **1974**.

[144] R. Sarala, M. A. Islam, S. B. Rabin, D. M. Stanburg, *Inorg. Chem.* **1990**, *29*, 1133–1142.

[145] Y. Park, D. Kang, K.-S. Choi, *Phys. Chem. Chem. Phys.* **2014**, *16*, 1238–1246.

[146] D. Souri, Z. E. Tahan, *Appl. Phys. B* **2015**, *119*, 273–279.

[147] Le Chen, F. M. Toma, J. K. Cooper, A. Lyon, Y. Lin, I. D. Sharp, J. W. Ager, *ChemSusChem* **2015**, *8*, 1066–1071.

[148] J. H. Kim, Y. Jo, J. H. Kim, J. W. Jang, H. J. Kang, Y. H. Lee, D. S. Kim, Y. Jun, J. S. Lee, *ACS nano* **2015**, *9*, 11820–11829.

[149] A. J. Bard, A. B. Bocarsly, F. R. F. Fan, E. G. Walton, M. S. Wrighton, *J. Am. Chem. Soc.* **1980**, *102*, 3671–3677.

[150] Y. Ma, S. R. Pendlebury, A. Reynal, F. Le Formal, J. R. Durrant, *Chem. Sci.* **2014**, *5*, 2964.

[151] B. Pattengale, J. Ludwig, J. Huang, *J. Phys. Chem. C* **2016**, *120*, 1421–1427.

[152] F. E. Osterloh, *Chem. Soc. Rev.* **2013**, *42*, 2294–2320.

[153] F. E. Osterloh, *Top. Curr. Chem.* **2016**, *371*, 105–142.

[154] P. M. Borsenberger, H. Bässler, *J. Appl. Phys.* **1994**, *75*, 967.

[155] A. Hirao, H. Nishizawa, *Phys. Rev. B* **1996**, *54*, 4755–4761.

[156] I. Hwang, C. R. McNeill, N. C. Greenham, *J. Appl. Phys.* **2009**, *106*, 94506.

[157] A. D. Smigelskas, E. O. Kirkendall, *Trans. Met. Soc. Aime* **1947**, 130–134.

[158] C.A.C. Sequeira, L. Amaral, *Trans. Nonferrous Met. Soc. China* **2014**, *24*, 1–11.

[159] J. D. Seader, E. J. Henley, D. K. Roper, *Separation process principles*. *Chemical and biochemical operations*.

[160] J. L. Plawsky, *Transport phenomena fundamentals*.

[161] L. Badia-Bou, E. Mas-Marza, P. Rodenas, E. M. Barea, F. Fabregat-Santiago, S. Gimenez, E. Peris, J. Bisquert, *J. Phys. Chem. C* **2013**, *117*, 3826–3833.

[162] T. Nakagawa, N. S. Bjorge, R. W. Murray, *J. Am. Chem. Soc.* **2009**, *131*, 15578–15579.

[163] L. Trotochaud, J. K. Ranney, K. N. Williams, S. W. Boettcher, *J. Am. Chem. Soc.* **2012**, *134*, 17253–17261.

[164] X. Yu, T. Hua, X. Liu, Z. Yan, P. Xu, P. Du, *ACS Appl. Mater. Interfaces* **2014**, *6*, 15395–15402.

[165] T. H. Jeon, W. Choi, H. Park, *Phys. Chem. Chem. Phys.* **2011**, *13*, 21392–21401.

[166] D. K. Zhong, J. Sun, H. Inumaru, D. R. Gamelin, *J. Am. Chem. Soc.* **2009**, *131*, 6086–6087.

[167] D. K. Zhong, D. R. Gamelin, *J. Am. Chem. Soc.* **2010**, *132*, 4202–4207.

[168] B. Klahr, S. Gimenez, F. Fabregat-Santiago, J. Bisquert, T. W. Hamann, *J. Am. Chem. Soc.* **2012**, *134*, 16693–16700.

[169] M. Barroso, C. A. Mesa, S. R. Pendlebury, A. J. Cowan, T. Hisatomi, K. Sivula, M. Gratzel, D. R. Klug, J. R. Durrant, *Proc. Natl. Acad. Sci. USA* **2012**, *109*, 15640–15645.

[170] M. Barroso, A. J. Cowan, S. R. Pendlebury, M. Gratzel, D. R. Klug, J. R. Durrant, *J. Am. Chem. Soc.* **2011**, *133*, 14868–14871.

[171] L. Fu, H. Yu, C. Zhang, Z. Shao, B. Yi, *Electrochim. Acta* **2014**, *136*, 363–369.

[172] T. Wang, H.-T. Hung, Y.-R. Cheng, M.-C. Huang, Y.-K. Hsieh, C.-F. Wang, *RSC Adv.* **2016**, *6*, 28236–28247.

[173] C. Jiang, S. J. A. Moniz, M. Khraisheh, J. Tang, *Chemistry* **2014**, *20*, 12954–12961.

[174] Y. Wang, Y. Wang, R. Jiang, R. Xu, *Ind. Eng. Chem. Res.* **2012**, *51*, 9945–9951.

[175] E. M. P. Steinmiller, K.-S. Choi, *Proc. Natl. Acad. Sci. USA* **2009**, *106*, 20633–20636.

[176] D. A. Lutterman, Y. Surendranath, D. G. Nocera, *J. Am. Chem. Soc.* **2009**, *131*, 3838–3839.

[177] S. K. Pilli, T. G. Deutsch, T. E. Furtak, J. A. Turner, L. D. Brown, A. M. Herring, *Phys. Chem. Chem. Phys.* **2012**, *14*, 7032–7039.

[178] J. A. Seabold, K.-S. Choi, *Chem. Mater.* **2011**, *23*, 1105–1112.

[179] J. A. Bearden, *Rev. Mod. Phys.* **1967**, *39*, 78–124.

[180] R. S. Khnayzer, M. W. Mara, J. Huang, M. L. Shelby, L. X. Chen, F. N. Castellano, *ACS Catal.* **2012**, *2*, 2150–2160.

[181] K. J. McDonald, K.-S. Choi, *Chem. Mater.* **2011**, *23*, 1686–1693.

[182] S. Hoang, S. Guo, N. T. Hahn, A. J. Bard, C. B. Mullins, *Nano Lett.* **2012**, *12*, 26–32.

[183] A. Rockett, *The materials science of semiconductors*, Springer, New York, NY, **2008**.

[184] X. Shi, I. Herraiz-Cardona, L. Bertoluzzi, P. Lopez-Varo, J. Bisquert, J. H. Park, S. Gimenez, *Phys. Chem. Chem. Phys.* **2016**, *18*, 9255–9261.

[185] H. W. Jeong, T. H. Jeon, J. S. Jang, W. Choi, H. Park, *J. Phys. Chem. C* **2013**, *117*, 9104–9112.

[186] S. K. Pilli, R. Janarthanan, T. G. Deutsch, T. E. Furtak, L. D. Brown, J. A. Turner, A. M. Herring, *Phys. Chem. Chem. Phys.* **2013**, *15*, 14723–14728.

[187] P. M. Rao, L. Cai, C. Liu, I. S. Cho, C. H. Lee, J. M. Weisse, P. Yang, X. Zheng, *Nano Lett.* **2014**, *14*, 1099–1105.

[188] X. Shi, I. Y. Choi, K. Zhang, J. Kwon, D. Y. Kim, J. K. Lee, S. H. Oh, J. K. Kim, J. H. Park, *Nat. Commun.* **2014**, *5*, 4775.

[189] E. Salje, K. Viswanathan, *Acta Cryst. A.* **1975**, *31*, 356–359.

[190] P. M. Woodward, A. W. Sleight, T. Vogt, *J. Solid State Chem.* **1997**, *131*, 9–17.

[191] E. Salje, *Ferroelectrics* **1976**, *12*, 215–217.

[192] R. Diehl, G. Brandt, E. Saije, *Acta Crystallogr. B. Struct. Crystallogr. Cryst. Chem.* **1978**, *34*, 1105–1111.

[193] B. O. Loopstra, H. M. Rietveld, *Acta Crystallogr. B. Struct. Crystallogr. Cryst. Chem.* **1969**, *25*, 1420–1421.

[194] E. Salje, *Acta Crystallogr. B. Struct. Crystallogr. Cryst. Chem.* **1977**, *33*, 574–577.

[195] W. L. Kehl, R. G. Hay, D. Wahl, *J. Appl. Phys.* **1952**, *23*, 212.

[196] C. V. Ramana, C. M. Julien, *Chem. Phys. Lett.* **2006**, *428*, 114–118.

[197] C. V. Ramana, R. J. Smith, O. M. Hussain, C. M. Julien, *J. Vac. Sci. Technol. A* **2004**, *22*, 2453.

[198] C. V. Ramana, S. Utsunomiya, R. C. Ewing, C. M. Julien, U. Becker, *J. Phys. Chem. B* **2006**, *110*, 10430–10435.

[199] Y. Zhang, J. Yuan, J. Le, L. Song, X. Hu, *Sol. Energ. Mat. Sol. Cells* **2009**, *93*, 1338–1344.

[200] C. Santato, M. Odziemkowski, M. Ulmann, J. Augustynski, *J. Am. Chem. Soc.* **2001**, *123*, 10639–10649.

[201] M. Regragui, M. Addou, A. Outzourhit, E. El Idrissi, A. Kachouane, A. Bougrine, *Sol. Energ. Mat. Sol. Cells* **2003**, *77*, 341–350.

[202] G. Li, T. Varga, P. Yan, Z. Wang, C. Wang, S. A. Chambers, Y. Du, *Phys. Chem. Chem. Phys.* **2015**, *17*, 15119–15123.

[203] A. J. Caruana, M. D. Cropper, *Mater. Res. Express* **2014**, *1*, 46408.

[204] S.-H. Baeck, K.-S. Choi, T. F. Jaramillo, G. D. Stucky, E. W. McFarland, *Adv. Mater.* **2003**, *15*, 1269–1273.

[205] Di Chen, J. Ye, *Adv. Funct. Mater.* **2008**, *18*, 1922–1928.

[206] D. W. Hwang, J. Kim, T. J. Park, J. S. Lee, *Catal. Lett.* **2002**, *80*, 53–57.

[207] E. I. Ross-Medgaarden, I. E. Wachs, *J. Phys. Chem. C* **2007**, *111*, 15089–15099.

[208] J. C. Hill, K.-S. Choi, *J. Phys. Chem. C* **2012**, *116*, 7612–7620.

[209] A. Izgorodin, E. Izgorodina, D. R. MacFarlane, *Energy Environ. Sci.* **2012**, *5*, 9496.

[210] S. R. Biaggio, R. C. Rocha-Filho, J. R. Vilche, F. E. Varela, L. M. Gassa, *J. Braz. Chem. Soc.* **1994**, *5*, 123–126.

[211] Y. Hou, F. Zuo, A. P. Dagg, J. Liu, P. Feng, *Adv. Mater.* **2014**, *26*, 5043–5049.

[212] D.-D. Qin, C.-L. Tao, S. A. Friesen, T.-H. Wang, O. K. Varghese, N.-Z. Bao, Z.-Y. Yang, T. E. Mallouk, C. A. Grimes, *Chem. Commun.* **2012**, *48*, 729–731.

[213] J. Premkumar, *Chem. Mater.* **2004**, *16*, 3980–3981.

[214] G. W. Scherer, T. J. Garino, *J. Am. Ceram. Soc.* **1985**, *68*, 216–220.

[215] O. Guillon, L. Weiler, J. Rödel, *J. Am. Ceram. Soc.* **2007**, *90*, 1394–1400.

[216] D. J. Green, O. Guillon, J. Rödel, *J. Europ. Ceram. Soc.* **2008**, *28*, 1451–1466.

[217] T. J. Garino, H. K. Bowen, *J. Am. Ceram. Soc.* **1990**, *73*, 251–257.

[218] R. K. Bordia, R. Raj, *J. Am. Ceram. Soc.* **1985**, *68*, 287–292.

[219] F. M. Toma, J. K. Cooper, V. Kunzelmann, M. T. McDowell, J. Yu, D. M. Larson, N. J. Borys, C. Abelyan, J. W. Beeman, K. M. Yu et al., *Nat. Commun.* **2016**, *7*, 12012.

[220] T. W. Kim, K.-S. Choi, *J. Phys. Chem. Lett.* **2016**, *7*, 447–451.

[221] A. G. Hufnagel, K. Peters, A. Müller, C. Scheu, D. Fattakhova-Rohlfing, T. Bein, *Adv. Funct. Mater.* **2016**, *26*, 4425.

[222] K. Sun, F. H. Saadi, M. F. Lichterman, W. G. Hale, H.-P. Wang, X. Zhou, N. T. Plymale, S. T. Omelchenko, J.-H. He, K. M. Papadantonakis et al., *Proc. Natl. Acad. Sci. USA* **2015**, *112*, 3612–3617.

[223] R. Liu, Z. Zheng, J. Spurgeon, X. Yang, *Energy Environ. Sci.* **2014**, *7*, 2504.

[224] Q. Wang, S. Zhu, Y. Liang, Z. Cui, X. Yang, C. Liang, A. Inoue, *J. Nanopart. Res.* **2017**, *19*.

[225] H. Vrubel, T. Moehl, M. Gratzel, X. Hu, *Chem. Commun.* **2013**, *49*, 8985–8987.

[226] K. Ding, B. Chen, Y. Li, Y. Zhang, Z. Chen, *J. Mater. Chem. A* **2014**, *2*, 8294.

[227] R. Li, F. Zhang, D. Wang, J. Yang, M. Li, J. Zhu, X. Zhou, H. Han, C. Li, *Nat. Commun.* **2013**, *4*, 1432.

[228] T. Liu, X. Zhou, M. Dupuis, C. Li, *Phys. Chem. Chem. Phys.* **2015**, *17*, 23503–23510.

[229] R. Munprom, P. A. Salvador, G. S. Rohrer, *J. Mater. Chem. A* **2015**, *3*, 2370–2377.

[230] V. Nair, C. L. Perkins, Q. Lin, M. Law, *Energy Environ. Sci.* **2016**, *9*, 1412–1429.

[231] P. Wang, J. Y. Zheng, D. Zhang, Y. S. Kang, *New J. Chem.* **2015**, *39*, 9918–9925.

[232] J. Zhu, F. Fan, R. Chen, H. An, Z. Feng, C. Li, *Angew. Chem.* **2015**, *127*, 9239–9242.

[233] J. H. Kim, J.-W. Jang, Y. H. Jo, F. F. Abdi, Y. H. Lee, R. van de Krol, J. S. Lee, *Nat. Commun.* **2016**, *7*, 13380.

14. List of Figures

Figure 5-1. Atmospheric CO_2 content over a time period of 800,000 years. Ice-core data considered for estimation of CO_2 content before 1958. Data after 1958 by Scripps CO_2 measurements at Mauna Loa, Hawaii, USA.[4] 2

Figure 5-2. Schematic illustration of a PEC cell comprised of a semiconductor photoanode and a metal counter electrode. 6

Figure 5-3. Energy diagram for the thermodynamically unfavorable water splitting reaction with E_A as activation energy. 8

Figure 5-4. Split-up of energy levels of atoms in a periodic lattice forming energy bands. 10

Figure 5-5. Energy diagram of a) an intrinsic semiconductor b) an n-type doped semiconductor and c) a p-type doped semiconductor. 13

Figure 5-6. Band diagrams of an n-type semiconductor-liquid junction. a) before being brought into contact and b) after beeing brought into contact. 15

Figure 5-7. Band diagram of an n-type semiconductor in contact with an electrolyte. a) unbiased and b) application of a positive bias potential to the semiconductor. 16

Figure 5-8. Band diagramm of an n-type semiconductor in contact with an aqueous electrolyte. a) in the dark and b) upon illumination. 17

Figure 5-9. Phase transitions of $BiVO_4$ according to Tokunaga et al.[67] 21

Figure 5-10. Unit cell and coordination polyhedra of monoclinic scheelite-type $BiVO_4$. Bi colored green, V colored blue, O colored red. V-O_4-tetrahedra colored blue, Bi-O_8-polyhedra colored yellow. 22

Figure 5-11. Energy diagram of monoclinic scheelite-type $BiVO_4$ according to Cooper et al.[23] 23

Figure 5-12. Evaporation-induced processes during dip coating according to Brinker et al.[92] 28

Figure 5-13. a) Sketch of EPD-setup b) Homogeneous electric field between electrodes. . 30

Figure 5-14. a) triangular voltage used for CV measurements, b) typical cyclic voltammogram for a reversible electrochemical reaction, c) cyclic voltammogram for an irreversible (photo-)electrochemical reaction conducted in darkness (red curve) and under illumination (blue curve). 31

Figure 5-15. Modified Randles circuit used to model the electrode-electrolyte interface for Mott-Schottky analysis. 34
Figure 5-16. Example of a photocurrent transient. 36
Figure 6-1. Scheme of the tube furnace used for fluorination of $BiVO_4$ and Mo:$BiVO_4$ thin films. 43
Figure 6-2. Photographs of the home-build photoelectrochemical cell. a) demounted cell, b) top-view of mounted cell, c) cell equipped with wired electrodes and installed light fiber of the light source in frontside illumination and d) cell under working conditions in frontside illumination mode. 47
Figure 6-3. Schematic illustration of frontside and backside illumination. 48
Figure 7-1. Sketch of fluorination apparatus. The inner corundum boat contains the sample to be fluorinated and the outer boat is filled with PVDF. 52
Figure 7-2. X-ray powder diffraction patterns of a) $BiVO_4$ and b) F:$BiVO_4$ with the results of the Rietveld refinements. Inset: Unit cell of F:$BiVO_4$ and polyhedral representation of the crystal structure. $Bi(O,F)_8$ polyhedra are drawn in yellow, $V(O,F)_4$ tetraheda are shown in blue. Reproduced from: Anke et al. Improved photoelectrochemical performance of bismuth vanadate by partial O/F-substitution. Solid State Sciences 2017, 63, 1-8. Copyright © 2017 Elsevier Masson SAS. All rights reserved. 53
Figure 7-3. Tauc plot for $BiVO_4$ and F:$BiVO_4$ based on UV/Vis diffuse reflectance spectroscopy. Reproduced from: Anke et al. Improved photoelectrochemical performance of bismuth vanadate by partial O/F-substitution. Solid State Sciences 2017, 63, 1-8. Copyright © 2017 Elsevier Masson SAS. All rights reserved. 58
Figure 7-4. TEM investigations of F:$BiVO_4$. a) bright field TEM overview image of F:$BiVO_4$ and b) high resolution TEM image with inset showing the corresponding FFT. Spots due to the (020) and (20-1) lattice planes of the [102] oriented particle are labelled. Reproduced from: Anke et al. Improved photoelectrochemical performance of bismuth vanadate by partial O/F-substitution. Solid State Sciences 2017, 63, 1-8. Copyright © 2017 Elsevier Masson SAS. All rights reserved. 59
Figure 7-5. High angle annular dark field image of F:$BiVO_4$ (left) with corresponding EDX maps of F (yellow), Bi (green) and V (red) (right from top to bottom). Reproduced from: Anke et al. Improved photoelectrochemical performance of bismuth vanadate by partial

O/F-substitution. Solid State Sciences 2017, 63, 1-8. Copyright © 2017 Elsevier Masson SAS. All rights reserved. 60
Figure 7-6. Illustration of synthesis steps for the preparation of electrodes out of the pre-synthesized $BiVO_4$ and F:$BiVO_4$ powders. 61
Figure 7-7. Illustration of electrode fabrication process: SEM top-view and cross-sectional images of a) as-prepared electrodes, b) calcined electrodes (450 °C, air), c) calcined electrodes with deposited CoPi co-catalyst layer and d) j-V-curves of as-prepared F:$BiVO_4$, calcined F:$BiVO_4$ and F:$BiVO_4$ with a deposited CoPi layer (0.1 M KPi buffer, pH 7.3, 20 mV/s, 150 W Xe-lamp, 400-700 nm, 100 mW/cm², backside illumination)..... 63
Figure 7-8. Illustration of electrode fabrication process: SEM top-view and cross-sectional images of a) as-prepared electrodes, b) calcined electrodes (550 °C, air), c) calcined electrodes with deposited CoPi co-catalyst layer and d) j-V-curves of as-prepared F:$BiVO_4$, calcined F:$BiVO_4$ and F:$BiVO_4$ with a deposited CoPi layer (0.1 M KPi buffer, pH 7.3, 20 mV/s, 150 W Xe-lamp, 400-700 nm, 100 mW/cm², backside illumination)..... 64
Figure 7-9. j-V curves of $BiVO_4$ and F:$BiVO_4$ photoanodes a) calcined at 450 °C, b) calcined at 550 °C and corresponding ABPE curves for $BiVO_4$ and F:$BiVO_4$ photoanodes c) calcined at 450 °C and d) calcined at 550 °C. 66
Figure 7-10. Photocurrent transients for $BiVO_4$ and F:$BiVO_4$ photoanodes calcined at 450 °C and 550 °C without CoPi and with CoPi deposited..... 68
Figure 7-11. Mott-Schottky-Plots for $BiVO_4$ and F:$BiVO_4$ electrodes calcined at 550 °C. Linear parts of the Mott-Schottky-plots are linearly extrapolated..... 72
Figure 7-12. Comparison of $BiVO_4$ and F:$BiVO_4$. a) materials properties and b) kinetics of the electrodes' surfaces and obtained photocurrent densities (illumination: 400-700 nm, 100 mW/cm²) regarding water oxidation..... 74
Figure 8-1. Synthesis scheme: a) precursor solution, b) as-deposited amorphous thin film and c) calcined, crystalline $BiVO_4$ thin film..... 77
Figure 8-2. Synthesis steps followed by TEM for a $BiVO_4$ thin film: a) as-deposited amorphous thin film and b) crystalline $BiVO_4$ thin film with FFT pattern of the HR-TEM image..... 80

Figure 8-3. GI-XRD and P-XRD pattern of $BiVO_4$ thin films on Si substrate (left) and $BiVO_4$ powder samples (right), reference pattern of monoclinic scheelite $BiVO_4$ (PDF 01-083-1698) included in both figures. 81
Figure 8-4. a) UV/Vis spectrum of $BiVO_4$ thin film on FTO substrate and b) Kr physisorption isotherm of $BiVO_4$ thin films, inset: corresponding BET plot. 82
Figure 8-5. a-c) SEM top-view images of $BiVO_4$ thin film Si substrate, d and e) SEM cross-section image of $BiVO_4$ thin films at Si substrate. Characteristic thin film features are highlighted. 83
Figure 8-6. TEM/SAED investigations of thin films scraped off the substrate and transferred to a TEM grid: a) overview image, b) corresponding SAED pattern, c) high resolution image and d) corresponding FFT pattern. 85
Figure 8-7. a) j-V-curves of BiVO4 thin films with and without a layer of CoPi water oxidation catalyst under continous illumination (inset: magnified view on j-V curves of pristine samples), b and c) j-V-curves of BiVO4 thin films without (b) and with (c) a layer of CoPi water oxidation catalyst under chopped illumination. 87
Figure 8-8. Results of PEC sulfite oxidation, a) j-V curves with and without CoPi water oxidation catalyst, b) photocurrent transients acquired in frontside and backside illumination mode. 88
Figure 8-9. UV/Vis spectra of synthesis solutions containing different amounts of Mo. ... 91
Figure 8-10. Overview of ICP-OES results for Mo:$BiVO_4$ thin films (left) and illustration of the relationship between Mo content in solution and in thin films (right). Mo-% is given in atomic ratios with respect to the used (synthesis solutions) or determined (thin films and powders) amount of Bi. 92
Figure 8-11. a) GI-XRD pattern of Mo:$BiVO_4$ thin films. Reflections marked with a star are measurement artefacts, b) magnified view on the (200) and (020) reflections (34.5 ° and 35.3 °) of the monoclinic scheelite structure. 93
Figure 8-12. a) X-ray diffraction pattern of Mo:$BiVO_4$ powder samples containing different amounts of Mo, b) magnified view on merging reflections at 33-37 ° and c) change of the a/b ratio and gamma-angle with increasing Mo content acc. to Rietveld refinements. 95
Figure 8-13. UV/Vis spectra of Mo:$BiVO_4$ thin films on FTO substrate. 97

Figure 8-14. Top view and cross section images of Mo:$BiVO_4$ with corresponding EDX spectra. The Mo-L peak overlaps with the Bi-M peak at 2.3 keV. 99
Figure 8-15. a) TEM/SAED investigations of one flake of a 5% Mo:$BiVO_4$ thin film (sample scraped-off the substrate and transferred to TEM grid), b) SEM/EBSD pattern of 5% Mo:$BiVO_4$ thin film with corresponding unit cells sketched in. 101
Figure 8-16. HR-STEM image of the interface between 10% Mo-doped BiVO4 and FTO substrate with corresponding FFT pattern, inset: overview of TEM lamella. Pt protection layer was deposited during the FIB-SEM lamella preparation. 102
Figure 8-17. STEM image of 10% Mo:$BiVO_4$ lamella and corresponding single element EDX maps. The EDX quantification was performed for the cation sites Bi, V, and Mo.. 103
Figure 8-18. j-V curves of pristine and Mo-doped $BiVO_4$ obtained in backside illumination, a) without water oxidation catalyst, b) with CoPi water oxidation catalyst deposited onto the $BiVO_4$ and Mo:$BiVO_4$ surface. 105
Figure 8-19. a) j-V curve in frontside and backside illumination and b) j-V curve in light on/off mode in frontside and backside illumination of a 10% Mo:$BiVO_4$ sample with and without CoPi deposited onto the surface. 108
Figure 8-20. Chronoamperometry in light on/off mode for pristine and Mo-doped $BiVO_4$ samples. 109
Figure 8-21. Results of Mott-Schottky-analysis: a) Mott-Schottky-Plot for all samples, b) magnified view on the Mo:$BiVO_4$ Mott-Schottky-Plots, c) Mott-Schottky-Plot of a 10% Mo:$BiVO_4$ sample measured at different frequencies. 114
Figure 8-22. a) Morphological features, b) Photoelectrochemical properties without CoPi surface functionalization, and c) Photoelectrochemical properties with CoPi surface functionalization of the $BiVO_4$ and Mo:$BiVO_4$ thin film photoanodes illustrated as a function of Mo content. 116
Figure 8-23. XRD (gracing incidence) patterns of domain-like and worm-like $BiVO_4$ thin films on FTO together with reference reflections acc. to PDF 01-083-1698 (monoclinic scheelite phase). 118
Figure 8-24. UV/Vis spectra of worm-like $BiVO_4$ and Mo:$BiVO_4$ thin films on FTO. a) comparison of a 5% Mo:$BiVO_4$ thin film with worm-like and domain-like morphology and b) comparison of worm-like $BiVO_4$ and Mo:$BiVO_4$ thin films. 119

Figure 8-25. SEM images comparing the morphology of domain-like 10% Mo:$BiVO_4$ thin films and worm-like 10% Mo:$BiVO_4$ thin films..... 120
Figure 8-26 SEM investigations of worm-like F127 templated $BiVO_4$ and Mo:$BiVO_4$ thin films on FTO calcined at 450 °C and EDX spectra. The Mo-L peak overlaps with the Bi-M peak at 2.3 keV. 123
Figure 8-27. TEM/SAED investigations of a worm-like $BiVO_4$ thin film. a) overview image, b) HR-TEM image with corresponding FFT (inset) and c) SAED pattern with indexed reflections acc. to $BiVO_4$ in momoclinic scheelite phase (PDF 01-083-1698).... 124
Figure 8-28. j-V-curves of worm-like $BiVO_4$ and Mo:$BiVO_4$ thin films on FTO substrate with and without CoPi deposited in frontside and backside illumination. 126
Figure 8-29. j-V curves of a) worm-like and domain-like $BiVO_4$ photoanodes and b) worm-like and domain-like 10% Mo:$BiVO_4$ photoanodes. 128
Figure 8-30. Photocurrent transients for a worm-like $BiVO_4$ (a) and a worm-like 5% Mi:$BiVO_4$ (b) photoanode with an without CoPi deposited. Measurements were performed using backside illumination..... 132
Figure 8-31. a) XRD patterns of 10% Mo:$BiVO_4$ powder samples calcined at different temperatures together with reference reflections acc. to PDF 01-083-1698 (monoclinic scheelite structure), b) magniefied view on the reflections at ~35°..... 136
Figure 8-32. SEM top view images of 10% Mo:$BiVO_4$ thin films on FTO substrate calcined at different temperatures..... 138
Figure 8-33. Results of TEM/SAED investigations of 10% Mo:$BiVO_4$ thin films on FTO substrate calcined at temperatures from 350 °C to 550 °C: overview images, HR-TEM images with corresponding FFT pattern given as inset and SAED patterns are shown. ... 141
Figure 8-34. Results of STEM/EDX mapping of lamella cut out of a 10% Mo:$BiVO_4$ thin film calcined at 450 °C. a) overview images of the lamella before and after irradiation of the electron beam and b) EDX mapping with corresponding single element maps and c) EDX point analysis spectra of thin film material (green) and knob material (red). 142
Figure 8-35. j-V curves and corresponding ABPE curves of 10% Mo:$BiVO_4$ thin films calcined at different temperatures: a and c) without CoPi water oxidation catalyst and b) and d) with CoPi catalyst deposited onto the surface. 144

Figure 8-36. Photocurrent transients of 10% Mo:$BiVO_4$ photoanodes calcined at different temperatures. Transients were acquired at an applied potential of 1.23 V vs RHE using backside illumination of blue light (440 nm, 2 mW/cm²). 148
Figure 8-37. Comparison of 10% Mo:$BiVO_4$ samples calcined at different temperatures. a) morphology features and b) kinetics at the electrodes' surfaces and PEC performance (illumination: 400-700 nm, 100 mW/cm²) regarding water oxidation. 151
Figure 8-38. Schematic illustration of a water oxidation cycle at a CoPi-modified semiconductor photoanode on an FTO substrate: a) as deposited, b) partially oxidized and c) fully oxidized. Mecahnism adapted from Jeon et al.[164] 154
Figure 8-39. Band diagram illustrating the band positions of $BiVO_4$ and the redox potential of Co^{2+}/Co^{3+}. 155
Figure 8-40. j-V curves of CoPi-modified 10% Mo:$BiVO_4$ photoanodes obtained in a) frontside illumination and b) backside illumination. Electrodeposition (ED) method was applied. j-V curves of all samples in the dark are not shown. 158
Figure 8-41. j-V curves of 10% Mo:$BiVO_4$ without CoPi and with electrodeposited CoPi (15 mC). 159
Figure 8-42. Photocurrent transients of 10% Mo:$BiVO_4$ photoanodes with electrodeposited CoPi. a) Q_{trans} = 5 mC, b) Q_{trans} = 15 mC and c) reference sample without CoPi. 161
Figure 8-43. SEM/EDX investigations of electrodeposited CoPi (15 mC) at a 10% Mo:$BiVO_4$ photoanode. a) lower magnification image showing unmodified areas and areas with concentrated CoPi depositions, b) higher magnification image highlighting area-like and dot-like CoPi depositions and c) EDX spectrum of CoPi-modified 10% Mo:$BiVO_4$ photoanode. Al-peak within EDX spectrum belongs to the sample holder. Theoretical position of Co-K peak is given as Co*. 164
Figure 8-44. j-V-curves of 10% Mo:$BiVO_4$ photoanodes modified with CoPi deposited by *frontside* PD and *backside* PD. j-V curves of all samples in the dark are not shown. 166
Figure 8-45. j-V curves of unmodified 10% Mo:$BiVO_4$ reference sample and 10% Mo:$BiVO_4$ anodes modified by frontside PD (30 min) and backside PD (35 min). . 169
Figure 8-46. Photocurrent transients of a) 10% Mo:$BiVO_4$ modified by frontside PD (30 min), b) 10% Mo:$BiVO_4$ modified by backside PD (35 min) and c) unmodified 10% Mo:$BiVO_4$ reference sample. 171

Figure 8-47. SEM/EDX investigations of photochemically deposited CoPi (*frontside* PD, 30 min) at a 10% Mo:$BiVO_4$ photoanode. a) lower magnification image showing nicely CoPi-covered areas and small areas without CoPi depositions, b) higher magnification image highlighting showing different CoPi morphologies deposited and c) EDX spectrum of CoPi-modified 10% Mo:$BiVO_4$ photoanode. Al peak belongs to the sample holder. .. 173
Figure 8-48. j-V curves of CoPi-modified 10% Mo:$BiVO_4$ photoanodes obtained in a) frontside illumination and b) backside illumination. Photo-assisted electrodeposition (PED) method was applied for CoPi deposition. j-V curves of all samples in the dark are not shown for clarity. 175
Figure 8-49. j-V curves of unmodified 10% Mo:$BiVO_4$ reference sample and 10% Mo:$BiVO_4$ anode modified by PED, Q_{trans} = 150 mC. 176
Figure 8-50. Photocurrent transients of a) 10% Mo:$BiVO_4$ modified by PED of CoPi, Q_{trans} = 150 mC and b) unmodified 10% Mo:$BiVO_4$ reference sample. 178
Figure 8-51. SEM/EDX investigations of a 10% Mo:$BiVO_4$ photoanode modified by CoPi according to the PED method, Q_{trans} = 150 mC. a) lower magnification image showing nicely CoPi-covered photoanode material, b) higher magnification revealing a roughened surface of the electrode material proofing CoPi deposition, c) EDX spectrum of CoPi-modified 10% Mo:$BiVO_4$ photoanode, d) image of an unmodified 10% Mo:$BiVO_4$ sample. 179
Figure 8-52 j-V curves of best-performing 10% Mo:$BiVO_4$ photoanodes, CoPi-modified by ED, PD and PED in a) frontside illumination and b) backside illumination along with the corresponding ABPE curves calculated from the j-V curves yielded in c) frontside illumination and d) backside illumination. 182
Figure 9-1. XRD pattern (gracing incidence) for pristine $BiVO_4$ thin films and fluorinated $BiVO_4$ thin films in line with the reference reflections acc. to PDF 01-083-1698. 185
Figure 9-2. UV/Vis spectrum of fluorinated and pristine $BiVO_4$ thin films, measurements carried out in transmission mode. 186
Figure 9-3. SEM top view and cross sectional images of $BiVO_4$ (left) and fluorinated $BiVO_4$ (right) thin films on FTO substrate and a calcination reference which was calcined in similar manner but leaving out the PVDF. Fluorination temperature: 370 °C, post-calcination temperature: 400 °C. 188

Figure 9-4. TEM investigations of fluorinated $BiVO_4$, a) overview image and corresponding SAED pattern, b) HR-TEM image with corresponding FFT pattern (inset) and c) EDX spectrum with a zoomed view on the fluorine peak. Sample was scraped-off the FTO substrate. 190
Figure 9-5. j-V curves of $BiVO_4$ and fluorinated $BiVO_4$ thin film photoanodes. a) j-V curves without CoPi deposited in constant illumination, b) j-V curves with CoPi deposited in constant illumination, c) j-V curves without CoPi deposited in chopped illumination and d) j-V curves with CoPi deposited in chopped illumination. 192
Figure 9-6. Photocurrent transients of $BiVO_4$ and F:$BiVO_4$ thin film photoanodes without (a) and with (b) a layer of CoPi deposited, obtained in frontside and backside illumination mode. 194
Figure 9-7. XRD pattern (gracing incidence) for a 10% Mo:$BiVO_4$ thin film and a F/10% Mo:$BiVO_4$ thin film in line with the reference reflections acc. to PDF 01-083-1698 for monoclinic scheelite structure. 198
Figure 9-8. UV/Vis spectrum of fluorinated and unmodified 10% Mo:$BiVO_4$ thin films, measurements carried out in transmission mode. 199
Figure 9-9. SEM top view and cross sectional images of 10% Mo:$BiVO_4$ (left) and F/10% Mo:$BiVO_4$ (right) thin films on FTO substrate. 200
Figure 9-10. TEM investigations of F/10% Mo:$BiVO_4$, a) overview image and corresponding SAED pattern, b) HR-TEM image with corresponding FFT pattern (inset) and c) EDX spectrum with a zoomed view on the fluorine peak. Sample was scraped-off the FTO substrate. 201
Figure 9-11. j-V curves of 10% Mo:$BiVO_4$ and F/10% Mo:$BiVO_4$ thin film photoanodes. a) j-V curves without CoPi deposited in constant illumination, b) j-V curves with CoPi deposited in constant illumination, c) j-V curves without CoPi deposited in chopped illumination and d) j-V curves with CoPi deposited in chopped illumination. 203
Figure 9-12. Photocurrent transients of 10% Mo:$BiVO_4$ and F/10% Mo:$BiVO_4$ thin film photoanodes without (a) and with (b) a layer of CoPi deposited, obtained in frontside and backside illumination mode. 205
Figure 10-1. a) Schematic illustration of different heterojunction types, b) staggered type heterojunction photoanode. 208

Figure 10-2. Illustration of WO_3 thin film synthesis a) WO_3 sol, b) as-prepared WO_3 thin film and c) WO_3 thin film after calcination. 212
Figure 10-3. a) GI-XRD of WO_3 thin film on FTO substrate and (reflection marked with a * belongs to the sample holder) b) powder XRD of WO_3 powder sample obtained by drying and calcination of the WO_3-sol used for dip coating, Reference pattern γ-WO_3 (JCPDS 71-2141). 213
Figure 10-4. a) UV/Vis spectrum of WO_3 thin film on FTO substrate and b) photograph of WO_3 thin film on FTO substrate next to bare FTO sample. 214
Figure 10-5. SEM/EDX investigations on WO_3 thin film deposited on FTO substrates. a+b) top view images, c) cross section image d) EDX spectrum (Sn peaks assigned to FTO substrate). 215
Figure 10-6. TEM/SAED investigations of a WO_3 thin film a) TEM overview image, b) HR-TEM image with corresponding FFT pattern and c) inverted SAED pattern with reflcetions assigned to monoclinic γ-WO_3 (JCPDS 71-2141). 216
Figure 10-7. a) j-V-curves of WO_3 thin films with and without CoPi deposited onto the surface, b) j-V-curves of WO_3 thin films with and without CoPi deposited onto the surface in light on/off mode and c) photocurrent transients of pristine and CoPi-decorated WO_3 photoanodes. 218
Figure 10-8. Mott-Schottky-Plots of a WO_3 thin film at frequencies of 500 Hz and 1 kHz. 220
Figure 10-9. Schematic potential energy diagramm of WO_3/$BiVO_4$ heterojunctions. 222
Figure 10-10. Gracing incidence XRD pattern of WO_3/10% Mo:$BiVO_4$ composite electrodes with reference patterns of monoclinc γ-WO_3 (JCPDS 71-2141) and monoclinic scheelite $BiVO_4$ (PDF 01-083-1698). 223
Figure 10-11. UV/Vis spectroscopy on WO_3/$BiVO_4$ and WO_3/Mo:$BiVO_4$ composite electrodes. a) Comparison of WO_3, 5% Mo:$BiVO_4$ and the junction WO_3/5% Mo:$BiVO_4$ on FTO substrates, b) results for different WO_3/$BiVO_4$ and WO_3/Mo:$BiVO_4$ junctions on FTO. 224
Figure 10-12. SEM top view images of WO_3/$BiVO_4$ and WO_3/Mo:$BiVO_4$ thin films on FTO substrate together with corresponding EDX spectra. The Mo-L peak overlaps with the Bi-M peak at 2.3 keV. 226

Figure 10-13. Schematic illustration of a thin film on a igid substrate. Coordinates are defined by x, y and z vectors. 228
Figure 10-14. SEM cross section images of a WO_3/10% Mo:$BiVO_4$ composite electrode with marked voids at the FTO/WO_3 and the WO_3/Mo:$BiVO_4$ interfaces. 229
Figure 10-15. a) HR-STEM investigations of a FIB lamella focusing on the WO_3/Mo:$BiVO_4$ interface. Corresponding FFT patterns are given for the WO_3 (blue), Mo:$BiVO_4$ (red) and the interface region (yellow) and b) STEM-EDX-Map of the WO_3/Mo:$BiVO_4$ composite electrode. 230
Figure 10-16. j-V-curves obtained for the WO_3/$BiVO_4$ and WO_3/Mo:$BiVO_4$ composite electrodes with and without CoPi deposited onto the surface in frontside and backside illumination. 233
Figure 10-17. UV/Vis spectrum of an optimized WO_3 thin film in comparison to a non-optimzed WO_3 thin film. 237
Figure 10-18. SEM investigations of optimized WO_3 thin films on FTO substrate: a and b) top view images, c) cross section image and d) EDX spectrum. 238
Figure 10-19. TEM/SAED investigations of optimized WO_3 thin films. a) Overview image, b) HR-TEM image with FFT illustrating crystallinity, c) SAED investigations of three different spots along one WO_3 flake. 240
Figure 10-20. Comparison of photoelectrochemical performance of WO_3 thin films before and after optimization. a) j-V curves obtained in frontside and backside illumination, b) j-V-curves in light on/off mode obtained in frontside and backside illumination and c) photocurrent transient measurements obtained in frontside and backside illumination. ... 242
Figure 10-21. a) Mott-Schottky-Plot of the optimized WO_3 thin film photoanodes at frequencies of 500 Hz and 1 kHz and b) comparison of Mott-Schottky-plots of optimized and non-optimized WO_3 thin film photoanodes obtained at a frequency of 1 kHz. 243
Figure 10-22. XRD pattern (gracing incidence) of optimized WO_3/$BiVO_4$ thin film on FTO substrate along with reference reflections acc. to JCPDS 71-2141 (γ-WO_3) and PDF 01-083-1698 ($BiVO_4$, monoclinic scheelite phase). 245
Figure 10-23. UV/Vis spectra of optimized composite electrodes. a) comparison of optimized and non-optimized WO_3/5% Mo:$BiVO_4$ composite electrodes along with single

layer spectra of WO_3 and 5% Mo:$BiVO_4$ and b) comparison of UV/Vis spectra of all optimized WO_3/$BiVO_4$ and WO_3/Mo:$BiVO_4$ composite electrodes. 246
Figure 10-24. SEM investigations (top view and cross section images) of the optimized WO_3/$BiVO_4$ and WO_3/Mo:$BiVO_4$ composite electrodes on FTO substrate. 248
Figure 10-25. TEM investigations of an optimized WO_3/$BiVO_4$ composite electrode. a) overview image, b) corresponding SAED pattern and c) HR-TEM image with corresponding FFT patterns. 250
Figure 10-26. j-V curves of optimized WO_3/$BiVO_4$ and WO_3/Mo:$BiVO_4$ composite electrodes in frontside and backside illumination with and without CoPi deposited onto the surface. 253
Figure 10-27. j-V curves and photocurrent transients of the WO_3/$BiVO_4$ and the WO_3/10% Mo:$BiVO_4$ composite electrodes. Measurements accomplished in frontside and backside illumination as well as with and without CoPi deposited. 255
Figure 10-28. ABPE curves of the WO_3/$BiVO_4$ and the WO_3/ Mo:$BiVO_4$ composite electrodes with CoPi deposited in frontside and backside illumination. Curves were calculated based on j-V curves. 256
Figure 10-29. Long-term stabiltiy test of an optimized CoPi-decorated WO_3/$BiVO_4$ photoanode using a 3-electrode configuration. 258
Figure 12-1. j-V curves of an F:$BiVO_4$ EPD electrode in frontside and backside illumination. 263
Figure 12-2. Mott-Schottky plots of $BiVO_4$ and F:$BiVO_4$ EPD electrodes calcined at 550 °C, electrochemical impedance spectroscopy was carried out at different frequencies. 264
Figure 12-3. Powder-XRD pattern of $BiVO_4$ and Mo:$BiVO_4$ powder samples, obtained out of the corresponding synthesis solutions. 265
Figure 12-4. Kr-physisorption isotherms and BET plots of $BiVO_4$ and Mo:$BiVO_4$ thin films. 269
Figure 12-5. SEM and EDX investigations of $BiVO_4$ and Mo:$BiVO_4$ thin films deposited on Si substrate. 270
Figure 12-6. TEM/SAED investigations of Mo:$BiVO_4$ thin films. Samples were scraped-off the substrate and transferred to a TEM grid. 271

Figure 12-7. j-v curves of $BiVO_4$ and Mo:$BiVO_4$ thin film photoanodes in frontside and backside illumination mode using continuous and chopped illumination. 272
Figure 12-8. Mott-Schottky plots of $BiVO_4$ and Mo:$BiVO_4$ thin film photoanodes, carried-out at different frequencies. 273
Figure 12-9. j-V curves of worm-like $BiVO_4$ and Mo:$BiVO_4$ thin film photoanodes with and without CoPi deposited in frontside and backside illumination. 274
Figure 12-10. Photocurrent transients of worm-like $BiVO_4$ and Mo:$BiVO_4$ thin film photoanodes with and without CoPi deposited in backside illumination mode. 275
Figure 12-11. j-V curves and ABPE curves for 10% Mo:$BiVO_4$ thin film photoanodes calcined at different temperatures with and without CoPi deposited in frontside and backside illumination. 276
Figure 12-12. j-V curves of single 10% Mo:$BiVO_4$ thin film photoanodes calcined at different temperatures with and without CoPi deposited in frontside and backside illumination. 277
Figure 12-13. Photocurrent transients of 10% Mo:$BiVO_4$ thin film photoanodes calcined at different temperatures with and without CoPi deposited in frontside and backside illumination. 279
Figure 12-14. j-V curves of 10% Mo:$BiVO_4$ thin film photoanodes with different amounts of electrodeposited CoPi in frontside and backside illumination. 282
Figure 12-15. j-V curves of 10% Mo:$BiVO_4$ thin film photoanodes with different amounts of photochemically deposited CoPi (*frontside PD*) in frontside and backside illumination. 283
Figure 12-16. j-V curves of 10% Mo:$BiVO_4$ thin film photoanodes with different amounts of photochemically deposited CoPi (*backside PD*) in frontside and backside illumination. 284
Figure 12-17. Figure 0 17. j-V curves of 10% Mo:$BiVO_4$ thin film photoanodes with different amounts of CoPi deposited by photo-assisted electrodeposition (PED) in frontside and backside illumination. 285
Figure 12-18. j-V curves of F:$BiVO_4$ thin film photoanodes fluorinated according to the conditions given in Table 12-7 with and without CoPi deposited in frontside and backside illumination. 287

Figure 12-19. j-V curves of a $BiVO_4$ thin film photoanode and a twice-calcined $BiVO_4$ thin film photoanode according to the heat treatment involved in the fluorination procedure. Results of samples with and without CoPi in frontside and backside illumination are shown. 288
Figure 12-20. SEM investigations of a twice-calcined $BiVO_4$ thin film photoanode according to the heat treatment involved in the fluorination procedure. 289
Figure 12-21. j-V curves of a 10% Mo:$BiVO_4$ thin film photoanode and a twice-calcined $BiVO_4$ thin film photoanode according to the heat treatment involved in the fluorination procedure. Results of samples with and without CoPi in frontside and backside illumination are shown. 290
Figure 12-22. j-V curves of WO_3/$BiVO_4$ and WO_3/Mo:$BiVO_4$ heterojunction photoanodes with and without CoPi deposited in frontside and backside illumination. 292
Figure 12-23. j-V curves of optimized WO_3/$BiVO_4$ and WO_3/Mo:$BiVO_4$ heterojunction photoanodes with and without CoPi deposited in frontside and backside illumination. ... 293
Figure 12-24. j-V curves of optimized WO_3/$BiVO_4$ and WO_3/Mo:$BiVO_4$ heterojunction photoanodes with and without CoPi deposited in chopped frontside and backside illumination. 294
Figure 12-25. Photocurrent transients of optimized WO_3/$BiVO_4$ and WO_3/Mo:$BiVO_4$ heterojunction photoanodes with and without CoPi deposited in frontside and backside illumination. 295

15. List of Tables

Table 6-1. Composition of the precursor solution used for the synthesis of X% Mo:$BiVO_4$ thin film photoanodes. 40
Table 7-1. Determined Bi/V-(O,F) bond lengths in $BiVO_4$ and F:$BiVO_4$. 54
Table 7-2. Refined structural parameters of $BiVO_4$ in comparison to F:$BiVO_4$. 54
Table 7-3. Structural parameters for $BiVO_4$ and F:$BiVO_4$. 56
Table 7-4. Particle sizes after thermal treatment for F:$BiVO_4$ and $BiVO_4$ photoanodes..... 62
Table 7-5. Summary of obtained photocurrents at 1.23 V vs RHE and ABPE maxima of $BiVO_4$ and F:$BiVO_4$ photoanodes calcined at 450 °C and 550 °C. 66
Table 7-6. Summary of results of the photocurrent transient analysis for $BiVO_4$ and F:$BiVO_4$ photoanodes calcined at 450 °C and 550 °C without CoPi and with CoPi deposited. 70
Table 8-1. Summary of analyzed thin film features. 100
Table 8-2. Summary of yielded photocurrents of the $BiVO_4$ and Mo:$BiVO_4$ photoanodes at an applied potential of 1.23 V vs RHE. 105
Table 8-3. Overview of literature reports on highly active $BiVO_4$-based photoanodes. ... 106
Table 8-4. Summary of photocurrent transient analysis for pristine and Mo-doped $BiVO_4$ samples. Transients acquired at 1.23 V vs RHE with 2 mW/cm² of 440 nm light in backside illumination. 111
Table 8-5. Summary of flatband potentials determined by Mott-Schottky analysis. 112
Table 8-6. Number of free charge carriers in $BiVO_4$ and Mo:$BiVO_4$ thin film photoanodes. Calculations are based on the Mott-Schottky equation, an applied potential of 1.23 V vs RHE, and the specific surface areas of the electrodes determined by Kr physisorption. .. 113
Table 8-7. Overview of particle and pore sizes and film thicknesses of worm-like $BiVO_4$ and Mo:$BiVO_4$ thin films on FTO substrate. 122
Table 8-8. Summary of yielded photocurrents at an applied potential of 1.23 V for worm-like $BiVO_4$ and Mo:$BiVO_4$ photoanodes with and without CoPi deposited in frontside and backside illumination. Corresponding photocurrents for domain-like $BiVO_4$ and Mo:$BiVO_4$ photoanodes given in brackets. 128

Table 8-9. Summary of photocurrent transient analysis for pristine and Mo-doped $BiVO_4$ samples. Transients acquired at 1.23 V vs RHE with 2 mW/cm² of 440 nm light in backside illumination. 133
Table 8-10. FWHM of the (004) reflections at 30.57 ° and crystallite sizes *L* determined using the Scherrer equation with K = 1 and λ = 0.154056 nm for 10% Mo:$BiVO_4$ powder samples calcined at different temperatures. 136
Table 8-11. Summary of analyzed morphological thin film features of 10% Mo:$BiVO_4$ thin films calcined at different temperatures. 139
Table 8-12. Summary of obtained photocurrents at 1.23 V vs RHE with and without CoPi for 10% Mo:$BiVO_4$ samples calcined at different temperatures togehter with ABPE maxima and ABPE maxima position with and without CoPi deposited. All values given for illumination from the backside. 146
Table 8-13. Summary of analyzed photocurrent transients of 10% Mo:$BiVO_4$ photoanodes calcined at different temperatures. Values given correspond to transients measured in backside illumination mode. 149
Table 8-14. Summary of photocurrents yielded at an applied potential of 1.23 V vs RHE are for CoPi-modified 10% Mo:$BiVO_4$ photoanodes. Electrodeposition (ED) method was applied. 158
Table 8-15. Summary of photocurrent transient analysis of a pristine 10% Mo:$BiVO_4$ photoanode and two 10% Mo:$BiVO_4$ photoanodes with electrodeposited CoPi, Q_{trans} = 5 mC and Q_{trans} = 15 mC. 163
Table 8-16. Summary of photocurrents yielded at an applied potential of 1.23 V vs RHE are for CoPi modified 10% Mo:$BiVO_4$ photoanodes. CoPi was deposited by *frontside* PD and *backside* PD. 167
Table 8-17. Summary of photocurrent transient analysis of an unmodified 10% Mo:$BiVO_4$ photoanode and two CoPi-modified 10% Mo:$BiVO_4$ photoanodes by frontside PD (30 min) and backside PD (35 min). 172
Table 8-18. Summary of photocurrents yielded at an applied potential of 1.23 V vs RHE are for CoPi modified 10% Mo:$BiVO_4$ photoanodes. Photo-assisted electrodeposition (PED) method was applied. 176

Table 8-19. Summary of photocurrent transient analysis of an unmodified 10% Mo:$BiVO_4$ photoanode and the Q_{trans} = 150 mC CoPi-modified 10% Mo:$BiVO_4$ photoanodes by usage of the PED method. 178
Table 9-1. Summary of fluorination reaction conditions in line with obtained photocurrents at an applied potential of 1.23 V vs RHE (0.1 M KPi buffer, pH = 7.3, light: 400-700 nm at 100 mW/cm²). For all fluorination reactions undoped $BiVO_4$ thin films were used. 184
Table 9-2. Summary of obtained photocurrents at 1.23 V vs RHE for $BiVO_4$ and F:$BiVO_4$ in frontside and backside illumination. 193
Table 9-3. Summary of photocurrent transient analysis of $BiVO_4$ and F:$BiVO_4$ thin film photoanodes with and without CoPi in frontside and backside illumination. 196
Table 9-4. Summary of obtained photocurrents at 1.23 V vs RHE for 10% Mo:$BiVO_4$ and F/10% Mo:$BiVO_4$ in frontside and backside illumination. 202
Table 9-5. Summary of photocurrent transient analysis of 10% Mo:$BiVO_4$ and F/10% Mo:$BiVO_4$ thin film photoanodes with and without CoPi in frontside and backside illumination. 206
Table 10-1. Phase transitions of WO_3. 212
Table 10-2. Summary of results of photocurrent transient analysis for CoPi modified WO_3 photoanodes. Transients were measured at an applied potential of 1.23 V vs RHE under illumination of blue light 440 nm at an intensity of 2 mW/cm²) 219
Table 10-3. Summary of analyzed average geometrical domain size and average inner domain material streak size for WO_3/$BiVO_4$, WO_3/Mo:$BiVO_4$ double layers on FTO in comparison with $BiVO_4$ and Mo:$BiVO_4$ monolayers on FTO. 227
Table 10-4. Summary of obtained photocurrents at an applied potential of 1.23 V vs RHE of the WO_3/$BiVO_4$ and WO_3/Mo:$BiVO_4$ composite electrodes with and without CoPi water oxidation catalyst deposited onto the surface in frontside and backside illumination. Values given in brackets are respective photocurrents for the $BiVO_4$ and Mo:$BiVO_4$ monolayer photoanodes. 232
Table 10-5. Overview of highest reported photocurrents for WO_3/(doped)$BiVO_4$/catalyst heterojunctions at neutral pH and under illumination of 100 mW/cm². 235
Table 10-6. Comparison of morphological thin film features of optimized WO_3 thin films and non-optimized WO_3 thin films. 239

Table 10-7. Summarizing comparison of yielded photocurrents at 1.23 V vs RHE of the optimized and non-optimized WO_3 thin films in frontside and backside illumination. 242
Table 10-8. Overview on analyzed morphology features of the $BiVO_4$ and Mo:$BiVO_4$ layers of the optimized and non-optimized composite electrodes. 249
Table 10-9. Summary of yielded photocurrents at 1.23 V vs RHE in frontside and backside illumination with and without a layer of CoPi for the optimized WO_3/$BiVO_4$ and WO_3/Mo:$BiVO_4$ composite electrodes. 252
Table 10-10. Summary of ABPE maxima for WO_3/$BiVO_4$ and WO_3/Mo:$BiVO_4$ composite electrode. 256
Table 12-1. Structural parameters for $BiVO_4$ and Mo:$BiVO_4$ powders obtained by Rietveld refinements. 266
Table 12-2. Structural parameters for $BiVO_4$ and Mo:$BiVO_4$ powders (continuation)..... 267
Table 12-3. Reasonable defect models for the substitution of V^{5+} by Mo^{6+} in $BiVO_4$ (formal defect equations, Kröger-Vink notation). 268
Table 12-4. Summary of obtained photocurrents and ABPE maxima for 10% Mo:$BiVO_4$ thin film photoanode obtained in *frontside illumination*. 278
Table 12-5. Summary of obtained photocurrents and ABPE maxima for 10% Mo:$BiVO_4$ thin film photoanode obtained in *backside illumination*. 278
Table 12-6. Summary of photocurrent transient analysis results for 10% Mo:$BiVO_4$ thin film photoanodes calcined at different temperatures with and without CoPi deposited in frontside and backside illumination. 280
Table 12-7. Summary of fluorination reaction conditions in line with obtained photocurrents at an applied potential of 1.23 V vs RHE (0.1 M KPi buffer, pH = 7.3, light: 400-700 nm at 100 mW/cm²). 286
Table 12-8. Data used to plot the energy diagramm of a WO_3/$BiVO_4$ and WO_3/Mo:$BiVO_4$ heterojunctions. 291

16. Acknowledgement

First of all, I would like to thank Prof. Dr. Anna Fischer for the kind supervision of my work during the last years, for giving me the possibility to work on this topic in a unconfined manner and for the confidence in me carrying out this work on my own in Berlin.

I would like to thank Prof. Dr. Arne Thomas for his kind support, for sharing his laboratory devices and for agreeing to be reviewer of my thesis.

Furthermore, I am grateful to Prof. Dr. Martin Lerch for the efficient work on solving problems in the field of solid state chemistry.

I am also grateful to the ZELMI at TU Berlin for providing access to their electon microscopes and for introducing me to the field of electron microscopy and its various applications. Especially Ulrich Gernert and Sören Selve are acknowledged for supervision and kind support in the field of SEM and TEM.

Additionally, I would like to thank:

My collegues from the Fischer group, especially the “residuals” in Berlin, Nina, Laura and Tomos and the Freiburg guys, especially Axel and Tobias.

The group of Prof. Dr. Lerch at TUB for creating a kind working atmosphere and especially Björn for various meetings and fruitful discussions.

My family for their unconditional support during the last years.

And last but not least, I would like to thank my wife and my children for being my biggest support throughout the whole PhD time and for giving a tangible meaning to research in the field of future energy.

17. Eidesstattliche Erklärung

Ich, Martin Rohloff, geboren am 11.08.1986 in Neubrandenburg, erkläre hiermit, dass ich diese Dissertation selbstständig ohne Hilfe Dritter und ohne Benutzung anderer als der angegebenen Quellen und Hilfsmittel verfasst habe. Alle den benutzten Quellen wörtlich oder sinngemäß entnommenen Stellen sind als solche einzeln kenntlich gemacht.

Diese Arbeit ist bislang keiner anderen Prüfungsbehörde vorgelegt worden und auch nicht veröffentlicht worden.

Ich bin mir bewusst, dass eine falsche Erklärung rechtliche Folgen haben wird.

_____

Berlin, Datum, Unterschrift